Cell Signaling Page 389

17 October 2008 | $10

Science

AAAS

Volume 322, Issue 5900

COVER

Detail from *The Last Automat III* by Max Ferguson. Sluggish operation of the reward circuitry in the brain may lead individuals to eat calorie-dense foods (such as pie) to try to compensate, placing them at risk for obesity. See page 449.

***Image:* The Last Automat III, *2003* (oil on panel); Max Ferguson/Bridgeman Art Library/Getty Images**

DEPARTMENTS

EDITORIAL

SPECIAL SECTION

Cell Signaling

INTRODUCTION

REVIEWS

For related online content, see page 339 or go to www.sciencemag.org/cellsignaling08/

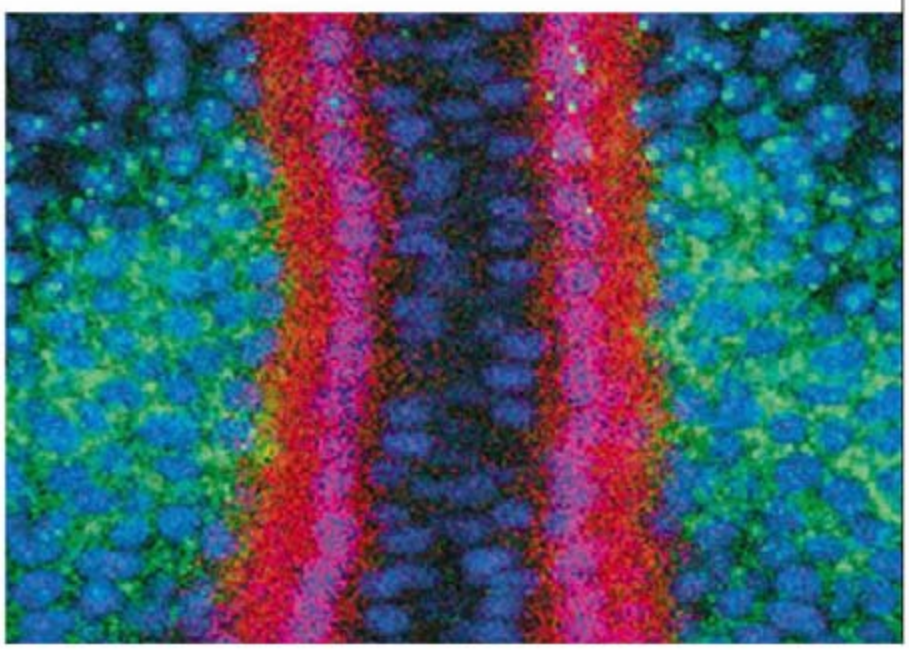

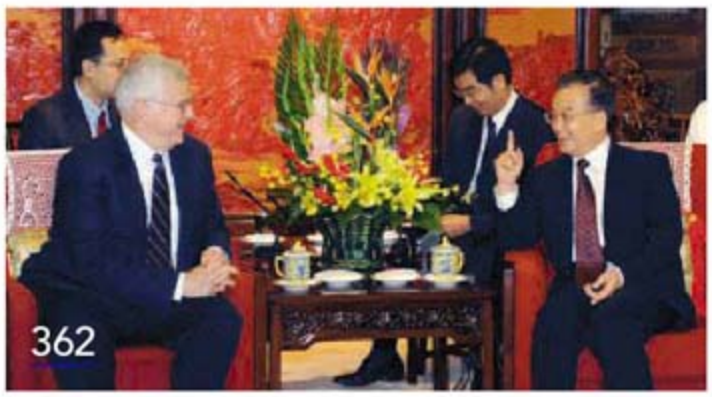

NEWS OF THE WEEK

NEWS FOCUS

CONTENTS continued >>

Science

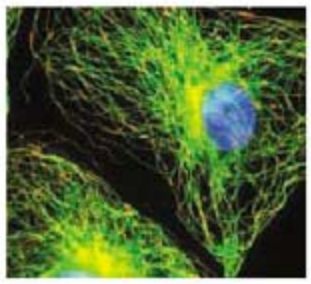

SCIENCE EXPRESS

www.sciencexpress.org

BIOCHEMISTRY

Structure and Molecular Mechanism of a Nucleobase-Cation-Symport-1 Family Transporter
S. Weyand et al.
The structure of a membrane transporter in an open state suggests that in- and out-facing cavities reciprocally open and close coordinated by two transmembrane segments.
10.1126/science.1164440

ASTRONOMY

The Fermi Gamma-Ray Space Telescope Discovers the Pulsar in the Young Galactic Supernova Remnant CTA 1
G. Kanbach et al.
The Fermi Space Telescope has detected a gamma-ray pulsar associated with a young supernova remnant, implying that such stars may be unidentified gamma-ray sources.
10.1126/science.1165572

CELL BIOLOGY

Detection of GTP-Tubulin Conformation in Vivo Reveals a Role for GTP Remnants in Microtubule Rescues
A. Dimitrov, M. Quesnoit, S. Moutel, I. Cantaloube, C. Poüs, F. Perez
GTP-bound tubulin is found at microtubule ends in living cells and also within microtubules, where it may promote repolymerization and avert microtubule collapse.
10.1126/science.1165401

ASTRONOMY

Observation of Pulsed γ-Rays Above 25 GeV from the Crab Pulsar with MAGIC
The MAGIC Collaboration
The MAGIC telescope has detected higher-energy, pulsed gamma rays from the Crab pulsar and a threshold suggesting that they are emitted from the outer magnetosphere.
10.1126/science.1164718

LETTERS

BOOKS *ET AL.*

POLICY FORUM

PERSPECTIVES

BREVIA

GEOCHEMISTRY

RESEARCH ARTICLE

GENETICS

REPORTS

PHYSICS

APPLIED PHYSICS

CHEMISTRY

CONTENTS continued >>

Science

REPORTS *CONTINUED...*

429

ADVANCING SCIENCE, SERVING SOCIETY

SCIENCE (ISSN 0036-8075) is published weekly on Friday, except the last week in December, by the American Association for the Advancement of Science, 1200 New York Avenue, NW, Washington, DC 20005. Periodicals Mail postage (publication No. 484460) paid at Washington, DC, and additional mailing offices. Domestic individual membership and subscription (51 issues): $144 ($74 allocated to subscription). Domestic institutional subscription (51 issues): $770; Foreign postage extra: Mexico, Caribbean (surface mail) $55; other countries (air assist delivery) $85. First class, airmail, student, and emeritus rates on request. Canadian rates with GST available upon request, GST #1254 88122. Publications Mail Agreement Number 1069624. SCIENCE is printed on 30 percent post-consumer recycled paper. **Printed in the U.S.A.**

Change of address: Allow 4 weeks, giving old and new addresses and 8-digit account number. **Postmaster:** Send change of address to AAAS, P.O. Box 96178, Washington, DC 20090–6178. **Single-copy sales:** $10.00 current issue, $15.00 back issue prepaid includes surface postage; bulk rates on request. The identification code for *Science* is 0036-8075. *Science* is indexed in the *Reader's Guide to Periodical Literature* and in several specialized indexes.

Printed on 30% post-consumer recycled paper.

CONTENTS continued >>

Separate and unequal.

SCIENCE**NOW**

www.sciencenow.org

HIGHLIGHTS FROM OUR DAILY NEWS COVERAGE

Don't Judge a Worm by Its Color
Scientists parse four species of earthworm from one, despite similarities in appearance.

Unconscious Brain Still Registers Pain
Some brain-injury patients may be hurting even if they can't show it.

The Come-Hither Voice
Pitch of a woman's voice rises during ovulation.

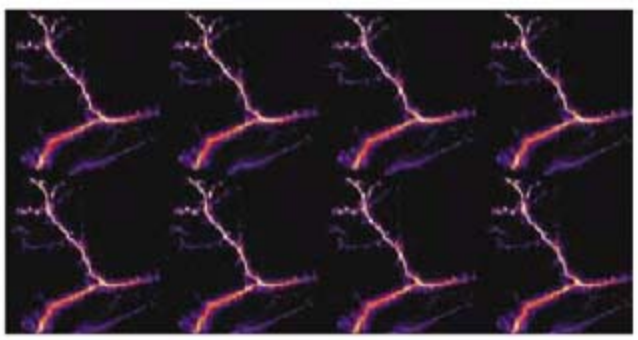

CREDITS: (*SCIENCE NOW*) BILL SYMONDSON; (*SCIENCE CAREERS*) PHOTODISC; (*SCIENCE SIGNALING*) SEVERINE CHAUMONT AND BALJIT S. KHAKH/UNIVERSITY OF CALIFORNIA, LOS ANGELES

VILIP1 interacts with P2X2 receptors in dendrites.

SCIENCE **SIGNALING**

www.sciencesignaling.org

THE SIGNAL TRANSDUCTION KNOWLEDGE ENVIRONMENT

RESEARCH ARTICLE: Regulation of P2X2 Receptors by the Neuronal Calcium Sensor VILIP1
S. Chaumont, V. Compan, E. Toulme, E. Richler, G. D. Housley, F. Rassendren, B. S. Khakh
Optics and electrophysiology reveal the dynamics of an ATP-gated ion channel signaling complex.

RESEARCH ARTICLE: BDNF Selectively Regulates $GABA_A$ Receptor Transcription by Activation of the JAK/STAT Pathway
I. V. Lund, Y. Hu, Y. H. Raol, R. S. Benham, R. Faris, S. J. Russek, A. R. Brooks-Kayal
Brain-derived neurotrophic factor regulates a GABA receptor subunit through the repressor ICER.

PERSPECTIVE: Acetylation of MKP-1 and the Control of Inflammation
H. Chi and R. A. Flavell
Toll-like receptor signaling is inhibited by acetylated MKP-1, a mitogen-activated protein kinase phosphatase.

PREVIEW
Get a sneak peek at articles coming up in the 21 October issue related to this week's *Science* special issue on cell signaling.
>> Cell Signaling section p. 389 and www.sciencemag.org/cellsignaling08/

Building a synthetic biology career.

SCIENCE **CAREERS**

www.sciencecareers.org/career_development

FREE CAREER RESOURCES FOR SCIENTISTS

Special Feature: Opportunities in Synthetic Biology
E. Pain
Synthetic biology may be in its infancy, but the field is growing rapidly and gaining support. >> Science *Podcast*

Getting Ready for Synthetic Biology
E. Pain
Synthetic biology offers new opportunities for scientists willing to challenge their ways of thinking and doing research.

A Multidisciplinary Approach to Life
E. Pain
A microbiologist, a mechanical engineer, and a chemist tell *Science* Careers how they ended up in synthetic biology.

***Science* Careers Podcast**
K. Travis
Hear three scientists talk about their career paths and the future of synthetic biology research.

SCIENCE**PODCAST**

www.sciencemag.org/multimedia/podcast

FREE WEEKLY SHOW

Download the 17 October *Science* Podcast to hear about a link between dopamine signaling and obesity, organic molecules from volcanic sparks, careers in synthetic biology, and more.

Separate individual or institutional subscriptions to these products may be required for full-text access.

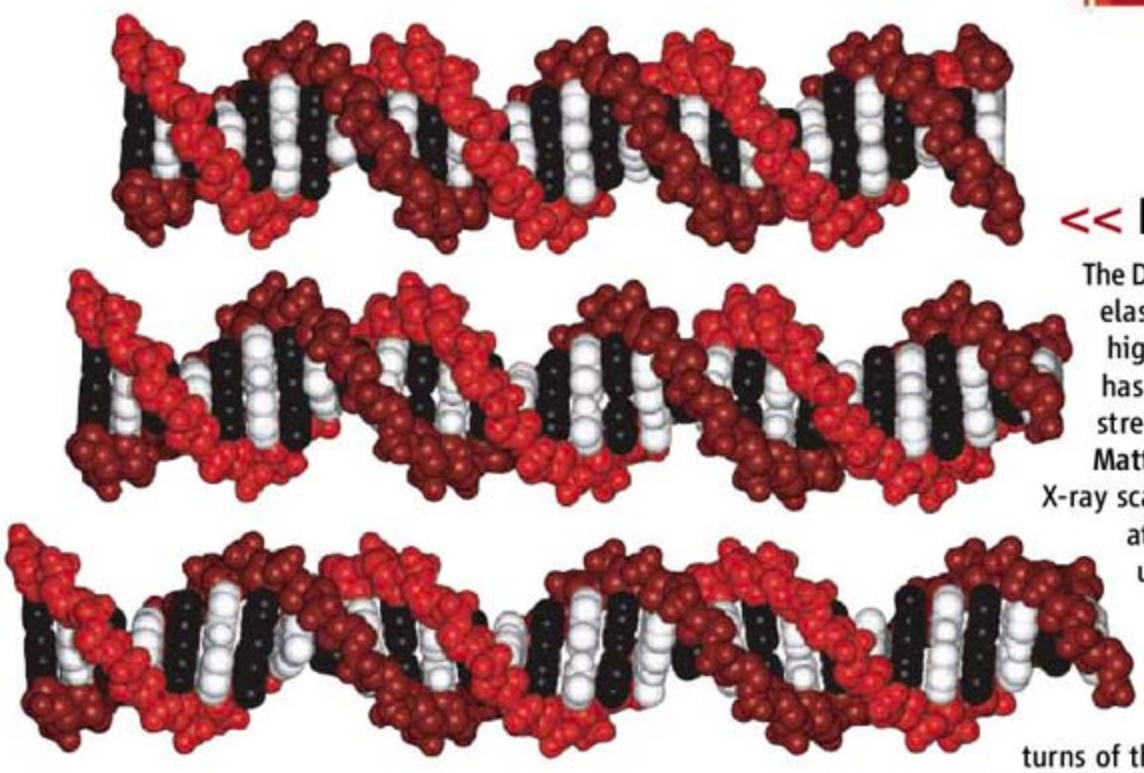

<< Flexing the Double Helix

The DNA duplex at equilibrium is generally viewed as an elastic rod. Recent experimental observations have highlighted that this is an oversimplification, but it has been difficult to resolve bending, twisting, and stretching fluctuations at a microscopic level. Now **Matthew-Fenn *et al.*** (p. 446) have used small-angle X-ray scattering interference between gold nanocrystals attached to the ends of DNA double helices to measure directly the distance distributions of DNA fragments short enough to limit bending. The results show that stretching fluctuations are much larger than expected for an ideal elastic rod and that stretching is correlated over at least two turns of the double helix. This correlated stretching could allow for allosteric communication along the DNA structure.

Riding the Spin-Wave

Much work is being undertaken that uses the spin property of electrons rather than, or as well as, its charge. Spin density waves are excitations of polarized electrons that propagate through magnetic systems. Determining the spin properties in a circuit, however, is a challenge. **Vlaminck and Bailleul** (p. 410; see the Perspective by **McMichael and Stiles**) demonstrate a long-proposed effect in which an injected current should result in the frequency-shift (or Doppler shift) of the propagating spin waves. Such a simple technique should prove invaluable in the development of spintronics.

Double Cosmic Rubble

About 70 small binary asteroids have been found in which two small bodies orbit each other. Many of these binary asteroids are weak objects composed of rubble held together by their weak gravity, and it has been suggested that some may have formed by the disruption of a single object. **Petit *et al.*** (p. 432) have now tracked one enigmatic binary in the Kuiper Belt, beyond Pluto, and show that its pairs are orbiting in an eccentric orbit more than 100,000 km apart. This great distance, 2000 times their radii, is difficult to create and maintain against disruption from the gravitation attraction of other objects. It is thus most likely that it formed from a collision, and its fragile existence could imply that such bodies would have been more common early in the solar system.

Fuel from Sorbitol

The chemical infrastructure for converting crude petroleum into fuel and functional compounds relies largely on breaking down and oxidizing long hydrocarbons. In contrast, a switch to carbohydrate biomass as the basic feedstock requires processing a set of very different building blocks that come excessively oxygenated. **Kunkes *et al.*** (p. 417, published online 18 September) present a two-stage strategy for converting abundant sugars such as glucose and sorbitol into fuels and commodity chemicals. In an initial reactor, a platinum-rhenium catalyst breaks down the aqueous sugar feed into alcohol and carbonyl compounds. The product can then be directed into a second reactor for catenation of these intermediates into chains, with an array of different catalysts available to select for either the highly branched structure of gasoline, or the longer-chain, more linear geometry used in Diesel and jet fuel mixtures.

Regulating Gene Regulation

Tissue-specific gene expression is established by sets of highly conserved transcription factors, common throughout mammals. However, the transcription factor binding sites themselves have changed dramatically during evolution. These changes could be the result of a variety of factors, including epigenetics, chromatin structure, underlying sequence changes, environment, and diet. To sort out the environmental versus genetic factors controlling gene expression, **Wilson *et al.*** (p. 434, published online 11 September; see the Perspective by **Coller and Kruglyak**) studied expression in the liver of mice that stably transmit a copy of human chromosome 21. This made it possible to study transcriptional regulation of complete homologous chromosomes of human and mouse sequences simultaneously in the same nuclei. In terms of protein-DNA binding, histone methylation, and transcription in vivo, DNA sequence was a more important determinant than the environment.

Imaging Internal Temperatures

Temperature is normally measured locally at the surface of a sample but, in many clinical situations, it would be useful to obtain temperature profiles inside the tissue, for example, during hyperthermic therapy. Such profiles can be obtained with contrast agents in conventional magnetic resonance imaging but drawbacks can arise from inhomogeneities in the magnetic fields as they pass through the body or from the technique's inability to work well in fatty tissue, such as the breast. **Galiana *et al.*** (p. 421) have developed a method that allows the temperature-dependent chemical shift of water to be measured relative to the temperature-independent chemical shift of lipids by using long-range intermolecular zero- and double-quantum coherences. The authors use their method to produce temperature profiles across the body of a living mouse.

CREDITS (TOP TO BOTTOM): MATTHEW-FENN ET AL.; GALIANA ET AL.

Continued on page 343

Continued from page 341

Ordered Solution

Block copolymers consisting of two chemically dissimilar covalently connected polymers will spontaneously phase separate into arrays of spheres or cylinders, depending on the concentration of the two blocks. With dissolution of one of the components, the materials can be used for templating semiconductor materials, for example, in the fabrication of memory chips. However, while the semiconductor industry is used to working with rectilinear patterns, the ordering of the spheres or cylinders tends to be hexagonal. **Tang *et al.*** (p. 429, published online 25 September) engineered two block copolymers to induce hydrogen bonding between the polystyrene blocks in each of them. When mixed, the polymers generated well-defined patterns with square symmetry.

Stochastic Changes

Cells that are genetically identical and in the same environment can display different phenotypes with a single cell switching stochastically between the phenotypes. A classic example is lactose metabolism in *Escherichia coli*—at intermediate inducer concentrations a fraction of cells in a population display an induced phenotype. **Choi *et al.*** (p. 442) examined the molecular basis of this switching by directly monitoring the expression of *lac* genes at a single molecule level. The tetrameric *lac* repressor, which binds to two operators on looped DNA, frequently dissociates from one operator to give basal level expression. Infrequently, there is complete dissociation from both operators to give large bursts of expression that trigger full induction. Thus, a stochastic molecular event acts to switch individual cells from an uninduced to an induced phenotype.

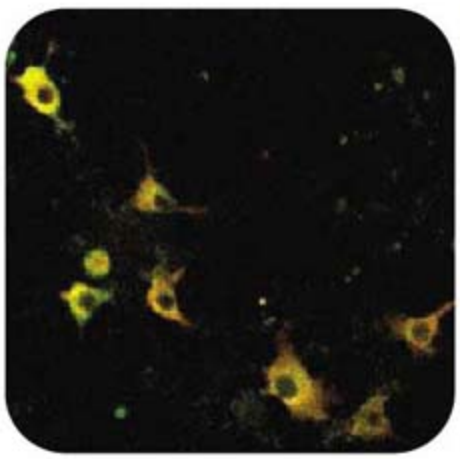

Mapping Out Redundancy

Living organisms often have compensatory signaling mechanisms that allow the loss of function of a single component to be tolerated, even in important regulatory pathways. This makes such pathways robust to potential challenges, but makes the job of unraveling and mapping the pathways more difficult. To work around such buffering or functional redundancy, **Bakal *et al.*** (p. 453) systematically tested more than 16,000 RNAi combinations in *Drosophila* tissue culture cells in order to identify regulators of *Drosophila* Jun NH_2-terminal Kinase (JNK). Further analysis with phosphoproteomic data and computational models of kinase specificity was used to establish where the components identified fit in a regulatory network. Similar approaches should help to unravel other critical targets for therapeutic modulation of cell function.

Genes and Weight Gain

What are the factors that increase an individual's risk of future weight gain? It has been hypothesized that obese individuals may have an underactive reward circuitry, which leads them to overeat in an effort to boost a sluggish dopamine reward system. Using brain imaging, **Stice *et al.*** (p. 449; cover) discovered a relationship between activation of the striatum and ingestion of a tasty calorific liquid compared with a neutral liquid that could differentiate between obese and non-obese individuals. This differential activation was accentuated in individuals bearing the A1 allele of the dopamine D2 receptor gene, which is associated with reduced dopamine transmission in the striatum. This relationship predicted an individual's weight gain when measured a year later.

Nematode Immune Defenses

Like all of us, the nematode worm, *Caenorhadbditis elegans*, is susceptible to illness and infection caused by bacteria. And, like all of us, worms mount an immune defense against infection. **Styer *et al.*** (p. 460, published online 18 September) now present data that suggest that the innate immune response of *C. elegans* requires expression of a G protein–coupled receptor, npr-1, in sensory neurons. The response also requires other signaling-related molecules, a cyclic GMP–gated ion channel and a soluble guanylate cyclase. The sensory neurons act to control the immune response throughout the worm. Thus, these neurons seem to control innate immunity in *C. elegans* by receiving signals from pathogens and then initiating an organism-wide immune response.

CREDIT: BAKAL *ET AL.*

Sergio Jorge Pastrana is the Foreign Secretary of the Academia de Ciencias de Cuba. E-mail: pastrana@ceniai.inf.cu.

Michael T. Clegg is the Foreign Secretary of the U.S. National Academy of Sciences and Donald Bren Professor of Biological Sciences, Ecology and Evolutionary Biology at the School of Biological Sciences, University of California, Irvine. E-mail: mclegg@uci.edu

U.S.-Cuban Scientific Relations

IN A FEW YEARS, THE TWO OLDEST NATIONAL ACADEMIES OF SCIENCE IN THE WORLD OUTSIDE of Europe—those of the United States and Cuba—will celebrate their 150th anniversaries. Yet despite the proximity of both nations and many common scientific interests, the U.S. embargo on exchanges with Cuba, which began in 1961 and is now based on the 1996 U.S. Helms-Burton Act and subsequent regulations, has largely blocked scientific exchange. It's time to establish a new scientific relationship, not only to address shared challenges in health, climate, agriculture, and energy, but also to start building a framework for expanded cooperation.

Restrictions on U.S.-Cuba scientific cooperation deprive both research communities of opportunities that could benefit our societies, as well as others in the hemisphere, particularly in the Caribbean. Cuba is scientifically proficient in disaster management and mitigation, vaccine production, and epidemiology. Cuban scientists could benefit from access to research facilities that are beyond the capabilities of any developing country, and the U.S. scientific community could benefit from high-quality science being done in Cuba. For example, Cuba typically sits in the path of hurricanes bound for the U.S. mainland that create great destruction, as was the case with Hurricane Katrina and again last month with Hurricane Ike. Cuban scientists and engineers have learned how to protect threatened populations and minimize damage. Despite the category 3 rating of Hurricane Ike when it struck Cuba, there was less loss of life after a 3-day pounding than that which occurred when it later struck Texas as a category 2 hurricane. Sharing knowledge in this area would benefit everybody.

Another major example where scientific cooperation could save lives is Cuba's extensive research on tropical diseases, such as dengue fever. This viral disease is epidemic throughout the tropics, notably in the Americas, and one of the first recorded outbreaks occurred in Philadelphia in the 18th century. Today, one of the world's most outstanding research centers dedicated to dengue fever is in Cuba, and although it actively cooperates with Latin America and Africa, there is almost no interaction with U.S. scientists. Dengue fever presents a threat to the U.S. mainland, and sharing knowledge resources to counter outbreaks of the disease would be an investment in the health security of both peoples.

Cuba has also made important strides in biotechnology, including the production of several important vaccines and monoclonal antibodies, and its research interests continue to expand in diverse fields, ranging from drug addiction treatment to the preservation of biodiversity. Cuban scientists are engaged in research cooperation with many countries, including the United Kingdom, Brazil, Mexico, China, and India. Yet there is no program of cooperation with any U.S. research institution.

The value system of science—openness, shared communication, integrity, and a respect for evidence—provides a framework for open engagement and could encourage evidence-based approaches that cross from science into the social, economic, and political arenas. Beyond allowing for the mutual leveraging of knowledge and resources, scientific contacts could build important cultural and social links among peoples. A recent Council on Foreign Relations report argues that the United States needs to revamp its engagement with Latin America because it is no longer the only significant force in this hemisphere. U.S. policies that are seen as unfairly penalizing Cuba, including the imposition of trade limitations that extend into scientific relations, continue to undermine U.S. standing in the entire region, especially because neither Cuba nor any other Latin American country imposes such restrictions.

As a start, we urge that the present license that permits restricted travel to Cuba by scientists, as dictated by the U.S. Treasury Department's Office of Foreign Assets Control, be expanded so as to allow direct cooperation in research. At the same time, Cuba should favor increased scientific exchanges. Allowing scientists to fully engage will not only support progress in science, it may well favor positive interactions elsewhere to promote human well-being. The U.S. embargo on Cuba has hindered exchanges for the past 50 years. Let us celebrate our mutual anniversaries by starting a new era of scientific cooperation. **– Sergio Jorge Pastrana and Michael T. Clegg**

10.1126/science.1162561

ECOLOGY/EVOLUTION

Not Kept Apart by Competition

According to the theory of limiting similarity, in order to minimize competition, species coexisting in the same habitat must differ enough in size, shape, or other variables. Ecologists and paleontologists have reported such differences in a wide range of organisms in modern environments or time-averaged deposits. To provide a temporal context, Huntley *et al.* examined the size and shape of Quaternary endemic land snails from the Canary Islands through the past 42,500 years. They considered two types of limiting similarity: ecological character displacement (differences between two closely related species are greater when speciation is ongoing in the same location) and community-wide character displacement (particularly large size or morphology variation among potentially competing species). The data showed that the two most abundant species of the pulmonate gastropod *Theba* exhibited a parallel reduction in size, but when one went extinct the other did not show convergence (a shift toward the other) or release (increased variation). Thus, limiting similarity appears to be a transient ecological phenomenon rather than a long-term evolutionary process. — SJS

Paleobiology **34**, 378 (2008).

Quaternary land snails.

CHEMISTRY

Odd Electron Chains

Organic materials that contain linear chains of metals in different valence states can behave as semiconductors or even exhibit metallic conductivity. Mitsumi *et al.* have explored a strategy for creating mixed-valence platinum (Pt) compounds by electrochemically oxidizing Pt(II) dimer precursors in organic solvents with noncoordinating ClO_4^- counterions. These dimers are stabilized by bridging dithiocarboxylato ligands (RCS_2–where R is an alkyl group), and, in the mixed-valence form, the Coulomb barrier that limits conductivity should be reduced by the presence of a shared unpaired electron in the Pt-Pt bonds and delocalized orbitals on the S atoms. For both methyl and ethyl analogs, the Pt dimers form linear chains with a mix of Pt_2^+ and Pt_3^+ centers (average oxidation states of 2.125 and 2.2, respectively). Crystal structures reveal that in the methyl analog, the chains arrange in parallel stacks separated by layers of solvent and ClO_4^- counterions. This compound, with one unpaired electron per chain repeat, exhibits high metallic conductivity at room temperature that persists to about 125 K (between 4 and 8 Siemens per cm). In the ethyl analog, in contrast, each chain is surrounded by solvent and counterions, and a longer repeat unit leads to pairing of the odd electrons and semiconducting behavior. — PDS

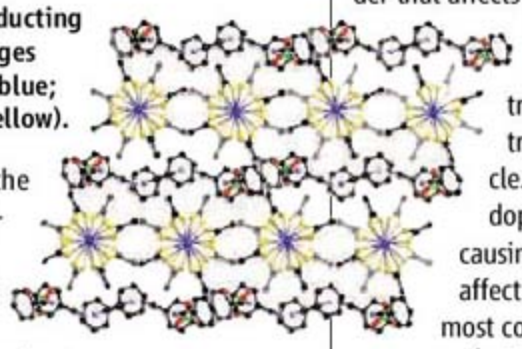

Conducting bridges (Pt, blue; S, yellow).

J. Am. Chem. Soc. **130**, 10.1021/ja805794a (2008).

CELL BIOLOGY

Losing Control

Parkinson's disease is a neurodegenerative disorder that affects 1% of people over 65, rising to 5% of those over 85. Nerve cells in the brain produce the neurotransmitter dopamine, which controls the smooth movement of muscle. In Parkinson's patients, these dopaminergic neurons are damaged, causing them to fire inappropriately and affect controlled body movements. The most common molecular cause of Parkinson's disease is a mutation in the gene encoding leucine-rich repeat kinase 2 (LRKK2); however, how this causes neuronal degeneration has been unclear. Now Imai *et al.* find that LRRK2 regulates the production of proteins in the cell during a stress response. When environmental conditions change, a cell needs to rapidly respond in order to survive. One effective way of doing this is by quickly generating additional proteins by translating existing mRNA. Both human and *Drosophila* forms of LRRK2 phosphorylated the translational regulator, eukaryotic initiation factor 4E-binding protein. This caused an increase in protein translation and attenuated resistance to oxidative stress and survival of dopaminergic neurons. In some patients, mutant LRRK2 has increased kinase activity, which could cause cells to lose control of translation. Thus, deregulated protein translation could affect the neurodegeneration seen in Parkinson's disease. — HP*

EMBO J. **27**, 2432 (2008).

IMMUNOLOGY

Mosaic Vaccines Are Not To Be Sneezed At

One of the few effective treatments for allergies to common substances such as pollen is allergen-specific immunotherapy. Doses of allergen too small to produce full-blown allergic reactions are administered to patients in an attempt to stimulate their immune systems to produce immunoglobulin G (IgG) molecules capable of blocking allergen recognition by the IgE molecules that orchestrate the inflammatory symptoms. Mothes-Luksch *et al.*

CREDITS (TOP TO BOTTOM): HUNTLEY *ET AL.*, *PALEOBIOLOGY* **34**, 378 (2008); MITSUMI *ET AL.*, *J. AM. CHEM. SOC.* **130**, 10.1021/JA805794A (2008)

report an alternative approach to modify allergens to produce immune response without triggering inflammation, making them potentially suitable for use as vaccines. A pollen allergen from timothy grass, Phl p 2, was divided it into equal-length peptides, none of which was recognized by IgE-containing serum from allergic patients. Neither Phl p 2 nor the peptide fragments produced an immune response in rabbits. However, a protein assembled from these peptides but in a different order produced a plentiful supply of IgG molecules capable of binding Phl p 2 and of blocking the binding of IgE. Changing the order of peptides stopped the mosaic protein from adopting the same three-dimensional structure as Phl p 2, making it hypoallergenic because it was effectively invisible to anti-Phl p2 IgE molecules. — CS*

J. Immunol. **181**, 4864 (2008).

ECOLOGY

Going My Way?

Genetic hitchhiking refers to the non-neutral fixation of nonselected alleles because of their physical proximity to loci under selection. If ecologically relevant loci are under divergent selection between populations, such as may occur during speciation, it may reduce recombination and further isolate these genomic regions, which in turn can facilitate the evolution of reproductive isolation. Via and West have tested this theory by measuring genetic differentiation in diverging host races of pea aphids found on clover and alfalfa. The authors identified highly diverged markers between aphids found on the different host plants, in particular near putative loci associated with ecologically important traits, and found that genetic differentiation between races extended much farther away from the loci under selection than expected. Divergence was also much less pronounced at markers linked to selected loci among aphids that shared the same crop type, even when these crops were geographically distant. — LMZ

Pea aphid.

CREDIT: SARA VIA

Mol. Ecol. **17**, 4334 (2008).

CHEMISTRY

How Holes Move

Quantum mechanics can explain how a single electron behaves in the presence of an oppositely charged proton. Add just one more electron, however, and the analysis becomes vastly more complicated. Because electrons affect one another, any motion by one of them must be considered in the context of correlated motion by the other—a scenario that proves ever more challenging to model as the number of electrons grows to molecular proportions. Lünnemann *et al.* explore the underlying effects of this correlated behavior in a computational study of how three molecules respond to ionization. After removing the most weakly bound electron from a phenyl, ethylene, or butadiene group tethered to an amine, the rate at which the resulting positive charge migrates to the nitrogen center was calculated. Because this delocalization is mediated by correlation effects rather than charge flow kinetics, the rates are extremely rapid (several femtoseconds). Migration is effectively total for the butadiene substrate, partial for the phenyl substrate, and minimal for the ethylene substrate. These trends are highly sensitive to molecular conformation and vary when the torsion angle of the amine is shifted. — JSY

J. Chem. Phys. **129**, 104305 (2008).

PHYSIOLOGY

Tick Tock Liver Clock

Rodents harbor an endogenous cycling clock with a period of about 24 hours. The so-called "master clock" in the brain is set by light, whereas subsidiary "peripheral" clocks are entrained by the animals' feeding schedule. Without these clocks, animals show impaired sleeping, eating, and activity rhythms, as well as pronounced problems in energy balance and glucose homeostasis. To understand how circadian clocks participate in glucose homeostasis, Lamia *et al.* selectively inactivated the clock in the liver by engineering mice with a conditional knockout allele for an essential clock component, the protein Bmal. These mice were unable to maintain steady levels of blood glucose, showing a drop in glucose during the fasting segment of their daily feeding cycle. This drop is normally prevented by a daily increase in the transcription of glucose transporter 2, a gene coding for the membrane protein that exports stored glucose from the liver into the blood. Other similarly regulated genes contribute to metabolic homeostasis. Thus, the liver circadian clock, entrained by the feeding cycle, has daily cycles of metabolic activity that ensure a steady supply of energy for the organism. — KK

Proc. Natl. Acad. Sci. U.S.A. **105**, 15172 (2008).

*Helen Pickersgill and Chris Surridge are locum editors in *Science*'s editorial department.

www.sciencemag.org

Science

1200 New York Avenue, NW
Washington, DC 20005
Editorial: 202-326-6550, FAX 202-289-7562
News: 202-326-6581, FAX 202-371-9227
Bateman House, 82-88 Hills Road
Cambridge, UK CB2 1LQ
+44 (0) 1223 326500, FAX +44 (0) 1223 326501

Subscription Services For change of address, missing issues, new orders and renewals, and payment questions: 866-434-AAAS (2227) or 202-326-6417, FAX 202-842-1065. Mailing addresses: AAAS, P.O. Box 96178, Washington, DC 20090-6178 or AAAS Member Services, 1200 New York Avenue, NW, Washington, DC 20005

Institutional Site Licenses please call 202-326-6755 for any questions or information

Reprints: Author Inquiries 800-635-7181
Commercial Inquiries 803-359-4578

Permissions 202-326-7074, FAX 202-682-0816

Member Benefits AAAS/Barnes&Noble.com bookstore www.aaas.org/bn; AAAS Online Store www.apisource.com/aaas/ code MKB6; AAAS Travels: Betchart Expeditions 800-252-4910; Apple Store www.apple/eppstore/aaas; Bank of America MasterCard 1-800-833-6262 priority code FAA3YU; Cold Spring Harbor Laboratory Press Publications www.cshlpress.com/affiliates/aaas.htm; GEICO Auto Insurance www.geico.com/landingpage/go51.htm?logo=17624; Hertz 800-654-2200 CDP#343457; Office Depot https://bsd.officedepot.com/portalLogin.do; Seabury & Smith Life Insurance 800-424-9883; Subaru VIP Program 202-326-6417; VIP Moving Services www.vipmayflower.com/domestic/index.html; Other Benefits: AAAS Member Services 202-326-6417 or www.aaasmember.org.

science_editors@aaas.org (for general editorial queries)
science_letters@aaas.org (for queries about letters)
science_reviews@aaas.org (for returning manuscript reviews)
science_bookrevs@aaas.org (for book review queries)

Published by the American Association for the Advancement of Science (AAAS), *Science* serves its readers as a forum for the presentation and discussion of important issues related to the advancement of science, including the presentation of minority or conflicting points of view, rather than by publishing only material on which a consensus has been reached. Accordingly, all articles published in *Science*—including editorials, news and comment, and book reviews—are signed and reflect the individual views of the authors and not official points of view adopted by AAAS or the institutions with which the authors are affiliated.

AAAS was founded in 1848 and incorporated in 1874. Its mission is to advance science, engineering, and innovation throughout the world for the benefit of all people. The goals of the association are to: enhance communication among scientists, engineers, and the public; promote and defend the integrity of science and its use; strengthen support for the science and technology enterprise; provide a voice for science on societal issues; promote the responsible use of science in public policy; strengthen and diversify the science and technology workforce; foster education in science and technology for everyone; increase public engagement with science and technology; and advance international cooperation in science.

Information for Authors
See pages 634 and 635 of the 1 February 2008 issue or access www.sciencemag.org/about/authors

EDITED BY CONSTANCE HOLDEN

Sumo Non Bonum

Rugby players call it scrumpox. Now sumo wrestlers are being plagued with their own version of the aptly named herpes gladiatorum.

It's a nasty strain of the herpes simplex virus that usually causes cold sores that are confined to the lips. But it spreads all over wrestlers, taking advantage of abrasions on faces, necks, arms, and legs to generate grotesque rashes of sores and blisters. Once acquired, the virus hides in nerve cells and periodically comes back to spread afresh.

Kazuo Yanagi, a virologist at the National Institute of Infectious Diseases in Tokyo, realized that sumo wrestlers, who live and train communally in sumo stables, were "a good group to study from an epidemiological point of view." Yanagi and colleagues studied serum samples collected from sumo wrestlers in the late 1980s and early 1990s, when a spike in infections appeared and one wrestler died. In the October issue of the *Journal of General Virology*, they report that a particularly virulent strain, BgK_L, entered the sumo community and quickly displaced a weaker strain, more readily infecting large parts of the body.

William Ruyechan, a virologist at the University at Buffalo in New York state, says the work shows how herpes can have drastic effects in certain subgroups. Yanagi believes but can't confirm that the virus is still circulating in the sumo community. "Information concerning diseases among sumo wrestlers is not released to outsiders," he says.

Bustling in the Deeps

Surprises still lurk in the deep. Last week, a school of snailfish was filmed for the first time at the record depth of 7700 meters in the Pacific Ocean's Japan Trench. The video shows the highly active, sociable fishes swarming over shrimps attracted by bait the scientists had deployed. It's one result of a 2-week expedition by a British-Japanese team working from the research ship *Hakuho-Maru*.

Deep-sea fish were thought to be mostly slow-moving, solitary species. But the busy snailfish, which are up to 23 cm long, belie that stereotype despite living in nearly freezing waters, under extreme pressure, and in total darkness. "What is really interesting is how many of them were rapidly attracted to bait and how active they seem," says oceanographer Jeffrey Drazen of the University of Hawaii, Honolulu, who was surprised to see the snailfish snapping at the large shrimps, which are themselves fish-eaters. The team operated a specially designed camera that took 5 hours to reach the bottom of the ocean and worked for 2 days in the high-pressure environment, offering a novel view of the deep-sea ecosystem at work.

The (B)ayes Have It

In the winner-take-all world of politics, candidates know that even a modest lead in the polls can spell almost certain victory. Sheldon Jacobson, an operations research specialist at the University of Illinois, Urbana-Champaign, and colleagues, including a group of students, have attempted to quantify that insight for the current United States presidential election, putting their predictions for the Electoral College on a Web site, election08.cs.uiuc.edu.

Using a statistical method known as Bayesian estimation, they combined an analysis of results from the 2004 Bush-versus-Kerry contest with current state-by-state polls for Obama versus McCain to produce probabilities for each candidate of carrying each state. They then converted the estimates into a probability distribution for the total number of Electoral College votes a candidate might receive.

In Indiana, for example, polls as of 4 October gave McCain a slight 2.5% lead. But given that Bush carried Indiana in 2004 by 20.7%, a Bayesian calculation indicates McCain's chance of winning the state's 11 Electoral College votes at about 87%.

Most states are now in the bag for one candidate or the other; only a handful are truly in Bayesian play. Current calculations give McCain no chance of victory. "However," Jacobson cautions, "if the polls move, then so will our forecasts."

A MAN'S REACH ...

This spaceship, designed for humans orbiting the moon, sprang from the fertile mind of pioneering rocket scientist Wernher von Braun in 1952, 16 years before Apollo 8 made the trip for real.

It's one of a collection of drawings, diagrams, and letters to be auctioned off this month for an estimated $15,000 to $20,000 at Bonhams in New York City. Von Braun created the materials in the course of writing a series of articles for *Collier's* magazine titled "Man Will Conquer Space Soon!" that ran from 1952 to 1954.

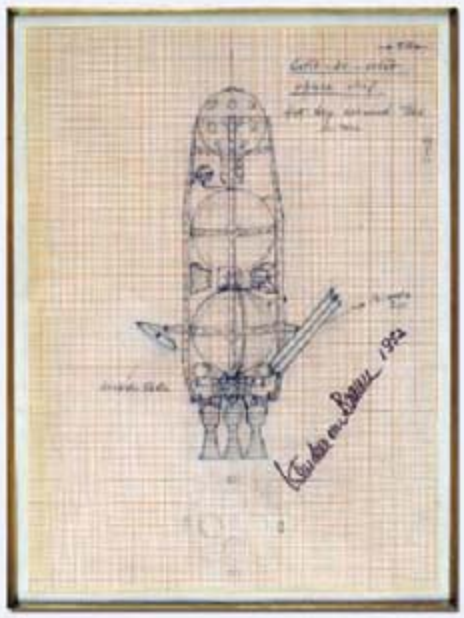

CREDITS (TOP TO BOTTOM): FRANCK ROBICHON/EPA/CORBIS; JAPAN AGENCY FOR MARINE-EARTH SCIENCE AND TECHNOLOGY; BONHAMS

EDITED BY YUDHIJIT BHATTACHARJEE

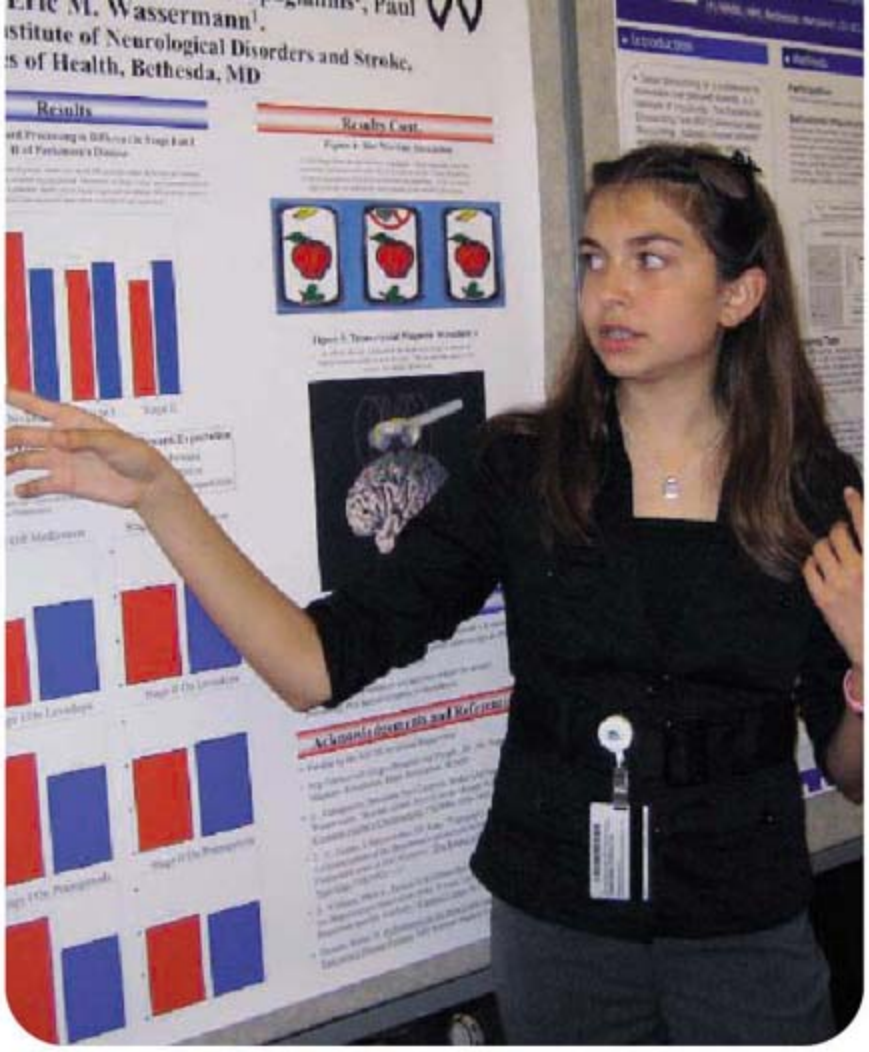

RISING STARS

SPEEDING. Many biologists get hooked on science as children, but Kelsey Curd Ladt's early experiences go far beyond the norm. A premed senior majoring in biology at the University of Kentucky (UK) in Lexington, the 13-year-old Ladt worked this summer in a neuroscience lab at the U.S. National Institutes of Health—probably the youngest NIH researcher ever, NIH officials say.

The daughter of a chemical engineer and a human resources consultant, Kelsey finished elementary school at age 7 and entered UK at age 11. NIH waived the requirement that summer interns be at least 16 because of her abilities, says NIH's Rita Ward. Working for Eric Wassermann of the National Institute of Neurological Disorders and Stroke, she recruited patients, ran experiments, and analyzed data for a study on whether transcranial magnetic stimulation can be used to assess how the human brain responds to a potential reward.

"Having someone young and excited with a different take on things, that makes science fun," says Wassermann, who expects Kelsey to be a co-author on an upcoming paper. Kelsey isn't planning to slow down, either: She plans to return to his lab after graduation before beginning an M.D./Ph.D. program in 2010.

ON CAMPUS

PARTIAL DISCLOSURE. Charles Nemeroff, the chair of psychiatry at Emory University School of Medicine, has stepped down from his post while the Atlanta, Georgia, university investigates Senate allegations that he failed to report at least $1.2 million in income from drug companies.

Nemeroff is the latest target of a probe by Senator Charles Grassley (R–IA) into financial conflicts of interest at more than 20 universities (*Science*, 27 June, p. 1708). According to documents released by Grassley last week, Nemeroff reported only half of at least $2.4 million that he earned from drug and device companies between 2000 and 2007 on financial disclosure forms. In 2004, for example, Nemeroff promised Emory officials that his income from GlaxoSmithKline (GSK) would not exceed $10,000 a year. But company records show that he was paid $282,000 from 2004 to 2007. At the time, Nemeroff was conducting a National Institutes of Health–funded study testing GSK drugs.

Possible outcomes of Emory's investigation could include firing Nemeroff, a university official has told reporters. Nemeroff said in an Emory statement that "to the best of my knowledge, I have followed the appropriate University regulations concerning financial disclosures."

Got a tip for this page? E-mail people@aaas.org

MONEY MATTERS

MIMICKING NATURE. A Harvard University alum is donating $125 million to the university to foster advances in biomedical engineering.

Hansjörg Wyss (below), the former head of Synthes—a global multibillion-dollar medical devices company—is a Swiss-born engineer who got an MBA from Harvard in 1965. His gift will create the Hansjörg Wyss Institute for Biologically Inspired Engineering, which will build on recent advances in nanotechnology, genetics, and cellular engineering.

Donald Ingber, a cell biologist and bioengineer who will be the institute's new director, says Wyss asked the university to develop a plan for bringing together faculty members from different schools of engineering, medicine, and Harvard's affiliated hospitals before making the donation, which will be given out over 5 years. Getting those departments and researchers on the same page, says Ingber, "took a lot of forethought and planning."

PRIVATE GOOD. Business Wire founder Lorry Lokey, 81, jokes that he has a selfish reason for donating $75 million for a new stem cell research center at Stanford University in Palo Alto, California. "I expect to live 20 years longer because of it," he says of the gift, announced last week. The 1949 Stanford journalism graduate, who made his fortune by establishing a wire service for distributing press releases, says he was also motivated by the Bush Administration's restrictions on federal funding for stem cell research.

The gift comes with few conditions on how it should be spent: Lokey says the recipients should be able to pick the paint color on their buildings. Officials at Stanford's School of Medicine are planning to break ground this month on an 18,580-m^2 facility, likely to be the nation's largest devoted to stem cell research.

CREDITS (TOP TO BOTTOM): SOURCE: KELSEY CURD LADT; STANFORD SCHOOL OF MEDICINE; HBS

Bad water and a mass extinction 359

Physics, chemistry, economics Nobels 360

SCIENTIFIC MISCONDUCT

Falsification Charge Highlights Image-Manipulation Standards

Controversy continues to plague work from the lab of prominent stem cell researcher Catherine Verfaillie. The University of Minnesota (UM) announced last week that an academic misconduct committee had concluded that Morayma Reyes, while a graduate student in Verfaillie's lab there, "falsified" four data images in figures in a 2001 stem cell article. The committee found that misconduct allegations against Verfaillie were unsubstantiated, but it did criticize her oversight and mentoring of lab personnel. The new charges come a year after questions were raised about the misuse of images in another key stem cell publication from the group (*Science*, 2 March 2007, p. 1207).

Reyes, now an assistant professor of pathology at the University of Washington (UW), Seattle, and Verfaillie, who now heads the Stem Cell Institute at the Catholic University of Leuven in Belgium, both acknowledge that errors were made in the preparation of the 2001 paper. But Verfaillie defends her supervision, and Reyes says that for several of the disputed images she merely globally adjusted the brightness and contrast in data images without any intent to deceive. "These errors were unintentional and were common and accepted practices at the time," Reyes wrote in an e-mail to *Science*.

The paper, published in *Blood*, claims that stem cells purified from human blood can form precursors of bone, fat, cartilage and muscle cells, as well as the endothelial cells that line blood vessels. At the time, blood stem cells weren't thought to be that versatile. Verfaillie and Reyes say the figure errors do not alter the *Blood* paper's conclusions, but Verfaillie has asked the journal to retract the paper, calling it "the proper course in this situation."

The *Blood* paper relates to work that the group later published in *Nature*, reporting that cells from mouse bone marrow could become a wide variety of cell types. Several groups have reported trouble reproducing that paper's results (*Science*, 9 February 2007, p. 760). Then last year, *Nature* conducted a re-review of the paper when a journalist at *New Scientist* questioned whether some data shown were identical to those in another paper. A UM investigation concluded that any duplication was the result of honest error. *Nature* published several corrections but said that the paper's conclusions were still valid and that Verfaillie continues to stand by the work.

New Scientist also alerted the university to an apparent duplicated image in the *Blood* paper (*Science*, 30 March 2007, p. 1779). The university then convened a new committee, which submitted its final report on 5 September. The school last week stated that the committee found that in four of the seven figures in the *Blood* paper, "aspects of the figures were altered in such a way that the manipulation misrepresented experimental data and sufficiently altered the original research record to constitute falsification." The committee cited "elimination of bands on blots, altered orientation of bands, introduction of lanes not included in the original figure, and covering objects or image density in certain lanes," the statement says.

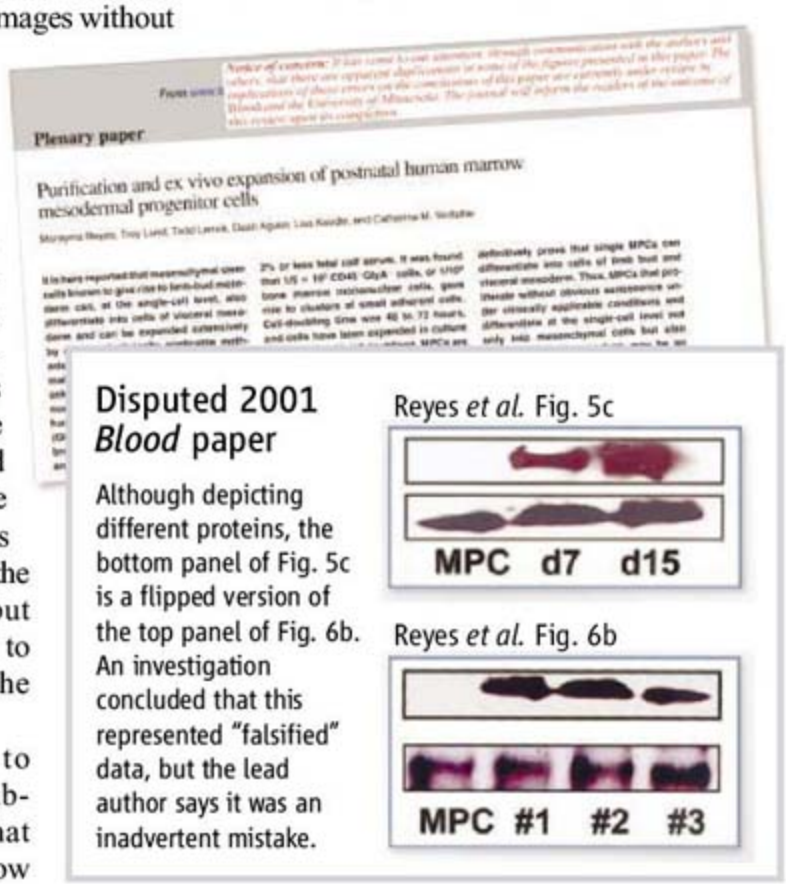

The university has not released the full report, citing privacy laws, and experts in image analysis say it is hard to determine intentional fraud solely from the original paper. James Hayden, manager of the microscopy core facility at the Wistar Institute in Philadelphia, Pennsylvania, says that to make a clear point, scientists often alter images, sometimes more than they should. Good laboratory practice means all such adjustments should be noted in a paper and copies of the original image files kept, he says. Jerry Sedgewick, head of the Biomedical Image Processing Lab at UM and one of Reyes's mentors, says he is not convinced that she did anything wrong with the image adjustments she made. "This is done routinely and has been done since film and imaging began," he says.

During the investigation, Reyes asked George Reis, who heads the consulting firm Imaging Forensics in Fountain Valley, California, to assess whether changes made between the original image scans and the published images could be due to "global" adjustments, which would imply there was no intent to deceive. Reis told *Science* that he did determine that significant global adjustments could account for "most of the changes in most of the images." But he says he did not examine the images specifically for signs of editing such as adding or deleting individual lanes.

UM says it has forwarded the panel's report and supporting materials to the federal Office of Research Integrity in Rockville, Maryland. UW is waiting for more information from UM before deciding whether to discipline Reyes, according to a spokesperson.

Both Verfaillie and Reyes say they have implemented much stricter rules for dealing with data images in their labs as a result of the case. "I have learned a hard lesson," Reyes e-mailed *Science*. "Now that I am a mentor ... I will make sure that my students will get the proper training, supervision and education."

–GRETCHEN VOGEL

With reporting by Rachel Zelkowitz.

Q&A with China's premier
364

Puzzling results from diabetes trials
367

GENETICS

DNA Test for Breast Cancer Risk Draws Criticism

It's been 8 years since the human genome was sequenced with the promise of revolutionizing medicine, and since then, efforts to put DNA discoveries into the doctor's office have only grown more controversial. The latest tussle came last week after deCODE Genetics, an Icelandic company, released the first-ever breast cancer risk test designed to cover common forms of the disease. The rollout and reaction were predictable: deCODE hailed the test as offering women a chance to take advantage of more aggressive screening if they're found at higher risk. Many oncologists and geneticists decried the $1625 test as premature because it includes just seven genetic variants out of the dozens or hundreds driving breast cancer that scientists expect to find soon.

Unlike some new genetic tests, this one is not in question over its science: The seven variants it uses, all single-nucleotide polymorphisms (SNPs) found in the last couple of years, have been linked to an increased risk of breast cancer in thousands of women, mainly of European descent. Five of the variants were identified by a group at the University of Cambridge, U.K., using genome-wide association. These SNPs are in the public domain, and companies can incorporate them into new products.

The test does not check for mutations in *BRCA1* and *BRCA2*, two genes that dramatically increase the risk of breast cancer. Those mutations are rare, accounting for only a small fraction of cases, and they have been patented by a company in Utah that holds exclusive rights to test for them in the United States.

The quandary presented by deCODE's breast cancer test, its sixth genetic risk test for a common disease, reflects a broader puzzle in genetics. Each new disease-linked SNP scientists uncover confers only a slight increase in risk, often no more than 20%. That might boost someone's lifetime chance of a chronic disease from 8% to 10%, so small as to be of questionable use to an individual. Even having several of these SNPs isn't likely to increase risk more than 100%, which amounts to a doubling. For breast cancer, that's roughly equivalent to having one family member with the disease.

Whereas some argue that such information isn't robust enough for clinical use, others see no reason to hold off. "It goes against our tradition to say, 'Let's wait until we discover more,'" says Kári Stefánsson, a neurologist and the chief executive officer of deCODE. The risk his test uncovers, he argues, is meaningful: Published work suggests that about 5% of women who use the company's test will find that they have a 20% risk of breast cancer; average risk is just over 12%. At 20% risk, U.S. guidelines recommend additional screening using magnetic resonance imaging (MRI).

Tipping point. A $1625 genetic test will inform women if they're at high enough risk to merit MRI screening for breast cancer, the manufacturer says.

"This is a suitable test for anyone," says Owen Winsett, a surgeon and director of the Breast Center of Austin in Texas. Winsett contacted deCODE last spring after learning about its work, and the company quotes his favorable comments in its press release. Winsett, who says he has not received any compensation, is backing his words with action. In the last month, he has offered the test to about 25 patients worried about breast cancer and recommended regular MRIs for some based on the results. Winsett says he would support prescribing tamoxifen, a drug taken to prevent breast cancer, based on the deCODE test results, though he hasn't done that yet.

Others are more wary. "Any test, even based on the best SNPs so far, will probably misclassify a substantial fraction of women," says David Hunter, a genetic epidemiologist at Harvard School of Public Health in Boston. That's because many believe the genetic risk identified in DNA so far is only a few percent of what will eventually be discovered. "Women need to know that their risk estimates might actually change over time as more variants become available," Hunter adds, noting that some labeled high-risk may later learn that the news isn't so bad, or vice versa.

"What you're seeing is someone's risk based on a small subset of variants," agrees Douglas Easton, a genetic epidemiologist at the University of Cambridge in the U.K. who led the team that identified five breast cancer SNPs last year. "You don't know what the whole hand is."

Mitchell Gail, a medical statistician at the National Cancer Institute in Bethesda, Maryland, who designed a commonly used breast cancer risk model, earlier this year analyzed how much risk predictions would be strengthened by testing for most of the SNPs in deCODE's test. (Predictions are now based on factors such as family history.) "I'm not seeing a lot of improvement," says Gail, who published his analysis in July. He estimates that about 300 SNPs are needed to dramatically improve risk forecasts for breast cancer.

Stefánsson finds such arguments infuriating. "They basically say we should wait until we have discovered everything about breast cancer," he says of his colleagues. "That is somewhere between ridiculous and incredibly dangerous." **–JENNIFER COUZIN**

CREDIT: JENNIFER HULSHIZER/THE STAR-LEDGER/CORBIS

RESEARCH FACILITIES

Hawaii Marine Lab Fights to Stay Afloat

Just a few kilometers down the coast from Waikiki Beach in Hawaii, the death knell is tolling for the University of Hawaii's (UH's) Kewalo Marine Laboratory. The university has agreed to give up its lease on the 35-year-old lab 17 years early and plans to move the lab's faculty to its other marine lab on Coconut Island, or to the main Manoa campus, or even to the Waikiki Aquarium. The state redevelopment agency, which owns the land, plans to tear down the waterfront lab to expand a park and set up a public arts place.

Word of the lab's demise is spreading through blogs and listservs, setting off protests across the globe. Last week, biologist Paul "PZ" Myers of the University of Minnesota, Morris, called the decision "short-sighted" in his blog, Pharyngula. In a letter to UH officials, Alessandro Minelli of the University of Padua in Italy praised the lab's evolutionary and developmental research and warned: "Stopping this activity would be a disaster for biology."

But Gary Ostrander, UH Manoa vice chancellor for research and graduate education, insists that he has no alternatives. "I don't like the idea of closing a marine lab, but we are a university that's struggling with budgets, and I have needs that are more pressing right now," he told *Science*.

The lab was established in 1972 with a focus on using marine animals and molecular methods to study cell and developmental biology. Given Hawaii's location and the central role marine resources play in Hawaii's economy, it would be "tragic" if the lab closes, says its director, Mark Martindale. "We will have the same number of marine labs as Alabama and Ohio."

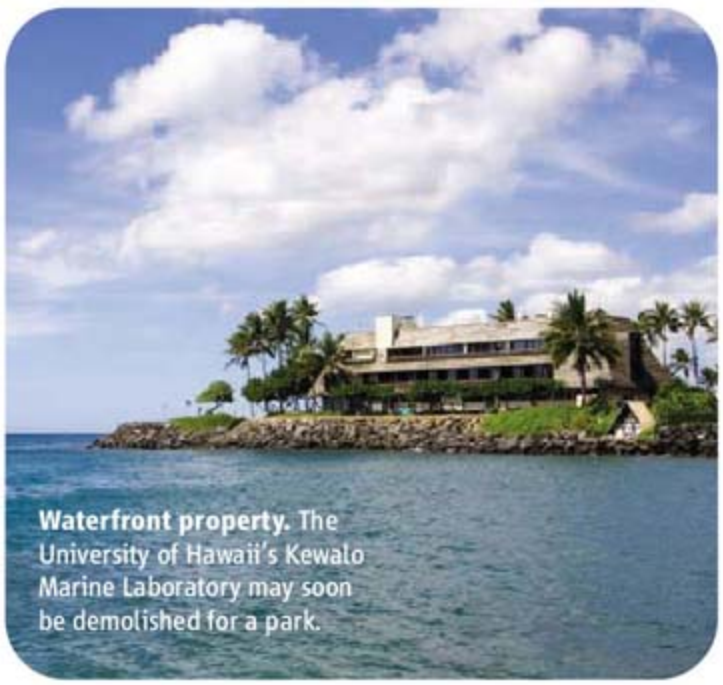

Waterfront property. The University of Hawaii's Kewalo Marine Laboratory may soon be demolished for a park.

The closure will be "really creating a deficit" both for Hawaii and the country, says George Boehlert, director of the Oregon State University Hatfield Marine Science Center in Newport. "You have very limited resources in the United States to do work on coral reefs, so this would be a significant blow to the research capacity of the United States."

But Ostrander says the lab is falling apart, and for several years the landlord, the Hawaii Community Development Authority, has been pushing to get the land back before the lease is up in 2030. Ostrander says he's looked into moving the lab a few blocks back from the water but has been unable to raise the $30 million estimated to be needed to rebuild the facility in this new location.

Places like the Kewalo lab "tend to have a fragile existence," being small and off campus and therefore more vulnerable to being closed down, says James Sanders, president of the National Association of Marine Laboratories and director of the Skidaway Institute of Oceanography in Savannah, Georgia. Indeed, Kewalo has been overshadowed by UH's other marine lab, the 15-year-old Hawaii Institute of Marine Biology, which also has dorms and conference facilities. But Sanders says that Kewalo is "well-respected" and that he would like to see it protected somehow. "We tend to view marine labs as windows on the ocean," he says. "I hate to see any of those windows shut."

–ELIZABETH PENNISI

NATIONAL INSTITUTES OF HEALTH

Two Strikes and You're Out, Grant Applicants Learn

Taking some by surprise, the National Institutes of Health (NIH) announced last week that scientists applying for grants will get only one chance to resubmit a rejected proposal. The current policy, which allows two revisions, bogged down the review process and forced investigators to wait in line for funding, NIH says. Giving applicants just one more try should fund the best science sooner.

The change is in response to an advisory panel that identified problems in peer review earlier this year. The panel found that because more researchers are applying for money at a time when NIH's budget has stopped growing, study sections are shying away from funding applications submitted for the first time. Instead, NIH data show, even investigators with very strong proposals must resubmit at least once. This has increased the workload for reviewers and applicants, and it means that many grantees wait up to 2 years for a decision. The advisory panel had a radical solution: Abolish revised proposals and consider all applications "new."

Some scientists, including the 80,000-member Federation of American Societies for Experimental Biology (FASEB), argued that was too harsh. In June, NIH officials said they planned to continue to permit more than one revision but would "rebalance" the system to lower the success rates for resubmitted proposals (*Science*, 13 June, p. 1404).

Over the summer, NIH decided to scrap the rebalancing idea, says Anthony Scarpa, director of NIH's Center for Scientific Review. "This goes further and achieves the same thing," he says. Beginning in January, only one amended application will be allowed. If that is rejected, the applicant "should substantially re-design the project," states an 8 October notice.

"It's a reasonable compromise," says Princeton University geneticist David Botstein, a member of the peer-review advisory committee. "It will push study sections in the direction that we want them to go." But "there has not been a lot of enthusiasm" among FASEB members, says Howard Garrison, the society's public-affairs director. He worries that "meritorious projects" will not get funded. But as Garrison notes, there is little point in protesting, as the new policy is final.

–JOCELYN KAISER

CREDIT: YALE PASSAMANECK

MASS EXTINCTION

Most Devastating Mass Extinction Followed Long Bout of Sea Sickness

Dying in a cesspool may not have the popular appeal of perishing in a giant asteroid impact, but fouled waters are looking more and more like the cause of the ocean's greatest mass extinction 252 million years ago. The witches' brew that may have wiped out 90% of marine species in a geologic moment "had been stewing for millions of years," says paleontologist David Bottjer of the University of Southern California in Los Angeles. Geochemists and paleontologists have new evidence that fouled ocean water "was a prelude to the mass extinction," Bottjer says, not just the immediate driving force behind it.

Geochemically, traces of bad water are preserved in the chemical and isotopic composition of marine sediments laid down late in the Permian Period. At the upcoming fall meeting of the American Geophysical Union (AGU) this December, biogeochemist Changqun Cao of the Nanjing Institute of Geology and Paleontology of the Chinese Academy of Sciences and his colleagues will report their analyses of organic matter from a rock core drilled at Meishan in southern China. Throughout the core, which spans the extinction and the 3 million years before it, they found distinctive hydrocarbons produced only by green sulfur bacteria. These bacteria live only in sunlit (and thus shallow) waters that are oxygen-free and loaded with usually noxious hydrogen sulfide. Toxic levels of carbon dioxide are common under such conditions as well.

Signs of similar circumstances inimical to higher life forms, much like those of the stagnant depths of the Black Sea today, are widespread in the geologic record of the Permian-Triassic mass extinction as well as the few million years before it, says geochemist Roger Summons of the Massachusetts Institute of Technology in Cambridge, a coauthor on the AGU presentation. Judging by his work and that of others, the encroachment of these foul waters was "progressive and pervasive" around the late Permian world, Summons says.

Bottjer and his colleagues found signs of the same progressive deterioration of environmental conditions in the fossil record of the late Permian. Reporting in the September issue of *GSA Today*, they summarize their published and in press analyses of the fossil records of three late Permian animals: clamlike, stalked brachiopods; encrusting, coral-like bryozoans; and bottom-dwelling mollusks. They counted not just the number of species but also the abundance of individual fossils as a clue to ecological changes. They found that starting as much as 8 million years before the extinction, the abundance of brachiopods in deeper, offshore waters began to drop; bryozoans started becoming less diverse there, while mollusks proliferated. The more mobile mollusks would dominate the oceans after the extinction.

"I certainly don't mean to say the mass extinction wasn't abrupt," Bottjer says, but "it was brewing for a long time, and it was coming from deep water." Perhaps all that the rising foul waters needed to precipitate the crisis of the extinction was a trigger, he says. The huge, climate-altering eruption of the Siberian Traps coincides with the extinction (*Science*, 17 September 2004, p. 1705) and could have sent foul waters shoreward.

The new results from the late Permian "are starting to swing the pendulum back" toward a more protracted episode of change for life, says paleontologist Paul Wignall of the University of Leeds, U.K. The exact nature of that episode—its pace throughout and the identity of the killer agent or agents—remain to be determined, he says. **–RICHARD A. KERR**

CREDIT: MATTHEW E. CLAPHAM

Early losers. Brachiopods (shells) and spongelike Bryozoa suffered an early battering.

SCIENCESCOPE

"Free" Gets Sold

Berlin-based publisher Springer is buying BioMed Central (BMC), the world's largest publisher of open-access journals. Launched in 2000 by entrepreneur Vitek Tracz, BMC pioneered the concept of making full-text articles freely available at the time of publication. Along the way, the company began charging authors, who once could publish for free; the fee for its priciest journals is now $2390 per article. The company publishes more than 180 titles and last year had profits of €15 million. The sale price was not disclosed. The deal shows that "open access is a successful business model," says epidemiologist R. Brian Haynes of McMaster University in Hamilton, Canada, a member of the board of trustees for London-based BMC. Springer will retain the open-access model and has "no immediate plans" to raise author fees, says a spokesperson. **–JOCELYN KAISER**

NASA Keeps Mars Mission on Track

Despite technical troubles, the Mars Science Laboratory remains on track for an October 2009 launch. But at a 10 October press conference, NASA officials said that although technical problems are under control, costs are rising. Originally budgeted at $1.6 billion, the lab is now pegged at $1.9 billion, says Doug McCuistion, director of NASA's Mars Exploration Program. Others at NASA expect the total to exceed $2 billion and say the overruns could affect additional efforts to study Mars and other planets. The program's next hurdle will be a NASA review in January. **–ANDREW LAWLER**

Legal Monkey Business

A legal battle is brewing over primate research in Bremen, Germany. Last year, Bremen's legislature passed a nonbinding resolution to phase out primate research in the city-state. Andreas Kreiter, a neuroscientist at the University of Bremen, is the only one conducting such studies, and his animal license runs out on 30 November. However, on 2 October, city authorities informed him that they intend to reject his application. The university and Germany's main research funding agency, DFG, have all said that that would violate Germany's constitutional guarantee of "research freedom." The university has threatened legal action if the city rejects the license, appealing all the way to the country's highest court if necessary, a move that experts say would impact other ongoing efforts to limit animal research across Germany. **–GRETCHEN VOGEL**

NOBEL PRIZE IN PHYSICS

Skewed Symmetries Net Honors for Particle Theorists

When Yoichiro Nambu won half of this year's Nobel Prize in physics he was surprised, ironically, because he had grown so used to others' saying that he deserved it. "I've been told that this is a possibility for many, many years," says Nambu, 87, who emigrated from Japan in 1952 and has been at the University of Chicago in Illinois since 1954. "I was not expecting it." Nambu's peers are happy to see him finally honored. "It's high time," says theorist Jonathan Ellis of the European particle physics laboratory, CERN, near Geneva, Switzerland. "This prize could have been awarded when I was a graduate student in 1968."

Triumphant trio. Nambu, Maskawa, and Kobayashi teased deep insight out of "broken" symmetries in interactions of subatomic particles.

Nambu is cited for applying a concept called spontaneous symmetry breaking to particle physics. The other half of the prize goes to Makoto Kobayashi, 64, of the High Energy Accelerator Research Organization (KEK) in Tsukuba and Toshihide Maskawa, 68, of Kyoto Sangyo University, both in Japan. While trying to explain an asymmetry between matter and antimatter, they correctly predicted the existence of new fundamental particles.

Spontaneous symmetry breaking occurs whenever the forces within a system are in some way symmetric but the lowest energy "ground state" that the system nestles into is not. Balance a pencil on its tip, for example, and gravity will pull the pencil down but won't tug it in any particular horizontal direction. The symmetry "breaks" only when the pencil flops onto the table in some random direction.

In the early 1960s, Nambu applied this concept to the interactions of protons and neutrons, known collectively as nucleons. Physicists knew the strong force that binds nucleons into atomic nuclei is conveyed by particles called pions whizzing between them. Nambu assumed a subtle symmetry among nucleons involving the way the particles spin and the fact that, to the strong force, a proton is essentially indistinguishable from a neutron. He showed that if the symmetry were spontaneously broken, pions had to emerge with exactly the mass and other properties they were already known to have.

Spontaneous symmetry breaking has since become a key tool in particle theory. Physicists think that spontaneous breaking of a different symmetry explains how fundamental particles obtain mass. That bit of conceptual calisthenics also predicts a new particle, the long-sought Higgs boson.

Kobayashi and Maskawa made one of science's more inspired educated guesses. In 1972, physicists knew of three types of ▶

NOBEL PRIZE IN ECONOMICS

Theorist Revolutionized Study of What Gets Made Where

A Nobel Prize often gives its winner a first taste of fame. The winner of this year's Sveriges Riksbank Prize in Economic Sciences in Memory of Alfred Nobel was already well known. Paul Krugman, an economist at Princeton University, a columnist for *The New York Times*, and a best-selling author, has won for his analyses of international trade and economic geography.

"The papers he writes are so simple and crystal clear that in hindsight, you might say, 'I could have thought of that,' " says Samuel Kortum, an economist at the University of Chicago. "But nobody did" until Krugman did. In 1979, Krugman reshaped the study of international trade. Economists had generally argued that countries trade with one another in response to differences between them. So a country that makes cars might trade with one that produces cotton to their mutual benefit. In reality, a country that produces cars often ends up trading with another country that makes cars.

Krugman explained that seemingly illogical "intra-industry trade" by taking into account "economies of scale"—the fact that the cost of producing an object decreases the more you make. If two countries trade, then each will effectively enlarge its economy, leading to a proliferation of goods and companies. However, to exploit economies of scale, each company will be based in one country or the other, even if that means Sweden sends Volvos to Germany as Germany sends BMWs to Sweden, Kortum explains.

In 1991, Krugman applied similar thinking to the growth of cities. He showed that, because more economically developed areas provide a wider variety of goods, they will also attract more people, further fueling economic growth and speeding the process of agglomeration. "Krugman's insight was that the towns themselves are sources for the demand for products," says Vernon Henderson, an economist at Brown University.

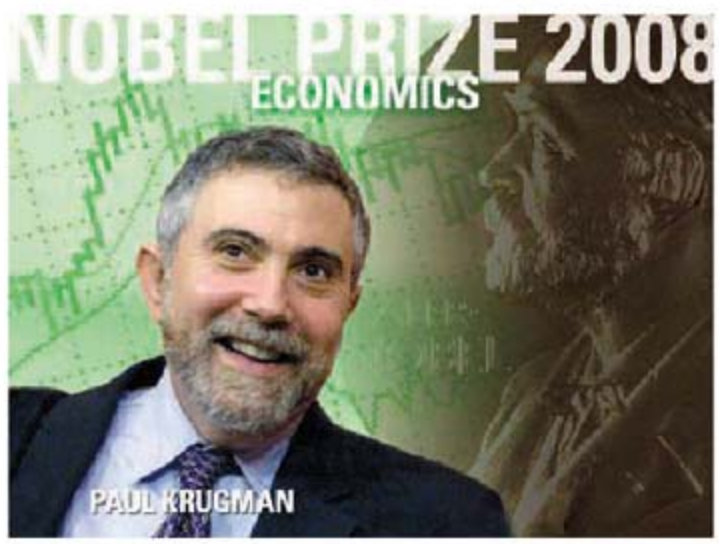

Back in the day. Perhaps best known now as a pundit, Krugman performed seminal analyses of trade and city formation.

A self-proclaimed liberal, Krugman has criticized the policies of President George W. Bush. But Henry Overman of the London School of Economics says Krugman won for his economic insights and not his politics—although he notes that Krugman's win is "not going to be very popular with Bush lovers."

–ADRIAN CHO

CREDITS: (TOP) KYODO/LANDOV; (BOTTOM) BRIAN WILSON/PRINCETON UNIVERSITY

particles called quarks: the up quark and down quark that make up nucleons, and the strange quark found in fleeting particles called K mesons. Kobayashi and Maskawa predicted that at least six types of quarks had to exist.

"It was very brave," says Michael Gronau, a theorist at Technion–Israel Institute of Technology in Haifa. "Nobody took the model seriously when it came out, but it turned out to be the right one." From ever-higher-energy particle collisions the charm quark emerged in 1974, the bottom quark in 1977, and the top quark in 1995.

Of course, the two theorists didn't just toss out a number. They were trying to explain an asymmetry between matter and antimatter called charge-parity (CP) violation that had been observed 8 years earlier in the decays of K and anti–K mesons. Kobayashi and Maskawa found that if there were six quarks, then there would be enough theoretical wiggle room so that, in particle decays, effects conceptually akin to the interference between waves could create differences between matter and antimatter.

Their scheme was confirmed to high precision when, starting in 1999, experimenters at KEK and the Stanford Linear Accelerator Center in Menlo Park, California, studied decays of B mesons, which contain bottom quarks and are the only other particles so far to exhibit CP violation. That was both a triumph and a disappointment. The Kobayashi-Maskawa "mechanism" produces too little CP violation to explain the bigger mystery of why the universe contains so much matter and so little antimatter. So, many physicists had hoped to see discrepancies that would lead to a more complete theory.

Even Kobayashi says, "in the sense that a deviation is a clue to new physics, then, of course, it's desirable." Nobels aside, science's most coveted prize is still a deeper understanding. **–ADRIAN CHO**

With reporting by Dennis Normile in Tokyo.

NOBEL PRIZE IN CHEMISTRY

Three Scientists Bask in Prize's Fluorescent Glow

Early in the summer of 1961, a young Japanese organic chemist named Osamu Shimomura wedged himself into a station wagon packed with lab equipment and three other passengers and drove across the United States looking for the secret of what makes certain jellyfish glow in the dark. The work was pure curiosity-driven basic research, Shimomura says. But his discovery—a luminescent protein known as green fluorescent protein (GFP)—blossomed into one of the most powerful imaging tools for molecular biology. Last week, it earned Shimomura and two Americans—Martin Chalfie of Columbia University in New York City and Roger Tsien of the University of California, San Diego—this year's Nobel Prize in chemistry.

Shimomura, who retired in 2001 from the Marine Biological Laboratory in Woods Hole, Massachusetts, set out from Princeton for San Juan Island off the coast of Washington state to collect samples of the jellyfish *Aequorea victoria*, whose outer edge glows green when the jellyfish is agitated. Initially, Shimomura, working with Princeton University biologist Frank Johnson, isolated a blue luminescent protein they called aequorin. But almost in passing, their 1962 paper describing aequorin also mentioned that they had found another protein, later called GFP, that puts out a soft green glow. "I had no idea" GFP would go on to become such a major tool for biologists, says Shimomura, who continues to study bioluminescence in a lab in his home.

Decades later, Douglas Prasher, a biologist then at the Woods Hole Oceanographic Institution in Massachusetts, did get an inkling of GFP's future utility. Unlike aequorin and other bioluminescent proteins, GFP doesn't need other proteins or cofactors to glow. That property raised the possibility that GFP's light-emitting capability could be transferred to other organisms by outfitting them with just a single extra gene. In a 1992 paper in *Gene*, Prasher reported sequencing and cloning the gene for GFP. Prasher and others later tried inserting the gene and expressing it in bacteria, without success.

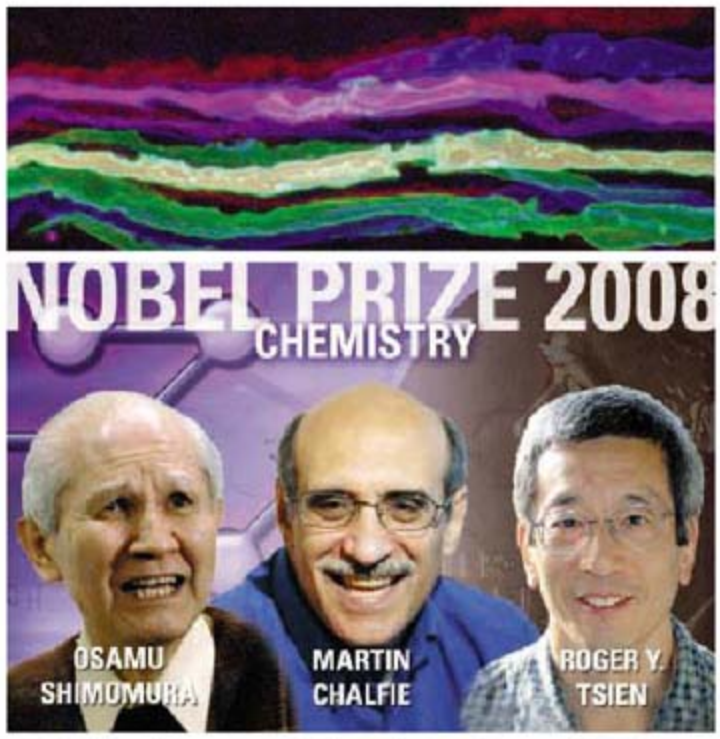

Bright idea. Shimomura, Chalfie, and Tsien discovered luminescent proteins that have cast a new light on cells and tissues (*top*).

In 1994, Prasher teamed up with Chalfie and three other colleagues. The team reported in *Science* that they had successfully cloned the gene for GFP into *Escherichia coli* bacteria and the *Caenorhabditis elegans* worm and could use its luminescence to track the expression of neighboring genes (*Science*, 11 February 1994, p. 802). The result set off an avalanche of interest in using GFP as a marker to investigate everything from how cells develop to what makes cancer cells metastasize. The fact that Prasher didn't share in the Nobel, Chalfie says, "is a very bittersweet aspect to this award."

But Chalfie and others agree that Tsien also richly deserves the recognition. Over the past 2 decades, Tsien has created an extended family of GFP relatives that fluoresce in a palette of colors across the visible spectrum. These enable biologists today to track the expression of multiple genes and other molecules inside cells simultaneously. Tsien says he periodically considers moving on from making fluorescent proteins, but the steady progress in the field "isn't making it easy to give it up."

"The fluorescent proteins have revolutionized medical research," says John Frangioni, an oncologist and imaging expert at Harvard Medical School in Boston. Last year, more than 12,000 papers reported using GFP and other fluorescent proteins, according to Marc Zimmer, a chemist at Connecticut College in New London whose book *Glowing Genes* recounts the discovery of fluorescent proteins. Today, GFP and other fluorescent proteins "are probably as important as the development of the microscope," he says. That underscores the value of basic research: If Shimomura's pursuit of jellyfish fluorescence were funded today, Zimmer says, it would be more likely to earn scorn than anything else. It would be "a great candidate for the Ig Nobels."

–ROBERT F. SERVICE

CREDITS: (TOP) LIVET, DRAFT, WEISSMAN, SANES, AND LICHTMAN; HARVARD UNIVERSITY, CAMBRIDGE MA; (BOTTOM, LEFT TO RIGHT) ADAM HUNGER/REUTERS/LANDOV; CHIP EAST/REUTERS/LANDOV; UCSD

Q&A:

China's Scientist Premier

In a rare one-on-one interview, Premier Wen Jiabao spoke with *Science* about China's efforts to ground its economic and social development in sound science

BEIJING—2008 has been a roller-coaster ride for China and for Premier Wen Jiabao. Recent highs were the spectacular Olympics and the successful space walk late last month during the Shenzhou-7 mission, a key step toward China's aspirations of building a space station and sending astronauts to the moon. Lows included the Tibet riot, a devastating earthquake in Sichuan Province, and the tainted milk scandal.

In 2003, early in his first term as head of China's government, Wen promoted measures to address the spread of AIDS and the emergence of SARS. His leadership qualities were tested again after the 12 May Wenchuan earthquake. Within hours, Wen was on the scene, rallying rescuers and comforting victims.

Wen led the earthquake response with technical authority few politicians anywhere could match. The Tianjin native studied geological surveying as an undergraduate and geological structure as a graduate student at the Beijing Institute of Geology from 1960 to 1968, then spent the next 14 years with Gansu Provincial Geological Bureau in western China. In the 1980s, Wen rose through the ranks of the Communist Party and became vice premier of the State Council, China's Cabinet, in 1998 and premier in 2003. Wen began a second 5-year term as premier last March.

In a 2-hour conversation with *Science* Editor-in-Chief Bruce Alberts at the Zhongnanhai leadership compound in the heart of Beijing on 30 September, Wen, 66, spoke candidly and forcefully, without notes, on everything from social and economic development being the "wellspring" of science and technology to cultivating scientific ethics and reducing China's reliance on fossil fuels. Here are highlights edited for clarity and brevity; a more complete version is posted on the *Science* Web site.

–HAO XIN AND RICHARD STONE

Online
sciencemag.org
A more complete Q&A is linked to this article online.

Bruce Alberts: *You were famous all over the world for going to the site of the earthquake as a professional geologist immediately afterwards and having a great effect on China's response. Could you tell us more about your response to the earthquake and what you see in the future in the way of earthquake protection for China?*

Wen Jiabao: When the Wenchuan earthquake occurred on 12 May, I was sitting in my office. Beijing shook, too. My instinct told me it was an earthquake. I instantly knew this disaster would affect a large area and the devastation would be severe.

I decided to go to the scene immediately. I understood clearly the importance of the [initial] 72 hours and especially the importance of the first day in saving people's lives. Simply put, the faster the better.

Within 3 days, we mobilized a force of more than 100,000 people and rescued some 80,000 from underneath the rubble. Often it is the inattention to aftershocks that causes more severe damage than the main shock. This required us to mobilize the residents to leave their homes and to find shelter.

More than 100 quake lakes were formed, the largest of which was Tangjiashan quake lake, which contained 300 million cubic meters of water. A possible bursting of the dammed-up quake lake would endanger large cities such as Mianyang and more than 10 million people along the path of the water. I went to the site of the quake lake many times and, together with engineers and experts, researched technical solutions and decided to solve the quake-lake problem quickly, safely, and efficiently. We dealt with perhaps the biggest quake lake in the world very success-

CREDIT: LIU WEIBING/XINHUA PRESS/CORBIS

Taking charge. Hours after the Sichuan earthquake struck, Wen was on the scene.

fully; not a single person was injured or died.

We need to gradually restore life, production, and ecological function in the region. This is a very arduous task.

B.A.: *Will new buildings in this area be built in a special way to make them highly resistant to future earthquakes?*

W.J.: We must establish building codes according to the magnitude and intensity of possible earthquakes in this region. Especially for public buildings such as schools and hospitals, we need to apply even safer standards, to assure parents and make children feel at ease.

B.A.: *In the United States, we read every day about what you were doing and the earthquakes ... but also how people came as volunteers from all over China to try to help.*

W.J.: We put into practice the principle of opening to the outside and announced news about the earthquake in real time to China and also to the world. The reason we did this is to tell people ways to avoid harm and help them properly settle [in shelters].

B.A.: *I assume that what you did in the earthquake is related to your new campaign to implement something you call "The Scientific Outlook on Development." I think most of us don't understand exactly what that is. Could you explain what the plans are and how Chinese scientists are going to contribute?*

W.J.: The number-one principle is to put people first. The second is comprehensive development, the integration of economic development with social development, the integration of economic reform with political reform, the integration of an opening-up and inclusive approach with independent innovation, and the integration of advanced civilization with traditional Chinese culture. Thirdly, we need to resolve the disparities—rich-poor disparity, regional disparity, and urban-rural disparity—in our country's developmental process. Fourthly, sustainable development: That is, to meet the challenges of population, resources, and environmental protection faced by a population of 1.3 billion in its modernization process. We want to achieve sustainable development by adopting a resource-conserving and environment-friendly approach. These four goals cannot be achieved without science and technology or without innovations.

B.A.: *We just published a major article from China (Science, 19 September, p. 1676) that shows that your transgenic cotton, used in your country, has reduced the need for pesticides not only for the cotton but also on other crops in the vicinity.*

W.J.: You know, 10 years ago, we did not have this transgenic technology in cotton plants. Back then, the cotton bollworms would not die even when immersed in pesticides. Since we began transgenic engineering of cotton, the plants not only increased their ability to resist bollworms but also increased yield. Therefore, I strongly advocate making great efforts to pursue transgenic engineering. The recent food shortages around the world have further strengthened my belief [in developing such technologies].

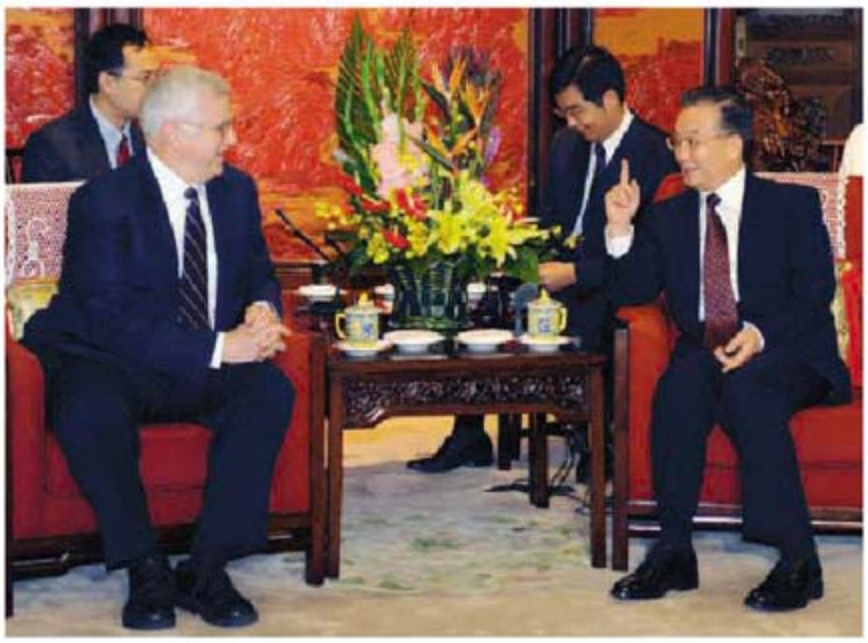

Meeting of the minds. Bruce Alberts and Wen Jiabao share a light moment during their 2-hour discussion of China's scientific challenges.

CREDIT: HUANG JINGWEN/XINHUA NEWS AGENCY

B.A.: *As you know, in Europe there's been a big reaction against transgenic crops, and this has affected the use of this important technology all across Africa as well.*

W.J.: Don't mix transgenic science with trade barriers. That would block the development of science.

B.A.: *May I turn to the issue of your attempts to create a more innovative system, which, of course, means you must attract innovative, talented people to China and train your own people to be innovative as well as smart. How is that going?*

W.J.: This has two aspects. One is we need to cultivate our own large numbers of innovative talents. This needs to start with children, to develop independent thinking from a young age. After they enter secondary schools and universities, there needs to be a free environment to enable them to develop creative thinking and critical thinking. I often say that to raise a question or to discover a problem is more important than solving a problem. This is exactly the kind of talents we need.

Secondly, we also need to integrate closely science and technology with economic and social development, because science and technology finds its wellspring in economic and social development. That's why we strongly push for integration of production, academic study, and research.

Thirdly, our scientists need to cultivate scientific ethics; most importantly, they need to uphold the truth, seek truth from facts, be bold in innovation and tolerant to failure. Only science and the spirit of seeking truth from facts can save China. I firmly believe in this.

We hold fast the policy of opening up to the outside world. To bring in the best brainpower and scientific and technological talents through opening up is most important.

From this perspective, scientists can leap over barriers of ideology and national boundaries to serve all of humanity. I can assure you that we will certainly create a good environment for scientists from the outside to work in China. But I don't believe this is the main thing. They should feel that they have the right conditions to develop their careers in China, that they are respected by China, that the results of their work are respected by China. This will require us to protect their independent creative spirits and intellectual-property rights.

B.A.: *In the United States, we often talk about the fact that the real innovation, if we look backwards, comes from fundamental science, basic science, that was done 20 to 25 years earlier. When I visited the Ministry of Science and Technology, I was told that China's investment in what we call basic research has been fixed at 5% of total research investment. Do you think that is the right number?*

W.J.: Personally, I attach great importance to research in fundamental sciences because I believe that no applied or developmental research can do without basic research as the wellspring and driving force. But, in this world of ours, often because of material gains and immediate interests, it is easy to neglect basic research. This should be avoided. In recent years, we have continuously increased

the level of support, but I think the [investment] ratio is still insufficient.

B.A.: *One of the things that I think is very impressive about China is the extent to which Chinese-Americans feel a great sense of belonging also to China. There's a very effective organization of Chinese scientists in the United States dedicated to helping China develop its own science. This is unusual—other countries do not have this kind of loyalty of their scientists to their homeland.*

W.J.: Our policy is to let them come and go freely. They can serve the motherland in different ways. We impose no restrictions on them and adopt a welcoming attitude.

B.A.: *As you probably know, the National Institutes of Health has put a very strong emphasis lately on supporting innovative young scientists. I met with many wonderful young scientists in China already, both students and young faculty, and having those kinds of opportunities would be very encouraging for them.*

W.J.: We should pay more attention to young scientists. I should say that we haven't done enough in this respect. In the future, we will definitely increase support for young scientists.

B.A.: *Your response to the milk crisis was very impressive, and it still needs, of course, a lot of attention. That terrible crisis awakens the need for more efforts in food safety, more broadly. Do you have new plans for food-safety protection in China?*

W.J.: We feel great sorrow about the milk incident. We feel that although problems occurred at the company, the government also has a responsibility. The important steps in making milk products—production of raw milk, collection, transportation, processing and making formula—all need to have clear standards and testing requirements and corresponding responsibilities, up to legal responsibilities. I once again solemnly emphasize that it is absolutely impermissible to sacrifice people's lives and health in exchange for temporary economic development. Food, all food, must meet international standards. Exported food must also meet the standards of importing countries. We have decided that the Ministry of Health will have main oversight responsibility over food safety.

B.A.: *There's another very important area in which scientists and engineers must collaborate all over the world, and that, of course, is in developing better ways to use and obtain energy. We have a world crisis with greenhouse gases and shortages of resources. What we do in China and the United States will be central with regard to how we treat this planet we're on and make sure that we don't destroy it. What are China's plans now for energy usage and development?*

W.J.: China is a main energy consumer and, therefore, is also a big greenhouse gas emitter. We must use energy resources rationally and must conserve. This needs us to adjust our economic structure, transform the mode of development, to make economic development more dependent on progress of science and technology and the quality of the work force.

We need to take strong measures, including economic, legal, and administrative measures when necessary, to restrict high energy consuming and heavily polluting enterprises and encourage the development of energy conserving and environmentally friendly enterprises.

Spilt milk. Wen, expressing sorrow, promises new food regulations after melamine-tainted milk poisoned thousands of babies.

Now every year, China produces about 180 million tons of crude oil and imports about 170 million tons. China's coal production exceeds 2.5 billion tons a year. This kind of huge consumption of energy, especially nonrenewable fossil fuel, will not be sustainable.

We have established a goal that our GDP [gross domestic product] growth every year must be accompanied by a 4% decrease in energy consumption and a 2% reduction in COD [chemical oxygen demand] and sulfur dioxide emissions every year. We will also adopt various measures to reduce the use of oil and coal in order to reduce the emission of greenhouse gases, including energy-conserving technologies and carbon-capture technologies.

We have only been industrializing for several decades, while developed countries have been on this road for over 200 years. But we will now begin to shoulder our due responsibilities, namely, the common but differentiated responsibilities set forth in the United Nations Framework Convention on Climate Change and the Kyoto Protocol.

B.A.: *The U.S. and China have a special role to play by working together. I wonder if we could imagine a really large-scale joint effort on issues like carbon capture. I know we're working on that in the United States, you're working on it in China, but working closely together on some of these things might make progress more rapid. It would also be a great symbol, for the world, that we are seriously, both of us, taking this issue to heart and are really going to do something about it.*

W.J.: China and the United States have just signed an agreement on a 10-year collaboration in energy conservation and adapting to climate change. This is a new highlight in our bilateral cooperation.

I agree to strengthen our cooperation. We can send a message to the world: We will make joint efforts to protect our common habitat.

B.A.: *Another area where I think we can be effective is using science for diplomacy. Scientists from all nations can work together effectively, even when their governments don't agree. I wonder if there is an enhanced role you might seek for cooperation of scientists, including China and the United States, with North Korean scientists who seem to be so isolated, and whether building new bridges to North Korea that way, through our scientific communities, might help the cause of world peace.*

W.J.: I believe that's entirely possible. Scientists from all over the world share the same desires and characteristics in their pursuit of scientific research, respect for science, and seeking truth through facts. Strengthening their collaboration and association will certainly make it easier to build consensus and mutual trust.

Secondly, the work scientists do has become increasingly relevant to economic and social development and everyday life: for example, the Internet. Therefore, exchanges and collaborations between scientists can help promote exchange and cooperation in economic and social realms between countries. More scientific language and less diplomatic rhetoric may make this world even better.

CREDIT: D. WONG/EPA/CORBIS

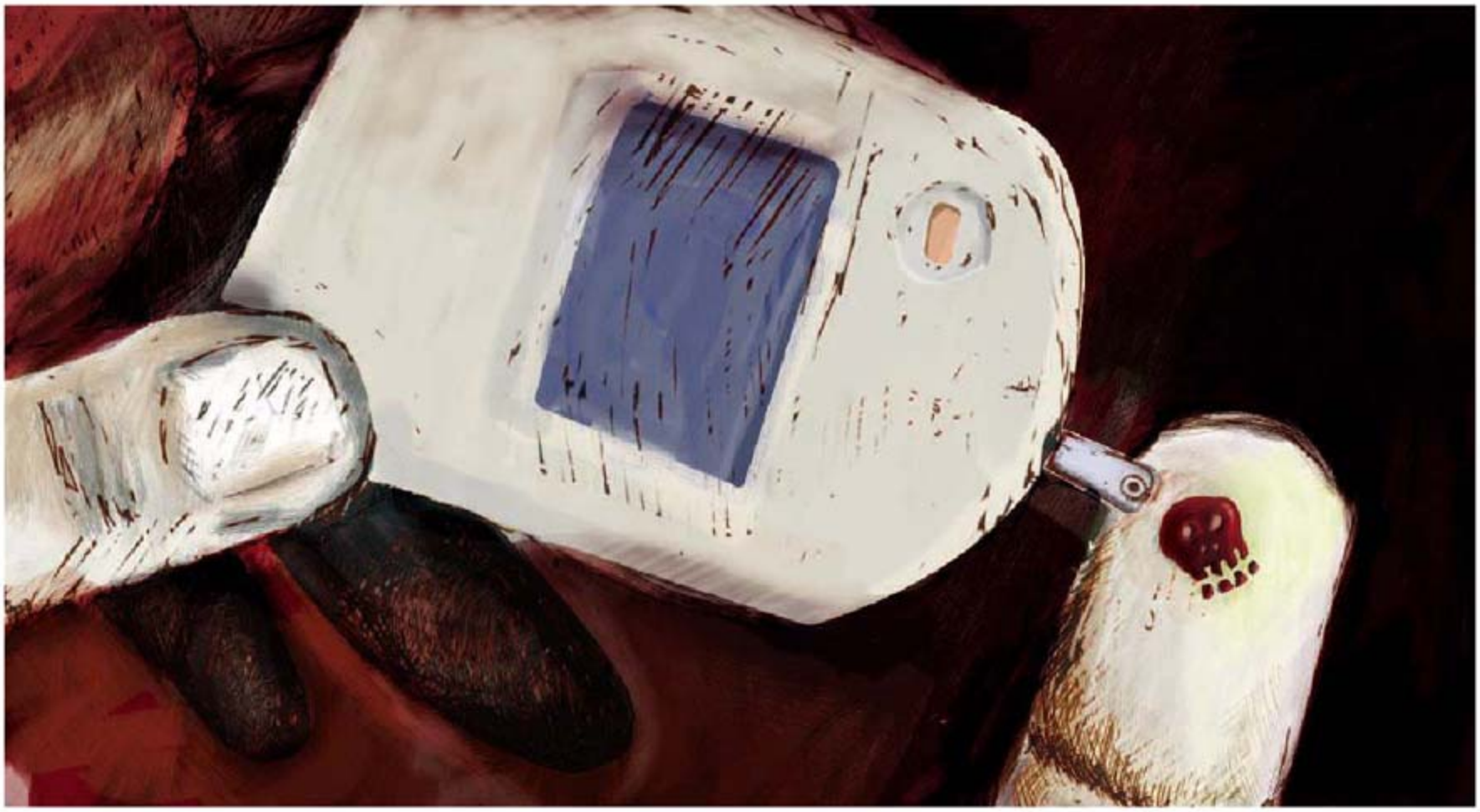

CREDIT: McDAVID HENDERSON

DIABETES

Paradoxical Effects of Tightly Controlled Blood Sugar

Researchers are puzzling over recent trials that had great success in lowering blood sugar in type 2 diabetics but no success in reducing deaths from cardiovascular disease

Last January, the steering committee overseeing a clinical trial on diabetes and heart disease received some disturbing news. One of the interventions being tested—intensive control of blood sugar in patients with type 2 (formerly called adult onset) diabetes—was anything but benign: The death rate among subjects undergoing the intensive therapy was higher than among those following the standard blood sugar–lowering strategy to which it was being compared. On 7 February, this part of the so-called ACCORD study (for Action to Control Cardiovascular Risk in Diabetes) came to an end, 17 months prematurely.

By the time the ACCORD collaboration released detailed results in early June, it was one of three major trials—comprising in total nearly 23,000 type 2 diabetics—reporting that lowering blood sugar in diabetics to levels considered normal provides no benefit in preventing heart attacks and strokes. If the ACCORD trial was any indication, more intensive therapy might even do more harm than good.

The three trials have intensified debate over what David Nathan, a diabetes specialist at Harvard Medical School (HMS) in Boston, calls "one of the most contentious issues in medicine"—the relationship between high blood sugar and the numerous long-term complications that beset diabetics. The results challenge a long-standing assumption that high blood sugar is the central villain, but they have left the field divided over where to cast the blame.

All three trials—ACCORD, a 20-country study called ADVANCE, and the Veterans Affairs Diabetes Trial (VADT)—were designed to see whether older patients with type 2 diabetes could reduce the risk of heart attacks and strokes—and thereby prolong their lives—by maintaining their blood sugar at near-healthy levels. The clinical results were clear: The trials failed to demonstrate the hoped-for benefit. Why they failed, though, and why ACCORD saw significantly more deaths in the intensive-therapy arm of the study are matters of dispute. "You can reach a lot of conclusions" based on these studies, says Derek LeRoith, an endocrinologist at the Mount Sinai School of Medicine in New York City. "The question is whether anybody concludes anything correctly."

Trouble in the blood

Type 1 diabetics, who lose their insulin-making cells and must take insulin to stay alive, are beset by a host of complications—from eye and nerve damage to extensive, accelerated atherosclerosis and a twofold to fivefold increased risk of dying from a heart attack. Since the 1940s, diabetes specialists have assumed that high blood sugar, or hyperglycemia, was at least partially responsible for these problems. It wasn't until the 1980s, when type 2 diabetes became a relatively common disorder and type 2 patients were living longer, says Nathan, that it became clear that these diabetics suffered many of the same complications.

Diabetologists divide these complications into two categories: macrovascular, including stroke and cardiovascular disease, and microvascular, including kidney disease, blindness, and nerve damage. In 1993, a North American trial, the Diabetes Control and Complications Trial (DCCT), reported that microvascular complications in type 1 diabetics could be delayed and suppressed by keeping blood sugar levels low and under very tight control. In 2005, an

Safe range. Diabetics monitor their blood to avoid high levels of blood sugar, but very low levels—below 70 mg/dL—can be dangerous as well. Clinical studies use a different, long-term measure of blood sugar, the percentage of glycated hemoglobin, or A1c, in circulation.

observational follow-up to DCCT reported that heart attacks and strokes could also be partially prevented.

The question since then has been whether the same cause and effect could be demonstrated in type 2 diabetics, who develop a resistance to the insulin they secrete. "There has always been a fair amount of evidence that chronic hyperglycemia in type 2 diabetics is associated with increased rates of cardiovascular events," says William Duckworth, co-chair of the VADT study and a diabetes special-zist at the Carl T. Hayden VA Medical Center in Phoenix, Arizona.

A range of biological mechanisms point to hyperglycemia as a possible cause. "There are several ways that glucose can alter vascular structure and function," says Duckworth. The accumulation of glucose molecules permanently bound to structural and functional molecules may contribute to stiffening of the arteries and the oxidation of low-density lipoprotein particles, an early and necessary step in the formation of atherosclerotic plaques. Hyperglycemia can also theoretically alter vascular function by altering oxygen delivery and nitric oxide in the cell, Duckworth adds. "There's also some suspicion it might cause turbulence in the vascular system, which can lead to increased clotting."

For decades, the notion that high blood sugar is a causal agent in cardiovascular disease remained a hypothesis; diabetologists wanted proof that lowering blood sugar in type 2 diabetics would prevent disease. "The only way to prove that halfway definitively is to take a group of people and lower their glucose and see if that decreases these macrovascular events," says Duckworth. "These three studies are unfortunately unanimous in saying, 'No, it doesn't.'"

What failed?

Interpreting the negative results is complicated, however, partly because the methods of controlling blood sugar varied from study to study and even patient to patient. The best measure of blood sugar control is a variable called hemoglobin A1c, the percentage of hemoglobin molecules in the blood that are bound to a glucose molecule, or glycated. Measuring blood sugar directly provides an indication of current blood sugar levels; hemoglobin A1c reflects the levels over the course of a few months. In healthy individuals, less than 6% of hemoglobin is glycated. In untreated diabetics, the levels are typically above 9.5% and can be far higher. Levels of 7.5% to 8.5% are reachable with standard insulin and insulin-sensitizing therapy. The ACCORD, ADVANCE, and VADT trials all compared these standard blood-sugar-lowering strategies with intensive therapies that lowered hemoglobin A1c below 6.5%.

The obvious explanation for why the three studies came up negative is that the hypothesis that high blood sugar causes macrovascular complications in type 2 diabetes is simply wrong. But these studies cannot absolutely rule it out; there are too many variables. Type 2 diabetes is associated with a spectrum of metabolic disorders, all of which are risk factors for cardiovascular disease: insulin resistance, obesity, hypertension, and cholesterol and lipid abnormalities known as diabetic dyslipidemia.

In all three trials, the investigators aggressively treated hypertension and diabetic dyslipidemia in all the subjects. As a result, mortality rates were so low that the trials may have had insufficient statistical power to demonstrate a beneficial effect from lowering blood sugar alone.

The ACCORD trial was planned with the expectation that 10% of the subjects would have a heart attack or stroke over 3.5 years. Instead, only 3% to 4% did. The same trend held true for ADVANCE. Its results were consistent with no benefit at all, says Anushka Patel, a co-chair of the ADVANCE trial and cardiologist at the George Institute for International Health in Sydney, Australia, but because of their statistical weakness, they were also "potentially consistent with a benefit on macrovascular disease." Even the ACCORD trial, despite being halted prematurely, showed a mild but insignificant benefit on nonfatal heart attacks and strokes and all deaths from cardiovascular disease.

One possibility is that, like the DCCT study of type 1 diabetics, these trials simply didn't run long enough to see a benefit. Just last week, British researchers published the latest results from the United Kingdom Prospective Diabetes Study (UKPDS) suggesting that this might be the case. UKPDS began in the late 1970s, comparing dietary therapy in type 2 diabetics with drug therapy that lowered hemoglobin A1c levels from 7.9% to 7%. The initial 5-year follow-up, published in 1998, reported no benefits on macrovascular complications. Now, after an average of 17 years of follow-up, slight reductions in heart attacks and mortality were seen. What caused this "legacy effect," however, was still open to speculation because glycemic control in the two groups had been identical for all but the first year of the study.

Lower may not be better

The most intriguing question is why, even with a slightly decreased risk of nonfatal heart attacks and strokes, the intensive-therapy subjects in the ACCORD trial had an increased risk of death. Here, again, hypotheses are plentiful, but not so the evidence to nail them down.

The goal of the ACCORD trial was to lower hemoglobin A1c levels in the intensive-therapy group below 6% rather than 6.5% in the ADVANCE and VADT trials. To do so, as LeRoith says, "they threw the kitchen sink" at these subjects. They were given more drugs than those in the intensive-therapy arms of ADVANCE or the VADT trial, at higher does, in more combinations, and more insulin itself.

As a result, one possible explanation for the excess deaths in ACCORD is that intensive therapy resulted in blood sugar so low—a condition known as hypoglycemia, defined as blood sugar below 70 milligrams/deciliter (mg/dL)—that it in turn caused deaths that would not necessarily have been identified as heart attacks or strokes. When blood sugar dips into the hypoglycemic range, it activates parasympathetic nerves, triggering hormonal responses that include secretion of

CREDIT: JUPITER IMAGES

epinephrine, glucagon, growth hormone, and cortisol, all aimed at limiting glucose uptake and exit from the bloodstream. It's possible, says Graham McMahon, a diabetes specialist at HMS and Brigham and Women's Hospital in Boston, that in the older type 2 diabetics recruited by ACCORD—with longer-standing disease and poorer underlying vascular function—these compensatory responses, combined with nerve damage in the autonomic nervous system, triggered fatal cardiac arrhythmias.

"We know when we drive people's blood sugar down this far," says William Friedewald, a biostatistician at the Columbia University Mailman School of Public Health and chair of the ACCORD Steering Committee, "they have a much higher rate of hypoglycemia and that, in fact, is what we observed in ACCORD." But when the ACCORD researchers searched for an association in their data between hypoglycemic events in the subjects and mortality, they came up empty.

But hypoglycemia still can't be ruled out. The more intensive the blood-sugar control in diabetics, says Stephen Davis, a diabetes researcher at Vanderbilt University in Nashville, Tennessee, the more frequently a patient suffers a hypoglycemic event, even a mild one, and the more likely they will be unaware of future hypoglycemic events. "Even quite minor levels of hypoglycemia," he says, "can down-regulate defenses against subsequent hypoglycemia. You get a vicious cycle whereby hypoglycemia begets more hypoglycemia." In these cases, blood sugar can drop to 30 or 40 mg/dL, without evoking compensatory responses or noticeable symptoms. In this hypothesis, the researchers running the trial would be unaware of many hypoglycemic events and therefore unable to link them directly to the death. "The data we have in ACCORD shows no tie-in to hypoglycemia," says Friedewald, "but it may still be a factor."

Is it the insulin?

Another possible explanation for the excess deaths in ACCORD is that some drug or combination of drugs turned out to have fatal side effects. One prime suspect is a drug called rosiglitazone, an insulin-sensitizing drug marketed by GlaxoSmithKline as Avandia and used widely to treat type 2 diabetics. Last year, both *The New England Journal of Medicine* and the *Journal of the American Medical Association* published meta-analyses reporting that rosiglitazone use was associated with an increased risk of heart attacks and, perhaps, an increased risk of death. Neither ACCORD nor the VADT trial, however, could find such an association. The researchers in the ADVANCE trial, says Patel, are not planning to do that analysis because of the many ways it can be confounded by other factors.

The most controversial hypothesis to explain the excess deaths in the intensive-therapy arm of ACCORD is that insulin therapy itself was responsible. Since the 1980s, when type 2 diabetes was widely accepted as a disease of insulin resistance rather than insulin deficit, diabetes specialists have debated whether macrovascular complications are caused primarily by high blood sugar or by chronically elevated insulin levels. This condition, known as hyperinsulinemia, arises when the beta cells of the pancreas compensate for insulin resistance elsewhere in the body by secreting ever-greater amounts of insulin. Many of the other metabolic disorders that accompany type 2 diabetes—obesity, hypertension, and diabetic dyslipidemia—may in turn be caused by hyperinsulinemia. "The idea has been around for a long time that insulin itself is a problem," says Friedewald, "and certainly people in the intensive group in ACCORD had higher exogenous insulin levels than people in the standard group."

Ralph DeFronzo, chief of the Diabetes Division at the University of Texas Health Science Center in San Antonio, is a leading proponent of the idea that heart disease in type 2 diabetics is not caused by high blood sugar but by insulin resistance, hyperinsulinemia, and the metabolic disorders that follow. "When you're treating and trying to control type 2 diabetes," says DeFronzo, "you have to understand that the basic defect is insulin resistance. You have to give enormous amounts of insulin to overcome that resistance, and when you do that, you activate growth-promoting inflammatory pathways." These in turn have direct effects on blood vessels and so can potentially cause or exacerbate cardiovascular disease, leading to heart attacks and death.

McMahon says that diabetologists don't like to think about this possibility because insulin is often lifesaving for type 2 diabetics. As these diabetics age, their beta cells eventually fail to maintain the excessive insulin secretion necessary to lower blood sugar in the face of insulin resistance. In those cases, says McMahon, insulin therapy "is the only rational treatment and the only treatment that works."

At the moment, the insulin hypothesis remains speculative. The ACCORD data revealed no link be-tween mortality and insulin use, says Friedewald, but this could be a product of the various biases and confounding factors inherent in these kinds of studies. "The fundamental problem in this area of investigation," says Harvard's Nathan, "is that the studies, almost by design, build in confounding elements. Whenever you're interpreting clinical trials, there's always other consequences of the intervention that affect the outcome. … The ideal study would have patients treated with exactly the same profile of medications, with the exception of one drug that you would ramp up in one group but not the controls. For example, if you put one group on a lower dose of insulin and one on a higher dose, that would be closer to an ideal trial."

Without such studies, the only thing that can be said with any confidence about the ACCORD, ADVANCE, and VADT results, as Friedewald says, is that they are more evidence against the hypothesis that high blood sugar is a fundamental cause of heart disease and stroke in type 2 diabetics.

–GARY TAUBES

ACCORD TRIAL: GLUCOSE LOWERING

	Intensive therapy Number (5128)	Percent	Standard therapy Number (5123)	Percent	Hazard ratio Intensive vs. Standard
Primary Outcome (First occurrence of nonfatal myocardial infarction, stroke, or death from cardiovascular causes)	352	6.9	371	7.2	0.90
Secondary Outcome					
Death, any cause	257	5.0	203	4.0	1.22
Death, cardiovascular causes	135	2.6	94	1.8	1.35
Nonfatal myocardial infarction	186	3.6	235	4.6	0.76
Nonfatal stroke	67	1.3	61	1.2	1.06
Fatal or nonfatal congestive heart failure	152	3.0	124	2.4	1.18

SOURCE: ACCORD STUDY GROUP, *THE NEW ENGLAND JOURNAL OF MEDICINE*, 12 JUNE 2008

Got milk? People in central Asia still milk mares (*left*), and residues on ancient potsherds (*inset*) show that this practice goes way back.

Trail of Mare's Milk Leads To First Tamed Horses

Herds of horses still race across the steppes of Northern Kazakhstan, and the people in that harsh environment have long depended on the animals, riding them, eating their meat, and exploiting their skins for clothes. Indeed, the oldest accepted evidence for horse domestication—equine bones and chariots found together and dated to 2000 B.C.E.—come from the region. Now, traces of ancient mares' milk may extend Northern Kazakhstan's equine roots another 1500 years.

Locals today still consume a fermented drink called koumiss made from mare's milk. Koumiss tastes "horrible" to her Western palate, confesses chemistry Ph.D. student Natalie Stear of the University of Bristol in the U.K., but an ancient version may have yielded some appetizing data: Stear reported at the meeting that she found the isotopic signature of mare's milk on 5500-year-old pottery fragments from Kazakhstan. "It is the smoking gun for horse domestication, since no one would attempt to milk a wild mare," says anthropologist Sandra Olsen of the Carnegie Museum of Natural History in Pittsburgh, Pennsylvania.

Many researchers believe people began domesticating horses about 4000 B.C.E., but finding clear evidence of that has been difficult. The shards Stear analyzed were made by the Botai, who dwelled in Central Asia between 3700 and 3100 B.C.E. In the 1990s, Olsen's team excavated one of their villages, revealing tons of animal bones, 90% of them equine. Olsen and others digging at Botai sites have uncovered other suggestive evidence of horse domestication, including signs of corrals and bit wear marks on horse teeth. But the bit wear conclusions have been hotly disputed, and some argued that the Botai primarily hunted wild horses for meat.

Stear's attempt to settle the issue evolved out of her work in Richard Evershed's group at Bristol, which has pioneered the technique of identifying milk residues on ancient pottery by carbon-isotope analysis. The varying amounts of such isotopes within lipids that permeate the vessels can sometimes reveal what species the fat came from and whether it was from meat or milk. In a paper that appeared online in *Nature* in August, for example, Evershed's team pushed the earliest dairy use back by 2000 years, to about 6050 B.C.E., after detecting milk fats in ancient Turkish pottery shards.

Stear used carbon isotopes to confirm the presence of equine fats on about 50 Botai shards, but the method couldn't distinguish between lipids from milk or meat. So she tested local horse meat and koumiss and confirmed a hypothesis posed by Evershed and Alan Outram of the University of Exeter, U.K.: that horse meat and milk contain different amounts of the hydrogen isotope deuterium. For reasons related to the isotope's heavier weight, summer rains in the region contain much more deuterium than winter precipitation. Because mares are only milked after they foal in the spring, researchers theorized that the isotope would be concentrated in milk, whereas horse meat's deuterium signal would be averaged over the course of each year.

Testing the ancient potsherds, Stear found that five had the horse-milk deuterium signature. "The way she did it was quite elegant," says Oliver Craig, a biomolecular archaeologist at the University of York. Stear also notes that colleagues have found new signs of bit use on the Botai horse teeth, giving her greater confidence that the animals were domesticated.

Still, some are reserving judgment. Marsha Levine of the McDonald Institute for Archaeological Research in Cambridge, U.K., has argued that the Botai primarily hunted wild horses, but she accepts that the deuterium evidence suggests that at least some horses there were domesticated. Levine cautions, however, that the new technique must be independently vetted before the Botai horses are definitively tamed.

Old Bones Reveal New Signs of Scurvy

By some estimates, scurvy killed or debilitated millions of early sailors before it was recognized that vitamin C can ward off the condition's connective tissue degradation, which results in spotty skin, gum disease, and bleeding throughout the body. Many researchers suspect that other ancient peoples were also vulnerable to scurvy, such as those facing famine or early farmers who ate little wild fruit as they transitioned to a cereal-based diet.

CREDITS (LEFT TO RIGHT): ALAN K. OUTRAM; VICTOR ZAIBERT, NATALIE STEAR

But such ideas are hard to prove because only the most severe cases leave telltale lesions on the slow-growing bones of adults.

At the meeting, however, postdoctoral researcher Hannah Koon of the University of York, U.K., described a new way to detect signs of scurvy in human skeletons. "Making a diagnosis with what you see on a skeleton is really problematic," says Megan Brickley of the University of Birmingham, U.K., a forensic anthropologist who specializes in scurvy and skeletal diseases. "This technique could potentially have a huge impact."

Koon focuses on collagen, the most abundant protein in the human body and the molecule at the heart of scurvy. Collagen molecules consist of three long chains of about 1000 amino acids, which twist and bind together and then pack into fibers that are the building blocks of bones and connective tissue. Collagen chains contain numerous proline amino acids, and for the fibers to become stable, many prolines must have hydroxyl groups attached to them through the work of an enzyme. For this hydroxylation, explains Koon, "one of the cofactors needed is vitamin C."

The prevailing wisdom had been that certain prolines in a collagen molecule were always hydroxylated and others never were. But in studying different collagen molecules from the same samples of modern cow and human bones, Koon found that certain prolines are only hydroxylated sometimes. She hypothesized that scurvy would alter how frequently these variable prolines are hydroxylated. Tests on guinea pigs raised on a low–vitamin C diet supported the idea.

Now Koon has begun to extend the work to humans, testing skeletons from a group of 17th to 18th century Dutch whalers excavated from the permafrost in the 1980s by George Maat of Leiden University in the Netherlands. Although they lack major bone lesions, most such sailors described scurvy symptoms in diaries or had scurvy-induced hemorrhages still evident in their well-preserved bodies. If the collagen assay "can't see scurvy in [the bones of] these guys, you won't see it anywhere," says Matthew Collins, Koon's lab chief.

Koon reported in York that collagen from the first two whalers does indeed reveal fewer hydroxylated prolines. "I'm cautiously optimistic" that the technique will work, she says. After more work on whalers, Koon plans to test bones of British sailors from before and after the turn of the 18th century, when the Royal and Merchant navies began to require sailors to drink lime juice daily to thwart scurvy, a practice resulting in the nickname of Limey.

Hope for the Rhone's Missing Sturgeon

Ancient DNA research typically provides a glimpse into a species' past, but work presented in York showed that it may also help give one species, the European sea sturgeon (*Acipenser sturio*), a new future.

Until the 19th century, this large fish thrived along the coast of Europe and spawned in most of the major rivers from the Baltic Sea to the Black Sea. Once a major source of food and caviar, it was fished almost to extinction. Today, only a few thousand remain, all breeding at a single site, the Gironde estuary, where the French rivers Dordogne and Garonne meet.

Good old days. In 1850, the European sea sturgeon roamed widely (blue) and spawned in many rivers. Today, few survive, but captive-bred larvae (*inset*) may be reintroduced.

SOURCE: MARIO LEPAGE/CEMAGREF; CREDIT: CEMAGREF

Captive-breeding efforts using sturgeon from this site were begun in the 1990s, and last year 11,000 larvae were born from captive-bred fish for the first time. France's Cemagref (Research Institute for Agricultural and Environmental Engineering) released those hatchlings into the Gironde last summer.

Now Cemagref and its partners want to reintroduce their hatchlings to other rivers in which the European sturgeon once swam. The Rhone is an obvious target—or is it? There's little doubt that some kind of sturgeon once densely populated the river, but no one has been sure whether the native Rhone fish was *A. sturio* or the Adriatic sturgeon, *A. naccarii*. The two fish are quite different ecologically—the European sturgeon spends much of its life at sea before briefly visiting rivers to spawn, and the Adriatic sturgeon is more of a freshwater homebody that struggles in sea migrations. Which one should be reintroduced to the Rhone?

In York, Olivier Chassaing of the École Normale Supérieure in Lyon described how he and colleagues used ancient DNA to find out. Researchers had previously analyzed DNA from museum specimens labeled as Rhone sturgeons, but the results were inconclusive. So Chassaing, Patrick Berrebi of the University of Montpellier, and colleagues in the Lyon lab of Catherine Hänni turned to an unusual collection of thousands of sturgeon bones found several decades ago on the Rhone river bank near Arles. Dated to between the 6th and 2nd century B.C.E. and apparently left by people fishing, the bones look like those of modern *A. sturio*. The DNA extracted from them clinched the case, Chassaing reported: All 14 samples tested were from the European sea sturgeon. There was no evidence of its Adriatic relative, or hybrids between the two. "We're convinced there was *A. sturio* in the Rhone," says Chassaing. "Our recommendation is to reintroduce *A. sturio* but not *A. naccarii*."

Although the ancient DNA work can't rule out that *A. naccarii* ever roamed the Rhone, the evidence is good enough for Cemagref fish biologist Mario Lepage, who has worked on the sturgeon recovery plan. Still, he cautions, it may be some time before the European sea sturgeon returns to its former home. He says researchers need to assess whether the modern Rhone is now suitable for young sturgeon and whether their reintroduction would harm species that took the sturgeon's ecological role decades ago. **–JOHN TRAVIS**

LETTERS

edited by Jennifer Sills

Quantifying Coauthor Contributions

FIFTY YEARS AGO IN *SCIENCE*, D. MCCONNELL ARGUED THAT "FOR anything short of a monographic treatment, the indication of more than three authors is not justifiable" (*1*). He was never cited. Coauthor numbers kept rising, and it has been recently suggested that in some fields "multiple authorship endangers the author credit system" (*2*). In 2006, more than 100 papers had over 500 coauthors, and one physics paper had a record 2512 coauthors (*3*). With research groups growing larger (*4*), this trend will continue. Given the increasing interest in the quantification and standardization of scientific impact with various metrics like the *h* index (*5*, *6*) and the growing debate on potential biases (*7*, *8*) and unethical behavior (*4*, *9*, *10*), a standardized method to quantify coauthor contributions is needed (*10*–*13*).

Rarely do all coauthors contribute to a paper equally. However, academic search engines (such as Google Scholar, Scopus, and Web of Science) calculate citations, *h* indices, and rankings without regard to author rank. Quantification of coauthor contributions will motivate coauthors to clarify each person's percent of contribution.

I propose that the *k*th ranked coauthor be considered to contribute 1/*k* as much as the first author. This way, coauthors' contributions can be standardized to sum to one, regardless of the author number or how authors are ranked. Author rank can be different from author order, provided that this is declared in the paper. Multiple authors can have the same rank, as long as this is stated and is reflected in the calculations.

Quantifying coauthors' contributions will encourage a healthy dialogue about the meaning of coauthorship and author rank (*2*, *4*, *10*, *13*), will promote better consideration of author rank in assessing scientific impact, and will lead to improved ways to measure and report coauthor contributions.

CAGAN H. SEKERCIOGLU

Department of Biology, Center for Conservation Biology, Stanford University, Stanford, CA 94305, USA. E-mail: cagan@stanford.edu

References

1. D. McConnell, *Science* **128**, 1157 (1958).
2. M. Greene, *Nature* **450**, 1165 (2007).
3. C. King, *Sci. Watch* **18**, 1 (2007).
4. P. A. Lawrence, *Curr. Biol.* **17**, R583 (2007).
5. J. E. Hirsch, *Proc. Natl. Acad. Sci. U.S.A.* **104**, 19193 (2007).
6. P. Ball, *Nature* **448**, 737 (2007).
7. C. D. Kelly, M. D. Jennions, *Nature* **449**, 403 (2007).
8. D. C. Mishra, *Nature* **451**, 244 (2008).
9. P. A. Todd, R. J. Ladle, *Nature* **451**, 244 (2008).
10. D. Kennedy, *Science* **301**, 733 (2003).
11. R. Hunt, *Nature* **352**, 187 (1991).
12. J. V. Verhagen, K. J. Wallace, S. C. Collins, T. R. Scott, *Nature* **426**, 602 (2003).
13. W. F. Laurance, *Nature* **442**, 26 (2006).

Biofuels: Clarifying Assumptions

THE REPORT BY T. SEARCHINGER *ET AL.* ("Use of U.S. croplands for biofuels increases greenhouse gases through emissions from land-use change," 29 February, p. 1238) provides one scenario for the conversion from a fossil-based energy economy to a bio-based, renewable-energy economy. However, Searchinger *et al.* failed to include several important considerations.

It is inaccurate and misleading to allocate the cutting down of Brazilian rainforest, which is done often for timber production, to biofuels use. The economic signals driving biofuels or agricultural land-use changes are different from the timber-driven economic signals driving land-use change patterns. The deforestation estimates of Searchinger *et al.* are appropriate for biodiesel production in the Far East. A cheaper and more likely use of land for increased biofuels production is the 6 billion acres of underutilized or unused rainfed agriculture land available, according to a Food and Agriculture Organization report (*1*).

Searchinger *et al.* analyze switchgrass as an energy crop when miscanthus and sorghum have much higher yields [a recent study estimated that miscanthus yields are 250% that of switchgrass (*2*)] and would dramatically reduce the demand for land. Furthermore, because these crops have not been optimized for biomass, they are likely to produce substantial further yield increases per acre. Given the theoretical maximum yield of 40 to 50 tons per acre in a region with an average of 40 inches of rain, practical yields of 50 to 60% of this maximum are likely. It has even been suggested that maximum theoretical yield values will be reached and possibly surpassed (*3*).

Searchinger *et al.* assume that crops grown in developing countries will have lower yields. The yields are lower because of low prices and lack of farmer income. In these conditions, farmers cannot afford the best seed crops and other inputs such as fertilizer (*1*). It is likely that if farmer incomes improve, yields will also increase.

Searchinger *et al.* state that "[h]igher prices triggered by biofuels will accelerate forest and grassland conversion there even if surplus croplands exist elsewhere." Energy

CREDIT: JOE SUTLIFF

costs influence the food Consumer Price Index (CPI) three times as much as does the basic price of corn (*4*, *5*). Implying that these price increases are principally caused by biofuels production is inaccurate.

Cellulosic ethanol will probably be so much cheaper to produce (even at $50 per dry ton feedstock costs) that it will displace all corn ethanol based on price alone, thus freeing up much of the more than 20 million acres of land used in 2007 for corn produced for ethanol.

The potential for biomass from other sources is grossly underestimated. If biomass-oriented winter crops were planted on annual crop lands, it would improve land ecology and produce substantial biomass for cellulosic biofuels. A yield of 3 tons per acre on 50 to 70% of our annual crop lands (320 million acres) would yield 480 to 672 million tons of biomass; a yield of 5 tons per acre by 2030 (assuming crop optimization for biomass by then) could yield 800 to 1120 million tons of biomass or sufficient biomass for more than 100 to 145 billion gallons with no additional land use. If corn stover and crop waste are included, even larger quantities of biomass can be made available without land use. Sustainable removal of stover from corn crops is estimated to be between 1.5 and 2.0 additional tons per acre.

The potential-for-waste outline in the U.S. Department of Energy biomass study (*6*) is completely ignored. The study concludes that up to 1.3 billion tons of sustainable biomass can be available "without a significant change in agricultural practices." Additional cellulosic and waste production will result from organic municipal waste, sewage, and other waste sources.

The authors assume that more marginal lands will be used for food cultivation, when in fact "land recovery" can happen with proper crop rotation practices on marginal and degraded agriculture lands and especially with perennial, polycultured energy crops, which are likely to dominate the energy crop field (*7*, *8*).

In allocating land displacement, Searchinger *et al.* fail to account for the most attractive regions in the world, namely, parts of Africa where biomass income is sorely needed.

Furthermore, the baseline for carbon emission costs of biofuels should be incremental alternative sources of new oil like tar sands and oil shales, not an average value of emissions for oil.

VINOD KHOSLA

Khosla Ventures, Menlo Park, CA 94028, USA. E-mail: vk@khoslaventures.com

References and Notes

1. FAO, *World Agriculture Towards 2015/2030: An FAO Perspective* (FAO, Rome, 2003).
2. S. P. Long *et al.*, *Global Change Biol.* **14**, 2000 (2008).
3. S. P. Long *et al.*, *Plant Cell Environ.* **29**, 315 (2006).
4. J. Urbanchuk, "The relative impact of corn and energy prices in the grocery aisle" (LECG Report, 2007); www.ncga.com/news/hotd/pdfs/061407_EthanolAndFoodPrices.pdf.
5. P. A. Sanchez, *Science* **295**, 2019 (2002).
6. R. D. Perlack *et al.*, *Biomass as Feedstock for a Bioenergy and Bioproducts Industry: The Technical Feasibility of a Billion-Ton Annual Supply* (U.S. Department of Energy and U.S. Department of Agriculture, April 2005); http://www.toyncrops.org/reports/Billion%20Ton%20Supply.pdf.
7. D. Tilman *et al.*, *Science* **294**, 843 (2001).
8. D. Tilman, J. Hill, C. Lehman, *Science* **314**, 1598 (2006).
9. Khosla Ventures is an investor in various biofuels startups; a full list can be seen at www.khoslaventures.com/presentations/Flower_Chart.ppt.

Response

ON BALANCE, KHOSLA'S LETTER PROMOTES hope for biofuels that use agricultural and forest residues, cover crops, and municipal

waste, and that therefore do not divert the capacity of productive land. Our Report also encouraged such biofuels. We similarly encouraged a focus on lands that would otherwise provide little food or carbon storage but that might produce ample biofuels. We even cited the U.S. Department of Energy's (DOE's) "billion-ton study," precisely because most of the potential biomass it estimates is waste. Yet DOE's full 1.3 billion tons also relied on diverting millions of hectares of cropland to grow biofuel crops. All cellulosic biofuels are not the same, and policies should support only those that do not use productive land.

Unfortunately, the Food and Agriculture Organization's (FAO's) estimate of roughly 6 billion acres of potential new rain-fed cropland referenced by Khosla in fact consists primarily of the world's wetter forests and grasslands, not "underutilized or unused" agricultural land (*1*). Studies predicting future cropland expansion point heavily to carbon-rich areas in Latin America and sub-Saharan Africa, which contain most of the best potential cropland (*1*, *2*). The U.S. Department of Agriculture now predicts that future food growth will rely more heavily on cropland expansion and less on yield growth than on past growth because cereal yield growth has fallen below 1% per year (*3*), well below the rate of population growth. Khosla correctly notes the capacity to boost yields in many developing countries, but the world must already unleash that capacity to feed a larger, selectively richer, world population while also reducing deforestation. Biofuels should not exacerbate this already imposing challenge.

The plight of the Amazon is a matter of both forestry and agriculture. Typical logging removes a few trees per hectare, causes collateral damage, and facilitates conversion through road-building, but forests regrow carbon if the land is not subsequently converted to agriculture (*4*). Biofuels that use good cropland anywhere in the world raise crop and meat prices and help spur the actual conversion to pasture or cropland by increasing their net economic return.

For cellulosic ethanol grown on corn land, our study found increased greenhouse gas emissions, even with dramatically higher yields (18 tons per hectare) and conversion rates (362 liters per hectare) than now broadly obtainable. As Khosla indicates, researchers using Illinois cropland to grow the hybrid miscanthus giganteus have obtained higher yields, but planting this hybrid requires digging up the roots to sever and then replant the rhizomes, which implies an expensive, slow process of expansion (*5*). Efforts to use seed-producing varieties continue to face obstacles (*5*). Yet even with major breakthroughs that double our assumed biomass yields, cellulosic ethanol grown on corn land would only reduce emissions compared with gasoline by 37% counting land-use change. By avoiding land use change, biofuels from wastes and residues could achieve far greater reductions.

Although Khosla correctly points out that rising crop prices only modestly increase food prices in U.S. grocery stores, the poor around the world eat basic cereals and vegetable oil. Their prices worldwide rose 300 and 400%, respectively, between 2000 and spring 2008 (*6*). Nearly all analyses assign a major role to biofuels (*6*, *7*): Biofuels consumed the vast bulk of the world's growth in cereals and vegetable oil between 2005 and 2007, requiring the world to deplete stocks to meet growing food demand (*8*).

Khosla's high confidence in a quick transition to better biofuels, however welcome, also seems excessive. Even the latest hopeful DOE research plan in 2005 envisions 15 years of research and development before cellulosic production can start to scale up (*9*). Optimistic scenarios predict modestly lower costs after many years (*10*), but some studies conclude that cellulose will indefinitely remain more expensive than corn ethanol (*11*). It will be a great achievement if cellulosic biofuels can supply the 21 billion gallons (79 billion liters) of noncorn biofuel now required by U.S. law in 2022, let alone the additional 15 billion gallons mandated (57 billion liters) that corn ethanol may supply. Yet, because some corn ethanol is cheaper than gasoline at reasonably high oil prices, corn ethanol from existing plants will probably remain with us, regardless of the supply of cellulosic biofuels (*7*, *11*).

Contrary to Khosla's claim, our analysis actually did predict a modest expansion of cropland in Africa in response to U.S. biofuels. More expansion there would not change our result because it generates greenhouse gases comparable to the world average (*12*). Sub-Saharan Africa already imports much of its food and has roughly 400 million hungry people who together suffer 85% of the world's calorie gap (*13*). Climate change could decrease yields by 50% in the region (*14*). Although small-scale bioenergy production might justifiably help local people fill unmet needs or switch from inefficient use of fuel wood, as a whole, sub-Saharan Africa needs to use its good arable land for food even more than other regions.

Finally, our result would change little even if all alternative gasoline to biofuels originated in tar sands (and only some will) (*15*).

TIMOTHY D. SEARCHINGER[1] AND R. A. HOUGHTON[2]

[1]Woodrow Wilson School, Princeton University, Princeton, NJ 08544, USA. [2]Woods Hole Research Center, Woods Hole, MA 02540, USA.

References

1. J. Bruinsma, Ed., *World Agriculture: Towards 2015/2030: An FAO Perspective* (FAO, Rome, 2003).
2. Millennium Ecosystem Assessment, *Ecosystems and Human Well-Being: Scenarios, Findings of the Scenarios Working Group* (Island Press, Washington, DC, 2005).
3. USDA Interagency Agricultural Projections Committee, *USDA Agricultural Projections to 2017* (OCE-1008-1, Washington, DC, 2008).
4. A. Verissimo, P. Barreto, M. Mattos, R. Tarifa, C. Uhl, *For. Ecol. Manag.* **55**, 169 (1992).
5. D. G. Christian, N. E. Yates, A. B. Roche, *Industrial Crops Prod.* **21**, 109 (2005).
6. D. Mitchell, *A Note on Rising Food Prices* (Policy Research Working Paper 4682, World Bank Development Prospects Group, Washington, DC, 2008).
7. P. C. Abbott, C. Hurt, W. E. Tyner, *What's Driving Food Prices* (Farm Foundation, Oak Brook, IL, 2008).
8. Organization for Economic Cooperation and Development, Food and Agricultural Organization of the UN, *OECD-FAO Agricultural Outlook 2008-2017 Highlights* (OECD-FAO, Paris, 2008), tables 2.3 and 2.5, pp. 41 and 43.
9. U.S. Department of Energy, *Breaking the Biological Barriers to Cellulosic Ethanol: A Joint Research Agenda* (DOE/SC-0095 2006).
10. International Energy Agency, *Energy Technology Perspectives 2008: Scenarios and Strategies to 2050* (IEA, Paris, 2008).
11. M. L. Baker, D. J. Hayes, B. A. Babcock, *Crop-Based Biofuel Production Under Acreage Constraints and Uncertainty* (Working Paper 08-WP 460, Center for Agricultural and Rural Development, Iowa State University, Ames, IA, 2008).
12. As shown in table E-1 in the supporting online material of our Report, the average hectare converted to cropland in the 1990s in sub-Saharan Africa caused carbon emissions comparable to the world average, yet African cropland also has lower yields and therefore requires more land for the same crops.
13. S. Meade, S. Rosen, S. Shapouri, *Food Security Assessment, 2006* (GFA-18 Economic Research Service, USDA , Washington, DC, 2007).
14. IPCC, *Climate Change 2007: Synthesis Report Summary for Policymakers* (2007).
15. H. K. Gibbs *et al.*, *Environ. Res. Lett.* **3**, 034001 (2008).

Letters to the Editor

Letters (~300 words) discuss material published in *Science* in the previous 3 months or issues of general interest. They can be submitted through the Web (www.submit2science.org) or by regular mail (1200 New York Ave., NW, Washington, DC 20005, USA). Letters are not acknowledged upon receipt, nor are authors generally consulted before publication. Whether published in full or in part, letters are subject to editing for clarity and space.

CORRECTIONS AND CLARIFICATIONS

Random Samples: "Motormouth" (22 August, p. 1023). "Silicon" in "silicon tongue" and "silicon skin" should have been "silicone."

Research Articles: "Essential cytoplasmic translocation of a cytokine receptor–assembled signaling complex" by A. Matsuzawa *et al.* (1 August, p. 663). There was inadvertent duplication of some of the loading control panels in two of the figures. In Fig. 1A, the JNK loading controls for the phospho-JNK blot (but not for the JNK kinase assay) were inadvertently duplicated between the *TRAF3*$^{-/-}$ and *TRAF6*$^{-/-}$ lanes. In Fig. 6D, the TAK1 loading controls in the TAK1 immunoprecipitate were inadvertently duplicated. The corrected figures are shown to the right. Neither error alters the scientific content of the figure or its interpretation.

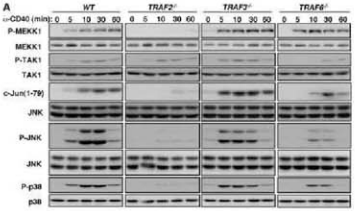

News Focus: "Reinventing rice to feed the world" by D. Normile (18 July, p. 330). The article should have included Dhaka University, in Bangladesh, as among the institutions collaborating on research on salt-tolerant rice varieties.

Perspectives: "Long-distance dispersal of plants" by R. Nathan (11 August 2006, p. 786). There was an error in the formula used to create Fig. 2, panels A and C. The corrected panels are shown to the right. The figure caption is correct, but the error affects two sentences in the text. On page 786, the text at the top of the second column should read "In the hypothetical case shown in Fig. 2, the expected time for a single effective dispersal event to occur is longer than 1 million years beyond 250 km. Nevertheless, an effective LDD event 415 km from the source, expected to occur once in almost 10 million years under the mean trend, may occur once in 25 years as a result of processes or events that 'break the rules.'"

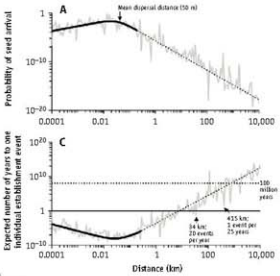

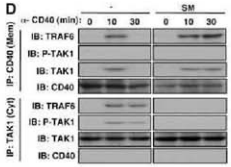

CLIMATE CHANGE

Taming the Angry Beast

Ken Caldeira

Fixing Climate
What Past Climate Changes Reveal About the Current Threat—and How to Counter It

by Wallace S. Broecker and Robert Kunzig

Hill and Wang (Farrar, Straus and Giroux), New York, 2008. 269 pp. $25. ISBN 9780809045013.

A brilliant and iconoclastic scientist, Wally Broecker is largely responsible for shaping the modern discipline of chemical oceanography. His pioneering work has improved our understanding of the ocean's roles in the carbon cycle and climate system and demonstrated that climate often shifts in unpredictable jumps and spurts. In *Fixing Climate*, Broecker teams with science journalist Robert Kunzig to offer a well-crafted description of the history of such research, our current climate predicament, and possible paths forward.

The book is mostly written by Kunzig, looking over Broecker's shoulder. It lacks the idiosyncratic prose, roughly hewn and prickling with personality, found in other books by Broecker [such as (*1*)]. Those books immerse readers in a panoply of slightly oblique and satiric references to his scientific colleagues and favor the vernacular over complex mathematical expressions. *Fixing Climate* has been shorn of such rough edges and eccentricities, producing mainstream science writing aimed at a general audience.

The book starts with a history of climate and carbon-cycle research, which emphasizes work Broecker and his contemporaries carried out in the mid-20th century. The authors then describe what we have learned about previous rapid and dramatic changes in climate. Nearly 13,000 years ago, temperatures in Greenland dropped 6°C within a few decades and then stayed there for 13 centuries. In the succeeding thousand warm years, sea level rose about 15 meters. Such swings have led Broecker to regard the climate system as an "angry beast" given to unpredictable outbursts. He likens our modern carbon dioxide emissions to "poking the angry beast." We can't be sure what will happen from doing so, and we might not want to find out.

Climate models suggest that global warming will tend to make wet places wetter and dry places drier. Broecker and Kunzig point out that the lack of water already impedes development in many areas of the world, and further drying is likely to magnify this impact. In addition, as warmer oceans expand and are supplemented by melting glaciers and ice sheets, they threaten to spill over today's coastlines onto the continents.

Nevertheless, the authors do not see climate change as an existential threat to human civilization. We are supremely adaptable animals, who already prosper in both the snowy Arctic and the sweltering tropics. However, climate change does threaten humans, especially those who have few resources at their disposal.

Broecker and Kunzig see alleviating human misery as more urgent than solving the climate problem. We need to help people escape poverty. Unfortunately, as the global economy develops, demand for cheap, reliable fossil fuels and the resulting carbon dioxide emissions increase.

To reduce the risks posed by climate change, the authors advocate a per capita allotment of carbon-emission allowances. The value of such allowances would give everyone incentive to reduce emissions. The poor could sell allowances to the rich to obtain the resources needed to deploy clean energy and transportation systems in impoverished parts of the world. (Developing a political consensus around this proposal may be even more daunting than developing the needed technologies. A physical scientist, Broecker seems to shy away from addressing the political challenges.)

Placing a price on carbon dioxide emission, however, does not solve the problem of meeting the demands for energy. Broecker and Kunzig dismiss wind and solar energy sources as too costly and unreliable, and they believe nuclear power cannot surmount the problems of nuclear proliferation, waste disposal, and public acceptance. Thus, they anticipate our continued reliance on fossil fuels.

The authors see as nearly inevitable the widespread deployment of systems that capture CO_2 from power plants and dispose of it underground. They find hope in the European carbon-trading market's track record and in the Bush administration's press releases. But the dominant activities on the carbon emissions front have been good-sounding talk and handouts to special interests. We have yet to witness effective action at a scale commensurate with the size of the problem. And since the book went to press, the Bush administration has pulled the plug on FutureGen, its flagship carbon capture and disposal demonstration project. Hence the optimism of Broecker and Kunzig seems hard to maintain.

Although carbon dioxide may be captured from large stationary power plants, no one has found ways to capture CO_2 from automobile exhaust or jet engines. Skeptical that affordable electric or hydrogen cars can be ready in time, the authors turn instead to the prospect of removing CO_2 from the atmosphere after it has already escaped from the tailpipe. This approach, pioneered by Klaus Lackner (*2*), appears to be costly but technically feasible.

Broecker and Kunzig believe that cobbling together a motley collection of existing technologies will not provide the vast amounts of power required later this century while reducing CO_2 emissions. Rather, they contend, we will come to depend on a small handful of energy technologies that are presently possible but not ready. Therefore, "we need a massive research program to get them ready—we need to be investing heavily in research into solar energy as well as carbon capture." Unfortunately, history reminds us that even experts are not good at picking technological successes. Instead of betting on a small handful of possibilities, we should support a broad but carefully selected research portfolio in energy technology.

The specific solutions proposed in *Fixing Climate* may not stand the test of time. But the book demonstrates that Broecker has again

Sign of the change. Record minimum extent of Arctic sea ice, 14 September 2007.

CREDIT: NASA/GODDARD SPACE FLIGHT CENTER SCIENTIFIC VISUALIZATION STUDIO

The reviewer is at the Department of Global Ecology, Carnegie Institution, 260 Panama Street, Stanford, CA 94305, USA. E-mail: kcaldeira@ciw.edu

identified an important and difficult problem for which he offers creative solutions that will open new lines of productive research.

References

1. W. S. Broecker, T.-H. Peng, *Tracers in the Sea* (Lamont-Doherty Geological Observatory, New York, 1982).
2. K. S. Lackner, *Science* **300**, 1677 (2003).

10.1126/science.1164254

CLIMATE CHANGE

Talk Instead of Yelling

Frank T. Manheim

Fred Krupp and Miriam Horn [respectively the president of and a writer at Environmental Defense Fund (EDF)] begin *Earth: The Sequel* with a prediction: The revolution needed to stop accelerating global warming "will depend on industrial technology—capital-intensive, shovel-in-the-ground industries." In Europe, such a statement might be unremarkable. But in the United States, positive reference to industry from a leading activist environmental organization, whose informal motto in the early 1980s was "Sue the bastards," is an attention-getter. A subtext of the opener is the conflict between environmentalists and industry in America. Kert Davies, of Greenpeace's Washington office, notes that EDF has "carved out a space that no one else has, dancing *with* companies, while groups like Greenpeace tend to dance *on* companies" (*1*).

Krupp and Horn focus their account on "inventors who will stabilize our climate, generate enormous economic growth, and save the planet." They offer a detailed review of technologies that could reduce carbon emissions. In addition to established methods, they discuss advanced coal options (such as separation, storage, or algal uptake of CO_2), cogeneration, energy storage, smart real estate development, and pay-as-you-drive insurance—and even mention futuristic geoengineering dazzlers like charged CO_2 molecules that can be moved to outer space.

To appreciate the vanguard role of Krupp and EDF, some background is necessary. Founded in 1967 by four Long Island scientists, EDF acquired skill in using citizen litigation provisions of the early 1970s environmental laws. It won a nationwide ban on DDT in 1972. Subsequently, EDF focused on industrial chemicals while expanding its activities, teaming with other environmental nongovernmental organizations in joint legal-political campaigns against industry.

Earth: The Sequel
The Race to Reinvent Energy and Stop Global Warming

by Fred Krupp and Miriam Horn

Norton, New York, 2008. 287 pp. $24.95, C$24.95. ISBN 9780393066906.

As a young environmental lawyer, Krupp interned with EDF and the Natural Resources Defense Council (NRDC), preparing himself to haul industry into court. But a chemical engineering professor at Yale convinced him that "people could create solutions if they would stop yelling at each other." Two years after assuming the presidency of EDF in 1984, Krupp announced in the *Wall Street Journal* "a new environmentalism," in which EDF's fight against pollution would include "coalitions of former enemies" (*2*).

Krupp's first major breakthrough was a proposal to the George H. W. Bush administration for a cap-and-trade system to reduce sulfur emissions. With support from Senator George Mitchell, other members of Congress, and Environmental Protection Agency (EPA) Administrator William Reilly and after intense debate, cap and trade was incorporated in the 1990 amendments to the Clean Air Act. Replacing the rigid provisions of the 1977 law with market incentives proved a huge success.

Krupp and EDF next pushed the Clinton administration to adopt cap and trade as the U.S.-proposed methodology for reducing global CO_2 emissions under the United Nations Framework Convention on Climate Change. Intensive debates among EPA and other U.S. officials, and later in the European Union and United Nations, led to a bizarre outcome. The Kyoto Protocol participants ultimately accepted the American approach for lowering carbon emissions, but the United States failed to ratify the convention.

Krupp is not one to hide his light under a bushel. However, the book does not dwell on his green deals negotiated with big companies like Wal-Mart, McDonald's, and FedEx or his personal role in other major initiatives. EDF, the World Resources Institute, the Pew Center on Global Climate Change, and NRDC helped achieve the breakthrough U.S. Climate Action Partnership in 2007. Ten major U.S. corporations called for a national cap on carbon emissions and "began operating as if a federal carbon cap were already in place" (*3*). That same year, EDF and NRDC brokered a compromise with Texas energy provider TXU that included scrapping 8 of 11 proposed coal-fired power plants.

Unlike some renewable energy projections, the authors' account considers practicalities. Though a believer in capitalist enterprise, Krupp keeps a figurative baseball bat in the corner for when extra persuasion is needed to achieve agreements with industry. He recognizes not only "tragedy of the commons" market failures but also misaligned incentives and counterproductive regulatory systems. *Earth: The Sequel* does not provide details about regulatory reform, such as are described in Daniel Fiorino's recommendations for performance-based alternatives (*4*) and my recent review of regulatory obstacles to green energy objectives (*5*). Krupp's approach has critics on the industrial side (*6*) and among environmentalists (*7*, *8*). Nonetheless, he and EDF may well become major players in future U.S. energy developments.

The reviewer is at the School of Public Policy, George Mason University, Fairfax, VA 22030, USA. E-mail: fmanhei1@gmu.edu

References and Notes

1. D. Wessel, *Wall Street Journal Online*, 1 March 2007; http://webreprints.djreprints.com/1912570891197.html.
2. F. D. Krupp, *Wall Street Journal*, 20 November 1986, p. 34.
3. See www.us-cap.org.
4. D. J. Fiorino, *The New Environmental Regulation* (MIT Press, Cambridge, MA, 2006).
5. F. T. Manheim, *The Conflict over Environmental Regulation in the United States: Origins, Outcomes, and Comparisons with the EU and Other Regions* (Springer, New York, 2008).
6. See, for example, comments by Marlo Lewis of the Competitive Enterprise Institute, quoted in P. Hill, *Washington Times*, 16 April 2007.
7. J. G. Speth, *The Bridge at the End of the World: Capitalism, the Environment, and Crossing from Crisis to Sustainability* (Yale Univ. Press, New Haven, CT, 2008).
8. S. Beder, *Free Market Missionaries: The Corporate Manipulation of Community Values* (Earthscan, London, 2006).

10.1126/science.1165165

BIOGRAPHY

From Tacoma to Thermal Diffusion

Charles T. Prewitt

A combination of autobiography and biography, *Uncle Phil and the Atomic Bomb* offers an enjoyable perspective on Philip Abelson's amazing career. John Abelson (an emeritus professor of biology at Caltech) primarily based the book on manuscripts and other documents given to him by his uncle. He weaves these together with additional comments and explanations to describe Philip Abelson's life. The book chronicles Abelson's story from his Norwegian parents' immigration to America; through his early childhood and education in Washington state, graduate work at Berkeley, the discovery of neptunium, and wartime research; to his work on the atomic submarine. A couple of pages summarize his subsequent years at the Carnegie Institution of Washington, as editor of *Science* (1962–1985), and with AAAS.

Uncle Phil and the Atomic Bomb
by John Abelson and Philip H. Abelson
Roberts, Greenwood Village, CO, 2007. 151 pp. $25. ISBN 9780974707778.

The book is full of Abelson's interesting adventures. For example, like many young men during the Depression, he caught rides on freight trains. At first, these were local trips. But eventually he rode the rails east to attend the 1933 world's fair in Chicago, returning to Tacoma by way of the Dust Bowl and Los Angeles.

Completing his physics doctorate in 1939, Abelson then joined the Carnegie Institution's Department of Terrestrial Magnetism. After Germany invaded France, he decided to examine the feasibility of large-scale separation of uranium isotopes and, after a search of the literature, elected to explore liquid thermal diffusion. Because of concerns about radioactivity contamination, his experiments were shifted to the National Bureau of Standards. There he synthesized 10 kg of uranium hexafluoride and used it in a thermal diffusion column that successfully separated small amounts of ^{235}U. Later, the project was transferred to the Naval Research Laboratory (for its high-temperature steam) and then to the Philadelphia Naval Base (which had even better facilities for uranium separation). The book describes a curious competition between personnel in the Army's Manhattan Project and those at the Naval Research Lab. They eventually collaborated, and the Navy's liquid thermal diffusion plant in Philadelphia was duplicated at Oak Ridge. It provided ^{235}U-enriched uranium for input to the electromagnetic and gaseous diffusion plants, which eventually produced substantial quantities of bomb-making material.

I very much enjoyed reading *Uncle Phil and the Atomic Bomb*. I met Abelson on a number of occasions during the years I was associated with the Carnegie Institution, but we never talked about his early days. It would have been wonderful to have known then the material described in the book, so that I could have asked more questions about his fascinating experiences.

The reviewer is at the Department of Geosciences, University of Arizona, Tucson, AZ 85721, USA. E-mail: prewitt@email.arizona.edu

10.1126/science.1162487

FILM: AGRICULTURE

The Value of Women

Would you use fire to cut a man's hair? No. This admonition lies at the heart of Brice Lainé's documentary *La forêt danse* (*The Dancing Forest*). With just £6000 at his disposal, Lainé (a student at Ravensbourne College of Design and Communication, London) has made a remarkable film that tells the history of a home-grown development project in northern Togo: Centre International pour le Développement Agro-Pastoral (CIDAP).

La forêt danse
[The Dancing Forest]
by Brice Lainé
United Kingdom, 2008. 76 minutes. In French and Nawdem with English subtitles.

The founder of the project was a village man who not only recognized that the source of their many problems lay in their exhausted land but also acknowledged the value of women as the primary guardians of the soil. CIDAP eschewed chemical fertilizers, likening their use to the futility of injecting blood into a corpse to make it live. The project therefore focused its efforts on educating the women in sustainable husbandry and soil restoration techniques. The resulting collective of Bakoté women was overwhelmingly successful until it almost foundered under the weight of their illiteracy, which prevented them from expanding into larger-scale commerce. Nevertheless, because of the huge benefits the women and their families reap from the more fertile soil, the movement persists despite threats from government officials and internal tensions. A poignant testimony came from one of the husbands, who simply declared he would be dead if it hadn't been for his wife's newly inspired efforts in their fields. I hope that this example of bottom-up development gives many governments pause for thought and also causes international agencies to rethink the ways they bestow benevolence. **–Caroline Ash**

10.1126/science.1166570

CREDITS: (TOP) COURTESY ROBERTS AND COMPANY; (BOTTOM) COURTESY BRICE LAINÉ

RESEARCH ETHICS

When Embryonic Stem Cell Lines Fail to Meet Consent Standards

It does not necessarily follow that just because an embryonic stem line was not derived according to current consent standards it ought not to be used.

Jeremy Sugarman* and Andrew W. Siegel

A recent review of the consent documents for obtaining the embryos used to create the human embryonic stem cell (hESC) lines approved for federal funding in the United States suggests that the consent provisions do not meet the current standards for hESC research specified by the U.S. National Academies of Sciences (NAS) and the International Society for Stem Cell Research (ISSCR) (*1*–*4*). Although the consent forms vary in the degree to which they conform to current guidelines, not a single one satisfies all of the provisions now deemed important for informed consent. An unsettling and unsettled issue has emerged (*5*–*7*) in the wake of this review: Should all research using these lines come to a halt? To address this question, it is helpful to review current research in light of evolving standards and to consider analogies to other biological materials.

Evolving Standards

In assessing ethical acceptability of research, it is important to consider the provenance of existing hESC lines. According to the NAS, assessing provenance "would include obtaining an assurance that the process by which the cells were obtained was approved by an IRB [Institutional Review Board] to ensure that donors provided voluntary informed consent and that risks were minimized" [(*2*) p. 6]. This is perfectly reasonable. However, the specific requirements for consent have shifted over time. For instance, before the release of the NAS and ISSCR guidelines, consensus was lacking about the necessity of obtaining the consent of gamete donors for stem cell research. In 1994, the Human Embryo Research Panel suggested that consent from gamete donors be obtained; but in 2000, the guidelines issued by the National Institutes of Health (NIH) did not (*8*, *9*).

In contrast is the requirement that consent documents include a statement that the research involves the destruction of embryos, which appears to have existed. Therefore, it is reasonable to conclude that hESC lines should not be used if they were derived without evidence that consent included some understanding that embryos would be destroyed.

Consider the University of California at San Francisco (UCSF) and WiCell lines that were approved for federal funding and were derived in the United States, which means that the documents described above are applicable. They fail to meet current standards for consent in some ways: for example, not providing for consent from gamete donors. However, each appears to be consistent at least with the relevant articulated standards existing at the time the consents would have been obtained. In particular, the consents for the lines derived at the University of California at San Francisco explicitly follow the NIH guidelines of 2000. The WiCell lines were derived before 2000 and do not seem to contravene the standards for consent at that time. Thus, these documents reflect a good-faith effort to abide by the principle of respect for autonomy. As such, the failure of the consent documents to satisfy current consent standards does not necessarily entail that it is morally impermissible to use these cell lines.

Stored Biological Materials

Many existing biological materials were procured without adequate consent according to current standards. The National Bioethics Advisory Commission has argued that it is appropriate to waive consent requirements for biological specimens collected before the adoption of the report's recommendations where (i) the study poses minimal risks to subjects and (ii) it is impracticable to obtain consent from them (*10*). This approach recognizes the importance of respect for autonomy but does not allow the lack of adequate consent for materials obtained prior to the report to interfere with potentially important scientific advances. One could reasonably apply a similar analysis to the hESC lines derived before the adoption of the NAS/ISSCR recommendations with respect to particular aspects of consent. Research with hESCs poses minimal risks to embryo and gamete donors. As to the practicability of obtaining new consents, it would likely be difficult to track down donors in many cases. Moreover, there may be legitimate ethical concerns about the practice, as donors may feel that they are contacted. It is important to note the potential moral distinctions between all biological materials and embryos (*11*). Here, it may be reasonable to be more lenient with respect to whether particular consent provisions were met with respect to gamete donors compared with embryo donors.

Conclusion

It seems naïve to expect that hESC lines derived in the past would meet current standards for consent. Yet, it seems perfectly reasonable to expect that consent was obtained for the donation of embryos and that those deriving these lines did so with appropriate oversight. Standards and guidelines can provide useful information about context, with the understanding that science does not sit still while such guidelines are being developed and promulgated (*12*). Diffusion of norms and expectations takes time. Regardless, scientific integrity mandates that those engaged in research keep abreast of such changes, as well as the fundamental ethical underpinnings of such policies.

Berman Institute of Bioethics, Johns Hopkins University, Baltimore, MD 21205, USA.

*Author for correspondence. E-mail: jsugarm1@jhmi.edu.

References

1. R. Streiffer, *Hastings Center Report* **38**, 40 (2008).
2. Committee on Guidelines for Embryonic Stem Cell Research, National Research Council, *Guidelines for Human Embryonic Stem Cell Research* (National Academies Press, Washington, DC, 2005).
3. ISSCR, *Guidelines for the Conduct of Human Embryonic Stem Cell Research* (ISSCR, Deerfield, IL, 2006); available at www.isscr.org/guidelines/index.htm
4. Human Embryonic Stem Cell Research Advisory Committee, National Research Council, *2007 Amendments to the National Academies' Guidelines for Human Embryonic Stem Cell Research* (National Academies Press, Washington, DC, 2007).
5. R. Weiss, "Ethically challenged," 25 July 2008; www.scienceprogress.org.
6. J. Keller, *Chron. Higher Educ.*, 28 July 2008; http://chronicle.com/daily/2008/07/3996n.htm.
7. M. Baker, *N. News*, 28 July 2008; www.nature.com/news/2008/080728/full/454556a.html.
8. NIH, *Report of the Human Embryo Research Panel*, National Institutes of Health, Bethesda, MD, 1994).
9. National Institutes of Health, "Guidelines for research using human pluripotent stem cells," *Fed. Regist.* **65**, 51976 (25 August 2000); http://stemcells.nih.gov/news/newsArchives/stemcellguidelines.asp.
10. National Bioethics Advisory Commission, *Research Involving Human Biological Materials: Ethical Issues and Policy Guidance*, vol. 1, *Report and Recommendations of the National Bioethics Advisory Commission* (National Bioethics Advisory Commission, Rockville, MD, 1999); http://bioethics.gov/reports/past_commissions/nbac_biological1.pdf (accessed 22 July 2008).
11. A. D. Lyerly, R. R. Faden, *Science* **317**, 46 (2007).
12. J. Sugarman, A. Siegel, *Cell Stem Cell* **3**, 238 (2008).

10.1126/science.1164441

GENETICS

It's the Sequence, Stupid!

Differences in regulatory DNA sequences drive species-specific gene expression.

Hilary A. Coller[1] and Leonid Kruglyak[2]

One of the surprises revealed by comparative genome sequencing is that closely related species share remarkably similar complements of genes. For example, a recent evaluation of the human gene catalog found at most 168 genes without close homologs in mouse or dog, with perhaps as few as 12 representing newly evolved protein-coding regions (*1*). Moreover, the corresponding genes tend not to differ much in their coding sequences: Nearly 80% of amino acids are identical between orthologous human and mouse proteins (*2*). Although this leaves many potentially functional coding changes, these observations lend further credence to the proposal, first made more than 30 years ago, that many of the observed differences between species likely stem from when and where the products of the genes are made (*3*). But what governs these changes in gene expression? There is no shortage of possible explanations—differences in external cues and cellular milieus, in how genomes are packaged, in the proteins that control transcription, and in the regulatory sequences to which they bind. Strikingly, on page 434 of this issue (*4*), Wilson *et al*. show that in human and mouse liver cells, the differences in regulatory sequences dominate all other factors.

Wilson *et al*. took advantage of an ideal system: a mouse model of Down syndrome in which mouse cells contain a copy of human chromosome 21 in addition to the complete mouse genome (*5*). In these cells, the human DNA sequence is placed in an otherwise murine context, including all external and cellular cues as well as regulatory proteins. This system allowed the authors to ask an otherwise impossible question: Is regulation of the genes on human chromosome 21 in these mouse cells (Tc1 hepatocytes) determined by the human DNA sequence, or by the mouse cellular environment and transcriptional machinery?

The authors compared the regulation of human genes in Tc1 cells to those of their mouse orthologs in these same cells. They then compared the observed patterns to those in mouse hepatocytes from littermates that did not inherit the extra human chromosome, as well as to those in normal human hepatocytes. The authors first confirmed that the protein binding and expression patterns of mouse genes in Tc1 hepatocytes match those in normal mouse hepatocytes, and that both differ from patterns for orthologous genes in human cells. What about the human genes in the Tc1 hepatocytes? If regulation is driven largely by sequence, then these genes should be regulated just as they are in normal human hepatocytes, whereas if species-specific developmental context, epigenetic factors, or differences in transcription factors themselves play a defining role, then the genes should most closely mimic their mouse orthologs.

The authors compared regulation at three levels: binding of transcription factors to DNA, modification of histones [proteins that bind chromosomal DNA and determine its packing and accessibility for binding (*6*)], and gene expression. The results were clear. The binding patterns of transcription factors HNF1α, HNF4α, and HNF6 on human chromosome 21 in mouse cells matched those seen in human cells, not those observed in mouse cells, with only a few exceptions (see the figure). Similarly, although histone H3K4me3 modifications at canonical transcription start sites were largely shared between the human and mouse chromosomes, these same modifications at other sites (thought to represent unannotated promoters) showed human-specific patterns on human chromosome 21 in Tc1 cells. Finally, gene expression (the amount of messenger RNA transcribed) from human chromosome 21 genes in Tc1 hepatocytes was more closely correlated to the expression of human chromosome 21 genes in human hepatocytes than to the expression of their mouse orthologs in the Tc1 cells. The authors thus concluded that it is the regulatory DNA sequence, rather than any other species-specific factor, that is the single most important determinant of gene expression.

This result raises many interesting questions about the transcriptional regulatory code. Wilson *et al*. show that the information required for species-specific regulation is encoded in cis-regulatory DNA sequence. Yet because essentially all of human chromosome

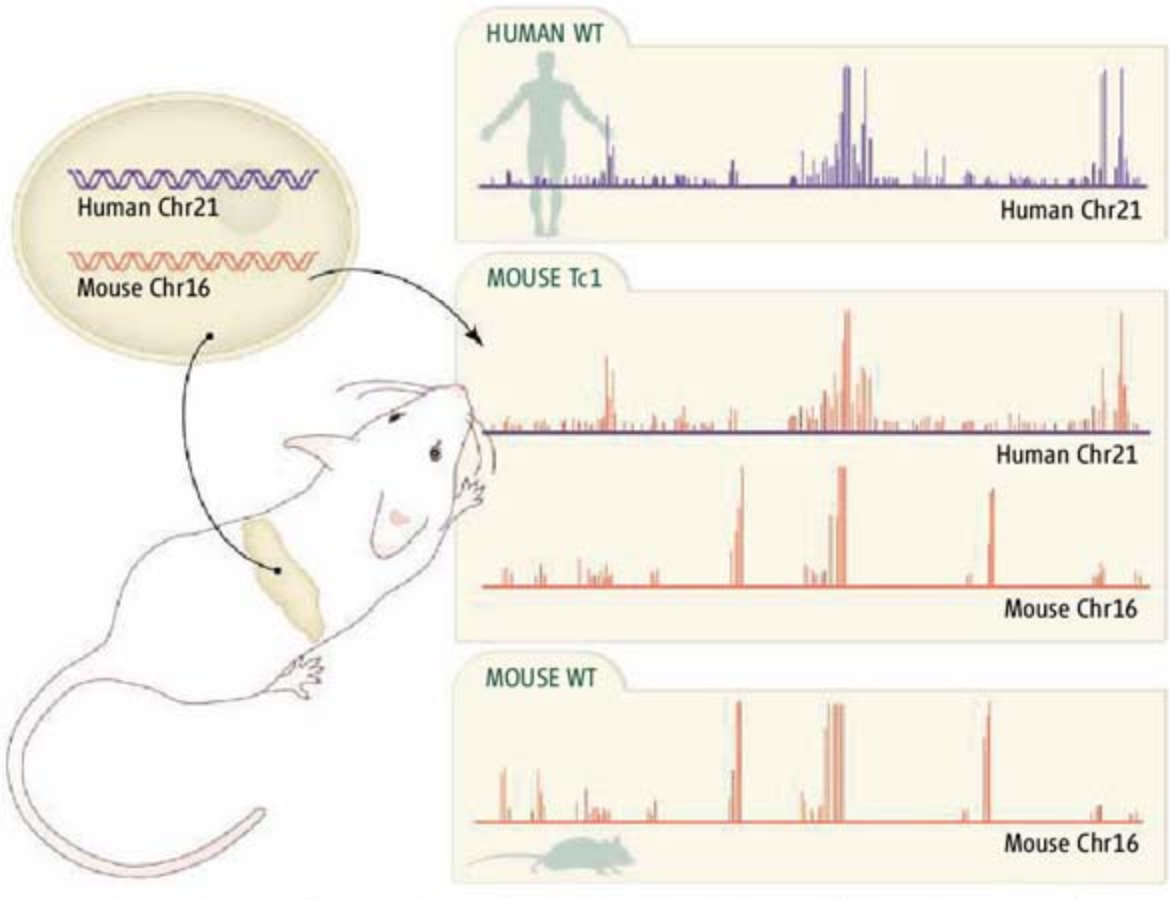

Reading the regulatory code. Transcription factor proteins in mouse Tc1 cells carrying a human chromosome (**middle**) bind to the human DNA in a human-specific pattern (**top**) and to the corresponding mouse DNA in a mouse-specific pattern (**bottom**).

CREDIT: P. HUEY/SCIENCE

[1]Department of Molecular Biology, Princeton University, Princeton, NJ 08544, USA. [2]Howard Hughes Medical Institute, Lewis-Sigler Institute for Integrative Genomics, and Department of Ecology and Evolutionary Biology, Princeton University, Princeton, NJ 08544, USA. E-mail: hcoller@princeton.edu; leonid@genomics.princeton.edu

21 is present, the data do not address whether the code is local. The results are consistent with either a few regulatory sites for each gene close to the corresponding start of transcription, or many interacting regulatory sites scattered across large swaths of human chromosome 21. Experiments that replaced a mouse gene by its human ortholog along with varying lengths of upstream and downstream regions might address how much human sequence is needed to recapitulate a human pattern of binding and expression. Would a few kilobases upstream be sufficient, as would be expected if only proximal transcription factor binding sites matter, or would much larger segments upstream and downstream be required, indicating that multiple types of poorly understood sequence elements are acting in concert?

The paper's findings also call into question one of the basic tenets of comparative genomics: that evolutionary conservation can serve as the primary tool for finding functional sequences (*2*, *7*, *8*). Clearly, nonconserved sequences are responsible for the observed functional differences in binding and expression of human and mouse genes in the same cells. Thus, although many conserved noncoding sequences are functional, and interspecies comparisons can help us to identify these motifs, narrowing our attention only to these sequences must result in an incomplete understanding of the regulatory code (*9*). Indeed, this approach guarantees missing the species-specific regulatory instructions that make us different from mice.

Finally, the transcriptional machinery of a mouse cell is able to read out human-specific gene expression instructions based solely on the sequence of the human chromosome, but today's bioinformatic methods cannot. Substantial progress has been made in predicting expression from sequence in yeast (*10*, *11*), whereas in mammals, known regulatory sequences are too short and degenerate, and extend too far from the start of transcription, for us to accurately predict gene expression from sequence information alone. So what would it take for us to predict how mouse cells would read out the regulatory code of, say, an armadillo chromosome, without doing the experiments? That is, how can we move toward reading the regulatory code as easily as we read the genetic code, which allows us to seamlessly go from the DNA sequence to the protein complement of any species? We anticipate that deciphering the regulatory code will require a combination of computational and experimental approaches, in concert with improved physical models of protein-DNA interaction (*12*). It will also require an understanding of the cellular context to an extent not necessary for the genetic code, because the complement of regulatory proteins operating to control transcription varies with the species, the cell type, and the environment. The ENCODE project provides one model of experimentally monitoring all accessible regulatory readouts, such as transcription itself, binding of regulatory proteins, histone modification states, and nucleosome positioning on a global scale (*13*). Our hope is that innovative approaches to the analysis of ENCODE-like data will ultimately allow us to crack the regulatory code.

References

1. M. Clamp *et al.*, *Proc. Natl. Acad. Sci. U.S.A.* **104**, 19428 (2007).
2. R. H. Waterston *et al.*, *Nature* **420**, 520 (2002).
3. M. C. King, A. C. Wilson, *Science* **188**, 107 (1975).
4. M. D. Wilson *et al.*, *Science* **322**, 434 (2008); published online 11 September 2008 (10.1126/science.1160930).
5. A. O'Doherty *et al.*, *Science* **309**, 2033 (2005).
6. T. Jenuwein, C. D. Allis, *Science* **293**, 1074 (2001).
7. Q. F. Wang *et al.*, *Genome Biol.* **8**, R1 (2007).
8. X. Xie *et al.*, *Nature* **434**, 338 (2005).
9. X. Y. Li *et al.*, *PLoS Biol.* **6**, e27 (2008).
10. M. A. Beer, S. Tavazoie, *Cell* **117**, 185 (2004).
11. C. T. Harbison *et al.*, *Nature* **431**, 99 (2004).
12. A. M. Moses *et al.*, *PLoS Comput. Biol.* **2**, e130 (2006).
13. E. Birney *et al.*, *Nature* **447**, 799 (2007).

10.1126/science.1165664

MATERIALS SCIENCE

In Praise of Pores

Advanced processing methods are used to tailor the properties of porous ceramics.

Paolo Colombo

Highly porous structures are found extensively in the natural world (*1*), because their design enables the efficient optimization of characteristics such as the strength-to-density and stiffness-to-density ratios. Moreover, synthetic porous ceramics have advantages over metallic or polymeric components, especially when resistance to high-temperature or corrosive environments or compatibility with biological materials is required. Recent progress in fabrication procedures has considerably widened the range of morphologies and properties achievable for porous ceramics, resulting in their use in an ever-expanding range of applications, including catalyst supports and chemical reactors (*2*), biomedical tracking and delivery platforms (*3*), electrodes, insulators, and heat exchangers (*4*). The introduction of nanopores in ceramics has opened possibilities for the development of smart devices such as photoactivated sensors and switches and drug delivery capsules.

All these applications require the porous component to have a specific range of values for different properties (see the figure) (*5*), which can only be achieved through judicious choice of starting materials and well-controlled processing. The manufacturing method strongly influences the amount of porosity (from a few percent to more than 95% in volume), the pore size (from nanometers to millimeters), the distribution of the pores within the solid, the shape and interconnectivity of the pores and other characteristics such as the flaw population (amount, size, and morphology of defects), and the size and cost of the component. The introduction of porosity is therefore an extremely versatile and powerful tool for greatly extending the range of properties offered by a ceramic component. No other single strategy enables the value of a given property to be varied to such an extent, often by orders of magnitude, in a single material.

Macroporous cellular (foam-like) ceramic structures are conventionally produced by dip-coating a polymeric foam into a ceramic slurry, followed by burnout of the preform and sintering. This approach leads to high-porosity, low-cost parts of limited strength, suitable for molten metal filters or kiln furniture. Similar porosity can also be created through the elimination of "sacrificial filler" materials by burnout or dissolution, providing tighter control on the average pore size distribution, with a wider range of cell size and amount of porosity. More recent methods use direct foaming of a ceramic slurry (for example, through mechanical frothing, gas injection, or in situ gas generation by decomposing an

Dipartimento di Ingegneria Meccanica–Settore Materiali, Università di Padova, 35131 Padova, Italy, and Department of Materials Science and Engineering, Pennsylvania State University, University Park, PA 16802, USA. E-mail: paolo.colombo@unipd.it

organic additive), followed by setting (for example, by gelling or particle stabilization of the liquid-gas interface) and sintering (*6*). This process yields components with higher strength, enabling the manufacture of smaller parts, such as thinner filters, and the use of porous ceramics in load-bearing applications, such as implants for bone substitutes. However, precise control of the cell size distribution remains a challenge.

Some applications, such as diesel particulate filters, require unidirectional macropores (as in honeycombs), in which alternate channel openings are blocked. This structure forces the gas to pass through the channel walls, depositing the soot on their surface. Such "wall-flow filters" are achieved by extrusion of a ceramic paste. An innovative development has been the production of such filters based on needle-shaped mullite crystals, which offer improved performance at high porosity volumes (*7*).

Other novel processing methods that enable fabrication of mainly unidirectional macropores include freeze casting (*8*) and pyrolysis of wood or assembled cardboard in an inert atmosphere (*9*). In the first process, the porous structure is templated by solidifying a solvent, leading to unique morphologies in which the lamellar surfaces exhibit dendritic-like features along the solidification direction. In the second process, complex carbon-based porous structures are obtained, which can be used as received or further reacted with gaseous or liquid precursors to form SiC or other advanced ceramic compositions that mimic the morphology of the parent component. These materials could be used in diesel trap applications, for biomedical applications (bone implants), as sandwich panel cores, in filtering devices, and as lightweight ceramic components.

Highly regular macroporous structures, offering a narrow range of variability in their morphology and hence their properties, can be achieved with computer-assisted fabrication methods. Three-dimensional periodic architectures comprising interconnected cylindrical rods have been produced by the extrusion of a continuous filament that is patterned in a layer-by-layer computer-controlled building sequence, using either particle-filled polymeric inks or concentrated colloidal gels. This method has the advantage, relative to competing techniques, of providing components with well-controlled properties. It also enables the precise placement of pores with desired size and shape within the component. Researchers have achieved submicrometer feature dimensions, and structures with an area of 1 m^2 can be printed at speeds of up to 10 cm/s (*10*). Use of multinozzle arrays will further reduce manufacturing times, making this a commercially viable approach for producing ceramic membranes and filters, catalyst supports, and structural materials with well-controlled properties. Moreover, infiltrating the polymeric structures with a ceramic or metallic material, followed by sintering, leads to inverse woodpile structures (a solid matrix with a periodic array of tubular holes), with possible applications as photonic crystals, in low-cost microelectromechanical systems, as microfluidic networks for heat dissipation, and in biological devices.

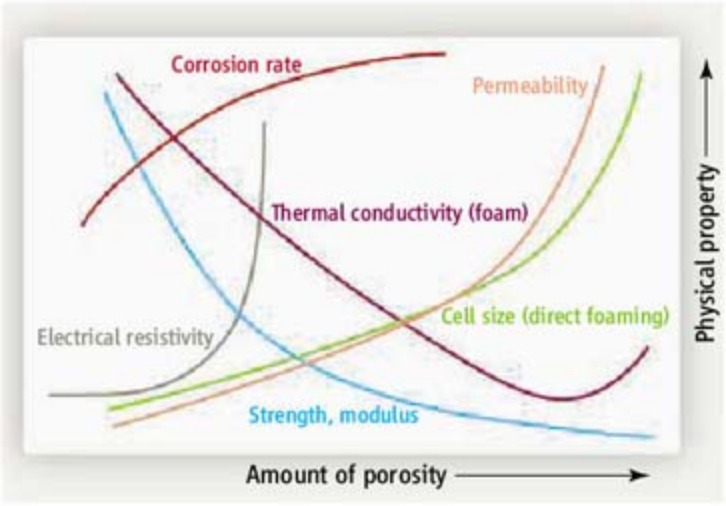

Porosity matters. A wide range of physical properties can be achieved by changing the amount of porosity through processing. Pore size, connectivity, and distribution also affect the properties of the component and can be used to further tailor its characteristics. No distinction is made in the graph between open and closed porosity.

The processing methods discussed so far use ceramic powders as the main starting materials. To build components with pores in the microscopic and mesoscopic range, ceramic precursors must instead be used. Two main approaches are used to fabricate ceramics with pores in these size ranges: sol-gel precursors, which mainly yield oxides, and preceramic polymers, which give more complex high-temperature ceramics.

Sol-gel precursors enable the fabrication of unique nanostructured porous morphologies and components. Via a self-assembly route that uses surfactants or via nanocasting, a highly ordered array of uniform pores in the mesoscopic range can be obtained, typically based on oxides such as silica or titania (*11*). The use of precursors such as silsesquioxane species leads to periodic mesoporous organosilicas, allowing for the precise tailoring of the size, thermal stability, and surface reactivity of the pores through the addition of organic chains and functional groups (*12*). Powders, fibers, monoliths, and thin and patterned films can be produced, although challenges remain in increasing the stability of the nanometer-scale pores at temperatures above a few hundred degrees Celsius and in achieving a uniformly well-ordered structure in large components. Applications include catalysis, sorption, gas sensing, optics, and photovoltaics. Alternatively, tunable mesoscale pores, coupled with very high specific surface area, can be achieved by etching carbides to selectively remove non-carbon atoms (*13*). These mesoporous carbons can be used as separation media, catalysts, and advanced electronic components for energy conversion and storage.

Preceramic polymers provide a route to SiC, SiCN, or BN mesoporous materials, which offer better high-temperature properties than oxides. Preceramic polymers are inorganic or organometallic polymers that can be converted into advanced ceramics via high-temperature pyrolysis. Owing to their polymeric behavior at low temperatures, these precursors can be processed by blowing, infiltration or coating of preforms, or warm pressing with sacrificial fillers to obtain macroporous components. Ceramics with a hierarchical pore structure and high specific surface area can be fabricated in a single process (*14*). Furthermore, with a fabrication method such as electrohydrodynamic spraying, a great variety of miniaturized polymeric porous structures—bubbles, capsules, nanofiber mats, microtubes, patterned microchannels—with controlled surface characteristics can be fabricated and then transformed into a ceramic (*15*). They can be used as lightweight fillers for syntactic foams, implantable capsules for drug delivery, components for tissue engineering, and microfluidic devices.

Further progress in fabrication methods is needed to increase component sizes and reduce their cost, and to widen even further the range of pore sizes and achieve a tighter control on their morphology. Advances in three-dimensional imaging techniques, such as computer-assisted tomography, would enable routine quantification of the pore morphology, providing much-needed data for modeling of the pore structure and properties and assisting in the design of reliable porous components. The coupling of porosity with other functionalities (such as electrical conductivity, piezoelectricity, or ferromagnetic properties) in the same element will lead to more versatile filters and to components with an even wider set of properties, for use in advanced applications

such as solid-oxide fuel cells, absorption of electromagnetic radiation, regenerable adsorption, and acoustic devices such as hydrophones.

References

1. S. Perkowitz, *Universal Foam: From Cappuccino to the Cosmos* (Walker, New York, 2000).
2. M. V. Twigg, J. T. Richardson, *Ind. Eng. Chem. Res.* **46**, 4166 (2007).
3. S. Oh, N. Oh, M. Appleford, J. L. Ong, *Am. J. Biochem. Biotech.* **2**, 49 (2006).
4. M. Scheffler, P. Colombo, Eds., *Cellular Ceramics: Structure, Manufacturing, Properties and Applications* (Wiley-VCH, Weinheim, Germany, 2005).
5. L. J. Gibson, M. F. Ashby, *Cellular Solids, Structure and Properties* (Cambridge Univ. Press, Cambridge, 1999).
6. A. R. Studart, U. T. Gonzenbach, E. Tervoort, L. J. Gauckler, *J. Am. Ceram. Soc.* **89**, 1771 (2006).
7. A. J. Pyzik, C. G. Li, *Int. J. Appl. Ceram. Tech.* **2**, 440 (2006).
8. S. Deville, *Adv. Eng. Mater.* **10**, 155 (2008).
9. P. Greil, *J. Eur. Ceram. Soc.* **21**, 105 (2001).
10. J. A. Lewis, *Adv. Funct. Mater.* **16**, 2193 (2006).
11. S. Polarz, B. Smarsly, *J. Nanosc. Nanotech.* **2**, 581 (2002).
12. W. J. Hunks, G. A. Ozin, *J. Mater. Chem.* **15**, 3716 (2005).
13. Y. Gogotsi *et al.*, *Nat. Mater.* **2**, 591 (2003).
14. P. Colombo, *J. Eur. Ceram. Soc.* **28**, 1389 (2008).
15. M. Nangrejo, Z. Ahmad, E. Stride, M. Edirisinghe, P. Colombo, *Pharm. Dev. Technol.* **13**, 425 (2008).

10.1126/science.1162962

MATERIALS SCIENCE

Toward Pore-Free Ceramics

Efforts are under way to create perfectly dense ceramics for use in applications ranging from lasers to health care.

Gary L. Messing and Adam J. Stevenson

Pore-free ceramics with grain sizes in the nanometer range promise to have unprecedented optical, mechanical, electrical, and other properties for use in lasers, health care, and electrical devices. Yet, in most of today's dense ceramics, pores with diameters of 100 to 1000 nm occupy about 2 to 5% of the volume of the material. Recent progress in nanoparticle processing, multiple-step sintering cycles, and novel densification techniques may yield fully dense nanoceramics.

Large pores can seriously impair the function of ceramic materials and components. For example, the zirconia or alumina balls used in hip prostheses must support load without failure for 15 years or more; pores can act as fracture initiation sites that lower mechanical strength and may cause catastrophic failure. Another example of the effect of pores is provided by transparent neodymium-doped yttrium-aluminum-garnet (Nd:YAG) ceramics, which have better lasing performance than single crystals (*1*) and may supplant Nd:YAG single crystals in next-generation high-power lasers. Because pores scatter light and reduce optical transmission in laser ceramics, such applications require 100% density. Ceramic components, like barium titanate ($BaTiO_3$) capacitors, in electronic devices also become increasingly vulnerable to the effects of pores as devices shrink, because pores in the ceramic create weak links that lead to dielectric breakdown and hence device and system failure.

Attempts to achieve fully dense ceramics with grain sizes below 100 nm start with 10- to 50-nm particles, which are consolidated into product-specific shapes from colloidal suspensions, dried, and then heated (sintered) to remove the porosity between the particles (see the figure). The driving force for pore elimination during sintering is the reduction of surface free energy of the ceramic particles, with a magnitude roughly equivalent to 1 megapascal (MPa). Pores are removed by mass transport to the pore surfaces. Because mass transport along grain boundaries is orders of magnitude faster than transport within grains, pores must be located along grain boundaries for a ceramic to become fully dense (that is, pore-free). As grains grow, pores can become trapped inside grains if their intrinsic mobility is lower than the mobility of the grain boundaries—a process called pore-boundary separation.

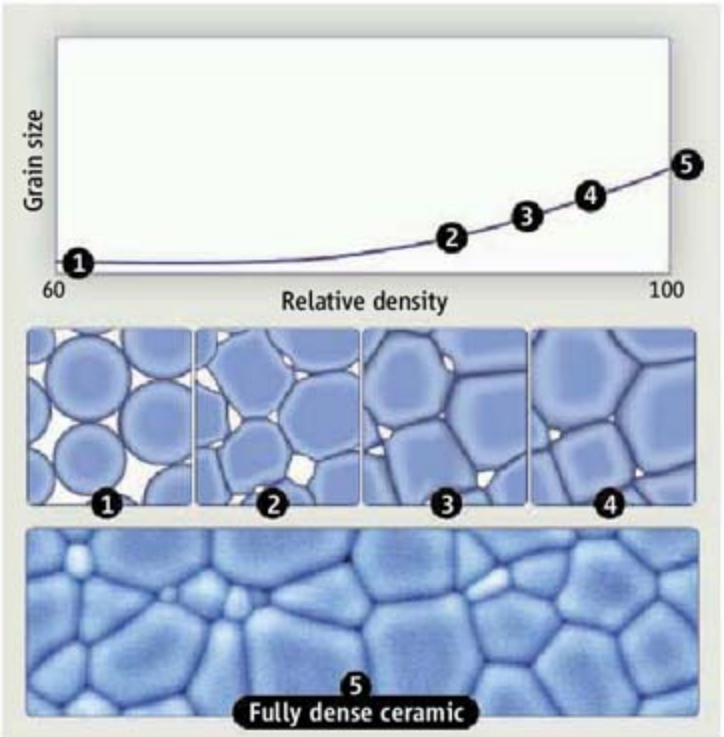

Density versus grain size. (Top) Plotting the grain size against the density helps to understand how to tailor sintering conditions to achieve fine-grain-size, fully dense ceramics (background image). **(Bottom)** (1) Initial random close particle packing. (2) At an intermediate stage of sintering, continuous pore channels limit grain growth. (3) At 92% density, pore channels pinch off to form isolated pores. (4) Grain growth increases rapidly in the fully dense areas, while sintering continues to eliminate the final pores. Controlling the slope during the final stage of densification is the key to obtaining nanograin-size fully dense ceramics. (5) Colorized scanning electron micrograph of a dense ceramic.

CREDIT: ADAPTED BY P. HUEY/SCIENCE

Department of Materials Science and Engineering, and Materials Research Institute, Pennsylvania State University, University Park, PA 16802, USA. E-mail: messing@matse.psu.edu; ajs515@psu.edu

The most effective approach to prevent pore-boundary separation is to ensure that all pores are smaller than the average particle size after the starting powder is consolidated into the desired shape. In practice, the best particle packing (and thus the smallest pore size and the narrowest pore size distribution) is achieved by consolidating discrete, narrowly sized, fine particles to random close-packed density (that is, 64% density). However, efforts to synthesize and form discrete particles with diameters of 10 to 50 nm and disperse them in a liquid for use in ceramic-part shaping are confounded by attractive interparticle forces, which increase with decreasing particle size. These forces cause flocculation into low-density particle networks, which evolve during drying and sintering into ceramics with pores larger than the average particle size. Sintering to full density is thus compromised.

On the plus side, nanoparticles substantially increase the driving force for sintering and reduce the sintering temperature. They thus hold considerable promise for lowering sintering temperature and reducing sintering time. Yet, there are only a few cases in which researchers have achieved small-grain-size, fully dense ceramics by pressureless densification of nanoparticles (*2*, *3*). An impressive demonstration of how to retain extremely

small grain size while achieving near full density is the work on $BaTiO_3$ capacitors (*4*, *5*). In this process, particles with diameters of 10 to 30 nm were dispersed in organic solvents of low dielectric constant to avoid particle solubility and to limit interparticle forces. With careful atmosphere control, multistep sintering cycles, and dopants, fully dense $BaTiO_3$ with grain sizes of <100 nm are commercially produced; experimentally, $BaTiO_3$ with <50-nm grain size has been achieved. These techniques are equally applicable to other ceramic systems but have only been demonstrated in $BaTiO_3$ such small dimensions are required to meet the demands for today's commercial, miniaturized electronic components.

An example of sintering pore-free, nanograined ceramics that enables new properties is the demonstration of transparent, polycrystalline Al_2O_3. Because it is optically birefringent, fully dense polycrystalline Al_2O_3 with micrometer-sized grains is translucent, but by refining the grain size to below 100 nm and sintering to over 99.9999% density, the dominant light-scattering mechanism is changed, allowing the material to become transparent (*3*). Despite the successes with $BaTiO_3$ and Al_2O_3, demonstrations of pore-free, nanograined ceramics remain rare; other methods have therefore been developed to aid densification.

For high-reliability ceramics like hip prostheses and optical components, pressure can be an additional driving force for densification. Mechanical hot pressing and hot isostatic pressing (where gas is used as the pressure-transmitting medium) are used commercially to achieve fully dense ceramics. By enabling pressures of 200 MPa or more, hot isostatic pressing has become the standard for commercial applications requiring total pore elimination, but cost and contamination limit its general applicability to a few ceramic systems.

Recently, novel heating methods like microwave and spark plasma sintering processes have gained much attention for sintering ceramics. Compared to conventional sintering, microwave sintering enables faster densification, but there are still no definitive physical mechanisms to explain this observation. Spark plasma sintering applies pressure like a hot press but simultaneously heats the ceramic by pulsing an electric current through it. It has been successful in limiting grain growth by reducing densification time from hours to minutes. Again, there is considerable controversy over why rapid densification happens. A recent model (*6*) shows that the electrical current induces local spatial temperature gradients that lead to enhanced diffusional processes. The authors contend that these spatial temperature gradients are the source of increased densification kinetics during spark plasma sintering. These novel electric field–enhanced methods challenge our thinking on thermal sintering. Improved understanding should lead to the development of even better electric-field densification techniques for fabricating bulk, pore-free nanostructured ceramics.

A major limitation in studying sintering is that we cannot probe the real-time, three-dimensional evolution of submicrometer pores during the last stage of densification. To appreciate the complexity of this problem, consider a material that is 99.9999% dense (a density that cannot be physically measured by conventional techniques). Such a material has ~5×10^{16} pores/cm^3 if the pores are 100 nm in diameter.

Magnetic resonance imaging and x-ray tomography have been used to study pore evolution but lack the resolution to observe submicrometer pores. Confocal optical microscopy, which has a lateral resolution of 200 to 300 nm, has been used to explore grain boundary structure in three dimensions (*7*) and has potential for observing submicrometer pores. Near-field scanning optical microscopy can image surface pores down to 40 to 50 nm. Scanning acoustic microscopy (*8*), scanning electron acoustic microscopy (*9*), and scanning near-field acoustic microscopy (*10*) have potential for detecting subsurface pores and can in principle achieve submicrometer resolution. Linear scattering spectroscopy can sensitively provide information on the size, size distribution, and shape of the pores (*11*).

Spectroscopists and microscopists must develop these tools with materials scientists so that we can observe nanopore changes inside the ceramic, preferably in real time and during sintering. The development of these new tools for the study of sintering would be a breakthrough in our ability to study this important process.

References and Notes

1. A. Ikesue *et al.*, *Annu. Rev. Mater.* **36**, 397 (2006).
2. V. V. Srdic *et al.*, *J. Am. Cer. Soc.* **83**, 729 (2000).
3. A. Krell *et al.*, *J. Am. Cer. Soc.* **86**, 12 (2003).
4. Y. Mizuno *et al.*, *J. Cer. Soc. Jpn.* **115**, 181 (2007).
5. A. V. Polotai *et al.*, *J. Am. Cer. Soc.* **88**, 3008 (2005).
6. E. Olevsky *et al.*, *J. Am. Cer. Soc.* **92**, 10.1111/j.1551-2916.2008.02705.x (2008).
7. M. O. Ramirez *et al.*, *Optics Express* **16**, 5965 (2008).
8. Z. Yu *et al.*, *Rev. Mod. Phys.* **67**, 863 (1995).
9. L. J. Balk, *Adv. Electron. Electron Phys.* **71**, 1 (1988).
10. P. Gunther *et al.*, *Appl. Phys. B* **48**, 89 (1989).
11. R. N. Johnston *et al.*, *Proc. Nat. Acad. Sci. U.S.A.* **76**, 3325 (1979).

12. The authors acknowledge the valuable scientific contributions of V. Gopalan and C. A. Randall, the artistic rendering of the figure by M. Fleck, and the support of NSF project DMR 749391.

10.1126/science.1160903

PHYSICS

Transforming Light

Vladimir M. Shalaev

Materials with optical properties not found in the natural world can now be designed, offering unprecedented control over light and enhanced device functionality.

Recent advances in micro- and nanofabrication methods are presenting opportunities to control light in a way that is not possible with the materials provided to us by nature. Synthetic structures built up from subwavelength elements can now be fabricated with a desired spatial distribution of effective electric permittivity ε and magnetic permeability μ, thereby offering the potential to guide and control the flow of electromagnetic energy in an engineered optical space. These "metamaterials" have opened the door to a number of applications that had been previously considered impossible. No longer are we constrained by the electromagnetic response of natural materials and their chemical compounds. Instead, we can tailor the shape and size of the structural unit of the metamaterial and tune their composition and morphology to provide new functionality.

The field of transformation optics, which is enabled by metamaterials, has inspired a fresh look to be taken at the very foundations of optics. Analogous to general relativity, where time and space are curved, transformation optics shows that the space for light can also be bent in an almost arbitrary way. The ability to design and engineer optical space provides the possibility of controlling the flow of light with nanometer spatial precision. Thus, general relativity may find practical use in a number of novel optical devices based on transformation optics, guiding how, using metamaterials, the space for light can be curved in a predesigned and well-controlled way. The relation between light propagation and effective space-time

Birck Nanotechnology Center and School of Electrical and Computer Engineering, Purdue University, West Lafayette, IN 47907, USA. E-mail: shalaev@ecn.purdue.edu

geometries was considered, for example, in early papers by Tamm (*1*, *2*), with the basics of transformation optics established later (*3*–*5*); these important early studies were not fully appreciated and were almost forgotten. Only recently has the field of transformation optics been reestablished (*6*–*10*).

Generally, light propagates so that the optical path, which is given by the product of the physical length and the refractive index, is minimized. Thus, by creating a complex distribution for the refractive index n, the geometrical path that minimizes the optical path can be curved in an almost arbitrarily complex way. One might think that such a molding of a light path is possible only in the limit of geometrical optics, which implies a scale much larger than the wavelength. Provided that the basic optical parameters of materials, ε and μ, are also transformed appropriately, and because of the generic invariance of Maxwell's equations, transformation optics makes it possible to mold and control light on all scales, from macroscopic sizes down to the deeply subwavelength scale. By creating a desired distribution of ε and μ, and thus a distribution of refractive index n, one can "curve" the space for light in a nearly arbitrary way, making it possible to propagate light not only in the backward direction (when n is negative) but also along nearly any curved line. As a result, a myriad of fascinating devices are achievable using transformation optics and metamaterials.

One of the most exciting applications is an electromagnetic cloak that can bend light around itself, similar to the flow of water around a stone, making invisible both the cloak and an object hidden inside (*6*, *11*). By excluding light from a certain area of space and bending the light around the space, one can make an object in that area invisible (*12*) (see the figure, left panel).

However, practical applications of transformation optics go far beyond just cloaking. Theory allows the control of light in an extreme and ultimate manner by providing a general recipe for obtaining complex spatial distributions of anisotropic permittivity and permeability. Using these distributions, a "curvilinear" optical space is molded, thereby creating the channel for the desired flow of light. The core challenge here is to approximate the required ideal optical space by manufacturable nanostructured metamaterials, with minimal loss of the required functionality, and thereby move from the theoretical description to actual prototypes.

One cannot only exclude light from some region, as in a cloak, but also do the opposite and concentrate light within a certain area of the space. In such a concentrator, light could be collected from all directions onto an arbitrarily small spot, leading to extremely high intensities [see the figure, middle left panel (*13*)]. The light concentrator may enable applications such as omnidirectional solar light collection and field-enhanced sensing.

Transformation optics can also enable a magnifying, planar hyperlens, which is probably the most exciting and promising metamaterial application to date. The information about the subwavelength features of an object is carried by evanescent waves that exponentially decay with distance. This decay results in the loss of the subwavelength details in the far-field image and thus limits the imaging resolution. The hyperlens transforms the evanescent fields into propagating waves, producing magnified far-field images of the subwavelength features (*14*–*17*).

However, the originally proposed hyperlens suffers from strong reflections at its inner and outer cylindrical surfaces, causing reduced light throughput. With local control of the electromagnetic response of metamaterials, the impedance matching at these boundaries can be improved (*18*) (see the figure, middle right panel). Moreover, the actual fabrication and use of the hyperlens is extremely challenging, as in its original concept it requires cylindrical symmetry. Such symmetry is needed to slowly increase the electromagnetic mode wavelength as the wave spreads away from the center of the device to the point where propagation in air becomes possible (*19*). In addition, its cylindrical symmetry limits applications, because placing an object of interest in the hyperlens' inner cylindrical cavity is often impossible. One would be better served by a planar hyperlens—if it were possible.

The approach of "engineering optical space" with local control of a metamaterial's response offers a direct solution to this problem. The process of "slowing down" the evanescent waves required for converting them into propagating waves in air can be achieved by properly varying the dielectric tensor within the hyperlens. Simulations for the proposed flat hyperlens (*13*) show that it can produce magnified far-field images of sub-λ structures (see the figure, right panel). Such a planar, magnifying hyperlens could eventually become a standard add-on to conventional microscopes. By enabling nanoscale resolution in optical microscopy, metamaterial-based transformation optics could allow one to literally see extremely small objects with the eye, including biological cells, viruses and, possibly, even DNA molecules.

Transformation optics enabled by metamaterials transforms the science of light and opens up many exciting applications that often go beyond what we could imagine until very recently.

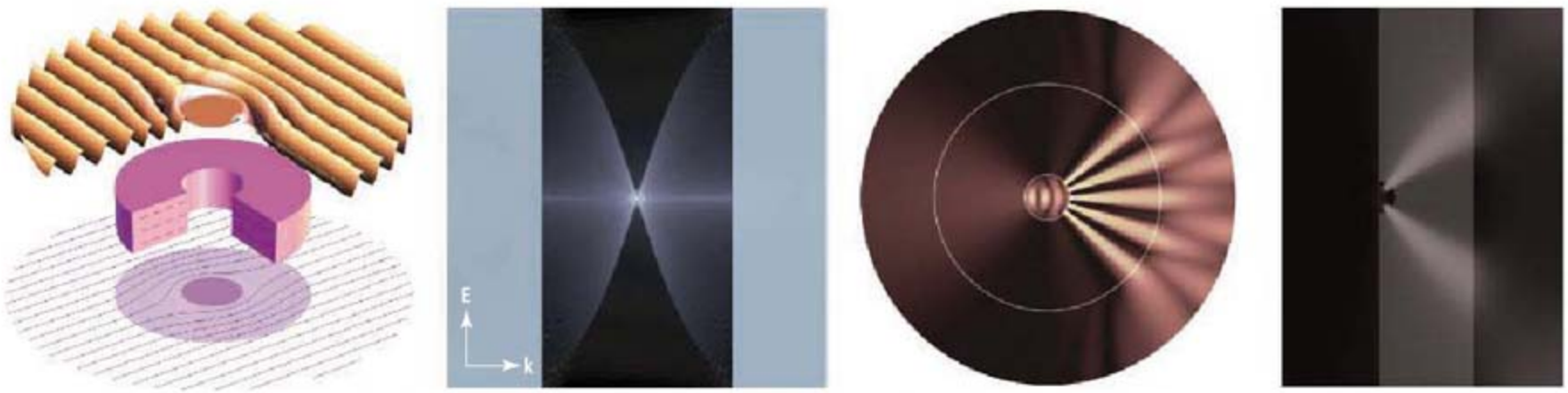

Optical transformations. **(Left)** Optical cloaking. **(Middle left)** Light concentrator [adapted from (*13*)]. **(Middle right)** Impedance-matched hyperlens [adapted from (*18*)]. **(Right)** Planar hyperlens [adapted from (*13*)].

CREDIT: A. V. KILDISHEV AND V. M. SHALAEV/PURDUE

References and Notes

1. I. Y. Tamm, *J. Russ. Phys. Chem. Soc.* **56**, 248 (1924).
2. I. Y. Tamm, *J. Russ. Phys. Chem. Soc.* **56**, 1 (1925).
3. L. S. Dolin, *Izv. Vyssh. Uchebn. Zaved., Radiofiz.* **4**, 964 (1961).
4. E. G. Post, *Formal Structure of Electromagnetics: General Covariance and Electromagnetics* (Interscience Publishers, New York, 1962).
5. M. Lax, D. F. Nelson, *Phys. Rev. B* **13**, 1777 (1976).
6. J. B. Pendry, D. Schurig, D. R. Smith, *Science* **312**, 1780 (2006).

7. W. C. Chew, W. H. Weedon, *Microwave Opt. Technol. Lett.* **7**, 599 (1994).
8. A. J. Ward, J. B. Pendry, *J. Mod. Opt.* **43**, 773 (1996).
9. U. Leonhard, *Science* **312**, 1777 (2006).
10. G. W. Milton, M. Briane, J. R. Willis, *New J. Phys.* **8**, 248 (2006).
11. D. Schurig *et al.*, *Science* **314**, 977 (2006).
12. W. Cai, U. K. Chettiar, A. V. Kildishev, V. M. Shalaev, *Nat. Photonics* **1**, 224 (2007).
13. A. V. Kildishev, V. M. Shalaev, *Opt. Lett.* **33**, 43, (2008).
14. Z. Jacob, L. V. Alekseyev, E. Narimanov, *Opt. Express* **14**, 8247 (2006).
15. A. Salandrino, N. Engheta, *Phys. Rev. B* **74**, 075103 (2006).
16. Z. Liu, H. Lee, Y. Xiong, C. Sun, X. Zhang, *Science* **315**, 1686 (2007).
17. I. I. Smolyaninov, Y.-J. Hung, C. C. Davis, *Science* **315**, 1699 (2007).
18. A. V. Kildishev, E. E. Narimanov, *Opt. Lett.* **32**, 3432 (2007)
19. E. E. Narimanov, V. M. Shalaev, *Nature* **447**, 266 (2007).
20. This work was supported in part by Army Research Office–Multidisciplinary University Research Initiative, ARO-MURI grant 50342-PH-MUR.

10.1126/science.1166079

PHYSICS

A New Spin on the Doppler Effect

Direct measurements can now be made of electron spin currents, which play a key role in advanced memory applications.

R. D. McMichael and M. D. Stiles

Electrical currents transport charge, but certain experimental setups allow them to transport spin as well. Such spin currents (excess flow of either spin-up or spin-down electrons) can by created by passing an electrical current through a ferromagnetic film; spins parallel to the film's spin orientation pass through more easily, whereas those of opposite sign are scattered more strongly. Spin currents are used in magnetic memories and are potentially useful in novel electronic switches (spintronics), because switching spin orientations may require less energy than is needed to turn a charge current on and off (*1*). One experimental challenge in developing such technology is that it is difficult to measure the flow of spin currents. On page 410 of this issue, Vlaminck and Bailleul (*2*) overcome this challenge by using a novel version of the Doppler effect to quantify the flow of spin currents in a ferromagnetic wire. They measure changes in the propagation of spin waves, which are oscillations of the spin orientation (see the figure, bottom panel).

The most prominent example of harnessing spin currents is the giant magnetoresistance (GMR) effect (*3*, *4*), which occurs when electrical current flows through two ultrathin ferromagnetic layers separated by a nonmagnetic spacer layer. When the magnetic domains of the ferromagnetic layers have parallel orientation, current flows more readily than when they are antiparallel, because the current of only one spin type (spin down, for example) undergoes extensive scattering. GMR has found numerous technological applications, including read heads in hard-disk drives, magnetic sensors, and magnetic random-access memory (MRAM). In many of these applications, the metallic spacer layer is replaced by a tunnel barrier made of oxides such as MgO. The associated resistance changes in such tunneling magnetoresistance (TMR) devices can be much greater than those in GMR devices.

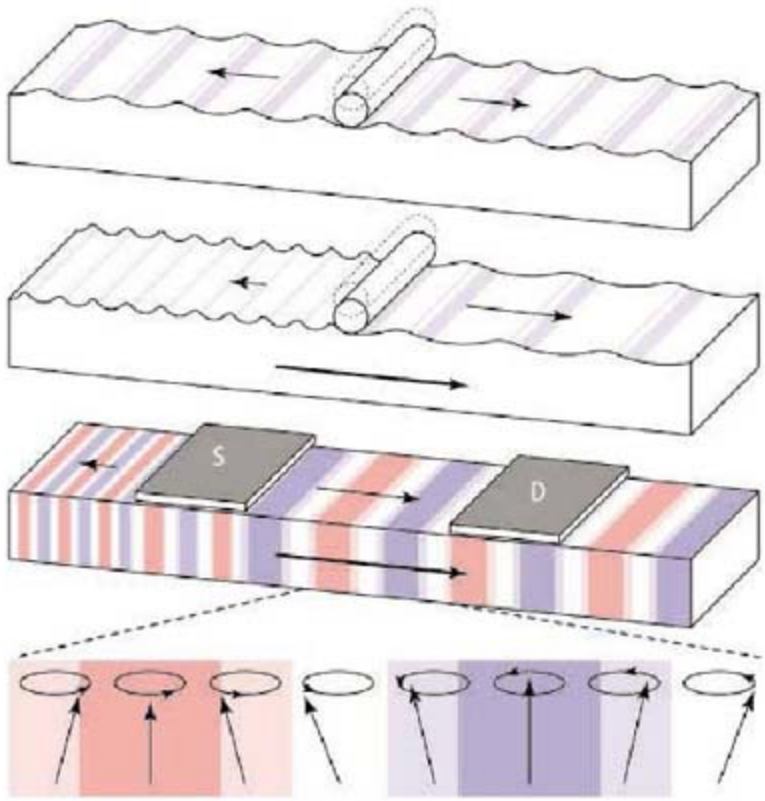

Doppler effects in moving media. **(Top)** Water waves propagate away from a moving cylinder with a frequency set by its oscillation frequency and a wavelength determined by the properties of the water. **(Middle)** Water flows past the cylinder (large arrow); the waves have the same frequency as before, but the downstream-propagating waves have a longer wavelength and the upstream-propagating waves have a shorter wavelength. The speed of the water can be determined from the change in the wavelength of the waves. **(Bottom)** A cartoon of the spin waves excited in the experiment of Vlaminck and Bailleul; the color shading corresponds to different points in the spin's precession (lower expanded view), while the different lengths of the blocks correspond to different propagation rates. Again, the spin waves propagating to the left and right of the source S have different wavelengths because of the spin current (large arrow) present in the system. The source and detector D are efficient only for a narrow range of wavelengths, so the maximum detector output occurs at a different frequency when the current flows. This transmission frequency shift yields the velocity of the effective magnetic medium of the spin waves.

In today's MRAM devices, spin currents are used only in the reading step through the GMR or TMR effects. In the writing step, the orientation of one of the ferromagnetic layers (the "soft layer") is changed by applying an external magnetic field. In a new generation of MRAM under development, spin currents are also used to write the bits (*5*). When a current passes through the spacer layer, the transport of angular momentum accompanying the spin current provides a spin transfer torque (*6*) that drives switching of one of the magnetic layers, performing the writing step.

If such development is successful, MRAM is projected to scale down to much smaller dimensions and could compete with dynamic random access memory (DRAM), which is presently used in computer memory. MRAM has the additional advantage of being nonvolatile like hard-disk drives, but even if MRAM could be scaled as far as conceivable with advanced lithographic fabrication methods, it will not approach the storage density available in hard-disk drives.

In MRAM applications, spin transfer torques act across a spacer layer; they also act within a single material and can be used to move the pattern of magnetic domain walls (which separate regions of opposite magnetic orientation) along a wire (*7*, *8*). A proposed "racetrack memory" (*9*, *10*), based on moving domain walls by spin

Center for Nanoscale Science and Technology, National Institute of Standards and Technology, Gaithersburg, MD 20899–6202, USA. E-mail: mark.stiles@nist.gov; robert.mcmichael@nist. gov

current, would compete with or exceed the memory density of mechanical hard-disk drives. These solid-state devices would stack bits on top of each other, storing information in the magnetic domains, regions of aligned spins, in vertically continuous magnetic wires. Similar to magnetic recording tape, bits of information represented by domain walls would be moved past a device that can read and write the information.

Unlike the tape, however, the magnetic racetrack wires are stationary. The magnetic information is moved by a spin current passing through the wire, so that the pattern of domains moves as the domain walls are carried "downstream" in the spin current. One difficulty in developing such devices has been characterizing the interaction between the spin-polarized current and the magnetic bits.

Direct measurements of the spin current are challenging, and the properties of the spin current are more often inferred from measurements of the magnetization or the electrical current. Some of the most interesting experiments are those that measure the current-induced motion of a domain wall. This motion is the basis for the racetrack memory mentioned above. However, one of the difficulties in interpreting these experiments is that unintentional inhomogeneities in the wires also influence the motion of domain walls (*11*). Thus, a basic property of the spin current, its polarization—the degree to which the current is carried by either spin-up or spin-down electrons—is not well known, and estimates generally depend on the experimental technique and the fabrication method. Because the polarization is often treated as a free parameter in the analysis of experiments, reliable polarization measurements would constrain experimental analysis and allow deeper understanding of the results.

Vlaminck and Bailleul introduce a reliable method for measuring the spin current polarization that makes use of the Doppler effect. In a common example of this effect, the pitch of a train whistle drops as the train passes the listener. In this case, there is relative motion between the source and the observer. The Doppler effect can also occur when the source and the observer are stationary, but the medium is flowing. An example is surface waves on a flowing body of water. The relation between how fast the waves go up and down (frequency) and the separation between the peaks (wavelength) as measured by the stationary observer is different than it would be if the water were not flowing (see the figure, top and middle panels). Measuring these changes can be used to determine the speed of the flowing water.

Vlaminck and Bailleul measured the change in the oscillation frequency of spin waves of a fixed wavelength in the presence of the current flow. They use the measured change to determine the effective flow rate of the magnetic medium in which the spin wave propagates. This flow rate is one of the fundamental quantities that characterize current-induced domain wall motion. We expect this experiment to be the first of a series that will enable the measurement of the spin characteristics of currents in ferromagnets. Such studies should also allow for a more quantitative analysis of experiments performed in the development of spin-based devices.

References

1. I. Zutic, J. Fabian, S. Das Sarma, *Rev. Mod. Phys.* **76**, 323 (2004).
2. V. Vlaminck, M. Bailleul, *Science* **322**, 410 (2008).
3. M. N. Baibich *et al.*, *Phys. Rev. Lett.* **61**, 2472 (1988).
4. G. Binasch, P. Grünberg, F. Saurenbach, W. Zinn, *Phys. Rev. B* **39**, 4828 (1989).
5. J. A. Katine, E. E. Fullerton, *J. Magn. Magn. Mater.* **320**, 1217 (2008).
6. D. C. Ralph, M. D. Stiles, *J. Magn. Magn. Mater*. **320**, 1190 (2008).
7. L. Berger, *J. Appl. Phys.* **49**, 2156 (1978).
8. L. Berger, *J. Appl. Phys.* **50**, 2137 (1979).
9. S. S. P. Parkin, M. Hayashi, L. Thomas, *Science* **320**, 190 (2008).
10. M. Hayashi, L. Thomas, R. Moriya, C. Rettner, S. S. P. Parkin, *Science* **320**, 209 (2008).
11. G. S. D. Beach, M. Tsoi, J. L. Erskine, *J. Magn. Magn. Mater.* **320**, 1272 (2008).

10.1126/science.1165717

CELL BIOLOGY

RNA Computing in a Living Cell

A system based on RNA can perform simple logical computations within a living cell, marking a step toward programming cell behavior.

Ehud Shapiro[1,2] and Binyamin Gil[2]

Engineering an autonomous, programmable molecular computing device that can operate inside a living cell, sense the presence or concentration of molecules, and act intelligently on what is sensed is a major goal of biomolecular computing. Such appropriately designed machines could potentially alter biological function and organism behavior by directly interacting with molecules within cells. An important step toward this goal is reported by Win and Smolke on page 456 in this issue (*1*).

The vision of autonomous programmable biomolecular computing devices has been advocated for some time (*2*–*9*). Initially, it was thought that these machines could perform with greater computational power than electronic counterparts (*3*). But this view changed when the true potential of molecular computers was recognized as their ability to operate in, and directly communicate with, a biological environment, a task not accessible to electronic computers (*4*, *10*, *11*). Previous milestones in this direction include in vitro demonstration of such a computing device (*7*) in which the software, input, and output were encoded in DNA and the hardware consisted of DNA-manipulating enzymes. The computer could be programmed to perform simple tasks such as determining whether a list of zeroes and ones had an even number of ones. It was later programmed with the ability to sense the concentrations of specific biomolecules [messenger RNA (mRNA)], perform a simple computation, and release a biomolecule (DNA) in response (*6*). Thus, it offered an in vitro proof-of-concept of disease diagnosis and therapy, by sensing abnormal concentrations of mRNA typical to a particular cancer, diagnosing the cancer, and releasing an agent to treat the diagnosed cancer in response. In another example, Seelig *et al.* (*11*) implemented Boolean logic gates over microRNA (miRNA) by using DNA strand displacement, rather than enzymes that manipulate DNA, and created multilayered circuits based on concepts borrowed from electronics (signal restoration, amplification, and feedback).

More recently, Rinaudo *et al.* (*12*) broke new ground by demonstrating a programmable biomolecular computing device that operates inside a living cell. The authors used the endogenous enzymatic machinery of the cell to compute, based on a "program" encoded in the DNA of a plasmid that was inserted into a

[1]Department of Computer Science and Applied Mathematics, Weizmann Institute of Science, Rehovot 76100, Israel. [2]Department of Biological Chemistry, Weizmann Institute of Science, Rehovot 76100, Israel. E-mail: ehud.shapiro@weizmann.ac.il

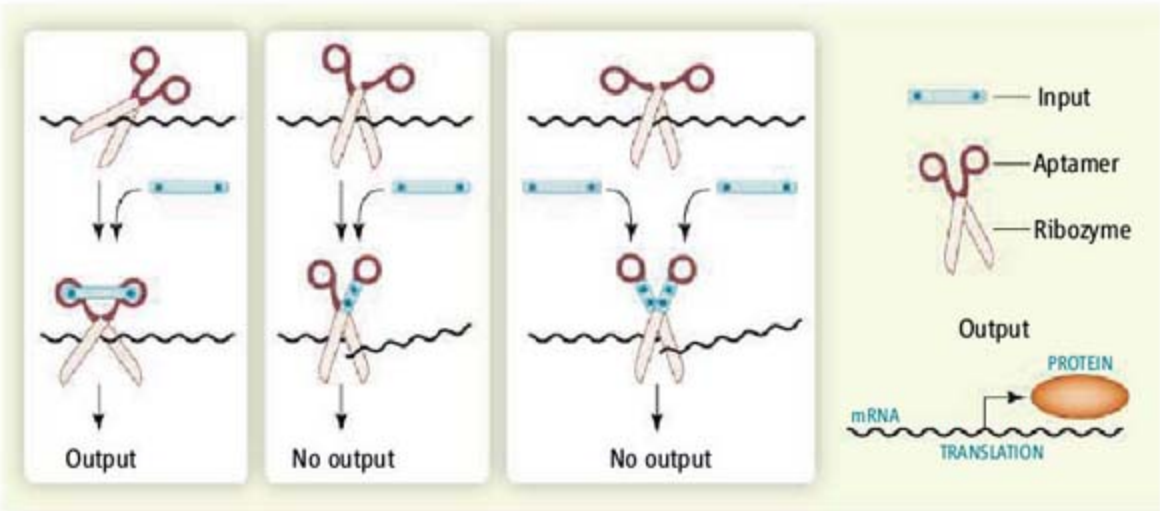

How does it compute? Shown is an analogy to the ribozyme-aptamer biomolecular computer designed by Win and Smolke. Controlling the ribozyme can be viewed as controlling the scissors' activity. Each of the scissors' handles corresponds to one aptamer and the patch is analogous to the input protein. **(Left)** Processing a simple logic operation (If Input, then Output): If the input protein (patch) is present, then aptamer-input interaction changes the ribozyme conformation, thus inhibiting ribozyme (scissors) cleavage activity, and output (translation of mRNA into protein) is achieved. **(Middle)** The opposed operation (If Not Input, then Output): Alternatively, the same input could bind to an aptamer and cause a conformational change that repairs the ribozyme and facilitate cleavage, thus blocking output. **(Right)** Processing a Boolean NAND operation (If Not input1 AND Input2 then Output]: If the two input proteins bind two aptamers, then the ribozyme cleaves the mRNA. Otherwise, the output protein is produced.

living cell. Computation was fully controlled by this externally provided program that was oblivious to the host cell's internal state. The program consisted of mRNA encoding a fluorescent protein. Target sequences for small interfering RNA (siRNA) were incorporated in the region that controls mRNA translation. The binding of externally provided siRNA to such a target would lead to mRNA degradation, allowing programmable siRNA control over the cell's level of fluorescence.

Win and Smolke further advance the state of the art by demonstrating programmable in vivo computation that is independent of the cell's own machinery and yet can respond to both endogenous and exogenous molecular signals. The authors achieve this feat by combining two of nature's most ancient inventions—ribozymes and RNA aptamers (*13*, *14*). Ribozymes are short, single-stranded RNA molecules that possess enzymatic activity. RNA aptamers are short RNA molecules that bind to specific target molecules, which could be almost any small molecule, including proteins, antibiotics, and dyes. Following other researchers who have harnessed these RNA molecules to perform molecular computation (*13*–*15*), Win and Smolke use ribozymes that can cleave RNA molecules and at the same time are aptamers, so that their cleaving ability can be regulated by another molecule that they specifically bind. The authors demonstrate, in yeast, several ways to use such combined ribozyme-aptamer molecules to implement Boolean logic operations like AND, OR, NAND (not-AND), and NOR (not-OR), using the concentrations of two proteins as input and the expression of green fluorescent protein (GFP) as output. Their system is modular and easy to program. It consists of mRNA encoding GFP with a modified control region (3′ untranslated region) in which one or more ribozyme-aptamer molecules are embedded. The modified mRNA can be translated into GFP only if it remains intact. Each ribozyme-aptamer embedded in the mRNA, if active, can cleave this mRNA, thus preventing its translation. However, ribozyme activity depends on whether its controlling aptamer is bound to its target. When the aptamer binds to its target, the ribozyme-aptamer undergoes a conformational change that alters ribozyme activity. The ribozyme-aptamer can be designed either so that aptamer binding allows cleavage or blocks cleavage by the ribozyme.

If we use scissors as an analogy for a ribozyme, then its controlling aptamer is a scissors' handle and the input is a patch that can bind the handle (see the figure). Following this analogy, the binding of an aptamer to its target obstructs the scissors' operation, or reconstructs a broken handle to yield proper operation (cleaving mRNA). To construct an AND gate using this molecular device, an mRNA can be designed to contain two ribozyme-aptamers, each responsive to one input molecule. Each input molecule could obstruct one ribozyme by binding to its aptamer, so that the mRNA molecule remains intact only when both inputs are present. A NAND operation is constructed by combining two aptamers with one ribozyme (see the figure). Win and Smolke show how one can combine simple gates to perform operations like AND, OR, NOR, and NAND, in response to different inputs—in this case, two small organic molecules (theophylline and tetracycline) that bind to the aptamers. Going beyond simple Boolean logic, a "bandpass" device that produces output only in response to a narrow concentration range of the input is constructed by combining two different gates for the same input.

As research in the past decade has shown, computing devices can be built from almost any combination of nature's basic tools. Win and Smolke have shown that one can go a very long way with the most basic and ancient natural devices. How far can we go once we learn to harness the more advanced machinery of the cell to our benefit? The challenges of biomolecular computer engineering are best illustrated by comparing them to those of electronic computer engineering. In the latter, one can conceive of an advanced and innovative computer design, use one's favorite computer-aided design software, send the design to a chip fabrication facility, and with luck have a working electronic device in short order. In the field of biomolecular computers, one can equally dream of innovative designs that can be made, in principle, from known protein building blocks (*4*). However, protein engineering is in its infancy compared to electronic circuit engineering. There is no protein design software to turn to, and no fabrication facility that can engineer a protein to a specification of its function. Therefore, researchers cannot construct their own advanced protein machinery and must make do with DNA (*3*, *5*, *6*, *11*), RNA (*1*, *12*–*15*), or naturally available proteins (*7*, *10*). A breakthrough in biomolecular computing is likely to come only on the heels of a breakthrough in protein engineering.

References

1. M. N. Win, C. D. Smolke, *Science* **322**, 456 (2008).
2. C. H. Bennett, *Int. J. Theor. Phys.* **21**, 905 (1982).
3. L. M. Adleman, *Science* **266**, 1021 (1994).
4. Y. Benenson, E. Shapiro, in *Dekker Encyclopedia of Nanoscience and Nanotechnology*, J. A. Schwarz, C. I. Contescu, K. Putyera, Eds. (Dekker, New York, 2004), pp. 2043–2056.
5. E. Winfree, F. R. Liu, L. A. Wenzler, N. C. Seeman. *Nature* **394**, 539 (1998).
6. C. Mao, T. H. LaBean, J. H. Reif, N. C. Seeman, *Nature* **407**, 493 (2000).
7. Y. Benenson, *et al. Nature* **414**, 430 (2001).
8. D. Sprinzak , M. B. Elowitz, *Nature* **438**, 443 (2005).
9. F. C. Simmel, *Nanomedicine* **2**, 817 (2007).
10. Y. Benenson *et al. Nature* **429**, 423 (2004).
11. G. Seelig, G. Soloveichik, D. Y. Zhang, E. Winfree, *Science* **314**, 1585 (2006).
12. K. Rinaudo *et al.*, *Nat. Biotechnol.* **25**, 795 (2007).
13. R. R. Breaker, *Curr. Opin. Biotechnol.* **13**, 31 (2002).
14. B. Suess, J. E. Weigand, *RNA Biol.* **5**, 1 (2008).
15. M. N. Stojanovic, D. Stefanovic, *Nat. Biotechnol.* **21**, 1069 (2003).

10.1126/science.1165665

CREDIT: ADAPTED BY P. HUEY/SCIENCE

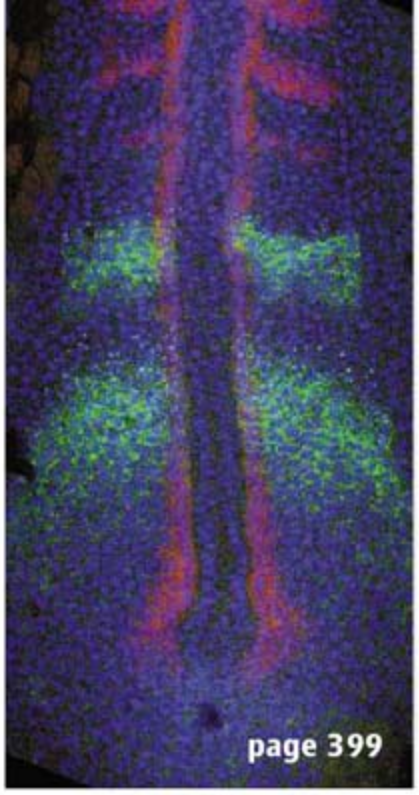

CREDIT: F. GIUDICELLI ET AL., PLOS BIOLOGY 5, 6 (7 JUNE 2008)

INTRODUCTION

Getting Your Loops Straight

COMPLICATED BIOCHEMICAL SIGNALING PATHWAYS REGULATE THE FUNCTION OF living cells. Such regulatory networks often have "downstream" components that provide input to components that act earlier in a pathway, creating feedback loops. These feedback loops have the potential to greatly alter the properties of a pathway and how it responds to stimuli. To fully understand these regulatory systems and exploit their vast potential as targets of therapeutic strategies, we need quantitative information on the flow of signals through a pathway and on the timing and location of signaling events within cells. We need to explore the properties that determine, for example, whether a system shows a graded response to a stimulus or turns on and off like a switch, how long a pathway stays activated, whether its output oscillates, which components can be perturbed to control the output of the system, and so on. The papers assembled in this special issue and in the companion issue of *Science Signaling* highlight recent progress in tackling these challenges.

The systems-level approaches required to understand signaling networks often integrate mathematical modeling with traditional biochemical analysis. Brandman and Meyer (p. 390) describe the ways in which feedback loops allow sophisticated regulatory responses, such as adaptable sensors that respond to changes in the amplitude of an input signal rather than the absolute amount of that signal. Lewis (p. 399) summarizes recent examples in which modeling approaches allow new insights into classical problems in development. Spemann's organizer, for example, emits a gradient of signaling molecules, and recent work explains how the system adjusts when an embryo is damaged, to recreate a complete body axis. Tools that allow precise noninvasive control and monitoring of biochemical components facilitate sorting out how a system responds. As Gorostiza and Isacoff explain (p. 395), it is now possible not only to sample the output of signaling systems by monitoring the fluorescence of reporter molecules but also to engineer proteins with light-dependent isomerization switches that, when reintroduced into cells, can be controlled precisely in time and space by exposure to light.

At *Science Signaling* (see www.sciencemag.org/cellsignaling08), an original research paper by Abdi *et al*. takes strategies that engineers use to understand the vulnerability of digital circuits and applies them to biological systems to identify key elements of cellular signaling networks. In Perspectives, Dohlman discusses how scaffolding molecules can determine the graded or switchlike response of a pathway. Elston summarizes how responses to pulsatile inputs are used to understand the dynamic behavior of a signaling system in yeast. Chiang and Muir outline advances in chemical approaches providing deeper insight into signaling mechanisms.

Getting your loops straight—or understanding how a complicated signaling network might respond in any given situation—does not come easily or intuitively. But the approaches mentioned here are clearly opening a large area of investigation of enormous practical potential.

– L. BRYAN RAY

Cell Signaling

CONTENTS

Reviews

Related material will be published in the 21 October issue of Science Signaling *(www.sciencesignaling.org).*

Science

REVIEW

Feedback Loops Shape Cellular Signals in Space and Time

Onn Brandman[1] and Tobias Meyer[2]

Positive and negative feedback loops are common regulatory elements in biological signaling systems. We discuss core feedback motifs that have distinct roles in shaping signaling responses in space and time. We also discuss approaches to experimentally investigate feedback loops in signaling systems.

Feedback loops are processes that connect output signals back to their inputs. The history of biological feedback goes back at least 130 years to observations by Eduard Pflüger that organs and other living systems "satisfy their own needs" (*1*). Feedback became an influential concept that led to Walter Cannon's theory of physiological homeostasis (*2*); Alan Turing's model of pattern formation (*3*); as well as investigations of metabolic end-product inhibition (*4*), metabolic oscillations (*5*), and transcriptional self-repression (*6*). Biological feedback concepts were further influenced by chemical oscillation theories (*7*) and the field of cybernetics (*8*). It has more recently become appreciated that the concept of feedback may be useful as a framework for understanding how intracellular signaling systems elicit specific cell behavior.

Mammalian species use over 3000 signaling proteins and over 15 second messengers to build hundreds of cell-specific signaling systems. Many of the signaling components have multiple upstream regulators and downstream targets, creating a web of connectivity within and between signaling pathways (*9*). The presence of multiple feedback loops in these systems (*10*) poses a challenge to understanding how receptor inputs control cellular behavior. We discuss how recurring feedback designs, or motifs (*11*), mediate biological functions such as bistability, oscillation, polarization, and robustness. Our goal was to generate a comprehensive guide for feedback in signal transduction that would also be instructive for understanding transcription networks, control of metabolism, pattern formation, the cell cycle, and the behavior of circadian oscillators.

We focus on two mammalian signaling systems: the receptor-triggered Ca^{2+} signaling system in nonexcitable cells (*12*) and the phosphoinositide 3-kinase (PI3K) signaling pathway in chemotactic neutrophils (*13*). These were chosen because of existing knowledge of feedback mechanisms that generate both simple and complex temporal and spatial signaling responses (Fig. 1). We use graphical representations of feedback motifs, with signaling components shown as vertices and directed negative and positive regulatory steps shown as arrows with and without minus symbols, respectively (Figs. 2 to 5, gray background). An arrow may consist of multiple steps so that a single positive arrow could reflect, for example, the net effect of two serial negative regulatory steps. Feedback loops are defined as paths that begin from and return to the same vertex. We also use mathematical representations with variables corresponding to vertices and equation terms corresponding to arrows (table S1). The simulated functions for each motif (Figs. 2 and 3) can be recreated by accompanying computer programs (table S2). We conclude by suggesting experimental approaches to investigate feedback loops.

[1]Department of Cellular and Molecular Pharmacology, University of California-San Francisco and Howard Hughes Medical Institute, San Francisco, CA 94158, USA. E-mail: Onn.Brandman@ucsf.edu [2]Department of Chemical and Systems Biology, 318 Campus Drive, Clark Building W200, Stanford University Medical Center, Stanford, CA 94305–5174, USA. E-mail: tobias1@stanford.edu

Signaling with a Single Negative Feedback Loop

Negative feedback loops are found in nearly all known signaling pathways and are defined as sequential regulatory steps that feed the output signal, inverted, back to the input (Fig. 2A). Depending on its characteristics and initial conditions, a single negative feedback motif can create four distinct signaling functions: basal homeostat, output limiter, adaptation, and transient generator.

The presence of a small-amplitude negative feedback loop stabilizes the basal signaling state without preventing strong input signals from triggering maximal pathway activation (Fig. 2A, basal homeostat). In this case, small deviations of an input signal are suppressed in the output, and only large changes in the input control the output. For example, a negative feedback involving the endoplasmic reticulum (ER) Ca^{2+}-sensing protein STIM2 (stromal interaction molecule 2) (*14*) keeps basal Ca^{2+} concentration in the cytosol and in the lumen of the ER at ~50 nM and ~400 μM, respectively. STIM2 triggers influx of extracellular Ca^{2+} at ER–plasma membrane junctions in response to a reduction in ER Ca^{2+} concentration, forming a negative feedback loop (*14*). Because many cellular processes are regulated by Ca^{2+}, maintaining proper resting levels is crucial.

A different use of negative feedback is to limit maximum signaling output (Fig. 2A, limiter). Upon stimulation, the output signal rapidly increases but is attenuated once it passes a threshold. For example, receptor-triggered increases of

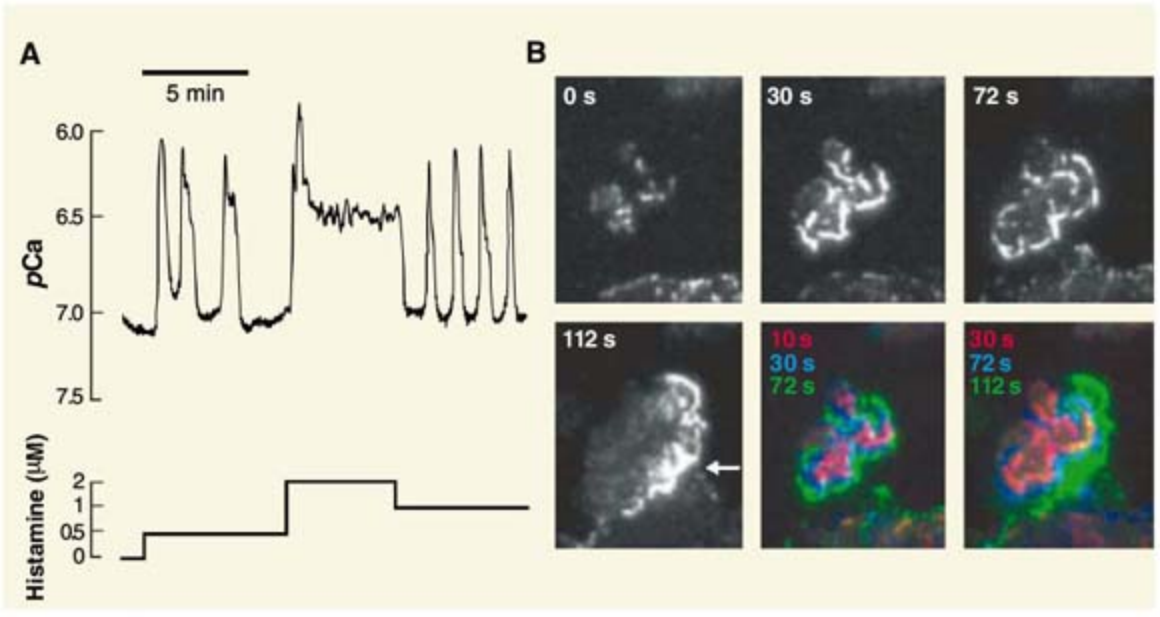

Fig. 1. Ca^{2+} and chemotaxis signaling systems exhibit complex temporal and spatial dynamics. (**A**) Histamine-triggered cytosolic Ca^{2+} signals in a single epithelial cell. The response includes spikes, oscillations, and plateaus. pCa is the negative log of the Ca^{2+} concentration (7 and 6 correspond to 10^{-7} and 10^{-6} M, respectively). [Adapted from (*28*)] (**B**) Total internal reflection fluorescence images of a neutrophil cells stimulated by chemoattractant. Hem-1 is a regulator of actin polymerization that initially concentrates in foci. It then relocalizes as part of outwardly propagating waves of actin polarization that terminate when the leading edge is reached (denoted by arrow at 112 s). The fifth and sixth images show overlays of successive Hem-1 distributions in red, blue, and green, respectively. [Adapted from (*29*)]

Ca^{2+} concentration in the cytosol are clipped and stabilized by a rapid negative feedback resulting from Ca^{2+} uptake by mitochondria. Mitochondrial Ca^{2+} uptake progressively increases when cytosolic Ca^{2+} concentration exceeds about 0.6 μM (*15*) and therefore occurs only during active signaling.

Negative feedback is also necessary to generate adaptive behavior. Adaptive signaling systems are built to respond to changes in input rather than the absolute amount of input signal (Fig. 2A, adaptive). Studies of bacterial chemotaxis (*16*) and vertebrate visual signal transduction (*17*) revealed sophisticated regulatory circuits that generate optimized adaptative behavior. In neutrophil chemotaxis, cells sense relative chemoattractant gradients by a mechanism that involves partial deactivation and subsequent internalization of activated cell surface receptors. The resulting lower input level prevents saturation of downstream signaling responses and allows for subsequent signaling when chemoattractant concentrations further increase (*18*). Most heterotrimeric guanine nucleotide–binding protein (G-protein)–coupled receptors, which include receptors involved in chemotaxis, exhibit adaptive behavior through use-dependent receptor down-regulation (*19*).

Lastly, a strong negative feedback loop that is triggered after a delay converts a constant input into a transient output signals with amplitudes that increase as a function of the amplitude of the input step (Fig. 2A, transient generator). An example of this function is the delayed activation of the Ca^{2+}/calmodulin (CaM)–regulated plasma membrane Ca^{2+} pump (PMCA) (*20*). After a 10- to 60-s delay that follows an increase in cytosolic Ca^{2+}, enhanced PMCA activity reduces the Ca^{2+} signals to create a transient signaling response.

Signaling with a Single Positive Feedback Loop

Positive feedback is often associated with uncontrolled, runaway processes such as nuclear chain reactions and models of catastrophic climate change. Nevertheless, functions of positive feedback in biological systems have been described for almost 100 years (*21*). Positive feedback is defined as a set of regulatory steps that feeds the output signal back to the input (Fig. 2B). If signaling output activity increases, positive feedback will further increase input levels, thereby enhancing the output signal. There are three common functions of a single positive feedback motif: amplifying a signal, changing the timing of a signaling response, and creating bistable switches.

Positive feedback can provide absolute as well as relative amplification (Fig. 2B, amplifier). Both types of amplification are exemplified in the activation of the inositol 1,4,5-trisphosphate (IP_3)–receptor (IP_3R), a ligand-gated ER-localized Ca^{2+} channel. The binding of four IP_3 molecules to a single IP_3R is believed to partially activate the channel, inducing an initial Ca^{2+} release from the ER. This, in turn, triggers a positive feedback

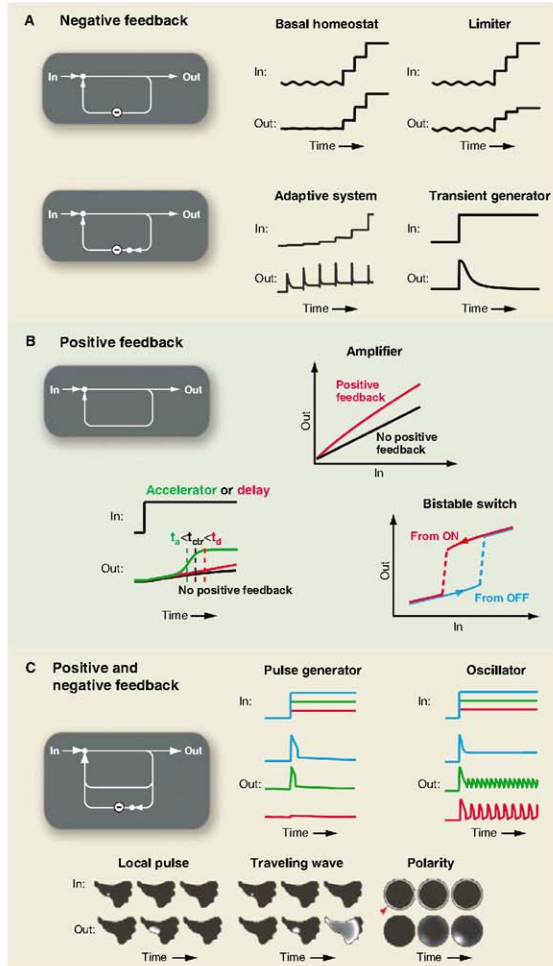

Fig. 2. Feedback motifs have important functions in signaling systems. **(A)** Negative feedback can stabilize basal signaling levels, limit maximal signaling output, enable adaptive responses, or create transient signal responses. **(B)** Positive feedback can amplify signaling responses, alter kinetics, or create bistable switches. **(C)** Mixtures of positive and negative feedback can create single pulses or oscillatory signal outputs. Mixed feedbacks can also trigger local signals, self-propagating waves, or cell polarization.

loop whereby the binding of multiple released Ca^{2+} molecules fully activates IP_3Rs (*22*). Thus, as a result of binding four IP_3 molecules, thousands of Ca^{2+} ions are released into the cytosol, providing for absolute amplification of the input signal. The ultrasensitive nature of the release process also results in relative amplification; a threefold increase in IP_3 can result in a 20-fold increase in cytosolic Ca^{2+} levels (*23*). Ultrasensitive regulatory steps are characterized by a sigmoidal dose-response curve (*24*).

As is the case for negative feedback (limiter and transient generator), positive feedback also changes the timing of the signaling response (Fig. 2B, accelerator or delay). In the case of IP_3-gated Ca^{2+} release, positive feedback accelerates the signaling response by opening more Ca^{2+} channels so that a saturating cytosolic Ca^{2+} concentration is more rapidly reached (green curve; half-maximal time: $t_a < t_{ctr}$). Positive feedback in nonsaturating conditions can also prolong the time required to reach a higher steady state (red curve; $t_d > t_{ctr}$) (*10*).

A positive feedback loop with an ultrasensitive regulatory step can trigger a bistable switch (Fig. 2B, bistability) (*25*). This is arguably one of the most important regulatory motifs in cell signaling. For inputs below a critical threshold, the signaling output remains near its basal state; for inputs above the threshold, the output increases to a high, active state. Bistable systems make use of hysteresis to remain in the active state, meaning that the input stimulus required to keep the system in the active state is lower than the input required for triggering the initial transition from basal to active state. Many cell signaling processes have been proposed to use positive feedback to implement either a reversible or irreversible bistable switch, such as Ca^{2+} spikes (*25*), chemotaxis (*26*), and oocyte maturation (*27*).

Mixed Positive and Negative Feedback

Delayed negative feedback can force a bistable system back to the inactive state and create a pulse in the signaling output that is typically characterized by a fixed amplitude and duration (Fig. 2C, pulse generator). Ca^{2+} pulses (*28*) are triggered by the aforementioned IP_3R fast positive feedback loop and a delayed negative feedback by which high levels of Ca^{2+} inhibit the IP_3R (*22*). Similarly, in neutrophil migration, a proposed fast positive feedback loop between the scaffold protein hematopoietic 1 (Hem-1) and actin nucleation enhances actin polymerization and local extension of lamellipods (*29*). Recruitment of a yet-unidentified inhibitor may break apart sites of nucleation, resulting in reversible local lamellipod extension. The common design principle is that the negative feedback that terminates the positive feedback is induced only at high concentrations of the output signal or after a time delay.

After a pulse in output activity, the negative feedback inhibition often recovers so that a new positive feedback cycle can be triggered. This results in a periodic cycling between high and low output states in response to a steady input (Fig. 2C, oscillator). In cell signaling, such a role of ultrasensitive positive and negative feedback in generating Ca^{2+} concentration oscillations was proposed 20 years ago (*25*). Model calculations showed that increases in stimulus amplitude increase the frequency of oscillation while keeping the duration and the amplitude of pulses constant. This behavior has been observed experimentally (*28*). Although there are feedback motifs without positive feedback that can produce oscillations (*30*), we believe that a more common mechanism in cell signaling consists of coupled positive and negative feedback loops (*31*).

Spatial Aspects of Mixed Positive and Negative Feedback

Biological systems often feature positive and negative feedbacks that are active in only part of the cell rather than the whole cell. This results in distinct functions such as local pulses, waves, and cell polarization (Fig. 2C, bottom images).

Local signal activation can occur without a global response (Fig. 2C, local pulse). In the case of Ca^{2+} signaling under weak stimulation, local positive feedback that activates IP_3R quickly inactivates, and the diffusing Ca^{2+} ions can be restricted to sub-micrometer distances from the source, creating local Ca^{2+} pulses (*32*). Local Ca^{2+} signaling pulses are useful to control cell functions such as secretion (*33*). In weakly stimulated neutrophils (and therefore in the absence of cell polarity), a chemoattractant triggers similar short-lived local pulses of actin polymerization (*29*).

If the local signal is sufficiently strong, new local pulses triggered at nearby sites can keep the signal alive and allow a self-propagating signal to move away from its source (Fig. 2C, traveling wave). Models combining positive and negative feedback with a diffusive second messenger predict the existence of such self-propagating Ca^{2+} waves (*34*). Ca^{2+} waves have been shown to propagate across gap junctions and synchro-

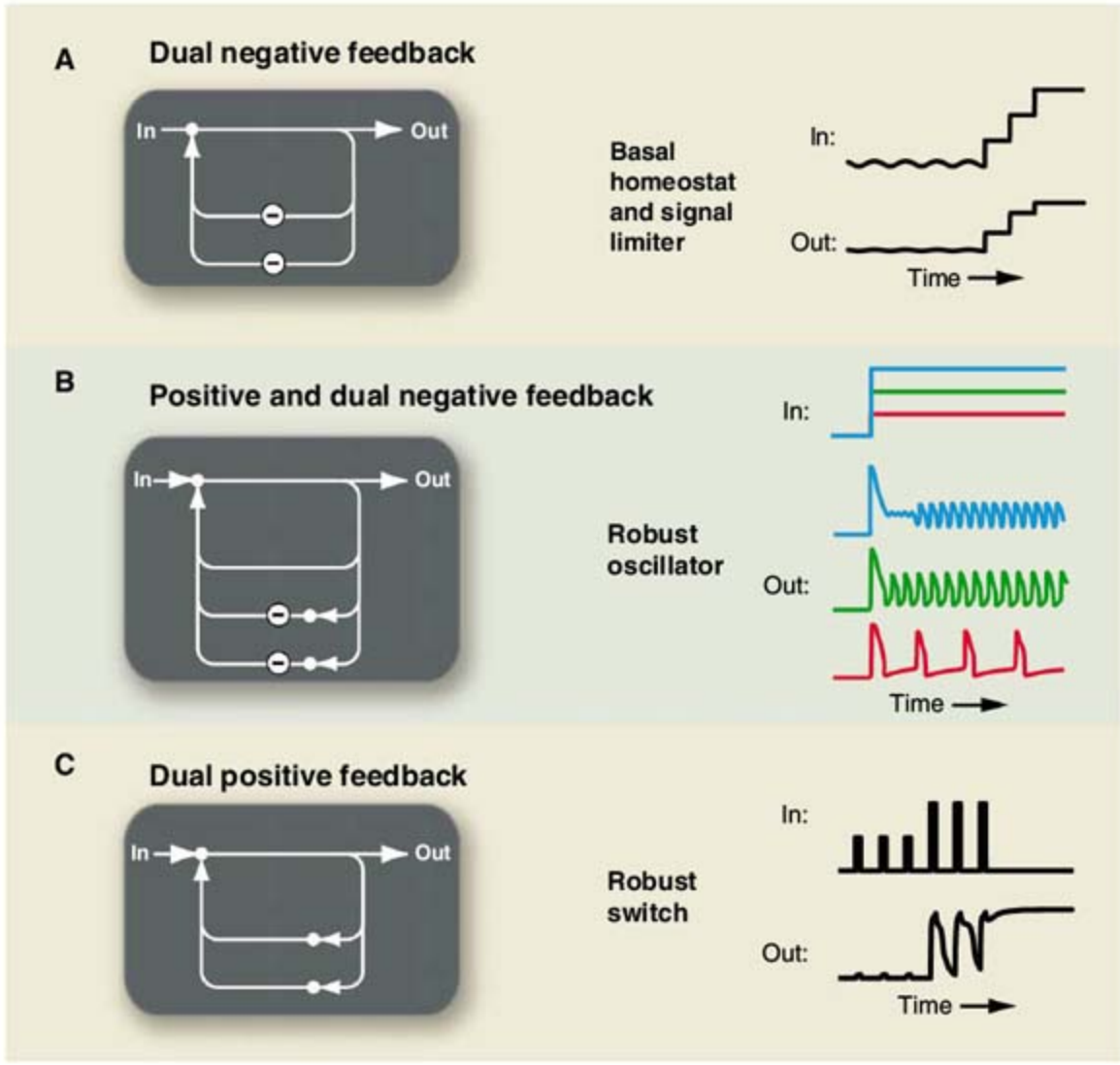

Fig. 3. Addition of extra feedback to core functions can be used to integrate key signaling characteristics or enhance the robustness of important functions. (**A**) Combining two negative feedback loops can independently stabilize basal signaling and limit maximal signal output. (**B**) Adding a negative feedback loop to the oscillator in Fig. 2C can result in sharper spikes, an increased input range over which oscillations occur and an increased output frequency range. (**C**) A system made up of a dual fast and slow positive feedback loops can exhibit transient or persistent bistable states if the fast or both positive feedbacks are engaged.

nize astrocyte, epithelial, and other cell assemblies (*35*). Similarly, under stimulated conditions, neutrophils generate local waves of actin polymerization that propagate over several micrometers toward the front of a cell until they reach a cell's leading edge, where they extend local lamellopdia and help propel the cell forward (*29*).

Combined positive and negative feedback can also polarize cells (Fig. 2C, polarity). Polarization and migration of neutrophils has been proposed to be regulated by a positive feedback loop whereby the guanylate exchange activator of the small guanosine triphosphatase Rac, Dock, both activates lamellipod extension and is recruited to locations where lamellipods extend (*13*, *36*). Once the positive feedback-driven local recruitment has been triggered (stochastically or in response to a local input), it diminishes the concentration of available Dock throughout the cell. This is a plausible mechanism for a negative feedback that can prevent a second front from forming. Mathematical modeling of a neuronal polarity system showed that reinforced local recruitment of a scarce activator is a robust mechanism for triggering cell polarization (*37*).

Enhancing Core Feedback Functions by Adding Feedback

Addition of extra feedback loops provides enhancements to the discussed core feedback functions. A design with two negative feedback loops allows cells to simultaneously stabilize the basal state and limit the activated signaling state (Fig. 3A, basal homeostat and limiter). Combined negative feedback through STIM2 and mitochondrial Ca^{2+} uptake is an example where two negative feedback loops function largely independent of each other. Combination of a basic oscillator (single positive and negative feedback loops) with an additional negative feedback loop can create patterns of repetitive spikes over a broader range of input stimuli and generate a wider range of output frequencies (Fig. 3B, robust oscillator). A reported calcium/calmodulin-dependent protein kinase II (CaMKII)–mediated inhibitory phosphorylation of the IP_3R (*38*) may serve as such a second negative feedback loop that prolongs the time between Ca^{2+} spikes and thereby extends the output frequency range.

A key function of a second positive feedback loop is to make a bistable signaling switch more robust in the presence of cell-to-cell variations resulting from noise in external inputs or copy numbers of internal signaling components (Fig. 3C, robust switch) (*39*). In the example shown, the first three stimulus pulses are not sufficient to engage the positive feedbacks, the next two stimuli trigger only the fast reversible positive feedback, whereas the last stimulus also engages the slow positive feedback and triggers a persistent output increase. This same motif also increases the overall ultrasensitivity and hysteresis if the two positive feedback loops are linked by an AND gate (*40*). Furthermore, coupling two positive feedback loops in which one loop is composed of two negative regulatory steps can delay the exit from the active state (*41*). Lastly, the added slower positive feedback loop can also spatially integrate and synchronize the activity of the faster loop, converting separate local bursts of signaling into a robust global signaling response. In the case of Ca^{2+} signaling, Ca^{2+} activation of IP_3R can provide rapid and localized positive feedback, whereas a second slow positive feedback from Ca^{2+} concentration to phospholipase C (*25*, *42*) and the production of the rapidly diffusible second messenger IP_3 yield global bistability and increased robustness to noise when triggering global Ca^{2+} responses.

Thus, although different types of network connectivity can generate dual positive feedback loops, these examples suggest that a common emerging property is enhanced robustness to noise. The robustness results from (i) increased hysteresis, (ii) increased spatial synchronization, (iii) delayed exit from the active state, or (iv) a combination thereof. It is plausible that addition of tailored positive or negative feedback loops to other functions described in Fig. 2 also make their functional properties more robust.

Signaling Systems Combine Multiple Feedback Functions to Orchestrate Cell Behavior

Feedback functions are combined in cells to produce a physiological output behavior. Graphic representations that reduce each of the feedback loops to a positive or negative regulatory step are useful to describe systems with multiple feedbacks. This is achieved by functionally annotating and ordering nested feedback loops according to increasing time constants. In the Ca^{2+} signaling

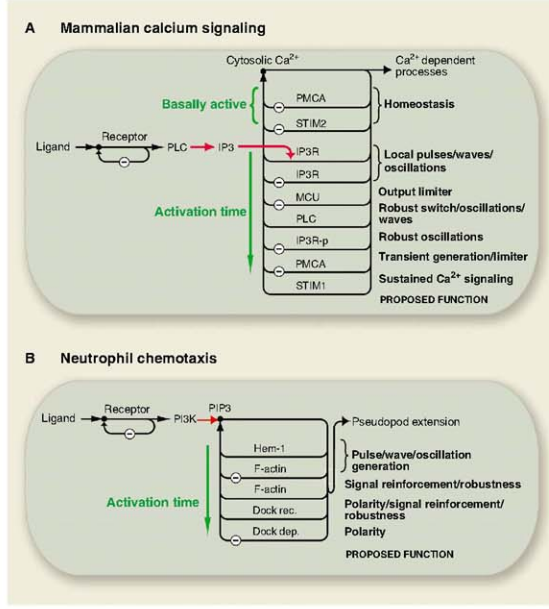

Fig. 4. Cell signaling systems take advantage of multiple feedback loops nested in time and space to generate desired signaling responses. Schematic representations of **(A)** mammalian Ca^{2+} signaling for nonexcitable cells and **(B)** neutrophil chemotaxis. The input signal spreads from membrane-bound receptors to a network of interlinked feedback loops. Feedback loops are arranged according to the loop time constant. PLC, phospholipase C; MCU, mitochondrial Ca^{2+} uniporter; PIP3, phosphatidylinositol (3,4,5)-trisphosphate; Dock, dedicator of cytokinesis; rec., recruitment; dep., depletion.

system (Fig. 4A), basal homeostasis involves negative loops that include the ER Ca^{2+} sensor STIM2 and the Ca^{2+} regulation of PMCAs. In the receptor-stimulated case, the fastest positive and negative feedback loops are the Ca^{2+} activation and inhibition of the IP_3R, which can create local or more-global spikes. Spatial synchronization of Ca^{2+} signals and robust bistability, oscillations, and waves are provided by a second positive feedback loop based on Ca^{2+} activation of phospholipase C and generation of more IP_3. A second negative feedback that phosphorylates and down-regulates the IP_3R may enhance the frequency range of Ca^{2+} oscillations. Mitochondria limit maximal Ca^{2+} signaling responses, whereas plasma membrane pumps ensure that cytosolic Ca^{2+} signals remain transient. Persistent Ca^{2+} signaling requires a third positive feedback in which the ER Ca^{2+} sensor STIM1 links the lowering of ER Ca^{2+} concentration to plasma membrane Ca^{2+} influx, which in turn triggers additional IP_3R-mediated Ca^{2+} release and lowering of Ca^{2+} in the ER (*43*). This triple positive feedback in the Ca^{2+} system comprises a robust switch and is likely critical in T cells, where Ca^{2+} concentration has to remain elevated for many hours in order to induce T cell differentiation (*44*). Note that separate feedback loops in the diagram can regulate the same target. For example, IP_3R is activated by Ca^{2+} concentrations below 0.2 μM (creating a positive feedback loop) and inhibited by higher Ca^{2+} levels (creating a negative feedback loop) (*22*).

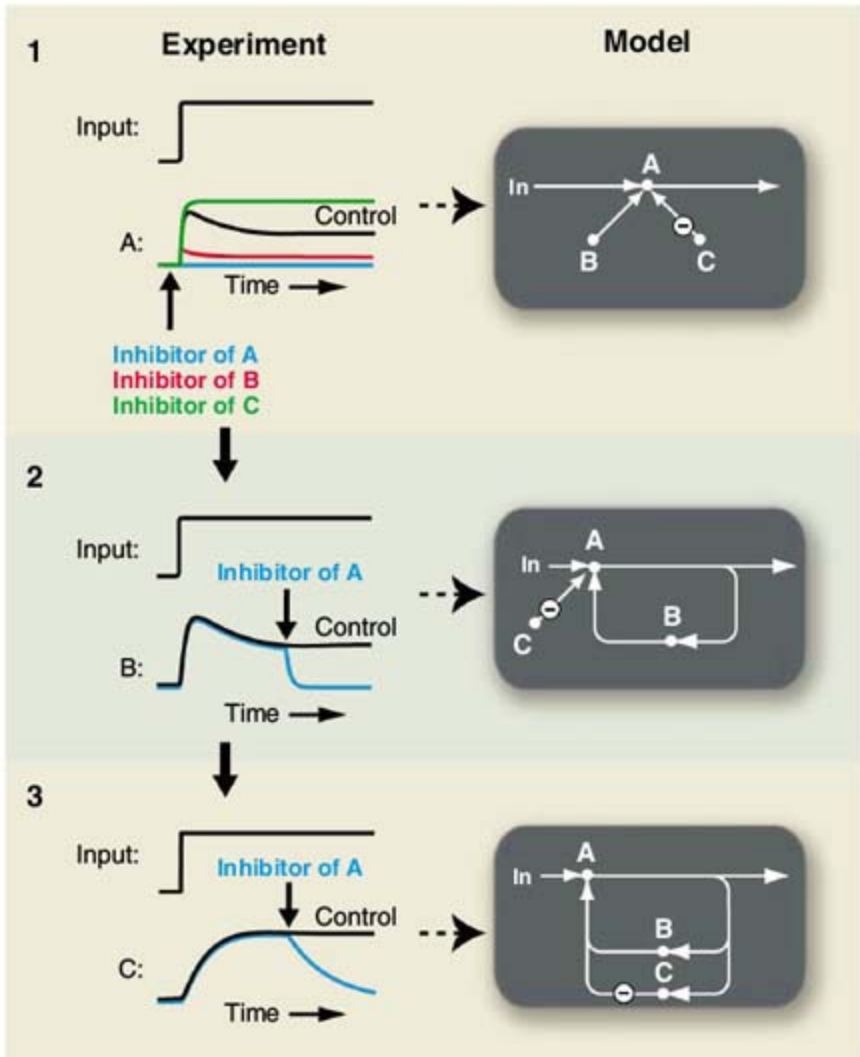

Fig. 5. Proposed rapid perturbation and monitoring strategy to experimentally investigate feedback loops. The shown graphs with proposed experiments use computer simulations of experiments to explain how fast perturbations and fast readouts can uncover feedback. Bold arrows denote the addition of inhibitors for the activities A, B, and C. Experiments in 1 show that the two players B and C regulate A. Experiments 2 and 3 reveal that B and C are part of a positive and a negative feedback loop, respectively.

In neutrophil chemotaxis, the balance between positive and negative feedback loops involving Hem-1 and other actin polymerization processes leads to small bursts in actin polymerization and local reversible lamellipod extensions (Fig. 4B) (*29*). When the proposed polarity-inducing positive feedback (e.g., Dock/Rac/PIP3) is engaged, actin polymerization and local lamellipod extension becomes restricted to the leading edge, resulting in cell migration (*13*, *29*). Key mechanisms for polarization are likely the recruitment of Dock and other components of the global positive feedback to the front and their concomitant depletion from the back. The time constants of feedback loops and the diffusion coefficients of their components define the spatial and temporal characteristics of local lamellipod extension and global cell polarization. Chemotaxis may then result from steering the front of these polarized cells by coupling local chemoattractant sensing to local lamellipod extension and creating small turns in the direction of migration toward a chemoattractant source (*45*). Additional feedback loops and regulatory components may further contribute to robust chemotaxis (*13*, *36*, *46*).

Experimental Investigation of Predicted Feedback Loops

Experimental investigation of signaling feedback in cells is challenging. Genetic, RNA interference, dominant negative, or chemical attenuation of a component's activity that results in an increased signaling response might indicate that the component (i) is part of a negative feedback loop, (ii) is part of a suppression step within the signaling pathway, or (iii) plays a housekeeping role by reducing protein stability, blocking endocytosis, or dephosphorylating an activation site. How can a postulated component in a signaling pathway be identified as part of a positive or negative feedback loop?

A direct approach to demonstrate that a positive or negative feedback controls a signaling pathway is to combine rapid perturbations of signaling steps with rapid monitoring of upstream and downstream signaling events (Fig. 5). We use a thought experiment to discuss this approach. In a first set of experiments, inhibitors of components A, B, and C are used to identify B and C as positive and negative regulators, respectively, of the signaling pathway leading to A. The second experiment monitors B and uses rapid inhibition of A to demonstrate a positive feedback from A back to B. The third experiment monitors C and uses rapid inhibition of A to demonstrate a negative feedback from A to C. Additional constrictions of a feedback model are gained from the kinetics of A, B, and C activity changes. There are three experimental challenges to the described approach: to develop perturbation tools to specifically and rapidly inhibit signaling steps, to develop biosensor or biochemical assays to rapidly measure their activity, and to set up single-cell experiments or use synchronized populations to be able to infer the existence and to measure the kinetics of putative feedback loops.

This strategy has been used in Ca^{2+} signaling to demonstrate the existence of a positive feedback from Ca^{2+} to phospholipase C. A rapid increase in cytosolic Ca^{2+} concentration by addition of Ca^{2+} ionophore increased the concentration of the phospholipase C product IP_3 within seconds (*42*). The kinetics of the other step in the feedback loop was measured by a rapid step increase in the concentration of IP_3 by photorelease of an inactive IP_3 precursor and measurement of the resulting subsecond Ca^{2+} release using a fluorescent biosensor (*47*). In neutrophils, the positive feedback for polarization was investigated by rapid chemical inhibition of PI3K (*48*) and by a chemical heterodimerization method whereby synthetic activators of endogenous PI3K and Rac proteins were forced to the plasma membrane within less than 30 s (*49*). These perturbations were combined with live-cell imaging of phoshoinositol 3,4,5-phosphate localization, lamellipod extension, and cell migration to infer the existence of a positive feedback (*48*, *49*).

Conclusions

Each feedback motif has a specific function in a signaling system, such as homeostasis or adaptation for a negative feedback motif, amplification or bistability for a positive feedback motif, and polarization or oscillations for a mixed feedback motif. The function of a particular feedback motif

depends on its characteristics and initial conditions. Cell signaling systems are made up of multiple feedback functions that together generate a cell's input-output behavior. We propose that working models of signaling systems can be based on graphic representations that show signaling components as part of feedback motifs with assigned functions and sorted by increasing feedback time constants. If the known feedback functions are insufficient to explain a cell's input-output behavior, this analysis can guide the search to identify control loops missing from a signaling model.

References and Notes

1. E. F. W. Pflüger, *Pflügers Arch.* **XV**, 57 (1877).
2. W. B. Cannon, *Physiol. Rev.* **IX**, 399 (1929).
3. A. M. Turing, *Philos. Trans. R. Soc. London Ser. B* **237**, 37 (1952).
4. H. E. Umbarger, *Science* **123**, 848 (1956).
5. B. Chance, R. W. Estabrook, A. Ghosh, *Proc. Natl. Acad. Sci. U.S.A.* **51**, 1244 (1964).
6. J. Monod, F. Jacob, *Cold Spring Harbor Symp. Quant. Biol.* **26**, 389 (1961).
7. I. Prigogine, *Thermodynamics of Irreversible Processes* (Interscience, New York, ed. 2, 1961).
8. N. Wiener, *Cybernetics: Or the Control and Communication in the Animal and the Machine* (MIT Press, Cambridge, MA, 1948).
9. J. D. Jordan, E. M. Landau, R. Iyengar, *Cell* **103**, 193 (2000).
10. M. Freeman, *Nature* **408**, 313 (2000).
11. U. Alon, *Nat. Rev. Genet.* **8**, 450 (2007).
12. D. E. Clapham, *Cell* **131**, 1047 (2007).
13. L. Stephens, L. Milne, P. Hawkins, *Curr. Biol.* **18**, R485 (2008).
14. O. Brandman, J. Liou, W.S. Park, T Meyer, *Cell* **131**, 1327 (2007).
15. D. Nicholls, K. Akerman, *Biochim. Biophys. Acta* **683**, 57 (1982).
16. U. Alon, M. G. Surette, N. Barkai, S. Leibler, *Nature* **397**, 168 (1999).
17. M. E. Burns, D. A. Baylor, *Annu. Rev. Neurosci.* **24**, 779 (2001).
18. S. H. Zigmond, S. J. Sullivan, *J. Cell Biol.* **82**, 517 (1979).
19. S. M. DeWire, S. Ahn, R. J. Lefkowitz, S. K. Shenoy, *Annu. Rev. Physiol.* **69**, 483 (2007).
20. D. M. Bautista, M. Hoth, R. S. Lewis, *J. Physiol.* **541**, 877 (2002).
21. A. Lotka, *J. Phys. Chem.* **14**, 271 (1910).
22. I. Bezprozvanny, J. Watras, B. E. Ehrlich, *Nature* **351**, 751 (1991).
23. D. O. Mak, S. McBride, J. K. Foskett, *Proc. Natl. Acad. Sci. U.S.A.* **95**, 15821 (1998).
24. D. E. Koshland Jr., A. Goldbeter, J. B. Stock, *Science* **217**, 220 (1982).
25. T. Meyer, L. Stryer, *Proc. Natl. Acad. Sci. U.S.A.* **85**, 5051 (1988).
26. H. Meinhardt, A. Gierer, *Bioessays* **22**, 753 (2000).
27. W. Xiong, J. E. Ferrell Jr., *Nature* **426**, 460 (2003).
28. R. Jacob, J. E. Merritt, T. J. Hallam, T. J. Rink, *Nature* **335**, 40 (1988).
29. O. D. Weiner, W. A. Marganski, L. F. Wu, S. J. Altschuler, M. W. Kirschner, *PLoS Biol.* **5**, e221 (2007).
30. M. B. Elowitz, S. Leibler, *Nature* **403**, 335 (2000).
31. T. Y. Tsai *et al.*, *Science* **321**, 126 (2008).
32. I. Parker, Y. Yao, *Proc. Biol. Sci.* **246**, 269 (1991).
33. G. J. Augustine, E. Neher, *Curr. Opin. Neurobiol.* **2**, 302 (1992).
34. T. Meyer, L. Stryer, *Annu. Rev. Biophys. Biophys. Chem.* **20**, 153 (1991).
35. A. H. Cornell-Bell, S. M. Finkbeiner, M. S. Cooper, S. J. Smith, *Science* **247**, 470 (1990).
36. J. Sai *et al.*, *J. Biol. Chem.*, in press.
37. M. Fivaz *et al.*, *Curr. Biol.* **18**, 44 (2008).
38. J. K. Foskett *et al.*, *Physiol. Rev.* **87**, 593 (2007).
39. O. Brandman, J. E. Ferrell Jr., R. Li, T. Meyer, *Science* **310**, 496 (2005).
40. A. Politi, L. D. Gaspers, A. P. Thomas, T. Hofer, *Biophys. J.* **90**, 3120 (2006).
41. J. E. Ferrell Jr., *Curr. Biol.* **18**, R244 (2008).
42. A. T. Harootunian, J. P. Kao, S. Paranjape, R. Y. Tsien, *Science* **251**, 75 (1991).
43. J. Liou *et al.*, *Curr. Biol.* **15**, 1235 (2005).
44. R. S. Lewis, *Annu. Rev. Immunol.* **19**, 497 (2001).
45. C. Arrieumerlou, T. Meyer, *Dev. Cell* **8**, 215 (2005).
46. P. A. Iglesias, P. N. Devreotes, *Curr. Opin. Cell Biol.* **20**, 35 (2008).
47. J. W. Walker, A. V. Somlyo, Y. E. Goldman, A. P. Somlyo, D. R. Trentham, *Nature* **327**, 249 (1987).
48. O. D. Weiner *et al.*, *Nat. Cell Biol.* **4**, 509 (2002).
49. T. Inoue, T. Meyer, *PLoS One* **3**, e3068 (2008).

50. We thank M. Hammer, J. Ferrell, M. Covert, A. Salmeen, Y. Brandman, and P. Vitorino for helpful discussion and suggestions and NIH grants R01GM063702, R01GM030179, and R01MH064801 for funding the work.

Supporting Online Material

www.sciencemag.org/cgi/content/full/322/5900/390/DC1
Tables S1 and S2

10.1126/science.1160617

REVIEW

Optical Switches for Remote and Noninvasive Control of Cell Signaling

Pau Gorostiza[1] and Ehud Y. Isacoff[2,3]*

Although the identity and interactions of signaling proteins have been studied in great detail, the complexity of signaling networks cannot be fully understood without elucidating the timing and location of activity of individual proteins. To do this, one needs a means for detecting and controlling specific signaling events. An attractive approach is to use light, both to report on and control signaling proteins in cells, because light can probe cells in real time with minimal damage. Although optical detection of signaling events has been successful for some time, the development of the means for optical control has accelerated only recently. Of particular interest is the development of chemically engineered proteins that are directly sensitive to light.

Signaling proteins operate in complex networks in cells. The networks are wired into long serial chains, and these chains are arrayed in numerous parallel pathways that diverge from common inputs, converge onto intermediate nodes, and diverge again to many different effectors. Signals from the external world that are detected at the cell membrane are transmitted in the plane of the membrane and through the cytoplasm, with feedback and feedforward loops onto organelles and the nucleus. The upshot of this complex connectivity is the control of outputs as diverse as membrane transport, cell metabolism, protein translation, cell shape and migration, gene transcription, cell cycle, and cell survival. The shear number of signaling proteins and complexity of their connectivity is staggering, and the depictions in textbooks and on glossy posters from chemical companies are as dense and as difficult to decipher as spirographs.

Optical detection of cellular signaling has been accomplished, first with chemical dyes and more recently with fluorescent protein sensors to measure ions, membrane potential, second messengers, enzyme activity, protein/protein interaction, and the structural changes in proteins that underlie their functional transitions (*1*). Methods for remote control of cell signaling have seen explosive growth. Early methods used caged compounds, which release a signaling molecule when exposed to an intense pulse of light. "Reversibly caged" photochromic ligands, whose ability to function can be toggled on and off, were also developed. Most recently, efforts here have led to the engineering of light-sensitivity into proteins by the attachment of photoswitched tethered ligands (PTLs) that turn the function of the protein on and off in response to light. Although demonstrated in only a limited number of cases, this form of protein engineering appears likely to be broadly applicable across protein classes, and it complements recently discovered naturally light-sensitive ion channels and pumps. We focus here on the optical methods of remote control of protein function for elucidating signaling circuits inside cells and in cell circuits.

The Power of Light

To manipulate cell signaling, it is essential to control the function of key proteins by means that differ from, and thus will not cross-react with,

[1]Institució Catalana de Recerca i Estudis Avançats and Institut de Bioenginyeria de Catalunya, Parc Científic de Barcelona, Edifici Hèlix. C/Baldiri Reixac 15, Barcelona 08028, Spain. [2]Department of Molecular and Cell Biology, University of California at Berkeley, 271 Life Sciences Addition, Berkeley, CA 94720, USA. [3]Divisions of Material and Physical Bioscience, Lawrence Berkeley National Laboratory, Berkeley, CA 94720, USA.

*To whom correspondence should be addressed. E-mail: ehud@berkeley.edu

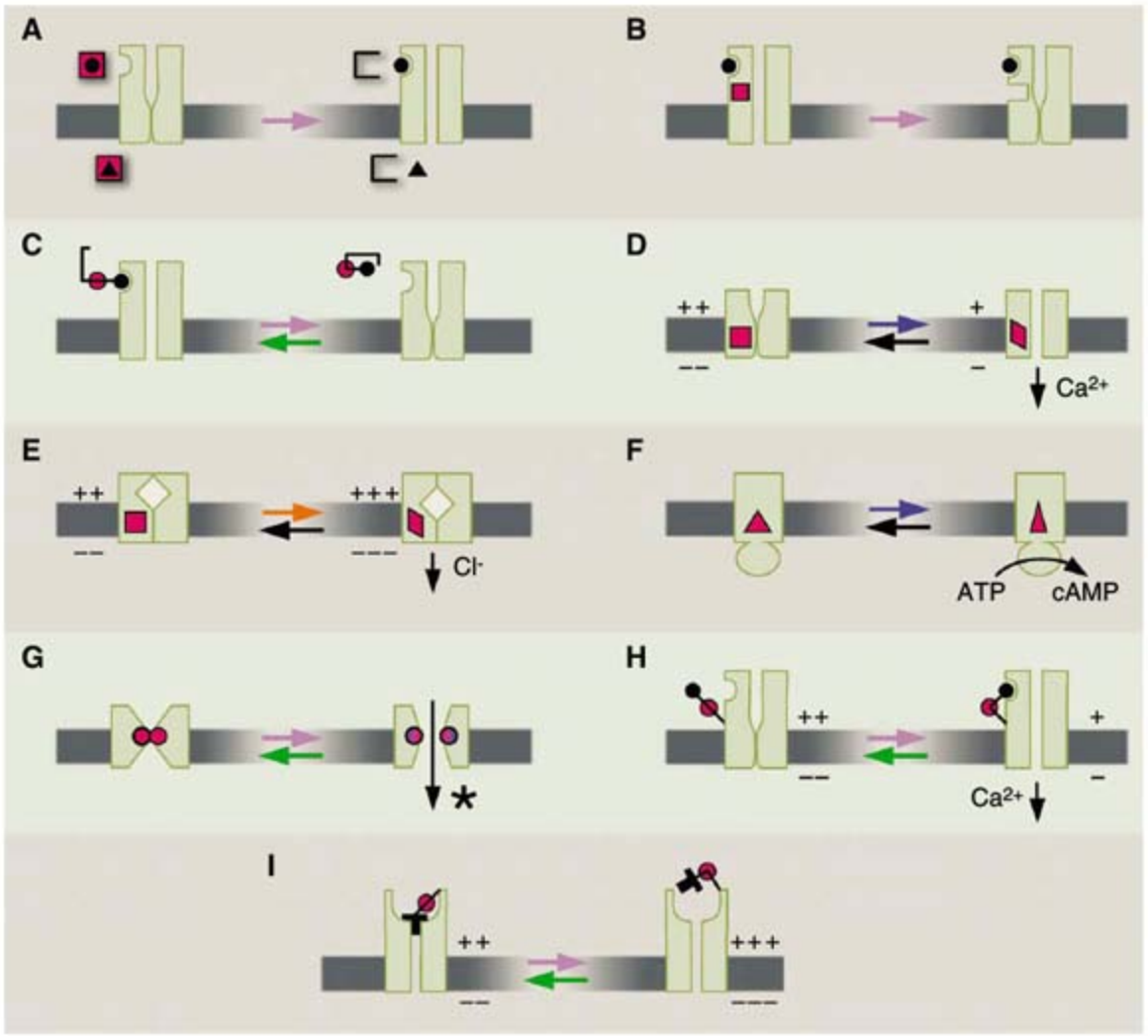

Fig. 1. Strategies for the manipulation of cell signaling with light. (**A**) Uncaging of ligands and ions (*9*, *37*). (**B**) Protein uncaging. (**C**) Free photoisomerizable ligands (*10*, *11*). (**D**) Light-gated cation channel Channelrhodopsin 2 (*38*). (**E**) Light-gated chloride pump NpHR (*16*). (**F**) PAC (*20*). ATP, adenosine triphosphate; cAMP, adenosine 3′,5′-monophosphate. (**G**) Light-gated mechanosensitive channel MscL (*22*). The asterisk indicates delivery of chemical. (**H**) Light-gated nAChR (*10*) and LiGluR (*33*). (**I**) Light-gated voltage-gated potassium channel (*31*).

normal cellular signaling. Optical manipulation is an appealing approach because light generally does not influence the system under study and can be used remotely and noninvasively. The high resolution with which light can be manipulated both temporally (microseconds) and spatially (microns) (*2*) should make it possible to investigate fast processes that are confined to specific cellular compartments or specific subsets of cells.

Caged Compounds and Proteins

Photolabile compounds can be used to "cage" ions (for example, Ca^{2+}), neurotransmitters (such as glutamate), and intracellular signaling molecules [for example, inositol triphosphate (IP3)] (Fig. 1A). The cage hides the bioactive compound until it is broken off with light. Alternatively, the cage can be attached to a protein at critical amino acids such that protein activity is enabled or disabled upon release (Fig. 1B). Spatiotemporally designated patterns of ligand release have been used to reveal the localization and function of channels (*3*, *4*) and to elucidate complex intracellular events regulated by signaling such as endocytosis (*5*) and also have made it possible to assume remote control of neuronal activity with the use of endogenous (*6*) and exogenous receptors (*7*). Many of these compounds are commercially available. Although most can act on multiple proteins in cells, their effect can be made specific in some cases through the use of an exogenous ligand that does not activate native proteins in the cell or organism in question, but that does activate a non-native receptor that is expressed heterologously (*8*). The use of caged compounds has been extensively reviewed (*9*) and is relatively widespread.

"Reversibly Caged" Photochromic Ligands

Because caging systems that rely on photodestruction of the cage are irreversible and can produce toxic photoproducts, it is attractive to think of alternative approaches to conditionally expose a ligand with light. An appealing alternative has been to replace the standard photo-cage with a photoisomerizable molecule that undergoes a large conformational change between two states in response to the absorption of light at two different wavelengths. The most common examples have used azobenzene, which interconverts between an extended, thermally relaxed trans isomer and a higher energy cis or "bent" isomer that is ~0.7 nm shorter than the trans isomer (Fig. 2). Illumination with near-ultraviolet (UV) irradiation at wavelengths preferred for absorption by the trans isomer (380 nm) leads to accumulation of the cis isomer, and visible light irradiation at wavelengths preferred for absorption by the cis isomer (500 to 600 nm) switches it back to the trans form. Photoisomerization cycles can be repeated many times without detectable photodestruction or loss of responsiveness.

When a ligand is chemically coupled through a very short connector to the azobenzene, the molecule in the cis state bends around the ligand and interferes with its ability to dock to its binding site in a target protein (Fig. 1C). This has been done successfully with nicotinic acetylcholine receptors (nAChRs) (*10*) and ionotropic glutamate receptors (iGluRs) (*11*). By driving the photoisomerizable "reversible cage" back and forth between its two configurations with two different wavelengths of light, it is possible to rapidly and reversibly turn the ligand from active to inactive without generating photoproducts, with great reproducibility over many rounds of illumination and at lower intensities (and thus a lower danger of collateral damage) than those required for photolysis of a cage. However, in the versions available so far, the obstructed state still has appreciable activity, so further refinement would be desirable.

Although caged and photochromic ligands are powerful, they have two limitations: (i) They are diffusible, so that they will act outside of the confines of the illumination volume, and (ii) they can never be completely selective for only one protein target. Indeed, they will usually act on a class of proteins. The class can be relatively narrow (for example, IP3-gated receptors), broad [such as the glutamate receptors class, which includes AMPA, *N*-methyl-D-aspartate, kainate receptor-channels, and metabotropic heterotrimeric guanine nucleotide-binding protein (heterotrimeric GTP-binding protein) coupled receptors], or very broad (like that including the numerous Ca^{2+}-activated channels, transporters, and enzymes in cells). Thus, there would be a major improvement in spatial and molecular specificity if a light-responsive "antenna" could be attached directly to the protein of interest. This has been done by attaching to proteins photoisomerizable molecules whose conformation can be changed by light, in turn changing the activity of the protein. This has been achieved by evolution, as described in the next section, and can be engineered into normally light-insensitive proteins, as described thereafter.

Naturally Light-Sensitive Proteins

Photoisomerizable chromophores are used in nature to switch the functional state of specific proteins rapidly and reversibly. The classical example is the chromophore retinal in the opsin proteins used for visual transduction in the eye

(rhodopsin) and as an energy source for pumping protons in bacteria (bacteriorhodopsin). Channelrhodopsin-2 (ChR2) [a light-gated cation channel (Fig. 1D) (*12*)], a recently discovered red-shifted channelrhodopsin (*13*), and halorhodopsin (Halo or NpHR) [a light-driven Cl^- pump (Fig. 1E) (*14*)] represent new and very useful members of the opsin family. They can be expressed heterologously in various cells and produce functional proteins. In mammals, retinal is available, so none needs to be added (*15*). This renders the expressing cells sensitive to light and thus confers the ability to influence the physiology of those cells with optical stimulation (*16*). ChR2 and NpHR are activated by light at distinct wavelengths, and so they can be independently controlled in the same neuron to excite (ChR2) and inhibit (NpHR) the neuron in alternation. These opsins can be used to manipulate activity in neurons for circuit mapping (*17*, *18*) and for studying the neural basis of behavior (*16*, *19*). The utility of opsins to remotely control neuronal firing has sparked the search for other phooactivated proteins. This search has already unearthed a photoactivated adenylyl cyclase (PAC) (Fig. 1F), which is endowed with photosensitivity by two flavin adenine dinucleotides (*20*). PAC can be used to optically control intracellular concentrations of cyclic adenosine monophosphate.

It is not known how many classes of proteins exist in nature in light-sensitive forms, how many of these could be made to work in other organisms, or whether their properties could be tuned in such a way as to obtain the desired kind of remote control over biochemical signaling in mammalian cells. Thus, a general strategy for engineering optical control into any protein of interest would have enormous benefit. We explore several approaches to this problem below.

Photoisomerizable Amino Acid Side Chains and Cross-Linkers

Light sensitivity can be engineered into proteins by covalently attaching the protein to photoisomerizable molecules such as azobenzene and spiropyran. If the attachment is near an important functional site, then the light-driven structural change in the azobenzene or spiropyran can alter activity. In this manner, azobenzene incorporated as an unnatural amino acid can photoregulate the binding affinity of catabolite activator protein to its promoter in response to light (*21*). A mechanosensitive channel was made sensitive to light by site-selective conjugation of spiropyran to an introduced cysteine (Fig. 1G) (*22*). Previous work has shown that mutating or chemically modifying a hydrophobic site in the pore with charges would result in spontaneous channel opening (*23*). The design exploited the change in dipolar moment of spiropyran upon isomerization to achieve optical gating of the channel. In both of these cases, the kinetics of photoswitching were slow and reversibility was limited, possibly because of steric hindrance to the photoisomerization rearrangement.

An alternative strategy has been to put cysteine-reactive groups on both ends of azobenzene, attach it as a cross-linker to a pair of introduced cysteines within a helical segment of a peptide or protein, and use the isomerization to either kink (moving from the trans to the cis configuration) or stretch (moving from cis to trans) the helix and thereby denature it and disrupt its function (*24*).

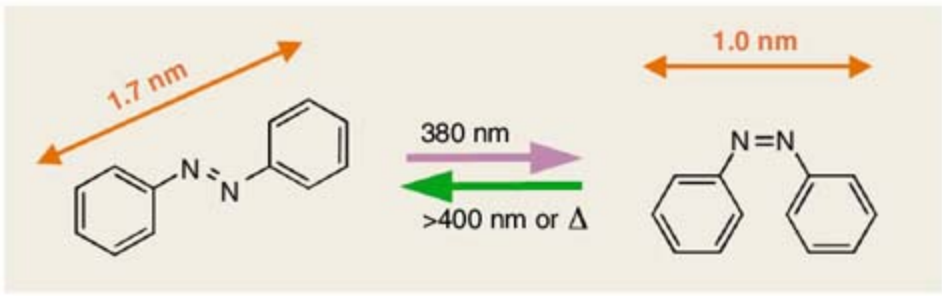

Fig. 2. Azobenzene photoisomerizes between an extended or trans configuration under visible light (left) and a bent or cis configuration under UV light (right), which is shorter by ~0.7 nm. Δ indicates thermal energy.

PTLs

In an alternative strategy for engineering optical control into proteins, azobenzene is attached through a cysteine-reactive group to an introduced cysteine on the protein surface, far enough away from the active site and from channel gates to avoid a direct effect of isomer configuration on protein function. Only the cysteine-reactive end of the azobenzene is attached to the protein (the other end is free) so that the protein exerts no direct force on it. This permits isomerization to proceed at rates with a reversibility that is comparable to that of free azobenzene. The functional effect on the protein is exerted by a ligand that dangles from the free end of the azobenzene. Photoisomerization back and forth between two states of the photoisomerizable moiety, in response to the two wavelengths of light, changes the location in space of the ligand, such that it can only bind in one of the isomeric states. The ligand of these PTLs can be an agonist, antagonist, or blocker. PTLs can be tuned by adjusting the chemistry of the reactive end, the wavelength and relative stability in the cis and trans states (and thus the rate of spontaneous interconversion in the dark), and the properties of the ligand (to adjust affinity and determine whether it operates as an agonist or antagonist) (*25*, *26*).

Light-gated nAChR. The muscle nAChR has been nanoengineered with PTLs (*10*). The design was based on the discovery that tethered agonist compounds can be conjugated to the native cysteines that give Cys-loop receptors their name. This loop is in the vicinity of the ACh binding site of the receptor. Tethering the ligand yields permanently active receptors, with the degree of activation proportional to the tether length (*27*). Using a tethered ligand compound of similar length but bearing an azobenzene within the tether (QBr) allowed the agonist to bind the receptor and activate it in the trans configuration, whereas in the cis configuration, the tether was too short for the agonist to bind (Fig. 1H) (*10*). Photoisomerization and subsequent induction of nAChR currents could be achieved reversibly with millisecond light pulses (*28*).

Light-gated K^+ channel. A PTL strategy has also been adapted to control a pore blocker on a K^+ channel and binding glutamate to an LiGluR. For the synthetic photoisomerizable azobenzene-regulated K^+ channel (SPARK), the design of a light-gated Shaker K^+ channel was based on two pieces of information: (i) the structure of a related K^+ channel pore from a bacterial channel with high similarity (*29*), and (ii) the demonstration that the channel could be permanently blocked by a quaternary ammonium compound, tetraethyl ammonium (TEA), that was conjugated through a passive linker to a cysteine introduced at a particular location on the external part of the pore (*30*). When an azobenzene group was included in the linker, the 0.7-nm length change induced by photoisomerization was enough to block the channel in the extended trans state, but the blocker was withdrawn in the shorter, bent cis state (*31*) (Fig. 1I). Mutations in the channel jammed its native gates in the open state, thus placing the conductance entirely under control of the "light-gate." Because the opening of a K^+ channel results in membrane hyperpolarization, SPARK allows photoinhibition of neuronal firing. SPARK was also converted into a photoswitchable, excitatory channel by mutational disruption of the ion selectivity filter, which rendered it permeable to Na^+, leading to membrane depolarization when the channel was unblocked and triggering action potentials in neurons in response to light (*32*).

Light-gated iGluR (*LiGluR*). A systematic, structure-based approach to the PTL strategy was used in the development of the photoswitchable LiGluR (Fig. 1H), for which no functional data on tethered ligands were available (*25*, *33*). A ligand attached to a model linker was tested and found to activate iGluR6, indicating that the conformational change induced by glutamate binding—that is, closure of the "jaws" of the ligand-binding domain (LBD) down over the glutamate—was not prevented by the linker (*33*). The full photoswitch, with a complete azobenzene in the linker and a maleimide cysteine-reactive end, was tested at many different attachment locations around the binding pocket, several of which gave rise to light-activation (Fig. 1H) (*33*). When attached to the

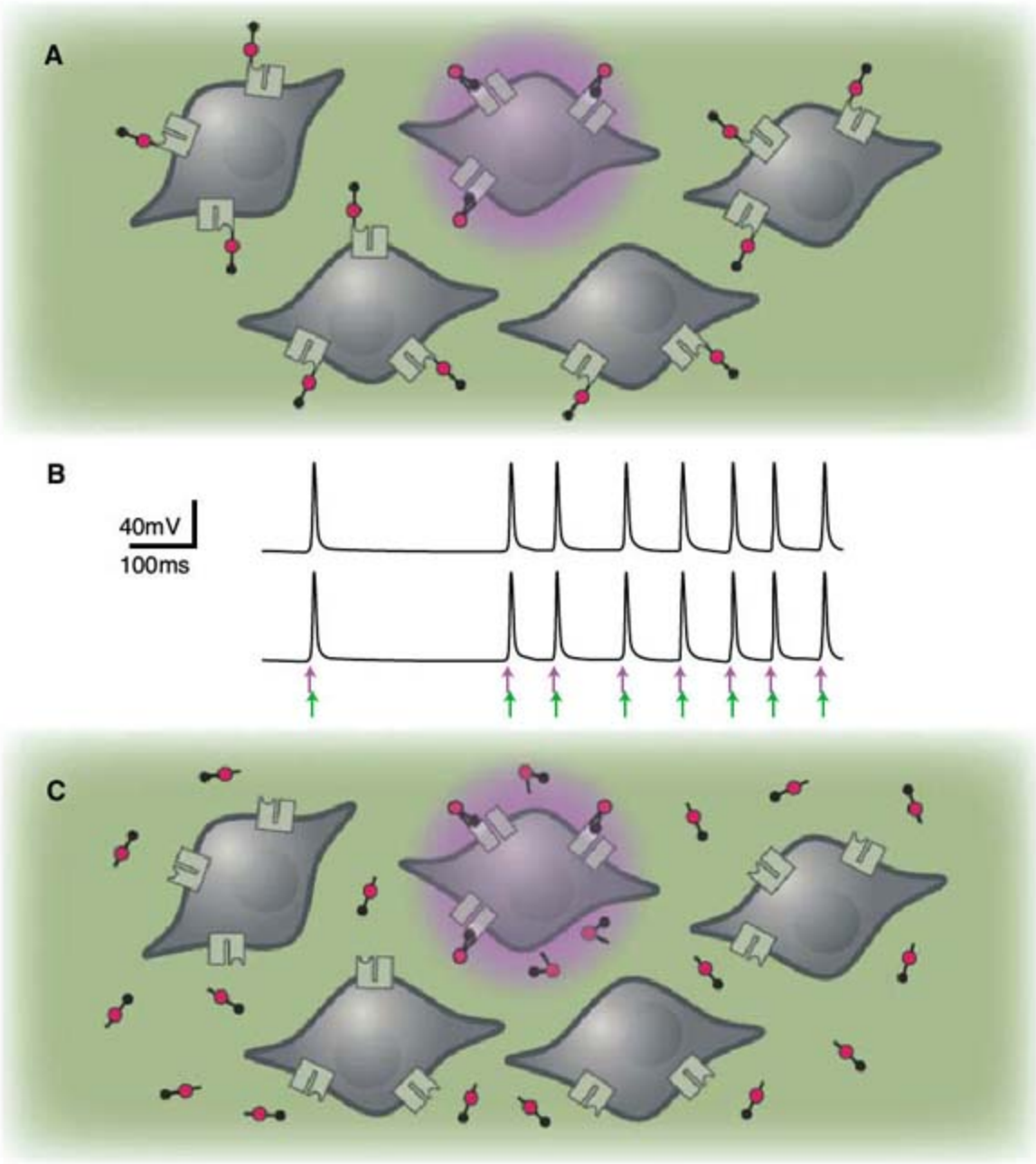

Fig. 3. Spatio-temporal control of cell signaling with light. **(A)** The use of spatially confined illumination on a group of cells expressing a photoswitchable protein allows selection of the particular cell (or cell region) to be manipulated. **(B)** LiGluR allows control of single action potential firing in neurons by millisecond light pulses. [Reproduced with permission from (*35*)]. **(C)** Region-selective conjugation of synthetic photoswitches using affinity labeling (*34*).

outer surface of the LBD, the linker must "turn" to point the glutamate into the binding pocket so that the cis state is the activating state. In the cis state, the local effective concentration of glutamate is ~40-fold higher than it is in the trans state (*34*).

The cation-selective pore of LiGluR supports the influx of Na^+ and Ca^{2+} into the cell, thus enabling both Ca^{2+} and voltage-activated processes to be triggered remotely. Millisecond light pulses were shown to elicit single action potentials at high frequency and reliability in cultured hippocampal neurons (Fig. 3, A and B), and light could be used to control specific behavior in zebrafish by regulating the activity of specific subsets of neurons (*35*). The intensity required for such fast switching is typical of what is used in confocal microscopy and is well tolerated by cells and live animals. Because the activating cis state of the LiGluR PTL is stable for minutes, the channel remains activated and the neuron continues to fire in the dark for many minutes after activation with a short pulse of light (*35*). This limits photodamage and permits behavioral experiments to be conducted without the confounding effects of light. The rate of cis-trans relaxation can be tuned by substitutions in and around the azobenzene and may range from milliseconds to days (*26*).

Photoswitch specificity arises from specialized geometry and affinity labeling. There are many native K^+ channels in a neuron that are blocked by TEA and many native receptors that are activated by glutamate, meaning that such ligands are not specific for the target protein. Moreover, cysteines are not very rare, so PTLs can attach at places other than those introduced into the target proteins. Nevertheless, the PTL approach turns out to be specific. This paradox is explained by two factors: (i) First, the short length of the PTLs restricts biological activity to only those PTLs that attach within ~1 nm of their ligand-binding site. Thus, in the example discussed, attachment must occur in the K^+ channel pore or in the glutamate binding pocket. As it turns out, K^+ channels and glutamate receptors do not have native cysteines at such locations. (ii) Second, the effective concentration of the cysteine-reactive end in the vicinity of the target cysteine is enhanced when the ligand end of the molecule docks in the binding site, leading to affinity labeling. Variants of the K^+ channel PTL have been developed that exploit affinity labeling by using electrophilic reactive groups to target native nucleophilic, non-cysteine residues, so that receptor mutagenesis can be avoided (*36*). Such compounds endow optical excitability onto endogenous potassium channels, thus allowing optical control of neuronal firing without the need for genetic manipulation. Affinity labeling is favored when the azobenzene in the linker is in the correct (activating or blocking) configuration, making it possible to use patterns of light to favor conjugation in specific locations—a form of optical lithography (Fig. 3C) (*34*, *36*).

Comparison Between PTLs and Naturally Light-Sensitive Proteins

Although the optical switches described here enable cell signaling to be controlled in a remote and noninvasive manner, the different approaches have distinct advantages. A major advantage to the naturally light-sensitive opsin proteins, like ChR2 and Halo, is that they are purely genetic in mammals, not requiring the addition of a photoswitch because their cofactor retinal is naturally present (*15*). In other organisms, such as flies and worms, retinal must be added. In addition, ChR2 and Halo are excited with visible light and at different wavelengths (ChR2-blue, Halo-yellow, VChR1-red) so that they can be controlled independently (*16*). On the other hand, PTL-controlled channels, such as iGluR6 and the Shaker K^+ channel, provide overall larger whole-cell currents than do ChR2 and Halo because of their larger single-channel currents. Moreover, PTLs can be actively turned off, providing a more precise control of timing (*35*). In addition, if one wants sustained excitation over a long period of time while avoiding the prolonged irradiation (and possible photodamage) that would be required for the opsin proteins, or if one wants to induce an activity change without the potential confound of light, then PTLs provide the advantage of remaining turned on in the dark for tens of minutes and still being switched off in milliseconds by the longer-wavelength light. PTL attachment to the target protein can be spatially patterned with light (*34*), and one can use a one-component version of PTLs in which they conjugate to native reactive proteins so that one need only supply the chemical photoswitch and avoid transgenesis (*36*). Many of the properties of the PTLs can be rationally tuned, including whether the ligand functions as a blocker, agonist, or antagonist; the wavelength-dependence; and the rate of spontaneous relaxation in the dark. Lastly, the PTL approach appears likely to be adapt-

able to many different protein classes, potentially including cytoplasmatic signaling proteins.

Conclusions

Remote and noninvasive manipulation of proteins with light provides a powerful approach for studying and reengineering signaling pathways by selectively establishing a fast and reversible remote control over specific proteins at specific locations within a cell or organism. The greatest specificity can be obtained from light-activated chemicals that are tethered to specific proteins. Naturally occurring photosensitive proteins have proven to be useful tools for experimentation and provide a major motivation to seek other naturally light-sensitive proteins. The success of synthetic PTL photoswitches introduces a tantalizing prospect of a general method that could be used to confer control of many proteins by light. The versatility of the approach comes from its superficiality. A PTL is attached to the bland surface of the protein in such a way that the covalent modification has little impact, except that presence of light of different wavelengths determines whether it presents or withdraws a ligand to and from a nearby binding site. The ligand can block or activate the site and thereby alter the function of the protein. The site can be an active site or an allosteric regulatory site. This logic should, in principle, be applicable across protein classes.

These optical approaches to the control of protein function provide an alternative to standard methods of controlling proteins through genetic or pharmacological means, which tend to be slow, difficult to reverse, and often not as specific as one would like. The contrast is particularly notable when one reflects that, in standard pharmacology, high specificity is associated with high affinity and thus with very slow dissociation and a lack of reversibility. In contrast, specificity of PTLs arises from the close relation between the geometry of the PTL and its change upon isomerization and the relative location of the attachment and ligand-binding sites. This even permits ligands of low affinity (or low specificity) to be used. The extremely rapid dissociation rates of such ligands and the subsequent fast reversal of signaling occur with rates similar to those of the fastest natural biological signals.

References and Notes

1. C. J. Weijer, *Science* **300**, 96 (2003).
2. C. Lutz *et al.*, *Nat. Methods* **5**, 821 (2008).
3. G. D. Housley, N. P. Raybould, P. R. Thorne, *Hear. Res.* **119**, 1 (1998).
4. J. Zhao *et al.*, *Biochemistry* **45**, 4915 (2006).
5. Y. Tong *et al.*, *J. Gen. Physiol.* **117**, 103 (2001).
6. S. Shoham, D. H. O'Connor, D. V. Sarkisov, S. S. Wang, *Nat. Methods* **2**, 837 (2005).
7. B. V. Zemelman, N. Nesnas, G. A. Lee, G. Miesenböck, *Proc. Natl. Acad. Sci. U.S.A.* **100**, 1352 (2003).
8. S. Q. Lima, G. Miesenböck, *Cell* **121**, 141 (2005).
9. M. Goeldner, R. Givens, *Dynamic Studies in Biology. Phototriggers, Photoswitches and Caged Biomolecules* (Wiley-VCH, Weinheim, Germany, 2005).
10. E. Bartels, N. H. Wassermann, B. F. Erlanger, *Proc. Natl. Acad. Sci. U.S.A.* **68**, 1820 (1971).
11. M. Volgraf *et al.*, *J. Am. Chem. Soc.* **129**, 260 (2007).
12. G. Nagel *et al.*, *Proc. Natl. Acad. Sci. U.S.A.* **100**, 13940 (2003).
13. F. Zhang *et al.*, *Nat. Neurosci.* **11**, 631 (2008).
14. B. Schobert, J. K. Lanyi, *J. Biol. Chem.* **257**, 10306 (1982).
15. A. Bi *et al.*, *Neuron* **50**, 23 (2006).
16. F. Zhang *et al.*, *Nature* **446**, 633 (2007).
17. K. Deisseroth *et al.*, *J. Neurosci.* **26**, 10380 (2006).
18. L. Petreanu, D. Huber, A. Sobczyk, K. Svoboda, *Nat. Neurosci.* **10**, 663 (2007).
19. G. Nagel *et al.*, *Curr. Biol.* **15**, 2279 (2005).
20. S. Schroder-Lang *et al.*, *Nat. Methods* **4**, 39 (2007).
21. M. Bose, D. Groff, J. Xie, E. Brustad, P. G. Schultz, *J. Am. Chem. Soc.* **128**, 388 (2006).
22. A. Koçer, M. Walko, W. Meijberg, B. L. Feringa, *Science* **309**, 755 (2005).
23. K. Yoshimura, A. Batiza, C. Kung, *Biophys. J.* **80**, 2198 (2001).
24. G. A. Woolley, *Acc. Chem. Res.* **38**, 486 (2005).
25. P. Gorostiza, E. Y. Isacoff, *Mol. Biosyst.* **3**, 686 (2007).
26. P. Gorostiza, E. Y. Isacoff, *Physiology* **23**, 238 (2008).
27. I. Silman, A. Karlin, *Science* **164**, 1420 (1969).
28. H. A. Lester, M. E. Krouse, M. M. Nass, N. H. Wassermann, B. F. Erlanger, *J. Gen. Physiol.* **75**, 207 (1980).
29. D. A. Doyle *et al.*, *Science* **280**, 69 (1998).
30. R. O. Blaustein, P. A. Cole, C. Williams, C. Miller, *Nat. Struct. Biol.* **7**, 309 (2000).
31. M. Banghart, K. Borges, E. Isacoff, D. Trauner, R. H. Kramer, *Nat. Neurosci.* **7**, 1381 (2004).
32. J. J. Chambers, M. R. Banghart, D. Trauner, R. H. Kramer, *J. Neurophysiol.* **96**, 2792 (2006).
33. M. Volgraf *et al.*, *Nat. Chem. Biol.* **2**, 47 (2006).
34. P. Gorostiza *et al.*, *Proc. Natl. Acad. Sci. U.S.A.* **104**, 10865 (2007).
35. S. Szobota *et al.*, *Neuron* **54**, 535 (2007).
36. D. L. Fortin *et al.*, *Nat. Methods* **5**, 331 (2008).
37. G. C. Ellis-Davies, *Nat. Methods* **4**, 619 (2007).
38. G. Nagel *et al.*, *Biochem. Soc. Trans.* **33**, 863 (2005).

39. P.G. is supported by the Human Frontier Science Program Organization through a Career Development Award and by the European Research Council through a Starting Grant. This work was supported by the NIH Nanomedicine Development Center for the Optical Control of Biological Function (grant 5PN2EY018241).

10.1126/science.1166022

REVIEW

From Signals to Patterns: Space, Time, and Mathematics in Developmental Biology

Julian Lewis

We now have a wealth of information about the molecular signals that act on cells in embryos, but how do the control systems based on these signals generate pattern and govern the timing of developmental events? Here, I discuss four examples to show how mathematical modeling and quantitative experimentation can give some useful answers. The examples concern the Bicoid gradient in the early *Drosophila* embryo, the dorsoventral patterning of a frog embryo by bone morphogenetic protein signals, the auxin-mediated patterning of plant meristems, and the Notch-dependent somite segmentation clock.

Developmental biologists are preoccupied with patterns in space and patterns in time. What causes cells in one part of an embryo regularly to adopt one character, and those elsewhere to adopt another? What controls the timing of these patterning events as the organism develops from the egg? What halts growth when a structure has reached its proper size?

Early discussions of developmental patterning considered, in abstract terms and in total ignorance of the molecules involved, how signals exchanged between cells might drive formation of the patterns we observe. Although they lacked a concrete molecular basis, several of these speculative theories turn out to have been remarkably prescient. Moreover, right or wrong, they drive home a general lesson. To explain how embryos generate their spatial patterns and their temporal programs, we need more than lists of the molecules involved and more than simple cartoon diagrams of the qualitative control relationships between them. To make sense of the control circuitry, qualitative data and unaided intuition are not enough. Even for the simplest cases, we need mathematics and detailed measurements, just as we need mathematics and measurements to explain the orbits of the planets or the swing of a pendulum.

The necessity arises especially because of the fundamental part that feedback plays in developmental control processes, as discussed elsewhere in this issue of *Science* by Brandman and Meyer (*1*). Positive feedback can give a system a flip/flop choice between alternative steady states; it can endow a system with enduring memory of its exposure to past signals; it can generate inhomogeneity in a system that starts out spatially uniform. Negative feedback can smooth out irregularities; it can enable a system to respond to a signal more

Vertebrate Development Laboratory, Cancer Research UK London Research Institute, London WC2A 3PX, UK.

rapidly; operating with a delay, it can give rise to temporal oscillations. These behaviors are not immediately obvious intuitively, but mathematics allows us to predict and compute them.

Molecular biology has been triumphant in identifying the key signaling molecules that govern development. Developmental biologists are now beginning to confront in earnest the problem of how these molecules work together as control systems to generate patterns in space and time. I discuss here a few examples to show how the interplay of quantitative experimentation and mathematical modeling leads to new insights and new ways of thinking about how molecular signals are used to pattern the embryo.

How a Morphogen Gradient Is Made and Used: The Bicoid Gradient in the *Drosophila* Embryo

Conceptually, at least, the simplest way to set up a spatial pattern is by means of a morphogen gradient. A signal substance, the morphogen, is synthesized at one end of a developing structure and diffuses away from this source, suffering degradation as it goes and thereby creating a concentration gradient. Cells at varying distances from the source experience different morphogen concentrations and somehow "read" those concentrations, adopting different characters as a result. We now have evidence for mechanisms of this sort in innumerable systems (*2*); a particularly clear example is that of the Bicoid gradient in the early *Drosophila* embryo. Recent quantitative analysis has provided a uniquely detailed and thought-provoking portrait of how this particular morphogen gradient works.

The early *Drosophila* embryo (Fig. 1) is a syncytium, in which repeated cycles of mitosis without cell division generate a steadily increasing number of nuclei. These nuclei are distributed uniformly in a cortical layer along the 500-μm length of the cigar-shaped embryo. Molecules of maternal *bicoid* mRNA are strictly localized at the anterior pole of the embryo and begin to be translated at the time of fertilization. Their product, the Bicoid protein, is a transcription regulator: It acts on the nuclei in the cortex, controlling their expression of genes such as *hunchback* (coding for another transcription regulator) that specify differences between regions of the embryo. The same molecules and the same mechanism operate in other related species of fly, some with embryos as little as 300 μm long, others as big as 1500 μm long. Curiously, the shape of the Bicoid gradient and the proportions of the resulting pattern are practically the same in every case, scaling with the size of the embryo (*3*).

Gregor *et al.* (*4*, *5*) used immunofluorescence staining and Bicoid protein tagged with green fluorescent protein (GFP) to see how the Bicoid concentration gradient in *Drosophila* is set up and how it controls *hunchback* expression. They measured the precise form of the concentration gradient, the time taken to establish it (about 1 hour), the rise and fall of Bicoid concentration in the nuclei with each mitotic cycle, and the surprisingly slow rate of diffusion of Bicoid protein through the cytoplasm. Putting all these measurements together, they showed how creation of the Bicoid gradient is related to the dynamics of release, reuptake, and degradation of Bicoid by the nuclei and argued that it must involve some sort of facilitated transit from nucleus to nucleus: The gradient is not explicable in terms of simple diffusion of Bicoid through the cytoplasm. The central role of the nuclei in localizing and degrading Bicoid hints, in a still-tantalizing way, at an explanation of how the pattern scales with size in embryos of different fly species: For if distance along the embryo is measured in units of the spacing between nuclei, instead of μm, all these embryos are alike.

Gregor *et al.* (*4*) examined how the Bicoid gradient controls expression of genes such as *hunchback* with such remarkable precision and sharpness that each nucleus behaves as though it knows its position along the 500-μm *Drosophila* embryo axis to an accuracy of better than 10 μm. They found that at the threshold for *hunchback* activation, about halfway along the embryo, there are on average 690 molecules of Bicoid protein per nucleus; through some statistical physics calculations, they showed that this means that the observed precision of patterning is close to the limit set by molecular noise (thermal fluctuations). They went on to measure the amazingly steep relationship between levels of Bicoid and Hunchback proteins in the critical neighborhood, and from this they were able to estimate that about five molecules of Bicoid must bind cooperatively to the *hunchback* regulatory locus to switch on *hunchback* expression.

These and many other ingenious deductions by the authors show how careful measurements and quantitative reasoning can highlight new questions and lead to deeper understanding, linking the simple concept of the morphogen gradient to other levels of description.

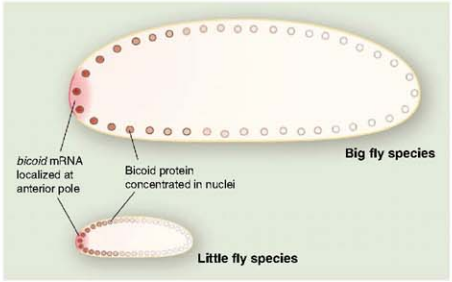

Fig. 1. The Bicoid gradient in a fly embryo. The early embryo is a syncytium, with its many nuclei distributed in a layer just beneath the cell cortex. *bicoid* mRNA is localized at the anterior end of this giant cell and is translated to produce Bicoid protein, which diffuses along the anteroposterior axis, creating an exponential gradient. During interphase, the protein is concentrated inside the nuclei, where it controls position-specific expression of other genes. Closely related fly species vary enormously in the sizes of their embryos but have closely similar numbers of nuclei at corresponding stages. The Bicoid gradient, remarkably, scales in proportion, giving a scaled body pattern.

How a Morphogen Gradient Is Scaled to the Size of the Organism: BMP Signaling and the Patterning of the Dorsoventral Axis of the Frog

The Bicoid gradient in *Drosophila* is intracellular: It is set up inside a single giant cell that only later becomes partitioned into many separate cells. Most of the morphogen gradients that pattern embryos are extracellular or at least based on signals that pass from one cell to another. An archetypal example is the gradient that originates in Spemann's organizer, the group of cells on the dorsal side of an early amphibian embryo that orchestrates the movements of gastrulation and governs creation of the main axes of the body (*6*). When cells from the organizer region are grafted to a new position in the embryo, opposite to their original location, they induce their new neighbors to join with them in forming a new body axis. Cells furthest from the organizer form ventral structures, and those closest to it form dorsal structures: Some sort of signal from the organizer apparently tells cells their position along the dorsoventral axis. The patterning mechanism has, however, a remarkable property, encountered also in many other systems (as we have just seen for fly embryos of different species): It scales with embryo size. Thus when an embryo is cut in half, the half that retains organizer tissue develops a miniature but perfectly proportioned body pattern (*7*). This would not be expected if the organizer were dictating the position-dependent characters of cells in the embryo by acting straightforwardly as the source of a simple morphogen gradient based on diffusion and degradation. The scaling mechanism in this multicellular system cannot be the same as in the syncytial fly embryo. Recent studies have revealed how it works (Fig. 2).

The critical condition governing the dorsoventral character of the cells is the strength of activation of the BMP (bone morphogenetic protein) signaling pathway: Strong activation causes cells to adopt a ventral character; weak or zero activation causes them to adopt a dorsal character. BMP itself is produced by cells at the ventral side of the embryo. Meanwhile, the organizer secretes at least eight different signal molecules, at least four of which are antagonists of BMP signaling, preventing activation of the pathway on the dorsal side of the embryo. Chordin, for example, is secreted by the organizer and binds to BMP, preventing it from activating the BMP receptor. Thus, it seems that a gradient of BMP inhibition, spreading out from the organizer, underlies dorsoventral patterning. Curiously, however, the organizer also secretes a BMP-related protein, called ADMP (antidorsalizing morphogenetic protein), that behaves, like BMP, as an activator of the BMP pathway and is also blocked in this action when bound to chordin. Reversade and De Robertis (*8*) analyzed the regulatory relationships between these components and showed that they all play essential parts in producing a dorsoventral pattern that scales with the size of the embryo. Their paper suggests in a qualitative way how they may do so, through feedback regulation of the expression of the various BMP agonists and antagonists, leading to a BMP "seesaw" between the ventral and dorsal poles of the embryo, with high levels of production of chordin and ADMP by the organizer at the dorsal pole somehow forcing creation of an opposite type of signaling center at the ventral pole. The paper ends with this remark: "Despite the complexity ... there is hope that, with the rise of systems biology, one day this intricate extracellular machinery will be understood as an integrated molecular circuit" (*8*).

Ben-Zvi *et al.* (*9*) have picked up the challenge. The first task is to discover whether the identified classes of molecules, interacting according to the rules proposed, really are sufficient in principle to give the observed scalable patterning. Unaided intuition is a feeble and often misleading guide to the behavior of systems with feedback, and all the more so for multiple cross-regulatory molecules diffusing in space. To answer the question of principle, therefore, one must turn to mathematics. It is easy enough to write down equations that represent the proposed rules of synthesis, diffusion, degradation, binding, and cross-regulation for each representative type of molecule—BMP, ADMP, and chordin—as revealed by the experiments. It is not too hard to program a computer to solve these equations. The difficulty is that different choices of the rate constants, diffusion coefficients, and other parameters in the mathematical model lead to wildly different outcomes. To make even qualitative predictions, we need quantitative data. In contrast with the case of the Bicoid gradient in *Drosophila*, the relevant quantitative data for BMP signaling in the frog embryo are largely lacking: We don't yet have properly developed tools to make the measurements in the context of the living organism.

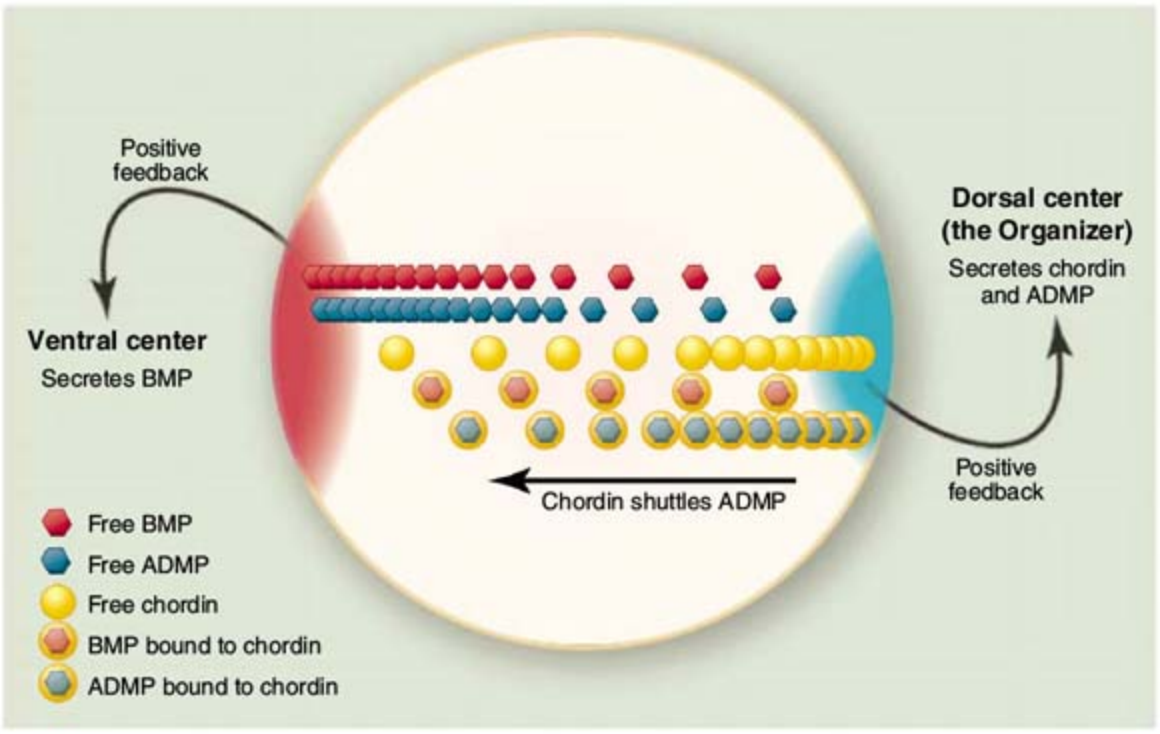

Fig. 2. Dorsoventral patterning in the *Xenopus* embryo: a current view. A self-organizing gradient of BMP signaling gives rise to a pattern that scales according to the size of the embryo. The gradient is set up by two signaling centers. The ventral center secretes BMP. The dorsal center (Spemann's organizer) secretes both a BMP-like molecule called ADMP and an inhibitor, chordin, which can bind to BMP and ADMP and block their action. High levels of BMP pathway activation stimulate expression of BMP and inhibit expression of ADMP and chordin; low levels do the opposite. Thus, local positive feedback maintains expression of BMP at the ventral center and maintains expression of chordin and ADMP at the dorsal center. At the same time, chordin, by binding to ADMP, speeds ADMP diffusion, thereby shuttling ADMP from the dorsal center toward the ventral, where the ADMP helps to stimulate BMP expression. This interaction between the two signaling centers coordinates their formation and ensures that the BMP gradient scales with the size of the embryo.

Ben-Zvi *et al.* (*9*), therefore, guided by their experience with a closely related dorsoventral patterning system in *Drosophila* (*10*), tried out different possibilities for the numerical parameters, systematically varying each one and exploring the behavior of the mathematical model for 26,000 different combinations of values. In this way, they showed that the model can indeed give the observed behavior, creating a pattern that scales in proportion to the size of the embryo. However, only a very small subset of parameter values, 21 out of the 26,000 combinations tested, will yield this outcome. These "successful" combinations share a striking feature: They correspond to conditions where BMP and ADMP molecules are only able to diffuse rapidly when they have their inhibitor, chordin, bound to them. In the process, the chordin itself undergoes degradation, creating a concentration gradient. The chordin, in these model cases, serves as a shuttle for movement of BMP and ADMP molecules across the embryo. Ben-Zvi *et al.* (*9*) therefore turned from mathematical modeling back to experimentation, asking whether such shuttling occurs in the real system: Does diffusion of BMP and ADMP through the tissue actually depend on binding to chordin? The answer is yes.

This work illustrates again how quantitative mathematical reasoning can sharpen understanding and suggest new lines of experimentation. At the same time, it highlights the central frustration of mathematical modeling in developmental biology: For most of the signaling systems that pattern the embryo, with their intricate feedback loops, we simply do not have the quantitative data that are needed to go beyond proof of plausibility to the type of solidly based quantitative theory that is commonplace in the physical sciences. But that is the challenge.

How Signaling Centers Are Created and Positioned: Auxin Transport in the Plant Meristem

Given a signaling center, one can easily imagine how it can organize the pattern of cell differentiation in its neighborhood. But how does the signaling center itself arise? If we start with a more or less homogeneous field of cells, what internal mechanism can make one region different from another and break the symmetry? Symmetry-breaking typically depends on positive feedback mechanisms that amplify small fluctuations into full-blown inhomogeneities. Turing (*11*) long ago showed with a mathematical model how this could happen in a developing tissue: Symmetry can be broken if the cells secrete two kinds of molecules that diffuse at different rates and cross-regulate one another's synthesis in an appropriate way; spatial variations

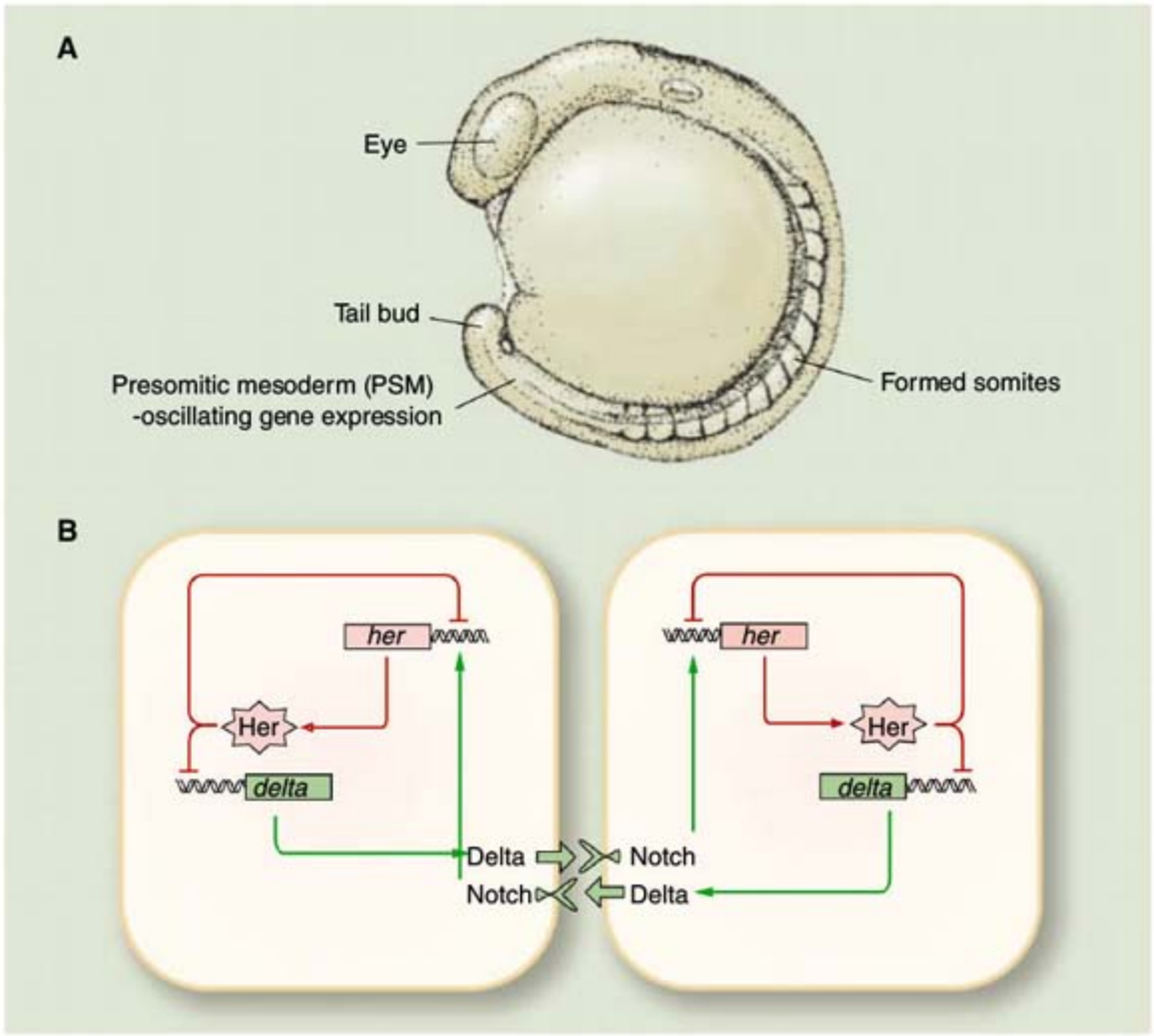

Fig. 3. The somite segmentation clock and its coordination. (**A**) Side view of a 14-somite zebrafish embryo. [Adapted from (*38*).] (**B**) Diagram of the gene control circuitry proposed to underlie the oscillations of gene expression in the cells of the PSM of the zebrafish. For simplicity, just two neighboring cells are shown. Oscillations arise from a very simple intracellular negative feedback loop: The protein product of a gene of the *her* family (or of a set of such genes) feeds back with a delay to shut off its own expression. Each cell is capable of oscillating independently, but neighboring cells are normally entrained to the same rhythm by Delta-Notch signaling. The oscillating levels of Her protein drive oscillating expression of a Notch ligand of the Delta family, which thus serves as a periodic time signal that each cell exchanges with its neighbors. This keeps them synchronized, provided that the delays in the signaling pathway are appropriate.

in their synthesis can then become self-amplifying. Gierer and Meinhardt (*12*, *13*) developed this abstract mathematical idea further, showing how the combination of a highly diffusible inhibitor molecule and a less diffusible activator can give rise to a self-organizing pattern in which tightly defined clusters of cells become signaling centers, secreting both types of molecules and thereby sustaining their own character while forcing different behavior in their neighbors. The organizer in the frog embryo, as we have just seen, is a signaling center that fits this description, and it probably arises more or less in this way.

Such self-organizing pattern formation is nicely exemplified in plant apical meristems, the tiny (~100 μm) growing tips of shoots in which the microscopic primordia of new leaves or floral organs are successively generated. As a meristem grows, the preexisting primordia act as signaling centers to control the positioning of new primordia, which go on to become signaling centers in their own right. But the molecular mechanism that creates these centers and governs their spacing turns out to be rather different from that imagined by Turing or Gierer and Meinhardt.

The crucial signal in this system is the plant hormone auxin (*14*, *15*). A dab of auxin placed at the side of the meristem will induce formation of an ectopic primordium. Converse effects result from mutation of the *PIN1* gene, coding for a protein that transports auxin out of cells into the extracellular space: The mutant meristem continues to grow but fails to generate any lateral organs, forming instead a single long thin unadorned stalk—a "pin." The dynamics of the normal auxin-dependent patterning process can be watched and measured in *Arabidopsis* by live imaging of the meristem using fluorescent reporters (*16*, *17*): A transgenic construct consisting of an auxin response element linked to a GFP coding sequence lights up cells in which auxin levels are high; a transgene coding for GFP-tagged PIN1 reveals the distribution of PIN1.

The patterning thus displayed involves movements of auxin in the epidermis, the outer surface layer of the meristem. Within this layer, auxin becomes concentrated at the site of each new primordium as it starts to form. The changing distribution of auxin goes hand in hand with a shifting epidermal distribution of PIN1 protein. This is most strongly expressed in the regions where levels of auxin are highest, that is, in the neighborhood of nascent primordia. Moreover, in each cell in these regions the PIN1 is localized predominantly on the side of the cell that faces toward the center of the nascent primordium. These and other findings suggest that the pattern of primordia is generated through a feedback loop in which auxin controls the synthesis and localization of its own transporter protein, PIN1: Where a local peak of auxin concentration starts to develop, the surrounding auxin gradient somehow orients the distribution of PIN1 transporters so as to drive still more auxin uphill toward the peak. This positive feedback based on active transport not only builds up the auxin concentration at the site of each nascent primordium, it also depletes auxin in the surrounding neighborhood, inhibiting formation of other primordia in that vicinity. Mathematical modeling shows that a mechanism of this type can explain the genesis of primordia in detail, including the precise geometry of primordium spacing and the quantitative data that come from live imaging (*15*, *18*–*20*).

How Cells Use Time Signals to Trace Out a Spatial Pattern: The Somite Segmentation Clock

Cells in embryos, like sailors at sea, use timers as well as spatial signals to tell them where they are and how they should behave. Such is the case for the cells that form the rudiments of the segments of the main vertebrate body axis, with their vertebrae, ribs, and axial muscles. These repetitive structures originate from somites, blocks of mesodermal cells that form sequentially, in head-to-tail succession and in two neat rows on either side of the midline of the embryo. Each somite is made out of cells that emerge from a region of apparently undifferentiated proliferative tissue at the tail end of the embryo, called the presomitic mesoderm, or PSM (Fig. 3). The PSM cells are kept in their special state by a combination of Wnt and FGF (fibroblast growth factor) proteins; the genes for these signal molecules are transcribed in the cells at the tail end of the PSM itself, creating a morphogen gradient that defines the PSM's extent (*21*, *22*). As the PSM cells grow and divide, the body axis elongates, but the morphogen gradient retreats in step with the tail bud, leaving behind a trail of cells that differentiate to form somites as the concentrations of FGF and Wnt to which they are exposed fall below a critical level.

The eye-catching feature of this process is its periodicity, the regular alternating pattern of the somites, each separated from the next by an intersomitic cleft. Cooke and Zeeman (*23*) speculated that this spatial periodicity could arise from a temporal oscillation in the PSM: a "clock" interacting with a signal, a "wavefront," that swept back along the embryo, marking the boundary between differ-

entiating somite cells and PSM cells. As the wavefront swept over them, cells would become consigned to different fates according to their clock phase at the critical moment, creating the periodic spatial pattern. Experiments by Palmeirim *et al.* (*24*) revealed that there is indeed a clock in the PSM, manifest in the oscillatory behavior of certain genes, which switch their expression on and off cyclically in this region. The period of the oscillation is equal to the time taken to form a somite: 2 hours in a mouse, 90 min in a chick, and 30 min in a zebrafish. The discovery of this segmentation clock has triggered an explosion of interest in somitogenesis and the mechanism of the clock (*25*).

Chick, mouse, and zebrafish all show the same phenomenon, and in all of them the Notch signaling pathway is critical for clock function. The first of the genes discovered to oscillate, in each of these species, were genes in the Notch pathway, especially members of the *Hes/her* family (called *Hes* genes in mouse and chick and *her* genes in zebrafish). These are all direct targets of regulation by Notch signaling, and all code for transcription regulators that bind to DNA to inhibit gene expression. Moreover, mutation of almost any component of the Notch pathway disrupts the organized oscillations and the regular pattern of somites (*26*). An obvious suggestion, therefore, is that Notch pathway components somehow generate the oscillations.

Notch signaling, unlike the other signaling pathways mentioned above, depends on direct cell-cell contact: A transmembrane protein, typically Delta, on the surface of one cell binds to a transmembrane receptor, Notch, on the surface of its neighbor. This triggers cleavage of Notch, releasing an intracellular fragment, NotchICD. NotchICD translocates to the cell nucleus and acts there as a transcription regulator, stimulating expression of the *Hes/her* genes. Notch signaling is famous for its role in lateral inhibition, a process that drives neighboring cells to become different as the result of a feedback loop based, in most cases, on negative regulation of *Delta* by Hes/Her proteins. But this is clearly not what is happening in the PSM, where neighboring cells remain similar and oscillate in synchrony. Indeed, experiments in the zebrafish suggested exactly the opposite: Notch signaling appeared to be needed to keep neighbors in synchrony. In mutants where signal transmission failed, it seemed as though the individual cells in the PSM continued to oscillate but gradually drifted out of synchrony over the course of half-a-dozen clock cycles, after having started out in synchrony (*27*).

Oscillations typically arise through delayed negative feedback. It is thus an attractive idea that the oscillations of the individual cells might be produced in a very simple way, through autoinhibition of *Hes/her* genes by their own products (*28*–*31*). Active transcription of a *Hes/her* gene would lead to synthesis of Hes/Her protein, which would act back on the promoter of the *Hes/her* gene, shutting off transcription; this would allow the protein levels to fall, thereby enabling transcription to start up again; and so on, cyclically.

Mathematical modeling of this simple feedback loop reveals properties that one might not otherwise have guessed. Sustained oscillations can indeed be generated, but only if certain conditions are satisfied. In particular, the delays involved in transcription and translation are critical: delays, that is, from the time when a fresh transcript or protein molecule begins to be synthesized to the time when synthesis of that molecule is completed and the functional molecule is delivered to its site of action. Without such delays, the system will not oscillate. If it is to oscillate, the lifetimes of the mRNA and protein molecules must be short compared with the sum of the delays. And if the system does oscillate, the predicted period is given by a simple formula: It is, to a good approximation, just twice the sum of the delays plus the lifetimes (*31*).

But is the model just a mathematical toy, or does it correspond to reality? In the zebrafish, it has been possible to estimate experimentally the transcriptional delays for the relevant *her* genes as well as their mRNA lifetimes. The estimates, although crude, support the model (*32*). The logic of the autoregulatory gene circuitry can also be checked experimentally and also fits the model. Moreover, the model can be extended to show how Notch signaling, through oscillating expression of a Delta gene, can serve to couple the oscillations in adjacent cells and keep them synchronized in the face of random fluctuations (*31*). Here too, delays are critical, and measurements indicate that the actual delays in Delta production have values consistent with the theory (*32*).

In the zebrafish, several independent lines of experimentation confirm that Notch signaling serves to keep the clocks of individual PSM cells synchronized. Cells grafted between embryos in different phases of the clock fall into step, and cells that misexpress Notch pathway components disturb the phase of their neighbors (*33*). When the strength of the coupling mediated by Notch is gradually reduced by increasing doses of an inhibitor that blocks Notch activation, synchrony is lost in just the manner predicted by the mathematical theory of systems of weakly coupled noisy oscillators and is regained when the block is removed (*34*). And when Notch signaling is blocked acutely with large doses of the same inhibitor at different stages in development, somitogenesis is disrupted only after a long delay, in a manner that implies that clock synchronization is the only function of Notch signaling in this system (*35*).

Despite all this evidence, we still lack proof that the proposed simple feedback circuitry is truly the pacemaker of the segmentation clock. Moreover, what is true for the zebrafish may not be true for mouse and chick. In the mouse and the chick, although not in the zebrafish, PSM cells are known to also show oscillating expression of various genes in the Fgf and Wnt signaling pathways (*21*, *36*, *37*). Which of these oscillators is the master and which the slave? Or do they operate in parallel, with loose coupling to keep them synchronized? Could there be some other as-yet undiscovered master oscillator at the root of it all, driving the oscillations in multiple signaling pathways? Firm answers, as for a host of other open questions about the systems of temporal and spatial signals that govern development, will require a combination of experiments, measurements, and mathematics.

References and Notes

1. O. Brandman, T. Meyer, *Science* **322**, 390 (2008).
2. L. Wolpert, *Principles of Development* (Oxford Univ. Press, Oxford, ed. 3, 2007).
3. T. Gregor, W. Bialek, R. R. de Ruyter van Steveninck, D. W. Tank, E. F. Wieschaus, *Proc. Natl. Acad. Sci. U.S.A.* **102**, 18403 (2005).
4. T. Gregor, D. W. Tank, E. F. Wieschaus, W. Bialek, *Cell* **130**, 153 (2007).
5. T. Gregor, E. F. Wieschaus, A. P. McGregor, W. Bialek, D. W. Tank, *Cell* **130**, 141 (2007).
6. H. Spemann, *Embryonic Development and Induction* (Yale Univ. Press, New Haven, CT, 1938).
7. J. Cooke, *Nature* **290**, 775 (1981).
8. B. Reversade, E. M. De Robertis, *Cell* **123**, 1147 (2005).
9. D. Ben-Zvi, B. Z. Shilo, A. Fainsod, N. Barkai, *Nature* **453**, 1205 (2008).
10. A. Eldar *et al.*, *Nature* **419**, 304 (2002).
11. A. Turing, *Philos. Trans. R. Soc. London Ser. B* **237**, 37 (1952).
12. H. Meinhardt, *Models of Biological Pattern Formation* (Academic Press, London, 1982).
13. H. Meinhardt, A. Gierer, *Bioessays* **22**, 753 (2000).
14. D. Reinhardt *et al.*, *Nature* **426**, 255 (2003).
15. T. Berleth, E. Scarpella, P. Prusinkiewicz, *Trends Plant Sci.* **12**, 151 (2007).
16. E. Benkova *et al.*, *Cell* **115**, 591 (2003).
17. M. G. Heisler *et al.*, *Curr. Biol.* **15**, 1899 (2005).
18. P. B. de Reuille *et al.*, *Proc. Natl. Acad. Sci. U.S.A.* **103**, 1627 (2006).
19. H. Jonsson, M. G. Heisler, B. E. Shapiro, E. M. Meyerowitz, E. Mjolsness, *Proc. Natl. Acad. Sci. U.S.A.* **103**, 1633 (2006).
20. R. S. Smith *et al.*, *Proc. Natl. Acad. Sci. U.S.A.* **103**, 1301 (2006).
21. A. Aulehla *et al.*, *Nat. Cell Biol.* **10**, 186 (2008).
22. J. Dubrulle, O. Pourquié, *Nature* **427**, 419 (2004).
23. J. Cooke, E. C. Zeeman, *J. Theor. Biol.* **58**, 455 (1976).
24. I. Palmeirim, D. Henrique, D. Ish-Horowicz, O. Pourquié, *Cell* **91**, 639 (1997).
25. M. L. Dequéant, O. Pourquié, *Nat. Rev. Genet.* **9**, 370 (2008).
26. S. A. Holley, *Dev. Dyn.* **236**, 1422 (2007).
27. Y. J. Jiang *et al.*, *Nature* **408**, 475 (2000).
28. Y. Bessho, H. Hirata, Y. Masamizu, R. Kageyama, *Genes Dev.* **17**, 1451 (2003).
29. C. A. Henry *et al.*, *Development* **129**, 3693 (2002).
30. A. C. Oates, R. K. Ho, *Development* **129**, 2929 (2002).
31. J. Lewis, *Curr. Biol.* **13**, 1398 (2003).
32. F. Giudicelli, E. M. Ozbudak, G. J. Wright, J. Lewis, *PLoS Biol.* **5**, e150 (2007).
33. K. Horikawa, K. Ishimatsu, E. Yoshimoto, S. Kondo, H. Takeda, *Nature* **441**, 719 (2006).
34. I. H. Riedel-Kruse, C. Müller, A. C. Oates, *Science* **317**, 1911 (2007); published online 15 August 2007 (10.1126/science.1142538).
35. E. M. Ozbudak, J. Lewis, *PLoS Genet.* **4**, e15 (2008).
36. M.-L. Dequéant *et al.*, *Science* **314**, 1595 (2006); published online 8 November 2006 (10.1126/science.1133141).
37. E. M. Ozbudak, O. Pourquié, *Curr. Opin. Genet. Dev.*, in press; published online 15 August 2008 (10.1016/j.gde.2008.06.007).
38. C. Kimmel *et al.*, *Dev. Dyn.* **203**, 253 (1995).

39. I thank N. Barkai, B. Reversade, R. Collins, A. Hanisch, C. Kuhlemeier, and an anonymous referee for comments and Cancer Research UK for funding.

10.1126/science.1166154

The Miller Volcanic Spark Discharge Experiment

Adam P. Johnson,[1] H. James Cleaves,[2] Jason P. Dworkin,[3] Daniel P. Glavin,[3] Antonio Lazcano,[4] Jeffrey L. Bada[5]*

In 1953, Miller (*1*) published a short paper describing the spark discharge synthesis of amino acids from a reducing gas mixture thought to represent the atmosphere of the early Earth. This experiment showed that the basic molecules of life could be synthesized from simple molecules, suggesting that Darwin's "warm little pond" was a feasible scenario.

After Miller's death on 20 May 2007, we found several boxes containing vials of dried residues. Notebooks (*2*) indicated that the vials came from his 1953–54 University of Chicago experiments that used three different configurations (*3*, *4*). One was the original apparatus used in (*1*). Another incorporated an aspirating nozzle attached to the water-containing flask, injecting a jet of steam and gas into the spark. The third incorporated the aspirator device but used a silent discharge instead of electrodes. Although Miller repeated his experiment in 1972 with use of the original architecture (*5*), the others were never tested again.

We were interested in the second apparatus because it possibly simulates the spark discharge synthesis by lightning in a steam-rich volcanic eruption (*6*) (Fig. 1A). Miller identified five different amino acids, plus several unknowns, in the extracts from this apparatus (*3*). Product yields appeared somewhat higher than those in the classical configuration, although Miller never confirmed this. We reanalyzed 11 vials in order to characterize the diversity of products synthesized in this apparatus.

The residues in the vials were resuspended in 1-ml aliquots of doubly distilled deionized water and characterized by high-performance liquid chromatography and liquid chromatography–time of flight mass spectrometry that allows for identification at the sub-picomolar ($<10^{-12}$ M) level (*2*). We identified 22 amino acids and five amines in the volcanic experiment (Fig. 1C), several of which had not been previously identified in Miller's experiments. Vials from the other two experiments were also reanalyzed and found to have a lower diversity of amino acids (table S1). The yield of amino acids synthesized in the volcanic experiment is comparable to, and in some cases exceeds, those found in the experiments Miller conducted (*1*, *3*, *5*). Hydroxylated compounds were preferentially synthesized in the volcanic experiment. Steam injected into the spark may have generated OH radicals that reacted with either the amino acid precursors or the amino acids themselves (*7*).

Geoscientists today doubt that the primitive atmosphere had the highly reducing composition Miller used. However, the volcanic apparatus experiment suggests that, even if the overall atmosphere was not reducing, localized prebiotic synthesis could have been effective. Reduced gases and lightning associated with volcanic eruptions in hot spots or island arc–type systems could have been prevalent on the early Earth before extensive continents formed (*8*). In these volcanic plumes, HCN, aldehydes, and ketones may have been produced, which, after washing out of the atmosphere, could have become involved in the synthesis of organic molecules (*3*, *4*, *8*). Amino acids formed in volcanic island systems could have accumulated in tidal areas, where they could be polymerized by carbonyl sulfide, a simple volcanic gas that has been shown to form peptides under mild conditions (*9*).

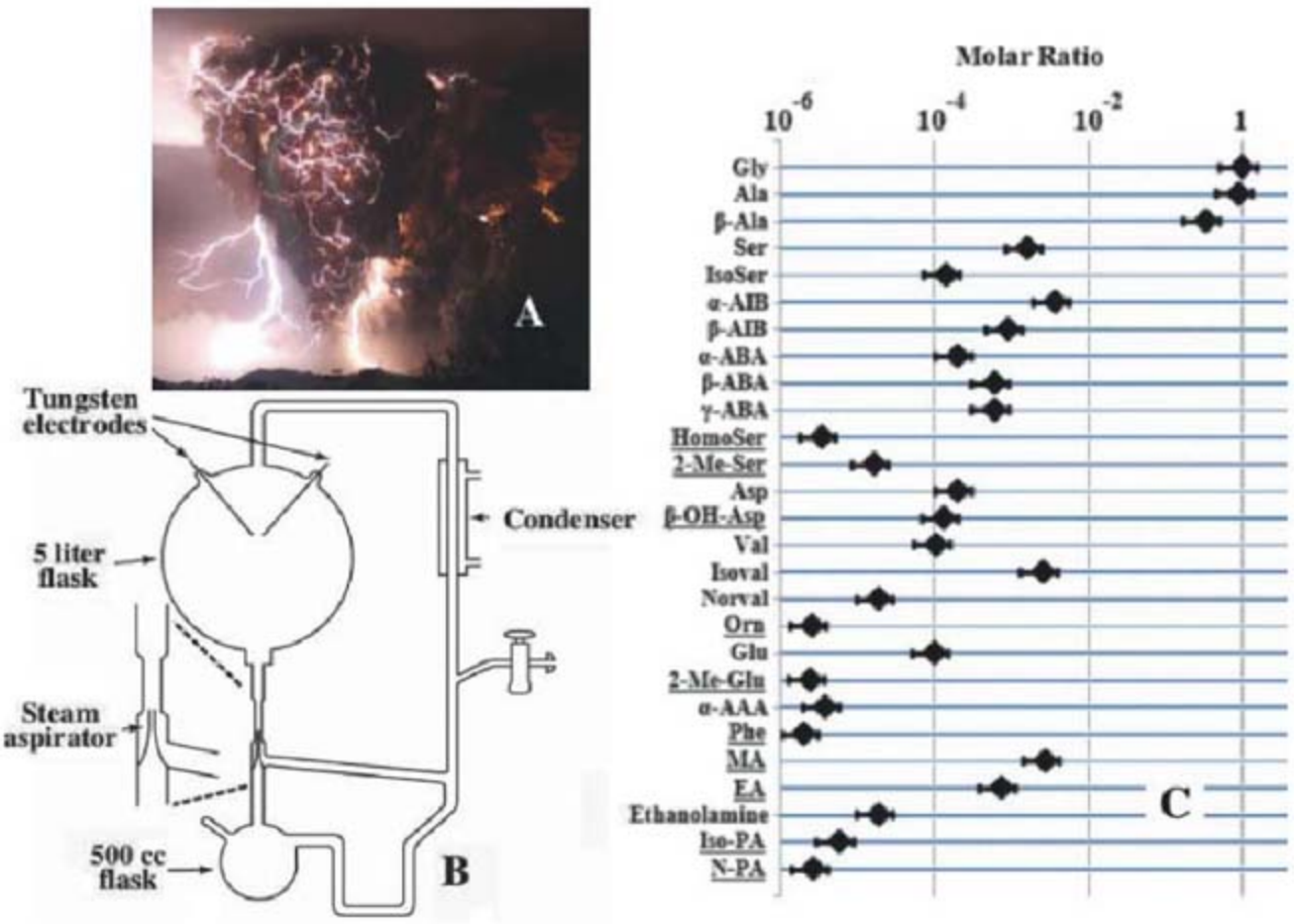

Fig. 1. (**A**) Lightning associated with the 3 May 2008 eruption of the Chaiten volcano, Chile. [Photo credit: Carlos Gutierrez/UPI/Landov] (**B**) The volcanic spark discharge apparatus used by Miller (*3*). Gas quantities added were 200 torr of CH_4, 200 torr of NH_3, and 100 torr of H_2 [these would have dissolved in the water according to their solubilities (*2*)]. Water was added to the 500-cm^3 (cc) flask and boiled, and the apparatus sparked with a Tesla coil for 1 week; (**C**) Moles (relative to glycine = 1) of the various amino acids detected in the volcanic apparatus vials [see (*2*) and table S1 for abbreviations]. Amino acids underlined have not been previously reported in spark discharge experiments. Values for amines are minimum values because of loss due to their volatility during workup.

References and Notes

1. S. L. Miller, *Science* **117**, 528 (1953).
2. Analytical details and additional data are available as supporting material on *Science* Online.
3. S. L. Miller, *J. Am. Chem. Soc.* **77**, 2351 (1955).
4. A. Lazcano, J. L. Bada, *Origins Life Evol. Biosph.* **33**, 235 (2003).
5. D. Ring, W. Yecheskel, N. Friedmann, S. L. Miller, *Proc. Natl. Acad. Sci. U.S.A.* **69**, 765 (1972).
6. S. R. McNutt, C. M. Davis, *J. Volcanol. Geotherm. Res.* **102**, 45 (2000).
7. D. Ring, S. L. Miller, *Origins Life Evol. Biosph.* **15**, 7 (1984).
8. R. D. Hill, *Origins Life Evol. Biosph.* **22**, 277 (1991).
9. L. Leman, L. Orgel, M. Reza Ghadiri, *Science* **306**, 283 (2004).

Supporting Online Material

www.sciencemag.org/cgi/content/full/322/5900/404/DC1
Materials and Methods
Figs. S1 and S2
Table S1
References and Notes

9 June 2008; accepted 8 August 2008
10.1126/science.1161527

[1]Interdisciplinary Biochemistry Program, Indiana University, Bloomington, IN 47401, USA. [2]Carnegie Institution of Washington, Washington, DC 20015, USA. [3]NASA Goddard Space Flight Center, Solar System Exploration Division, Greenbelt, MD 20771, USA. [4]Facultad de Ciencias, Universidad Nacionale Autónoma de México, Mexico Distrito Federal 04510, Mexico. [5]Scripps Institution of Oceanography, La Jolla, CA 92093–0212, USA.

*To whom correspondence should be addressed. E-mail: jbada@ucsd.edu

Conservation and Rewiring of Functional Modules Revealed by an Epistasis Map in Fission Yeast

Assen Roguev,[1,2] Sourav Bandyopadhyay,[3] Martin Zofall,[4] Ke Zhang,[4] Tamas Fischer,[4] Sean R. Collins,[1,2,5] Hongjing Qu,[1,2] Michael Shales,[1,2] Han-Oh Park,[6] Jacqueline Hayles,[7] Kwang-Lae Hoe,[8] Dong-Uk Kim,[8] Trey Ideker,[3]* Shiv I. Grewal,[4]* Jonathan S. Weissman,[1,2,5]* Nevan J. Krogan[1,2]*

An epistasis map (E-MAP) was constructed in the fission yeast, *Schizosaccharomyces pombe*, by systematically measuring the phenotypes associated with pairs of mutations. This high-density, quantitative genetic interaction map focused on various aspects of chromosome function, including transcription regulation and DNA repair/replication. The E-MAP uncovered a previously unidentified component of the RNA interference (RNAi) machinery (*rsh1*) and linked the RNAi pathway to several other biological processes. Comparison of the *S. pombe* E-MAP to an analogous genetic map from the budding yeast revealed that, whereas negative interactions were conserved between genes involved in similar biological processes, positive interactions and overall genetic profiles between pairs of genes coding for physically associated proteins were even more conserved. Hence, conservation occurs at the level of the functional module (protein complex), but the genetic cross talk between modules can differ substantially.

Genetic interactions report on the extent to which the function of one gene depends on the presence of a second. This phenomenon, known as epistasis, can be used for defining functional relationships between genes and the pathways in which the corresponding proteins function. Two main categories of genetic interactions exist: (i) negative (e.g., synthetic sickness/lethality) and (ii) positive (e.g., suppression). We have developed a quantitative approach, termed epistasis map (E-MAP), allowing us to measure the whole spectrum of genetic interactions, both positive and negative (*1*, *2*). In budding yeast, *Saccharomyces cerevisiae*, it has been demonstrated that positive genetic interactions can identify pairs of genes whose products are physically associated and/or function in the same pathway (*1*, *2*), whereas negative interactions exist between genes acting on parallel pathways (*3*, *4*).

We developed the Pombe Epistasis Mapper (PEM) approach (*5*) that allows high-throughput generation of double mutants in the fission yeast, *Schizosaccharomyces pombe*. Fission yeast is more similar to metazoans than is *S. cerevisiae*, owing to its large complex centromere structure, the restriction of spindle construction to mitotic entry, gene regulation by histone methylation and chromodomain heterochromatin proteins, gene and transposon regulation by the RNA interference (RNAi) pathway, and the widespread presence of introns in genes. To further study these processes and to try to understand how genetic interaction networks have evolved (*6*), we generated an E-MAP in *S. pombe* that focuses on nuclear function, designed to be analogous to one we created in budding yeast (*2*).

An E-MAP in *S. pombe*. Using our PEM system (*5*), we generated a quantitative genetic interaction map in *S. pombe*, comprising ~118,000 distinct double mutant combinations among 550 genes involved in various aspects of chromosome function (Fig. 1A and tables S1 and S4) (*7*). The genes on the map were chosen on the basis of a previous budding yeast E-MAP (*1*, *2*) and also included factors present in human (but not in *S. cerevisiae*), including the RNAi machinery. We used colony size (measured from high-density arrays) as a quantitative phenotypic read-out to compute a genetic interaction score (S score) and previously described quality control measures to ensure a high-quality data set (*7*, *8*) (fig. S1A).

We have previously observed two prominent general trends between genetic interactions and protein-protein interactions (PPIs): (i) a propensity for positive genetic interactions and (ii) strong correlations of genetic interaction profiles between genes coding for proteins participating in PPIs (*2*). Using a high-confidence set of 151 PPI pairs from *S. pombe* (*9*) (table S2), we observed the same trends in this organism (Fig. 1, B and C). Thus, it appears these relationships are evolutionarily conserved and may represent a general feature of biological networks.

Exploring nuclear function in fission yeast. We generated a highly structured representation of the genetic map by subjecting the data to hierarchical clustering (Fig. 2). By scrutinizing several interaction-rich regions, we were able to recapitulate known, and identify previously unknown, functional relationships.

Genes required for DNA repair/recombination and various checkpoint functions form clusters enriched in negative interactions (Fig. 2, region 1). The *rad9-hus1-rad1* (9-1-1) checkpoint complex (*10*) clusters together with rad17 (the homolog of budding yeast *RAD24*), which loads it onto DNA (*11*). We found two genes linked to tRNA biogenesis, *sen1* and *trm10*, within the DNA repair cluster. tRNA regulation has been linked to the DNA damage response pathway in *S. cerevisiae* (*12*), and these genetic patterns suggest that a similar mechanism may exist in fission yeast. To genetically interrogate the function of essential genes, we used the decreased abundance by mRNA perturbation (DAmP) strategy for generating hypomorphic alleles (*1*) (table S1) and found that the DAmP allele of *mcl1*, involved in DNA replication control and repair, is highly correlated with components of the replication checkpoint (*mrc1* and *csm3*).

The fission yeast homologs of the components of the SWR complex (SWR-C)—which, in budding yeast, incorporates the histone H2A variant Htz1 (Pht1 in fission yeast) into chromatin (*13*–*15*)—form a highly correlated group (Fig. 2, region 2). A jumonji domain–containing protein, Msc1, whose *S. cerevisiae* ortholog *ECM5* is not part of the budding yeast's SWR-C, is found within the fission yeast SWR-C cluster, consistent with the demonstration that Msc1 acts through Pht1 to promote chromosome stability (*16*).

The E-MAP reveals functional specialization of the fission yeast Set1 histone H3 lysine 4 methyltransferase complex (SET1-C, COMPASS) (*17*–*20*). In *S. pombe*, five of its subunits (core SET1-C: *set1*, *spp1*, *swd1*, *swd21*, and *swd3*) are indispensable for H3-K4 methylation (*19*) and form a highly correlated cluster on the E-MAP (Fig. 2, region 3). In budding yeast, another component of COMPASS, Swd2, is essential and is part of two distinct complexes: (i) SET1-C and the (ii) Cleavage and Polyadenylation Factor (CPF) (*17*, *21*). *S. pombe* contains two nonessential paralogs of *SWD2* (*swd21* and *swd22*), which have previously been shown to act independently in the *S. pombe* SET1-C and CPF, respectively (*22*). Consistent with this observation, on our map, *swd21* is part of the core SET1-C, whereas *swd22* is strongly correlated with the *SSU72* ortholog, a part of CPF (*21*, *23*) (Fig. 2, region 3).

[1]Department of Cellular and Molecular Pharmacology, University of California, San Francisco, CA 94158, USA. [2]California Institute for Quantitative Biosciences, University of California, San Francisco, CA 94158, USA. [3]Department of Bioengineering and Program in Bioinformatics, University of California–San Diego, La Jolla, CA 92093, USA. [4]Laboratory of Biochemistry and Molecular Biology, Center for Cancer Research, National Cancer Institute, NIH, Bethesda, MD 20892, USA. [5]Howard Hughes Medical Institute, San Francisco, CA 94158, USA. [6]Bioneer Corporation, Daejeon, Korea. [7]Cell Cycle Laboratory, Cancer Research UK, London Research Institute, 44 Lincoln's Inn Fields, London WC2A 3PX, UK. [8]Genomic Research Center, Korea Research Institute of Bioscience and Biotechnology, Daejeon, Korea.

*To whom correspondence should be addressed. E-mail: trey@bioeng.ucsd.edu (T.I.); grewals@mail.nih.gov (S.I.G.); weissman@cmp.ucsf.edu (J.S.W.); krogan@cmpmail.ucsf.edu (N.J.K.)

The Ash2-Sdc1 heterodimer within the SET1-C also behaves differently. In *S. cerevisiae*, its orthologous pair (Bre2p-Sdc1p) is exclusively found in the SET1-C (*17*), whereas in fission yeast it is shared between the SET1-C and LID2-C (*19*). Consistent with this result, the dimer does not cluster next to core Set1-C [as is observed in budding yeast (*2*)] but is more similar to *snt2*, a member of LID2-C (Fig. 2, region 3).

Genetic dissection of the RNAi pathway. The RNAi pathway in *S. pombe* is composed of several components, including CLR4-C, RDR-C, RITS, dicer (Dcr1), and the HP1 homolog Swi6 (*24*). All known components of the RNAi machinery that were analyzed cluster next to each other and primarily display positive genetic interaction with one another (Fig. 3A). Within this cluster are subclusters corresponding to the different protein complexes. Consistent with previous reports, we found positive genetic interactions between the RNAi machinery and *epe1*, an antisilencing factor involved in the transcription of heterochromatic regions by RNA polymerase II (RNAPII) (*25*) and required for RNAi-mediated heterochromatin assembly (*24*). Conversely, we found negative interactions between RNAi components involved in posttranscriptional gene silencing and factors implicated in transcriptional gene silencing (TGS) of repeat sequences and other loci. In particular, *clr3*, a histone deacetylase and catalytic subunit of the Snf2/Hdac-containing repressor complex (*26*) that is involved in TGS at centromeric repeats (*24*) and Tf2 retrotransposons (*27*, *28*), shows negative interactions with RNAi components (Fig. 3A).

Within the RNAi cluster, we also found a previously unknown component of the RNAi pathway, SPCC1393.05, which we named *rsh1* (involved in RNAi silencing and heterochromatin formation) (Fig. 3A). The gene encodes a 110-kD protein with no obvious homologs or apparent sequence motifs. We used chromatin immunoprecipitation to determine that Rsh1 is localized to heterochromatic centromeric regions. Its absence causes a substantial reduction of silencing at these loci and a loss of small interfering RNAs (siRNAs) expressed from the centromeric dg/dh repeats (Fig. 3, B to F). Additionally, *rsh1*Δ leads to a marked reduction of H3-K9 dimethylation and Swi6/HP1 binding that correlates with lowered levels (more than sixfold decrease) of Ago1 (a component of RITS) recruitment to the outer (*otr*) centromeric repeat region (Fig. 3, G and H).

We also observed positive interactions between the RNAi machinery and homologs of factors involved in the transition between transcriptional initiation and elongation, including *rpb9* and *iwr1*, components of RNAPII (*21*, *29*), and the Mediator complex (*pmc2*, *rox3*, *pmc5*, and *med2*) (*30*, *31*). Deletions of *rpb9*, *rox3*, *pmc5*, or *pmc2* lead to moderate loss of silencing at the centromere (Fig. 3, I and J).

We observed numerous negative genetic interactions between the RNAi machinery and other cellular complexes and processes (Fig. 3A), including the spindle-checkpoint pathway (*mad1*, *mad2*, *bub3*, and *alp14*) (*32*); components of the DASH complex (*33*) (*dad1*, *dad2*, *ask1*, and *spc34*); and *mal3*, *tub1*, and *alp31* involved in microtubule stability (*34*), consistent with the involvement of RNAi/heterochromatin apparatus in proper chromosome segregation (*35*). The acetyltrasferase complex Elongator (*36*) interacts negatively with the RNAi machinery and clusters next to factors regulating spindle function, consistent with the observation that Elongator may be responsible for tubulin acetylation, required for microtubule-based protein trafficking (*37*). Finally, components of the DNA repair, checkpoint, and recombination apparatus display negative genetic interactions with the RNAi machinery, suggesting that the RNAi pathway is also involved in maintaining genomic stability.

Conservation of modular organization of genetic interaction networks. The large evolutionary distance between *S. cerevisiae* and *S. pombe* [~400 million years (*38*)] allowed us to study the evolution of genetic interactomes. We directly compared the data from this *S. pombe* E-MAP to an analogous database from *S. cerevisiae* (database S4) (*2*). The overlap of one-to-one annotated orthologs (*39*) between the two E-MAPs encompasses 239 genes (table S3). First, we analyzed individual negative pairwise interactions in the two organisms. Recently, it has been suggested (*6*) that negative interactions between yeast and *Caenorhabditis elegans* were not conserved. Although not strong, we did find a conservation of negative interactions (17.3% for S score ≤ –2.5), which became more pronounced (33%) when the analysis was restricted to genes that shared the same functional annotations (Fig. 4A and fig. S2B). To confirm this observation, we used an independent data set from BioGRID (*9*) and observed similar conservation rates [18% for all and 31% among functionally related genes (*7*)]. Part of the discrepancy seen in *C. elegans* could be due to functional redundancy, multicellularity, or incomplete knockdowns by RNAi. Furthermore, this comparison was not restricted to functionally related genes (*6*). In our analysis, we also found a very strong conservation (>50%) of positive interactions (S score ≥ 2.0) [that were not considered by (*6*)] between pairs of genes whose corresponding proteins are physically associated (Fig. 4A and fig. S2, A to D) (*7*).

The set of genetic interactions for a given gene provides a sensitive phenotypic signature or profile. Although a global comparison of all correlations of genetic profiles between orthologous pairs in each species (table S3)

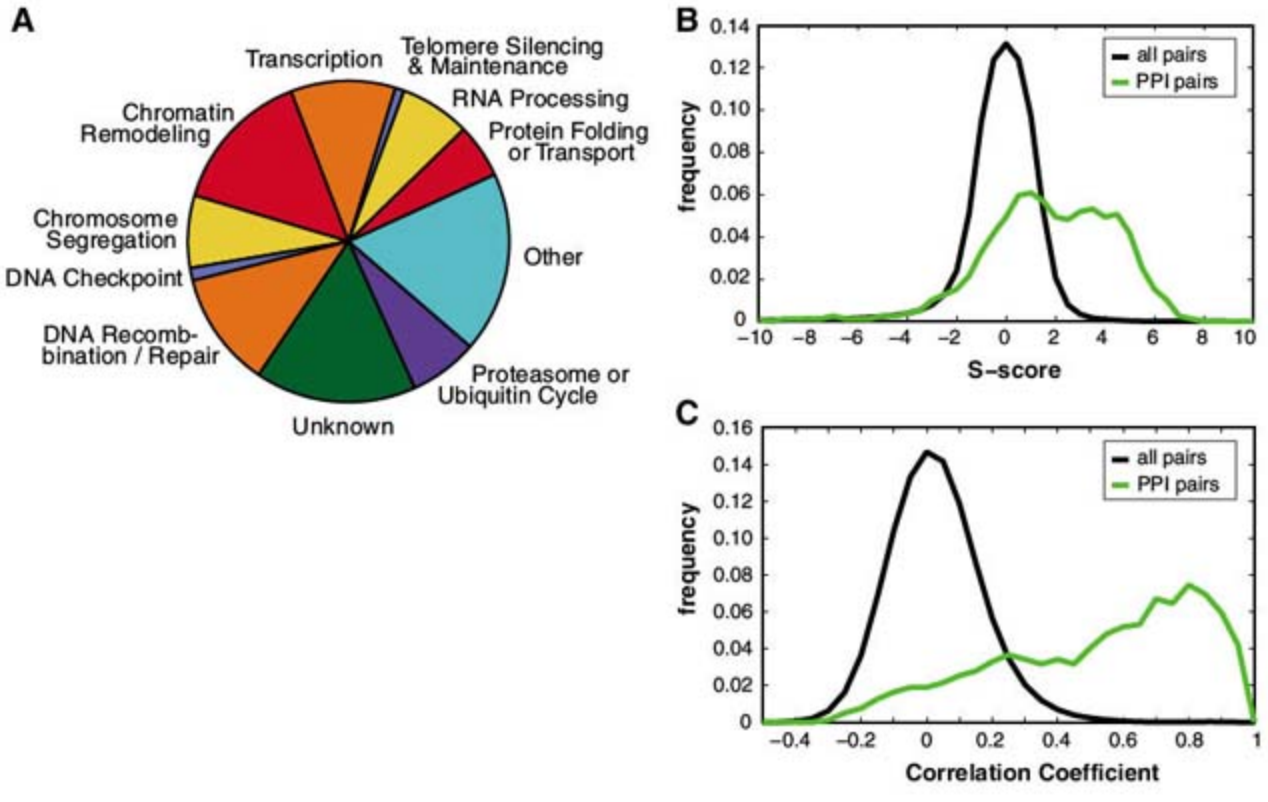

Fig. 1. Data set overview. (**A**) Functional classification of the genes contained within the *S. pombe* E-MAP. The map contains 550 genes that were classified into 11 functional categories (table S4). (**B**) Distribution of interaction scores for pairs of genes corresponding to physically interacting proteins (green) and noninteracting proteins (black). (**C**) Distribution of Pearson correlation coefficients of the genetic interaction profiles for the same set of genes used in (B). For a complete list of PPIs used in this analysis, see table S2.

revealed a weak overall conservation (correlation coefficient $r = 0.14$) (Fig. 4B), pairs corresponding to PPIs were much more highly correlated ($r = 0.60$) (Fig. 4B). An aggregate measure for the likelihood of two proteins to carry out a common function, many of which correspond to PPI pairs, is the complex or linear pathway (COP) score (*8*), which integrates the individual genetic interaction score and correlation coefficient of genetic interaction profiles. Pairs of genes displaying high COP scores in both organisms almost exclusively correspond to PPIs (fig. S2E).

To further explore the extent of conservation of genetic networks, the profiles of each of the 239 orthologs in both species were compared to all profiles from the other organism (Fig. 4C). We found some conservation between direct orthologs ($P = 8 \times 10^{-20}$), suggesting that genetic interaction profiles of orthologs across species tend to be similar (fig. S2F). There is, however, a stronger conservation of genetic profiles between a gene and the ortholog of its interacting partner when only co-complex members were considered (Fig. 4C) ($P = 9 \times 10^{-51}$). Thus, genetic profiles of members of PPI pairs tend to correlate better, not only to their interaction partners within the same species, but also to the orthologs of their interaction partner in an evolutionarily distant organism.

Collectively, these data demonstrate that genetic interactions between particular subsets of genes are conserved between *S. cerevisiae* and *S. pombe*. Specifically, we find conservation of negative interactions when genes involved in the same cellular process are considered. Better conserved are positive interactions and genetic profiles of genes whose products are physically associated. Therefore, we argue that conservation primarily exists at the level of the functional module (protein complex), and perhaps PPIs pose a constraint on functional divergence in evolution.

Rewiring of conserved functional modules. Biological modules can be defined as highly interconnected groups of physically or functionally associated factors, and they often correspond to protein complexes. In addition to identifying functional modules, high-density genetic interaction data reports on the functional relationships between modules (i.e., the wiring of the network).

To compare the genetic cross talk between modules in the two organisms, we merged and clustered the genetic interaction matrix of *S. pombe* with that of *S. cerevisiae* for the 239 1:1 orthologs (database S2). Inspection of this database revealed a partial overlap of negative interactions between protein complexes (Fig. 5A). For example, in both organisms, SWR-C display negative genetic interactions with the SET1-C and the histone deacetylase (HDAC) complex, SET3-C. However, substantial differences were found as well. For instance, only in budding yeast are there

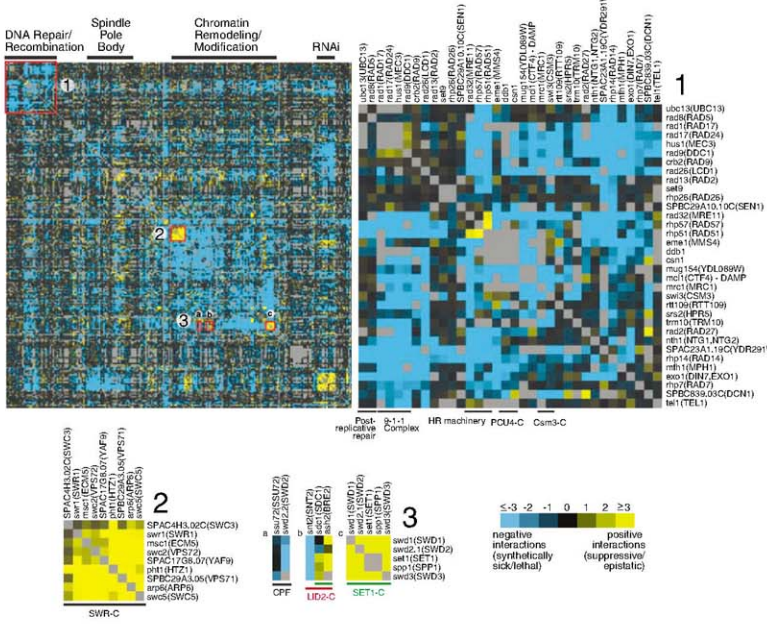

Fig. 2. The *S. pombe* chromosome function E-MAP. A section of the E-MAP with specific regions of interest annotated. Further highlighted are the factors involved in DNA repair/recombination (1), as well as two complexes contained within the chromatin remodeling/modification region: the SWR-C chromatin remodeling complex (2) and the Set1, Lid2, and CPF complexes (3). The names of the budding yeast orthologs are shown in parentheses (table S3). The final data set consists of 118,575 measurements and contains 5772 negative (S score ≤ −2.5) and 1812 positive (S score ≥ 2) interactions.

negative interactions between SWR-C and components of the spindle checkpoint, the chaperone complex Prefoldin, the HDAC complex, Rpd3C(L), and Mediator (Fig. 5A).

Several possible explanations can be offered. First, the additional subunit unique to the fission yeast SWR-C, Msc1, may alter the function of the complex. Also, species-specific posttranslational modifications may result in different genetic behavior. Msc1 has been shown to harbor ubiquitin ligase activity (*40*) and may be involved in ubiquitinating proteins related to the function of SWR-C. Another reason could be the presence or absence of particular cellular machinery. For example, the rewiring of the genetic space surrounding the SWR-C in *S. pombe* may be due to the presence of the RNAi machinery, which shows negative interactions with the complex (Fig. 5B). Consequently, dramatic alterations in the network topology of budding yeast may have been necessary to compensate for the absence of the RNAi pathway. We cannot rule out the possibility that many of the interactions do exist under different environmental conditions. Nonetheless, a major rewiring of other complexes [e.g., the histone regulatory (HIR) chromatin assembly complex and Prefoldin] (fig. S3) was also observed under the conditions used.

The modularity of biological networks is believed to be one of the main contributors to their robustness, as it implies enhanced functional flexibility. Much like an electronic cir-

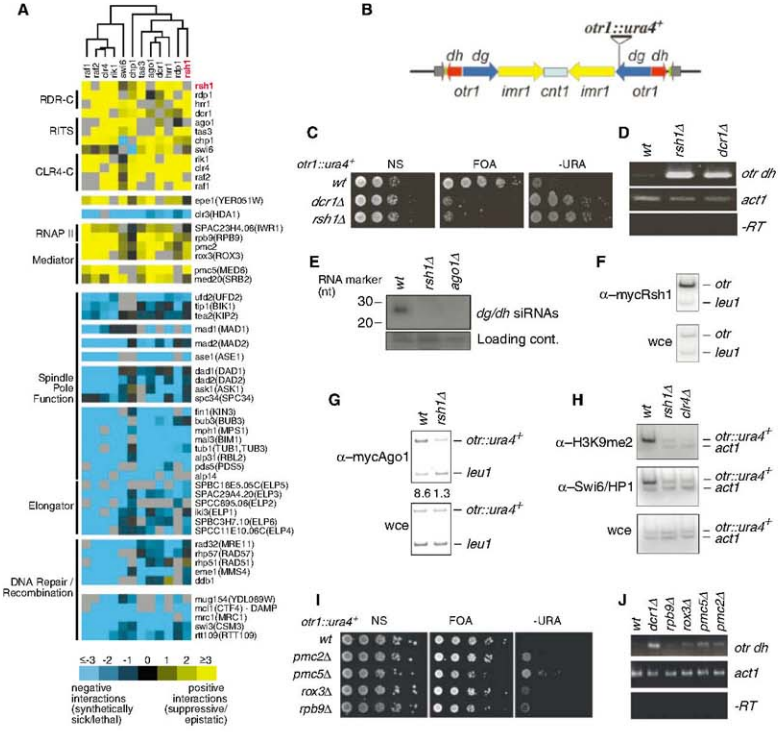

Fig. 3. Characterization of genes involved in the RNAi pathway. **(A)** Genetic profiles for genes involved in RNAi with individual protein complexes or processes annotated. **(B)** Schematic of the centromeric region of chromosome 1 with the position of the *ura4*$^+$ reporter gene within the *otr1* region. **(C)** Loss of Rsh1p abolishes heterochromatic silencing of the *ura4*$^+$ reporter gene inserted at the outer repeat region of centromere 1 (*otr1::ura4*$^+$). NS, nonselective; FOA, counterselective; -URA, uracil-deficient media. **(D)** Levels of *dh* transcripts analyzed by reverse transcription polymerase chain reaction (RT-PCR) using RNA prepared from indicated strains. **(E)** Loss of siRNAs derived from *dg/dh* repeats in *rsh1Δ* detected by Northern blotting. nt, nucleotides. **(F)** Rsh1 localizes to outer (*otr*) centromeric repeats. An epitope-tagged version of Rsh1 (mycRsh1) was used to perform chromatin immunoprecipitation (ChIP). wce, whole-cell extract. **(G)** Rsh1 is required for localization of Ago1. Localization of mycAgo1 at *otr1::ura4*$^+$ in wild-type and *rsh1Δ* cells was assayed using ChIP. leu1 is an internal loading control for ChIP experiments. **(H)** Effect of *rsh1Δ* on heterochromatin assembly at centromeric repeats. Levels of histone H3 lysine 9 dimethylation (H3K9me2) and Swi6/HP1 at *otr1::ura4*$^+$ were assayed using ChIPs. **(I** and **J)** Loss of Mediator and RNAPII subunits affects centromeric silencing. The levels of transcripts corresponding to *dh* centromeric repeats were analyzed by RT-PCR. leu1 and act1 are used as internal loading controls.

cuit, such modular architecture allows different tasks to be accomplished with the same minimal set of components by changing the wiring (or flow of information) between them. Rewiring because of addition or removal of modules allows for economical design of sophisticated networks that are able to adapt to different conditions and environmental niches at a low cost. We observe this behavior derived from high-density genetic-

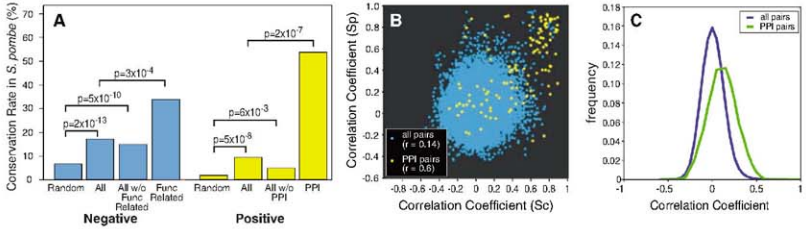

Fig. 4. Modular conservation of genetic interaction patterns. A set of 239 one-to-one orthologs (table S3) was used for the analysis. **(A)** Conservation of positive and negative genetic interactions based on comparison with *S. cerevisiae*. Conservation rates are higher for the subset of negative interactions between genes with the same functional annotation and the subset of positive interactions corresponding to known PPIs in *S. cerevisiae*. Pairs of genes whose proteins are physically associated or functionally related did not contribute significantly to the general trends (second bar), because removal of these pairs (third bar) resulted in similar conservation rates. *P* values were determined using a two-sided Student's *t* test (*7*). **(B)** Scatter plot of Pearson correlation coefficients of genetic interaction profiles. Sc, *S. cerevisiae*; Sp, *S. pombe*. **(C)** Distribution of the cross-species Pearson correlation coefficient of genetic profiles.

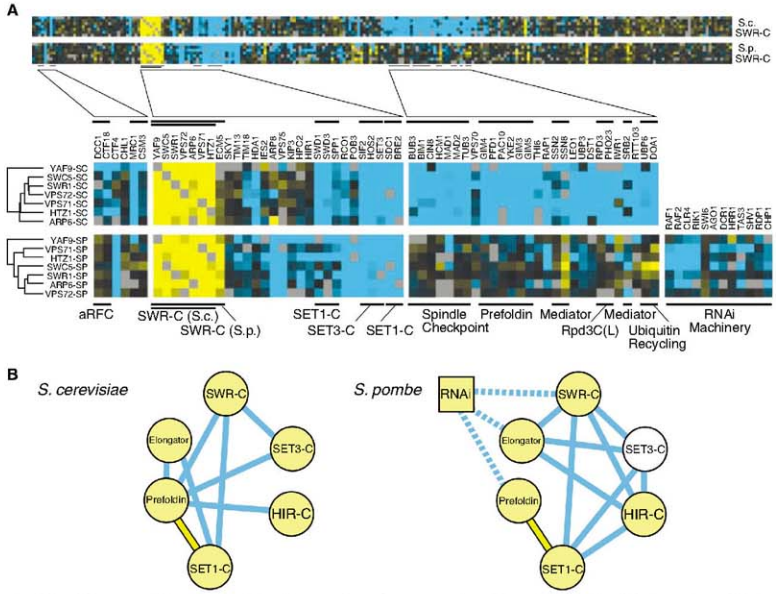

Fig. 5. Rewiring of the conserved functional modules. **(A)** Comparison of genetic interaction profiles of the SWR-C in *S. cerevisiae* and *S. pombe*. Analogous sets of genetic interactions from the two organisms are shown (database S2). **(B)** Genetic cross talk between functional modules. Modules are represented as circles or boxes (in yellow if the interactions within the module are primarily positive). Negative and positive interactions between modules are represented as blue and yellow lines, respectively. The diagram was generated using the method described in (*41*).

interaction data from two evolutionarily distant species. Our data strongly support the idea that functional modules are highly conserved, but the wiring between them can differ substantially. Thus, the use of model systems to make inferences about biological network topology may be more successful for describing modules than for describing the cross talk between them.

References and Notes

1. M. Schuldiner *et al.*, *Cell* **123**, 507 (2005).
2. S. R. Collins *et al.*, *Nature* **446**, 806 (2007).
3. X. Pan *et al.*, *Methods* **41**, 206 (2007).
4. A. H. Y. Tong *et al.*, *Science* **303**, 808 (2004).
5. A. Roguev, M. Wiren, J. S. Weissman, N. J. Krogan, *Nat. Methods* **4**, 861 (2007).
6. J. Tischler, B. Lehner, A. G. Fraser, *Nat. Genet.* **40**, 390 (2008).
7. Materials and methods are available as supporting material on *Science* Online.
8. S. R. Collins, M. Schuldiner, N. J. Krogan, J. S. Weissman, *Genome Biol.* **7**, R63 (2006).
9. C. Stark *et al.*, *Nucleic Acids Res.* **34**, D535 (2006).
10. R. Kaur, C. F. Kostrub, T. Enoch, *Mol. Biol. Cell* **12**, 3744 (2001).
11. J. Majka, P. M. Burgers, *Proc. Natl. Acad. Sci. U.S.A.* **100**, 2249 (2003).
12. A. Ghavidel *et al.*, *Cell* **131**, 915 (2007).
13. N. J. Krogan *et al.*, *Mol. Cell* **12**, 1565 (2003).
14. G. Mizuguchi *et al.*, *Science* **303**, 343 (2004), published 26 November 2003; 10.1126/science.1090701.
15. M. S. Kobor *et al.*, *PLoS Biol.* **2**, E131 (2004).
16. S. Ahmed, B. Dul, X. Qiu, N. C. Walworth, *Genetics* **177**, 1487 (2007).
17. A. Roguev *et al.*, *EMBO J.* **20**, 7137 (2001).
18. N. J. Krogan *et al.*, *J. Biol. Chem.* **277**, 10753 (2002).
19. A. Roguev *et al.*, *J. Biol. Chem.* **278**, 8487 (2003).
20. P. L. Nagy, J. Griesenbeck, R. D. Kornberg, M. L. Cleary, *Proc. Natl. Acad. Sci. U.S.A.* **99**, 90 (2002).
21. A. C. Gavin *et al.*, *Nature* **415**, 141 (2002).
22. A. Roguev *et al.*, *Mol. Cell. Proteomics* **3**, 125 (2004).
23. B. Dichtl *et al.*, *Mol. Cell* **10**, 1139 (2002).
24. S. I. Grewal, S. Jia, *Nat. Rev. Genet.* **8**, 35 (2007).
25. M. Zofall, S. I. Grewal, *Mol. Cell* **22**, 681 (2006).
26. T. Sugiyama *et al.*, *Cell* **128**, 491 (2007).
27. K. R. Hansen *et al.*, *Mol. Cell. Biol.* **25**, 590 (2005).
28. H. P. Cam, K. Noma, H. Ebina, H. L. Levin, S. I. Grewal, *Nature* **451**, 431 (2008).
29. N. J. Krogan *et al.*, *Nature* **440**, 637 (2006).
30. H. Spahr *et al.*, *J. Biol. Chem.* **275**, 1351 (2000).
31. H. Sakurai, M. Kimura, A. Ishihama, *Gene* **221**, 11 (1998).
32. D. N. Millband, K. G. Hardwick, *Mol. Cell. Biol.* **22**, 2728 (2002).
33. X. Liu, I. McLeod, S. Anderson, J. R. Yates III, X. He, *EMBO J.* **24**, 2919 (2005).
34. K. Asakawa *et al.*, *Mol. Biol. Cell* **17**, 1421 (2006).
35. I. M. Hall, K. Noma, S. I. Grewal, *Proc. Natl. Acad. Sci. U.S.A.* **100**, 193 (2003).
36. G. Otero *et al.*, *Mol. Cell* **3**, 109 (1999).
37. J. Gardiner, D. Barton, J. Marc, R. Overall, *Traffic* **8**, 1145 (2007).
38. M. Sipiczki, *Genome Biol.* **1**, REVIEWS1011 (2000).
39. C. J. Penkett, J. A. Morris, V. Wood, J. Bahler, *Nucleic Acids Res.* **34**, W330 (2006).
40. B. E. Dul, N. C. Walworth, *J. Biol. Chem.* **282**, 18397 (2007).
41. S. Bandyopadhyay, R. Kelley, N. J. Krogan, T. Ideker, *PLOS Comput. Biol.* **4**, e1000065 (2008).

42. We thank P. Beltrao and G. Cagney for critical reading of the manuscript; M. Wiren and S. Forsburg for discussion; P. Kemmeren for setting up the web database; S. Wang, C. Wen, and D. Avdic for technical help; and F. Stewart for sharing unpublished data. This work was supported by NIH [National Institute of General Medical Sciences grant GM084279 (T.I. and N. J.K.)], the Sandler Family Foundation (N.J.K), the Howard Hughes Medical Institute (J.S.W.), National Cancer Institute (S.I.G.), Center for Cancer Research (S.I.G.), and the California Institute of Quantitative Biology (N.J.K.).

Supporting Online Material

www.sciencemag.org/cgi/content/full/1162609/DC1
Materials and Methods
SOM Text
Figs. S1 to S5
Tables S1 to S8
References
Databases S1 to S4

1 July 2008; accepted 12 September 2008
Published online 25 September 2008;
10.1126/science.1162609
Include this information when citing this paper.

REPORTS

Current-Induced Spin-Wave Doppler Shift

Vincent Vlaminck and Matthieu Bailleul

Spin transfer appears to be a promising tool for improving spintronics devices. Experiments that quantitatively access the magnitude of the spin transfer are required for a fundamental understanding of this phenomenon. By inductively measuring spin waves propagating along a permalloy strip subjected to a large electrical current, we observed a current-induced spin wave Doppler shift that we relate to the adiabatic spin transfer torque. Because spin waves provide a well-defined system for performing spin transfer, we anticipate that they could be used as an accurate probe of spin-polarized transport in various itinerant ferromagnets.

Spin transfer—the transfer of angular momentum produced by a flow of electrons through an inhomogeneous magnetization configuration (*1*, *2*)—has many potential applications for data storage and microwave electronics. It has been demonstrated recently in nanostructured multilayers [current-induced magnetic switching (*3*, *4*) and precession (*5*, *6*)] and extended magnetic strips [current-induced domain-wall motion (*7*, *8*)]. It is usually difficult to measure the magnitude of the spin transfer with such experiments because they involve a complex spatio-temporal evolution of the magnetization (*4*, *8*). As recently suggested, spin transfer can also occur when an electrical current flows through a spin wave (*9*, *10*), which has the advantage of being a system that is stationary both in time and space: The low-amplitude magnetization perturbation is entirely determined by the wave vector $\vec{k}$ and pulsation ω of the spin wave (Fig. 1A), and the standard adiabatic gradient expression of spin transfer torque (STT) for continuously variable magnetization (*11*–*14*) results in a simple shift of the frequency of the spin wave (*10*, *15*)

$$\Delta\omega_{STT} = \frac{P\mu_B}{-|e|M_s}\cdot\vec{J}\vec{k} \qquad (1)$$

where P is the degree of spin polarization of the electrical current, μ_B is the Bohr magneton, $\vec{J}$ is the electrical current density, e is the electron charge, and M_s is the saturation magnetization. Although this current-induced frequency shift should not be confused with a true Doppler shift (*16*) that occurs, for example, when a detector is moved along the ferromagnet in which the spin wave propagates (*17*), it can be identified formally as the Doppler shift that would occur if the full electron system were simply drifting with respect to the lab frame with a velocity of $P\mu_B\vec{J}/-|e|M_s$, as suggested 40 years ago by Lederer and Mills (*18*).

We used a micrometer-sized version of the propagating spin wave spectroscopy (PSWS) technique (*19*–*21*). The microfabricated sample (Fig. 1, B and C) consisted of a permalloy ($Ni_{80}Fe_{20}$) strip [width (w) = 2 μm, thickness (t) = 20 nm], at the extremities of which four metal pads served to inject the current I_{dc} and measure the resistance. An external field H_0 ($\mu_0 H_0 \sim 1$ T, where μ_0 is the permeability of the vacuum) magnetized the permalloy strip out of plane so that spin waves propagated in the so-called magnetostatic forward volume waves (MSFVW) geometry (*19*, *20*). Spin waves were emitted and detected with a pair of spin wave antennae (center-to-center distance D = 7.7 μm) located above the central part of the strip and connected to a 20-GHz vector network analyzer via coplanar waveguides (CPW). Each antenna consists of a sub-micrometer–sized meander terminated with a short circuit. In the operating principle of PSWS (Fig. 1E), a microwave current $i(\omega)$ is injected into one antenna and generates a microwave magnetic field $h(\omega)$ that couples to the spin wave modes $m(\omega,k)$. These spin waves propa-

Institut de Physique et Chimie des Matériaux de Strasbourg, UMR 7504 CNRS–Université Louis Pasteur, 23 Rue du Loess, 67034 Strasbourg Cedex 2, France.

gate in both directions along the strip and induce an additional magnetic flux on the excitation antenna and on the second antenna. The signature of the spin waves is therefore a magnetic resonance behavior for the self-inductance $\Delta L_{11}(\omega)$ of the excitation antenna and for the mutual inductance $\Delta L_{12}(\omega)$ between the two antennae (*15*, *21*). The spatial periodicity of the microwave current density $j(x, \omega)$, as fixed by the meander shape of the antennae, determines the wave vector k of the excited spin waves. The Fourier transform $\tilde{j}(k, \omega)$ displayed in Fig. 1D shows a main peak at $k_M = 7.4\ \mu m^{-1}$ [that is, a wavelength (λ) ~ 0.8 μm corresponding to the spatial periodicity of the design] with a full width at half maximum (FWHM) of about 0.8 μm^{-1} alongside a secondary peak centered at $k_S = 2.8\ \mu m^{-1}$. In addition to the sample shown in Fig. 1, B and C, three other devices with different dimensions ($w = 3.5$ or 8 μm, $\lambda \sim 0.8$ or 1.6 μm, and $D = 5.4$ to 14.5 μm) were fabricated and studied.

We first characterized the permalloy strip and the propagation between the two antennae without dc current. Figure 2A shows the real and imaginary parts of the self-inductance ΔL_{11} for the $w = 8$ μm, $\lambda \sim 1.6$-μm sample under an applied field $\mu_0 H_0 = 0.993$ T. The absorption $Im(\Delta L_{11})$ displays two peaks: a main one at resonance frequency $f_{res} = 3.48$ GHz with a FWHM of 150 MHz and a secondary one at $f_{res} = 3.24$ GHz. They are attributed to the excitation of spin waves around k_M and k_S, respectively. The insets in Fig. 2A show the magnetic field dependency of the frequency of the main resonance (left) and the frequency dependence of its FWHM (right). These data are accounted fairly well by using the MSFVW dispersion (*15*) with a gyromagnetic ratio $\gamma/2\pi = 30.0$ GHz T^{-1}, an effective magnetization $\mu_0 M_{eff} = 0.88$ T, and a Gilbert damping factor $\alpha = 0.009$. These values compare reasonably well with the values obtained by broadband ferromagnetic resonance measurements on the unprocessed film (29.3 GHz T^{-1}, 0.94 T, and 0.006 T respectively) and with published values for permalloy/alumina thin films (*22*). Figure 2B shows the real and imaginary parts of the mutual inductance that were measured in the same run. One sees clear oscillations that are convoluted with the two absorption peaks observed in Fig. 2A. This is attributed to the propagation delay of the spin waves. When the frequency is swept around the f_{res}, slightly different wave vectors are selected within the FWHM of the $\tilde{j}(k,\omega)$ peaks so that the phase delay of the transmitted signal ($\phi = -kD$) changes continuously. From the period f_P of these oscillations, we estimate the spin wave group velocity to be $Vg = D f_P \sim 0.8\ \mu m\ ns^{-1}$, in reasonable agreement with the value of 0.72 μm ns^{-1} deduced from the MSFVW dispersion. The mutual inductances ΔL_{21} and ΔL_{12}, which correspond respectively to signal propagating in the forward (antenna 1 → 2) and reverse (antenna 2 → 1) directions, are identical (Fig. 2B), which confirms that the transmission of these volume spin waves is reciprocal (*19*, *20*) in the absence of a dc current.

Next, we proceeded to transmission measurements with a dc current. Figure 3A shows the imaginary part of the forward and reverse mutual inductances ΔL_{21} and ΔL_{12} measured for the $w = 2$ μm, $\lambda \sim 0.8$ μm sample upon injecting $I_{dc} = +6$ mA through the strip. The curves are shifted horizontally with respect to each other. The blue curve [$Im(\Delta L_{12})$], which corresponds to spin waves traveling in the same direction as the electron flow (Fig. 3A, inset), is shifted about 18 MHz higher in frequency than the red curve [$Im(\Delta L_{21})$], which accounts for spin waves traveling against the electron flow. When the polarity of the dc current is reversed (Fig. 3B), it is the red curve [$Im(\Delta L_{21})$], now corresponding to spin waves propagating along the electron flow, that is shifted about 18.5 MHz higher in frequency than the blue one. These observations were reproduced on all four samples, for different values of the dc current and for different values of the applied field (*15*). We also verified that the polarity of H_0 has no influence on the effect. To quantitatively compare these results, we plotted the measured frequency shifts Δf normalized by the wave vector k_M versus the electrical current density J (Fig. 3C). Aside from the data points corresponding to the highest current densities, we recognize a clear linear dependence in agreement with the STT Doppler shift. Upstream and downstream spin waves are Doppler-shifted in opposite ways so that the measured frequency shift Δf is two times the Δf_{STT} of Eq. 1. From the slope of the line shown in Fig. 3C, the spin polarization of the current in our permalloy film is estimated to be $P = 0.5 \pm 0.05$ (*15*), which indicates that the electrical current is mostly carried by the majority spins. The order of magnitude is consistent with the previous estimates derived from a detailed modeling of the low-temperature magnetoresistance of spin valves containing permalloy layers ($P = 0.6$ to 0.8) (*23*) and of the residual resistivity of bulk dilute alloys ($P = 0.8$ to 0.95) (*24*).

These results can be examined within the two-current model for which $P = \frac{\rho_\downarrow - \rho_\uparrow}{\rho_\downarrow + \rho_\uparrow}$, where the resistivities $\rho_\uparrow$ for the majority and $\rho_\downarrow$ for

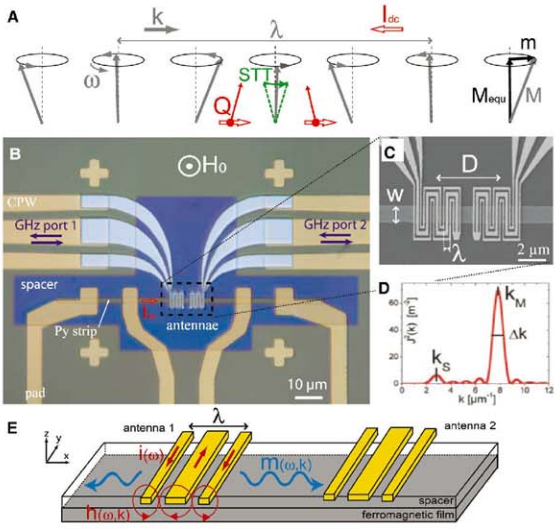

Fig. 1. Principle of the spin wave measurements. **(A)** Sketch of a spin wave subjected to STT [case of a spin wave propagating against the dc current (along the electron flow) with a spin polarization $P > 0$]. The red arrows represent the flow of spin-polarized electrons (the spin current Q) (*15*). **(B)** Optical micrograph of the device with a $w = 2$-μm permalloy strip ($t = 20$ nm) and a pair of $\lambda = 0.8$-μm antennae. **(C)** Scanning electron micrograph of the central region. **(D)** Fourier transform of the microwave current density for the antenna shown in (C). It was calculated by assuming a uniform current density across each branch of the meander. **(E)** Sketch of the operating principle of propagating spin wave spectroscopy.

the minority spin channels are determined by adding the contributions from the different sources of electron scattering (*24*). For bulk alloys at low temperature, the substitutional disorder dominates. Because the atomic potentials on Ni and Fe sites nearly align for the majority channel but differ substantially for the minority channel (*25*), this type of scattering is strongly spin-polarized in Ni-Fe ($\rho_\downarrow \sim 100$ microhm cm $>> \rho_\uparrow$) (*26*), which explains the very high value of P measured in these conditions (*24*). We estimate that several other sources of scattering contributed to the 30-microhm-cm room-temperature resistivity of our 20-nm polycrystalline film (to be compared with the residual resistivity 4 microhm cm of bulk permalloy): phonons and magnons (*24*), spin-mixing processes (*24*, *26*), grain boundaries, and film surfaces (*27*). This could explain the quantitative differences between our value of P and the previous estimates (*23*, *24*). Our experimental conditions were very close to those used to observe current-induced domain-wall motion (*7*, *8*, *28*), and so the polarization we measured is probably the most relevant in this context. The deviations from the linear dependence of $\Delta f/k$ versus J observed in Fig. 3C for current densities $|J| > 1.2\ 10^{11}$ A m^{-2} could reflect the enhancement of magnon and phonon scattering (*24*) due to a sizable Joule heating ($\Delta T \sim 100$ K for the $w = 3.5$-μm sample under $|J| = 1.7\ 10^{11}$ A m^{-2}, as estimated from the changes of the strip resistance and resonance frequency) (*15*). In line with these observations, a systematic study of the dependence of the Doppler shift on temperature, film thickness, and material microstructure could help to elucidate the scattering mechanisms that govern the adiabatic spin transfer in various materials. Spin waves could also be used to test the existence of the controversial nonadiabatic term of STT (*8*, *12*–*14*). Such a term would result in a simple change of the propagating attenuation of the spin waves, which could be accessed by improving the am-

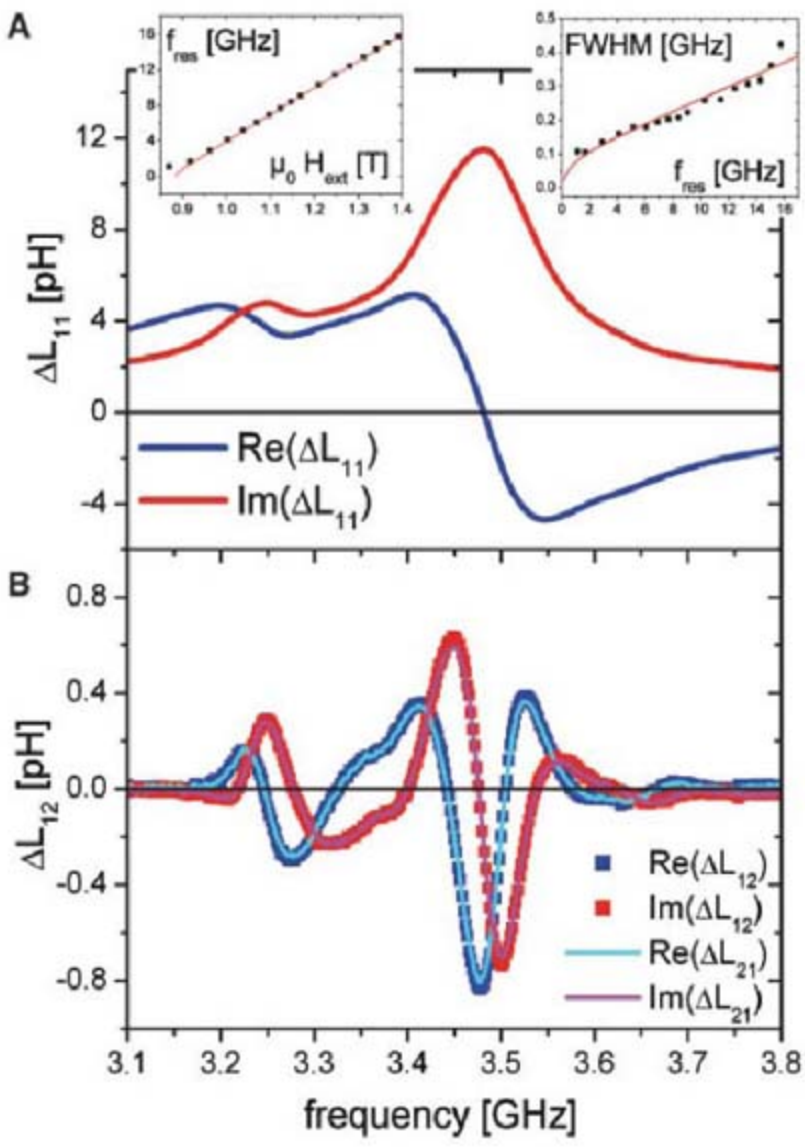

Fig. 2. Characterization of the spin wave signals in the absence of dc current. (**A**) Self-inductance measurement for a $\lambda = 1.6$-μm antenna coupled to a $t = 20$-nm, $w = 8$-μm permalloy strip subjected to a $\mu_0 H_0 = 0.993$ T field. (Left) Magnetic field dependence of the main resonance frequency. The continuous line was calculated with the dispersion of MSFVW (SOM text) (*15*). (Right) Frequency dependence of the frequency-swept linewidth (FWHM) of the main resonance. The continuous line was calculated by adding the intrinsic Gilbert contribution (*15*) to the inhomogeneous broadening because of the finite wave vector spreading of the excitation (Fig. 1D). (**B**) Mutual inductance measurements for the same experimental conditions ($D = 8.7$ μm).

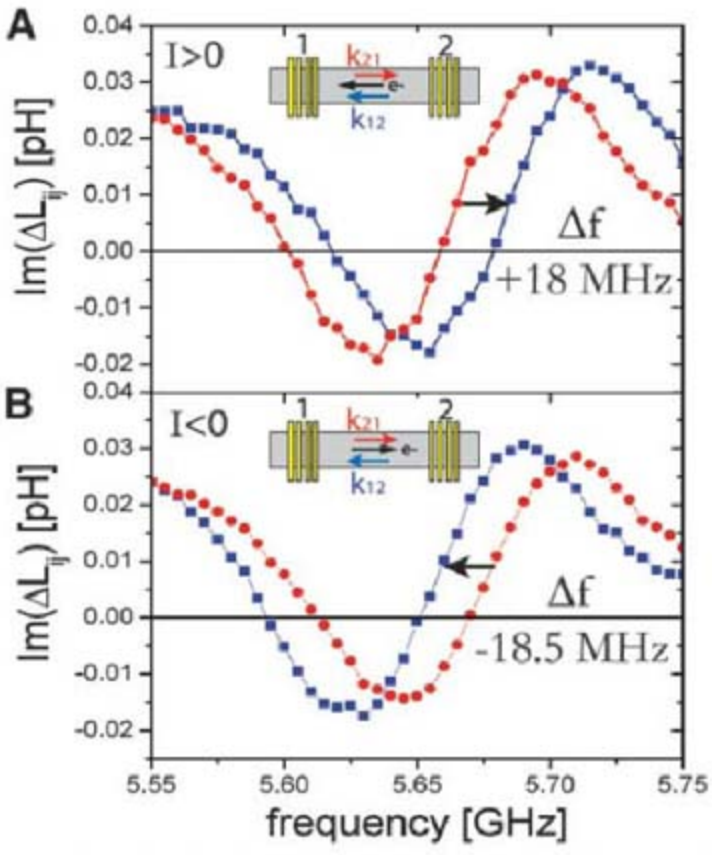

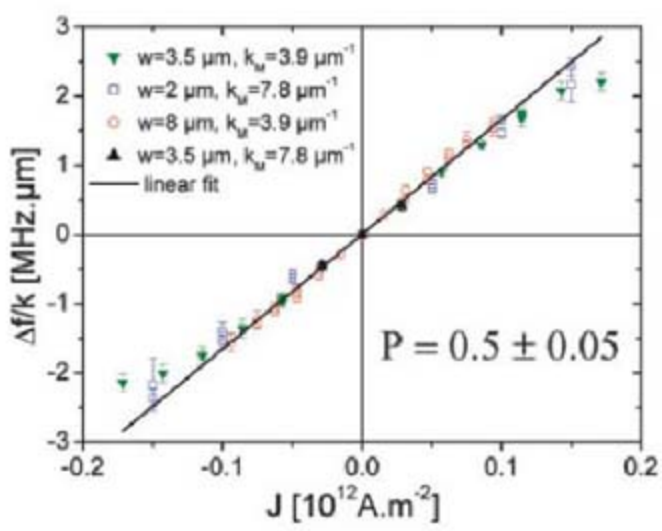

Fig. 3. Influence of a dc current on the spin wave propagation. (**A**) Mutual-inductance measurement in the presence of a $I = +6$ mA dc current for the $w = 2$ μm, $\lambda = 0.8$ μm sample under $\mu_0 H_0 = 1.029$ T. ΔL_{21} is shown as a red curve and corresponds to spin waves propagating from antenna 1 to antenna 2. ΔL_{12} is shown as a blue curve and corresponds to spin waves propagating from antenna 2 to antenna 1. The orientations of the spin wave wave vector and of the electron flow are shown in the inset. The measured frequency shift Δf is indicated on the graph. For clarity, only the imaginary part and only the frequency range corresponding to the main peak ($k \approx k_M$) are shown. (**B**) I_{dem} for $I = -6$ mA. (**C**) Experimental k-normalized frequency shifts versus current density. The data has been collected on four different devices and, in most cases, for two different magnetic fields (so that the main resonance falls in the ranges of 3 to 4 GHz and 4 to 7 GHz). The linear fit was performed in the range $|J| < 1.2\ 10^{11}$ A m^{-2}. P was determined with Eq. 1 and a product $M_s t$, which was deduced from the resonance data (*15*).

plitude stability of the PSWS experiment. Such studies could help to promote a fundamental understanding of spin-polarized transport in various itinerant ferromagnets, in that spin waves provide both a well-defined inhomogeneous magnetization configuration for performing spin transfer and an accurate probe with which to measure it.

References and Notes

1. J. C. Slonczewski, *J. Magn. Magn. Mater.* **159**, L1 (1996).
2. L. Berger, *Phys. Rev. B* **54**, 9353 (1996).
3. E. B. Myers, D. C. Ralph, J. A. Katine, R. N. Louie, R. A. Buhrman, *Science* **285**, 867 (1999).
4. M. D. Stiles, J. Miltat, in *Spin Dynamics in Confined Magnetic Structures* (Springer, New York, 2006), vol. 3, pp. 225–308.
5. M. Tsoi *et al.*, *Nature* **406**, 46 (2000).
6. W. H. Rippard, M. R. Pufall, in *Handbook of Magnetism and Advanced Magnetic Materials*, H. Kronmüller, S. Parkin, Eds (Wiley, New York, 2007), vol. 2, pp. 1167–1191.
7. A. Yamaguchi *et al.*, *Phys. Rev. Lett.* **92**, 077205 (2004).
8. L. Thomas, S. Parkin, in *Handbook of Magnetism and Advanced Magnetic Materials*, H. Kronmüller, S. Parkin, Eds (Wiley, New York, 2007), vol. 2, pp. 942–982.
9. Y. B. Bazaliy, B. A. Jones, S. C. Zhang, *Phys. Rev. B* **57**, R3213 (1998).
10. J. Fernández-Rossier, M. Braun, A. S. Nuñez, A. H. MacDonald, *Phys. Rev. B* **69**, 174412 (2004).
11. L. L. Hirst, *Phys. Rev.* **141**, 503 (1966).
12. S. Zhang, Z. Li, *Phys. Rev. Lett.* **93**, 127204 (2004).
13. A. Thiaville, Y. Nakatani, J. Miltat, Y. Suzuki, *Europhys. Lett.* **69**, 990 (2005).
14. J. Xiao, A. Zangwill, M. D. Stiles, *Phys. Rev. B* **73**, 054428 (2006).
15. Materials and Methods are available as supporting material on *Science* Online.
16. T. P. Gill, *The Doppler Effect, An Introduction to the Theory of the Effect* (Logos Press, London, 1965).
17. D. D. Stancil, B. E. Henty, A. G. Cepni, J. P. Van't Hof, *Phys. Rev. B* **74**, 060404 (2006).
18. P. Lederer, D. L. Mills, *Phys. Rev.* **148**, 542 (1966).
19. A. G. Gurevich, G. A. Melkov, *Magnetization Oscillations and Waves* (CRC Press, 1996).
20. D. D. Stancil, *Theory of Magnetostatic Waves* (Springer, New York, 1993).
21. M. Bailleul, D. Olligs, C. Fermon, *Appl. Phys. Lett.* **83**, 972 (2003).
22. H. Hurdequint, *J. Magn. Magn. Mater.* **242–245**, 521 (2002).
23. J. Bass, W. P. Pratt Jr., *J. Magn. Magn. Mater.* **200**, 274 (1999).
24. I. A. Campbell, A. Fert, in *Ferromagnetic Materials*, E. P. Wohlfarth, Ed. (North-Holland, Amsterdam, 1982), vol. 3, pp. 747–804.
25. P. E. Mijnarends, S. Sahrakorpi, M. Lindroos, A. Bansil, *Phys. Rev. B* **65**, 075106 (2002).
26. J. Banhart, H. Ebert, A. Vernes, *Phys. Rev. B* **56**, 10165 (1997).
27. A. F. Mayadas, J. F. Janak, A. Gangulee., *J. Appl. Phys.* **45**, 2780 (1974).
28. G. S. D. Beach, C. Knutson, C. Nistor, M. Tsoi, J. L. Erskine, *Phys. Rev. Lett.* **97**, 057203 (2006).

29. We thank J. Grollier and C. Deranlot (UMR CNRS/Thalès) for providing the permalloy films, H. Hurdequint for advice, A. Carvalho for assistance with e-beam lithography, A. Boulard for the fabrication of the measurement set-up, and K. Hajjia for measurements on unprocessed films. Support from the staff of the Consortium de Nanosciences et de Nanotechnologies de Strasbourg nanofabrication facilities and financial support from Agence Nationale de la Recherche "spectrospin" and from Region Alsace are gratefully acknowledged.

Supporting Online Material

www.sciencemag.org/cgi/content/full/322/5900/410/DC1
Materials and Methods
SOM Text
Figs. S1 and S2
References

7 July 2008; accepted 10 September 2008
10.1126/science.1162843

Complex Patterning by Vertical Interchange Atom Manipulation Using Atomic Force Microscopy

Yoshiaki Sugimoto,[1] Pablo Pou,[2] Oscar Custance,[3]* Pavel Jelinek,[4] Masayuki Abe,[1,5] Ruben Perez,[2] Seizo Morita[1]

The ability to incorporate individual atoms in a surface following predetermined arrangements may bring future atom-based technological enterprises closer to reality. Here, we report the assembling of complex atomic patterns at room temperature by the vertical interchange of atoms between the tip apex of an atomic force microscope and a semiconductor surface. At variance with previous methods, these manipulations were produced by exploring the repulsive part of the short-range chemical interaction between the closest tip-surface atoms. By using first-principles calculations, we clarified the basic mechanisms behind the vertical interchange of atoms, characterizing the key atomistic processes involved and estimating the magnitude of the energy barriers between the relevant atomic configurations that leads to these manipulations.

Scanning tunneling microscopy (STM) has proven to be the method of excellence for creating nanostructures on surfaces, manipulating atoms and molecules one at a time (*1*–*3*). A new panorama has recently been opened by the capability of atomic force microscopy (AFM) to create similar nanostructures atom by atom (*4*) and to quantify the forces involved in these lateral manipulations (*5*, *6*).

When exploring a surface with these scanning probe methods, the apex of the probe can be contaminated with atomic species present at the surface (*7*) by picking up atoms in accidental or intended mechanical contacts with the surface. Advantage could be taken of this situation, and an atomic version of the dip-pen nanolithography (*8*) may be implemented: Atoms wetting the tip apex could be individually deposited to write patterns at heterogeneous surfaces. We provide evidence that such an atomic pen can be implemented by using AFM.

We performed the AFM experiments (*9*) in dynamic mode under the frequency modulation detection scheme (*10*), keeping the cantilever oscillation amplitude constant. Commercial silicon cantilevers, which have very sharp tips at their free ends, were used to image the Sn/Si(111) – $(\sqrt{3} \times \sqrt{3})$R30° surface (*11*) by detecting the short-range chemical interaction force between the closest tip and surface atoms (*9*).

The inset of Fig. 1A shows topographic images of a single atomic layer of tin (Sn) atoms, which appear as bright protrusions, grown over a silicon (111) single-crystal substrate. Among the atomic defects this surface exhibits (*11*), the most representative ones are substitutional silicon (Si) atoms (*12*) at the perfect Sn atomic layer, and these appear as protrusions with diminished contrast. We have observed that these Si defects can be vertically manipulated during force spectroscopy (*13*, *14*) experiments. After imaging the surface and positioning the AFM tip with a lateral precision better than ±0.1 Å (*15*) over the topmost part of the marked Si atom, we moved the sample toward the oscillating AFM probe. At a given tip-surface distance, an instability in the frequency shift occurs, as highlighted by the arrow in the graph. In an image taken after the sample was retracted, the Si atom was no longer visible, and a Sn atom was found to occupy the corresponding lattice position instead (Fig. 1A, bottom right inset). One hypothesis to explain this event is that the Si atom at the surface has been replaced by a Sn atom originally located at the tip apex, as sketched out by the illustration in Fig. 1A. The same procedure can be consecutively applied to the freshly deposited Sn atom (marked with a circle in Fig. 1B, left inset), resulting in the replacement of this surface atom by a Si atom coming from the tip and in a partial loss of atomic contrast (Fig. 1B, bottom right inset). Because all the images shown in Fig. 1 were acquired under the same experimental parameters,

[1]Graduate School of Engineering, Osaka University, 2-1 Yamada-Oka, 565-0871 Suita, Osaka, Japan. [2]Departamento de Física Teórica de la Materia Condensada, Universidad Autónoma de Madrid, 28049 Madrid, Spain. [3]National Institute for Materials Science, 1-2-1 Sengen, 305-0047 Tsukuba, Ibaraki, Japan. [4]Institute of Physics, Academy of Sciences of the Czech Republic, Cukrovarnicka 10, 1862 53 Prague, Czech Republic. [5]Precursory Research for Embryonic Science and Technology, Japan Science and Technology Agency (JST), 332-0012 Saitama, Japan.

*To whom correspondence should be addressed. E-mail: custance.oscar@nims.go.jp

this contrast change should correspond to a modification of the tip apex (fig. S4) (*9*). This tip modification is, however, not irreversible. By scanning aside a region that neighbors the imaged area at vertical distances slightly closer to the surface than that used for imaging, we recovered good atomic contrast again for most of the test performed (fig. S1) and were able to repeat these manipulation processes multiple times (fig. S2). Dissipation signals (*16*) of up to 1.2 eV per cycle accompanied these atomic interchanges between the tip and surface (fig. S1). Although the vertical manipulations described here were performed at room temperature, they have also been accomplished at low temperature (80 K).

This vertical interchange of strongly bound atoms between the tip and the surface differs from methods previously reported using STM, in which an atom weakly bonded on a metallic surface can be reversibly transferred between the tip and the surface by applying an appropriate bias voltage (*17*). It also diverges from other methods of controlled atom manipulations recently achieved with AFM (*4*–*6*) that make use of the attractive part of the tip-surface interaction to laterally manipulate atoms without any active participation of the tip, which is only used to tune the interaction of the manipulated atom with the surface. In contrast, the mechanism of the manipulations reported here is based on a process in which the vertical interchange of atoms is controlled by the mechanical properties of a hybrid tip-surface structure formed in the repulsive regime of the tip-surface interaction force.

Although imaging and manipulation in the attractive regime involve mainly the bonding interaction between the closest tip-surface atoms, in the repulsive regime a larger contact involving several atoms is expected, leading to a very complex energy landscape. The structure of the contact at the closest approach determines the most likely outcome among the different competing processes: atom interchange, atom transfer to the tip, or deposition of tip atoms when the tip is pulled out from the surface. However, the reproducibility of the vertical atomic interchange and the resemblance of recorded frequency shift and force curves in experiments performed with different tips (figs. S1 and S2) point toward a common basic microscopic mechanism.

To characterize the atomistic processes, we performed simulations of the tip-surface approach and retraction events. These simulations (*9*) are based on density functional theory first-principles calculations implemented with a local orbital basis using the FIREBALL code (*18*). To model the experimental tip apex, we considered a rigid tip (Fig. 2B) on which only the two atoms in the dimer defining the apex were allowed to relax upon interaction with the surface. We imposed this constraint on the tip model in order to simplify the complex configuration space associated with the tip mechanical response.

Figure 2A illustrates, using the total energy, the evolution of the system during an alternate deposition of a Sn atom (solid lines) and Si atom (dashed lines); the most relevant atomic configurations during both processes are depicted in Fig. 2B. For the Sn deposition, the system follows branch A (squares), starting at A_1, where there is no substantial interaction, and enters the attractive regime as the tip approaches the surface. At A_2, the system is near the total energy minima, and further tip-surface approach leads to a repulsive force that increases up to structure A_3, in which the atoms are considerably compressed but still keep their original bonding topology. Upon retraction from any tip-surface distance larger than the one corresponding to A_3, the system follows the same energy curve back to the original structure A_1. Approaching the tip beyond A_3, the system undergoes a discontinuous jump to a new energy branch B (triangles) with a substantially different bonding topology (Fig. 2B, image B_1). During further approach and consecutive retraction, the system follows this energy branch up to B_2, where a jump takes it to another energy solution [branch C (circles)], leading to the bonding topology (structure C_2) and the atomic interchange. The Si deposition case presents the same basic features. During approach, the system follows the C branch until reaching C_3, where it jumps to branch D (pentagons). Retraction from any distance along the D branch after this jump leads to a new jump from D_2 to A_2 and to the atom interchange. Comparing the two deposition cases, although the atomistic details are slightly different, overall the atom interchange mechanism seems to be the same. The key step in these processes is to reach the dimer-like structure shown in B_1 and D_1. In these atomic configurations, the outermost atom of the tip and the atom at the surface now have an equal number of bonds with the surrounding atoms, losing their association as being part of the tip or the surface. Our simulations confirm that the dimer structure that minimizes the stored elastic energy under compression is the lowest energy configuration for other tip-surface orientations and even for different tip structures.

The energy landscape of these atomic interactions sheds light on some of the features observed in the associated experimental curves. The frequency shift signals (Fig. 1) display a shoulder at closer tip-surface distances that develops into a double well structure in the corresponding short-range chemical interaction forces (figs. S1 and S2), in contrast to canonical force spectroscopy curves that for this system can be found in figures 3 and 5 of (*12*). The presence of several possible pathways in either a Sn or a Si deposition manifests in different solutions of the tip-surface interaction force. However, because the frequency shift is proportional to a weighted average of the tip-surface interaction force over one oscillation cycle (*19*, *20*), the existence of these pathways is blurred (*16*) in the frequency shift and thus in the short-range chemical interaction force derived from it. Both the frequency shift and the obtained interaction force should not a priori bear information about nonconservative tip-surface interactions (*19*, *21*, *22*) that lead to a dissipation of energy from the

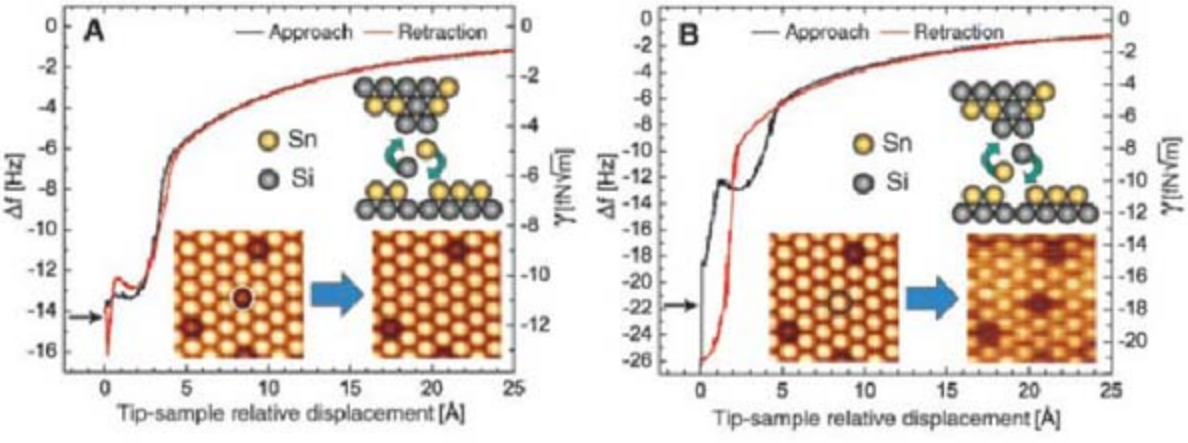

Fig. 1. Alternate vertical interchange atom manipulations. (**A**) Frequency shift (Δf) signal upon approach (black) and retraction (red) of the tip over the Si atom marked with a white circle in the left inset image. In a consecutive topographic image to the curve acquisition (bottom right inset), a Sn atom appears at the same surface location instead. The Si atom was replaced by a Sn atom coming from the tip (Sn deposition). (**B**) Frequency shift signal upon approach (black) and retraction (red) of the tip above the Sn atom deposited in (A), pointed out by a black circle (left inset). After the curve acquisition, the replacement of this Sn atom by a Si atom coming from the tip (Si deposition) and a partial loss of atomic contrast are obtained (bottom right inset). For comparison with other curves, the normalized frequency shift (γ) (*19*) is displayed in the vertical axis on the right. The black arrows in the plots indicate instabilities representative of the corresponding concerted vertical interchange of atoms between the tip and surface. The origin of the horizontal axes denotes the point of maximum proximity between the tip and sample; this criterion was adopted for all the experimental curves shown in this work. The illustrations are representations of the corresponding vertical atomic interchange, with yellow and gray spheres symbolizing Sn and Si atoms, respectively; they do not bear any realistic information about the tip-apex structure or composition. For the acquisition parameters and analysis of the short-range forces associated with these manipulations, see fig. S1.

cantilever oscillation (*16*, *23*, *24*). The energy barriers between branches as a function of the tip-surface distance dictate where the system jumps during either approach or retraction and thus determine the details of both frequency shift and force curves (fig. S3) (*9*). The shoulder in the frequency shift curves, the double-well structure in the short-range chemical forces, and the energy dissipation indicate that the system is evolving between two different bonding configurations during an approach-and-retraction cycle. These configurations must be stable enough to be reproduced over multiple approach-and-retraction cycles of the oscillating tip at the closest tip-surface distances.

These vertical interchange atomic manipulations require a tip rigid enough to endure high loads over the repulsive part of the short-range chemical interaction without undergoing major structural modifications, which is the norm under these conditions. We have found tips that can alternatively deposit Sn and Si atoms (Fig. 1 and fig. S2), others that can just deposit Sn atoms (fig. S5) (*9*), and some tips that only deposit Si atoms. We have not been able to develop a systematic way of producing such tips yet, and success in identifying them relies on making a number of gentle tip-surface contacts using the same cantilever over different measurement sessions. From our extensive force spectroscopy experiments on this surface (*14*), we have found that 29% of the tips produced vertical interchange atom manipulation, being almost equally probable to find tips producing either Si deposition or alternate deposition of Sn and Si atoms and less probable to have a tip depositing only Sn atoms. Once an atom exchanging tip is found, it is possible to perform the manipulations in a reproducible way. Figure 3 illustrates an example of the creation of complex atomic patterns by successively depositing individual Si atoms coming from the tip in processes similar to the one shown in Fig. 1B. The tip used to create these atomic patterns was only able to deposit Si atoms (Figs. 3B to 3M). Thus, to put aside the Si defect beside the "i" character in Fig. 3M, several in-plane lateral interchange manipulation steps performed as described in (*4*) (fig. S7) were successively applied. In contrast to previous atomic assemblies based on lateral atom manipulation with AFM (*4*), this vertical manipulation method reduces by almost a factor of 10 the time needed to create similar atomic patterns: it took us only 1.5 hours of mostly imaging time to build the structures shown in Fig. 3.

The creation of these atomic patterns must involve not only the repeated interchange of atoms between the tip and surface but also diffusion and segregation processes at the tip apex to guarantee the presence of the required chemical species in the appropriate atomic arrangement. The simulation of the whole process is far beyond the capabilities of current first-principles methods, yet insights into the influence of the tip mechanical response can be gained just by approaching our initial tip model with a more realistic situation. To this end, we have allowed the four outermost atoms of the tip apex to relax. This option considerably enlarges the configuration space with processes including tip modifications and extraction of atoms from the surface (fig. S6) (*9*) that lead the system to a final state of energy higher than that for the vertical atomic interchange. Although at room temperature thermodynamics would favor the lowest energy final configurations, the feasibility of the process is controlled by the energy barriers among the different local minima. Figure 4A depicts the energy for an approach (squares) and retraction (triangles) cycle over a Si atom resulting in a tip change, in which the Sn atom at the apex is deposited over the surface atoms. Upon retraction, the system crosses an energy branch (circles) that corresponds to a tip retraction in which the surface Si atom is located at the dimer structure forming the tip apex and the tip Sn atom is now at the surface in a vertical atomic interchange similar to the one shown in Fig. 1A. Using the nudge elastic band method (*25*), we studied the transition between two atomic configurations very close in energy (points α and β) belonging to these two different energy solutions: The starting atomic arrangement (α) is a dimer-like configuration in which both atoms have lost their association as being part of the tip or the surface; the final state (β) is the deposition of the Sn atom. We found that

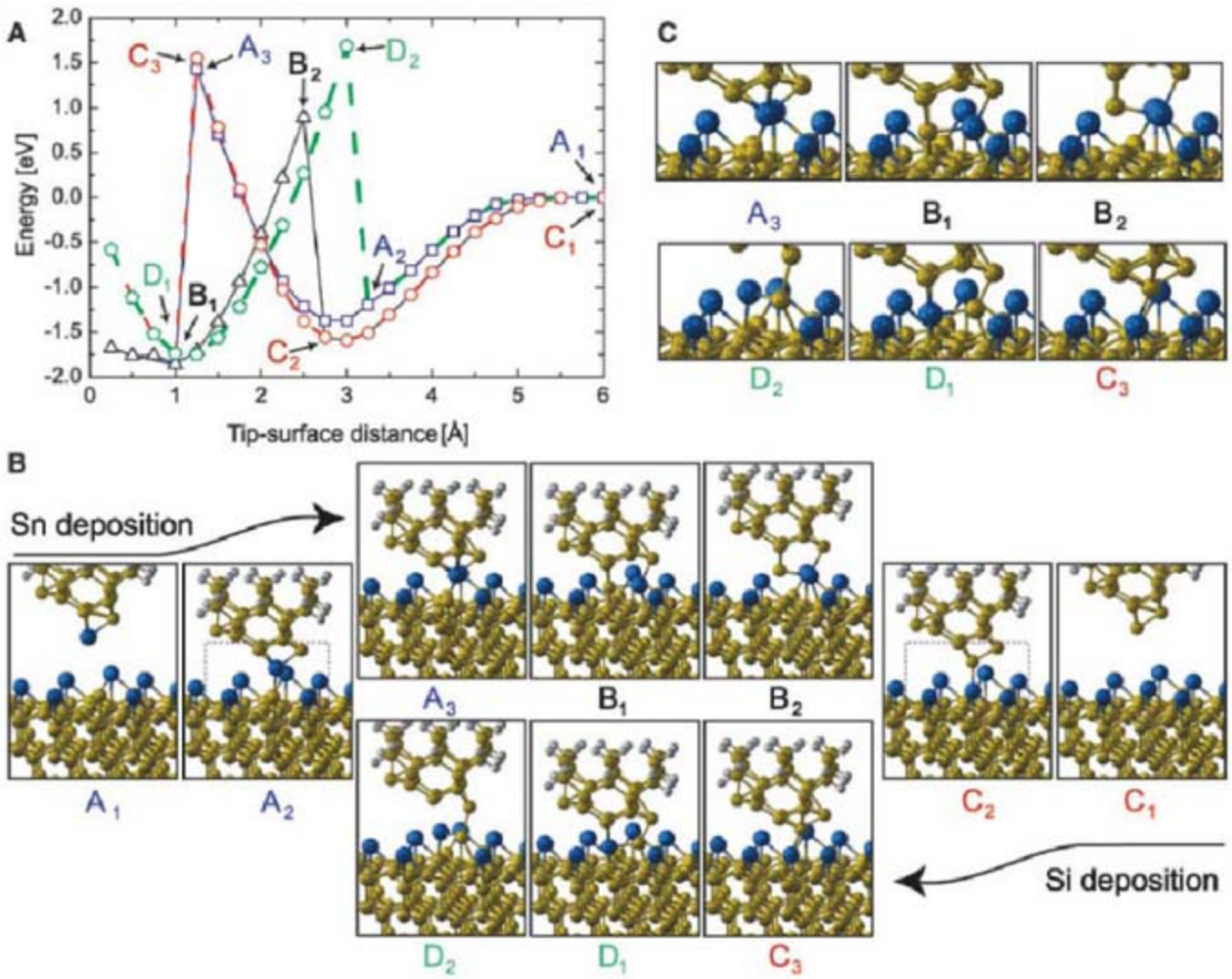

Fig. 2. First-principles simulations of vertical interchange atom manipulation proceses. (**A**) Evolution of the total energy upon two consecutive approach-and-retraction cycles using a model rigid tip (only the two atoms in the dimer defining the apex are allowed to relax) over the same location of a Sn/Si(111) – $(\sqrt{3} \times \sqrt{3})$R30° surface, which results in the alternate deposition of a Sn atom [first cycle (continuous lines)] and a Si atom [second cycle (dashed lines)], respectively. Upon increasing the load of the tip apex over the surface and consecutive retraction, atoms at both the tip and surface undergo a series of structural relaxations that manifest in jumps between different solutions that correspond to local energy minima. (**B** and **C**) Atomic configurations associated with the transitions between energy branches labeled in (A) showing the most relevant atomistic details involved in the concerted vertical interchange of atoms between the tip and surface. A detail of the bonding configuration evolution within the dashed line rectangles displayed in A_2 and C_2 of (B) is shown in (C).

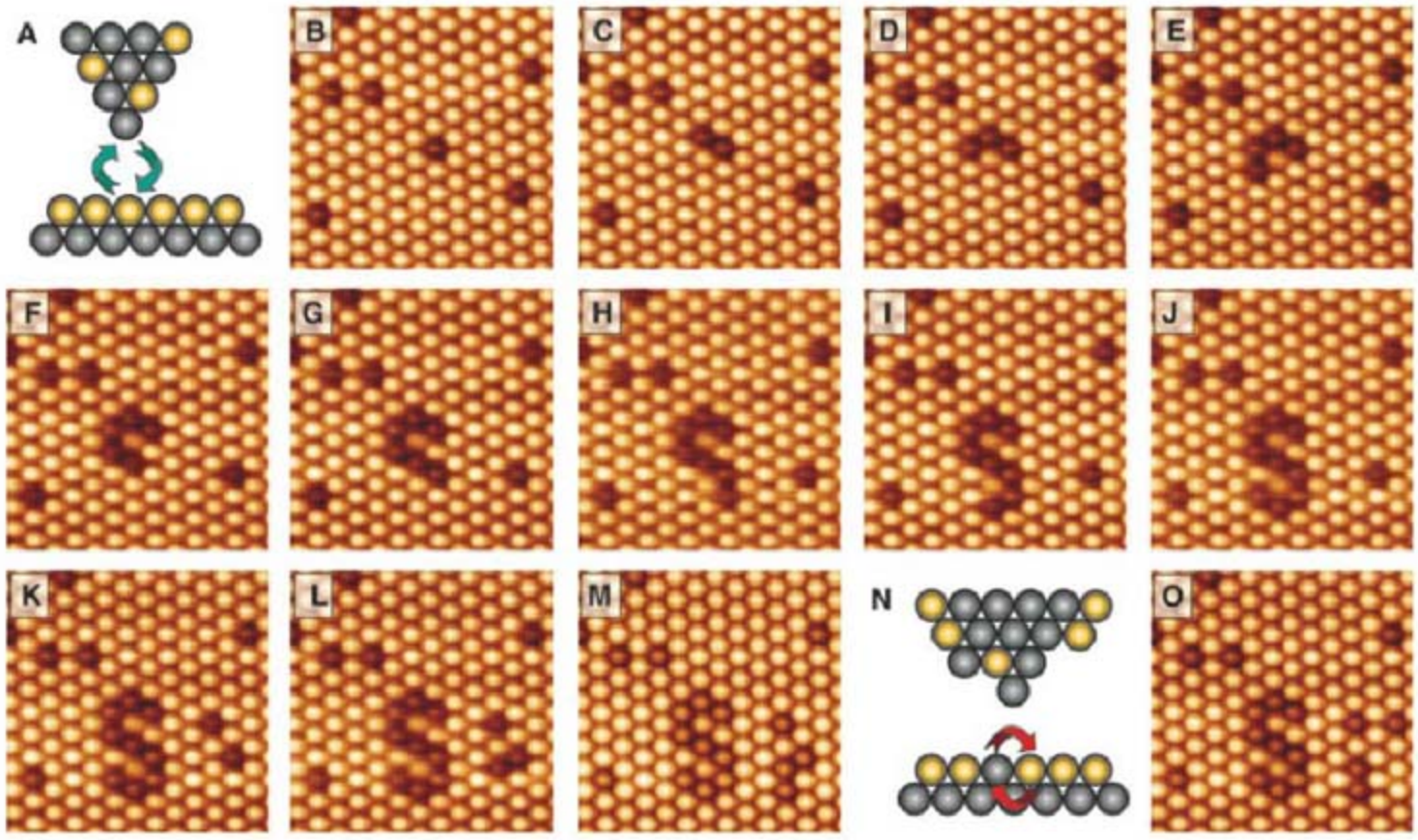

Fig. 3. Complex atomic patterning by vertical interchange atom manipulation at room temperature. (**A**) Illustration denoting the concerted vertical interchange of atoms between the tip and surface. (**B** to **M**) Series of topographic images showing the creation of atomic patterns displaying the symbol of silicon. These patterns were constructed by the successive substitution of Sn atoms at the surface one atom at a time with Si atoms coming from the tip. (**N**) Illustration denoting the concerted lateral interchange of surface atoms. (**O**) The Si atom adjacent to the "i" character in (M) was relocated to a nearby position in several in-plane lateral interchange atom-manipulation (*4*) events similar to the one depicted in fig. S7 (*9*). Acquisition parameters were a cantilever first mechanical resonant frequency of 193744.2 Hz, cantilever oscillation amplitude of 226 Å, and cantilever static stiffness of 48.8 N/m, with imaging Δf set point values between –5.5 Hz and –6.6 Hz.

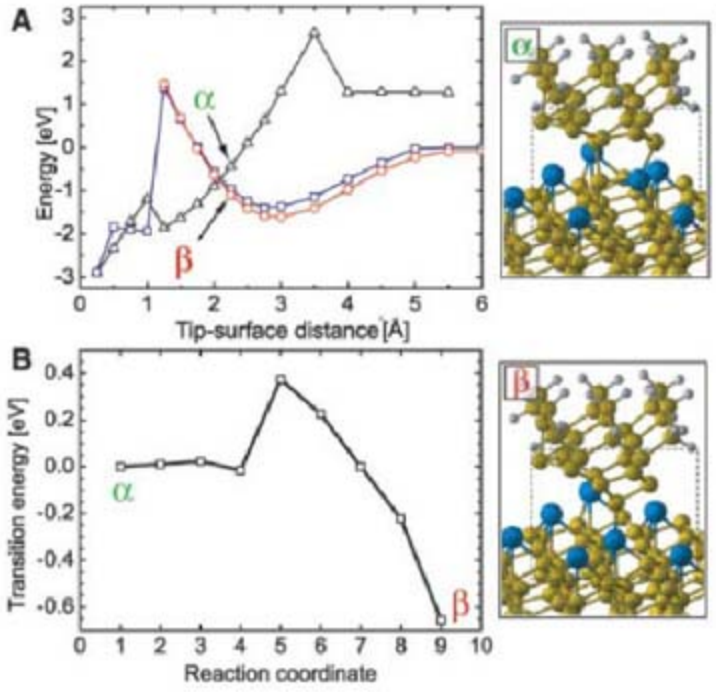

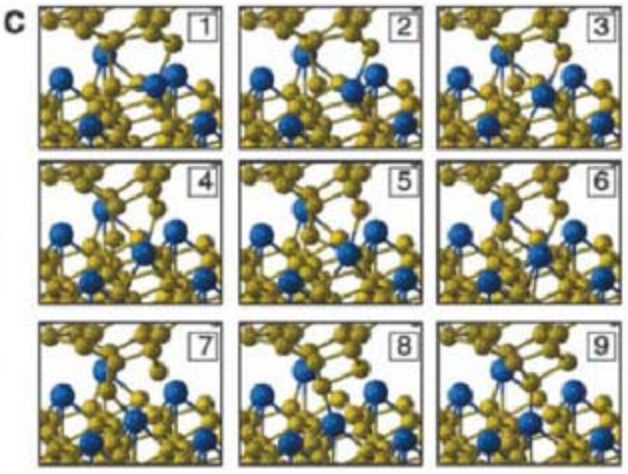

Fig. 4. Typical energy barriers involved in the concerted vertical interchange of atoms between the tip and surface. (**A**) Total energy solutions (squares and triangles) for a tip-surface approach-and-retraction cycle over a Si atom producing a tip modification in which the Sn atom at the apex is lost and left on the surface. The energy solution upon retraction (triangles) crosses an energy branch (circles) that would result in the concerted vertical interchange of these atoms. (**B**) Transition energy between two atomic configurations close in total energy labeled as α and β in (A). Energy barriers of a magnitude similar to the one shown in (B) can be easily overcome by atomic thermal fluctuations at room temperature. The atomic configurations corresponding to the points marked in (A) and (B) are displayed on the right. (**C**) Details of the bonding configurations, reaction coordinate (*9*) in (B), through the minimum energy path for the transition from state α to state β. The area displayed matches the dashed-line rectangles shown on the images on the right.

there is an energy barrier of 0.4 eV for the transition between these two configurations (Fig. 4B), which corresponds to the breaking of the remaining bond of the Si atom with the surface and the formation of a second bond of the Sn atom with the surface (Fig. 4C, images 4 to 6). This relatively small energy barrier does not prevent the process from taking place at room temperature, accounting as well for the presence of a considerable dissipation signal (fig. S1) at the closest tip-surface distances (*16*, *23*, *24*). Therefore, in the experiments it is not necessary to reach the high loads predicted in Fig. 2 for the atomic interchange taking place; just by exploring tip-surface distances close to the location of the repulsive zero short-range force (near the crossing point of the different energy branches available for the system), we are very likely to obtain a thermally activated vertical interchange atom manipulation.

The results reported here provide evidence that AFM can be used for the controlled deposition of individual atoms in semiconductor surfaces with the possibility of patterning complex atomic structures. Although our results focus on the Sn/Si system, we have found these vertical interchange atomic manipulations in other semiconductor surfaces (fig. S8). This manipulation technique may pave the way toward selective semiconductor doping (*26*), practical implementation of quantum computing (*27*), or atomic-based spintronics (*28*). The possibility of combining sophisticated vertical and lateral atom manipulations (*4*, *6*) with the capability of AFM for single-atom chemical identification (*14*) may bring closer the advent of future atomic-level applications, even at room temperature.

References and Notes

1. D. M. Eigler, E. K. Schweizer, *Nature* **344**, 524 (1990).
2. M. F. Crommie, C. P. Lutz, D. M. Eigler, *Science* **262**, 218 (1993).

3. A. J. Heinrich, C. P. Lutz, J. A. Gupta, D. M. Eigler, *Science* **298**, 1381 (2002).
4. Y. Sugimoto *et al.*, *Nat. Mater.* **4**, 156 (2005).
5. Y. Sugimoto *et al.*, *Phys. Rev. Lett.* **98**, 106104 (2007).
6. M. Ternes, C. Lutz, C. Hirjibehedin, F. Giessibl, A. Heinrich, *Science* **319**, 1066 (2008).
7. O. Paz, I. Brihuega, J. M. Gómez-Rodríguez, J. M. Soler, *Phys. Rev. Lett.* **94**, 056103 (2005).
8. R. D. Piner, J. Zhu, F. Xu, S. Hong, C. A. Mirkin, *Science* **283**, 661 (1999).
9. Materials and methods are available as supporting online material on *Science* Online. In AFM experiments we used the easyPLL Plus (Nanosurf, Liestal, Switzerland) for the detection and regulation of the cantilever dynamics, and data acquisition and representation was performed using a Dulcinea SPM controller (Nanotec Electrónica, Madrid, Spain) (*29*).
10. T. R. Albrecht, P. Grütter, D. Horne, D. Rugar, *J. Appl. Phys.* **69**, 668 (1991).
11. S. T. Jemander, N. Lin, H. M. Zhang, R. I. G. Uhrberg, G. V. Hansson, *Surf. Sci.* **475**, 181 (2001).
12. Y. Sugimoto *et al.*, *Phys. Rev. B* **73**, 205329 (2006).
13. M. A. Lantz *et al.*, *Science* **291**, 2580 (2001).
14. Y. Sugimoto *et al.*, *Nature* **446**, 64 (2007).
15. M. Abe, Y. Sugimoto, O. Custance, S. Morita, *Appl. Phys. Lett.* **87**, 173503 (2005).
16. N. Oyabu *et al.*, *Phys. Rev. Lett.* **96**, 106101 (2006).
17. D. M. Eigler, C. P. Lutz, W. E. Rudger, *Nature* **352**, 600 (1991).
18. P. Jelinek, H. Wang, J. P. Lewis, O. F. Sankey, J. Ortega, *Phys. Rev. B* **71**, 235101 (2005).
19. F. J. Giessibl, *Phys. Rev. B* **56**, 16010 (1997).
20. J. E. Sader, S. P. Jarvis, *Appl. Phys. Lett.* **84**, 1801 (2004).
21. H. Hölscher *et al.*, *Phys. Rev. B* **64**, 075402 (2001).
22. U. Dürig, *Appl. Phys. Lett.* **75**, 433 (1999).
23. N. Sasaki, M. Tsukada, *Jpn. J. Appl. Phys.* **39**, L1334 (2000).
24. L. N. Kantorovich, T. Trevethan, *Phys. Rev. Lett.* **93**, 236102 (2004).
25. G. Mills, H. Jónsson, *Phys. Rev. Lett.* **72**, 1124 (1994).
26. T. Shinada, S. Okamoto, T. Kobayashi, I. Ohdomari, *Nature* **437**, 1128 (2005).
27. B. E. Kane, *Nature* **393**, 133 (1998).
28. D. Kitchen, A. Richardella, J.-M. Tang, M. E. Flatté, A. Yazdani, *Nature* **442**, 436 (2006).
29. I. Horcas *et al.*, *Rev. Sci. Instrum.* **78**, 013705 (2007).

30. S.Y., O.C., M.A., and S.M. acknowledge support from grants in aid for scientific research from the Ministry of Education, Culture, Sports, Science and Technology (MEXT), JST, Handai Frontier Research Center, the Project Atomic Technology funded by MEXT, and Global Center of Excellence program "Center for Electronic Devices Innovation." O.C. also acknowledges support from the Air Force Office of Scientific Research–Asian Office of Aerospace Research and Development. The work of Y.S. is supported by the Frontier Research Base for Global Young Researchers funded by MEXT. P.P. and R.P. acknowledge the support of Ministerio de Educación y Ciencia (Spain) and computer time provided by Red Española de Supercomputación at the Barcelona Supercomputing Center. P.J. acknowledges the support of Grantová Agentura Akademie Věd (Czech Republic)

Supporting Online Material

www.sciencemag.org/cgi/content/full/322/5900/413/DC1
Materials and Methods
Figs. S1 to S8
References

16 May 2008; accepted 9 September 2008
10.1126/science.1160601

Catalytic Conversion of Biomass to Monofunctional Hydrocarbons and Targeted Liquid-Fuel Classes

Edward L. Kunkes, Dante A. Simonetti, Ryan M. West, Juan Carlos Serrano-Ruiz, Christian A. Gärtner, James A. Dumesic*

It is imperative to develop more efficient processes for conversion of biomass to liquid fuels, such that the cost of these fuels would be competitive with the cost of fuels derived from petroleum. We report a catalytic approach for the conversion of carbohydrates to specific classes of hydrocarbons for use as liquid transportation fuels, based on the integration of several flow reactors operated in a cascade mode, where the effluent from the one reactor is simply fed to the next reactor. This approach can be tuned for production of branched hydrocarbons and aromatic compounds in gasoline, or longer-chain, less highly branched hydrocarbons in diesel and jet fuels. The liquid organic effluent from the first flow reactor contains monofunctional compounds, such as alcohols, ketones, carboxylic acids, and heterocycles, that can also be used to provide reactive intermediates for fine chemicals and polymers markets.

Diminishing petroleum reserves and growing concerns about global climate change necessitate the development of fuel production pathways based on renewable resources, such as biomass-derived carbohydrates. The conversion of biomass-derived carbohydrates to liquid transportation fuels requires removal of most, or all, of the oxygen atoms in the reactants to form molecules having desirable properties for combustion. To produce nonoxygenated liquid fuels, this removal of oxygen must be accompanied by isomerization to form branched hydrocarbons for gasoline, and/or by C-C coupling reactions to increase the molecular weight for diesel and jet fuels. We have previously outlined a strategy involving dehydration of sugars (e.g., fructose) over acid catalysts to form furan derivatives (e.g., hydroxymethylfurfural, HMF) that can subsequently undergo aldol condensation with ketones (e.g., acetone), followed by hydrodeoxygenation to form C_9 to C_{15} alkanes for use in diesel and jet fuels (*1*, *2*). Here, we outline a strategy that begins the oxygen-removal process by converting sugars and polyols over a Pt-Re catalyst to form primarily hydrophobic alcohols, ketones, carboxylic acids, and heterocyclic compounds (Fig. 1). This process can be used to produce ketones for C-C coupling with HMF, thereby replacing the acetone in our previous process with ketones derived directly from biomass. This alternative process does not require the separate formation of HMF, because we demonstrate that the ketones produced can undergo self-coupling reactions. In addition, this process provides a route to highly branched alkanes and olefins, as well as alkylated aromatics, these compounds being high-octane components of gasoline (*3*, *4*). Moreover, intermediate compounds formed during the conversion of biomass-derived carbohydrates to liquid transportation fuels can serve as valuable compounds for the chemical and polymer industries.

The conversion of carbohydrates over metal catalysts proceeds via reaction pathways involving C-C and C-O bond scission (*5*, *6*). High rates of C-C cleavage lead to the formation of CO, CO_2, and H_2 (denoted as "reforming"), whereas high rates of C-O cleavage produce alkanes (*5*, *6*). Our approach here is to achieve controlled rates of C-C and C-O cleavage, leading to the formation of monofunctional hydrocarbons. This behavior is analogous to achieving selective hydrogenation of acetylene to ethylene, without undergoing further reaction to form ethane over metal catalysts (*7*), where strongly adsorbed reactants preferentially occupy surface sites compared to more weakly adsorbed reaction intermediates, thus allowing the production of these reaction intermediates with high yield.

In the initial step of our process, a fraction of the polyol or sugar feed is reformed over Pt-Re/C to supply the hydrogen required to partially deoxygenate the remainder of the feed to monofunctional hydrocarbons. Endothermic reforming reactions are balanced with exothermic deoxygenation reactions in the same reactor, such that the overall conversion is mildly exothermic and more than 90% of the energy content of the polyol or sugar feed is retained in the reaction products. As outlined schematically in Fig. 1 for a polyol feed, we propose that reforming reactions involve adsorption and dehydrogenation of the polyol, followed by C-C cleavage, leading to CO adsorbed on the catalyst surface, which reacts with water to produce H_2 and CO_2 by the water–gas shift reaction. (This production of CO_2 is required for the overall conversion of polyols to monofunctional hydrocarbons, because a fraction of the polyol feed must be converted to H_2 and CO_2 to generate the hydrogen required for deoxygenation reactions.) Adsorbed polyol species

Department of Chemical and Biological Engineering, University of Wisconsin–Madison, Madison, WI 53706, USA.

*To whom correspondence should be addressed. E-mail: dumesic@engr.wisc.edu

can also undergo C-O bond cleavage to form surface intermediates with lower susceptibility toward reforming reactions and with lower binding energies on the surface, facilitating desorption and resulting in the formation of alcohols and ketones, carboxylic acids (following OH migration analogous to the benzilic acid rearrangement), and heterocyclic compounds (following intramolecular dehydration). These monofunctional hydrocarbons can undergo further conversion to alkanes.

Results from density functional theory calculations suggest that cleavage of C-C bonds on Pt for an oxygenated hydrocarbon takes place through transition states that have lower energy and that are more dehydrogenated compared to transition states for cleavage of C-O bonds (*8*), suggesting that C-O cleavage should be favored versus C-C cleavage by operating at reaction conditions in which the surface is highly covered by strongly adsorbed species, such as adsorbed CO and highly oxygenated reaction intermediates (*8*). Furthermore, Re has been shown to promote the rate of C-O hydrogenolysis reactions for oxygenated hydrocarbons (*9*). Because the binding energies of oxygen atoms and hydroxyl groups are stronger on Re than on Pt (*10*), the effects of Re in Pt-Re/C catalysts may be mediated by the presence of oxygen and/or hydroxyl groups associated with Re atoms on the surface of Pt-Re alloy particles.

The primary biomass-derived reactants addressed in this work are glucose and sorbitol, the latter of which can be formed in nearly 100% yield by hydrogenation of glucose (*11*). Glucose can be derived from the acid hydrolysis of cellulose (*12*), the most abundant carbohydrate found in nature, or obtained more directly from edible crops such as sugar cane (with cellulose being the most desirable long-term source of sugar). We show here that sorbitol and glucose can be converted over a carbon-supported Pt-Re catalyst at temperatures near 500 K to a hydrophobic organic liquid containing alcohols, ketones, carboxylic acids, and alkanes containing four, five, or six carbon atoms, as well as heterocyclic tetrahydrofuran and tetrahydropyran compounds (Fig. 1). Biomass can also be converted to fuels and chemicals by pyrolysis at high temperatures (>770 K) to form a liquid product commonly referred to as "bio-oil," followed by upgrading to naphtha-like products or conversion to synthesis gas or H_2 (*13*, *14*). Whereas bio-oil from pyrolysis is a complex mixture of more than 300 highly oxygenated compounds and can contain up to 50 weight percent (wt %) water (*13*, *14*), the liquid product from catalytic conversion of sorbitol or glucose over Pt-Re/C contains a well-defined mixture of hydrophobic species. Moreover, we have demonstrated additional catalytic processes to convert the carbohydrate-derived organic liquid stream to liquid alkanes, olefins, and/or aromatics with molecular weights and structures appropriate for use as transportation fuels. An advantage of this approach is the removal in the first catalytic step of more than 80% of the oxygen contained in the carbohydrate, allowing subsequent upgrading processes to operate at reduced capacity and with increased efficiency (*15*).

Figure 2 and Table 1 show the effects of temperature, pressure, and space velocity on the selectivities and carbon distributions, respectively, for conversion of a 60 wt % sorbitol in water solution over a 10 wt % Pt-Re (1:1)/C catalyst. Increasing the pressure from 18 to 27 bar at 483 K results in a shift of the effluent carbon from aqueous-phase species to organic-phase species (Table 1). Increasing the pressure at 503 K results in a shift from aqueous-phase species to gaseous species, whereas pressure has a negligible effect at 523 K on the carbon distribution (Table 1). The production of alkanes increases at the expense of oxygenated species as pressure increases at constant temperature, and raising the temperature at constant pressure leads to an increase in the production of alkanes and a decrease in high molecular weight oxygenates (Fig. 2A). An increase in the space velocity from 0.60 to 1.2 hours^{-1} at constant temperature and pressure causes an increase in production of organic-phase species at the expense of gaseous products (Fig. 2B and Table 1), and more specifically, an increase in the yield of ketones, alcohols, and acids, with a concurrent reduction in alkane yield. A further increase of space velocity to 2.4 hours^{-1} shifts the carbon distribution toward aqueous-phase oxygenates. All reaction conditions were tested for at least 24 hours time-on-stream, and the carbon balances closed to within 10%. At 503 K and 18

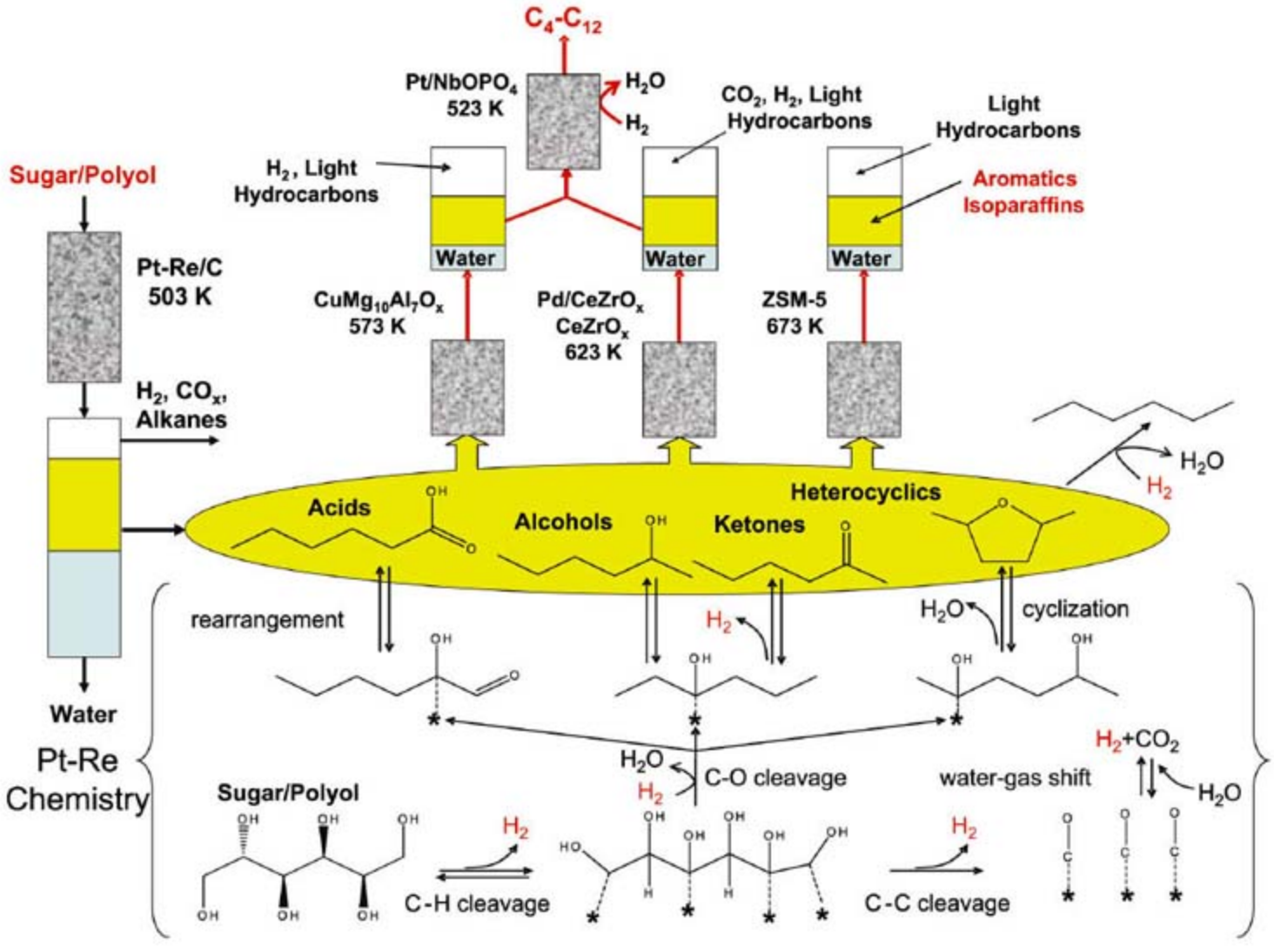

Fig. 1. Schematic representation of reactor sequence used to generate monofunctional organic compounds from catalytic processing of sorbitol or glucose, providing a platform for the production of liquid transportation fuels. The proposed chemistries involved in the conversion of sugars and polyols over Pt-Re catalysts are shown schematically in the lower portion of this figure. The asterisks represent catalytic sites.

bar, Pt-Re/C showed excellent stability for longer than 1 month time-on-stream. This organic liquid product stream, designated as Sorb_503_18, was used for subsequent catalytic processing.

If the rates of reforming and deoxygenation reactions are balanced such that all of the H_2 produced by reforming is utilized by deoxygenated reactions, then the maximum carbon conversion to Sorb_503_18 would be equal to 75%, with the remainder of the carbon being converted to CO_2 (*16*). The actual conversion of the carbon in sorbitol to Sorb_503_18 is 52%, corresponding to a yield of 70% of the maximum value. Deviations from the maximum yield result from the production of CO_2 associated with excess hydrogen, and the formation of gas-phase alkanes. The aforementioned yield corresponds to the production of 1 kg of Sorb_503_18 for every 3.5 kg of sorbitol. If Sorb_503_18 is converted into alkane-based fuels, then these fuels would retain 65% of the energy content of the sorbitol feed (*16*).

We have explored catalytic processes to produce transportation fuel components from the organic liquid effluent produced by conversion of sorbitol over Pt-Re/C (*16*). (The chemistries involved in these catalytic upgrading steps are outlined in the supporting online material.) For example, with respect to gasoline components, we have shown that the organic liquid produced from sorbitol can be converted to aromatic compounds by first hydrogenating the ketones to alcohols (at 433 K and 55 bar H_2 pressure over 5 wt % Ru/C), and then heating to 673 K at atmospheric pressure over H-ZSM-5 (*17*). Of the carbon in the sorbitol-derived organic phase, 25% and 29% is converted to paraffins and olefins containing three and four carbon atoms, respectively, whereas 38% of the carbon is converted to aromatic species (Fig. 3A). Of this aromatic fraction, 12% (5% of total) is converted to benzene, 37% (14% of the total) is converted to toluene, and 30% (11% of the total) is converted to a C_2 benzene (a benzene with two additional carbon atom substituents such as xylenes or ethyl benzene). The remaining 22% of the aromatic fraction (8% of the total) is split between C_3 to C_6 substituted benzene. Overall, 40% of the carbon in the Sorb_503_18 feed is converted into C_{6+} fuel-grade components. In addition, we have shown that gasoline components can be produced by dehydration of secondary pentanols and hexanols (such as the ones present in hydrogenated Sorb_503_18) over an acidic niobia catalyst to form branched C_4 to C_6 olefins, and also by oligomerization of these olefins combined with cracking reactions over H-ZSM-5 to form a distribution of branched olefins centered at C_{12}. The overall process converts 50% of the carbon present in the secondary alcohols into fuel-grade components.

Diesel and jet fuels are composed primarily of hydrocarbons containing carbon atoms linearly arranged to achieve high cetane numbers, whereas gasoline typically contains more highly branched hydrocarbons and aromatic compounds having high octane numbers (*3*, *4*). The heterocyclic compounds present in Sorb_503_18 serve directly as high-octane additives in gasoline (*4*, *18*, *19*). To produce C_8 to C_{12} compounds that contain primarily a single carbon branch and are suitable for conversion to diesel-fuel components, we passed Sorb_503_18 in the presence of H_2 over a bifunctional $CuMg_{10}Al_7O_x$ catalyst to achieve C-C coupling of the C_4 to C_6 ketones and secondary alcohols by aldol condensation [at 573 K and 5 bar pressure with 20 cm^3(STP) min^{-1} H_2 co-feed,

Table 1. Molar carbon distributions (mol %) for the conversion of sorbitol over 10 wt % Pt-Re/C at varying process conditions.

Temperature and pressure study*		
523 K	18 bar	27 bar
% Gas	53	54
% Organic	43	44
% Aqueous	4	2
503 K	18 bar	27 bar
% Gas	36	49
% Organic	52	48
% Aqueous	12	4
483 K	18 bar	27 bar
% Gas	26	30
% Organic	46	57
% Aqueous	29	13

Space velocity study†			
503 K, 27 bar	0.6 $hours^{-1}$	1.2 $hours^{-1}$	2.4 $hours^{-1}$
% Gas	49	33	28
% Organic	48	60	49
% Aqueous	4	7	24

*Three grams of 10 wt % Pt-Re/C catalyst with an atomic Pt:Re ratio of 1:1 was used with a 60 wt % sorbitol feed at a flow rate of 0.04 cm^3 min^{-1} (weight hourly space velocity of 0.6 $hours^{-1}$). †Feed flow rates from 0.04 to 0.16 cm^3 min^{-1} (weight hourly space velocities from 0.6-2.4 $hours^{-1}$) were used with 3.0 g of 10 wt % Pt-Re/C catalyst with an atomic Pt:Re ratio of 1:1.

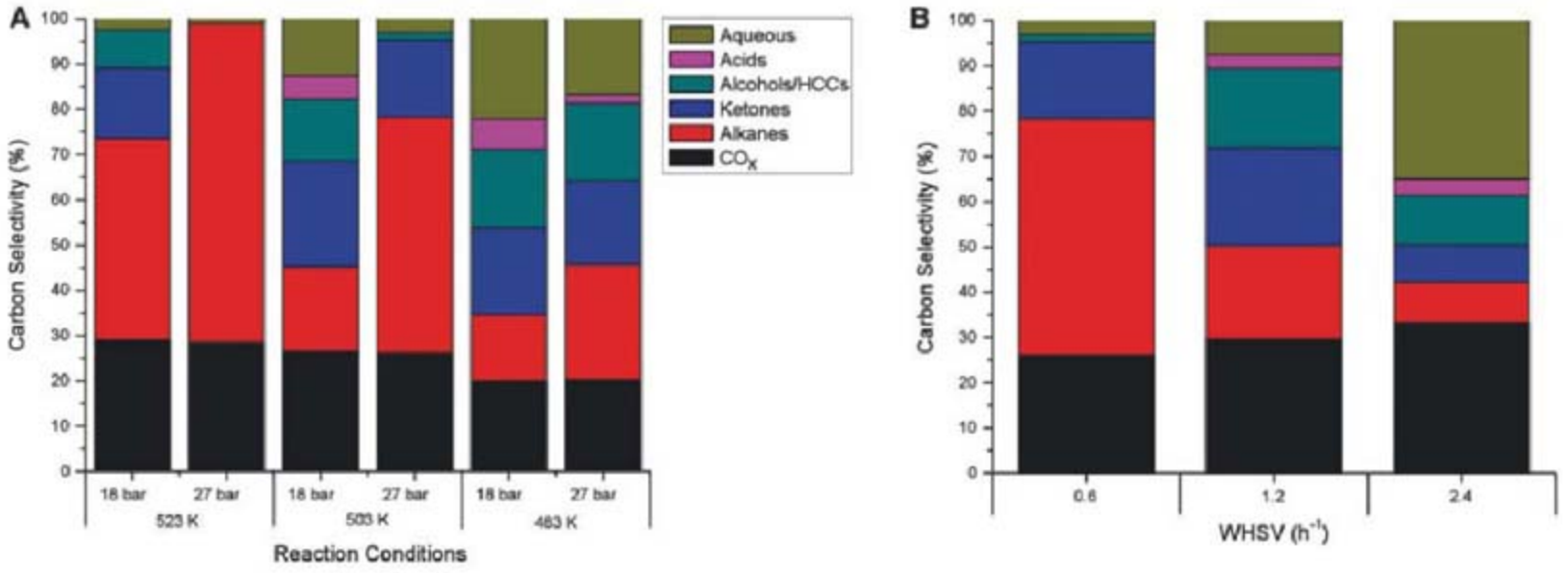

Fig. 2. Carbon selectivities for the conversion of sorbitol over Pt-Re/C. (**A**) Carbon selectivities at pressures between 18 and 27 bar and temperatures between 483 and 523 K. (**B**) Carbon selectivities at feed flow rates between 0.04 and 0.16 cm^3 min^{-1} (weight hourly space velocities between 0.60 and 2.4 $hours^{-1}$) at 27 bar and 503 K. HCCs: heterocyclic hydrocarbon species such as tetrahydrofurans and tetrahydropyrans.

giving a weight hourly space velocity of feed equal to 0.4 hours^{-1}] (*20*, *21*). At these reaction conditions, two-ketones undergo self-aldol condensation or crossed aldol condensation with three-ketones, and primary alcohols are oxidized to aldehydes, which in turn undergo crossed aldol condensation with ketones (*22*, *23*). Self-aldol condensation of three-ketones takes place at a slower rate because of steric and electronic effects (*24*). The small amounts of organic acids and esters in Sorb_503_18 cause deactivation of the basic $Mg_{10}Al_7O_x$ catalyst (*25*). Thus, before condensation, Sorb_503_18 was refluxed with a 20 wt % NaOH solution at 343 K and atmospheric pressure to hydrolyze the esters and neutralize the organic acids.

Figure 3B shows the product distribution following aldol condensation over the $CuMg_{10}Al_7O_x$ catalyst. Light species containing between four and six carbon atoms and one or no oxygen atoms (C_4 to C_6) constitute 55% of the carbon in the products, caused primarily by the low reactivity toward condensation of three-ketones (*26*). These light species contain C_4 alcohols (3% of total carbon) and heterocyclic compounds (substituted tetrahydrofurans and tetrahydropyrans, constituting 9% of total carbon), which would form C_4 to C_6 alkanes upon hydrodeoxygenation (*27*). The C_5 to C_6 ketones and secondary alcohols contribute 32% of the carbon in the products, whereas hexane and pentane contribute 10% of the carbon. The remaining carbon (45%) is associated with condensation products containing between 8 and 12 carbon atoms and one or no oxygen atoms (C_8 to C_{12}). The condensation products can be converted by hydrodeoxygenation over a $Pt/NbOPO_4$ catalyst to the corresponding alkane products (*27*), leading to a distribution similar to that shown in Fig. 3B. Because of the low oxygen content of the condensation products produced in the aforementioned process, the scale of the subsequent hydrodeoxygenation process is reduced in comparison to our previously reported process involving hydrodeoxygenation of the condensation products of acetone with furfural and HMF. The overall aldol-condensation process transforms 40% of the carbon contained in Sorb_503_18 into C_8 to C_{12} species, and converts 90% of the readily condensable methyl ketones present in the feed.

Ketonization reactions, in which two carboxylic acid molecules react to form a ketone with release of CO_2 and H_2O (*28*), can be performed in lieu of the aforementioned neutralization/ester hydrolysis step, to minimize product loss and the use of nonrenewable reagents (NaOH), and simultaneously to provide an additional pathway for C-C coupling. This approach should be particularly effective when the organic phase derived from the conversion of sugars or polyols is rich in carboxylic acids, as is the case for the conversion of a 40 wt % glucose solution over Pt-Re/C at 483 K and 18 bar, giving rise to production of an organic phase containing 40% of the feed carbon. This organic phase, designated Gluc_483_18, consists of 30% C_4 to C_6 carboxylic acids, with the remainder of the carbon present as ketones, alcohols, and alkanes.

Ketonization of Gluc_483_18 was carried out in a fixed bed flow reactor over a $CeZrO_x$ catalyst (weight hourly space velocity = 0.24 hours^{-1}) at two sets of reaction conditions (temperature/pressure): 648 K/1 bar and 573 K/20 bar. The effluent from the reactor was cooled to room temperature and passed to a gas-liquid separator that operated with a continuous flow of inert sweep gas at 20 cm^3(STP) min^{-1}. The first set of ketonization conditions resulted in a 65% carbon yield to liquid organic products, with the remainder of the carbon present in the vapor phase. The vapor phase consisted of C_4 to C_6 oxygenates (60%) resulting from evaporation, CO_2 (15%) resulting from ketonization, and alkanes and alkenes (25%) resulting from dehydration of alcohols. The second set of conditions was used to decrease evaporation and dehydration of light oxygenates, and it yielded 85% conversion to a liquid organic product stream. Both sets of conditions achieved greater than 98% conversion of the carboxylic acids in the feed to C_7 to C_{11} ketones.

The ketones in ketonized Gluc_483_18 can be coupled by aldol condensation to increase the yield of C_{7+} products. We attempted this aldol-condensation step using a $CuMg_{10}Al_7O_x$ catalyst; however, we observed that trace amounts of acids and esters present in the ketonized Gluc_483_18 cause deactivation of the catalyst over a period of 8 hours. In contrast, we found that a bifunctional catalyst consisting of 0.25 wt % Pd on $CeZrO_x$ is stable at 623 K versus time-on-stream for aldol condensation of the ketonized

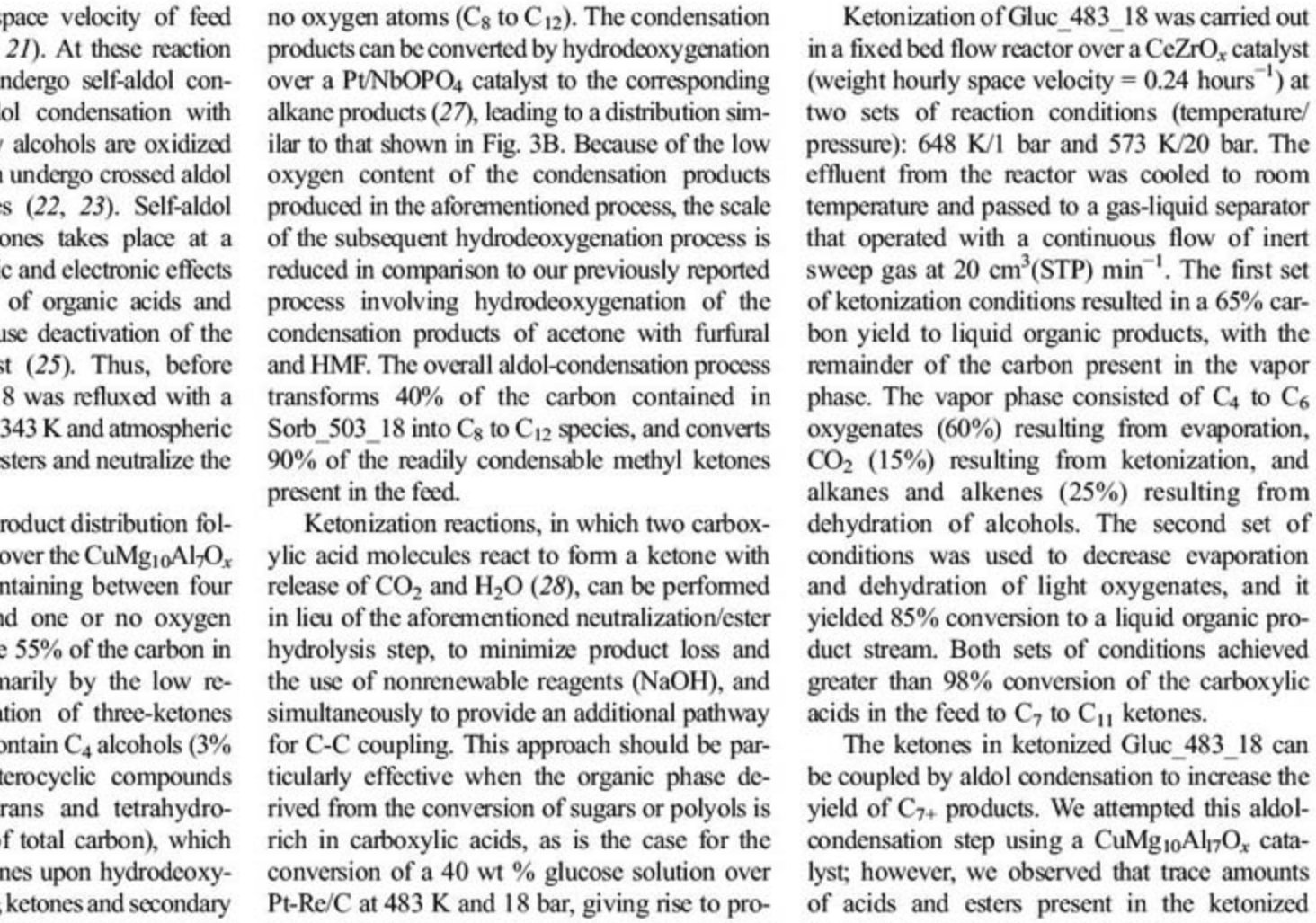

Fig. 3. Product distributions for the upgrading of the organic liquid product from sorbitol or glucose conversion over Pt-Re/C. (**A**) Sorb_503_18 upgrading to olefins and aromatic species over H-ZSM-5 at 673 K and atmospheric pressure. C_x: species containing x carbon atoms; C_{1-2}: CO_2, CH_4, C_2H_4, and C_2H_6; C_x Benzene: benzene rings functionalized with x additional carbon groups. (**B**) Sorb_503_18 aldol condensation to C_8 to C_{12} species over $CuMg_{10}Al_7O_x$ at 573 K and 5 bar. (**C**) Gluc_483_18 ketonization over $CeZrO_x$. (**D**) Aldol condensation of ketonized Gluc_482_18 over 0.25 wt % $Pd/CeZrO_x$ at 623 K and 5 bar.

Gluc_483_18. The feed used for aldol condensation over the Pd/$CeZrO_x$ catalyst consisted of a mixture of the organic products obtained at the two different sets of ketonization conditions mentioned previously: 34% C_7 to C_{11} ketones and 66% C_4 to C_6 alkanes and oxygenates (Fig. 3C). This ketonized organic feed was then subjected to aldol condensation over Pd/$CeZrO_x$ at 623 K, with all other conditions being the same as those used for the condensation of refluxed Sorb_503_18. Of the total carbon in the liquid organic product stream, 57% is in the form of C_{7+} ketones (Fig. 3D), with 34% resulting from ketonization and 23% resulting from aldol condensation. Products with carbon-chain length greater than C_{12} were also observed, likely resulting from aldol condensation of methyl ketones with C_{7+} ketones formed during ketonization. The combined ketonization and aldol-condensation process completely converted the carboxylic acids found in Gluc_503_18 into C_{7+} ketones, whereas 65% of the readily condensable two-ketones in ketonized Gluc_503_18 were converted to heavy products during the aldol-condensation step. Improving the efficiency of the aldol-condensation step and minimizing evaporation during the ketonization step has the potential to increase the overall conversion of Gluc_50_18 to C_{7+} ketones to ~63%. The comparable operating conditions of the ketonization and aldol-condensation processes should permit the integration of these C-C coupling steps into a two-bed single reactor system.

The cost of producing transportation fuels from ligno-cellulosic biomass is controlled primarily by the costs associated with the processing of biomass to produce the fuel (*29*), making it imperative to develop new processes for the conversion of biomass to liquid fuels that involve a limited number of processing steps (*15*). The catalytic approach shown in Fig. 1 is sufficiently simple that it can be used in a limited number of flow reactors, thus achieving low capital costs, but it is sufficiently flexible that it can be employed to produce a variety of liquid-fuel components. Although we have demonstrated promising yields of monofunctional hydrocarbons from conversion of sorbitol and glucose over Pt-Re/C catalysts, it will be important to understand how the composition of the monofunctional hydrocarbon stream is controlled by the nature of the biomass-derived feed, the catalyst, and the reaction conditions, such that high yields of targeted classes of transportation fuels can be achieved during subsequent catalytic upgrading steps.

References and Notes

1. Y. Roman-Leshkov, J. N. Chheda, J. A. Dumesic, *Science* **312**, 1933 (2006).
2. G. W. Huber, J. N. Chheda, C. J. Barrett, J. A. Dumesic, *Science* **308**, 1446 (2005).
3. C. H. Bartholomew, R. J. Farrauto, *Fundamentals of Industrial Catalytic Processes* (Wiley, Hoboken, NJ, 2006).
4. M. T. Barlow, D. J. H. Smith, D. G. Gordon, in European Patent 82689 A2 (1983).
5. R. R. Davda, J. W. Shabaker, G. W. Huber, R. D. Cortright, J. A. Dumesic, *Appl. Catal. B* **56**, 171 (2005).
6. G. W. Huber, R. D. Cortright, J. A. Dumesic, *Angew. Chem. Int. Ed.* **43**, 1549 (2004).
7. G. C. Bond, P. B. Wells, *J. Catal.* **4**, 211 (1965).
8. R. Alcala, M. Mavrikakis, J. A. Dumesic, *J. Catal.* **218**, 178 (2003).
9. V. Pallassana, M. Neurock, *J. Catal.* **209**, 289 (2002).
10. J. Zhang *et al.*, *J. Am. Chem. Soc.* **127**, 12480 (2005).
11. A. Perrard *et al.*, *Appl. Catal. A* **331**, 100 (2007).
12. D. L. Klass, *Biomass for Renewable Energy, Fuels and Chemicals* (Academic Press, San Diego, 1998).
13. S. Czernik, A. V. Bridgwater, *Energy Fuels* **18**, 590 (2004).
14. A. V. Bridgwater, *Appl. Catal. A* **116**, 5 (1994).
15. A. J. Ragauskas *et al.*, *Science* **311**, 484 (2006).
16. Materials, methods, calculations and detailed reaction schemes are available as supporting material on *Science* Online.
17. A. G. Gayubo, A. T. Aguayo, A. Atutxa, R. Aguado, J. Bilbao, *Ind. Eng. Chem. Res.* **43**, 2610 (2004).
18. D. J. Barratt, J. Lin, U.S. Patent 5,925,152 (1999).
19. T. H. Takizawa, S. A. Shimizu, S. S. Yamada, S. H. Ikebe, S. H. Hara, U.S. Patent 5,925,152 (1994).
20. J. I. Di Cosimo, G. Torres, C. R. Apesteguia, *J. Catal.* **208**, 114 (2002).
21. A. A. Nikolopoulos, B. W. L. Jang, J. J. Spivey, *Appl. Catal. Gen.* **296**, 128 (2005).
22. C. Carlini *et al.*, *J. Mol. Catal. A* **220**, 215 (204).
23. C. S. Cho, *J. Mol. Catal. A* **240**, 55 (2005).
24. J. McMurry, Ed., *Organic Chemistry* (Pacific Grove, CA, ed. 5, 2000), pp. 938–940.
25. J. Lopez, J. Sanchez Valente, J.-M. Clacens, F. Figueras, *J. Catal.* **208**, 30 (2002).
26. S. G. Powell, A. T. Nielsen, *J. Am. Chem. Soc.* **70**, 3627 (1948).
27. R. M. West, Z. Y. Liu, M. Peter, J. A. Dumesic, *ChemSusChem* **1**, 417 (2008).
28. O. Nagashima, S. Sato, R. Takahashi, T. Sodesawa, *J. Mol. Catal. A* **227**, 231 (2005).
29. C. N. Hamelinck, A. P. C. Faaij, H. den Uil, H. Boerrigter, *Energy* **29**, 1743 (2004).

30. This work was supported by the U.S. Department of Energy Office of Basic Energy Sciences and the NSF Chemical and Transport Systems Division of the Directorate for Engineering. We thank M. Mavrikakis for valuable discussions throughout this project, and E. I. Gürbüz for help with flow reactor experiments. J.C.S.-R. thanks the Spanish Ministry of Science and Innovation for postdoctoral support; C.A.G. thanks the German Academic Exchange Service (DAAD) for a scholarship. J.A.D. owns founders stock in Virent Energy Systems, a company with interest in the area of this research. The Wisconsin Alumni Research Foundation at University of Wisconsin has applied for a patent based partly on the work described here.

Supporting Online Material

www.sciencemag.org/cgi/content/full/1159210/DC1
Materials and Methods
Fig. S1
Table S1
References

16 April 2008; accepted 5 September 2008
Published online 18 September 2008;
10.1126/science.1159210
Include this information when citing this paper.

Accurate Temperature Imaging Based on Intermolecular Coherences in Magnetic Resonance

Gigi Galiana,[1,2] Rosa T. Branca,[2] Elizabeth R. Jenista,[2] Warren S. Warren[2]*

Conventional magnetic resonance methods that provide interior temperature profiles, which find use in clinical applications such as hyperthermic therapy, can develop inaccuracies caused by the inherently inhomogeneous magnetic field within tissues or by probe dynamics, and work poorly in important applications such as fatty tissues. We present a magnetic resonance method that is suitable for imaging temperature in a wide range of environments. It uses the inherently sharp resonances of intermolecular zero-quantum coherences, in this case flipping up a water spin while flipping down a nearby fat spin. We show that this method can rapidly and accurately assign temperatures in vivo on an absolute scale.

Temperature, one of the most fundamental intrinsic quantities of matter, is very difficult to measure noninvasively beneath the surface of an object. A general method to image interior temperatures in soft matter could find a wide range of experimental applications in fields ranging from bulk catalysis and process chemistry to clinical treatment. In medicine alone, temperature distributions in the body have been linked to the critical regulation of metabolism, immune function, and longevity. (*1*) Hyperthermic cancer treatments and radiation therapy are used to kill cancer cells at different stages of growth (*2–7*), and numerous groups have developed thermally sensitive formulations (e.g., liposomes) that release drugs selectively within a heated region (*8–11*). In practice, however, the utility of all of this work is compromised by the difficulty of accurate temperature imaging in vivo. (*12*) In general, current methods break down in the very systems that are of greatest interest, those that are inhomogeneous and that change with time.

Here, we present a magnetic resonance imaging approach for rapid, high-resolution in vivo temperature imaging. It involves selective detection of intermolecular multiple quantum coherences (iMQCs), (*13–21*) which in this case correspond to exciting water spin resonances while simultaneously de-exciting lipid resonances from molecules that are separated by the "correlation distance,"

[1]Department of Chemistry, Princeton University, Princeton, NJ 08544, USA. [2]Center for Molecular and Biomolecular Imaging, Duke University, Durham, NC 27708, USA.

*To whom correspondence should be addressed. E-mail: warren.warren@duke.edu

typically tens of micrometers. The method is not restricted to biological tissues; in essence, it uses a temperature-insensitive resonance to clean up the response of a temperature-sensitive resonance, with the critical advantage that the two types of spins need not be in the same molecule or even in exactly the same position. It required the development of a new generation of pulse sequences that enable efficient and rapid iMQC detection to reduce the effects of physiological noise. In contrast to existing methods, it is intrinsically insensitive to static and transient inhomogeneity, does not require exogenous contrast, and can rapidly provide accurate temperature measurement on an absolute scale.

Image-compatible methods of obtaining absolute temperatures are an intense area of research, but most techniques require injection of exogenous contrast agents, such as paramagnetic species. The best current approach to clinical MR thermometry (*22*–*24*) uses the change in resonance frequency of water protons with temperature (0.01 parts per million/°C, or 3 Hz/°C in a 7 tesla magnet). The water frequency has been used as a thermometer for decades in traditional nuclear magnetic resonance (NMR) (*25*), where line shapes are narrow and shifts are unambiguous, and in that case absolute temperatures can be measured by the frequency difference between water and a reference peak (*26*–*28*). However, line shapes in vivo are broad and shifting, because the topography of the local magnetic field changes dramatically with motion, heating, drift, and susceptibility gradients; this field is heterogeneous over the sampling volume, thus generating a range of resonance frequencies that leads to an inhomogeneous line shape. These macroscopic effects easily overshadow the thermal coefficient and, even with elaborate approximations and correction factors (*29*), can lead to large inaccuracies.

Chemical shift imaging (CSI) methods, such as two-dimensional (2D) CSI or computational techniques that decompose the fat and water images, are also promising, but these compare fat spins (S) and water spins (I) distributed across the entire voxel, typically of much larger dimensions (1 to 10 mm) than the correlation distance (*30*). As a result, the proton frequency shift method is the one commonly used, and only to image relative temperatures, for example, during a heating therapy. In that case, the temperature gradients themselves give rise to complicated, nonlinear gradients in the local magnetic field. (*31*) Furthermore, the heating probe itself induces large magnetic susceptibility gradients that amplify the consequences of motion, so that a 1- to 5-mm displacement of the probe falsifies the temperature measured 1.5 cm away by 10°C or more (*32*). Finally, current methods are unsuitable for fatty tissue such as breast, although breast cancer treatment is anticipated to be one of the most promising targets of hyperthermic therapies.

One approach to detection that is insensitive to the problem of inhomogeneity in the macroscopic field is to use so-called zero-quantum transitions, which conventionally involve flipping two spins on the same molecule in opposite directions. The frequency shifts that arise from microscopic phenomena (including those related to temperature, if the two resonances have a different temperature dependence) are retained. However, water's magnetically equivalent spins cannot be used, and other molecules with multiple peaks found in vivo (such as in fat or lipid) have no appreciable temperature dependence (*33*).

Flipping two separated spins in different directions [intermolecular zero-quantum coherences (iZQCs)] removes most of the inhomogeneous broadening (*34*), as demonstrated, for example, in the HOMOGENIZED sequence (*16*). In addition, water-fat iZQCs maintain the frequency difference between the spins (and hence the temperature dependence of the water chemical shift) because the chemical shift of lipids does not change with temperature over a biologically relevant range. Flipping both spins in the same direction [intermolecular double-quantum coherences (iDQCs)] could do this as well if the iDQCs are ultimately detected by echoing them into conventional coherences (which inherently evolve at the water or fat frequency, but not both). However, iZQCs and iDQCs are normally indirectly detected by incrementing an internal delay in a repeated pulse sequence. Imaging using only the iMQCs between two inequivalent spins is not easily accomplished; signal intensity from like-spin iZQCs, such as the water-water iZQCs in vivo, is often simultaneously detected and is often much larger than the desired mixed-spin or crosspeak signal. Resolving the temperature-dependent crosspeak frequency from the water-water signal would generally require a full 4D (two spatial, two spectral) Nyquist-sampled experiment. Any such sequence is both relatively slow and highly sensitive to physiological noise.

Ultrafast imaging methods have previously been applied to speed up iZQC data acquisition; these methods allow coherences to evolve along the same pathways for slightly different times and acquire signal by partial transfer into observable magnetization (*19*). We now introduce a new generation of pulse sequences (Fig. 1) that simultaneously excite coherences along multiple different paths without signal loss, which permits acquisition of two independent points in a single shot to measure a temperature change. Data acquired with this sequence demonstrates that temperature maps can rapidly and accurately monitor temperature, both in vitro and in vivo.

By modern magnetic resonance standards, the sequence is very simple: two broadband radio frequency (rf) pulses (shown as striped ovals), two selective rf pulses (solid color ovals), and several gradient pulses (trapezoids). Conventional MR experiments start from I_z or S_z in the equilibrium density matrix, and it is straightforward to show that this sequence then produces no signal, because no combination of the gradient areas provides any possible echo for arbitrary values of m and n in the gradient pulses. However, iMQCs result from two-spin (or higher) terms in the equilibrium density matrix, which in this sequence produce two echoes at two different times via two completely separate coherence pathways. After

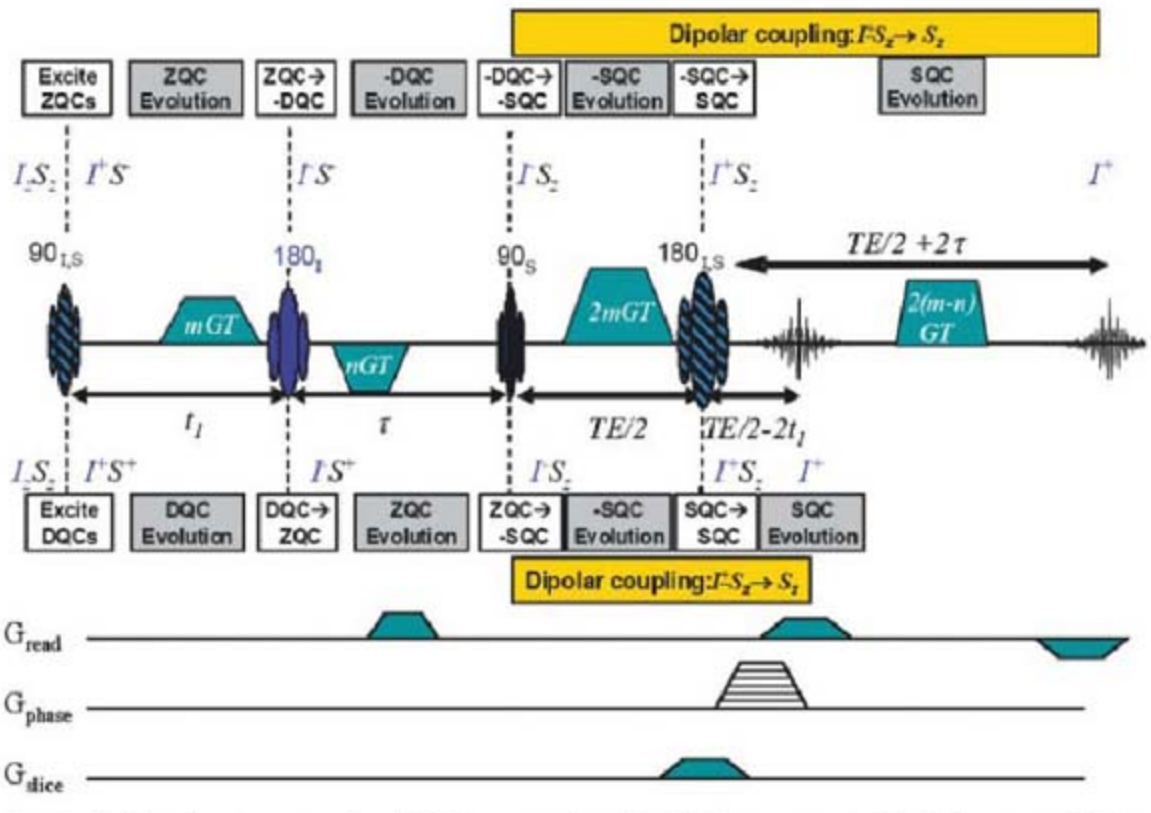

Fig. 1. HOT pulse sequences for iZQC thermometry. The HOT sequence excites inhomogeneity-free transitions at the difference frequency between water (spin I, in blue) and fat (spin S, in black). It acquires two separate echoes, which evolve for $\pm(t_1 + \tau)$ at the difference frequency $\omega_I - \omega_S$, so the phase difference gives an absolute measure of temperature. Single-line image acquisition (using the gradients on the bottom three lines) gives a full image in a few minutes; EPI could be even faster.

the first pulse, the two-spin term in the equilibrium density matrix I_zS_z is transformed into I_xS_x, which contains ZQ, –DQ, and +DQ contributions. All of these terms are transformed in the usual way by subsequent pulses, as illustrated in Fig. 1, and the evolution follows the standard "spin physics" well known in the NMR community. Simple algebra (adding up the expected effect of inhomogeneous broadening or a gradient on the listed operators during the different time periods) predicts all of the observed properties, including the insensitivity to local field variations. All four gradient pulses are needed to rephase the pathway at the top, which echoes 2 τ late because of the −DQ evolution in τ; at the echo, the coherence has a net evolution at the water-fat difference frequency for a total of $t_1 + \tau$. Only the first three gradient pulses are needed to rephase the pathway at the bottom, which echoes 2 t_1 early because of the +DQ evolution in t_1; at the echo, it evolved at the negative of this frequency for $t_1 + \tau$. Using the same evolution rules, it can be shown that the water-water or fat-fat two-spin terms ($I_{z1}I_{z2}$ or $S_{z1}S_{z2}$) never refocus. This sequence selectively transfers coherences that evolve off-resonance in the indirectly detected dimension, prompting its acronym to be HOMOGENIZED with Off-resonance Transfer, or the HOT sequence.

As with all intermolecular multiple-quantum experiments, the two-spin operators are ultimately made observable by dipolar interactions in solution (*35*). During the period indicated in gold in Fig. 1, n dipolar couplings of the form $D_{1n}I_{z1}S_{zn}$ all interact with terms such as $I_{x1}S_{zn}$ (which would be called antiphase coherences in 2D NMR) to create observable magnetization such as I_{y1}. Because of the gradients, the sign in front of the term $I_{x1}S_{zn}$ depends on the relative orientation and separation of spins 1 and n (as does the sign of the dipolar coupling D_{1n} itself). At a specific distance dictated by these areas (which we call the correlation distance), spherical symmetry is completely broken, the effects of the many couplings constructively interfere, and observable signals are produced (iMQC signals in vivo are typically 5 to 10% of the equilibrium magnetization). In imaging applications, we add conventional imaging gradients [single-line, as shown in the bottom panel of Fig. 1, or echo planar imaging (EPI)] to acquire two images at once, and the phase difference is a direct measure of local temperature, with dramatically reduced contributions from physiological noise compared to single-echo acquisitions.

As a calibration of the accuracy of HOT thermometry, we used a single-window version of Fig. 1 to acquire temperature images of a fat-

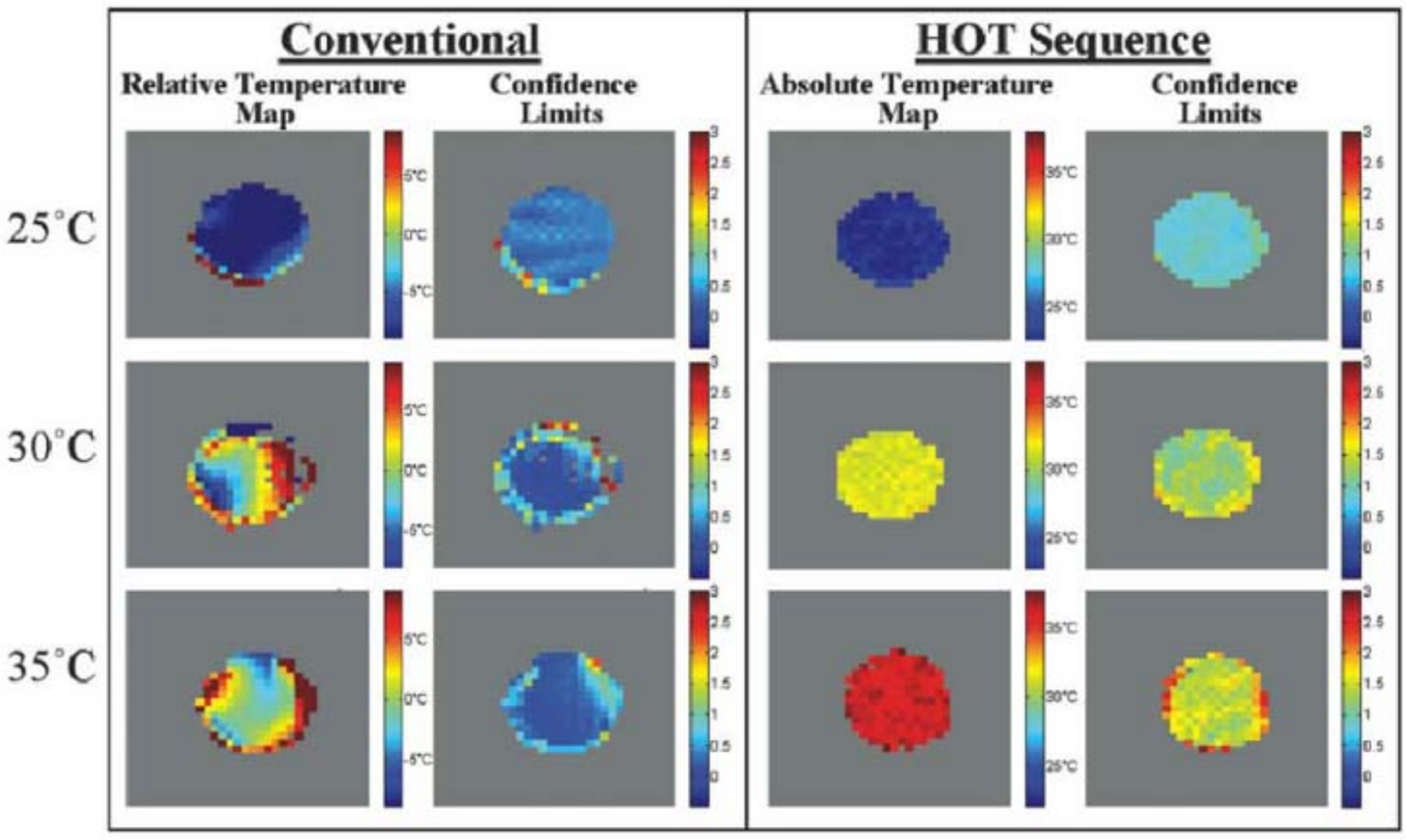

Fig. 2. Temperature maps of a phantom at three uniform temperatures. Conventional thermometry (color bar shows relative temperature inferred by water frequency) and iZQC thermometry (color bar shows absolute temperature from iZQC frequency) of an equilibrated fat-water phantom. The conventional method is precise but inaccurate, reporting a wide range of temperatures that are actually variations in local B_0. In contrast, HOT thermometry gives more uncertainty in the observed slope because of the lower signal-to-noise ratio, but these images accurately reflect the uniform temperature of the phantom.

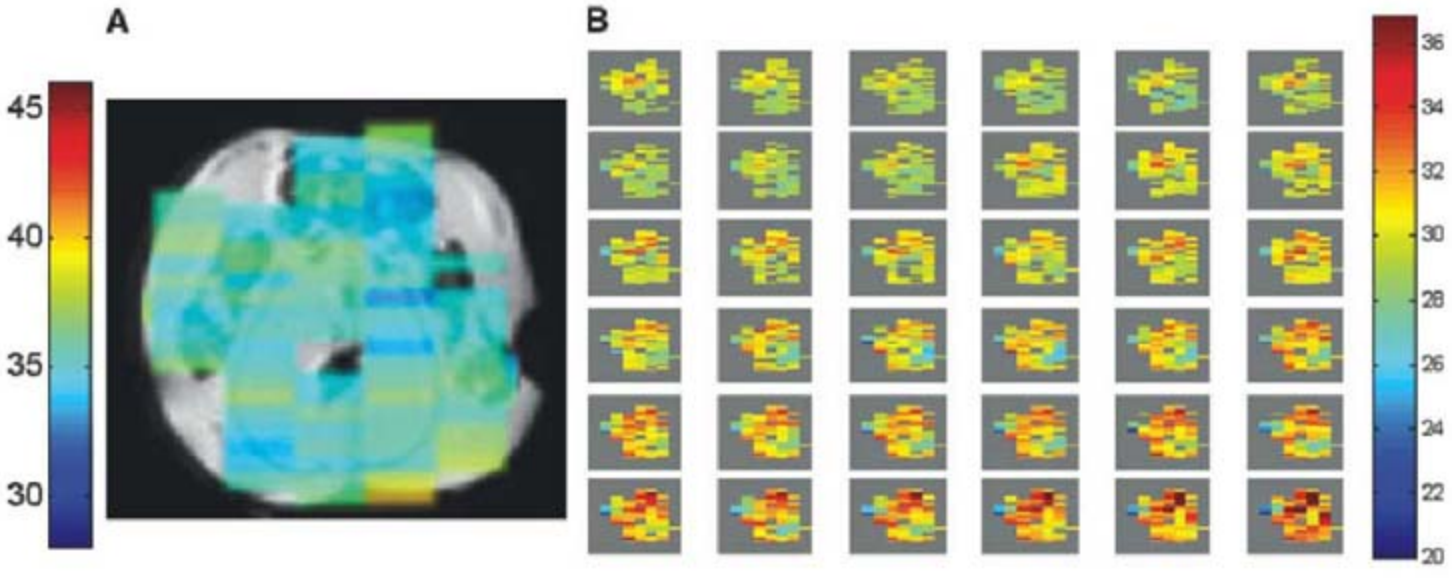

Fig. 3. (**A**) A 2-min HOT temperature image of OBM superimposed on an anatomical image of a thinner slice shows a relatively uniform distribution, as would be expected. These ungated images were acquired from the hindquarters of a live mouse at 7 T. (**B**) A series of HOT images on a different OBM heated by contact with a warm water tube. Images were taken every 2 min, and rectal temperature increased from 28.6°C to 39°C during the course of the experiment.

water phantom that was allowed to equilibrate to a uniform temperature (Fig. 2) (TE = 60 ms; pulse sequence repetition time TR = 5 s; τ = 2.67 ms; t_1 = 3 to 11 ms). Alongside each image at each temperature, we also show 90% confidence intervals based on the quality of the fit in each voxel to a single evolution frequency. In each case, what is shown here is not the absolute signal intensity but the measured resonance frequency of the voxel (and its associated error bars). Whereas the conventional data report large temperature gradients in these uniformly heated samples (an error caused by susceptibility-induced frequency shifts), HOT signals only change with temperature. In other words, the conventional method is precise but not accurate; HOT is less precise (because it has less signal) but far more accurate.

Figure 3 demonstrates HOT thermography in vivo using the two-window protocol in Fig. 1, which acquires images in just 2 min (ungated images of hindquarters of a live mouse, with TE = 40 ms; TR = 2 s; mGT = 1 ms*8.4 G/cm; nGT = 1 ms*21 G/cm; t_1 = 3 ms; τ = 10.66 ms; voxel size 0.25 cm^3). In Fig. 3A, an in vivo image is shown of an obese mouse (OBM), superimposed on a structural image of a thinner slice, which is an excellent model for the fatty tissue in breast. The temperature image shows considerable uniformity, as would be expected at the natural body temperature of the mouse. This data was acquired using single-line acquisition; EPI could provide still greater acceleration factors. The 2-min protocol was sufficiently fast, however, to allow us to dynamically image a heating procedure in vivo. A series of temperature images is shown in Fig. 3B of a different OBM that is being heated by contact with an external warm water tube (same imaging parameters as previously described and using no spatial smoothing or image coregistration between temperature images). These images further establish that the phases of iZQC images reflect temperatures in vivo in a clinically accessible scan time.

Further extensions of the HOT pulse-sequence are possible. For example, this scan used a separately acquired reference image to correct the phases for sequence imperfections, but we have shown that adding an additional module consisting of [$(n-m)$GT gradient pulse, delay T', 180 pulse] at the end of this sequence gives yet another echo after T'-t_1-τ that is purely I spin conventional magnetization and hence can be used for phase correction or coregistration. Phase-shift effects of heterogeneity in the fat composition can be minimized by judicious choice of pulse delays. This technique can be used to generate accurate temperature maps on almost any sample with at least two abundant components (assuming their electronic screenings do not have identical thermal shifts) on an absolute scale. However, it is notable that the signal from a HOT experiment scales as the product of the two magnetizations, $M_I M_S$, so optimal signal is attained when both spins are in high abundance. At lower fields, such as those found in clinical settings, temperature shifts are smaller, but in general T_2 is longer. Thus, the iZQC coherences can evolve for longer periods, giving an adequate separation of phase. Furthermore, because iZQC signal intensity grows in during TE, a longer T_2 can offset the lower magnetization available at higher field. Thus, the method can easily be adapted to a wide range of applications that would benefit from real-time imaging of this fundamental physical property.

References and Notes

1. B. Conti *et al.*, *Science* **314**, 825 (2006).
2. J. Overgaard, in *Hyperthermic Oncology*, vol. 2, J. Overgaard, Ed. (Taylor & Francis, London, 1985), pp. 325–338.
3. J. Van der Zee, *Ann. Oncol.* **13**, 1173 (2002).
4. E. L. Jones *et al.*, *J. Clin. Oncol.* **23**, 3079 (2005).
5. P. Wust *et al.*, *Lancet* **3**, 487 (2002).
6. T. Hehr, P. Wust, M. Bamberg, W. Budach, *Oncologie* **26**, 295 (2003).
7. G. P. Raaphorst, in *An Introduction to the Practical Aspects of Clinical Hyperthermia*, S. B. Field, J. W. Hand, Eds. (Taylor & Francis, London, 1990), pp. 10–54.
8. M. B Yatvin, J. N. Weinstein, W. H. Dennis, R. Blumenthal, *Science* **202**, 1290 (1978).
9. G. Kong, R. D. Braun, M. W. Dewhirst, *Cancer Res.* **60**, 4440 (2000).
10. M. H. Gaber *et al.*, *Int. J. Radiat. Oncol. Biol. Phys.* **36**, 1177 (1996).
11. D. Needham, G. Anyarambhatla, G. Kong, M. W. Dewhirst, *Cancer Res.* **60**, 1197 (2000).
12. M. Dewhirst *et al.*, *Int. J. Hyperthermia* **21**, 779 (2005).
13. W. S. Warren, W. Richter, A. H. Andreotti, B. T. Farmer II, *Science* **262**, 2005 (1993).
14. Q. He, W. Richter, S. Vathyam, W. S. Warren, *J. Chem. Phys.* **98**, 6779 (1993).
15. S. Lee, W. Richter, S. Vathyam, W. S. Warren, *J. Chem. Phys.* **105**, 874 (1996).
16. S. Vathyam, S. Lee, W. S. Warren, *Science* **272**, 92 (1996).
17. Y.-Y. Lin, N. Lisitza, S. Ahn, W. S. Warren, *Science* **290**, 118 (2000).
18. C. Faber, D. Balla, *J. Magn. Reson.* **161**, 265 (2003).
19. G. Galiana, R. T. Branca, W. S. Warren, *J. Am. Chem. Soc.* **127**, 17574 (2005).
20. Z. Chen, Z. Z. Chen, J. H. Zhong, *J. Am. Chem. Soc.* **126**, 446 (2004).
21. Y. Y. Lin *et al.*, *Phys. Rev. Lett.* **85**, 3732 (2000).
22. B. Denis de Senneville, B. Quesson, C. T. W. Moonen, *Int. J. Hyperthermia* **21**, 515 (2005).
23. J. Gellermann *et al.*, *Int. J. Hyperthermia* **21**, 497 (2005).
24. Y. Ishihara *et al.*, *Magn. Reson. Med.* **34**, 814 (1995).
25. J. Hindman, *J. Chem. Phys.* **44**, 4582 (1966).
26. N. McDannold *et al.*, *Radiology* **230**, 743 (2004).
27. S. K. Hekmatyar, P. Hopewell, S. K. Pakin, A. Babsky, N. Bansal, *Magn. Reson. Med.* **53**, 294 (2005).
28. C. Li, X. Pan, Q. Zhang, K. Ying, *Proc. Intl. Soc. Magn. Reson. Med.* **15**, 3372 (2007).
29. V. Rieke *et al.*, *Magn. Reson. Med.* **51**, 1223 (2004).
30. K. Kuroda *et al.*, *Magn. Reson. Med.* **43**, 220 (2000).
31. R. D. Peters, R. S. Hinks, R. M. Henkelman, *Magn. Reson. Med.* **41**, 909 (1999).
32. A. Boss *et al.*, *J. Magn. Reson. Imaging* **22**, 813 (2005).
33. A. Abragam, *The Principles of Nuclear Magnetism* (Clarendon, Oxford, 1961).
34. Susceptibility changes that occur over the correlation distance, typically tens of microns, still do contribute to the iZQC linewidths. However, in almost any realistic samples, susceptibility changes that occur over this distance are necessarily far smaller than those seen across an entire voxel, leading to substantial line narrowing.
35. Although we use the iZQC nomenclature here, as discussed in (*17*), (*27*), and numerous other places, it is also possible in principle to calculate these effects using Bloch equations adapted to include a nonlinear term—the distant dipolar field—and this method is useful for numerical simulations. However, the nonlinearities in that picture dramatically reduce its intuitive value; for example, it is very hard to explain why peaks at the difference frequency are insensitive to inhomogeneous broadening.

36. This work was funded by NIH grants EB2122 and EB5979. We thank M. Dewhirst for useful discussions.

14 July 2008; accepted 5 September 2008
10.1126/science.1163242

Molecular Layering of Fluorinated Ionic Liquids at a Charged Sapphire (0001) Surface

Markus Mezger,[1] Heiko Schröder,[1] Harald Reichert,[1]* Sebastian Schramm,[1] John S. Okasinski,[1] Sebastian Schöder,[1,2] Veijo Honkimäki,[2] Moshe Deutsch,[3] Benjamin M. Ocko,[4] John Ralston,[5] Michael Rohwerder,[6] Martin Stratmann,[6] Helmut Dosch[1,7]

Room-temperature ionic liquids (RTILs) are promising candidates for a broad range of "green" applications, for which their interaction with solid surfaces plays a crucial role. In this high-energy x-ray reflectivity study, the temperature-dependent structures of three ionic liquids with the tris(pentafluoroethyl)trifluorophosphate anion in contact with a charged sapphire substrate were investigated with submolecular resolution. All three RTILs show strong interfacial layering, starting with a cation layer at the substrate and decaying exponentially into the bulk liquid. The observed decay length and layering period point to an interfacial ordering mechanism, akin to the charge inversion effect, which is suggested to originate from strong correlations between the unscreened ions. The observed layering is expected to be a generic feature of RTILs at charged interfaces.

Organic room-temperature ionic liquids (RTILs) were first synthesized a century ago (*1*), but research on RTILs has grown explosively during the past decade (*2*), spurred by the RTILs' potential role in "green" chemical synthesis (*3*, *4*), catalysis (*5*), batteries (*6*), fuel and solar cells (*7*, *8*), and even telescope construction (*9*). The RTILs' high functionality is a result of their nonvolatility, good solvent properties, wide liquidus range, low viscosity, high

ion mobility, and wide electrochemical window (*2*, *10*). Moreover, they are easily tunable to specific needs by combining judiciously chosen anions and cations (*2*, *11*). More than 1000 RTILs have been synthesized to date, already outnumbering all conventional inorganic salts.

RTILs are governed by a complex combination of van der Waals, (unscreened) Coulomb, dipole, and hydrogen bonding interactions, which seldom occur together in other materials (*12*). The theoretical understanding of the specific role and relative importance of these interactions in determining the bulk and surface structure and properties is one of the most challenging tasks of current RTIL research. The challenge is exacerbated by the scarcity of molecular-resolution structural information for the RTILs' bulk and interfaces. RTILs also allow addressing other issues. As ionic melts with no solvent, they constitute infinite-concentration electrolytes. These were studied very little theoretically and experimentally for lack of appropriate samples (*13*).

The vast majority of processes in RTIL applications involve interfaces, mostly the solid-liquid interface. To date, such interfaces have been investigated mostly by optical methods such as sum frequency spectroscopy (*14*), which yield only the molecular orientation of the first interfacial layer. The only x-ray measurement of the structure of a liquid-vapor interface of two imidazolium-based RTILs revealed a single surface layer ~6 Å thick, which is ~12% denser and 15% anion-richer than the bulk (*13*). This conclusion is consistent with low-resolution neutron measurements on the same liquid-vapor interface (*15*). An x-ray study of a solid-supported thin (~100 to 200 Å) RTIL film provided evidence for molecular layering throughout the film thickness, although only after an annealing treatment. The layering vanishes gradually with increasing film thickness (*16*). Even these few pioneering measurements span too restricted a momentum transfer range to allow for the determination of the near-interface structure with a molecular-scale resolution. Such high-resolution structural information should provide insight into the complex interplay of all of the relevant interactions, which may be different and/or complementary at the solid-liquid and air-liquid interfaces. We report here on high-resolution studies of the temperature-dependent structure of three FAP-based ionic liquids {[FAP]$^-$ is tris(pentafluoroethyl)trifluorophosphate anion} at a charged solid Al_2O_3 (0001) interface (Fig. 1A) (*17*). By using high-energy x-ray reflectivity, we have determined the electron density profile across the interface. The measurements span a momentum transfer range up to $q = 1.4$ Å^{-1}, resulting in a submolecular-scale resolution of 4.5 Å.

The measurements were carried out in a temperature-controlled (±0.01 K, operable at 200 K < T < 500 K) vacuum cell (Fig. 1B) mounted on the high-energy microdiffraction setup HEMD (*18*) at beamline ID15A of the European Synchrotron Radiation Facility (Grenoble, France). The monochromatic x-rays ($E = 72.5$ keV) with a flux of ~5×10^{10} photons per s were focused by a compound refractive lens (CRL) to a 5 μm–by–20 μm spot at the sample position. The samples were prepared in several steps: (i) The Al_2O_3 substrates (Saint-Gobain Crystals, Newbury, Ohio, 10 mm by 6 mm

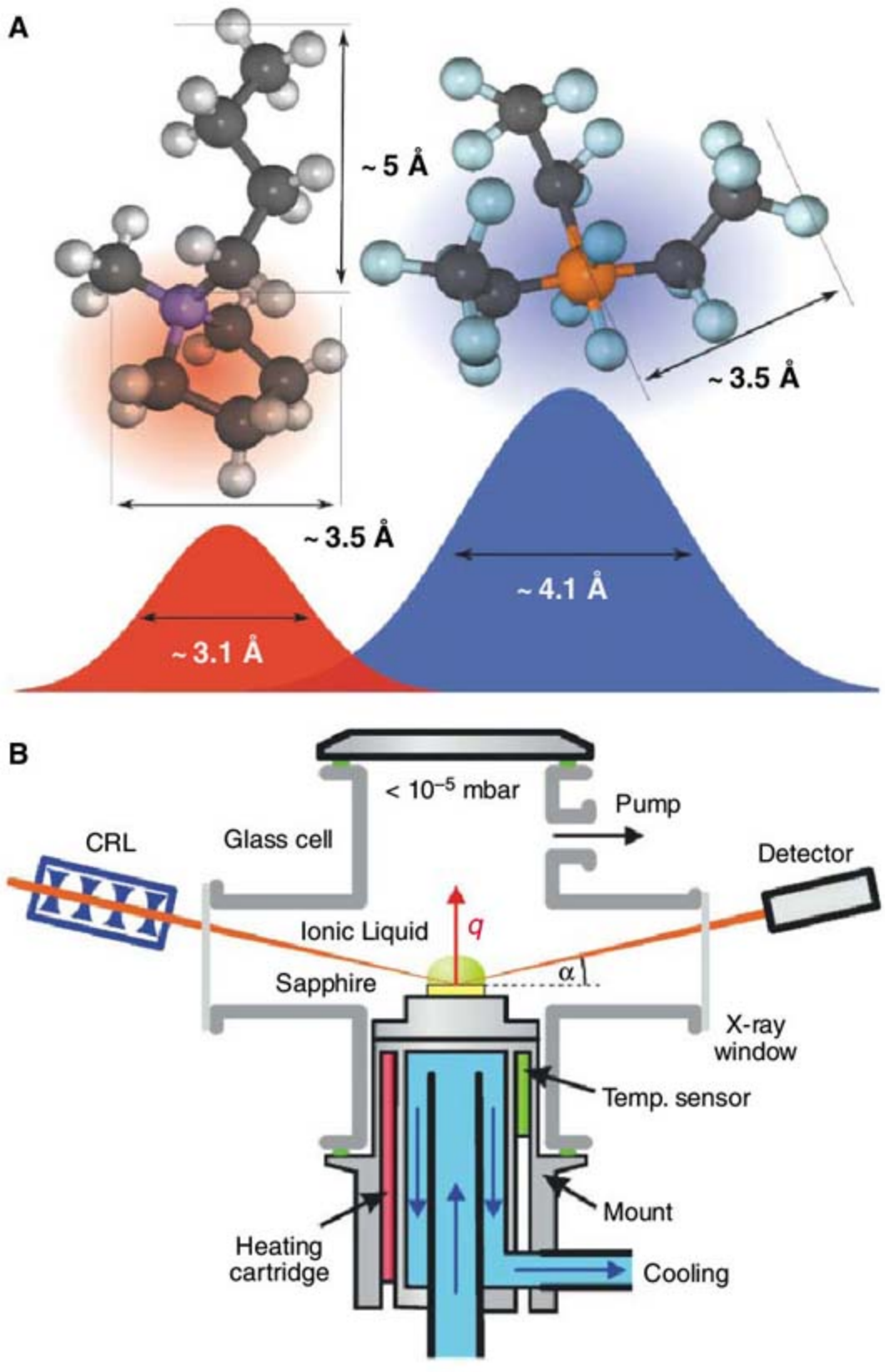

Fig. 1. (**A**) Sketch of the two ions of the RTIL [bmpy]$^+$[FAP]$^-$ with the delocalized charge shown as colored clouds. The total electron density distribution of each ion (red is cation and blue is anion) is modeled by a Gaussian with width $\sigma_0^c = 3.1$ Å and $\sigma_0^a = 4.1$ Å. Typical distances in the molecular ions are indicated. (**B**) Experimental setup. The microfocused high-energy x-ray beam penetrates the droplet from the side, illuminating only the interface to be studied. The temperature is adjusted by four heating cartridges and a cooling fluid from a recirculating bath or cold N_2 gas.

[1]Max-Planck-Institut für Metallforschung, D-70569 Stuttgart, Germany. [2]European Synchrotron Radiation Facility, F-38043 Grenoble, France. [3]Physics Department and Institute of Nanotechnology and Advanced Materials, Bar-Ilan University, Ramat-Gan 52900, Israel. [4]Condensed Matter Physics and Materials Science Department, Brookhaven National Laboratory, Upton, NY 11973, USA. [5]Ian Wark Research Institute, University of South Australia, Mawson Lakes, SA 5095, Australia. [6]Max-Planck-Institut für Eisenforschung, D-40237 Düsseldorf, Germany. [7]Institut für Theoretische und Angewandte Physik, Universität Stuttgart, D-70550 Stuttgart, Germany.

*To whom correspondence should be addressed. E-mail reichert@mf.mpg.de

by 0.35 mm) were chemically cleaned with standard methods (solvent treatment in ultrasonic bath and H_2SO_4/H_2O_2 piranha etch), followed by ultraviolet (172 nm) irradiation. Typical values for the substrate surface roughness, σ_S, were 2 to 2.5 Å, as determined by x-ray reflectivity. (ii) The high-purity grade RTILs (Merck KGaA, Darmstadt, Germany) were degassed at temperature $T \sim 70$°C in a vacuum oven for several hours. Karl Fischer titration confirmed a water content well below 100 parts per million (ppm). (iii) Before the deposition of the RTIL, the substrate was heated to 110°C. (iv) The cell was evacuated to 10^{-5} mbar immediately after depositing the RTILs onto the substrate to evaporate volatile contaminants. This protocol allowed us to obtain reproducible x-ray results.

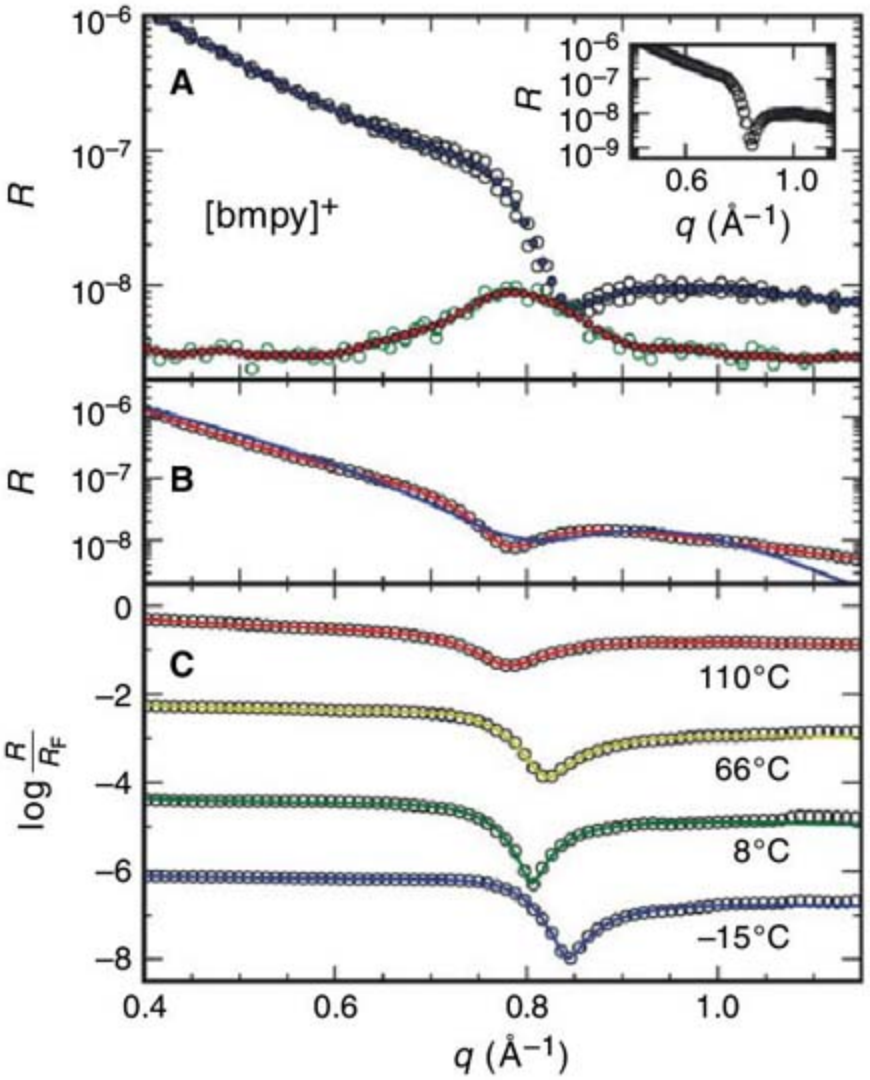

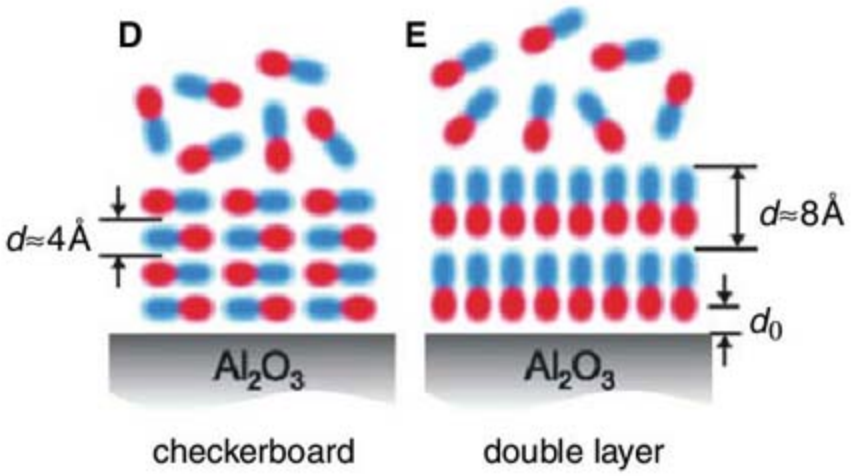

Fig. 2. Experimental results for the $[bmpy]^+[FAP]^-$-Al_2O_3 interface. (**A**) Measured reflectivity (black open circles) and background (green open circles) at $T = -15$°C. The blue and red circles mark the corresponding interpolated data on a regularly spaced grid. (Inset) Background-corrected reflectivity curve. (**B**) Reflectivity at 110°C together with best fits using a checkerboard [blue line and (D)] and a double-layer [red line and (E)] model, respectively. (**C**) Normalized reflectivities (symbols) together with best fits (solid lines) at different temperatures (the curves are shifted vertically for clarity). (**D** and **E**) Different possible layering arrangements of correlated ions at a hard wall with checkerboard-type stacking (D) and double-layer stacking (E).

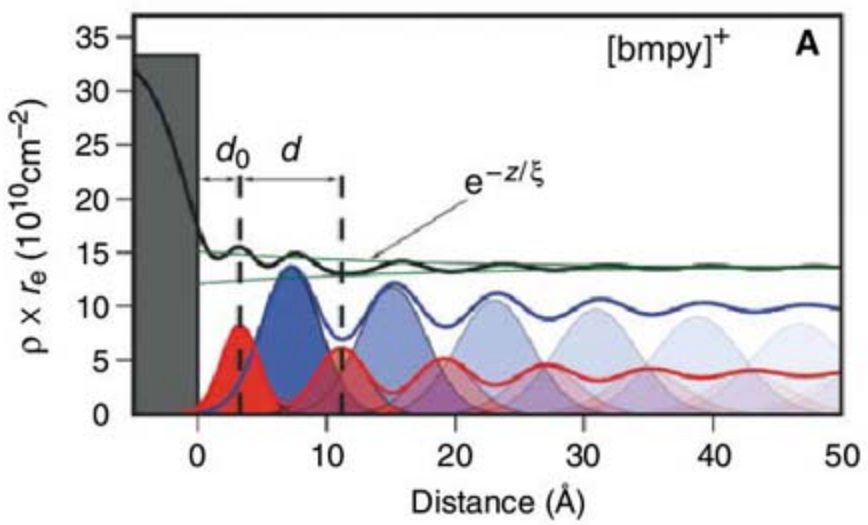

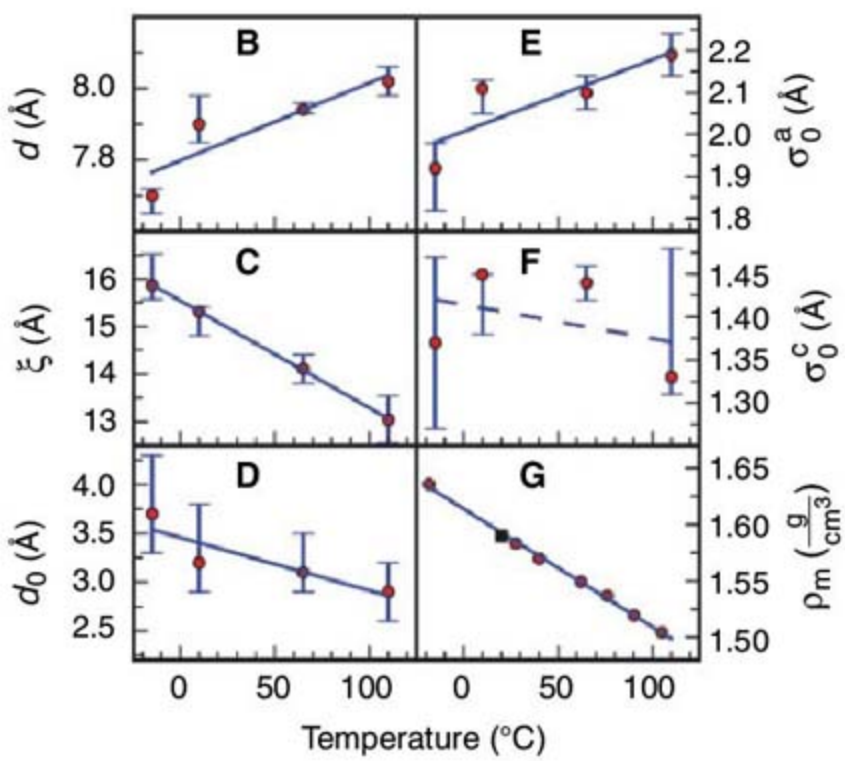

Fig. 3. (**A**) Cation (red), anion (blue), and total (black) electron densities obtained from the best fit at $T = -15$°C. Red and blue lines indicate cation and anion Gaussian distributions contributing to the respective partial electron density profiles; black line, total electron density profile; and gray bar, electron density of the sapphire substrate without roughness. (**B** to **F**) Best-fit values of d, ξ, d_0, σ_δ^a, and σ_δ^c. Linear fits (blue) are also shown. Error bars were derived from parameter space maps and indicate a 50% decrease in fit quality. (**G**) RTIL mass density ρ_m obtained from bulk density pycnometry (red circles) with a linear fit (blue) and the supplier's room temperature value (black square) (*17*).

The x-ray reflectivity of the interface, $R(q)$, was measured as a function of the normal momentum transfer (*19*), $q = (4\pi/\lambda)\sin\alpha$, where α is the angle of incidence onto the interface. At this short x-ray wavelength, $\lambda = 0.171$ Å associated with a quantum x-ray energy of $E = 72.5$ keV, the setup requires high stability (*18*). Beam damage was avoided by translating the sample perpendicular to the incident beam during the measurements (*20*). In order to minimize the influence of random factors, we measured and averaged several $R(q)$ curves on a given sample. The background, originating mainly from bulk liquid scattering, was measured with the incident angle detuned by 0.05° from the specular position within the reflection plane and subtracted from the signal (Fig. 2A).

The reflectivity of the $[bmpy]^+[FAP]^-$-Al_2O_3 interface ($[bmpy]^+$ is 1-butyl-1-methylpyrrolidinium) was measured at −15°C (deeply undercooled), 8°C (near the melting point at 5°C), 66°C, and 110°C (far above the melting point) and normalized by the Fresnel reflectivity $R_F(q)$ (Fig. 2C). The most pronounced feature in all four curves is a strong dip at $q_0 \sim 0.8$ Å^{-1}, which implies the presence of pronounced interfacial layering, with a layer spacing $d = 2\pi/q_0 \sim 8$ Å. The position of the dip shifts toward smaller q values with increasing temperature, indicating an increase in the layer spacing. The position of the dip is very close to the position of the first peak of the liquid structure factor (Fig. 2A), which corresponds to the average molecular distance in the bulk ionic liquid. Furthermore, a broadening of the dip was observed with increasing temperature, indicating a decrease in the thickness of the layered structure.

In a two-component ionic system, layered structures can be formed in two generically different ways. Systems dominated by electrostatic interactions between the ions should order in a checkerboard-type structure with an equal amount of anions and cations in each layer (Fig. 2D). However, systems with strong correlations between the ions and a preference for either cations or anions at the interface might form double-layer structures with anions and cations clearly separated into distinct layers. The two models differ in both their density distributions and the periodicity, d, of the layering. The large layer spacing of $d \sim 8$ Å deduced from the position of the dip indeed suggests the double-layer model (Fig. 2E) for the density profile of the RTIL.

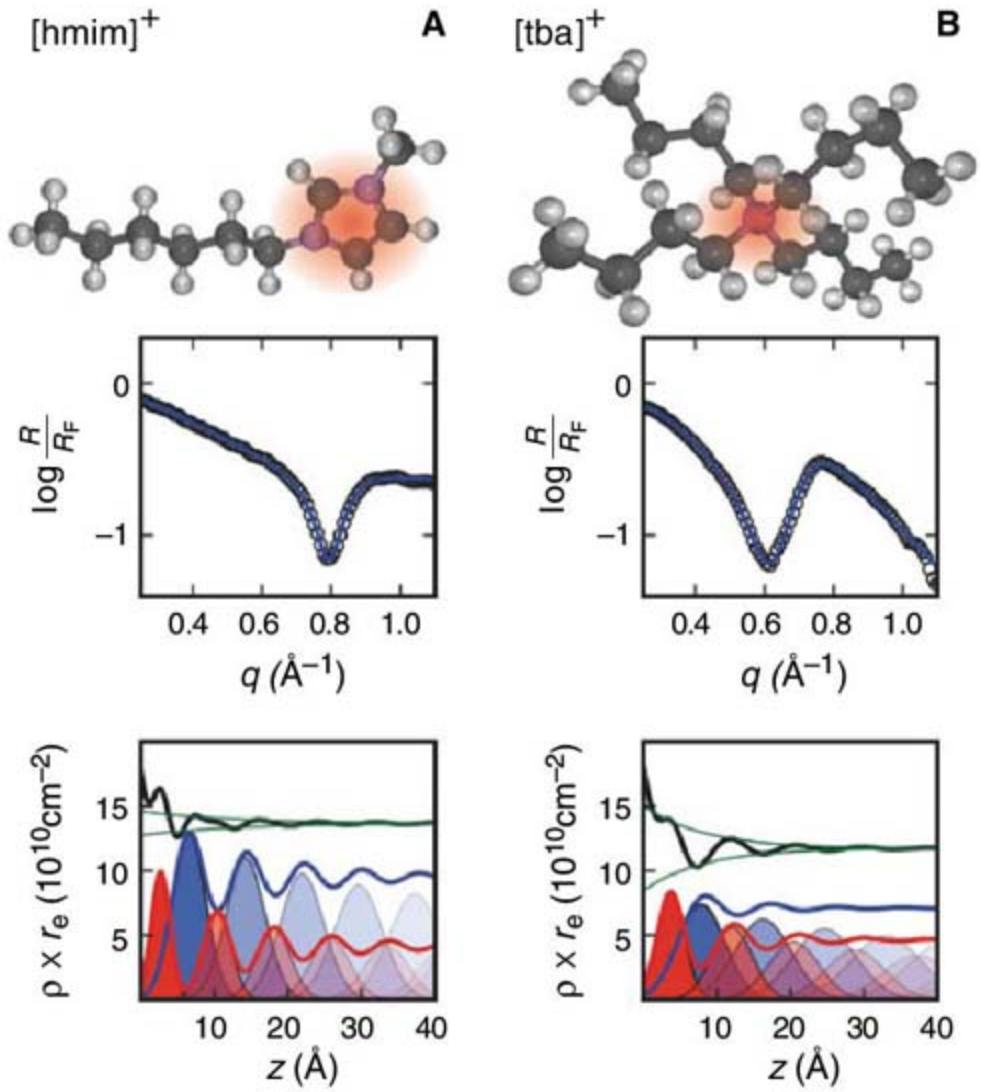

Fig. 4. Molecular layering at the $[hmim]^+[FAP]^-$-Al_2O_3 interface (**A**) and $[tba]^+[FAP]^-$-Al_2O_3 interface (**B**). Each column displays a sketch of the corresponding cation; the normalized reflectivity (open circles) measured at $T = -34$°C (A) and $T = 56$°C (B), including the best fit (solid line); and the cation (red line), anion (blue line), and total (black line) electron densities obtained from the best fit.

The electron density of the layered RTIL is parameterized by a modification of the distorted-crystal model used successfully in several studies to describe surface-induced layering in single-component liquid metals (*21*, *22*). In this model, the ionic liquid is stratified parallel to the interface with the periodically modulated density profile decaying toward the constant bulk density

$$\rho(z) = (2\pi)^{-1}\sum_{n=0}^{\infty} \times \left\{\frac{\rho_c}{\sigma_n^c}e^{-\frac{1}{2}\left(\frac{d_0+nd-z}{\sigma_n^c}\right)^2} + \frac{\rho_a}{\sigma_n^a}e^{-\frac{1}{2}\left[\frac{d_0+(n+\varepsilon)d-z}{\sigma_n^a}\right]^2}\right\} + \sigma_S erf\left(\frac{-z}{\sqrt{2}\sigma_s}\right) \quad (1)$$

This density profile parameterizes both checkerboard-type layering ($\varepsilon = 0$) and the double-layer model ($\varepsilon = 0.5$), which consists of alternating layers of cations (c) and anions (a), required to preserve charge neutrality. Each of the d-spaced ion layers has a Gaussian electron density distribution (Fig. 1A). The decay in the layering with distance from the interface is described by the increasing width of the Gaussian distribution $(\sigma_n^{c,a})^2 = (\sigma_0^{c,a})^2 + n\sigma_b^2$. σ_b controls the broadening of the Gaussians, and $\sigma_0^{c,a}$ is the first cation or anion layer width, respectively, including the interfacial roughness. d_0 is the distance between the substrate's surface and the center of the first ion layer. $\rho_{c,a} = dZ_{c,a}\rho_m N_A/M_{c,a}$ is the areal electron density of the ions, where Z is the number of electrons of the respective ion, M its molar mass, ρ_m the bulk mass density, and N_A the Avogadro constant. Each Gaussian represents a single ionic layer, and the model conserves the locally averaged mass and electron densities. The substrate's density is modeled by an error function with an interfacial roughness σ_S and a sapphire electron density ρ_S.

We modeled $\rho(z)$ by fitting the measured reflectivities using Parratt's multilayer formalism within a simulated annealing procedure (*23*). The following six parameters were varied in the fit: d_0, d, $\sigma_0^{c,a}$, σ_b, and σ_S. The bulk liquid density of the RTIL and its temperature dependence were determined independently by pycnometry (Fig. 3G). Consistent fitting results with physically acceptable values could only be obtained by taking the near-substrate layer to be a cation layer. The resulting fits are in excellent agreement with the measured reflectivity curves (Fig. 2, B and C).

Other models for the electron density profile, such as single adsorbed layers, nonlayered models, or the simple distorted crystal model with a single Gaussian layer per molecule, could not reproduce the measured reflectivity. Figure 2B shows the best fit of the checkerboard model to the reflectivity at $T = 110$°C, resulting in a poor

fit and an unphysical large gap of d_0 = 10 Å. Figure 3A presents the partial and total electron density profiles at the $[bmpy]^+[FAP]^-$-Al_2O_3 interface for $T = -15$°C. The extracted density profiles exhibit pronounced layering extending several nm deep into the bulk liquid. The contribution of the cations and anions are shown separately. The layering decays exponentially into the bulk where ξ, the decay length for the layering, is related to the broadening parameter σ_b.

The results for the temperature dependence of the model parameters for the $[bmpy]^+[FAP]^-$-Al_2O_3 interface are summarized in Fig. 3, B to G. The double-layer spacing d expands with temperature in agreement with the linear thermal expansion coefficient $\alpha_T = 2.2 \times 10^{-4}$ K^{-1} extracted from the bulk liquid density (Fig. 3G). The initial width σ_0^a of the anion distribution shows a thermal smearing, whereas σ_0^c is roughly temperature-independent. The range of the molecular layering can be deduced from the decay of the moduli of the normalized electron density profiles. Figure 3A shows the result of a fit of an exponentially decaying envelope function to the total electron density profile. At $T = -15$°C, we find a decay length $\xi = 15.9$ Å $\sim 2d$, which decreases slowly with temperature to $\xi = 1.6d$ at $T = 110$°C (Fig. 3C). We also note that, within the error bars, no additional increase in ξ was observed near the melting point or at deep undercooling ($T = -15$°C). A rather unexpected result is that the distance d_0 of the first molecular layer from the interface decreases with increasing temperature, which implies that the soft side of the anharmonic potential experienced by the first molecule is located at the substrate side.

Independent kelvin probe measurements confirmed that the observed layering is triggered by a negatively charged sapphire surface. A series of experiments were carried out on (i) a bare substrate surface without x-ray illumination, (ii) a bare substrate surface with x-ray illumination, (iii) a substrate covered with RTIL and without x-ray illumination, and (iv) a substrate covered with RTIL under x-ray illumination. These measurements uncovered a strong effect of the x-ray beam on the insulating sapphire substrate. Exposing the bare substrate and the RTIL-covered substrate to the full microfocused x-ray beam resulted in potential drops of –550 mV and –1300 mV, respectively, in the kelvin probe. The sign and the magnitude of the potential drop at the bare substrate's surface and at the RTIL-substrate interface clearly demonstrated that the substrate surface gets noticeably charged by the x-ray beam exposure (*24*).

In further studies, we varied systematically the RTIL's cation, replacing the $[bmpy]^+$ cation by $[hmim]^+$ (1-hexyl-3-methylimidazolium) and $[tba]^+$ (tetrabutylammonium) (Fig. 4). X-ray reflectivities have been measured at several temperatures at the $[hmim]^+[FAP]^-$-Al_2O_3 interface (Fig. 4A) and the $[tba]^+[FAP]^-$-Al_2O_3 interface (Fig. 4B). The measurements exhibit molecular layering features that are similar to those found for the $[bmpy]^+[FAP]^-$-Al_2O_3 interface. The parameter values obtained from the best fits by using the double-layer distorted crystal model above are (i) $d = 7.7$ Å, $d_0 = 2.7$ Å, and $\xi = 7.7$ Å for $[hmim]^+[FAP]^-$ and (ii) $d = 8.4$ Å, $d_0 = 3.7$ Å, and $\xi = 8.1$ Å for $[tba]^+[FAP]^-$. Both RTILs show no significant variation of the model's parameters with temperature. These results strongly suggest that the observed molecular layering is a generic feature of RTILs at charged walls.

Dilute aqueous electrolytes contain water-screened weakly interacting ions, the ordering of which near a charged wall has been successfully treated within mean field theories of charge double layers (e.g., the Debye-Hückel and the Gouy-Chapman models) based on the Poisson-Boltzmann equation (*25*). This equation neglects, however, correlations between ions. In contrast, the interaction between the oppositely charged RTIL ions is very strong because no water or other molecules are available for screening. The ions are, therefore, strongly correlated. When cations are attracted to the negatively charged sapphire interface and form the first counterion layer, their strongly associated anions are carried along. These anions are repelled from the negatively charged sapphire, so a checkerboard arrangement of cations and anions is not possible within the first sapphire-adjacent ion layer and the anions form a second charged layer above the first cation one. Such correlations lead also to other apparently counterintuitive phenomena like charge inversion (*25*, *26*) and attraction between like-charged objects (*27*, *28*). They also stabilize alternately charged polyelectrolyte multilayers (*29*), which, however, are created artificially and are stabilized by kinetic barriers only. In contrast, the ionic multilayers reported here self-assemble spontaneously and are thermodynamic-equilibrium structures. The theoretical study of highly correlated ionic systems is still in its infancy, and a general theory, akin to those based on the Poisson-Boltzmann equation for uncorrelated ions, is not currently available for a quantitative theoretical comparison with our results (*25*, *26*).

Our measurements reveal the existence of pronounced molecular layering of FAP-based RTILs at an Al_2O_3 (0001) interface. Molecular dynamics simulations of the structure of a much simpler RTIL with a large size difference between the anion and the cation have produced density profiles in slit pores that are similar to the ones observed in our experiments (*30*, *31*). By using Lennard-Jones potentials for the dispersion interactions of the molecules, as well as for the wall-molecule interaction, a clear separation of the anions and cations into double layers was observed in the simulations. A very recent simulation of a RTIL near a graphite surface (*32*) also found a distinct alternate-ion layering of the type reported here, albeit only for the first three ionic layers rather than the five to six layers observed here. This difference may stem from the fact that the sapphire is charged, whereas the simulated graphite is not. Clearly, simulations of more complex RTILs, without confinement effects and using more realistic force fields, are called for to achieve a fuller understanding of the physical behavior of RTILs at a single-charged hard wall, which is a prerequisite for the rational design of RTILs for applications.

References and Notes

1. P. Walden, *Bull. Acad. Imper. Sci. St. Petersbourg* **8**, 405 (1914).
2. P. Wasserscheid, T. Welton, *Ionic Liquids in Synthesis* (Wiley-VCH, Weinheim, Germany, 2007).
3. T. Welton, *Chem. Rev.* **99**, 2071 (1999).
4. L. A. Blanchard, D. Hancu, E. J. Beckman, J. F. Brennecke, *Nature* **399**, 28 (1999).
5. H. Zhao, J. E. Holladay, H. Brown, Z. C. Zhang, *Science* **316**, 1597 (2007).
6. M. J. Earle *et al.*, *Nature* **439**, 831 (2006).
7. U. Bach *et al.*, *Nature* **395**, 583 (1998).
8. P. Wang, S. M. Zakeeruddin, P. Comte, I. Exnar, M. Grätzel, *J. Am. Chem. Soc.* **125**, 1166 (2003).
9. E. F. Borra *et al.*, *Nature* **447**, 979 (2007).
10. R. D. Rogers, K. R. Seddon, *Science* **302**, 792 (2003).
11. I. Krossing, J. M. Slattery, *Z. Phys. Chem.* **220**, 1343 (2006).
12. L. Crowhurst, N. L. Lancaster, J. M. P. Arlandis, T. Welton, *J. Am. Chem. Soc.* **126**, 11549 (2004).
13. E. Sloutskin *et al.*, *J. Am. Chem. Soc.* **127**, 7796 (2005).
14. C. S. Santos, S. Rivera-Rubero, S. Dibrov, S. Baldelli, *J. Chem. Phys. C* **111**, 7682 (2007).
15. J. Bowers, M. C. Vergara-Gutierrez, *Langmuir* **20**, 309 (2004).
16. A. Carmichael, C. Hardacre, J. D. Holbrey, M. Nieuwenhuyzen, K. R. Seddon, *Mol. Phys.* **99**, 795 (2001).
17. N. V. Ignat'ev, U. Welz-Biermann, A. Kucheryna, G. Bissky, H. Willner, *J. Fluor. Chem.* **126**, 1150 (2005).
18. H. Reichert, V. Honkimäki, A. Snigirev, S. Engemann, H. Dosch, *Physica B* **336**, 46 (2003).
19. J. Als-Nielsen, D. McMorrow, *Elements of Modern X-ray Physics* (Wiley, New York, 2001).
20. M. Mezger *et al.*, *Proc. Natl. Acad. Sci. U.S.A.* **103**, 18401 (2006).
21. O. M. Magnussen *et al.*, *Phys. Rev. Lett.* **74**, 4444 (1995).
22. M. J. Regan *et al.*, *Phys. Rev. B* **55**, 15874 (1997).
23. L. Ingber, *Math. Comput. Model.* **18**, 29 (1993).
24. In addition, we have studied systematically radiation damage effects at the interface. All experiments reported here were performed under conditions excluding radiation damage.
25. A. Y. Grosberg, T. T. Nguyen, B. I. Shklovskii, *Rev. Mod. Phys.* **74**, 329 (2002).
26. A. Shafir, D. Andelman, *Eur. Phys. J. E* **19**, 155 (2006).
27. B. Ha, A. J. Li, *Phys. Rev. Lett.* **79**, 1289 (1997).
28. Y. G. Chen, J. D. Weeks, *Proc. Natl. Acad. Sci. U.S.A.* **103**, 7560 (2006).
29. G. Decher, *Science* **277**, 1232 (1997).
30. R. M. Lynden-Bell *et al.*, *Acc. Chem. Res.* **40**, 1138 (2007).
31. C. Pinilla, M. G. Del Popolo, J. Kohanoff, R. M. Lynden-Bell, *J. Phys. Chem. B* **111**, 4877 (2007).
32. S. Maolin *et al.*, *J. Chem. Phys.* **128**, 134504 (2008).

33. This work was supported by the German-Israeli Foundation for Scientific Research and Development (no. I 779-42.10/2003), the U.S.–Israel Binational Science Foundation (Jerusalem), the Division of Materials Science of the U.S. Department of Energy under contract no. DE-AC02-98CH10886, and the Australian Research Council Special Research Centre Scheme.

11 August 2008; accepted 8 September 2008
10.1126/science.1164502

Evolution of Block Copolymer Lithography to Highly Ordered Square Arrays

Chuanbing Tang,[1] Erin M. Lennon,[1,2] Glenn H. Fredrickson,[1,2,3]* Edward J. Kramer,[1,2,3]* Craig J. Hawker[1,3,4]*

The manufacture of smaller, faster, more efficient microelectronic components is a major scientific and technological challenge, driven in part by a constant need for smaller lithographically defined features and patterns. Traditional self-assembling approaches based on block copolymer lithography spontaneously yield nanometer-sized hexagonal structures, but these features are not consistent with the industry-standard rectilinear coordinate system. We present a modular and hierarchical self-assembly strategy, combining supramolecular assembly of hydrogen-bonding units with controlled phase separation of diblock copolymers, for the generation of nanoscale square patterns. These square arrays will enable simplified addressability and circuit interconnection in integrated circuit manufacturing and nanotechnology.

One of the main limitations in the manufacture of integrated circuits is the difficulty in scaling the photolithographic techniques currently used during fabrication of complementary metal oxide semiconductor transistors to below 30 nm (*1*, *2*). One promising technique to achieve this scaling is block copolymer (BCP) lithography, which affords feature sizes that are dictated by the molecular weight of the block copolymer and are typically 10 to 30 nm (*3*–*8*). BCP lithography was recently used in the development of air-gap technology, in which hexagonal arrays of cylindrical pores are combined with photolithography to create multiple levels of porous dielectric nanostructures (*9*). Although BCP lithography is attractive because it can be done under simplified processing conditions with no requirement for expensive projection tools, a number of challenges exist (*10*). These include the development of strategies for producing a wide range of nanoscale patterns—for example, easily obtained hexagonal arrays as well as square arrays that are compatible with semiconductor integrated circuit design standards (*11*)—and of methods for controlling long-range order in the self-assembled BCP structures (*12*, *13*).

To address these challenges, we have focused on the fabrication of highly ordered square arrays of sub–20-nm features, without the need for an underlying square chemical pattern (*14*). For bulk materials, the traditional approach to preparing more complex self-assembled structures from block copolymers has been to progress from A-B diblock copolymers to more sophisticated A-B-C triblock copolymer systems. Multistep control of the precise composition of each segment of such A-B-C triblock copolymers, combined with the intricacies of controlling their thin-film morphologies, prompted our investigation into a simplified, modular approach to defining nanoscale features in polymeric thin films. In terms of modularity, simple blending of different diblock copolymers, such as A-B/B-C and A-B/C-D alloys, would seem to be attractive for combining physical properties and broadening the processing window (*15*–*17*). However, uniform long-range order has not been achieved in thin-film blends of block copolymers (*18*) because of the overwhelming tendency of such mixtures to exhibit macrophase separation (*19*–*22*).

In an attempt to limit macrophase separation in these blends, we have exploited supramolecular (H-bonding) interactions in addition to the nonspecific dispersive interactions typically present in a copolymer alloy (*23*, *24*). These attractive interactions between complementary H-bonding groups are designed to suppress macrophase separation in favor of microphase separation, thereby producing large-scale assembly of nanoscale features. By controlling the level of incorporation of H-bonding units, the molecular weights and compositions of the block copolymers, and the relative amounts of the two block copolymers in the alloy, a highly modular and tunable system can be developed that allows diverse families of ordered features to be achieved, including square arrays of cylinders.

The block copolymers were based on poly(ethylene oxide)-*b*-poly(styrene) (PEO-*b*-PS) and poly(styrene)-*b*-poly(methyl methacrylate) (PS-*b*-PMMA). Such a blend system combines the photodegradability of PMMA with the long-range ordering characteristics of the PEO block copolymer under solvent annealing at controlled humidity (*25*), as demonstrated by earlier work on PEO-*b*-PMMA-*b*-PS triblock copolymers (*26*). The respective PS segments were modified with small fractions of randomly incorporated 4-hydroxystyrene and 4-vinylpyridine units (*26*). Diblock copolymers of poly(ethylene oxide)-*b*-poly(styrene-*r*-4-hydroxystyrene) [PEO-*b*-P(S-*r*-4HS), denoted as A-B] and poly(styrene-*r*-4-vinylpyridine)-*b*-poly(methyl methacrylate) [P(S-*r*-4VP)-*b*-PMMA), denoted as B′-C] (Fig. 1) with B and B′ blocks as the majority segments in each copolymer were prepared using controlled free-radical polymerizations (for synthesis and characterization, see figs. S1 to S5). This allows the molecular weight of each block to be accurately controlled and the level of incorporation of the H-bonding units to be tailored by simple random copolymerization. A

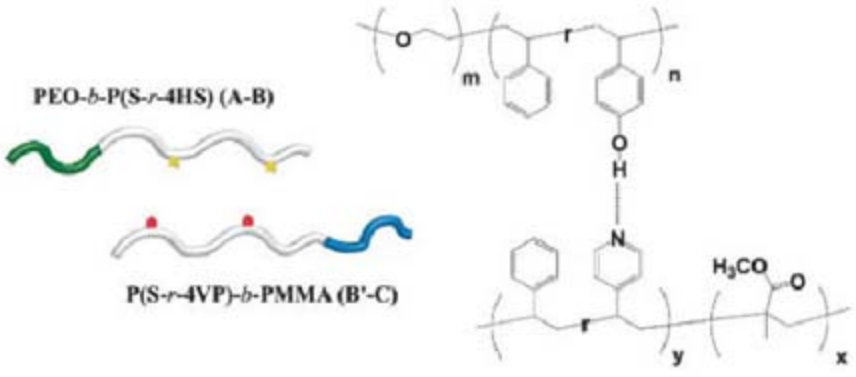

Fig. 1. Hierarchical self-assembly and target morphology for a blend of supramolecular A-B and B′-C diblock copolymers stabilized by H-bonding.

Table 1. Molecular weight and compositions of A-B and B′-C block copolymers (the last digit of each sample name denotes the average number of H-bonding units per chain). DP is the degree of polymerization for each of the components.

PEO-*b*-P(S-*r*-4HS)	DP_{EO}:DP_S:DP_{4HS}	f_{PEO} (wt %)	f_{PS} (wt %)	f_{P4HS} (wt %)
1) A-B_7	113:147:7	23.8	72.4	3.8
P(S-*r*-4VP)-*b*-PMMA	DP_{MMA}:DP_S:DP_{4VP}	f_{PMMA} (wt %)	f_{PS} (wt %)	f_{P4VP} (wt %)
2a) B′-C_6	120:220:6	33.7	64.4	1.9
2b) B′-C_8	120:195:8	36.3	61.3	2.4
2c) B′-C_14	120:188:14	36.4	59.1	4.5
2d) B′-C_25	120:219:25	32.1	61.0	6.9

[1]Materials Research Laboratory, University of California, Santa Barbara, CA 93106, USA. [2]Department of Chemical Engineering, University of California, Santa Barbara, CA 93106, USA. [3]Department of Materials, University of California, Santa Barbara, CA 93106, USA. [4]Department of Chemistry and Biochemistry, University of California, Santa Barbara, CA 93106, USA.

*To whom correspondence should be addressed. E-mail: hawker@mrl.ucsb.edu (C.J.H.); edkramer@mrl.ucsb.edu (E.J.K.); ghf@mrl.ucsb.edu (G.H.F.)

representative selection of diblock copolymers is shown in Table 1. Initially, the number of H-bonding units in the respective polystyrene blocks was kept low to minimize the chemical difference between the blocks while still enabling an overall attraction characterized by a negative Flory-Huggins parameter ($\chi < 0$).

Supramolecular block copolymer films, ~50 nm thick, were prepared by spin-coating polymer solutions in benzene onto silicon wafers, with the blends formulated by simply mixing the phenolic containing PEO A-B diblock, **1**, with the corresponding PMMA B′-C diblock, **2**, containing various levels of 4-vinylpyridine substitution. In these samples, a 1:1 molar ratio of A-B chains to B′-C chains was maintained and the films were solvent-annealed under saturated toluene vapor in a controlled high-humidity atmosphere (*26*, *27*). Figure 2 shows the atomic force microscopy (AFM) phase images of films from four representative blends, which indicate that the nanoscale morphology and grain size are affected by the composition of H-bonding components. For a blend of **1** with **2d** (ratio of phenolic groups to pyridyl groups is approximately 1:3.5), vertical cylinders were obtained, but little order, either hexagonal or square packing, was observed (Fig. 2D). Upon decreasing the phenolic:pyridyl ratio to 1:2, distinct square arrays were observed, although the ordering was poor (Fig. 2C). However, for blends with approximately equal numbers of phenolic and pyridyl units per chain, the corresponding thin films exhibited square arrays with a high degree of in-plane order. In the case of the blend of **1** and **2a**, an extremely high degree of ordering was observed, with grains of the square array morphology that were larger than 5 μm by 5 μm (Fig. 2A).

To confirm the critical role of supramolecular interactions in these systems, we examined control samples that did not have H-bonding interactions: blends of the parent polymers, PEO-*b*-PS/PS-*b*-PMMA, and blends where the phenolic unit was exchanged for an acetoxy group, PEO-*b*-P(S-*r*-4AS)/P(S-*r*-4VP)-*b*-PMMA. In each case, blends prepared using the same solvent-annealing procedure showed macrophase-separated structures with no long-range order (fig. S6). In the case of PEO-*b*-P(S-*r*-4AS)/P(S-*r*-4VP)-*b*-PMMA, we found small regions with nanoscale morphology; however, these showed hexagonal local order. The lack of uniform microphase-separated structures in these systems is not surprising and is consistent with previous studies of diblock copolymer blends (*19*–*22*). These control experiments demonstrate the critical role of supramolecular interactions in producing both long-range order and novel square arrays of nanoscale features.

The presence of square arrays of features for the blend of **1** and **2a** with near-stoichiometric numbers of H-bonding units was confirmed by a series of studies. The film-substrate interface was examined by etching the underlying oxide and lifting the polymer film off the substrate, followed by flipping and imaging by AFM (figs. S7 and S8). We observed square arrays of features with similar periodicity for the substrate interface, which suggests a perpendicular cylindrical structure spanning the entire thickness of a film. Transmission electron microscopy (TEM) images of the solvent-annealed films (Fig. 3) confirmed the square array of cylinders. A highly ordered square lattice was observed with distinct contrast between bright features, gray features, and a dark matrix (no stain was used). Further observation of the films revealed that each gray domain is surrounded by four white domains and vice versa. The dark, continuous regions are presumably PS, whereas the PMMA domains (which undergo degradation under electron beam irradiation, leading to enhanced Z-contrast with the matrix) appear white when compared to the gray regions, which correspond to PEO domains. The center-to-center spacing of the square arrays corresponds to 51 nm, which is in very good agreement with the AFM measurements.

We used numerical self-consistent field theory (SCFT) (*28*) to examine the stability of tetragonal cylinder packing in this system. In previous studies of symmetrical (bulk) ABC triblock copolymers, square lattices were experimentally observed by Mogi *et al.* (*29*, *30*) and the energetic preference of square over hexagonal cylinder packing was theoretically verified using SCFT (*31*). Applying similar methods, we examined a model A-B/B′-C diblock copolymer blend in which the supramolecular interactions are described by a simple (nonspecific) contact attraction between B and B′ segments. The diblocks were assumed to be 70% B (or B′) by volume and of equal overall molecular weight. The products of the chain length N and the segmental Flory interaction parameters were fixed at $\chi_{AB}N = \chi_{AB'}N = \chi_{B'C}N = \chi_{BC}N = 14$, $\chi_{BB'}N = -3.5$, and $\chi_{AC}N = 55$. Earlier studies indicated that during solvent annealing under high-humidity conditions, water absorption into the PEO domains increases the effective χ between PEO and PMMA segments, hence the relatively large value of $\chi_{AC}N$ used in the model (*27*, *32*). Large-cell SCFT simulations of this model launched from random initial conditions revealed no evidence of macrophase separation or hexagonal cylinder packings. In all cases, microphase-separated morphologies with well-ordered square lattices of A and C cylinders were obtained.

Figure 4 shows the microdomain structure and density plots from such a simulation. The A and C blocks (red and black) form cylinders with coronas of B and B′ (yellow and blue), respectively. The green polymer matrix reflects regions where the yellow B and blue B′ blocks are intermixed. Similar to ABC triblock copolymers, unit-cell simulations reveal that square-packed cylinders in the A-B/B′-C system have a lower free energy density than do hexagonally packed cylinders, which constitute the stable phase in simple AB diblock copolymers. In ABC triblock copolymers, the square lattice allows for a more uniform distribution of the C domains around each A domain (and vice versa), which lessens the stretching penalty of the B blocks despite not providing an optimal close packing of cylinders

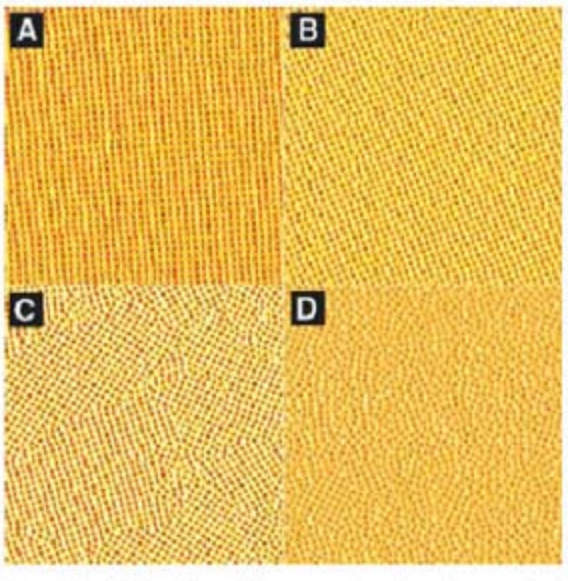

Fig. 2. AFM phase images of solvent-annealed films from blends of supramolecular block copolymers: **(A) 1** and **2a**; **(B) 1** and **2b**; **(C) 1** and **2c**; **(D) 1** and **2d**. Image sizes, 2 μm by 2 μm.

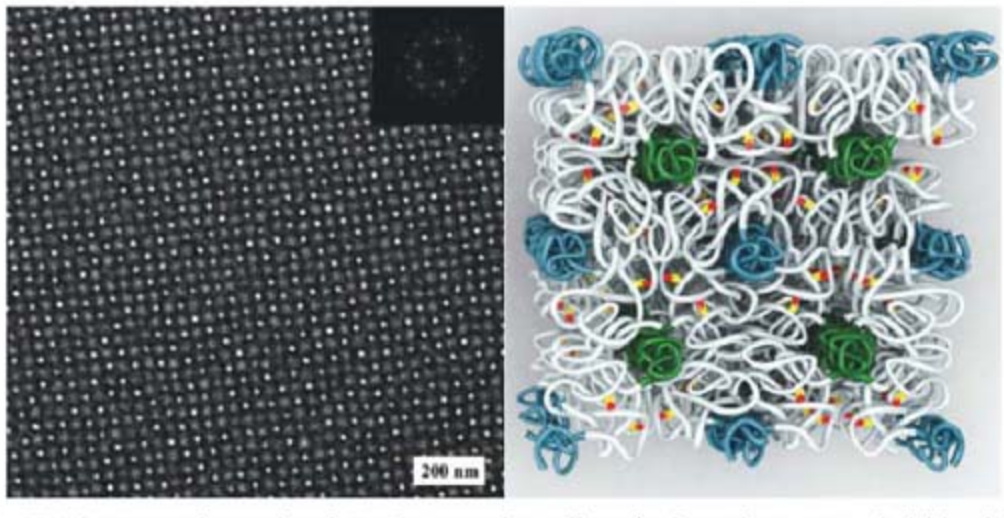

Fig. 3. TEM image and associated Fourier transform (**inset**) of a solvent-annealed blend film of supramolecular block copolymers **1** and **2a**. A cartoon (right panel) illustrates proposed chain packings.

(*31*). Although the A and C blocks do not connect on the same chain in the present blend system, favorable supramolecular interactions between B and B′ blocks mimic triblock-like behavior by encouraging B-B′ segmental mixing at relatively uniform B and B′ block extensions.

Additional evidence for the nanoscale morphology of these self-assembled films was obtained by using these materials as lithographic masks to transfer the template image into the underlying silicon substrate. A schematic route to fabricating square arrays of holes in silicon oxide from a supramolecular block copolymer film is shown in Fig. 5. The film is first irradiated with deep-UV light to degrade the PMMA domains and cross-link the PS matrix. The UV-degraded films served as masks for reactive ion etching (RIE) using CHF_3 to etch the silicon oxide; the remaining organic material was removed by O_2 plasma. Scanning electron microscope (SEM) images are also shown in Fig. 5. In the top-view SEM micrograph, the cylindrical pores from the UV-degraded regions appear darker and have a diameter of ~22 nm. The period of the holes is 50 nm, which is consistent with the AFM results for the nondegraded thin films and demonstrates a high degree of fidelity in the pattern transfer process. Of particular note is the retention of the corresponding features due to the co-registered PEO domains, which lead to small "dimples" due to the topological and etch rate differences between the PEO domains and the polystyrene matrix. Additional confirmation of the formation of cylindrical pores was obtained from the 75° cross-section images, which clearly show the formation of holes with depths of 15 to 20 nm.

By combining supramolecular assembly of H-bonding phenolic and pyridyl units with controlled microphase separation of well-defined diblock copolymers, we have shown that near-stoichiometric ratios of the H-bonding groups are critical for achieving good order as well as controlling the local packing of cylindrical domains. Degradation of the PMMA domains and subsequent etching allowed nanoscale features to be lithographically transferred with high fidelity, leading to highly ordered square arrays of ~20-nm cylindrical pores.

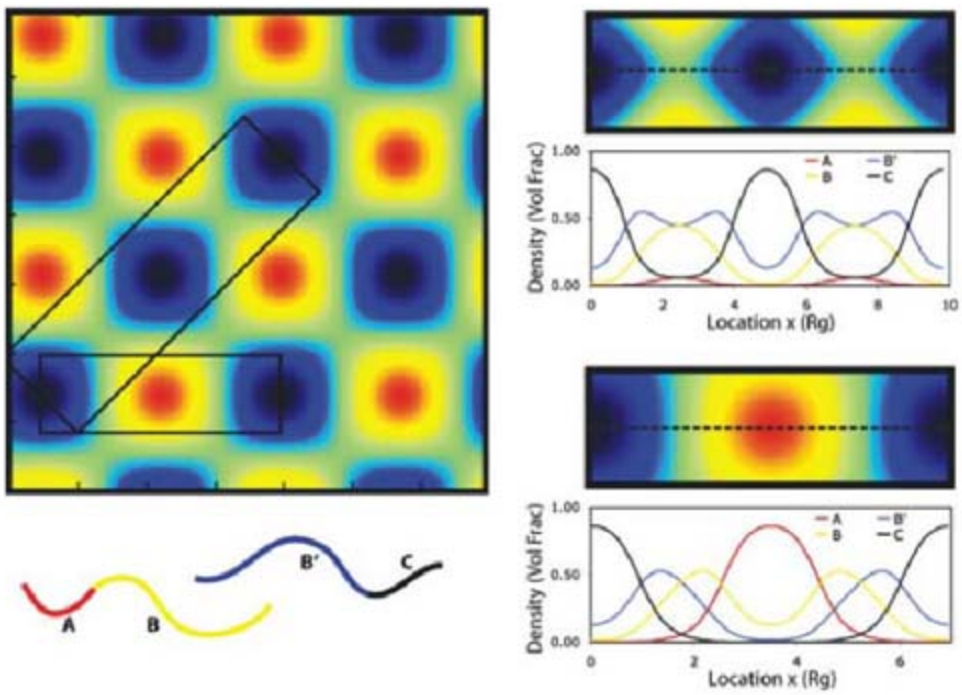

Fig. 4. SCFT simulated morphology and density profiles of an A-B/B′-C diblock copolymer blend. Regions of high A, B, B′ and C density are colored red, yellow, blue, and black, respectively. The green regions represent mixed B and B′. The boxed regions are reproduced at right, with line density profiles taken along the dashed lines.

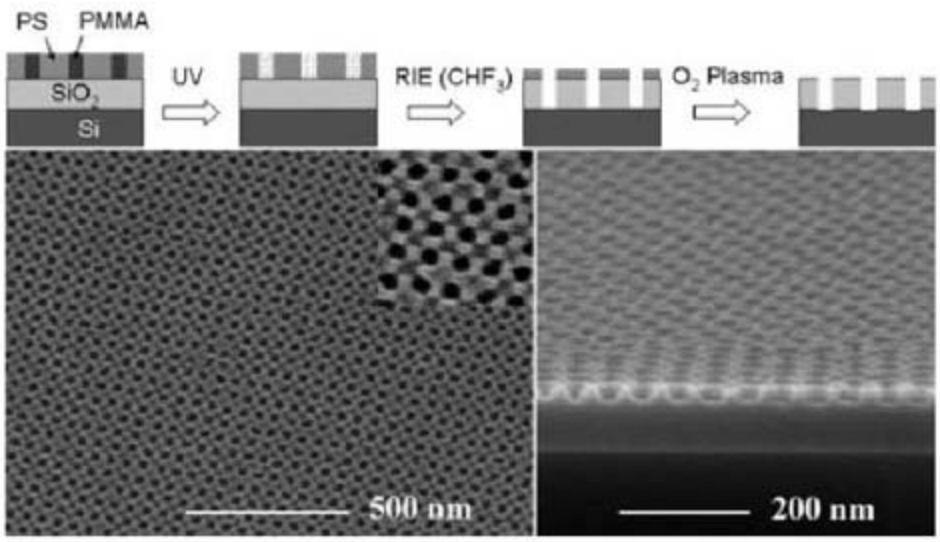

Fig. 5. (**Top**) Schematic representation of pattern transfer from supramolecular block copolymer thin films; PEO domains are omitted for clarity. (**Bottom**) SEM top view and 75° cross-section images of square arrays of cylindrical pores in silicon oxide after RIE and O_2 plasma treatment of a UV-degraded thin-film blend of supramolecular block copolymers **1** and **2a**. (Inset) Magnified SEM top view.

References and Notes

1. C. T. Black *et al.*, *Appl. Phys. Lett.* **79**, 409 (2001).
2. T. Skotnicki, J. A. Hutchby, T. J. King, H. S. P. Wong, F. Beouff, *IEEE Circuits Devices Mag.* **21**, 16 (2005).
3. M. Park, C. Harrison, P. M. Chaikin, R. A. Register, D. H. Adamson, *Science* **276**, 1401 (1997).
4. S. O. Kim *et al.*, *Nature* **424**, 411 (2003).
5. D. Y. Ryu, K. Shin, E. Drockenmuller, C. J. Hawker, T. P. Russell, *Science* **308**, 236 (2005).
6. P. Mansky, Y. Liu, E. Huang, T. P. Russell, C. J. Hawker, *Science* **275**, 1458 (1997).
7. R. A. Segalman, H. Yokoyama, E. J. Kramer, *Adv. Mater.* **13**, 1152 (2001).
8. J. Y. Cheng, C. A. Ross, E. L. Thomas, H. I. Smith, G. J. Vancso, *Appl. Phys. Lett.* **81**, 3657 (2002).
9. S. Hamm, *BusinessWeek Online*, www.businessweek.com/technology/content/may2007/tc20070502_768360.htm?chan=top+news_top+news+index_businessweek+exclusives.
10. International Technology Roadmap for Semiconductors, ITRS 2007 Edition (www.itrs.net/Links/2007ITRS/2007_Chapters/2007_ERM.pdf), pp. 22–26.
11. Square arrays are a major goal because of the considerable investment by the semiconductor industry in circuit design software, fabrication processes, etc., all based on a rectilinear coordinate system. A hexagonal pattern of vias, for example, would require extensive and very expensive reworking of the design software and fabrication protocols, whereas a square array would not. As a result, the Semiconductor Industry Association several years ago posed a challenge to researchers in block copolymer lithography to develop square arrays of etchable block copolymer domain patterns (see www.itrs.net/Links/2007ITRS/LinkedFiles/ERM/DSAR11%20082107.DOC).
12. R. A. Segalman, *Mater. Sci. Eng. Rep.* **R48**, 191 (2005).
13. J. Y. Cheng, C. A. Ross, H. I. Smith, E. L. Thomas, *Adv. Mater.* **18**, 2505 (2006).
14. S.-M. Park, G. S. W. Craig, Y.-H. La, H. H. Solak, P. F. Nealey, *Macromolecules* **40**, 5084 (2007).
15. V. Abetz, T. Goldacker, *Macromol. Rapid Commun.* **21**, 16 (2000).
16. N. Y. Vaidya, C. D. Han, *Macromolecules* **33**, 3009 (2000).
17. H. Mao, P. L. Arrechea, T. S. Bailey, B. J. S. Johnson, M. A. Hillmyer, *Faraday Discuss.* **128**, 149 (2005).
18. T. Asari, S. Matsuo, A. Takano, Y. Matsushita, *Macromolecules* **38**, 8811 (2005).
19. P. D. Olmsted, I. W. Hamley, *Europhys. Lett.* **45**, 83 (1999).
20. H. Frielinghaus *et al.*, *Macromolecules* **34**, 4907 (2001).
21. K. Kimishima, H. Jinnai, T. Hashimoto, *Macromolecules* **32**, 2585 (1999).
22. H. G. Jeon, S. D. Hudson, H. Ishida, S. D. Smith, *Macromolecules* **32**, 1803 (1999).
23. O. Ikkala, G. ten Brinke, *Chem. Commun.* **2004**, 2131 (2004).
24. R. Hoogenboom, D. Fournier, U. S. Schubert, *Chem. Commun.* **2008**, 155 (2008).
25. S. H. Kim, M. J. Misner, T. Xu, M. Kimura, T. P. Russell, *Adv. Mater.* **16**, 226 (2004).
26. J. Bang *et al.*, *J. Am. Chem. Soc.* **128**, 7622 (2006).
27. C. Tang *et al.*, *Macromolecules* **41**, 4328 (2008).

28. The SCFT simulations were run using a pseudo-spectral method with 256^2 spatial collocation points, periodic boundary conditions, and a spatial resolution of 0.05 Rg (radius of gyration) in the x and y directions. As we are primarily interested in the packing of cylinders, uniformity is assumed in the z direction. The free energy per chain was minimized with respect to the box size. The chains were modeled as continuous Gaussian threads and were discretized using 200 contour steps.
29. Y. Mogi *et al.*, *Macromolecules* **25**, 5408 (1992).
30. Y. Mogi *et al.*, *Macromolecules* **27**, 6755 (1994).
31. M. W. Matsen, *J. Chem. Phys.* **108**, 785 (1998).
32. J. Bang *et al.*, *Macromolecules* **40**, 7019 (2007).
33. We thank E. Pressly and M. Dimitriou for synthesis assistance. Supported by the Nanoelectronics Research Initiative under contract RID#1549 (SRC/NRI), the Focus Center Research Program (FCRP) Center on Functional Engineered Nano Architectonics, and NSF under the Materials Research Science and Engineering Center program (UCSB MRL, DMR-0520415).

Supporting Online Material
www.sciencemag.org/cgi/content/full/1162950/DC1
Materials and Methods
Figs. S1 to S8
References

8 July 2008; accepted 5 September 2008
Published online 25 September 2008;
10.1126/science.1162950
Include this information when citing this paper.

The Extreme Kuiper Belt Binary 2001 QW_{322}

J.-M. Petit,[1,3]* J. J. Kavelaars,[2] B. J. Gladman,[3] J. L. Margot,[4] P. D. Nicholson,[4] R. L. Jones,[5] J. Wm. Parker,[6] M. L. N. Ashby,[7] A. Campo Bagatin,[8] P. Benavidez,[8] J. Coffey,[3] P. Rousselot,[1] O. Mousis,[1] P. A. Taylor[4]

The study of binary Kuiper Belt objects helps to probe the dynamic conditions present during planet formation in the solar system. We report on the mutual-orbit determination of 2001 QW_{322}, a Kuiper Belt binary with a very large separation whose properties challenge binary-formation and -evolution theories. Six years of tracking indicate that the binary's mutual-orbit period is ≈25 to 30 years, that the orbit pole is retrograde and inclined 50° to 62° from the ecliptic plane, and, most surprisingly, that the mutual orbital eccentricity is <0.4. The semimajor axis of 105,000 to 135,000 kilometers is 10 times that of other near-equal-mass binaries. Because this weakly bound binary is prone to orbital disruption by interlopers, its lifetime in its present state is probably less than 1 billion years.

A combination of survey strategies and adaptive optics technologies has led to a surge in the discovery rate of binary minor planets. Since 2001, newly discovered binaries in the main asteroid and Kuiper Belts have been announced at the rate of about seven per year (*1*, *2*). There are now more than 100 known binaries, nearly half of which are Kuiper Belt objects (KBOs). Measurements of the frequency of binary objects and their sizes and orbital configurations constrain their formation and evolution mechanisms, theories of planetesimal accretion and disruption, and the collisional history of the Kuiper Belt.

Discovering and studying the mutual orbits of binary systems is currently the only way to directly determine KBO masses. Assuming that the optical properties of the KBO binaries are representative of the whole KBO population, one can link mass to apparent magnitude and hence estimate the total mass of the Kuiper Belt without requiring assumptions on albedo and density. Recent Hubble Space Telescope observations (*3*) indicate that KBOs display a wide range of albedos (8 to 40%, assuming unit density), which complicate the estimation of the total mass of the Kuiper Belt using a luminosity function. Combined with thermal infrared observations, phase-function photometry, or star occultation observations, direct determination of KBO masses leads to the determination of their density and bulk composition.

Here we report the mutual-orbit determination of the large-separation Kuiper Belt binary, 2001 QW_{322} (*4*). This KBO was discovered in data acquired on 24 August 2001 at the Canada-France-Hawaii Telescope by the Canada-France Ecliptic Plane Survey team. The two components had identical magnitudes of $m_R \simeq 24.0$ within the measurement uncertainties, implying essentially equal sizes. Only one other equal-component binary was known at the time, asteroid (90) Antiope, with a magnitude difference of ~0.1 mag (*5*). However, 2001 QW_{322} was obviously exceptional because the measured separation of ~4″ at its distance of 43 astronomical units (AU) corresponds to a sky-projected physical separation of 125,000 km (about one-third of the distance from Earth to the Moon), far larger than any other small-body binary.

The large separation implied a mutual-orbit period of at least several years. Six years of tracking with the use of 4- to 8-m class telescopes (Fig. 1) resolved that 2001 QW_{322}, an object in the main classical Kuiper Belt (*6*), has a low-eccentricity mutual orbit with a separation of 105,000 to 135,000 km, greater than any other

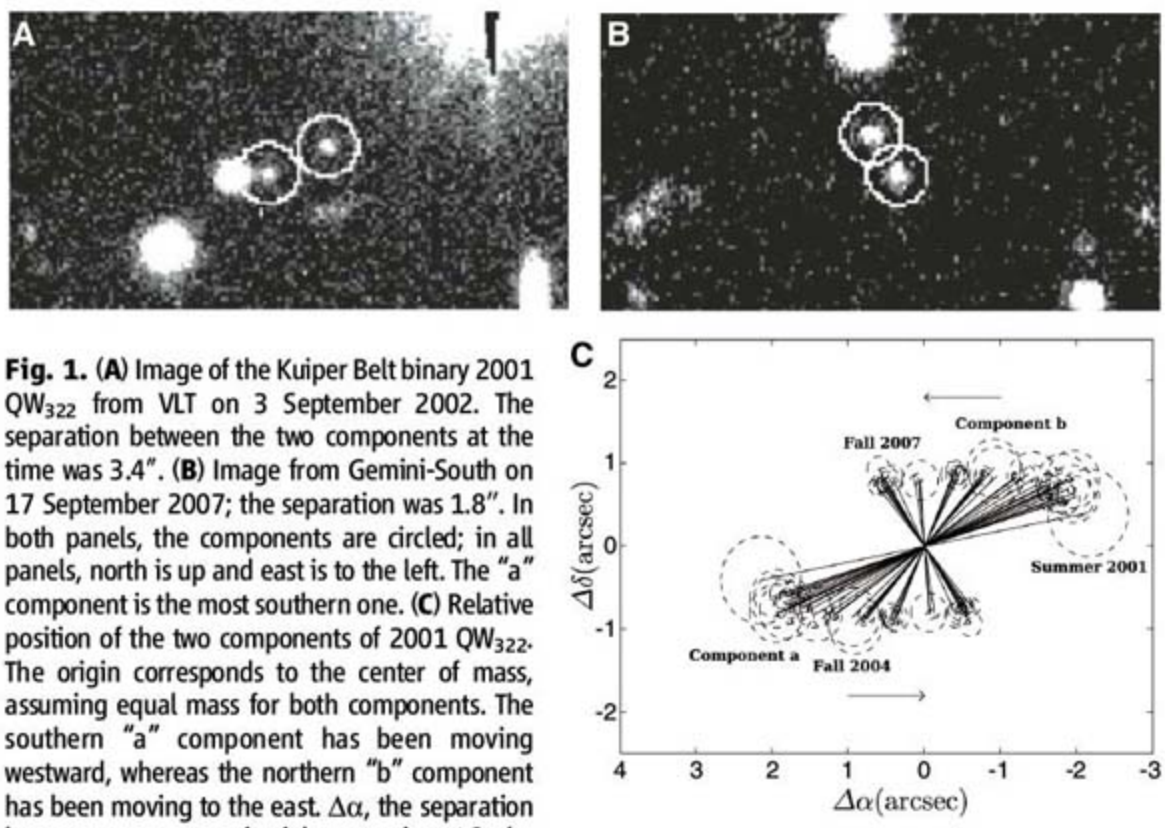

Fig. 1. (**A**) Image of the Kuiper Belt binary 2001 QW_{322} from VLT on 3 September 2002. The separation between the two components at the time was 3.4″. (**B**) Image from Gemini-South on 17 September 2007; the separation was 1.8″. In both panels, the components are circled; in all panels, north is up and east is to the left. The "a" component is the most southern one. (**C**) Relative position of the two components of 2001 QW_{322}. The origin corresponds to the center of mass, assuming equal mass for both components. The southern "a" component has been moving westward, whereas the northern "b" component has been moving to the east. $\Delta\alpha$, the separation between components in right-ascension; $\Delta\delta$, the separation of declination.

[1]Observatoire de Besançon, Universite de Franche Comte, Besancon, Doubs 25010, France. [2]Herzberg Institute of Astrophysics, National Research Council, Victoria, BC V9E 2E7, Canada. [3]Department of Physics and Astronomy, University of British Columbia, Vancouver, BC V6T 1Z1, Canada. [4]Department of Astronomy, Cornell University, Ithaca, NY 14853, USA. [5]Department of Astronomy, University of Washington, Seattle, WA 98195–1580, USA. [6]Southwest Research Institute, Boulder, CO 80302–5150, USA. [7]Harvard-Smithsonian Center for Astrophysics, Cambridge, MA 02138, USA. [8]Escuela Politecnica Superior, University of Alicante, Alicante 03080, Spain.

*To whom correspondence should be addressed. E-mail: petit@obs-besancon.fr

known minor-planet binary (*7*). The separation is so large that this nearly equal-mass binary should be incredibly fragile to dynamical disruption, and its continued existence in the middle of the main Kuiper Belt puts strong constraints on the history of the Belt (*8*).

Within the roughly 0.1-magnitude observational uncertainties at discovery, the two components had identical brightnesses, a finding confirmed in 2002 (*9*). Assuming identical albedos, object size is proportional to the square root of flux, so it is unclear which component is the largest (and thus the primary). We therefore obtained higher-precision photometric observations from 8-m class telescopes [Very Large Telescope (VLT), Gemini-North, and Gemini-South] between 2002 and 2007, including broadband colors in *R*-band (~570 to ~750 nm), *I*-band (~720 to ~880 nm), and *V*-band (~500 to ~600 nm) filters (tables S1 to S3). From these data, it appears that the relative magnitudes of the two components are essentially the same in all measured colors; the color similarity implies a surface similarity that strengthens the assumption of equal albedos. The plentiful *R*-band data give a mean relative magnitude $m_b - m_a = -0.03 \pm 0.02$. For what follows, we therefore take the two components to have the same physical size. Using the magnitude $r_{G0303} = 23.7$ for both components (measured at a geocentric distance of $\Delta = 43.4$ AUs), we derive a radius of $r = 54$ km for an assumed *R*-band albedo $p = 0.16$. The color of 2001 QW_{322} is on the blue extreme of the color distribution of the cold classical Kuiper Belt (*10*) or the Kuiper Belt core (*11*). At the 1σ confidence level, both components could have a light curve of amplitude ~0.4 magnitude, but no rotation period could be derived.

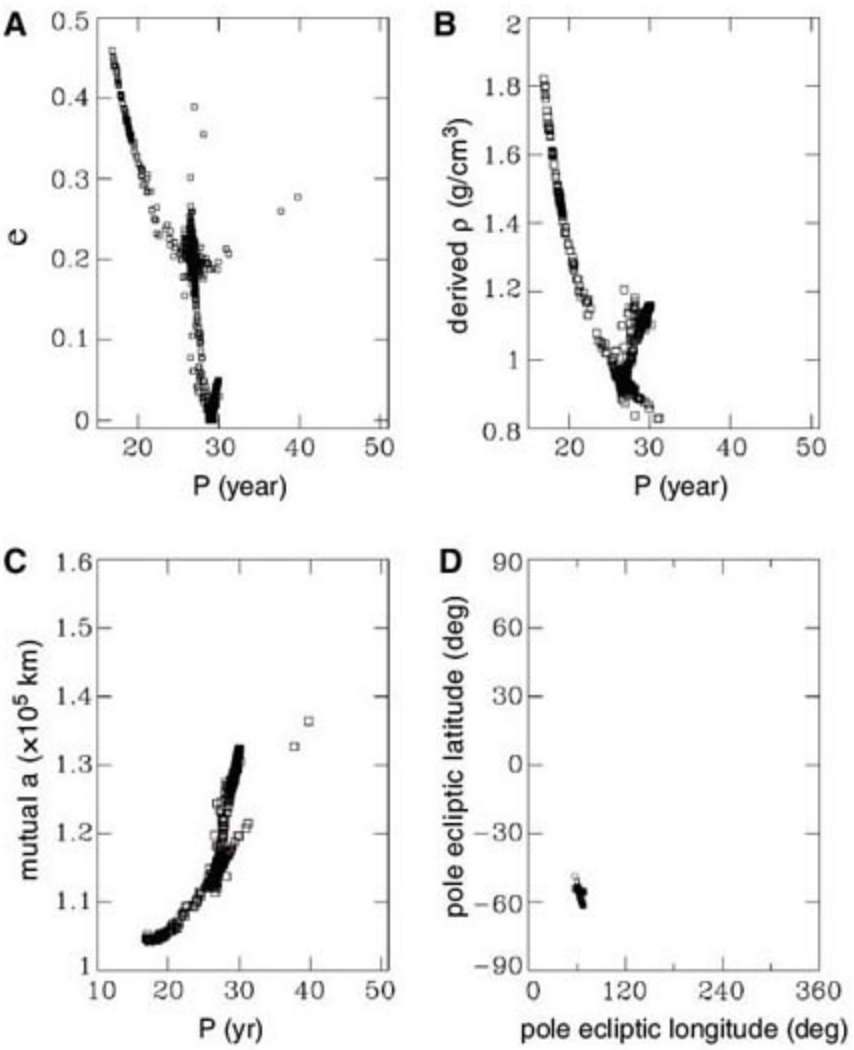

Fig. 2. Range of plausible orbital parameters and densities for 2001 QW_{322}. These have been obtained by nonlinear minimization of χ^2 statistics, starting from several thousand initial conditions, retaining only those solutions with a reduced χ^2 value that is close enough to the overall best fit, as explained in (*7*). The fitted parameters are the binary's *P*, *a*, *e*, pole orientation, and argument of pericenter. *e* (**A**), ρ (**B**), and *a* (**C**) are given as a function of the period, and the pole's ecliptic latitude versus its ecliptic longitude is shown in (**D**). The density was derived assuming a radius for each component of 54 km. (D) The precision with which the mutual-orbit pole is now known on the sky is shown.

We measured (table S4) right ascension and declination of the center of mass (assuming equal mass components) of the binary, along with position angle and separation between components (Fig. 1). Fits to the astrometric measurements up to and including 2006 were equally consistent with a large-eccentricity mutual orbit either pole-aligned or anti-aligned with the line of sight, as well as a low-eccentricity orbit viewed nearly edge-on. Additional measurements were acquired in October 2006 (from Gemini-South) and fall 2007 [September from Gemini-South, October from VLT, and November from Multi Mirror Telescope (MMT) and VLT], which ruled out nearly all $e > 0.3$ solutions (where *e* is eccentricity). This observation is surprising, as it is difficult to imagine how to bind two small bodies that never come closer to each other than a distance of 85,000 km. The mutual orbit of 2001 QW_{322} is retrograde, with a pole's ecliptic latitude between –50° and –62°, and is viewed somewhat edge-on (inclined at 55° to 70° to the line of sight).

Three main groups of acceptable orbits remain: (i) one group with $e \approx 0.2$, $a \approx 114{,}000$ km, $P \approx 27$ years, and $\rho \approx 0.94$ g cm^{-3}; (ii) another group with nearly circular orbits $e \lesssim 0.05$, $a \approx 128{,}000$ km, $P \approx 29$ years, and $\rho \approx 1.11$ g cm^{-3}; and (iii) a smaller group with $e \lesssim 0.4$, $a \approx 105{,}000$ km, $P \approx 18$ years, and $\rho \approx 1.6$ g cm^{-3} (where *a* is the semimajor axis; *P* is the orbital period; and ρ is density) (Fig. 2). We mildly prefer the non-circular orbits, which have a goodness-of-fit that is 10% better than that for the nearly circular group. The stability region for binary orbits can be expressed in terms of the ratio a/R_H, where R_H is the Hill radius (*7*), with prograde orbits becoming instable for $a/R_H > 0.3$ to 0.4 (*12*), whereas the limit of stability of retrograde orbits is 0.5 to 0.6. This may explain why the first such system was found to be retrograde. It also indicates that 2001 QW_{322} is very fragile to disruption, as mentioned in (*8*). For our acceptable orbits, a/R_H varies mostly between 0.27 and 0.32, with the first group of orbits centered at 0.29 and the second group centered at 0.31.

According to Kepler's third law, the total mass of the binary is 0.9×10^{18} to 2.4×10^{18} kg; and most of the estimated values are between

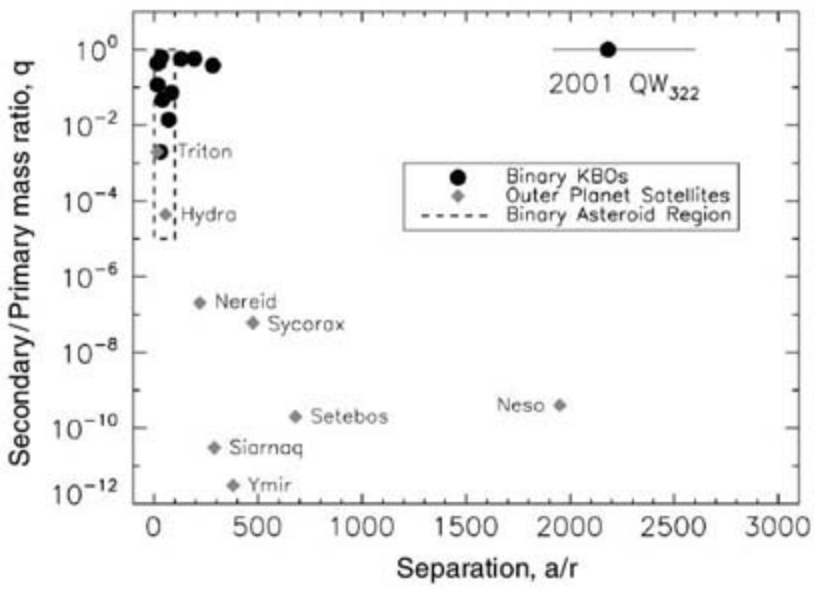

Fig. 3. Secondary-to-primary mass ratio versus average separation (in units of the primary's radius). The dashed box represents the known binary asteroids, all on the left side of the plot (the largest separation barely exceeds 100). Also shown are the most-extreme, outer-planet irregular satellites and several other binary KBOs. The mass ratio *q* is estimated from the published difference in magnitude between the components, assuming an equal albedo and density for both components. The error bar on the separation for 2001 QW_{322} accounts only for the uncertainty in the estimated *a*; it does not account for the (unlikely) possibility that the radius could be off by up to a factor of 2. Nevertheless, with equal mass component and a separation that is more than 2000 times the radius of each component, 2001 QW_{322} clearly stands out in the top-right corner of this diagram as the widest-orbit, near-equal-mass binary of the solar system.

1.1×10^{18} and 1.5×10^{18} kg. With the photometrically derived nominal size of $r = 54$ km for each component (assumed albedo of 0.16), the density of 2001 QW_{322} (Fig. 2B) is probably 0.8 to 1.2 g cm^{-3}. This is a little higher than that of comparably sized outer solar system bodies [figure 5 of (*13*); 0.6 to 0.8 g cm^{-3}]. Our nominal albedo of 0.16 is approximately double that estimated from optical and thermal infrared photometry for similar-size KBOs (*14*, *15*) but about a factor of 2 below that of (58534) Logos/Zoe ($p = 0.37 \pm 0.04$) (*2*), which is of comparable size. Estimated density from eqs. S2 and S3 is proportional to the assumed albedo to the power of $^3/_2$. Halving our albedo would increase our radius estimates by $\sqrt{2}$ and decrease the estimated density by a factor of $2^{3/2} = 2.8$, below the range of published densities (*13*) for such small bodies.

The nominal densities shown in Fig. 2 are at the boundary between the density of a low-porosity, pure-water ice body and that of a mixture of water ice and silicate rocks (*13*). A thermal detection, mutual eclipse, or stellar occultation by the binary (all unlikely) would be necessary to further constrain the size, albedo, density, and hence the bulk composition of 2001 QW_{322}.

Given the very large separation (Fig. 3), such a binary is difficult to create and maintain. Of all the proposed KBO binary-formation scenarios (*16*–*19*), only the collision of two bodies close to a third one (*16*) can simply explain the primordial formation of such a system (*7*).

A study of the long-term stability of the large-separation KB binaries (*8*) led to the conclusion that the major destabilizing factor is unbinding due to direct collisions of impactors on the secondary. Applying their method to the newly determined orbital and physical parameters for 2001 QW_{322} and our nominal albedo, we find that the lifetime of this binary is 0.3 to 1 billion years, which is two to three times shorter than the previous estimate. This finding implies one of two things: (i) Either 2001 QW_{322} was created with its current mutual orbit early in the history of the solar system, in which case it is one of the few survivors of a population at least 50 to 100 times larger, or (ii) this is a transitory object, evolving because of perturbation from interactions with smaller KBOs, from a population of more tightly bound binaries. Asserting this latter hypothesis would require better orbital statistics for moderately large KB binaries (separation of 1 to 2″).

For the likely mutual-orbit parameters, the average orbital speed is $\langle v \rangle \simeq 0.85$ m/s or a mere 3 km hour^{-1}, a slow human walking pace. An observer standing on one of the components (a very precarious situation, as the gravity is only 0.02 m/s^2 or nearly 600 times smaller than on Earth) would see the other component subtend an angle of only 3 arc min, which corresponds to a pinhead seen at arm's length. The existence of the other component would not be in doubt, however, because when viewed at full phase it would be as luminous as Saturn seen from Earth, and it would move perceptibly from week to week.

References and Notes

1. W. J. Merline *et al.*, in *Asteroids III*, W.F. Bottke Jr., A. Cellino, P. Paolicchi, R.P. Binzel, Eds. (Univ. of Arizona Press, Tucson, AZ, 2002), pp. 289–312.
2. K. S. Noll, W. M. Grundy, E. I. Chiang, J. L. Margot, S. D. Kern, in *The Solar System Beyond Neptune*, A. Barucci, H. Boehnhardt, D. Cruikshank, A. Morbidelli, Eds. (Univ. of Arizona Press, Tucson, AZ, 2008), pp. 345–363.
3. J. L. Margot, M. E. Brown, C. A. Trujillo, R. Sari, J. A. Stansberry, *Bull. Am. Astron. Soc.* **37**, 737 (2005).
4. J. J. Kavelaars, J.-M. Petit, G. Gladman, M. Holman, *IAU Circ.* **7749**, 1 (2001).
5. W. J. Merline *et al.*, *Bull. Am. Astron. Soc.* **32**, 1017 (2000).
6. B. Gladman, B. G. Marsden, C. Van Laerhoven, in *The Solar System Beyond Neptune*, A. Barucci, H. Boehnhardt, D. Cruikshank, A. Morbidelli, Eds. (Univ. of Arizona Press, Tucson, AZ, 2008), pp. 43–57.
7. See supporting online material text.
8. J.-M. Petit, O. Mousis, *Icarus* **168**, 409 (2004).
9. J. Burns, V. Carruba, B. Gladman, B.G. Marsden, *Minor Planet Electron. Circ.* **L30**, 1 (2002).
10. O. R. Hainaut, A. C. Delsanti, *Astron. Astrophys.* **389**, 641 (2002).
11. A. A. S. Gulbis, J. L. Elliot, J. F. Kane, *Icarus* **183**, 168 (2006).
12. D. Nesvorný, J. L. A. Alvarellos, L. Dones, H. F. Levison, *Astron. J.* **126**, 398 (2003).
13. W. M. Grundy *et al.*, *Icarus* **191**, 286 (2007).
14. J. A. Stansberry *et al.*, *Astrophys. J.* **643**, 556 (2006).
15. J. R. Spencer, J. A. Stansberry, W. M. Grundy, K. S. Noll, *Bull. Am. Astron. Soc.* **38**, 546 (2006).
16. S. J. Weidenschilling, *Icarus* **160**, 212 (2002).
17. P. Goldreich, Y. Lithwick, R. Sari, *Nature* **420**, 643 (2002).
18. Y. Funato, J. Makino, P. Hut, E. Kokubo, D. Kinoshita, *Nature* **427**, 518 (2004).
19. S. A. Astakhov, E. A. Lee, D. Farrelly, *Mon. Not. R. Astron. Soc.* **360**, 401 (2005).

20. This work was partially supported by NASA/Planetary Astronomy Program grant NNG04GI29G. A.C.B. also acknowledges support from Ministerio de Educacion y Ciencia (Spain), National project n. AYA2005-07808-C03-03. J.L.M. was partially supported by grant NNX07AK68G from the NASA Planetary Astronomy program. This research used the facilities of the Canadian Astronomy Data Centre operated by the National Research Council of Canada with the support of the Canadian Space Agency. The Canada-France-Hawaii Telescope is operated by the National Research Council of Canada, the Institut National des Sciences de l'Univers of the Centre National de la Recherche Scientifique of France, and the University of Hawaii. Observations at Palomar Observatory are carried out under a collaborative agreement between Cornell University and the California Institute of Technology. Observations made with European Southern Observatory Telescopes at the La Silla or Paranal Observatories under program IDs 069.C-0460, 071.C-0497, 072.C-0542, 074.C-0379, 075.C-0251, and 380.C-0791. The Gemini Observatory is operated by the Association of Universities for Research in Astronomy, under a cooperative agreement with NSF on behalf of the Gemini partnership: NSF (US), the Science and Technology Facilities Council (UK), the National Research Council (Canada), Comisión Nacional de Investigación Científica y Tecnológica (Chile), the Australian Research Council (Australia), Ministério da Ciência e Tecnologia (Brazil), and Secretaría de Ciencia y Technología (Argentina). Observations were obtained at the WIYN Observatory, a joint facility of the University of Wisconsin–Madison, Indiana University, Yale University, and the National Optical Astronomy Observatories; the William Herschel Telescope, at Roque de los Muchachos Observatory (La Palma, Canary Islands, Spain), operated by the Instituto de Astrofisica de Canarias; and the MMT Observatory, a joint facility of the Smithsonian Institution and the University of Arizona.

Supporting Online Material

www.sciencemag.org/cgi/content/full/322/5900/432/DC1
SOM Text
Figs. S1 and S2
Tables S1 to S4
References

11 July 2008; accepted 12 September 2008
10.1126/science.1163148

Species-Specific Transcription in Mice Carrying Human Chromosome 21

Michael D. Wilson,[1]* Nuno L. Barbosa-Morais,[1,2]* Dominic Schmidt,[1,2] Caitlin M. Conboy,[3] Lesley Vanes,[4] Victor L. J. Tybulewicz,[4] Elizabeth M. C. Fisher,[5] Simon Tavaré,[1,2,6] Duncan T. Odom[1,2]†

Homologous sets of transcription factors direct conserved tissue-specific gene expression, yet transcription factor–binding events diverge rapidly between closely related species. We used hepatocytes from an aneuploid mouse strain carrying human chromosome 21 to determine, on a chromosomal scale, whether interspecies differences in transcriptional regulation are primarily directed by human genetic sequence or mouse nuclear environment. Virtually all transcription factor–binding locations, landmarks of transcription initiation, and the resulting gene expression observed in human hepatocytes were recapitulated across the entire human chromosome 21 in the mouse hepatocyte nucleus. Thus, in homologous tissues, genetic sequence is largely responsible for directing transcriptional programs; interspecies differences in epigenetic machinery, cellular environment, and transcription factors themselves play secondary roles.

Higher eukaryotes are organized collections of different cell types, each of which is created from differential transcription of a common genome (*1*). Evolutionarily conserved sets of tissue-specific transcription factors establish each cell's transcription during development and maintain it during adulthood by binding to DNA in a sequence-specific manner (*1*–*3*). These proteins typically recognize short consensus motifs, often between 6 and 16 nucleotides, found at high frequency throughout a genome. How transcription factors discriminate among nearly identical motifs is poorly understood, although chromatin state, cellular environ-

ment, and surrounding regulatory sequences have all been suggested to direct transcription factors to specific cognate sites (*4*, *5*). Sequence comparisons alone can identify only a fraction of regulatory regions (*6*), because the protein–DNA binding events linking transcription factors with genetic control sequences, and thus gene expression, change on a rapid evolutionary time scale (*7*–*10*). For instance, the targeted genes and precise binding locations of conserved, tissue-specific transcription factors for mouse and human differ significantly (*7*). Even when transcription factors bind near orthologous genes in two species, the precise locations of the large majority of the binding events do not align (*7*, *9*). In numerous cases, transcription factors frequently bind one highly conserved motif near a gene in one species and a different conserved motif near the orthologous gene in a second species (*7*, *9*). This divergence of transcription factor–binding locations among related species is a widely occurring phenomenon, and similar observations have been made in yeast, *Drosophila*, and mammals (*7*–*10*). Thus, the mechanisms that determine tissue-specific transcriptional regulation must be more complex than simple gain and loss of the immediately bound, local sequence motifs.

The role that DNA sequence plays in directing histone modifications is also not well understood. It has been previously shown on human chromosomes 21 and 22 that, at the sequence level, sites of methylation at lysine 4 of histone H3 (H3K4) are no more conserved relative to mouse genome than background sequence (*11*). Genomic locations where H3K4 methylation occurred in both species did not show high levels of overall sequence conservation (*11*). One interpretation of this observation is that sequence comparisons alone have a limited capability for identifying epigenetic landmarks.

Ultimately, transcription factor binding and epigenetic state contribute to tissue-specific gene expression (*4*, *5*). A complete understanding of the mechanisms underlying divergence of transcriptional regulation and transcription itself is central to the debate surrounding the relative roles that cis-regulatory mutations and protein-coding mutations play during evolution (*12*, *13*).

Here, we isolate the role that genetic sequence plays in transcription by using a mouse model of Down syndrome that stably transmits human chromosome 21 (*14*, *15*). In this mouse, we compared transcriptional regulation of orthologous human and mouse sequences in the same nuclei and, thereby, eliminated most environmental and experimental variables otherwise inherent to interspecies comparisons.

Tc1 mice are partially mosaic, and ~60% of their hepatic cells contain human chromosome 21, which we confirmed by quantitative genotyping (fig. S1). Historically, human chromosome 21 has been extensively studied to explore transcription and transcriptional regulation on a chromosomewide basis (*11*, *16*, *17*), and the corresponding orthologous mouse regions are located primarily in chromosome 16, with additional regions in chromosomes 10 and 17 (*14*).

We chose liver as a representative tissue for these experiments because most liver cells are hepatocytes that are easy to isolate and highly conserved in structure and function. A set of conserved, well-characterized transcription factors (including HNF1α, HNF4α, and HNF6) are responsible for hepatocyte development and function (*2*, *18*), and orthologous liver-specific mouse and human transcription factors recognize the same consensus sequences (*7*). Despite almost perfect conservation in their DNA binding domains, the mouse orthologs of HNF1α, HNF4α, and HNF6 can vary in amino acid composition by up to 5% from their human orthologs in regions that could mediate protein-protein interactions (table S1) (*19*, *20*). No liver-specific transcription factor genes we profiled reside on human chromosome 21 (HsChr21); therefore, binding events identified are due to mouse transcription factors.

Because approximately three-quarters of the conserved synteny between human chromosome 21 and the mouse genome resides on mouse chromosome 16, we used tiling microarrays to obtain genomic information in four chromosome-nuclear combinations: human chromosome 21 located in human hepatocytes (indicated as WtHsChr21), human chromosome 21 located in Tc1 mouse hepatocytes (TcHsChr21), mouse chromosome 16 located in Tc1 mouse hepatocytes (TcMmChr16), and mouse chromosome 16 located in wild-type mouse hepatocytes (WtMmChr16).

For every experiment, we subtracted all potentially mouse-human degenerate probes computationally, as well as experimentally, by cross-hybridizing each platform with nucleic acids from the heterologous species [details in (*15*)]. Taken together, our genomic microarrays, in principle, could interrogate more than 28 Mb of human and mouse DNA sequence shared in both HsChr21 and MmChr16, which would capture information on ~145 genes embedded in their native chromosomal context. After subtraction of regions deleted from TcHsChr21, ~20 Mb and 105 genes are interrogated herein.

Three aspects of this system are of particular note: (i) the primary Tc1 hepatocytes used in these experiments are indistinguishable in liver function, tissue architecture, and mouse genome–based gene expression and transcription factor binding from that profiled from wild-type littermates (see below); (ii) TcHsChr21 and TcMmChr16 are in an identical dietary, developmental, nuclear, organismal, and metabolic environment in Tc1 hepatocytes; and (iii) as all profiled transcription factors arise from the mouse genome, species-specific effects are eliminated for antisera used in chromatin immunoprecipitation (ChIP) experiments.

We first confirmed the substantial divergence in transcription factor binding between wild-type mouse and human hepatocytes by performing ChIP assays against HNF1α, HNF4α, and HNF6, which are members of three different protein families (Fig. 1). As expected, most transcription factor–binding events were species-specific (*7*) and were located distal to transcriptional start sites (TSSs) (*10*, *21*). We define human-specific (or human-unique) as ChIP enrichment on the human genome that does not have detectable signal in the orthologous region of the mouse genome (and vice versa) (Fig. 1A, and fig. S2).

To determine the role that human DNA sequence can play in directing mouse transcription factor binding, we performed ChIP experi-

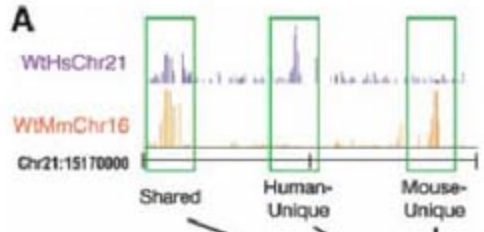

B

Chromatin IP		Shared	Human-Unique	Mouse-Unique
HNF1α		76	38	300
HNF4α		137	119	146
HNF6		28	60	115
H3K4me3	at TSS:	77	8	0
	Non-TSS:	24	28	22

Fig. 1. Transcriptional regulation of human hepatocytes varies from mouse hepatocytes across a complete chromosome. (**A**) Genome track showing ChIP enrichment of HNF1α binding in wild-type mouse and human hepatocytes across 30 kb of genomic sequence. The species of bound DNA sequences and ChIP signal are indicated by color: Purple represents human; orange represents mouse. Highlighted in green are HNF1α-bound regions that are shared by both species, human-unique, or mouse-unique. (**B**) The total number of genomic regions occupied by three transcription factors (HNF1α, HNF4α, and HNF6) and H3K4me3 that are shared between the species, human-unique, or mouse-unique. ChIP data were obtained in wild-type mouse and human hepatocytes across the homologous regions of human chromosome 21 and mouse chromosome 16.

[1]Cancer Research UK, Cambridge Research Institute, Li Ka Shing Centre, Robinson Way, Cambridge CB2 0RE, UK. [2]Department of Oncology, Hutchison/MRC (Medical Research Council) Research Centre, Hills Road, Cambridge CB2 0XZ, UK. [3]Medical Scientist Training Program, University of Minnesota Medical School, Minneapolis, MN 55455, USA. [4]Division of Immune Cell Biology, National Institute for Medical Research, The Ridgeway, Mill Hill, London NW7 1AA, UK. [5]Institute of Neurology, University College London, Queen Square, London WC1N 3BG, UK. [6]Department of Applied Mathematics and Theoretical Physics, University of Cambridge, Cambridge CB3 0WA, UK.

*These authors contributed equally to this work
†To whom correspondence should be addressed. E-mail: duncan.odom@cancer.org.uk

ments against HNF1α, HNF4α, and HNF6 in hepatocytes from the Tc1 mouse (Fig. 2). For each transcription factor, we simultaneously hybridized DNA from replicate ChIP enrichment experiments to microarrays representing human chromosome 21 and mouse chromosome 16 (*15*). We found that transcription factor binding on TcMmChr16 and WtMmChr16 is largely identical; thus, the presence of an extra human chromosome does not perturb transcription factor binding to the mouse genome (fig. S3).

We then asked whether transcription factor binding to transchromic TcHsChr21 aligned with the positions found on (human) WtHsChr21 or (mouse) TcMmChr16. Although binding events could also be present uniquely on TcHsChr21 that do not align to either WtHsChr21 or TcMmChr16, this was rarely observed. If the transcription factor–binding positions on TcHsChr21 align with positions found on WtHsChr21, then that would indicate that this binding is largely determined by cis-acting DNA sequences, as the transcription factors are present in both mouse and human hepatocytes and regulate key liver functions. If more than a small number of binding events on TcHsChr21 were found at locations that align elsewhere in the genome (for instance, with binding events on TcMmChr16), then other mechanistic influences besides genome sequence, such as chromatin structure, interspecies differences in developmental remodeling, diet, and/or environment must contribute substantially toward directing the location of transcription factor binding.

Remarkably, almost all of the transcription factor–binding events on HsChr21 are found in both human and Tc1 mouse hepatocytes (85 to 92%) (Fig. 2A and fig. S4). The few peaks that appear to be unique to WtHsChr21 or TcHsChr21 are generally of lower intensity and difficult to evaluate reliably by using standard peak-calling algorithms (fig. S5). Indeed, as can be seen in Fig. 3, the pattern of conservation and divergence in transcription factor binding found in both WtHsChr21 (located in human liver) and WtMmChr16 (located in mouse liver) is recapitulated in TcHsChr21 and TcMmCh16 (both located in mouse liver) (see also figs. S6 and S7). Because transcription factors often bind to regions that do not contain their canonical binding sequences (*7*, *9*, *21*), this result is further notable.

Despite the evolutionary divergence of primate and rodent lineages, mouse genome–encoded transcription factors can bind to human sequences in a manner identical to the human genome–coded transcription factors in a homologous tissue. These data eliminate the possibility that protein concentration differences or small coding variations in the mouse versions of transcription factors (or within larger transcriptional complexes) could redirect transcription factor binding to locations different from those found in human. Taken together, underlying genetic sequences appear to be the dominant influence on where transcription factors bind in homologous mammalian tissues.

We then explored how the mouse chromatin remodeling machinery interacts with TcHsChr21 (Fig. 1) (*22*). Using ChIPs, we isolated nucleosomes containing the trimethylated lysine 4 of histone H3 (H3K4me3) to identify the genomic anchor points for basal transcriptional machinery (*11*, *22*–*25*). Although most H3K4me3 enrichment occurs at TSSs and correlates with gene expression, it recently has been shown that most TSSs are H3K4me3-enriched, regardless of whether they are being actively elongated (*11*, *22*–*25*). Depending on the cell type, approximately a quarter of genes can show differential H3K4 methylation, and many of these genes have been shown to be cell type–specific (*22*).

We first identified how well trimethylation of the H3K4 position is shared in both the wild-

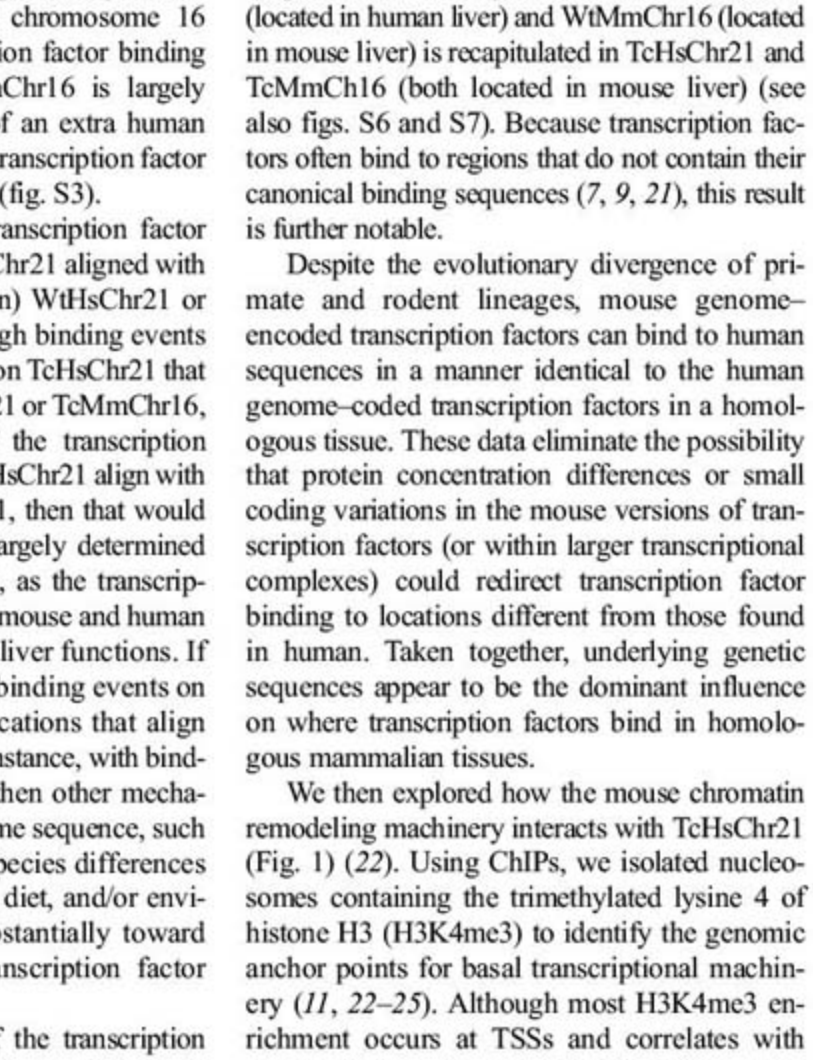

		Shared	Cis-directed	Trans-directed
HNF1α		38	39	1
HNF4α		58	93	4
HNF6		11	36	0
H3K4me3	at TSS:	43	2	5
	Non-TSS:	10	16	2

Fig. 2. Comparison of the binding of the liver-specific transcription factors HNF1α, HNF4α, and HNF6, and enrichment of H3K4me3 on TcHsChr21 with the corresponding data obtained in mouse TcMmChr16 and human WtHsChr21 regions. The color scheme is the same as in Fig. 1; notably, the primary difference from Fig. 1 is the addition of the human chromosome in a mouse environment, which is indicated as a purple bar (representing the human chromosomal sequences) with an orange peak (from mouse transcription factor binding). The binding events on TcHsChr21 are sorted into categories on the basis of whether they align with similar peaks in mouse and human (shared), align only with peaks in human (cis-directed), or align only with peaks in mice (trans-directed).

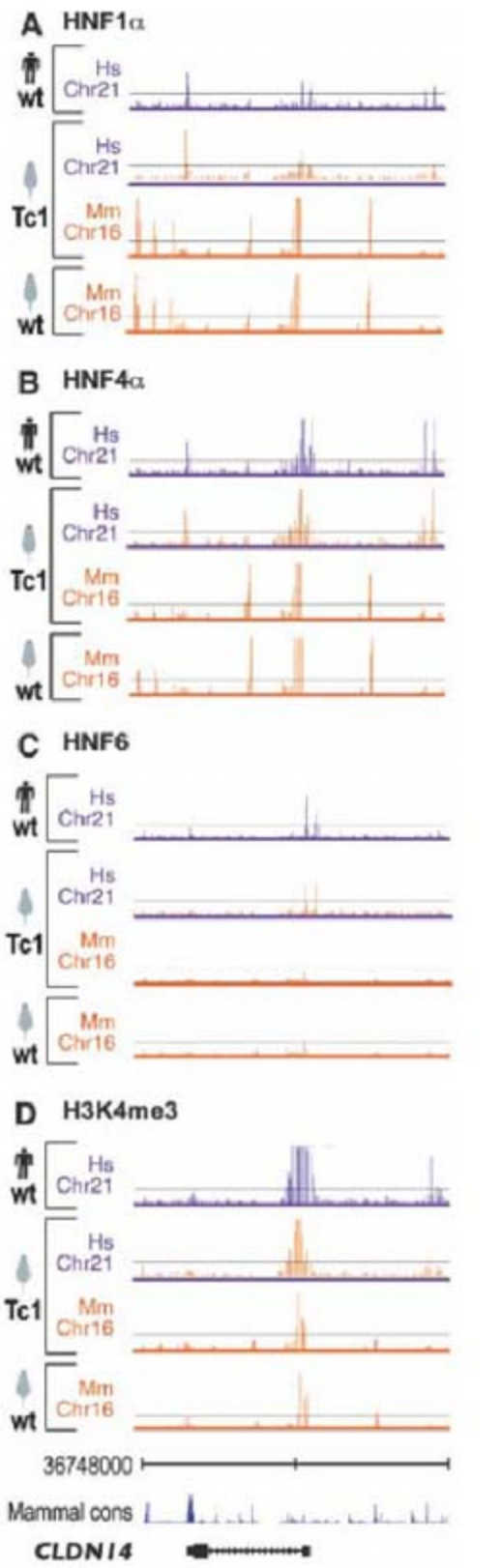

Fig. 3. Patterns of transcription factor binding and transcription initiation are determined by genetic sequence. ChIP enrichment for **(A)** HNF1α, **(B)** HNF4α, **(C)** HNF6, and **(D)** H3K4me3 are shown across a 50-kb region surrounding the liver-expressed gene *CLDN14*. The human chromosome 21 coordinates and the vertebrate sequence conservation track (Seq Cons; genome.ucsc.edu) are shown flanking *CLDN14*. Each panel shows the species of genetic sequence as a bar colored by species (human, purple; mouse, orange) below a track showing ChIP enrichment, similarly colored by species.

type mouse and human hepatocytes. We found that 77% of the regions of H3K4me3 enrichment were shared in both WtHsChr21 and WtMmChr16. These regions are similar in a number of features, including proximity to TSSs (77 out of 101) and presence of CpG islands (80 out of 101). Consistent with H3K4me3 serving as an anchor for the basal transcriptional machinery, for almost every shared region enriched for H3K4me3 in human hepatocytes (97 out of 101), RNA transcripts were found in the liver-derived cell line HepG2 (*16*).

Regions enriched in trimethylation of H3K4 located distal to known TSSs are thought to represent unannotated promoter regions (*11*, *25*). The vast majority of the species-specific regions enriched in H3K4me3 in human hepatocytes (28 out of 36) and mouse hepatocytes (22 out of 22) were distal to TSSs (Fig. 1 and fig. S8). These species-specific sites of H3K4me3 enrichment were less likely to have CpG islands (3 out of 36 and 2 out of 22, respectively) and showed somewhat lower enrichment than the conserved regions (fig. S8). Consistent with their association with unannotated TSSs, human-specific regions enriched for trimethylation of H3K4 also showed evidence of transcription in HepG2 (26 out of 36 and 12 out of 22, respectively). In sum, H3K4me3 enrichment was found to be shared in both wild-type mouse and human hepatocytes at the majority of TSSs, yet largely divergent elsewhere.

On the basis of the presence of the trimethylated form of H3K4 in both mouse and human we observed at TSSs, we expected that a human chromosome subject to mouse developmental remodeling would have enrichment of H3K4me3 at similar positions near TSSs. It was unclear, however, whether the mouse transcriptional machinery would successfully recreate the human-specific histone modifications at uncharacterized promoters distal to known TSSs. Observing H3K4me3 enrichment on TcHsChr21 at either the human-unique sites on WtHsChr21 or the mouse-unique sites on WtMmChr16 could suggest what mechanisms direct the location of transcriptional initiation.

We found that virtually all of the TSSs and about three-quarters of non-TSS H3K4me3-enriched regions on WtHsChr21 were found at the same location on TcHsChr21 (Fig. 2 and fig. S4). We found a minority of cases (7 out of 78) where H3K4me3 enrichment occurred at sites on the TcHsChr21 that aligned with H3K4me3-enriched sites on TcMmChr16, without significant signal in WtHsChr21 (Fig. 2). Although these could be examples where human sequence in a mouse environment is handled in a mouse-specific manner, most are marginally enriched for H3K4me3 (see supporting online text 1). Taken as a whole, close inspection of the patterns of enrichment of H3K4me3 on TcHsChr21 reveals that 85% of H3K4me3-enriched regions found on WtHsChr21 were reproduced on TcHsChr21 (fig. S4); the remarkable extent of this similarity is shown for the liver-expressed gene *CLDN14* as a typical example (Fig. 3). Independent ChIP sequencing (ChIP-seq) experiments confirmed 93% (77 out of 82) of the sites of H3K4me3 enrichment on TcHsChr21 and 73% of sites on TcMmChr16 (70 out of 95); the majority of non-confirmed sites on TcMmChr16 (20 out of 25) were mouse-unique, half of which (13 out of 25) were found in the *Tiam1* gene (see supporting online text 1 and fig. S9).

In addition to expanding the examples of functionally conserved H3K4me3 sites, our results demonstrate that the regions of differential H3K4 methylation between divergent species are primarily dictated by cis-acting genetic sequence. Neither the cellular environment nor differences among the mouse and human chromatin–remodeling complexes substantially influence the placement of key chromatin landmarks associated with transcriptionally active regions.

Having shown that transcription factor binding and transcription initiation occurred in positions largely determined by underlying genetic sequences, we finally examined how the Tc1 mouse environment affects gene expression originating from the human chromosome. Using human gene expression microarrays that had been computationally and experimentally confirmed to be unaffected by the presence of mouse transcripts, we identified a distinct set of human genes that was expressed reproducibly in Tc1 mouse hepatocytes (Fig. 4A). Genes located in regions known to be deleted from TcHsChr21 were not detected as expressed (fig. S10) (*14*). Unsupervised clustering and principal component analysis of transcriptional data from the human gene expression microarrays clearly separated Tc1 and wild-type littermates by the presence of TcHsChr21 (fig. S10). Conversely, we asked whether the presence of the human chromosome perturbs mouse genome–based gene expression. No differential expression of mouse hepatocyte mRNA between Tc1 mice and wild-type littermates was detected by mouse-specific Illumina BeadArrays [note vertical scale in (Fig. 4B)]. Unsupervised clustering of the normalized mouse array data accurately grouped mice by litter and strain, independently of the absence or presence of the human chromosome (fig. S10).

We asked how well the transcripts originating from TcHsChr21 correlated with the transcripts originating from WtHsChr21 in human hepatocytes (Fig. 4C and fig. S11). Gene expression in Tc1 mouse hepatocytes originating from the human chromosome was determined by using the probes representing the 121 genes present on TcHsChr21 and then compared with matching gene expression data for the same 121 genes obtained from human hepatocytes. We found a strong correlation between the expression levels of the human genes located in Tc1 mouse hepatocytes and their counterparts located in wild-type human hepatocytes (Fig. 4C and fig. S11). This correlation ($R \approx 0.90$) was slightly lower than that found between replicate individual human livers (fig. S12), yet appears to be higher than similar correlations previously reported between human and other primates (*26*, *27*). The expression of orthologous genes within Tc1 hepatocytes (i.e., TcHsChr21 versus TcMmChr16) is substantially more divergent, with $R \approx 0.28$ (Fig. 4D). It is possible that the correlation between mouse and human orthologs could be influenced by the experimental differences between platforms, as well as by microarray design peculiarities. To address this concern, we determined the relative rank-order of expression among the genes on WtHsChr21, TcHsChr21, and TcMmChr16 and then compared the ranked results. We found correlation trends similar to the above (fig. S11) (*15*).

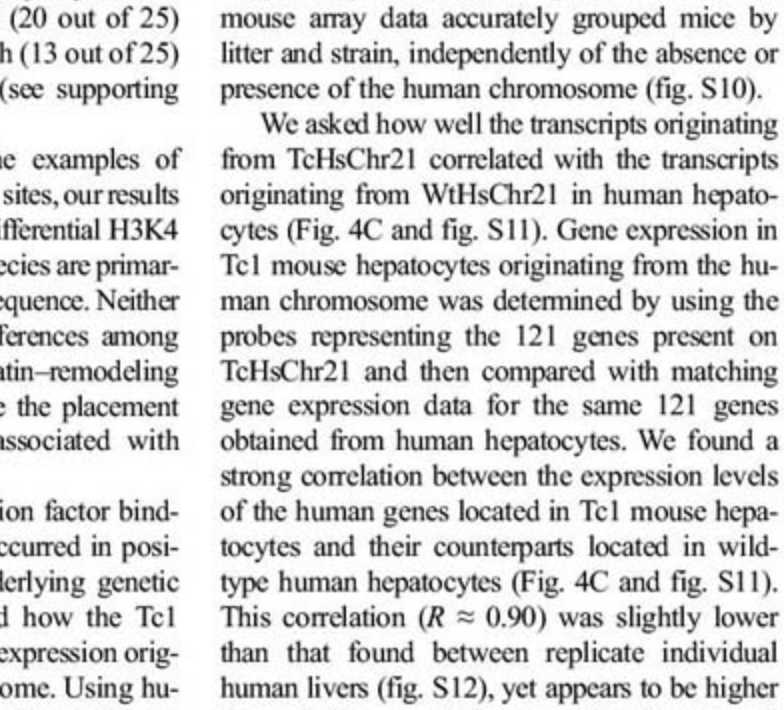

Fig. 4. Gene expression in the Tc1 mouse originating from the mouse and human chromosomes is largely indistinguishable from comparable wild-type nuclear environments. Volcano plots (empirical Bayes log odds of differential expression versus average log fold change) make several points. (**A**) Tc1 hepatocytes have high transcription occurring from the transplanted human chromosome 21, when we used human genomic arrays and wild-type littermate mRNA as a reference (black probes map to human genes; blue probes map to genes located on HsChr21; red probes map to regions absent from TcHsChr21); however, (**B**) wild-type and Tc1 mouse gene expression on mouse genomic arrays have indistinguishable patterns of transcription (black probes map to mouse genes). (**C**) Plot of the log expression of TcHsChr21 (*y* axis) transcripts versus WtHsChr21 (*x* axis) transcripts ($R \approx 0.90$). (**D**) Plot of the log expression of TcHsChr21 (*y* axis) transcripts versus WtMmChr16 (*x* axis) orthologous transcripts ($R \approx 0.28$).

Our results test the hypothesis that variation in gene expression is dictated by regulatory regions, extending recent studies of expression by quantitative trait-loci mapping and comparative expression studies that have been confined to closely related species (*26*–*30*). The apparent absence of overt trans influences could be explained by the modest amount of human DNA provided by a single copy of human chromosome 21 when compared with the complete mouse genome, as well as the absence of liver-specific transcriptional regulators on chromosome 21. The extent to which protein coding and cis-regulatory mutations contribute to changes in morphology, physiology, and behavior is actively debated in evolutionary biology (*3*, *12*, *13*). Myriad points of control influence gene expression; however, it has also been an unresolved question as to which of these mechanisms has the most influence globally. Here, we show that each layer of transcriptional regulation within the adult hepatocyte, from the binding of liver master regulators and chromatin remodeling complexes to the output of the transcriptional machinery, is directed primarily by DNA sequence. Although conservation of motifs alone cannot predict transcription factor binding, we show that within the genetic sequence there must be embedded adequate instructions to direct species-specific transcription.

References and Notes

1. E. H. Davidson, D. H. Erwin, *Science* **311**, 796 (2006).
2. K. S. Zaret, *Mech. Dev.* **92**, 83 (2000).
3. G. A. Wray, *Nat. Rev. Genet.* **8**, 206 (2007).
4. B. Li, M. Carey, J. L. Workman, *Cell* **128**, 707 (2007).
5. E. Guccione *et al.*, *Nat. Cell Biol.* **8**, 764 (2006).
6. L. Elnitski, V. X. Jin, P. J. Farnham, S. J. Jones, *Genome Res.* **16**, 1455 (2006).
7. D. T. Odom *et al.*, *Nat. Genet.* **39**, 730 (2007).
8. A. M. Moses *et al.*, *PLOS Comput. Biol.* **2**, e130 (2006).
9. A. R. Borneman *et al.*, *Science* **317**, 815 (2007).
10. E. Birney *et al.*, *Nature* **447**, 799 (2007).
11. B. E. Bernstein *et al.*, *Cell* **120**, 169 (2005).
12. H. E. Hoekstra, J. A. Coyne, *Evolution* **61**, 995 (2007).
13. S. B. Carroll, *Cell* **134**, 25 (2008).
14. A. O'Doherty *et al.*, *Science* **309**, 2033 (2005).
15. Materials and methods are available as supporting material on *Science* Online.
16. D. Kampa *et al.*, *Genome Res.* **14**, 331 (2004).
17. J. S. Carroll *et al.*, *Cell* **122**, 33 (2005).
18. S. Cereghini, *FASEB J.* **10**, 267 (1996).
19. J. Eeckhoute, B. Oxombre, P. Formstecher, P. Lefebvre, B. Laine, *Nucleic Acids Res.* **31**, 6640 (2003).
20. F. M. Sladek, M. D. Ruse Jr., L. Nepomuceno, S. M. Huang, M. R. Stallcup, *Mol. Cell. Biol.* **19**, 6509 (1999).
21. A. Rada-Iglesias *et al.*, *Hum. Mol. Genet.* **14**, 3435 (2005).
22. M. G. Guenther, S. S. Levine, L. A. Boyer, R. Jaenisch, R. A. Young, *Cell* **130**, 77 (2007).
23. M. Vermeulen *et al.*, *Cell* **131**, 58 (2007).
24. R. J. Sims 3rd *et al.*, *Mol. Cell* **28**, 665 (2007).
25. A. Barski *et al.*, *Cell* **129**, 823 (2007).
26. Y. Gilad, A. Oshlack, G. K. Smyth, T. P. Speed, K. P. White, *Nature* **440**, 242 (2006).
27. P. Khaitovich *et al.*, *Science* **309**, 1850 (2005).
28. P. J. Wittkopp, B. K. Haerum, A. G. Clark, *Nat. Genet.* **40**, 346 (2008).
29. C. C. Park *et al.*, *Nat. Genet.* **40**, 421 (2008).
30. Y. Gilad, S. A. Rifkin, J. K. Pritchard, *Trends Genet.* **24**, 408 (2008).

31. We are grateful to E. Jacobsen, R. Stark, I. Spiteri, B. Liu, J. Marioni, A. Lynch, J. Hadfield, N. Matthews, the Cambridge Research Institute (CRI) Genomics Core, CRI Bioinformatics Core, and Camgrid for technical assistance, and B. Gottgens and J. Ferrer for insightful advice. Supported by the European Research Council (D.T.O.); Royal Society Wolfson Research Merit Award (S.T.); Hutchison Whampoa (D.T.O., ST); Medical Research Council (E.F., VT); Wellcome Trust (E.F., V.T.); University of Cambridge (D.T.O., D.S., N.B.M., S.T.); and Cancer Research U.K. (D.T.O., M.D.W., N.B.M., S.T., D.S.). Data deposited under ArrayExpress accession numbers E-TABM-473 and E-TABM-474. M.D.W., N.B.M., D.S., D.T.O., and C.M.C. designed and performed experiments; N.B.M., M.D.W., and D.S. analyzed the data; L.V., V.T., M.D.W., and E.F. created, prepared, and provided Tc1 mouse tissues; and M.D.W., N.B.M., D.T.O., and S.T. wrote the manuscript. D.T.O. oversaw the work. The authors declare no competing interests.

Supporting Online Material

www.sciencemag.org/cgi/content/full/1160930/DC1
Materials and Methods
SOM Text
Figs. S1 to S12
Table S1

27 May 2008; accepted 3 September 2008
Published online 11 September 2008;
10.1126/science.1160930
Include this information when citing this paper.

Surface Sites for Engineering Allosteric Control in Proteins

Jeeyeon Lee,[1]* Madhusudan Natarajan,[2]* Vishal C. Nashine,[1] Michael Socolich,[2] Tina Vo,[2] William P. Russ,[2] Stephen J. Benkovic,[1] Rama Ranganathan[2]†

Statistical analyses of protein families reveal networks of coevolving amino acids that functionally link distantly positioned functional surfaces. Such linkages suggest a concept for engineering allosteric control into proteins: The intramolecular networks of two proteins could be joined across their surface sites such that the activity of one protein might control the activity of the other. We tested this idea by creating PAS-DHFR, a designed chimeric protein that connects a light-sensing signaling domain from a plant member of the Per/Arnt/Sim (PAS) family of proteins with *Escherichia coli* dihydrofolate reductase (DHFR). With no optimization, PAS-DHFR exhibited light-dependent catalytic activity that depended on the site of connection and on known signaling mechanisms in both proteins. PAS-DHFR serves as a proof of concept for engineering regulatory activities into proteins through interface design at conserved allosteric sites.

Proteins typically adopt well-packed three-dimensional structures in which amino acids are engaged in a dense network of contacts (*1*, *2*). This emphasizes the energetic importance of local interactions, but protein function also depends on nonlocal, long-range communication between amino acids. For example, information transmission between distant functional surfaces on signaling proteins (*3*), the distributed dynamics of amino acids involved in enzyme catalysis (*4*–*6*), and allosteric regulation in various proteins (*7*) all represent manifestations of nonlocal interactions between residues. To the extent that these features contribute to defining biological properties of protein lineages, we expect that the underlying mechanisms represent conserved rather than idiosyncratic features in protein families.

[1]Department of Chemistry, Pennsylvania State University, University Park, PA 16802, USA. [2]Green Center for Systems Biology and Department of Pharmacology, University of Texas Southwestern Medical Center, Dallas, TX 75390, USA.

*These authors contributed equally to this work.
†To whom correspondence should be addressed. E-mail: rama.ranganathan@utsouthwestern.edu

On the basis of this conjecture, methods such as statistical coupling analysis (SCA) quantitatively examine the long-term correlated evolution of amino acids in a protein family—the statistical signature of functional constraints arising from conserved communication between positions (*8*, *9*). This approach has identified sparse but physically connected networks of coevolving amino acids in the core of proteins (*8*–*12*). The connectivity of these networks is remarkable, given that a small fraction of total residues are involved and that no tertiary structural information is used in their identification. Empirical observation in several protein families shows that these networks connect the main functional site with distantly positioned secondary sites, enabling predictions of allosteric surfaces at which binding of regulatory molecules (or covalent modifications) might control protein function. Both literature studies and forward experimentation in specific model systems confirm these predictions (*8*–*12*). Thus, techniques such as SCA may provide a general tool for computational prediction of conserved allosteric surfaces.

The finding that certain surface sites might be statistical "hotspots" for functional interaction with active sites suggests an idea for engineering new regulatory mechanisms into proteins. What if two proteins were joined at surface sites such that their statistically correlated networks were juxtaposed and could form functional interactions (Fig. 1A)? If the connection sites are functionally linked to their respective active sites

through allosteric mechanisms intrinsic to each protein, it should be possible to couple the activity of one protein to that of the other.

Evidence from natural systems supports this design concept (Fig. 1B). Ligand binding in a PDZ (PSD95/Dlg1/ZO1) protein interaction module in the human Par6 protein is allosterically regulated by interaction with the guanine nucleotide–binding protein (G protein) Cdc42 at a distant surface site (*13*, *14*). SCA for the PDZ and G protein families reveals a contiguous network of amino acids that connects the nucleotide-binding pocket of Cdc42 with the ligand-binding pocket of the PDZ domain through specific interactions across an allosteric interaction surface (Fig. 1B and figs. S1 to S3). Mutagenesis studies confirm that these networks in PDZ and G proteins contribute to allosteric signaling (*11*, *14*). In both proteins, the allosteric site is uniquely identified as the surface-exposed residues of the SCA network that are nonetheless distant from the active site (fig. S3).

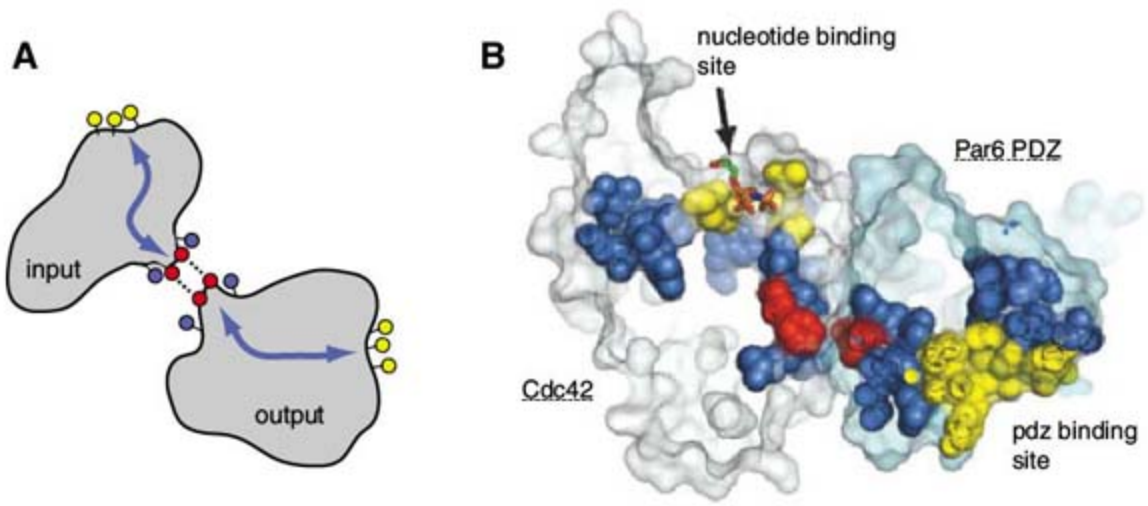

Fig. 1. A design concept for allosteric communication. (**A**) The SCA computational method identifies networks of statistically interacting amino acids in proteins (blue arrows). These networks often link primary functional sites (yellow) with distant surface positions (red) through the core (blue). This motivates the idea of functionally coupling the two proteins (denoted "input" and "output" modules) through linkage at the predicted allosteric sites. (**B**) A slice through the structure of a complex between the PDZ domain of the cell polarity protein Par6 (cyan surface) with its allosteric regulator, the Cdc42 G protein (white surface) shows an example of SCA network linkage in a natural protein-protein interaction. SCA residues [in CPK representation and colored as in (A)] constitute a contiguous network linking the site of nucleotide exchange on Cdc42 with the ligand-binding pocket of the PDZ domain (both in yellow) through specific residues at the allosteric interface (red).

Can statistically correlated allosteric networks be joined to engineer functional communication between proteins? To test this idea, we selected two protein modules as components for creation of a non-natural allosteric two-domain protein in which a signal originating in one domain (the "input" module) is transmitted to influence the activity of the second domain (the "output" module) (Fig. 1A). For the input module, we chose a light-sensing domain from plant phototropin [*Avena sativa* LOV2 (*15*)], a member of the Per/Arnt/Sim (PAS) family of signaling modules (*16*). PAS domains mediate biological responses to a diverse set of stimuli, including aromatic hydrocarbons, gases, redox potential, and light, and share a conserved core structure comprising a five-stranded antiparallel β sheet with two flanking α helices (*17*) (fig. S4A). A deep ligand-binding pocket opens to one surface of the domain. In the phototropin LOV2 domain, signaling is initiated by light absorption by a flavin mononucleotide (FMN) chromophore bound within the binding pocket, which then transmits the signal through the structure to cause two large conformational changes at the opposite surface: destabilization and unbinding of helical extensions at both the C terminus (the Jα helix) and the N terminus of the core PAS domain (*18*, *19*) (Fig. 2A and fig. S4A). The structural details of the N- and C-terminal extensions varies among members of the PAS domain family, but conformational change at these regions appears to be a

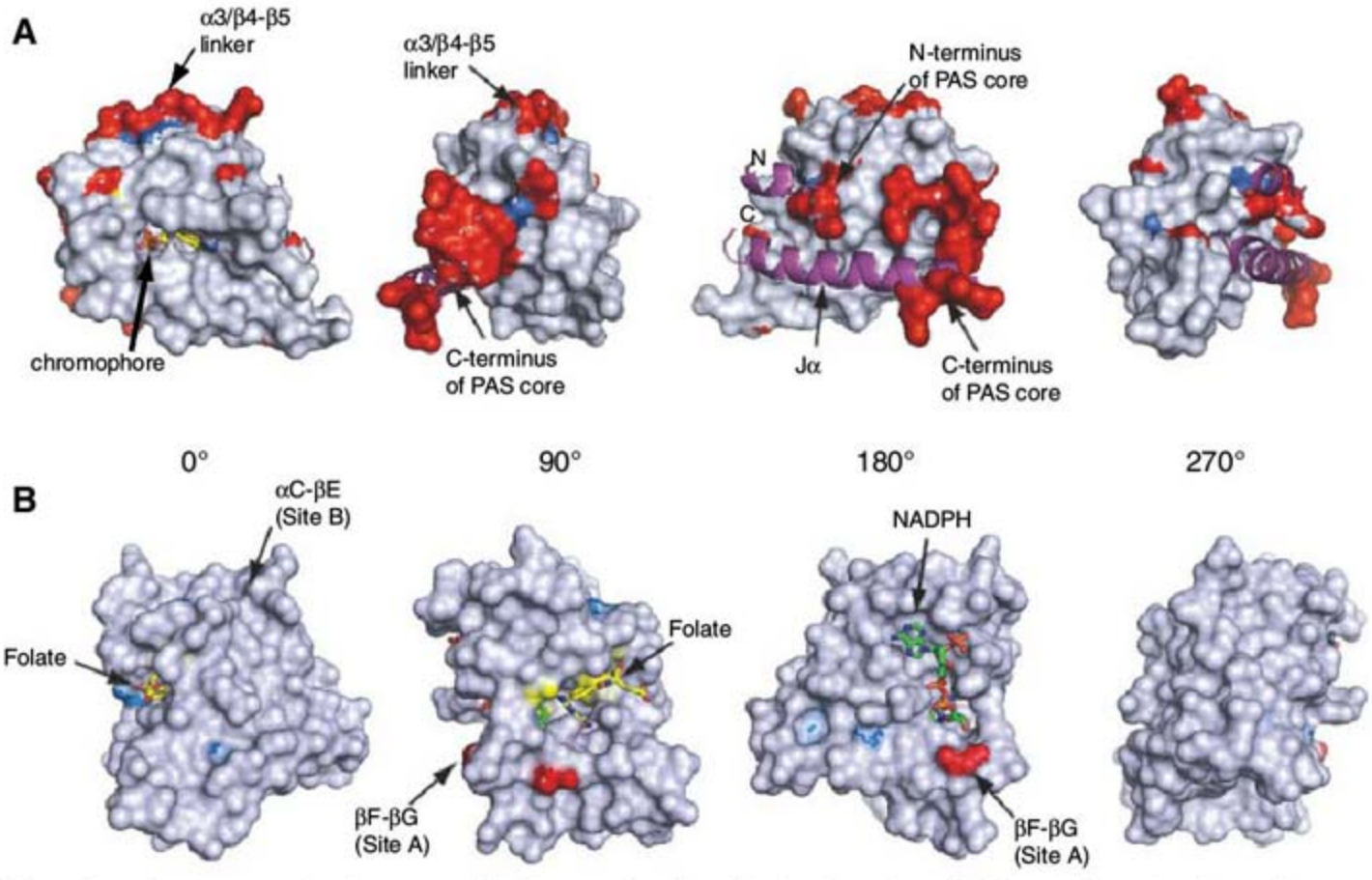

Fig. 2. Design principle of the PAS-DHFR chimera. (**A** and **B**) Surface-exposed SCA sites shown on the LOV2 PAS domain [(A), PDB code 2VOU] and *E. coli* DHFR [(B), PDB code 1RX2] shown in four successive rotations of each molecule. As in Fig. 1A, SCA network positions are colored yellow (within 5 Å of substrate), red (surface-exposed), or blue (buried). A residue is considered buried if its fractional solvent-accessible surface area is <0.1. In the core PAS domain, this analysis reveals two surface-exposed nonsubstrate proximal SCA sites: (i) the N- and C-terminal regions that, in LOV2, mediate light-dependent interaction with the Jα and N-terminal helical extensions, and (ii) the α3/β4-β5 region (see text and fig. S4). In DHFR, SCA reveals a network (fig. S5) that relates the enzyme active site to a specific distant surface loop (βF-βG, site A, in red). The experiment is to insert the LOV2 domain into several DHFR positions at site A and at a control surface (site B, αC-βE loop).

conserved feature of allosteric signaling in this protein family (*20*, *21*).

SCA for a multiple sequence alignment of 1104 core PAS domains mirrors the experimental findings. A spatially contiguous network of correlated amino acids links the ligand-binding pocket to surface-exposed residues at the N- and C-terminal regions of the core domain that, in LOV2, make direct interactions with the Jα and N-terminal helices (Fig. 2A and fig. S4, B and C). A second surface-exposed site is also evident (the α3 helix and β4-β5 linker); this site undergoes light-dependent conformational change in another member of the PAS family, the photoactive yellow protein, but is close to the chromophore-binding pocket (*22*). These data uniquely identify the N- and C-terminal regions of the LOV2 domain as the logical connection sites in our design experiment.

As the output module, we chose *E. coli* dihydrofolate reductase (EcDHFR), an enzyme system in which extensive prior structural, biochemical, and theoretical work has established the basic catalytic mechanism and evidence for long-range control of activity. DHFR is an essential enzyme required for folate metabolism in all organisms; it catalyzes the stereospecific reduction of 7,8-dihydrofolate (H_2F) to 5,6,7,8-tetrahydrofolate (H_4F; Fig. 2B, yellow stick bonds), using nicotinamide adenine dinucleotide phosphate (NADPH; Fig. 2B, green stick bonds) as a cofactor (*23*). The structure of DHFR comprises a central eight-stranded β sheet (β strands A to H) and four flanking α helices (αB, αC, αE, and αF) that make up an active-site cleft that positions the substrate and cofactor for the catalytic step: transfer of the pro-R hydride from NADPH to position C-6 of H_2F (fig. S5A) (*24*). Changes in both the structure and dynamics of loops surrounding the active site are implicated in DHFR activity (*25*); in particular, the dynamics of the βF-βG loop (residues 116 to 132) is thought to control transition-state stabilization and to enhance the rate of hydride transfer (k_{hyd}). Consistent with these findings, SCA for an alignment of 418 members of the DHFR family uniquely identifies the βF-βG loop as the most distant surface-exposed site showing strong correlated evolution with the enzyme active site (Fig. 2B). [See (*26*) and fig. S5B for details about SCA mapping and known allosteric mechanism in DHFR.]

To functionally couple the light-dependent allosteric mechanism in the LOV2 domain with the DHFR catalytic mechanism, we created sets of chimeric proteins in which the core LOV2 domain is inserted via its N- and C-terminal helical extensions into DHFR at two different surface sites (sites A and B; Fig. 2B and Fig. 3, A and B). Site A chimeras interrogate the computationally and experimentally defined allosteric surface (A120 to A122, βF-βG loop), and site B chimeras interrogate another surface site (B86 to B89, αC-βE loop) that is similarly distant but statistically uncorrelated with the active site; site B serves as a control for potential nonspecific coupling between the two domains.

We began by evaluating the independent activities of the DHFR and LOV2 domains in context of the chimeras. All LOV2-DHFR chimeras were well expressed and rescued growth in the DHFR auxotropic *E. coli* strain (ER2566Δ*fol*Δ*thy*) under minimal media conditions (*27*) (fig. S6), which indicated that insertion of the LOV2-Jα domain did not abolish DHFR activity in any instance. Consistent with the known mutagenic sensitivity of the βF-βG loop (*25*), site A chimeras showed a factor of ~1000 reduction in hydride transfer rate (Fig. 3B, wild-type k_{hyd} = 220 s^{-1}), a value that translates to a factor of ~60 change in the overall turnover rate k_{cat}. Site B chimeras showed a more modest decrease in catalytic activity (by a factor of 5 to 7), consistent with the prediction that this site is less influential for active-site function. With regard to LOV2 domain function, the absorbance spectra of dark-equilibrated proteins showed clear evidence of a 447-nm peak consistent with a noncovalently bound FMN chromophore (*28*), and light activation of all the chimeric enzymes triggered a char-

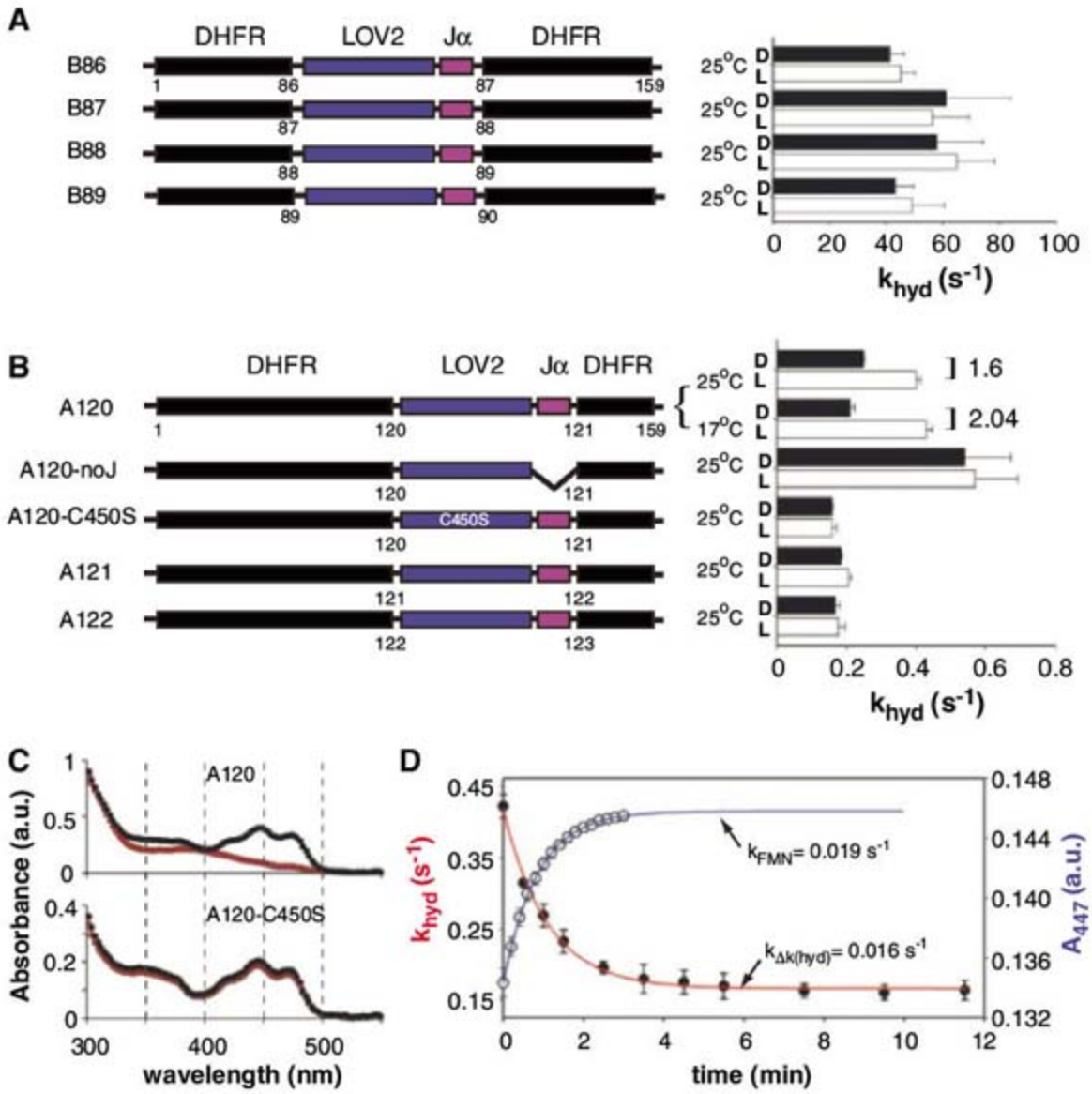

Fig. 3. Light-dependent catalysis in a LOV2-DHFR chimera. (**A** and **B**) Schematics of the chimeric constructs in sites A and B and associated hydride transfer rates (k_{hyd}) carried out under single-turnover conditions. Data are measured either upon dark adaptation (black bars) or immediately after a 5-min exposure to intense white light (white bars) (*26*). The A120-noJ chimera lacks the C-terminal Jα helix (a major site of light-dependent conformational change in LOV2), and the A120-C450S chimera carries a point mutation that locks LOV2 in the dark state. No site B chimeras show light-dependent catalysis, but one site A chimera (A120) shows a modest but clear increase in k_{hyd} upon light activation. (**C**) Dark (black curves) and light-activated (red curves) absorbance spectra in the A120 and A120-C450S chimeras show the characteristic 447-nm peak of the FMN chromophore in the dark state of LOV2; in A120 alone, light activation shows the expected transition to the 390 nm–absorbing lit-state species. (**D**) The kinetics of dark recovery of the catalytic rate follows a single-exponential process (red curve), which closely mimics that kinetics of recovery of the 447 nm–absorbing dark state of LOV2 (blue curve). In all panels, error bars indicate SD.

acteristic spectral shift to a 390 nm–absorbing species due to formation of a covalent thiol-FMN adduct (Fig. 3C and fig. S7). This species showed single-exponential relaxation to the dark-state spectrum (Fig. 3D and table S4) with a rate constant (0.019 s^{-1}) nearly identical to that reported for the isolated domain (*29*). These findings show that the basic intrinsic features of the PAS domain and DHFR are structurally and functionally intact in the LOV2-DHFR chimeras.

We next examined the chimeras for light-dependent DHFR activity by comparing k_{hyd} for matched samples either maintained in the dark or immediately after exposure to light. Rates were measured under single-turnover conditions designed to minimize the effects of dark relaxation of the LOV2 domain. Consistent with the prediction that site B is uncoupled from active-site function, none of the site B chimeras showed light-dependent changes in enzyme activity (Fig. 3A). In contrast, one of the site A chimeras (A120) showed a modest but clear light-dependent DHFR activity (Fig. 3B and table S3). By varying temperature and pH conditions (fig. S8), we determined that light increased the catalytic rate of the enzyme by a factor of 2 at 17°C and by a factor of 1.6 at 25°C (Fig. 3B). The light-dependent effect depends on the known mechanism of signaling in the LOV2 domain; an A120 variant lacking the Jα helix (*19*) (A120-noJ) or an A120 variant carrying a point mutation in LOV2 that is known to lock the molecule in the dark state (A120-C450S) (*30*, *31*) showed no light dependence, although both constructs showed absolute DHFR activities similar to that of A120 (Fig. 3B). Shifting light-exposed A120 to the dark caused a decay of the light-dependent increase in k_{hyd} that followed a single-exponential relaxation ($k_{\Delta k(hyd)}$, 0.016 s^{-1}) (Fig. 3D), observable through several cycles of excitation. The relaxation of enzyme activity nearly matched the rate of thermal relaxation of the LOV2 domain to the dark state (0.019 s^{-1}, Fig. 3D) (*29*); this result implies that the light-dependent enzymatic activity in A120 is due to establishment of allosteric communication between LOV2 and DHFR.

The magnitude of the effect is small and hardly optimal, given the factor of ~600 allosteric effect intrinsic to LOV2-Jα (*32*). In addition, it is clear that not every chimera made at site A showed light-dependent activity (Fig. 3B). Nonetheless, these results show that site-specific connections at allosteric surfaces can, even without directed optimization or mechanism-based design, begin to produce coupled activities in designed chimeric proteins.

In addition to the hydride transfer step, the overall turnover cycle of DHFR involves several other reactions, including $NADP^+$/NADPH exchange after reduction of substrate and rate-limiting release of the product H_4F (*26*, *33*). To examine potential allosteric control of these processes in the A120 chimera, we measured the light dependence of the H_4F off-rate and of the equilibrium dissociation constant for NADPH (Fig. 4). The H_4F off-rate, measured via methotrexate (MTX) competition under conditions saturating in H_4F, NADPH, and MTX (*34*), showed a factor of ~3 decrease in the A120 chimera, a value comparable to a previously characterized point mutation in the βF-βG loop [G121V (*25*)] (Fig. 4A). We observed a small but statistically significant light dependence on H_4F off-rate that was abrogated in the background of the dark-locked LOV2 mutant (C450S) (table S4). In contrast, we observed no light dependence in the equilibrium dissociation constant for the NADPH cofactor, although the LOV2 insertion into the βF-βG loop showed an effect on NADPH binding similar to that of the G121V mutant (Fig. 4B). Previous work shows that, separate from the structural contributions of the βF-βG loop to cofactor or substrate binding, the dynamics of this loop specifically controls k_{hyd} and product release (*35*). Thus, the engineered interdomain allostery in the A120 chimera likely works mechanistically through light-dependent modulation of βF-βG loop dynamics.

Taken together, the data presented here are consistent with the notion that modular allosteric networks in each protein can be brought together to initiate the formation of new allosteric control. The installation of light-dependent enzymatic activity in the A120 LOV2-DHFR chimera occurred with minimal disruption of the internal biochemical features of each module. Few discernible alterations to the photodynamics of LOV2 were noted, and the changes in DHFR properties were no greater than the effect of point mutation at the surface site used for connection. Although the number of sites tested here is small, the emergence of interdomain allostery through insertion at the βF-βG loop but not at the αC-βE loop is in agreement with the proposal that specific surface locations might act as evolutionarily conserved hotspots for allosteric control. Allosteric effects in proteins could also arise through idiosyncratic variation in individual family members (*36*), but these results suggest the notion that the linkage of conserved networks of amino acid interactions might represent a statistically preferential strategy for the evolution of allosteric signaling in multidomain proteins.

The engineering of light-dependent allosteric control in the LOV2-DHFR chimera represents an initial step toward a general scheme for the creation of allosteric multidomain systems. As methods become more refined, the computational prediction of potential allosteric surface sites should be combined with physics-based interface design and experimental screening to design high-performance allosteric systems.

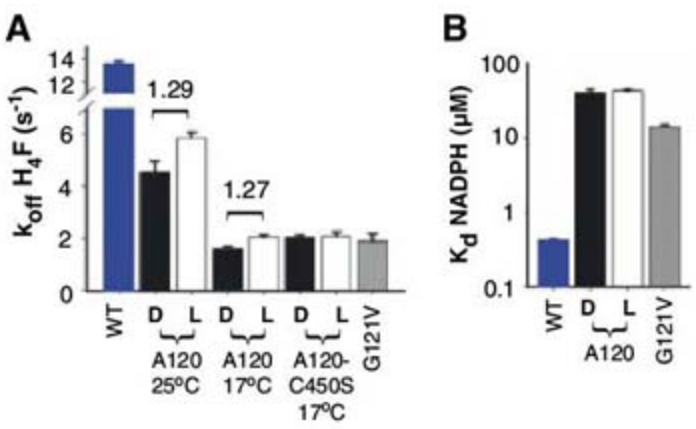

Fig. 4. Light dependence of product off-rate (**A**) and cofactor binding (**B**) in the A120 chimera. In (A), the product dissociation rate (k_{off}, H_4F) shows a small light dependence in A120 (factor of ~1.3) that is abrogated in the background of the dark-locked C450S mutation. (B), Cofactor binding (K_d, NADPH) shows no light dependence. In both assays, the overall effect of LOV2 domain insertion between positions 120 and 121 in the βF-βG loop is similar to that of the point mutation G121V. Error bars indicate SD.

References and Notes

1. F. M. Richards, W. A. Lim, *Q. Rev. Biophys.* **26**, 423 (1993).
2. J. Tsai, R. Taylor, C. Chothia, M. Gerstein, *J. Mol. Biol.* **290**, 253 (1999).
3. J. F. Swain, L. M. Gierasch, *Curr. Opin. Struct. Biol.* **16**, 102 (2006).
4. S. J. Benkovic, S. Hammes-Schiffer, *Science* **301**, 1196 (2003).
5. S. Hammes-Schiffer, S. J. Benkovic, *Annu. Rev. Biochem.* **75**, 519 (2006).
6. K. Henzler-Wildman, D. Kern, *Nature* **450**, 964 (2007).
7. I. Luque, S. A. Leavitt, E. Freire, *Annu. Rev. Biophys. Biomol. Struct.* **31**, 235 (2002).
8. S. W. Lockless, R. Ranganathan, *Science* **286**, 295 (1999).
9. G. M. Suel, S. W. Lockless, M. A. Wall, R. Ranganathan, *Nat. Struct. Biol.* **10**, 59 (2003).
10. A. D. Ferguson *et al.*, *Proc. Natl. Acad. Sci. U.S.A.* **104**, 513 (2007).
11. M. E. Hatley, S. W. Lockless, S. K. Gibson, A. G. Gilman, R. Ranganathan, *Proc. Natl. Acad. Sci. U.S.A.* **100**, 14445 (2003).
12. A. I. Shulman, C. Larson, D. J. Mangelsdorf, R. Ranganathan, *Cell* **116**, 417 (2004).
13. S. M. Garrard *et al.*, *EMBO J.* **22**, 1125 (2003).
14. F. C. Peterson, R. R. Penkert, B. F. Volkman, K. E. Prehoda, *Mol. Cell* **13**, 665 (2004).
15. M. Salomon *et al.*, *Proc. Natl. Acad. Sci. U.S.A.* **98**, 12357 (2001).
16. B. L. Taylor, I. B. Zhulin, *Microbiol. Mol. Biol. Rev.* **63**, 479 (1999).
17. Y. Z. Gu, J. B. Hogenesch, C. A. Bradfield, *Annu. Rev. Pharmacol. Toxicol.* **40**, 519 (2000).
18. A. S. Halavaty, K. Moffat, *Biochemistry* **46**, 14001 (2007).
19. S. M. Harper, L. C. Neil, K. H. Gardner, *Science* **301**, 1541 (2003).
20. M. A. Cusanovich, T. E. Meyer, *Biochemistry* **42**, 4759 (2003).
21. P. J. Erbel, P. B. Card, O. Karakuzu, R. K. Bruick, K. H. Gardner, *Proc. Natl. Acad. Sci. U.S.A.* **100**, 15504 (2003).
22. R. Brudler *et al.*, *J. Mol. Biol.* **363**, 148 (2006).
23. P. T. Rajagopalan, S. J. Benkovic, *Chem. Rec.* **2**, 24 (2002).
24. M. R. Sawaya, J. Kraut, *Biochemistry* **36**, 586 (1997).
25. C. E. Cameron, S. J. Benkovic, *Biochemistry* **36**, 15792 (1997).
26. See supporting material on *Science* Online.

27. M. C. Saraf, A. R. Horswill, S. J. Benkovic, C. D. Maranas, *Proc. Natl. Acad. Sci. U.S.A.* **101**, 4142 (2004).
28. J. M. Christie, M. Salomon, K. Nozue, M. Wada, W. R. Briggs, *Proc. Natl. Acad. Sci. U.S.A.* **96**, 8779 (1999).
29. M. Salomon, J. M. Christie, E. Knieb, U. Lempert, W. R. Briggs, *Biochemistry* **39**, 9401 (2000).
30. J. M. Christie, T. E. Swartz, R. A. Bogomolni, W. R. Briggs, *Plant J.* **32**, 205 (2002).
31. S. M. Harper, J. M. Christie, K. H. Gardner, *Biochemistry* **43**, 16184 (2004).
32. X. Yao, M. K. Rosen, K. H. Gardner, *Nat. Chem. Biol.* **4**, 491 (2008).
33. C. A. Fierke, K. A. Johnson, S. J. Benkovic, *Biochemistry* **26**, 4085 (1987).
34. J. T. Chen, K. Taira, C. P. Tu, S. J. Benkovic, *Biochemistry* **26**, 4093 (1987).
35. D. M. Epstein, S. J. Benkovic, P. E. Wright, *Biochemistry* **34**, 11037 (1995).
36. J. Kuriyan, D. Eisenberg, *Nature* **450**, 983 (2007).
37. We thank members of the Ranganathan and Benkovic labs for discussions, M. Rosen and K. H. Gardner for discussions and sharing of unpublished data and materials, and J. Wang for solvent accessibility calculations. Supported by the Robert A. Welch foundation (R.R.) and a grant from the Defense Advanced Research Projects Agency (R.R. and S.J.B.).

Supporting Online Material
www.sciencemag.org/cgi/content/full/322/5900/438/DC1
Materials and Methods
Figs. S1 to S8
Tables S1 to S4
References

14 April 2008; accepted 9 September 2008
10.1126/science.1159052

A Stochastic Single-Molecule Event Triggers Phenotype Switching of a Bacterial Cell

Paul J. Choi,* Long Cai,*† Kirsten Frieda,‡ X. Sunney Xie§

By monitoring fluorescently labeled lactose permease with single-molecule sensitivity, we investigated the molecular mechanism of how an *Escherichia coli* cell with the *lac* operon switches from one phenotype to another. At intermediate inducer concentrations, a population of genetically identical cells exhibits two phenotypes: induced cells with highly fluorescent membranes and uninduced cells with a small number of membrane-bound permeases. We found that this basal-level expression results from partial dissociation of the tetrameric lactose repressor from one of its operators on looped DNA. In contrast, infrequent events of complete dissociation of the repressor from DNA result in large bursts of permease expression that trigger induction of the *lac* operon. Hence, a stochastic single-molecule event determines a cell's phenotype.

Genetically identical cells in the same environment can exhibit different phenotypes, and a single cell can switch between distinct phenotypes in a stochastic manner (*1*–*4*). In the classic example of lactose metabolism in *Escherichia coli*, the *lac* genes are fully expressed for every cell in a population under high extracellular concentrations of inducers, such as the lactose analog methyl-β-D-thiogalactoside (TMG). However, at moderate inducer concentrations, the *lac* genes are highly expressed in only a fraction of a population, which may confer a fitness advantage for the entire population (*5*). We studied the molecular mechanism that controls the stochastic phenotype switching of a single cell.

Lactose metabolism is controlled by the *lac* operon (*6*, *7*), which consists of the *lacZ*, *lacY*, and *lacA* genes encoding β-galactosidase, lactose permease, and transacetylase, respectively. Expression of the operon is regulated by a transcription factor, the *lac* repressor (*8*), which dissociates from its specific binding sequences of DNA, the *lac* operators, in the presence of an inducer to allow transcription (Fig. 1A). The production of the permease increases inducer influx (*9*), which results in positive feedback on the permease expression level. Above a certain threshold of permease numbers, a cell will remain in a phenotype that is capable of lactose metabolism, and below this threshold, a cell will remain in a phenotype that is incapable of lactose metabolism (*10*, *11*). The former has high fluorescence from the cell membrane when the permease is labeled with a yellow fluorescent protein (YFP), whereas the latter has low fluorescence. The image in Fig. 1B shows the coexistence of both phenotypes in a cell population at intermediate inducer concentrations, characterized by the bimodal distributions of fluorescence intensity in Fig. 1C.

Although it is known that the bistability in the *lac* operon arises from positive feedback (*12*, *13*), the molecular mechanism underlying the initiation of switching between two phenotypes remains unclear. Novick and Weiner deduced that switching from the uninduced state to the induced state occurs through a single rate-limiting molecular process (*12*) rather than a multistep process. They further hypothesized that the random expression of one molecule of permease was enough to trigger induction. However, this has never been observed experimentally because of insufficient sensitivity.

Our group has previously shown that a single fluorescent protein molecule can be visualized in a living bacterial cell by using the method of detection by localization (*14*–*16*). Because a permease molecule is a membrane protein with slow diffusion, its fluorescence label is highly localized as compared with a fluorescent protein in the cytoplasm, which allows for its detection above the background of cellular autofluorescence. Thus, we generated strain SX700, which possesses intact *lac* promoter elements and expresses a functional LacY-YFP fusion protein (fig. S1) from *lacY*'s native chromosomal position (fig. S2). Figure 1B shows a fluorescence image of SX700 cells that allows us to directly count the number of single LacY-YFP molecules present in a cell.

Figure 1D shows the histogram of permease copy numbers in the uninduced fraction of cells, free from the complication of autofluorescence background in the lower peak of Fig. 1C. Evidently, the uninduced cells have 0 to 10 LacY molecules with significant probability, independent of the inducer concentration. Had one permease been enough to trigger induction, all cells in the uninduced subpopulation would have contained zero LacY molecules. Thus, we conclude that a single copy of LacY is not sufficient to induce switching of the phenotype, and the threshold for induction must be much higher than several molecules per cell.

We then set out to determine the threshold of permease molecules for induction. It is experimentally difficult to capture the rare events of phenotype switching in real time. To overcome this difficulty, we prepared cells covering a broad range of permease copy numbers by first fully inducing the cells and subsequently washing out the inducer. We then allowed the cells to divide for one to six generations, during which the initial permeases were partitioned into daughter cells (*17*). Figure 2A shows fluorescence time traces of the cells, normalized by cell size, upon the reintroduction of 40 μM TMG. Although the fluorescence in cells with low permease numbers continued to decay because of cell division and photobleaching, cells with more than 300 initial permease molecules induced again within 3 hours and showed increased fluorescence. Figure 2B shows the probability of induction as a function of initial permease number, which is well fit by a Hill equation with a Hill coefficient of 4.5 and a threshold of ~375 molecules. The large value of the threshold indicates that hundreds of permease molecules are necessary to switch the phenotype.

If the induction is due to a single rate-limiting event as Novick and Weiner argued, there must be a single large burst of permease expression to reach this high threshold. However, only small

Department of Chemistry and Chemical Biology, Harvard University, Cambridge, MA 02138, USA.
*These authors contributed equally to this work.
†Present address: Division of Biology, California Institute of Technology, Pasadena, CA 91125, USA.
‡Present address: Biophysics Program, Stanford University, Stanford, CA 94305, USA.
§To whom correspondence should be addressed. E-mail: xie@chemistry.harvard.edu

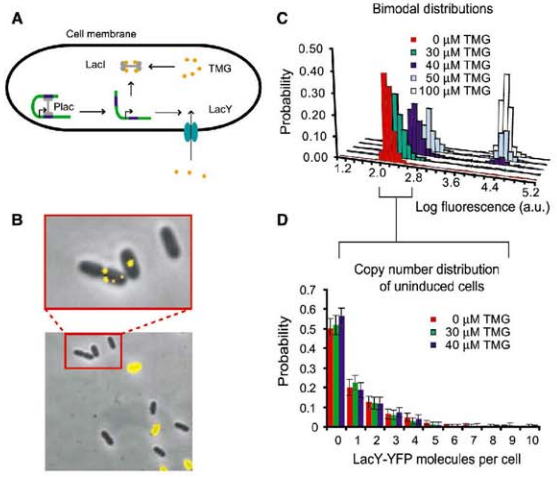

Fig. 1. The expression of lactose permease in *E. coli*. **(A)** The repressor LacI and permease LacY form a positive feedback loop. Expression of permease increases the intracellular concentration of the inducer TMG, which causes dissociation of LacI from the promoter, leading to even more expression of permeases. Cells with a sufficient number of permeases will quickly reach a state of full induction, whereas cells with too few permeases will stay uninduced. **(B)** After 24 hours in M9 medium containing 30 μM TMG, strain SX700 expressing a LacY-YFP fusion exhibits all-or-none fluorescence in a fluorescence-phase contrast overlay (bottom, image dimensions 31 μm × 31 μm). Fluorescence imaging with high sensitivity reveals single molecules of permease in the uninduced cells (top, image dimensions 8 μm × 13 μm). **(C)** After 1 day of continuous growth in medium containing 0 to 50 μM TMG, the resulting bimodal fluorescence distributions show that a fraction of the population exists either in an uninduced or induced state, with the relative fractions depending on the TMG concentration. **(D)** The distributions of LacY-YFP molecules in the uninduced fraction of the bimodal population at different TMG concentrations, measured with single-molecule sensitivity, indicate that one permease molecule is not enough to induce the *lac* operon, as previously hypothesized (*12*). More than 100 cells were analyzed at each concentration. Error bars are SE determined by bootstrapping.

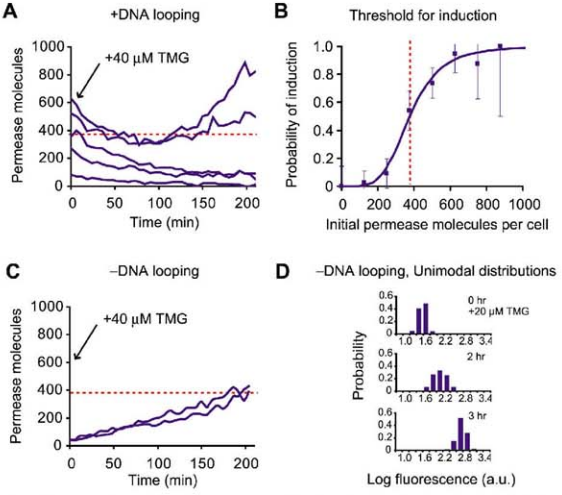

Fig. 2. Measurement of the threshold of permease molecules for induction. **(A)** Single-cell time traces of fluorescence intensity, normalized by cell size, starting from different initial permease numbers. The initial LacY-YFP numbers were prepared through dilution by cell division of fully induced cells after removal of the inducer. Upon adding 40 μM TMG at time 0, those cells with low initial permease numbers lost fluorescence with time as a result of dilution by cell division and photobleaching, whereas those cells with high initial permease numbers exhibited an increase in fluorescence as a result of reinduction. Permease molecule numbers were estimated from cell fluorescence (*28*). The dashed red line indicates the determined threshold. **(B)** The probability of induction of a cell within 3 hours as a function of the initial permease number was determined using traces from 90 cells. The probability of induction (p) was fit with a Hill equation $p = y^{4.5}/(y^{4.5} + 375^{4.5})$ for the initial permease number y. The threshold of permease numbers for induction was thus determined to be 375 molecules. Error bars are the inverse square root of the sample size at each point. **(C)** To prove that the complete dissociation of tetrameric repressor from two operators triggers induction, we constructed strain SX702 with auxiliary operators removed (no DNA looping). The figure shows single-cell traces of permease numbers in single cells grown in 40 μM TMG as a function of time. Unlike the looping strain SX700, the rapid induction of SX702 is no longer dependent on the initial number of permease molecules. This proves that phenotype switching is the result of a complete dissociation of the tetrameric repressor, as shown in (B). **(D)** In the absence of DNA looping, the entire population of strain SX702 rapidly induces in a coordinated manner from far below the threshold for a concentration as low as 20 μM TMG. DNA looping is necessary for bistability of the *lac* operon under these conditions.

bursts have been observed in previous studies of the repressed *lac* promoter (*14*, *18*). Large bursts, if any, would be infrequent and insufficiently sampled in the previous work. To explain why both small and large bursts may occur from the *lac* promoter, we considered the tetrameric repressor that is doubly bound to two operators, forming a DNA loop (*19*, *20*). We hypothesized that more frequent partial dissociations of the tetrameric repressor from one operator lead to single transcripts and small bursts of protein expression, whereas rare complete dissociations from all operators lead to multiple transcripts and large bursts of expression. In this model, the complete dissociation of the tetrameric repressor would be the molecular event that causes a change in phenotype.

To test this model experimentally, we first removed the auxiliary operators from SX700 to generate SX702 (fig. S2), which cannot form DNA loops. As a result, every dissociation event of LacI from the remaining O1 operator results in a complete dissociation event that would generate a large burst of expression. In this case, we predicted frequent and large bursts of expression with

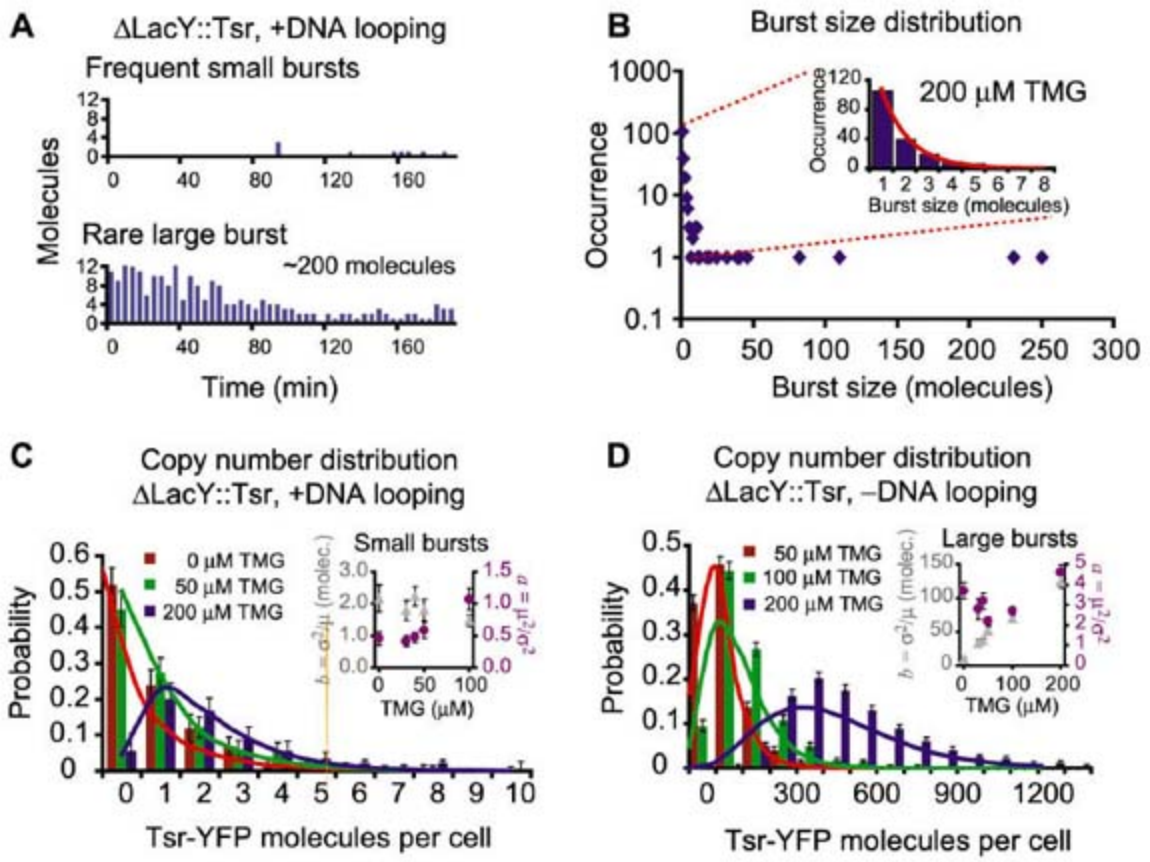

Fig. 3. Small and large bursts in the absence of positive feedback. In order to eliminate positive feedback from permease transport, we constructed strain SX701 by replacing the lactose permease with the membrane protein fusion Tsr-YFP. (**A**) Real-time traces of protein production in SX701 in 200 μM TMG. The fluorescent proteins were photobleached immediately after detection to ensure that only newly produced proteins were measured after each 4-min interval. Representative traces of single cells show frequent small bursts, associated with partial dissociation events, and a rare large burst, associated with a complete dissociation event, of protein production. (**B**) Distribution of burst sizes determined for 208 bursts from the real-time experiment depicted in (A). Although the majority of bursts are small, a number of unusually large bursts are observed. The former are attributed to partial dissociations and the latter to complete dissociations of the tetrameric repressor. (Inset) The occurrence of burst sizes smaller than 10 molecules is well-fit by an exponential distribution (red line). (**C**) Analysis of small bursts from partial dissociations of the tetrameric repressor shows that the distribution of YFP molecules in the range of 0 to 10 molecules does not change in the range of 0 to 200 μM TMG. A small percentage of cells have much more than 10 molecules and do not appear on the axis of this plot (fig. S7C). Over 100 cells were analyzed for each concentration. (Inset) The number of bursts per cell cycle (purple circles) increases slightly whereas the average number of proteins per burst (gray triangles) remains approximately constant. These kinetic parameters are determined from the steady-state distribution of YFP in those cells with fewer than 10 molecules (see SOM text). Error bars are standard errors determined by bootstrapping. Gamma distributions using the determined parameters are overlayed as solid lines. The gamma distribution for 200 μM is normalized for the subpopulation of cells with fewer than 10 molecules. (**D**) In addition to having the permease replaced with Tsr-YFP, strain SX703 has the auxiliary operators removed, eliminating DNA looping so that every dissociation event is a complete dissociation. The protein number distributions should reflect the bursts of protein expression from complete dissociations alone. (Inset) the noise parameters μ^2/σ^2 (purple circles) and σ^2/μ (gray triangles) suggest that the frequency of large bursts is independent of the TMG concentration but that the burst size is not.

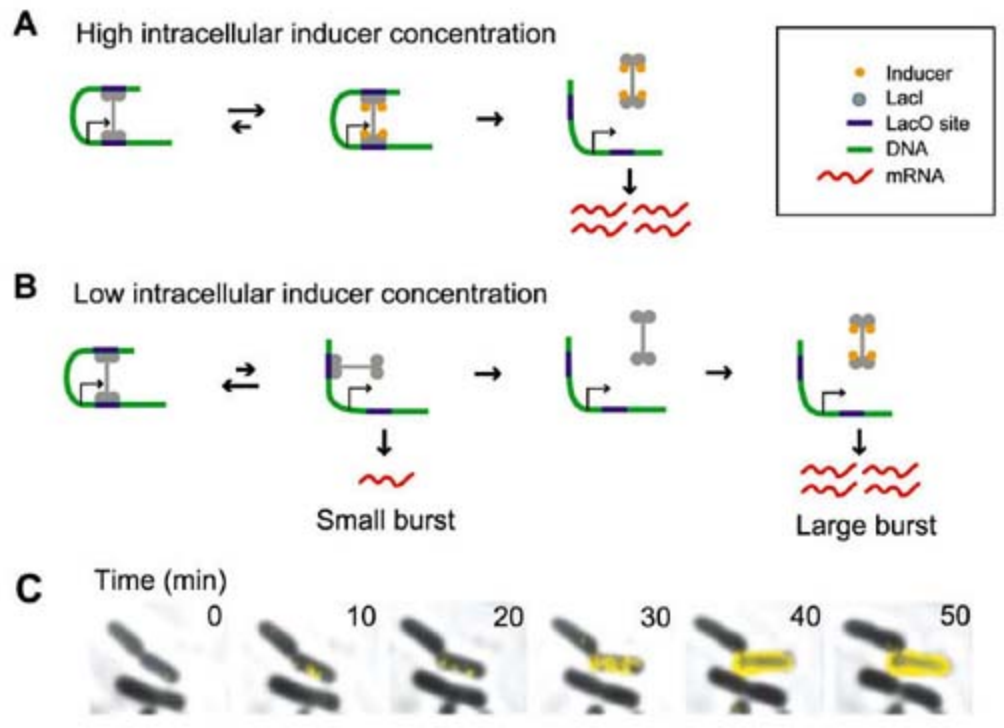

Fig. 4. Complete dissociation of the tetrameric repressor triggers induction. (**A**) A high concentration of intracellular inducer can force dissociation of the repressor from its operators, as described by Monod and Jacob (*6*). (**B**) At low or intermediate concentrations of intracellular inducer, partial dissociation from one operator by the tetrameric LacI repressor is followed by a fast rebinding. Consequently, no more than one transcript is generated during such a brief dissociation event. However, the tetrameric repressor can dissociate from both operators stochastically and then be sequestered by the inducer so that it cannot rebind, leading to a large burst of expression. (**C**) A time-lapse sequence captures a phenotype-switching event. In the presence of 50 μM TMG, one such cell switches phenotype to express many LacY-YFP molecules (yellow fluorescence overlay) whereas the other daughter cell does not (movie S1).

a faster rate of phenotype switching. Indeed, Fig. 2C shows that without DNA looping, SX702 induces rapidly upon the addition of inducer, even though the initial permease numbers are much smaller than the threshold in Fig. 2, A and B [see supporting online material (SOM) text]. The removal of DNA looping eliminated bistability. This was manifested by the unimodal distributions of an inducing population in Fig. 2D at 20 μM TMG.

To directly observe large bursts, we replaced the *lacY* gene of the *E. coli* chromosome with a membrane-localized protein, Tsr, fused to YFP, which generated strain SX701 (fig. S2). Eliminating LacY's positive feedback served two purposes: to allow the resolution of distinct large bursts and to prove that large bursts do not require permease activity. The Tsr-YFP fusion functioned as a surrogate reporter for protein production with single-molecule sensitivity.

When we acquired time-lapse fluorescence microscopy movies of SX701 cells with 200 μM TMG, we observed that Tsr-YFP was produced mostly in small bursts, but occasionally in a large burst (Fig. 3A). The distribution of burst sizes (Fig. 3B) taken from these real-time traces shows both the frequent exponentially distributed small bursts and the rare unusually large bursts.

We next analyzed the inducer concentration dependence of burst frequency and size by using population distributions. Figure 3C shows that SX701 has a protein copy number distribution in a cell population very similar to the distributions of uninduced cells in Fig. 1D within the range of 0 to 10 molecules. We have shown that these copy-number distributions manifest the stochasticity in gene expression characterized by two parameters, transcription rate (a) and the burst size of proteins per mRNA (b), and can be well fit with a gamma distribution $p(n) = b^{-a}n^{a-1}e^{-n/b}/\Gamma(a)$ (*18*, *21*). The inset in Fig. 3C shows a and b determined in this fashion for cells with fewer than 10 molecules for different TMG concentrations. The small burst size is independent of the inducer concentration, whereas the small burst frequency has only a weak concentration dependence. In fact, within the range of 0 to 50 μM TMG, the small burst frequency does not change appreciably, suggesting that the partial repressor dissociation is predominantly spontaneous at low inducer concentrations.

Because characterization of the rare, large bursts is difficult for the wild-type operators, we generated strain SX703, in which the permease gene was replaced with Tsr-YFP and the O2 and O3 operators were removed to eliminate DNA looping. Every dissociation event in the SX703 should be a complete dissociation, and hence should lead to a large burst. Because there is a 20- to 100-fold difference in the inducer-binding affinity to the repressor in DNA-bound form (~1 mM) relative to the free form (~10 μM) (*22*, *23*), we expected to observe the stochastic dissociation of the repressor from the sole operator site and sequestration of the free repressor by the inducers at the concentrations we used (0 to 50 μM) rather than inducer-driven dissociation events.

Consequently, we expected the frequency of dissociation to remain constant as the inducer concentration increased but expected the length of the dissociation time to increase. When we analyzed the steady-state protein distributions at different inducer concentrations (Fig. 4C) by applying a generalized interpretation of the *a-b* model, which estimates the number of proteins per expression bursts (SOM text), we found that inducer concentration affects the size of large bursts but not the frequency. This observation supports our model that the inducer sequesters the repressor after it stochastically dissociates from the operator and prolongs its lifetime in the non–DNA-bound state, leading to larger burst sizes (SOM Text).

Figure 4 summarizes the model of induction in the *lac* operon. In the case of high inducer concentration (Fig. 4A), the repressor is actively pulled off both operator sites by the inducer, as described in Monod and Jacob's model (*6*). Under low or intermediate TMG concentrations, however, the repressor can stochastically dissociate from one operator independently of the inducer, as shown in Fig. 4B. When the repressor partially dissociates from one operator, a small protein burst from a single copy of mRNA is generated (*14*) before the repressor rapidly rebinds to the vacant operator. When the repressor completely dissociates from both operators, multiple mRNAs are transcribed, which leads to a large protein burst that surpasses the LacY threshold, initiates positive feedback, and maintains a switch in phenotype.

Why do complete dissociation events give rise to large bursts? Our group has recently shown that if a repressor dissociates from DNA, it takes a time scale of minutes for the repressor to rebind to the operator because the repressor spends most of its time binding to nonspecific sequences and searching through the chromosomal DNA (*15*). In addition, there are only a few copies of the tetrameric repressors (*8*). Such a slow repressor rebinding time, relative to transcript-initiation frequencies (*24*), would allow multiple copies of *lacY* mRNA to be made following a complete repressor dissociation event. Furthermore, in the presence of inducer, the nonspecific binding constant remains unchanged (*25*), but the affinity of the inducer-bound repressor to the operator is substantially reduced, rendering specific rebinding unlikely. The large burst that results from slow repressor rebinding is an example of how a single-molecule fluctuation under out-of-equilibrium conditions can have considerable biological consequences, which has been discussed theoretically in the context of cell signaling (*26*) and gene expression (*27*) but has not previously been experimentally observed.

Because the binding affinity of inducers for operator-bound repressors is weaker than for free repressors by a factor of 20 to 100 (*22*, *23*), the inducer's role under low concentrations is not to force a dissociation event but to simply sequester repressors that stochastically dissociated from their operators in order to aid in creating a large burst (SOM text) (Fig. 3D). When the inducer concentration increases, the size of the large bursts increases because the duration of complete dissociations increases, improving the probability that a large burst can cross the positive-feedback threshold. Consequently, it is this higher probability of successful switch-on events that shifts the bimodal population toward the fully induced state as inducer concentration increases.

The biological importance of DNA looping has been discussed in the literature in terms of facilitating interactions between distance sequences and enhancing the local concentration (*19*, *20*). Here, we show that DNA looping allows the control of gene regulation on multiple time scales through different kinds of dissociation events. The presence of DNA looping allows the use of rare complete dissociation events to control a bistable genetic switch.

We have shown that a stochastic single-molecule event can cause a change in phenotype. It is not difficult to imagine that similar molecular events might determine more complicated phenotypes of other cells or organisms. The ability to observe and probe the properties of genetic switches at the molecular level is crucial for understanding how cells make decisions.

Referenes and Notes

1. A. Arkin, J. Ross, H. H. McAdams, *Genetics* **149**, 1633 (1998).
2. M. Ptashne, *A Genetic Switch: Phage Lambda Revisited* (Cold Spring Harbor Laboratory Press, Woodbury, NY, 2004).
3. M. Kaern, T. C. Elston, W. J. Blake, J. J. Collins, *Nat. Rev. Genet.* **6**, 451 (2005).
4. D. Dubnau, R. Losick, *Mol. Microbiol.* **61**, 564 (2006).
5. E. Dekel, U. Alon, *Nature* **436**, 588 (2005).
6. J. Monod, F. Jacob, *J. Mol. Biol.* **3**, 318 (1961).
7. B. Müller-Hill, *The Lac Operon: A Short History of a Genetic Paradigm* (de Gruyter, New York, 1996).
8. W. Gilbert, B. Müller-Hill, *Proc. Natl. Acad. Sci. U.S.A.* **56**, 1891 (1966).
9. G. N. Cohen, J. Monod, *Bacteriol. Rev.* **21**, 169 (1957).
10. J. M. G. Vilar, C. C. Guet, S. Leibler, *J. Cell Biol.* **161**, 471 (2003).
11. T. Mettetal, D. Muzzey, J. M. Pedraza, E. M. Ozbudak, A. van Oudenaarden, *Proc. Natl. Acad. Sci. U.S.A.* **103**, 7304 (2006).
12. A. Novick, M. Weiner, *Proc. Natl. Acad. Sci. U.S.A.* **43**, 553 (1957).
13. E. M. Ozbudak, M. Thattai, H. N. Lim, B. I. Shraiman, A. van Oudenaarden, *Nature* **427**, 737 (2004).
14. J. Yu, J. Xiao, X. Ren, K. Lao, X. S. Xie, *Science* **311**, 1600 (2006).
15. J. Elf, G. W. Li, X. S. Xie, *Science* **316**, 1191 (2007).
16. X. S. Xie, P. J. Choi, G. W. Li, N. K. Lee, G. Lia, *Annu. Rev. Biophys.* **37**, 417 (2008).
17. N. Rosenfeld, J. W. Young, U. Alon, P. S. Swain, M. B. Elowitz, *Science* **307**, 1962 (2005).
18. L. Cai, N. Friedman, X. S. Xie, *Nature* **440**, 358 (2006).
19. H. Krämer *et al.*, *EMBO J.* **6**, 1481 (1987).
20. S. Oehler, E. R. Eismann, H. Krämer, B. Müller-Hill, *EMBO J.* **9**, 973 (1990).
21. N. Friedman, L. Cai, X. S. Xie, *Phys. Rev. Lett.* **97**, 168302 (2006).
22. M. D. Barkley, A. D. Riggs, A. Jobe, S. Bourgeois, *Biochemistry* **14**, 1700 (1975).
23. M. Dunaway *et al.*, *J. Biol. Chem.* **255**, 10115 (1980).
24. D. Kennell, H. Riezman, *J. Mol. Biol.* **114**, 1 (1977).
25. A. Revzin, P. H. von Hippel, *Biochemistry* **16**, 4769 (1977).
26. M. N. Artyomov, J. Das, M. Kardar, A. K. Chakraborty, A. K. *Proc. Natl. Acad. Sci. U.S.A.* **104**, 18958 (2007).

27. J. E. M. Hornos *et al.*, *Phys. Rev. E* **72**, 051907 (2005).
28. Materials and methods are available as supporting material on *Science* Online.
29. We would like to thank G. Church, A. Miyawaki, and B. Wanner for bacterial strains and plasmids; J. Hearn for technical assistance; and J. Elf, N. Friedman, and G. W. Li for helpful discussions. This work was supported by the NIH Director's Pioneer Award. P.J.C. acknowledges the John and Fannie Hertz Foundation.

Supporting Online Material
www.sciencemag.org/cgi/content/full/322/5900/442/DC1
Materials and Methods
SOM Text
Figs. S1 to S8
Movie S1
References

5 June 2008; accepted 12 September 2008
10.1126/science.1161427

Remeasuring the Double Helix

Rebecca S. Mathew-Fenn,[1,2]* Rhiju Das,[2,3]*† Pehr A. B. Harbury[1,2]‡

DNA is thought to behave as a stiff elastic rod with respect to the ubiquitous mechanical deformations inherent to its biology. To test this model at short DNA lengths, we measured the mean and variance of end-to-end length for a series of DNA double helices in solution, using small-angle x-ray scattering interference between gold nanocrystal labels. In the absence of applied tension, DNA is at least one order of magnitude softer than measured by single-molecule stretching experiments. Further, the data rule out the conventional elastic rod model. The variance in end-to-end length follows a quadratic dependence on the number of base pairs rather than the expected linear dependence, indicating that DNA stretching is cooperative over more than two turns of the DNA double helix. Our observations support the idea of long-range allosteric communication through DNA structure.

Since the double helical structure of DNA was discovered 50 years ago (*1*), its average structure and internal fluctuations have been objects of intense study. Near its equilibrium structure, the DNA duplex is generally viewed as an ideal elastic rod. Current estimates put the bending rigidity B at ~230 pN·nm^2, the torsional rigidity C at 200 to 500 pN·nm^2, and the stretching modulus S (the extrapolated force required to double the length of the DNA) at ~1000 pN (*2*–*7*). Recent experimental observations, however, have called into question the accuracy of this simple mechanical picture. For example, single-molecule measurements show that overtwisting of DNA induces helix stretching (*8*). This twist-stretch coupling leads to a revised picture of DNA in which the helix core is modeled as an elastic rod while the phosphodiester backbone is modeled as a rigid wire. Analysis of DNA bending on short length scales has also yielded surprises. Specifically, ~100–base pair (bp) DNA helices circularize two to four orders of magnitude faster than would be predicted by the elastic rod model, leading to the idea that discrete kinks contribute to DNA bending (*9*, *10*).

The most straightforward way to characterize DNA structural fluctuations would be to directly visualize them under nonperturbing solution conditions. Kilobase-sized DNA structures have been imaged in real time, but it has not been possible to resolve bending, twisting, and stretching fluctuations at the microscopic level. Alternatively, analyzing the motions of very short DNA fragments simplifies the problem by limiting the contributions from bending. In practice, this has proved technically challenging. The experimental tools suited to the job, molecular rulers, provide an indirect readout of distance that is difficult to relate quantitatively to variation in end-to-end length. Indeed, short DNA duplexes are often assumed to be completely rigid and are used as length standard controls for new molecular rulers (*11*–*14*).

Our investigations apply a recently developed technique for measuring distance distribu-

[1]Biophysics Program, Stanford University, Stanford, CA 94305, USA. [2]Department of Biochemistry, Stanford University, Stanford, CA 94305, USA. [3]Department of Physics, Stanford University, Stanford, CA 94305, USA.

*These authors contributed equally to this work.
†Present address: Department of Biochemistry, University of Washington, Seattle, WA 98195, USA.
‡To whom correspondence should be addressed. E-mail: harbury@cmgm.stanford.edu

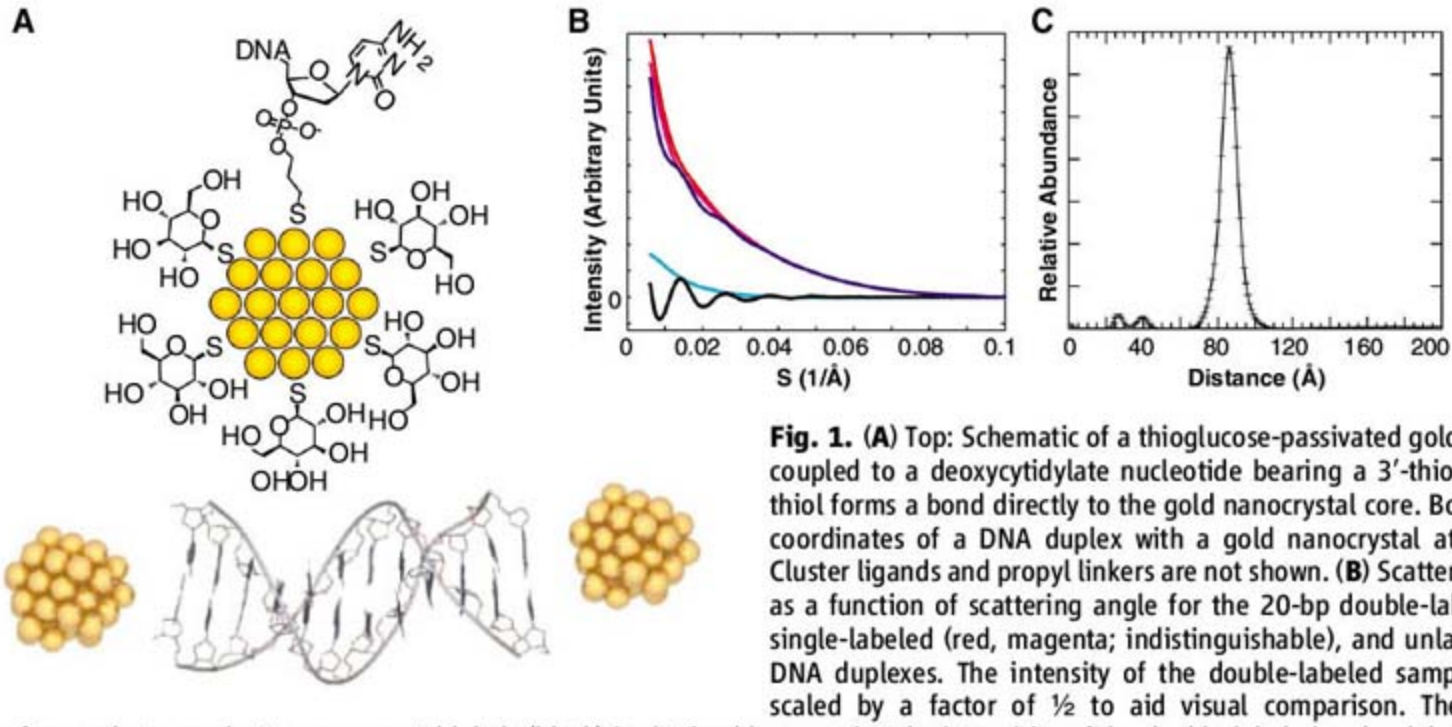

Fig. 1. (**A**) Top: Schematic of a thioglucose-passivated gold nanocrystal coupled to a deoxycytidylate nucleotide bearing a 3′-thiol group. The thiol forms a bond directly to the gold nanocrystal core. Bottom: Model coordinates of a DNA duplex with a gold nanocrystal at either end. Cluster ligands and propyl linkers are not shown. (**B**) Scattering intensity as a function of scattering angle for the 20-bp double-labeled (blue), single-labeled (red, magenta; indistinguishable), and unlabeled (cyan) DNA duplexes. The intensity of the double-labeled sample has been scaled by a factor of ½ to aid visual comparison. The pattern of scattering interference between the two nanocrystal labels (black) is obtained by summing the intensities of the double-labeled and unlabeled samples, then subtracting the intensities of the two single-labeled samples (*15*). The data were obtained at 200 μM DNA and are averages of 10 exposures of 1 s each. Measurements were made at 25°C in the presence of 70 mM Tris-HCl (pH 8.0), 100 mM NaCl, and 10 mM ascorbic acid. The scattering parameter S is defined as $(2 \sin \theta)/\lambda$, where 2θ is the scattering angle and λ is the x-ray wavelength. (**C**) Transformation of the nanocrystal scattering interference pattern into a weighted sum of sinusoidal basis functions (corresponding to different interprobe distances) yields the probability distribution for nanocrystal center-of-mass separation (*15*).

tions based on small-angle x-ray scattering interference between heavy-atom nanocrystals (*15*). Gold nanocrystals with radii of 7 Å are site-specifically attached to the ends of DNA double helices of varying length, as illustrated for a 20-bp DNA segment in Fig. 1A. The experimental scattering profile for this molecule (Fig. 1B) displays a characteristic oscillation with an inverse period of 86 Å, due to the scattering interference between the nanocrystals. This interference pattern is decomposed into a linear combination of basis scattering functions corresponding to discrete separation distances between the nanocrystals, providing the interparticle distance distribution (Fig. 1C). Distributions measured this way can be extremely sharp if the probes are at fixed distances, and they reveal broadened, highly skewed, or even bimodal distance distributions if they are present (*15*). The x-ray ruler reads out an effectively instantaneous distribution of distances, due to the short time scale of x-ray scattering from bound electrons. The nanocrystal labels produce no detectable disruption of the structure of DNA double helices (as monitored by circular dichroism spectroscopy) and negligibly alter the melting thermodynamics of the helices into single strands (table S1 and fig. S1). As a further precaution against any undetected effects on DNA structure from the gold probes, we base our conclusions below on the change in probe separation as the helix length is increased, and not on the absolute value of the measurement for a single DNA construct.

We prepared labeled DNA duplexes with lengths between 10 and 35 bp in 5-bp increments (table S2). The scattering interference profiles for these molecules (Fig. 2A) give end-to-end distance distributions with approximately symmetric fluctuations around a well-defined mean distance (Fig. 2B). The interprobe distance increases approximately linearly with the number of helix base pairs (Fig. 3A). A fit to these data that takes into account the potential displacement of the gold probes off of the helix axis (fig. S2) gives an average rise per base pair of 3.29 ± 0.07 Å (Fig. 3A), in close agreement with the average crystallographic value of 3.32 ± 0.19 Å (*16*). To estimate measurement errors, we compared distributions from independently prepared samples exposed at two different x-ray beamlines and with different detectors and calibration standards (fig. S3). The scatter in the mean was 0.4 Å for the shortest duplex and 0.9 Å for the longest duplex, with intermediate values for the other constructs (the error bars are smaller than the marker size in Fig. 3A). The deviation of the fit from the data exceeds the measurement error and may reflect sequence-dependent variation in the rise per base pair (*16*). The x-ray ruler gives a rise per base-pair intermediate between the lower values (2.9 to 3.1 Å) observed in microscopy experiments (*17*–*19*) and the somewhat higher "canonical"

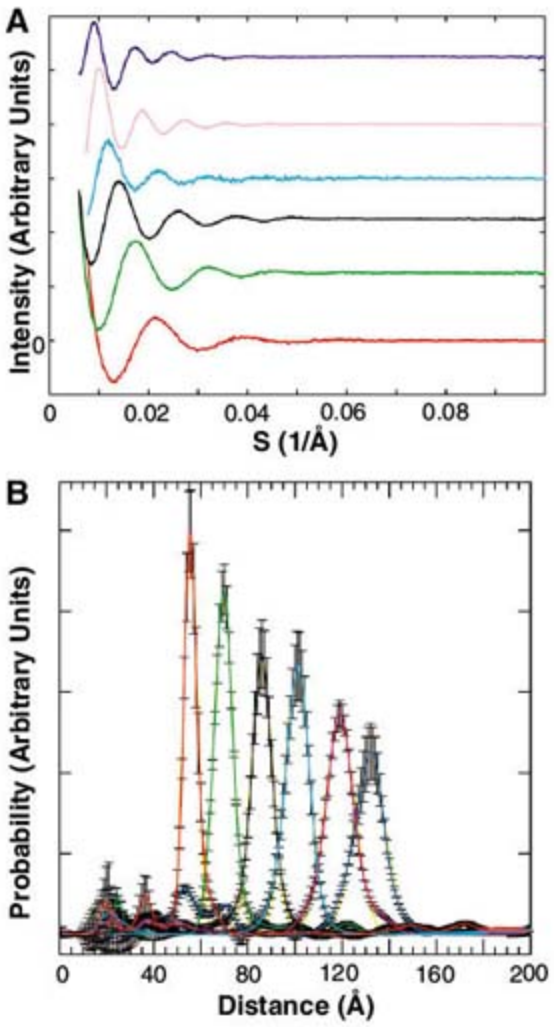

Fig. 2. (**A**) Nanocrystal scattering interference patterns obtained for the 10-bp (red), 15-bp (green), 20-bp (black), 25-bp (cyan), 30-bp (magenta), and 35-bp (blue) duplexes are offset vertically. See table S2 for DNA sequences. (**B**) Probability distance distribution curves for the 10-bp (red), 15-bp (green), 20-bp (black), 25-bp (cyan), 30-bp (magenta), and 35-bp (blue) duplexes. The distributions are normalized to sum to unity. Each distribution was fit to a Gaussian curve (yellow) using the "fminsearch" function in MATLAB. See fig. S10 for distance distribution curves plotted individually with error bars, and fig. S3 for repeated measurements using independently prepared samples at two different x-ray synchrotron beamlines.

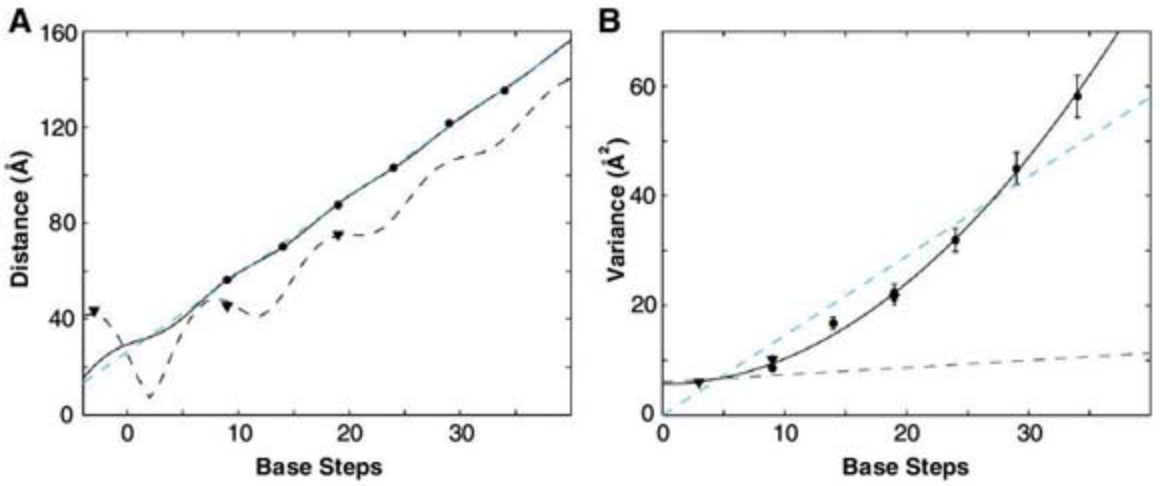

Fig. 3. (**A**) Mean nanocrystal-nanocrystal separation distance of end-labeled duplexes (circles) and internally labeled duplexes (triangles), plotted with respect to the number of intervening DNA base-pair steps. The distances for the end-labeled duplexes oscillate around a straight line (dashed blue line). A three-variable fit accounting for rotation of the nanocrystal probes around the helix axis (solid black line, fig. S2, $R^2 = 0.9995$) gives a rise per base pair of 3.29 ± 0.07 Å and a 9 Å radial displacement of the nanocrystals off of the helix axis. A similar two-variable fit to the internally labeled duplex distances (dashed black line, $R^2 = 0.9992$) gives a rise per base pair of 3.27 ± 0.1 Å and a 21 Å radial displacement of the nanocrystals off of the helical axis. Each fit takes into account the reduction in end-to-end length expected from bending fluctuations (table S3). The distance data points derive from the Gaussian curves in Fig. 2B. The measurement errors are estimated to be ±0.5%, according to repeat experiments with independently prepared samples at two different synchrotrons, and are smaller than the graph symbols (fig. S3). (**B**) Variance in nanocrystal-nanocrystal separation distance of end-labeled duplexes (circles) and internally labeled duplexes (triangles), plotted with respect to the number of intervening DNA base-pair steps. The variance predictions for an ideal elastic rod with a stretching modulus of 1000 pN (the value measured in single-molecule stretching experiments) are shown (dashed black line) and deviate grossly from the data. A linear relationship between variance and base-pair steps (dashed cyan line, two variables, $R^2 = 0.919$) is expected if the stretching of base-pair steps is uncorrelated along the DNA duplex (*24*). Alternatively, a quadratic relationship (solid black line, two variables, $R^2 = 0.997$) should hold if the DNA stretches cooperatively. The quadratic fit indicates that each base-pair step contributes 0.21 Å of standard deviation to the end-to-end length of a duplex. The *y* intercept of 5.7 Å^2 corresponds to variance arising from experimental factors. The variance data points derive from the Gaussian curves in Fig. 2B. Each fit takes into account the variance expected from bending fluctuations (table S3). The uncertainties in the variance values are estimated to be ±6.6%, based on the standard deviation of repeated measurements for the 25-bp duplex at independent beamlines and with independently prepared samples (fig. S3).

value (3.4 Å) obtained for DNA in condensed states or under tension (*20*, *21*).

Structural fluctuations of the DNA should be reflected in the width of the measured distance distributions after other sources of variance, such as linker flexibility and nanocrystal size heterogeneity, have been taken into account (Fig. 3B). DNA-independent factors are expected to contribute the same amount of variance to measurements with different duplexes (~6 $Å^2$ as fit in Fig. 3B). Thus, the increase in distribution width with DNA length must derive from structural changes in the DNA itself. Three facts argue that stretching fluctuations, rather than bending fluctuations or twisting fluctuations, dominate the approximately ±10% spread in end-to-end distance that we observe: (i) The DNA samples studied here are shorter than the bending persistence length of double-helical DNA (*22*). Both Monte Carlo calculations and an analytical approximation (table S3) (*23*) yield 7 $Å^2$ as the maximum contribution of bending fluctuations to the end-to-end length variance of the 35-bp duplex. This value accounts for only 14% of the observed variance. (ii) DNA bends produce asymmetrical distributions with shoulders at shorter distances (*15*), whereas the distributions we observe are symmetrical (Fig. 2B). (iiii) Because the nanocrystals lie close to the helical axis (Fig. 3A and fig. S2), twisting fluctuations have small effects on the measured end-to-end distances and cannot account for the observed variance.

The distance distributions are not consistent with the conventional model of the DNA duplex as an ideal elastic rod with a stretch modulus of ~1000 pN. To illustrate the point, suppose that the entire 8.5 $Å^2$ variance of the 10-bp duplex distribution arises from experimental sources unrelated to DNA stretching. Presumably, the same 8.5 $Å^2$ applies to the other duplex samples, which differ only by addition of base pairs to the center of the duplex sequence. The conventional model predicts that for the longest 35-bp duplex, DNA stretching should contribute an additional 3.3 $Å^2$ of variance, for a total variance of 11.8 $Å^2$ (dashed black line in Fig. 3B) (*24*). In fact, the observed variance is 51 $Å^2$; the contribution of DNA stretching to the variance is larger than predicted by a factor of ~13. A linear fit of the observed variances with respect to DNA length (dashed cyan line in Fig. 3B) indicates an apparent stretch modulus of ~91 pN. The resistance of DNA to stretching is thus weaker in the absence of tension, as measured herein, than in the presence of high tension, as in single-molecule stretching experiments.

A notable feature of the x-ray scattering data is the change in variance with duplex length (Fig. 3B). The elastic rod model predicts that the variance should increase linearly with the number of base steps (dashed lines in Fig. 3B). In contrast, we observe a quadratic dependence of variance on DNA length. The errors in the measured variances fall between 0.2 and 2.0 $Å^2$, according to replicate measurements at different x-ray beamlines with independently prepared samples (fig. S3). The data fit a quadratic dependence to within this measurement error (black line; $\chi^2 = 7.5$ with 7 degrees of freedom; $P = 0.39$), but not a linear dependence (cyan dashed line; $\chi^2 = 91$ with 7 degrees of freedom; $P = 7.4 \times 10^{-17}$). A quadratic increase in variance can only occur if the stretching fluctuations of neighboring base steps in a duplex are tightly correlated (*24*). Fits to models that interpolate between linear and quadratic dependences with a range of correlation lengths are given in fig. S4. These fits demonstrate that the stretching correlation must persist over at least two turns of a double helix. Thus, short DNA fragments stretch cooperatively: As the first two bases move farther apart, so do the last two bases.

We performed numerous controls to rule out experimental artifacts. One worry was that the nanocrystals or DNA might be damaged by x-ray radiation. A variety of tests showed that, in the presence of the radical scavenger ascorbate, the samples were not damaged during data collection (fig. S5) (*15*). Another concern was that as the synthetic DNA fragments became longer, the incidence of single base deletions might increase, resulting in an anomalous length-variance trend. However, electrophoretic and chromatographic analyses showed that all of the samples were >94% pure (figs. S5 and S6). A third possibility was that a lower signal-to-noise ratio in the longer-duplex data sets might lead to broadened distributions. However, when all of the data sets were degraded by truncation at low scattering angles and by addition of white noise so as to match the 35-bp data set, the measured means and variances did not change appreciably (fig. S7). To control for possible end effects, three duplexes were labeled internally by attaching gold probes to the DNA bases (fig. S8). The distance measurements for these internally labeled duplexes were consistent with the measurements for the end-labeled duplexes (Fig. 3).

Finally, we examined how long-range electrostatic forces might affect the end-to-end distance distributions. The nanocrystals prepared for these studies possess a weak net negative charge (as assessed by gel electrophoresis). Nonetheless, measurements at 10 mM, 100 mM, and 1 M NaCl (Debye screening lengths of 30 Å, 10 Å, and 3 Å, respectively) gave indistinguishable variances, indicating a negligible role of electrostatic repulsion between the two probes and between the probe and DNA in the variance measurements. The melting temperatures for the unlabeled, singly labeled, and doubly labeled duplexes also indicated a negligible interaction energy between the nanocrystals (table S1).

In light of our findings, we reexamined previous structural studies of short DNA duplexes (*24*). A comprehensive analysis of the end-to-end lengths for DNA duplexes in the Nucleic Acid Database reveals a range of distances that is consistent with our solution observations (fig. S9). However, this crystallographic distribution might be artificially broadened because it includes many different DNA sequences and crystallization conditions, or artificially narrowed because it includes many structures solved at 109 K. A plot of crystallographic length variance with respect to number of base steps is noisy and can be fit equally well with linear or quadratic curves. These data are therefore inconclusive with respect to the cooperativity of DNA stretching. We also reevaluated recently published time-resolved single-molecule fluorescence resonance energy transfer (FRET) (*25*) and electron spin resonance data (*26*) measured on DNA duplex samples. Plots of the end-to-end length variance derived from these data with respect to duplex length are clearly better fit by a quadratic relationship than by a linear relationship (fig. S9; both fits have 2 degrees of freedom). Although the data are noisy, the independent molecular-ruler measurements support the conclusion that short DNA duplexes stretch cooperatively.

A remaining puzzle is why DNA under tension appears to be much stiffer than relaxed DNA. One possibility is that the soft stretching mechanism we observe has a limited range and is fully extended at tensions greater than ~10 pN (the force above which helix stiffness is

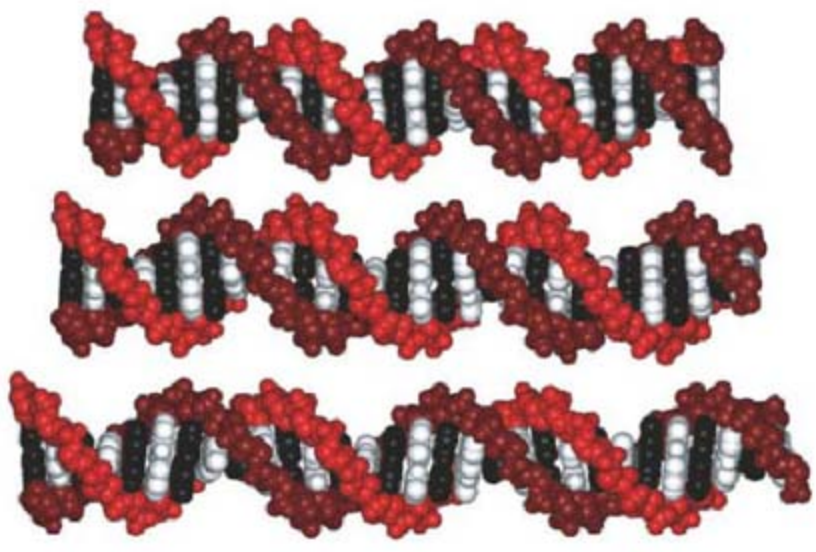

Fig. 4. Molecular models of 30-bp B-form DNA double helices with lengths 10% smaller (top) and 10% larger (bottom) than the canonical length (center) preserve base pairing geometry and are sterically allowed. The models were produced using Rosetta with constraints on local rise parameters to induce compression or stretching (*30*). The starting model coordinates were generated by the DNA Star Web Server (*31*). The figure was rendered with PovScript+ (*32*).

typically measured in single-molecule force-extension curves). For example, suppose that each base step can adopt either a short or a long conformation (say 3.3 Å ± 10%) of equivalent energy, and that the conformational state of contiguous bases is correlated over a length of 35 nucleotides. In the absence of tension, short DNA duplexes would populate equally the short and long conformations and therefore exhibit end-to-end distance distributions covering ±10% of the mean length (Fig. 4). The variance of these distributions would grow quadratically with duplex length (*24*). Under a stretching force, however, the DNA would preferentially adopt the long conformation, and this degree of freedom would saturate at modest tensions. At room temperature, 99% of the base steps would exist in the long conformation under 8 pN of applied force, and the apparent stretching modulus would be 1000 pN (*24*). Thus, a very soft stretching degree of freedom in the absence of tension can behave as a very stiff stretching degree of freedom when the duplex is under tension. The stretching of DNA at larger forces would presumably occur by a different mechanism. We note that this two-state model is oversimplified with respect to our data because our measurements would spatially resolve the short and long states if only two existed. However, the saturation behavior holds for models with a larger number of states.

Additional theoretical and experimental work will be required to reveal the microscopic basis for correlated DNA stretching fluctuations and its potential relation to other recently discovered nonideal properties of DNA (*8*–*10*). Whereas FRET experiments with nanosecond time resolution indicate large DNA stretching fluctuations (*25*), alternative FRET experiments that average single-molecule FRET signals over hundreds of microseconds do not (*27*). Thus, DNA stretching dynamics likely occur on a time scale between 10^{-8} and 10^{-5} s. Molecular simulations intended to model DNA stretching will have to access this time regime.

The presence of long-range stretching correlations implies that DNA double helices can, in principle, transmit information over at least 20 bp through an allosteric "domino effect" (*28*, *29*). For example, in the context of the two-state model, a protein that favors binding to a stretched segment of double helix would disfavor the binding of another protein that prefers a compressed conformation. This effect would propagate to sites within 20 bp, and possibly farther. Whether such DNA-mediated allosteric communication alters how the double helix and its specific binding partners interact to regulate biological processes remains to be tested.

References and Notes

1. J. D. Watson, F. H. Crick, *Nature* **171**, 737 (1953).
2. Z. Bryant *et al.*, *Nature* **424**, 338 (2003).
3. S. B. Smith, Y. Cui, C. Bustamante, *Science* **271**, 795 (1996).
4. D. Shore, R. L. Baldwin, *J. Mol. Biol.* **170**, 957 (1983).
5. D. Shore, R. L. Baldwin, *J. Mol. Biol.* **170**, 983 (1983).
6. M. D. Wang, H. Yin, R. Landick, J. Gelles, S. M. Block, *Biophys. J.* **72**, 1335 (1997).
7. D. E. Depew, J. C. Wang, *Proc. Natl. Acad. Sci. U.S.A.* **72**, 4275 (1975).
8. J. Gore *et al.*, *Nature* **442**, 836 (2006).
9. T. E. Cloutier, J. Widom, *Mol. Cell* **14**, 355 (2004).
10. T. E. Cloutier, J. Widom, *Proc. Natl. Acad. Sci. U.S.A.* **102**, 3645 (2005).
11. A. Hillisch, M. Lorenz, S. Diekmann, *Curr. Opin. Struct. Biol.* **11**, 201 (2001).
12. C. Sönnichsen, B. M. Reinhard, J. Liphardt, A. P. Alivisatos, *Nat. Biotechnol.* **23**, 741 (2005).
13. P. Zhu, J. P. Clamme, A. A. Deniz, *Biophys. J.* **89**, L37 (2005).
14. L. S. Churchman, Z. Okten, R. S. Rock, J. F. Dawson, J. A. Spudich, *Proc. Natl. Acad. Sci. U.S.A.* **102**, 1419 (2005).
15. P. A. B. Harbury, *PLoS ONE* **3**, e3229 (2008).
16. W. K. Olson, A. A. Gorin, X. J. Lu, L. M. Hock, V. B. Zhurkin, *Proc. Natl. Acad. Sci. U.S.A.* **95**, 11163 (1998).
17. J. D. Griffith, *Science* **201**, 525 (1978).
18. C. Rivetti, M. Guthold, C. Bustamante, *J. Mol. Biol.* **264**, 919 (1996).
19. K. Sakata-Sogawa, M. Kurachi, K. Sogawa, Y. Fujii-Kuriyama, H. Tashiro, *Eur. Biophys. J.* **27**, 55 (1998).
20. S. B. Zimmerman, B. H. Pheiffer, *J. Mol. Biol.* **135**, 1023 (1979).
21. N. B. Ulyanov, T. L. James, *Methods Enzymol.* **261**, 90 (1995).
22. C. G. Baumann, S. B. Smith, V. A. Bloomfield, C. Bustamante, *Proc. Natl. Acad. Sci. U.S.A.* **94**, 6185 (1997).
23. J. M. Schurr, B. S. Fujimoto, *Biopolymers* **54**, 561 (2000).
24. See supporting material on *Science* Online.
25. T. A. Laurence, X. Kong, M. Jager, S. Weiss, *Proc. Natl. Acad. Sci. U.S.A.* **102**, 17348 (2005).
26. Q. Cai *et al.*, *Nucleic Acids Res.* **34**, 4722 (2006).
27. E. Nir *et al.*, *J. Phys. Chem. B* **110**, 22103 (2006).
28. J. M. Schurr, J. J. Delrow, B. S. Fujimoto, A. S. Benight, *Biopolymers* **44**, 283 (1997).
29. K. M. Kosikov, A. A. Gorin, V. B. Zhurkin, W. K. Olson, *J. Mol. Biol.* **289**, 1301 (1999).
30. A. V. Morozov, J. J. Havranek, D. Baker, E. D. Siggia, *Nucleic Acids Res.* **33**, 5781 (2005).
31. Y. Liu, D. L. Beveridge, *J. Biomol. Struct. Dyn.* **18**, 505 (2001).
32. T. D. Fenn, D. Ringe, G. A. Petsko, *J. Appl. Crystallogr.* **36**, 944 (2003).

33. We thank C. J. Ackerson for discussions on nanocrystal synthesis; R. L. Baldwin, F. E. Boas, Z. D. Bryant, L. S. Churchman, A. R. Dunn, D. R. Halpin, D. Herschlag, W. L. Martin, B. H. Robinson, J. M. Schurr, A. L. Smith, R. M. Weisinger, and S. J. Wrenn for insights into DNA; Y. Bai, S. Doniach, K. Ito, J. Lipfert, I. S. Millett, S. Seifert, P. Thiyagarajan and H. Tsuruta for assistance and advice on x-ray scattering; T. D. Fenn for writing code that was used to calculate crystallographic dispersion values and for valuable discussions throughout this work; P. A. Walker for expert assistance with DNA synthesis; and P. Bradley and D. Baker for permitting use of unpublished code to prepare Fig. 4. Supported by NIH grants GM068126-01 and DP OD000429-01 (P.A.B.H.), an NIH training grant fellowship (R.S.F.), an NSF graduate fellowship (R.D.), and the U.S. Department of Energy (contract W-31-109 Eng-438 to the Advanced Photon Source, and support of Stanford Synchrotron Radiation Laboratory).

Supporting Online Material

www.sciencemag.org/cgi/content/full/322/5900/446/DC1
Materials and Methods
SOM Text
Figs. S1 to S10
Tables S1 to S4
References

9 April 2008; accepted 3 September 2008
10.1126/science.1158881

Relation Between Obesity and Blunted Striatal Response to Food Is Moderated by *Taq*IA A1 Allele

E. Stice,[1,2]* S. Spoor,[1] C. Bohon,[1,3] D. M. Small[4,5]

The dorsal striatum plays a role in consummatory food reward, and striatal dopamine receptors are reduced in obese individuals, relative to lean individuals, which suggests that the striatum and dopaminergic signaling in the striatum may contribute to the development of obesity. Thus, we tested whether striatal activation in response to food intake is related to current and future increases in body mass and whether these relations are moderated by the presence of the A1 allele of the *Taq*IA restriction fragment length polymorphism, which is associated with dopamine D2 receptor (*DRD2*) gene binding in the striatum and compromised striatal dopamine signaling. Cross-sectional and prospective data from two functional magnetic resonance imaging studies support these hypotheses, which implies that individuals may overeat to compensate for a hypofunctioning dorsal striatum, particularly those with genetic polymorphisms thought to attenuate dopamine signaling in this region.

Although twin studies suggest that biological factors play a major role in the etiology of obesity, few prospective studies have identified biological factors that increase risk for future weight gain. Dopamine is involved in the reinforcing effects of food (*1*). Feeding is associated with dopamine release in the dorsal striatum, and the degree of pleasure from eating correlates with amount of dopamine release (*2*, *3*). The dorsal striatum responds to

ingestion of chocolate in lean humans and is sensitive to its devaluation by feeding beyond satiety (*4*). In contrast, the ventral striatum appears to respond to food receipt only if it is unexpected (*5*) and plays a preferential role in encoding the value of cues associated with food receipt, reacting preferentially to cues versus receipt (*6*) and showing sensitivity to the devaluation of food cues, but not food receipt (*4*, *7*). Thus, the dorsal and ventral striatum may serve distinct roles in encoding food reward, with the former playing a more prominent role in encoding consummatory food reward. Dopamine antagonists increase appetite, energy intake, and weight gain, whereas dopamine agonists reduce energy intake and produce weight loss (*8*, *9*). Dopamine D2 receptors are reduced in obese relative to lean individuals (*10*, *11*). Obese rats have lower basal dopamine levels and reduced D2 receptor expression compared with lean rats (*12*, *13*). It has therefore been postulated that obese individuals have hypofunctioning reward circuitry, which leads them to overeat to compensate for a hypofunctioning dopamine reward system (*14*).

We used blood oxygen level–dependent (BOLD) functional magnetic resonance imaging (fMRI) to test whether obese, relative to lean, individuals show abnormal activation of the dorsal striatum, which encodes consummatory food reward (*2*, *4*), in response to receiving a highly palatable food. Although BOLD response reflects blood flow, and not dopamine signaling, it has been argued that the BOLD signal in regions that register as a dopamine source or target probably reflects dopaminergic activity (*15*–*17*). In addition, in genetically homogeneous and heterogeneous samples, individuals with an A1/A1 or A1/A2 allele of the *Taq*IA (rs1800497) are more likely to be obese than those without this allele (*18*–*20*). Furthermore, six post mortem and positron emission tomography (PET) studies have found that individuals with at least one A1 allele of the *Taq*IA restriction fragment length polymorphism associated with the dopamine D2 receptor (*DRD2*) gene evidenced 30 to 40% fewer D2 receptors than those with the A2/A2 allele (*21*–*26*), which suggests that reduced D2 receptor availability in obese individuals may be related to this polymorphism. The one study in which this effect did not emerge used single-photon emission computed tomography (SPECT) (*27*), which implies that SPECT may not be sufficiently sensitive to detect this difference (*28*). Thus, we further hypothesized that any evidence of abnormal striatal activation in response to food receipt for obese, relative to lean, individuals would be amplified among those with the A1 allele.

In two fMRI studies, we investigated striatal activation in response to receiving a chocolate milkshake versus a tasteless solution (*29*). Tastes were delivered using programmable syringe

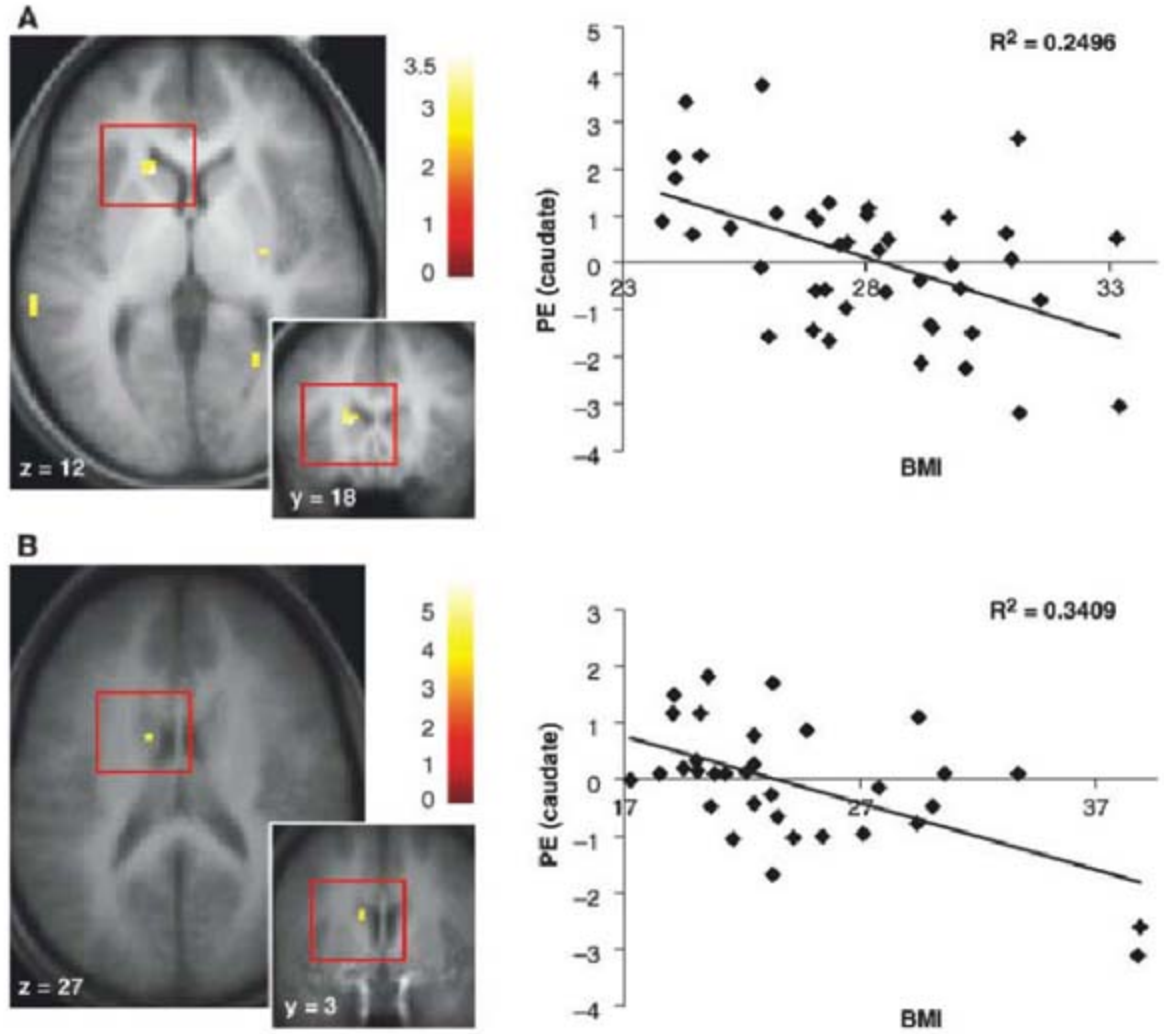

Fig. 1. (**A**) Coronal section of weaker activation in the left caudate nucleus (–15, 18, 12, $t = 3.65$, $P < 0.05$ FDR corrected) in response to receiving a milkshake versus a tasteless solution as a function of BMI with the graph of parameter estimates from that region (study 1). (**B**) Coronal section of weaker activation in the left caudate nucleus (–12, 3, 27, $t = 4.00$, $P < 0.05$ FDR corrected) in response to receiving a milkshake versus a tasteless solution as a function of BMI with the graph of parameter estimates from that region (study 2).

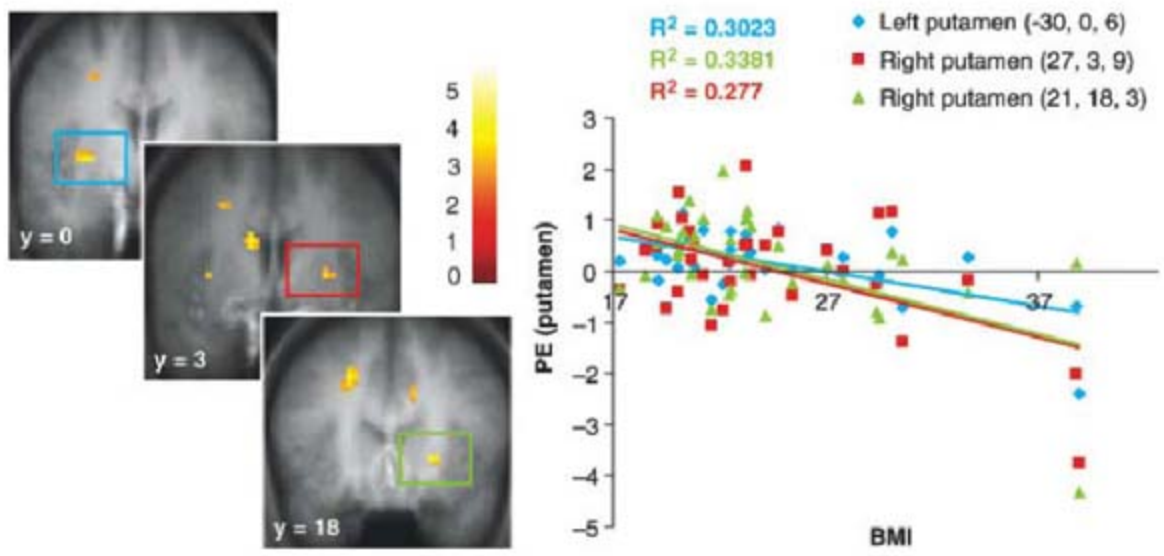

Fig. 2. Coronal section of weaker activation bilaterally in the putamen (–30, 0, 6, $t = 3.98$, $P < 0.05$ FDR corrected; 27, 3, 9, $t = 3.45$, $P < 0.05$ FDR corrected) in response to milkshake receipt versus tasteless solution receipt as a function of BMI with the graph of parameter estimates from that region (study 2).

[1]Oregon Research Institute, 1715 Franklin Boulevard, Eugene, OR 97403, USA. [2]Department of Psychology, University of Texas, Austin, TX 78712, USA. [3]Department of Psychology, University of Oregon, Eugene, OR 97403, USA. [4]The John B. Pierce Laboratory, New Haven, CT 06519, USA. [5]Department of Psychiatry, Yale University School of Medicine, New Haven, CT 06511, USA.

*To whom correspondence should be addressed. E-mail: estice@ori.org.

pumps to ensure consistent volume, rate, and timing of taste delivery. This procedure has been used successfully in previous studies (*6*).

In study 1, 43 female college students (mean age = 20.4, range 18 to 22; mean body mass index (BMI) = 28.60; range 23.8 to 33.2) were scanned while viewing pictures of a glass of chocolate milkshake and a glass of water that predicted taste delivery and while they tasted the milkshake and tasteless solution. The paradigm used in study 2 was similar, but the cues were geometric shapes (diamond, square, or circle) rather than pictures of glasses of milkshake or water. Study 2 involved 33 adolescent girls (mean age = 15.7, range 14 to 18 years; mean BMI = 24.3; range 17.5 to 38.9). Genetic data were obtained from 27 of these 33 participants. Because our hypothesis focused on dorsal striatal involvement in consummatory food reward, analyses focused on response to receiving a milkshake or a tasteless solution, not on response to cues signaling impending receipt of these tastes.

Individual statistical parametric mapping (SPM) contrast maps were entered into regression models with BMI scores as a covariate. In all analyses, *t*-maps (voxelwise levels of significance) were set at a threshold of $P < 0.005$ with a minimum cluster criterion of three. We then performed region-of-interest searches using peaks in the dorsal striatum identified previously (*2*, *4*) as centroids to define 10-mm diameter spheres. Peaks within these regions were considered significant at $P < 0.05$, false-discovery rate (FDR) corrected across the small volume.

We found a negative correlation between BMI and response in the left caudate nucleus to receiving a milkshake versus a tasteless solution in study 1 ($r = -0.50$) (Fig. 1A) and in study 2 ($r = -0.58$) (Fig. 1B). We also found a negative correlation between BMI and response bilaterally in the putamen to receiving a milkshake versus a tasteless solution in study 2 ($r = -0.53, -0.58$) (Fig. 2). In study 1, presence of the A1 allele significantly moderated the negative relation between BMI and activation in the left caudate while receiving a milkshake versus a tasteless solution ($r = -54$, $P < 0.001$); activation in this region showed a strong inverse relation ($r = -0.83$) to BMI for

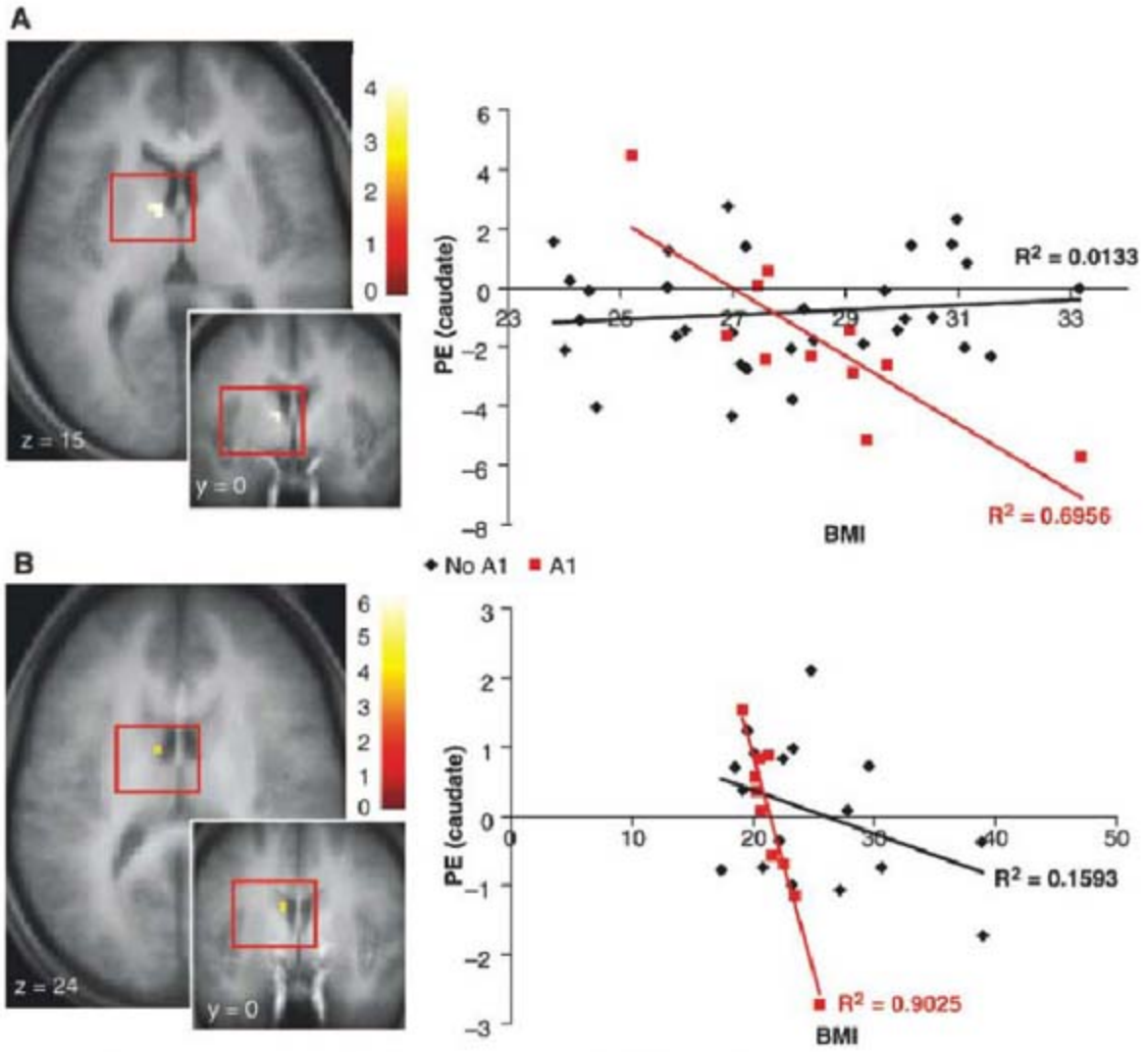

Fig. 3. (**A**) Sagittal section of weaker activation in the left caudate nucleus (–12, –3, 24, $t = 4.00$, $P < 0.05$ FDR corrected; –9, 0, 15. $t = 4.00$, $P < 0.05$ FDR corrected) while receiving a milkshake versus a tasteless solution as a function of BMI depending upon A1 allele status. The graph shows the parameter estimates of the contrast (milkshake receipt versus tasteless solution receipt) across BMI scores for each DRD2 allele type (study 1). (**B**) Coronal section of weaker activation in the left caudate nucleus (–9, 0, 24, $t = 3.81$, $P < 0.05$ FDR corrected) while receiving a milkshake versus a tasteless solution across BMI scores for each DRD2 allele type, with the graph showing the parameter estimates of the contrast (milkshake receipt versus tasteless solution receipt) versus BMI for each allele type (study 2).

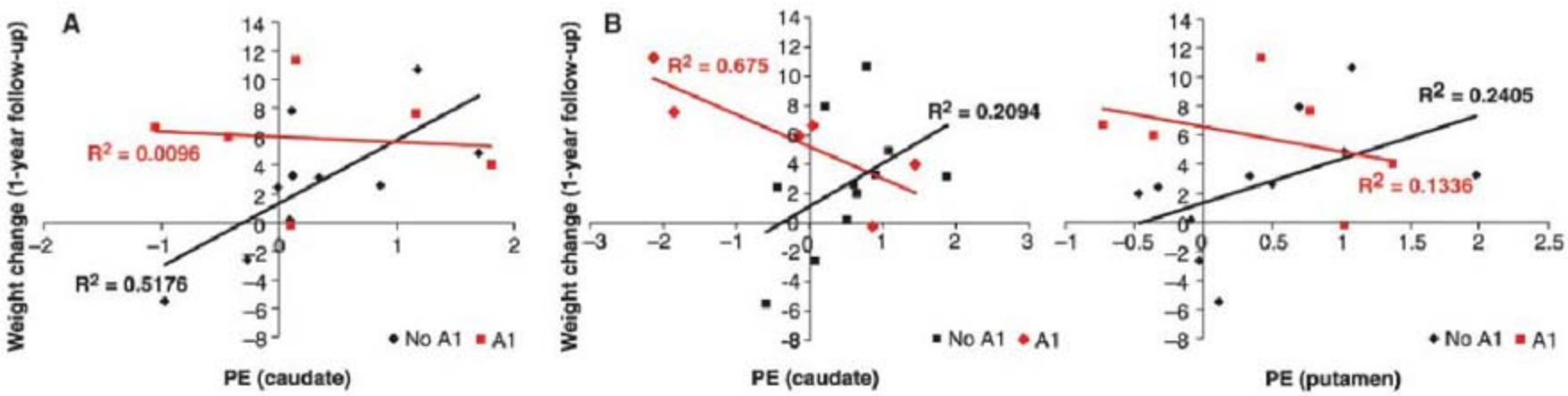

Fig. 4. (**A**) Activation in the caudate nucleus (–12, 3, 27) was negatively related to future weight gain for participants with the A1 allele, but positively related to future weight gain for participants without the A1 allele (study 1). (**B**) Activation in the caudate (6, 9, 15) and putamen (21, 18, 3) was negatively related to future weight gain for participants with the A1 allele, but positively related to future weight gain for participants without the A1 allele (study 2). Note that the graph generated from the caudate peak (left) showed the strongest interaction but just missed significance in the main SPM analysis ($t = 3.0$, $P = 0.002$ uncorrected).

those with the A1 allele, but a weak relation ($r = 0.12$) to BMI for those without this allele (Fig. 3A). In study 2, the A1 allele significantly moderated the negative relation between BMI and activation in the left caudate nucleus during receipt of milkshake versus a tasteless solution ($r = –0.68$, $P < 0.001$); activation in this region showed a strong inverse relation ($r = –0.95$) to BMI for those with the A1 allele, but a weaker relation ($r = –0.40$) to BMI for those without this allele (Fig. 3B). Note that participants with, rather than without, the A1 allele did not differ in their ratings of milkshake pleasantness ($r = 0.16$). Thus, as hypothesized, in both studies obese individuals, relative to lean individuals, showed a blunted striatal response to milkshake receipt, and this effect was amplified in those with the A1 allele.

In study 2, multiple regression models [Statistical Package for the Social Sciences (SPSS)] tested whether presence of the A1 allele moderated the relation between blunted dorsal striatal activation and future increases in BMI (from an increased positive energy balance) over a 1-year follow-up ($n = 17$, mean BMI percent change, 3.63, range –5.5 to 11.3). We controlled for initial BMI, A1 allele status, and dorsal striatal activation. Analyses were performed using the parameter estimates from the most significant peaks from the cross-sectional analyses of study 2. The interaction between A1 status and activation in the right putamen ($r = –0.45$, $P = 0.01$) and activation in the left caudate ($r = –0.42$, $P = 0.02$) while receiving a milkshake versus a tasteless solution in relation to change in BMI were significant and medium in magnitude (Fig. 4). Activation in the putamen ($r = 0.19$) and caudate ($r = 0.26$) and A1 allele status ($r = 0.30$) did not show significant main effects in the prediction of increases in BMI over follow-up.

Collectively, results from these two studies are consistent with the hypothesis that the dorsal striatum is less responsive to food reward in obese, relative to lean, individuals, potentially because the former have reduced D2 receptor density and compromised dopamine signaling, which may prompt them to overeat in an effort to compensate for this reward deficit. We did not observe effects (positive or negative) in the ventral striatum or midbrain, even when we reduced the significance threshold. Because we measured BOLD response, we can only speculate that the effects reflect reduced dopaminergic signaling. However, this interpretation seems reasonable because the presence of the A1 allele, which has been associated with reduced dopaminergic signaling in six studies (*21*–*26*), significantly moderated the observed BOLD effects, and because prior work has found that this region shows increased blood flow and increased dopamine release in response to ingestion of palatable food (*2*, *4*). Our findings converge with evidence that obese, relative to lean, humans have fewer D2 receptors in the striatum (*10*, *11*), and obese, relative to lean, rats have lower basal dopamine levels and reduced D2 receptor density (*12*, *13*). Our findings extend these results by showing that response in the dorsal striatum is blunted during ingestion of palatable food. Our findings also extend work implicating the A1 allele in obesity (*30*) by providing evidence that the negative relation between striatal response to food receipt and BMI was significantly stronger for individuals with the A1 allele, presumably because these individuals have reduced dopamine signaling capacity in the striatum. Most important, although striatal activation in response to food intake was positively related to weight gain for those without the A1 allele, it was negatively related to weight gain for those with the A1 allele, which provides evidence that blunted dorsal striatal response to food intake temporally precedes weight gain for those with this allele. This finding is consistent with the theory that it represents a vulnerability factor for obesity (*31*). However, an important alternative explanation to consider is that the hypofunctioning dopamine system results from down-regulation of reward circuitry secondary to overconsumption of high-fat and high-sugar foods (*31*, *32*). Indeed, animal studies indicate that chronic excessive intake of such foods results in down-regulation of postsynaptic D2 receptors, increased D1 receptor binding, and decreased D2 sensitivity and μ-opioid receptor binding (*32*–*34*)—changes that also occur in response to chronic substance use. Although we controlled for initial BMI in our prospective analyses, which reduces the risk that a history of overeating explains the prospective effects, we cannot rule out the possibility that the blunted striatal response is caused by overeating, particularly among individuals with the A1 allele. Paradoxically, such an adaptation may further increase the risk for the persistence of overeating.

One cautionary note is that, although studies suggesting that obesity is related to striatal hypofunctioning have included both women and men (*10*, *11*, *14*) and obesity is equally prevalent for the two genders, our result should be generalized to males with caution, because we only studied females. Moreover, the evidence that hypofunctioning of the striatum and the A1 allele of *Taq*I are associated with both obesity and substance abuse (*1*) implies that individual difference factors, such as affect regulation expectancies, modeling of overeating versus substance abuse, or environmental exposure (to high-fat foods versus psychoactive substances), interact with these general vulnerability factors to determine whether an at-risk individual develops obesity, substance abuse, or neither adverse outcome.

In conclusion, the present results strongly suggest that individuals who show blunted striatal activation during food intake are at risk for obesity, particularly those at genetic risk for compromised dopamine signaling in brain regions implicated in food reward. Thus, behavioral or pharmacologic interventions that remedy striatal hypofunctioning may assist in the prevention and treatment of this pernicious health problem.

References and Notes

1. D. E. Comings, K. Blum, *Prog. Brain Res.* **126**, 325 (2000).
2. D. M. Small, M. Jones-Gotman, A. Dagher, *Neuroimage* **19**, 1709 (2003).
3. M. S. Szczypka *et al.*, *Neuron* **30**, 819 (2001).
4. D. M. Small, R. J. Zatorre, A. Dagher, A. C. Evans, M. Jones-Gotman, *Brain* **124**, 1720 (2001).
5. G. Pagnoni, C. F. Zink, P. R. Montague, G. S. Berns, *Nat. Neurosci.* **5**, 97 (2002).
6. D. M. Small, M. G. Veldhuizen, J. Felsted, Y. E. Mak, F. McGlone, *Neuron* **57**, 786 (2008).
7. J. A. Gottfried, J. O'Doherty, R. J. Dolan, *Science* **301**, 1104 (2003).
8. J. de Leon *et al.*, *J. Clin. Psychopharmacol.* **27**, 22 (2007).
9. J. J. Leddy *et al.*, *Obes. Res.* **12**, 224 (2004).
10. G. J. Wang *et al.*, *Lancet* **357**, 354 (2001).
11. N. D. Volkow *et al.*, *Neuroimage* **42**, 1537 (2008).
12. S. O. Fetissov, M. M. Meguid, T. Sato, L. H. Zhang, *Am. J. Physiol. Regul. Integr. Comp. Physiol.* **283**, R905 (2002).
13. M. Orosco, C. Rouch, S. Nicolaidis, *Appetite* **26**, 1 (1996).
14. G. J. Wang, N. D. Volkow, J. S. Fowler, *Expert Opin. Ther. Targets* **6**, 601 (2002).
15. K. D'Ardenne, S. M. McClure, L. E. Nystrom, J. D. Cohen, *Science* **319**, 1264 (2008).
16. W. Schultz, P. Dayan, P. R. Montague, *Science* **275**, 1593 (1997).
17. B. Knutson, S. E. B. Gibbs, *Psychopharmacology (Berlin)* **191**, 813 (2007).
18. K. Blum *et al.*, *Pharmacogenetics* **6**, 297 (1996).
19. M. R. Spitz *et al.*, *Nutr. Res.* **20**, 371 (2000).
20. P. A. Tataranni *et al.*, *Diabetes* **50**, 901 (2001).
21. E. P. Noble *et al.*, *Arch. Gen. Psychiatry* **48**, 648 (1991).
22. J. Thompson *et al.*, *Pharmacogenetics* **7**, 479 (1997).
23. T. Pohjalainen *et al.*, *Mol. Psychiatry* **3**, 256 (1998).
24. E. G. Jonsson *et al.*, *Mol. Psychiatry* **4**, 290 (1999).
25. T. Ritchie, E. P. Noble, *Neurochem. Res.* **28**, 73 (2003).
26. E. Tupala *et al.*, *Neuroimage* **19**, 145 (2003).
27. M. Laruelle, J. Gelernter, R. Innis, *Mol. Psychiatry* **3**, 261 (1998).
28. E. P. Noble, *Am. J. Med. Genet.* **116B**, 103 (2003).
29. Materials and methods are available as supporting material on *Science* Online.
30. L. H. Epstein *et al.*, *Behav. Neurosci.* **121**, 877 (2007).
31. N. D. Volkow, J. S. Fowler, G. J. Wang, *Behav. Pharmacol.* **13**, 355 (2002).
32. N. T. Bello, L. R. Lucas, A. Hajnal, *Neuroreport* **13**, 1575 (2002).
33. C. Colantuoni *et al.*, *Neuroreport* **12**, 3549 (2001).
34. A. E. Kelley *et al.*, *Eur. J. Neurosci.* **18**, 2592 (2003).

Supporting Online Material

www.sciencemag.org/cgi/content/full/322/5900/449/DC1
Materials and Methods
Figs. S1 to S4
References

9 June 2008; accepted 11 September 2008
10.1126/science.1161550

Phosphorylation Networks Regulating JNK Activity in Diverse Genetic Backgrounds

Chris Bakal,[1,2*†] Rune Linding,[3*] Flora Llense,[4*] Elleard Heffern,[2] Enrique Martin-Blanco,[4] Tony Pawson,[5] Norbert Perrimon[1,2]

Cellular signaling networks have evolved to enable swift and accurate responses, even in the face of genetic or environmental perturbation. Thus, genetic screens may not identify all the genes that regulate different biological processes. Moreover, although classical screening approaches have succeeded in providing parts lists of the essential components of signaling networks, they typically do not provide much insight into the hierarchical and functional relations that exist among these components. We describe a high-throughput screen in which we used RNA interference to systematically inhibit two genes simultaneously in 17,724 combinations to identify regulators of *Drosophila* JUN NH_2-terminal kinase (JNK). Using both genetic and phosphoproteomics data, we then implemented an integrative network algorithm to construct a JNK phosphorylation network, which provides structural and mechanistic insights into the systems architecture of JNK signaling.

Signaling networks, especially those maintaining cell viability and proliferation in response to environmental fluctuations and stress, may be more robust to perturbation than others (*1*). One signaling network dedicated to maintaining cell, tissue, and organism fidelity in the face of cellular stress involves stress-activated protein kinases (SAPKs), also known as JUN NH_2-terminal kinases (JNKs) (*2*). Classical in vivo genetic approaches in *Drosophila* have identified a highly conserved pathway consisting of a single JNK, a JNK-kinase (JNKK), and a mixed-lineage kinase (MLK) that serves as a JNKK-kinase (*3*), but little is known as to how other signaling networks feed into this canonical cascade. To expand our understanding of JNK regulation, we conducted cell-based RNA interference (RNAi) screens to systematically investigate JNK activity in various genetic backgrounds. Furthermore, to gain insight into the systems architecture of JNK signaling, we used a probabilistic computational framework to reconstruct a JNK phosphorylation network among components identified in the screen on the basis of phosphoproteomics data.

To measure JNK activity in live migratory *Drosophila* cells, we devised an RNAi screen based on a dJUN-FRET sensor (fluorescence resonance energy transfer or FRET). dJUN-FRET is a single polypeptide composed of a modified *Drosophila* JUN phosphorylation domain and a FHA phosphothreonine-binding module (*4*) separated by a flexible linker and flanked by a cyan fluorescent protein (CFP) donor and yellow fluorescent protein (YFP) acceptor modules (Fig. 1A). *Drosophila* BG-2 migratory cells were transfected with a plasmid that drives dJUN-FRET expression from an *actin* promoter and, 2 days later, were transfected with a set of 1565 double-stranded RNAs (dsRNAs) targeting all 251 known *Drosophila* kinases, 86 phosphatases (PPases), and predicted kinases and PPases, as well as regulatory subunits and adapters (the "KP" set). JNK activity in single cells was determined by calculating the ratio of FRET signal (generated by FRET between YFP and CFP) to the level of CFP intensity (which provides the baseline level of dJUN-FRET expression in each cell regardless of JNK activity) within each cell boundary. A mean ratio is then derived for all cells treated with a particular dsRNA (Fig. 1B). The mean fold change in dJUN-FRET reporter activity for 16,404 control wells was 1.00 ± 0.04 (SD); however, in a screen of the KP set, multiple dsRNAs targeting *JNK* (Z = –2.06 and –2.05) and *MLK* (Z = –5.06, –2.60, and –2.13) produced significant decreases in dJUN-FRET reporter activity (*5*). Moreover, dsRNAs targeting the JNK PPase *puckered* (*puc*) (*6*) resulted in significant increases in reporter activity (Z = 2.13, 3.44, and 4.81), consistent with the role of Puc as a negative regulator of JNK (Fig. 1C). In the KP screen, we identified 24 genes (5% of genes tested) as putative JNK regulators and reidentified the 6 out of 7 positive and negative JNK regulators previously identified in vivo (*3*) (Fig. 1D). Although the KP screen identified both previously known and novel JNK components and regulators, the results are notable in the genes that the screen failed to isolate. For example, the only *Drosophila* JNKK, encoded by the *hemipterous* gene (*7*), was not identified in the KP screen. Furthermore, although *ERK* emerged from the KP screen as a JNK suppressor because of ERK's

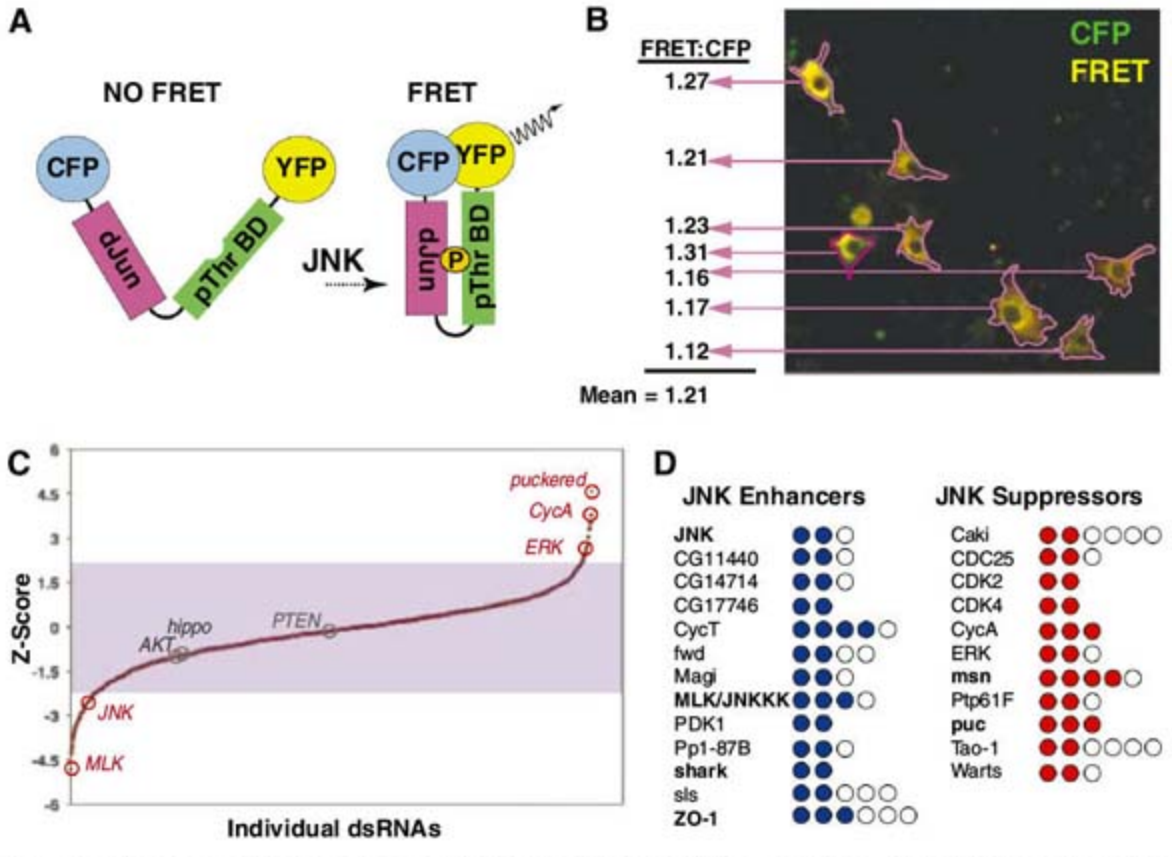

Fig. 1. Overview of FRET-based screen for JNK regulators. (**A**) Schematic of dJUN-FRET construct. (**B**) Representative image of dJUN-FRET transfected BG-2 cells and image analysis protocol. (**C**) Graph of Z scores for individual dsRNAs in KP screen. (**D**) List of 11 JNK suppressors and 13 enhancers identified in the KP screen. Genes are considered JNK regulators if two or more independent dsRNAs result in mean changes in dJUN-FRET activity above or below a Z score of +2.0 or –2.0, respectively. Circles represent the number of dsRNAs tested per gene; filled circles represent dsRNAs that contribute to the average Z score. Genes in bold indicate previously described JNK regulators (*3*).

[1]Department of Genetics, Harvard Medical School, 77 Avenue Louis Pasteur, Boston, MA 02215, USA. [2]Howard Hughes Medical Institute, Harvard Medical School, Boston, MA 02215, USA. [3]Cellular & Molecular Logic Team, The Institute for Cancer Research, 237 Fulham Road, London SW3 6JB, UK. [4]Institut de Biologia Molecular de Barcelona, CSIC (Spanish Council for Scientific Research), Parc Científic de Barcelona, 08028 Spain. [5]Samuel Lunenfeld Research Institute, Mount Sinai Hospital, 600 University Avenue, Toronto, Ontario M5G 1X5, Canada.

*These authors contributed equally to this work
†To whom correspondence should be addressed. E-mail: cbakal@receptor.med.harvard.edu

potential positive effects on *puc* transcription (fig. S1), we did not identify dsRNAs targeting other components of the ERK pathway. A high false-negative rate appears to be present in this genetic screen; therefore, we developed a combinatorial strategy to further enhance the sensitivity of the screen.

We performed 12 different sensitized screens in which we incubated cells with dsRNAs targeting a "query" gene in combination with dsRNAs of the KP set. In choosing query genes, we focused primarily on components of Rho guanosine triphosphatase (GTPase) signaling, such as *Rac1*, *Cdc42*, the Rho guanine nucleotide exchange factor *still-life* (*sif*), and *p190RhoGAP* (GTPase-activating protein), because Rho activity couples JNK activation to a number of upstream signaling events (*3*). We also sensitized cells by targeting canonical JNK components, such as *JNK*, *puc*, and *MLK*; other strong candidates from the KP screen, such as *ERK*; and genes, such as *AKT*, *PTEN*, *hippo*, and *VHL*, whose inhibition could result in the activation stress pathways even though they were themselves not identified in the KP screen (*4*). Genes were then identified as likely JNK regulators if two or more independent dsRNAs resulted in average increases or decreases in dJUN-FRET reporter activity in each screen, and we assigned a significance score based on how many total dsRNAs were tested for each gene across all screens (*4*, *26*). For example, a gene targeted by two to four dsRNAs was considered a JNK regulator if isolated in two or more screens, but a gene targeted by five to seven dsRNAs must be isolated in three or more screens to be included in the list of high-confidence regulators. No genes were isolated in the background of *JNK* inhibition (Fig. 2), which showed that increases or decreases in dJUN-FRET reporter activity in both unmodified and modified backgrounds are JNK-dependent. Using this combinatorial approach, we identified 55 new JNK suppressors and enhancers in a test of 17,724 dsRNA combinations, which, together with results from the nonsensitized initial screen, provide a list of 79 likely JNK regulators (17% of the genes tested) (*26*). We validated some of the hits identified in multiple screens as bona fide JNK regulators by quantifying mRNA abundance of the JNK-specific transcriptional target *MMP1* (*8*, *9*) after dsRNA-mediated inhibition of candidate genes by quantitative real-time polymerase chain reaction (fig. S2).

We wished to obtain insight into why depletion of certain kinases and PPases had effects in both unmodified and modified backgrounds, while others were isolated only in sensitized contexts. Therefore, we integrated our genetic screen with phosphoproteomics data and computational models of kinase specificity to derive networks on the basis of all of these experimental sources using the NetworKIN algorithm (*10*). NetworKIN was deployed on more than 10,000 unique high-confidence phosphorylation sites identified in a recent mass spectrometry study of *Drosophila* cells (*11*). This resulted in an initial network that was subsequently overlaid with the genetic hits in order to derive a model of the JNK phosphorylation network (Fig. 3) (*25*, *26*). Last, to determine which phosphorylation events make functional contributions to JNK signaling, we looked in data sets derived from combinatorial screens for epistatic interactions among kinases and substrates and performed hierarchical clustering of mean *Z* scores for components of the JNK phosphorylation network across several combinatorial RNAi screens to look for shared patterns of genetic interaction (Fig. 4). Thus, through integrating genetic and phosphoproteomics data using a computational framework, we undertook a systems-level strategy to describe the protein networks underlying genetic interactions.

JNK regulators identified in all screens could be broadly grouped into different classes on the basis of previously described biological functions and/or structural similarity of protein products (Fig. 3). Specifically, we identified a number of protein and lipid kinases involved in axon guidance and cell migration, such as *FER* (*12*), *Ptp69d* (*13*), *otk* (*14*, *15*), *thickveins* (*16*), *RET* (*17*), *wunen2* (*18*), *GSK3* (*19*), *PDK1* (*20*), and *JAK* (*21*). We also identified genes encoding components of apicobasal polarity complexes, such as *ZO-1*, *Caki*, *Magi*, and *discs large 1 (dlg1)*, largely as JNK suppressors (*22*), which is consistent with in vivo studies demonstrating unrestrained JNK activation associated with breakdown of polarity in backgrounds of hyperactivated Ras/ERK signaling (*8*, *23*). Furthermore, our results implicate the Warts-Hippo complex (*24*) as a potential link between JNK activity and the remodeling of cytoskeletal structures (Fig. 3). NetworKIN predicts that Hippo-mediated activation of JNK can occur through phosphorylation of MLK and that Hippo is also a direct target for JNK, which suggests that a feedback loop exists between JNK and Warts-Hippo signaling. Notably, we also predict Dlg1 to be extensively phosphorylated by a number of kinases in the JNK network, including JNK itself (Fig. 3). This suggests that JNK, and other kinases such as ERK and CDK2, can act upstream of Dlg1 to remodel or dismantle polarized cell-cell adhesion

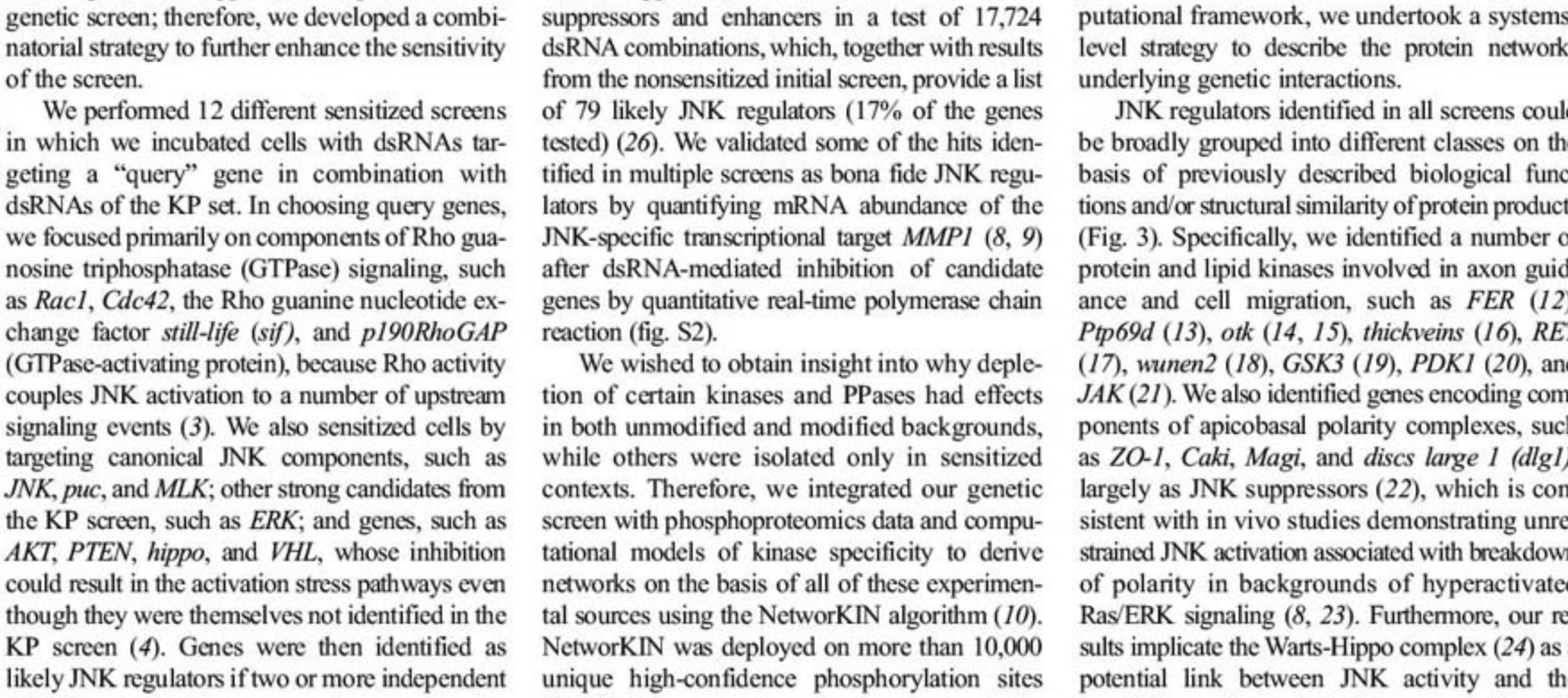

Fig. 2. Overview of the ability of dsRNAs to enhance or suppress dJUN-FRET reporter activity in diverse sensitized backgrounds. Genes are considered hits in individual screens if two or more independent dsRNAs result in a mean dJUN-FRET reporter activity that is considered in the top or bottom 5% of each screen. Shading indicates 0.05 to 0.95 percentile in each screen. Blue boxes indicate the number of JNK enhancers in each screen; red boxes indicate the number of JNK suppressors.

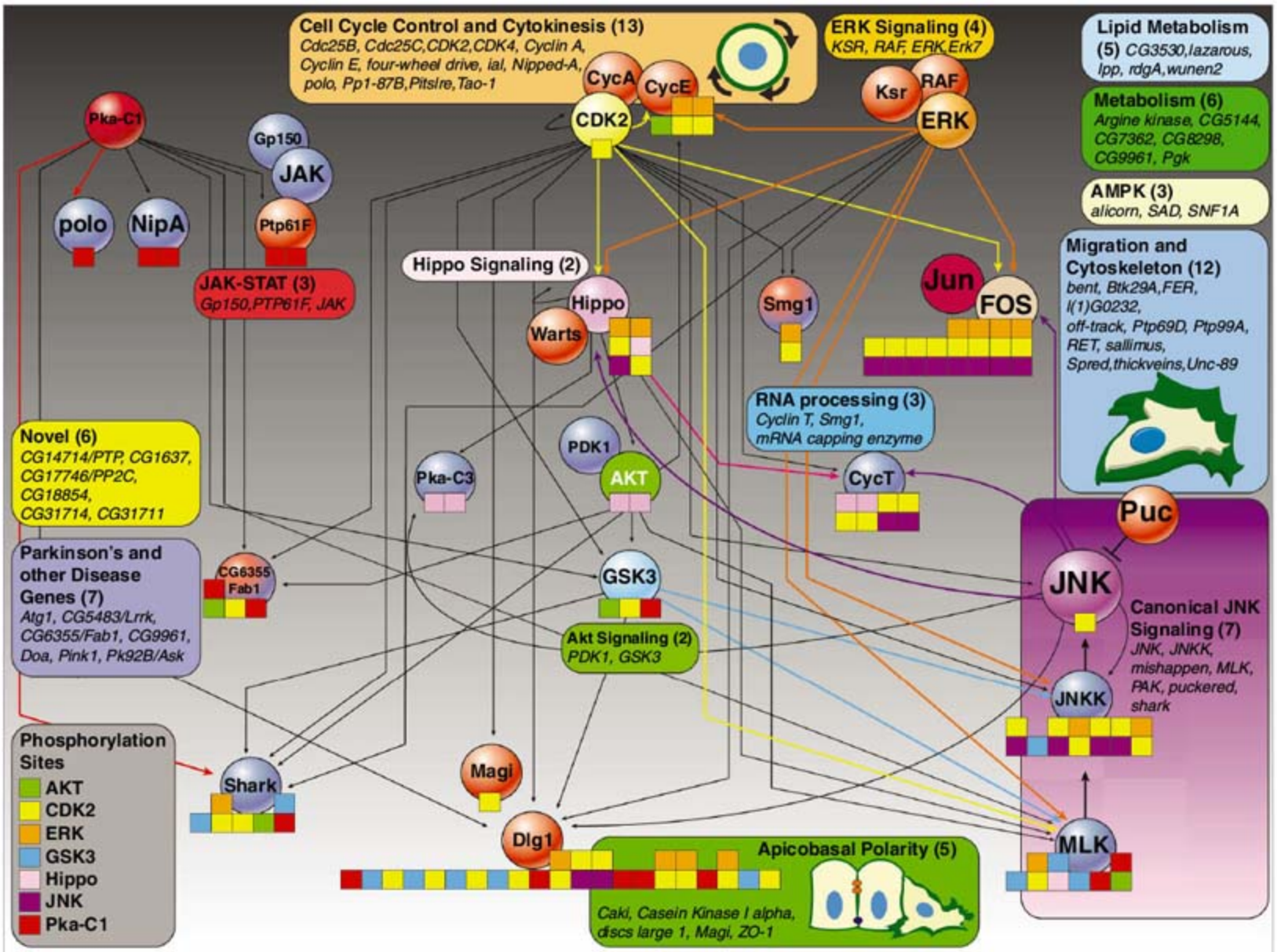

Fig. 3. Information flow through the JNK network. Kinases with predicted substrates in the JNK signaling network are shown in various colors, and the corresponding phosphorylation sites are indicated with similarly colored boxes on the corresponding targets. Stacked boxes indicate instances where the same motif is predicted to be phosphorylated by multiple kinases. Colored lines indicate either that we have detected an epistatic interaction among kinases and substrates or that kinase and substrate have correlated scores across sensitized screens (Fig. 4). Curved arrows emanating from JNK represent instances for which we predict the existence of regulatory feedback in the JNK network. Additionally, we show components of the networks that we did not predict as either kinases or substrates, but that have well-characterized functional relations with particular components of the JNK phosphorylation network. For example, KSR (kinase suppressor of Ras), RAF (a family of serine-threonine protein kinases), and ERK are well-characterized components of the same pathway (*26*). Unless predicted as a kinase by NetworKIN, JNK regulators are colored according to whether they were identified as JNK enhancers (blue) or JNK suppressors (red) in this study. AKT, FOS, and JUN were not isolated in this screen. All other JNK regulators are listed in the colored boxes and were grouped according to GO annotation (www.flybase.org). AMPK, adenosine monophosphate (AMP)–activated protein kinase. Numbers in parentheses correspond to the number of JNK regulators identified in this study that make up each group.

complexes, which, in turn, promote the morphological changes required to complete division, migration, or extrusion from tissue during apoptosis. Compelling support of this idea is provided by the fact that mammalian Dlg1 is regulated by phosphorylation, is a substrate of JNKs, and becomes highly phosphorylated during mitosis (*25*). These findings highlight the ability of integrated genetic and computational approaches to provide systems-level insight into the complex regulation of JNK activity.

In summary, we demonstrate that combinatorial RNAi screening is a powerful strategy to reduce the false-negatives present in current screens and reveals functions for a large fraction of genes. Moreover, our data-integrative–powered approach unraveled both mechanistic and hierarchical associations of components in the JNK regulatory system and provides an invaluable starting point for understanding the genetic interactions and signaling networks that underpin various diseases.

References and Notes

1. M. A. Felix, A. Wagner, *Heredity* **100**, 132 (2008).
2. C. R. Weston, R. J. Davis, *Curr. Opin. Cell Biol.* **19**, 142 (2007).
3. Y. Xia, M. Karin, *Trends Cell Biol.* **14**, 94 (2004).
4. Materials and methods are available as supporting material on *Science* Online.
5. Supplemental tables and files are available at http://genepath.med.harvard.edu/~cbakal/Supplemental.
6. E. Martin-Blanco *et al.*, *Genes Dev.* **12**, 557 (1998).
7. B. Glise, H. Bourbon, S. Noselli, *Cell* **83**, 451 (1995).
8. M. Uhlirova, D. Bohmann, *EMBO J.* **25**, 5294 (2006).
9. A. Srivastava, J. C. Pastor-Pareja, T. Igaki, R. Pagliarini, T. Xu, *Proc. Natl. Acad. Sci. U.S.A.* **104**, 2721 (2007).
10. R. Linding *et al.*, *Cell* **129**, 1415 (2007).
11. B. Bodenmiller *et al.*, *Mol. Biosyst.* **3**, 275 (2007).
12. M. J. Murray, C. M. Davidson, N. M. Hayward, A. H. Brand, *Development* **133**, 3063 (2006).
13. C. J. Desai, J. G. Gindhart Jr., L. S. Goldstein, K. Zinn, *Cell* **84**, 599 (1996).
14. M. L. Winberg *et al.*, *Neuron* **32**, 53 (2001).
15. X. Lu *et al.*, *Nature* **430**, 93 (2004).
16. M. Affolter, D. Nellen, U. Nussbaumer, K. Basler, *Development* **120**, 3105 (1994).
17. M. Chiariello *et al.*, *Oncogene* **16**, 2435 (1998).
18. M. Starz-Gaiano, N. K. Cho, A. Forbes, R. Lehmann, *Development* **128**, 983 (2001).
19. S. Etienne-Manneville, A. Hall, *Nature* **421**, 753 (2003).
20. L. Primo *et al.*, *J. Cell Biol.* **176**, 1035 (2007).
21. S. X. Hou, Z. Zheng, X. Chen, N. Perrimon, *Dev. Cell* **3**, 765 (2002).
22. L. Funke, S. Dakoji, D. S. Bredt, *Annu. Rev. Biochem.* **74**, 219 (2005).
23. T. Igaki, R. A. Pagliarini, T. Xu, *Curr. Biol.* **16**, 1139 (2006).

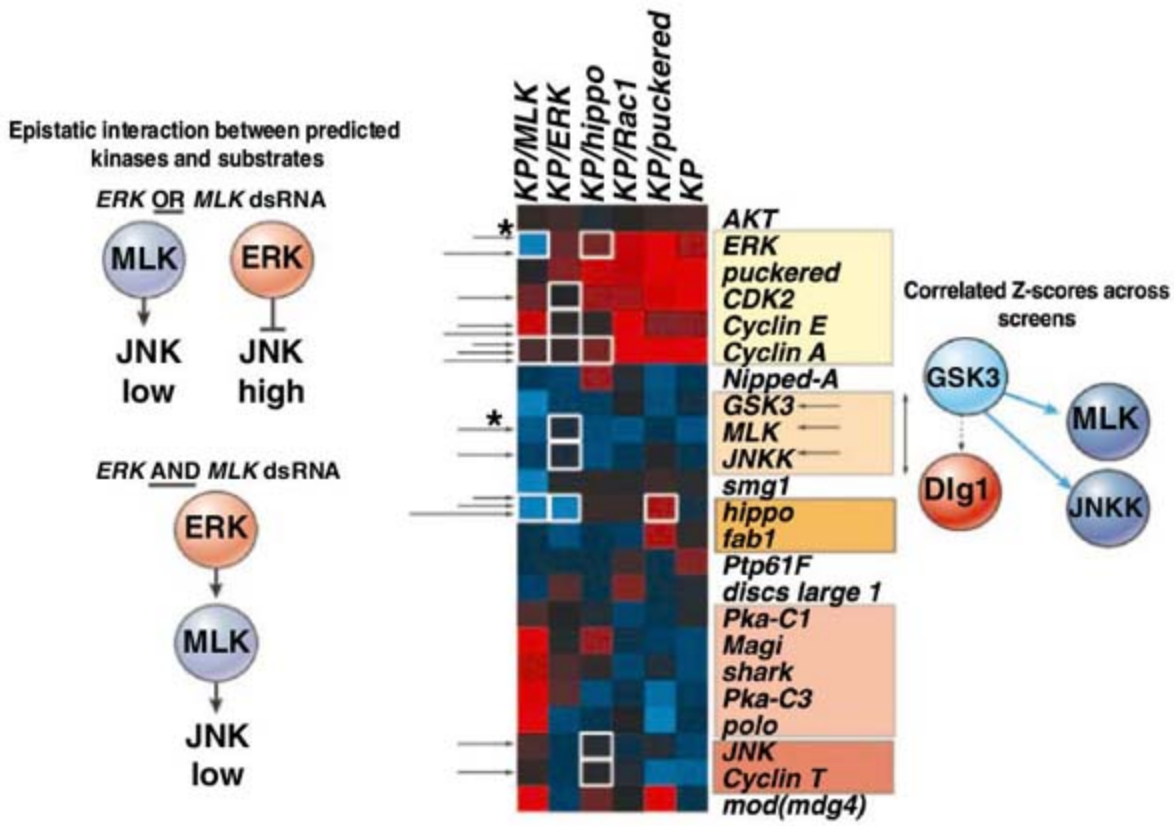

Fig. 4. Determining functional interactions among kinases and substrates in the JNK network. Hierarchical clustering of average dJUN-FRET *Z* scores after inhibition by RNAi of components in the JNK phosphorylation network in unmodified (KP), as well as in backgrounds deficient in *ERK*, *hippo*, *MLK*, or *puc*. Functional interactions are defined by the detection of an epistatic interaction between kinase and substrate (white boxes) or when the average *Z* scores of kinases and substrate dsRNAs across all sensitized screens cluster together with a cluster distance metric (an average of uncentered Pearson correlation coefficients) greater than 0.67 (shaded boxes). For example, whereas typically ERK acts as a JNK suppressor, *ERK* RNAi in *MLK*-deficient background (asterisk) leads to a notable decrease in dJUN-FRET reporter activity, which suggests that the ERK can act upstream of JNK via predicted phosphorylation of MLK and JNKK. Alternatively, GSK3 is predicted to target MLK, JNKK, and Dlg1, but only *Z* scores for GSK3, MLK, or JNKK dsRNAs cluster across screens, which suggests that GSK3-mediated phosphorylation of MLK and JNKK, but not Dlg1, is functionally relevant to JNK signaling.

24. L. J. Saucedo, B. A. Edgar, *Nat. Rev. Mol. Cell Biol.* **8**, 613 (2007).
25. P. Massimi, D. Gardiol, S. Roberts, L. Banks, *Exp. Cell Res.* **290**, 265 (2003).
26. A. Friedman, N. Perrimon, *Nature* **444**, 230 (2006).

27. We are deeply indebted to the *Drosophila* RNAi Screening Center and to J. Aach, S. Lee, C. Jørgensen, B. Mathey-Prevot, and B. Bodenmiller. The NetworKIN and NetPhorest algorithms are available at http://networkin.info and http://NetPhorest.info, respectively. This work is supported by Genome Canada through the Ontario Genomics Institute, the Spanish Ministerio de Ciencía e Innovación (BFU/Consolider 2007), and the European Union (FP6). C.B. is a Fellow of the Leukemia and Lymphoma Society. N.P. is an Investigator of the Howard Hughes Medical Institute.

Supporting Online Material
www.sciencemag.org/cgi/content/full/322/5900/453/DC1
Materials and Methods
SOM Text
Figs. S1 and S2

7 April 2008; accepted 20 August 2008
10.1126/science.1158739

Higher-Order Cellular Information Processing with Synthetic RNA Devices

Maung Nyan Win and Christina D. Smolke*

The engineering of biological systems is anticipated to provide effective solutions to challenges that include energy and food production, environmental quality, and health and medicine. Our ability to transmit information to and from living systems, and to process and act on information inside cells, is critical to advancing the scale and complexity at which we can engineer, manipulate, and probe biological systems. We developed a general approach for assembling RNA devices that can execute higher-order cellular information processing operations from standard components. The engineered devices can function as logic gates (AND, NOR, NAND, or OR gates) and signal filters, and exhibit cooperativity. RNA devices process and transmit molecular inputs to targeted protein outputs, linking computation to gene expression and thus the potential to control cellular function.

Genetically encoded technologies that perform information processing, communication, and control operations are needed to produce new cellular functions from the diverse molecular information encoded in the various properties of small molecules, proteins, and RNA present within biological systems. For example, genetic logic gates that process and translate multiple molecular inputs into prescribed amounts of signaling through new molecular outputs would enable the integration of diverse environmental and intracellular signals to a smaller number of phenotypic responses. Basic operations such as signal filtering, amplification, and restoration would also enable expanded manipulation of molecular information through cellular networks.

Molecular information processing systems have been constructed that perform computation with biological substrates. For example, protein-based systems can perform logic operations to convert molecular inputs to regulated transcriptional events (*1*–*4*). Information processing systems that perform computation on small-molecule and nucleic acid inputs can be constructed from nucleic acid components (*5*–*11*). RNA-based systems can process single inputs to regulated gene expression events (*12*, *13*) and integrate multiple regulatory RNAs for combinatorial gene regulation (*14*, *15*). We sought to combine the rich capability of nucleic acids for performing information processing, transduction, and control operations with the design advantages expected from the relative ease by which RNA structures can be modeled and designed (*16*, *17*).

We proposed a framework for the construction of single input–single output RNA devices (*18*) based on the assembly of three functional components: a sensor component, made of an RNA aptamer (*19*); an actuator component, made of a hammerhead ribozyme (*20*); and a transmitter component, made of a sequence that couples the sensor and actuator components. The resulting devices distribute between two primary conformations: one in which the input cannot bind the sensor, and the other in which the input can bind the sensor as a result of competitive hybridization events within the transmitter component. Input binding shifts the distribution to favor the input-bound conformation as a function of increasing input concentration and is translated to a change in the activity of the actuator, where a "ribozyme-active" state results in self-cleavage of the ribozyme (*21*).

Division of Chemistry and Chemical Engineering, California Institute of Technology, 1200 East California Boulevard, MC 210-41, Pasadena, CA 91125, USA.

*To whom correspondence should be addressed. E-mail: smolke@cheme.caltech.edu

The RNA device is coupled to the 3′ untranslated region (UTR) of the target gene, where ribozyme self-cleavage inactivates the transcript and thereby lowers gene expression independent of cell-specific machinery. We made simple RNA devices that function as single-input Buffer and Inverter gates that convert a molecular input to increased and decreased gene expression output, respectively (*18*).

The utility of a proposed composition framework depends partly on the extensibility of the framework itself. A framework that provides a general approach for the forward engineering of multi-input devices will allow the combinatorial assembly of many information processing, transduction, and control devices from a smaller number of components. Thus, we used defined points of integration to facilitate the assembly of putatively modular RNA components into sophisticated information processing devices (Fig. 1A) and specified three signal integration (SI) schemes (Fig. 1B). SI 1 was used to construct RNA devices that acted as logic gates (AND or NOR gates) and signal and bandpass filters through the assembly of independent single-input gates. SI 2 was used to construct devices that allowed other logic operations (NAND or OR gates) through the assembly of sensor-transmitter components linked to both stems of the ribozyme. SI 3 was used to construct devices that acted as logic gates (AND or OR gates) and exhibited cooperativity through the assembly of two sensor-transmitter components linked to a single ribozyme stem. The various operations were achieved by altering the function or input responsiveness of the single-input gates in SI 1 or sensor-transmitter components in SI 2 and 3. We assembled multiple RNA devices from various components for all operations to demonstrate the generality of the integration schemes.

In SI 1, the single-input gates act independently such that computation is performed through integration of individual gate operations in the 3′ UTR of the target transcript. Because only one of the ribozymes needs to be in an active state to inactivate the transcript, the device output (gene expression activity) is high only when both ribozymes of the single-input gates are in their inactive states. We engineered signal filters by coupling representative Buffer or Inverter gates (*18*) responsive to either theophylline or tetracycline (SI 1.1; Fig. 2A). Coupled-gate devices exhibited a device response that was shifted lower compared to that of the single-input gate, indicating the independent action of each single-input gate (Fig. 2B, SOM text S1 and S2, and table S1).

We constructed an AND gate that exhibited high output only when both inputs were present by coupling a theophylline-responsive Buffer gate and a tetracycline-responsive Buffer gate (SI 1.2; Fig. 2C). In this composition, only in the presence of both molecular inputs (theophylline and tetracycline) did both Buffer gates favor the ribozyme-inactive state, resulting in high device output (Fig. 2D and fig. S1).

We constructed a NOR gate that exhibited high output only when both inputs were absent by coupling a theophylline-responsive Inverter gate and a tetracycline-responsive Inverter gate (SI 1.3; Fig. 2E and fig. S2). In this composition, only in the absence of both inputs did both Inverter gates favor the ribozyme-inactive state, resulting in high device output (Fig. 2F and fig. S3). We also engineered a bandpass filter that exhibited high output only over intermediate input concentrations by coupling theophylline-responsive Buffer and Inverter gates (fig. S4). The various devices demonstrated that diverse information processing operations can be assembled through SI 1, where layering strategies can extend the attainable operations (SOM text S3).

Devices constructed through SI 2 and 3 consisted of multiple sensor-transmitter components, or internal gates (Fig. 1B). An internal Inverter or Buffer gate is defined as a sensor-transmitter component that activates or inactivates, respectively, a coupled component, such as an actuator or other internal gate, in the presence of input. In SI 2, the internal gates act independently through the linked ribozyme stems and therefore computation is performed through the integration of individual internal gate operations in the ribozyme core. The single ribozyme is only in the active state, corresponding to low device output, when both sensor-transmitter components are in states that activate the coupled ribozyme. We constructed a NAND gate by coupling a theophylline-responsive internal Inverter gate through stem I and a tetracycline-responsive internal Inverter gate (fig. S2) through stem II (SI 2.1; Fig. 3A). The device exhibited low output only in the presence of both inputs, because both internal Inverter gates favored the ribozyme-active state (Fig. 3B and fig. S5). Other logic operations can be performed by SI 2 devices, such as an OR operation, through the coupling of two internal Buffer gates (SOM text S4).

In SI 3, the sensor-transmitter components are coupled within a ribozyme stem, and computation occurs via the integrated operations of the internal gates. Internal gates were linked through the aptamer loop of the lower gate, IG(n), and the transmitter of the higher gate, IG(n + 1). The operation of the higher internal gate determines the state of the lower internal gate, where an internal gate can perform its encoded operation when it is in an active state, and the state of the internal gate linked to the ribozyme (IG1) determines the state of the device. We constructed an alternative AND gate by coupling a theophylline-responsive internal Buffer gate (IG1) and a tetracycline-responsive internal Inverter gate (IG2) at stem II (SI 3.1; Fig. 4A). In this composition, only in the presence of both inputs did

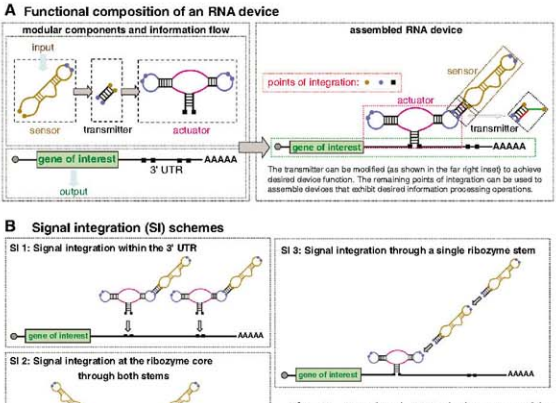

Fig. 1. Functional RNA device composition framework. The color scheme for all figures is as follows: brown, aptamer or sensor component; purple, catalytic core of the ribozyme or actuator component; blue, loop regions of the actuator component; green and red, strands within the transmitter component that participate in the competitive hybridization event. **(A)** A functional composition framework for assembling RNA devices from modular components. Information in the form of a molecular input is received by the sensor and transmitted by the transmitter to a regulated activity of the actuator, which in turn controls the translation of a target transcript as an output. **(B)** Three signal integration schemes represent different component assembly strategies to build higher-order RNA devices. The RNA device in SI 1 involves multiple actuator components controlled by single sensor-transmitter components, whereas those in SI 2 and 3 involve multiple sensor-transmitter components controlling a single actuator component.

IG1 change the state of the RNA device to favor the ribozyme-inactive state, resulting in high device output (Fig. 4B and fig. S6). We also constructed RNA devices that perform an OR operation through SI 3 (SOM text S4).

We engineered RNA devices that exhibited programmed cooperativity through SI 3 by manipulating the relative energies required to switch the device between different states (SOM text S5). RNA devices were composed of theophylline-responsive internal Buffer (IG1) and Inverter (IG2) gates (SI 3.2; Fig. 4C), in which the energetic differences between the input-unbound (**1**) and single-input–bound (**2**) states were varied (programmed through IG2; $\Delta\Delta G_{IG2}$; table S2) and the

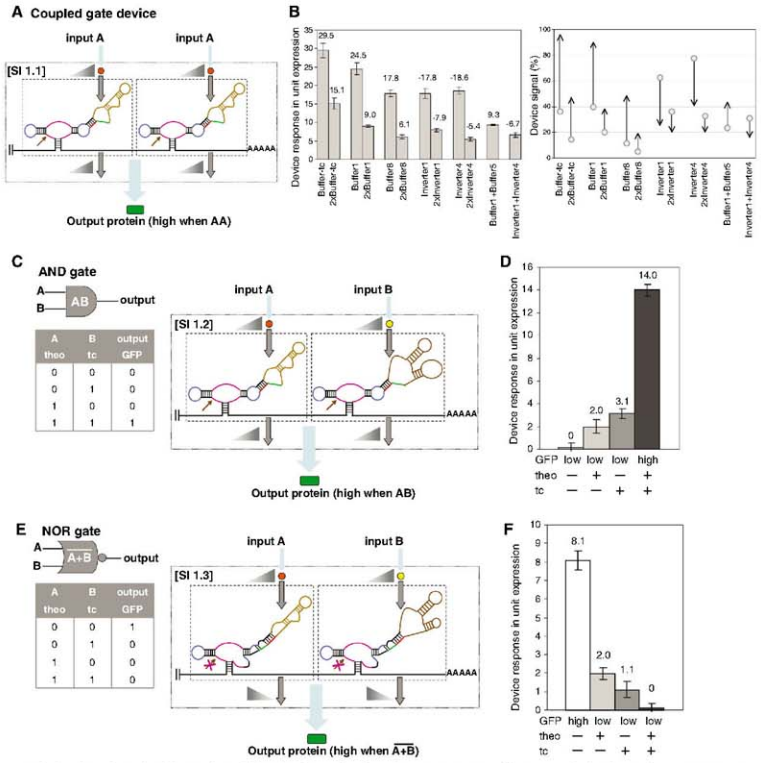

Fig. 2. RNA devices based on signal integration within the 3′ UTR (SI 1). Single-input gates are indicated in dashed boxes, and triangles indicate relationships between associated gate inputs and outputs. (**A**) An RNA device composed of two Buffer gates responsive to the same input functions to shift the device response lower than that of the single-input gate. (**B**) The device output of RNA devices composed of two single-input gates and their single-input gate counterparts. (Left) Device response (bars) is reported as the difference between gene expression activities in the absence and presence of the appropriate inputs [10 mM theophylline (theo) or 1 mM tetracycline (tc)] (*21*). (Right) Device signal (arrows) is reported over the full transcriptional range of the promoter system used as a percentage of the expression activity relative to that of an inactive ribozyme control, where circles and arrowheads indicate device signals in the absence and presence of input, respectively. The negative sign indicates the down-regulation of target gene expression by the Inverter gates. (**C**) An RNA device that performs an AND operation by coupling two Buffer gates responsive to different inputs and the associated truth table. (**D**) The device response of an AND gate (L2bulge1 + L2bulge1tc). Device response under different input conditions [theo or tc (–), 0 mM; theo (+), 5 mM; tc (+), 0.25 mM] is reported as the difference between expression activity in the absence of both inputs and that at the indicated input conditions. (**E**) An RNA device that performs a NOR operation by coupling two Inverter gates responsive to different inputs and the associated truth table. (**F**) The device response of a NOR gate (L2bulgeOff1 + L2bulgeOff1tc). Device response under different input conditions [theo or tc (–), 0 mM; theo (+), 10 mM; tc (+), 0.5 mM] is reported as the difference between expression activity in the presence of both inputs and that at the indicated input conditions. Error bars represent the SD from at least three independent experiments.

differences between the single-input–bound and two-input–bound (**3**) states were kept constant (programmed through IG1; $\Delta\Delta G_{IG1}$ = 1 kcal/mol). The devices exhibited Buffer operations and substantial degrees of cooperativity (Fig. 4D and fig. S7), where one device exhibited a degree of cooperativity [Hill coefficient (n_H) ≈ 1.65; Fig. 4E] similar to that of a naturally occurring cooperative riboswitch (*22*). We also placed internal Inverter gates into IG1 to construct a device that performed an Inverter operation and exhibited cooperativity (figs. S8 and S9). Control studies indicated that the value of $\Delta\Delta G_{IG1}$ was important to the observed cooperative response (figs. S10 and S11) and verified that the response was achieved through input binding to both sensors (figs. S12 to S15).

We have developed a composition framework for constructing higher-order RNA devices. Functional modularity is a critical element of any composition framework and was achieved in this study partly through the separation of device functions into distinct components. Although the functions of sensing and actuation frequently rely on tertiary interactions, which are not accounted for in this framework, the integration of these functions into a device is simplified via a transmitter that insulates component functions and controls the interactions between components through predictive hybridization interactions. The variety of information processing operations demonstrated from a small number of standard components emphasizes the utility of modular assembly. In addition, three of the devices have naturally occurring functional counterparts (*22*–*24*), supporting the biological

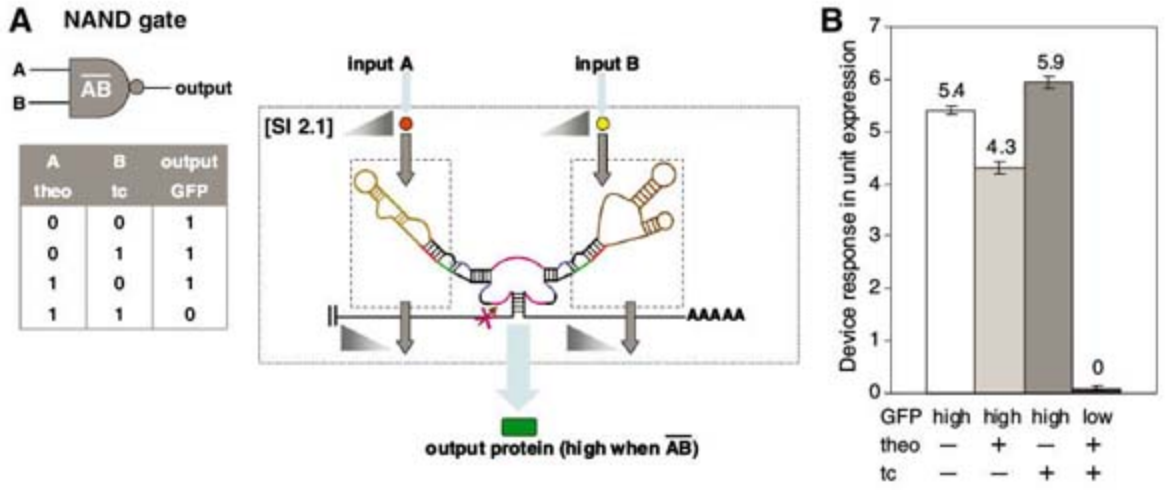

Fig. 3. RNA devices based on signal integration at the ribozyme core (SI 2). Internal gates are indicated in dashed boxes, and triangles indicate relationships between associated internal gate inputs and outputs. (**A**) An RNA device that performs a NAND operation by coupling two internal Inverter gates responsive to different inputs to different ribozyme stems and the associated truth table. (**B**) The device response of a NAND gate (L1cm10 – L2bulgeOff3tc). Device response under different input conditions [theo or tc (–), 0 mM; theo (+), 10 mM; tc (+), 1 mM] is reported as in Fig. 2F. Error bars represent the SD from at least three independent experiments.

Fig. 4. RNA devices based on signal integration at a single ribozyme stem (SI 3). Internal gates (IG*n*) are indicated in dashed boxes, and triangles indicate relationships between associated internal gate inputs and the device output. (**A**) An RNA device that performs an AND operation by coupling internal Buffer (IG1) and Inverter (IG2) gates responsive to different inputs to a single ribozyme stem. (**B**) The device response of an AND gate (tc-theo-On1). Device response under different input conditions [theo or tc (–), 0 mM; theo (+), 2.5 mM; tc (+), 0.5 mM] is reported as in Fig. 2D. (**C**) An RNA device composed of internal Buffer (IG1) and Inverter (IG2) gates responsive to the same input coupled to a single ribozyme stem. (**D**) The device response of RNA devices composed of internal Buffer and Inverter gates and their single-internal gate device counterpart (L2bulge1). Device response is reported as in Fig. 2B. Theo-theo-On10, -On11, -On12, and -On13 exhibit varying degrees of cooperativity, as quantified by Hill coefficients (n_H) greater than 1 (*26*). (**E**) The device output response of theo-theo-On13 shows a high degree of programmed cooperativity. The device response is normalized to the response at 10 mM theophylline (*21*). Error bars represent the SD from at least three independent experiments.

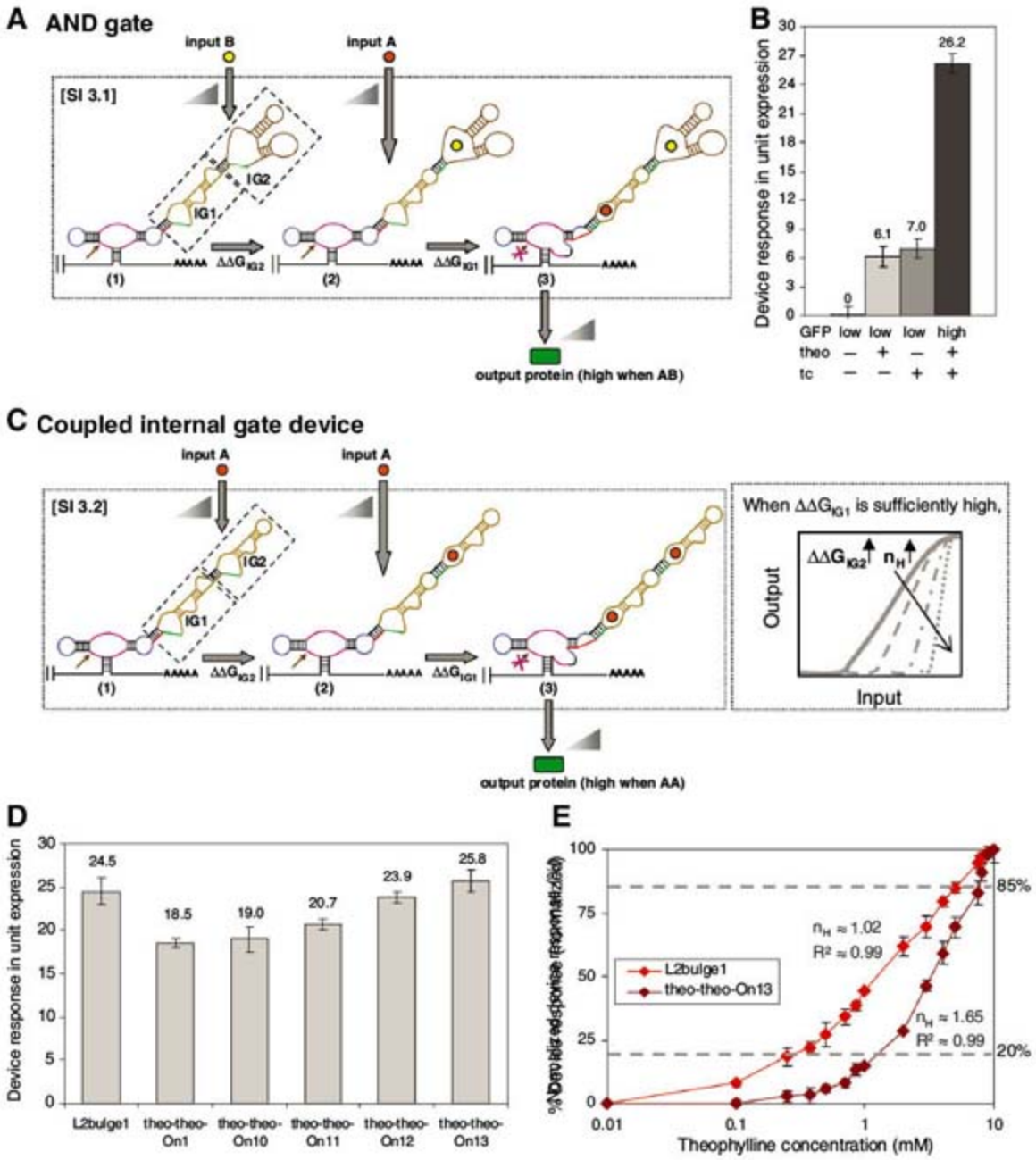

relevance of such information processing operations. The framework may be further extended to more complex devices by combining multiple SI schemes within a device and implementing layering strategies. We anticipate that further insight into RNA structure-function relationships (*25*), and improved predictions of RNA secondary and tertiary structures (*16*), may allow the development of improved modular assembly schemes, in which an important design challenge will be to insulate device functions across distinct components and control interactions between these components.

References and Notes

1. C. C. Guet, M. B. Elowitz, W. Hsing, S. Leibler, *Science* **296**, 1466 (2002).
2. B. P. Kramer, C. Fischer, M. Fussenegger, *Biotechnol. Bioeng.* **87**, 478 (2004).
3. R. S. Cox III, M. G. Surette, M. B. Elowitz, *Mol. Syst. Biol.* **3**, 145 (2007).
4. J. C. Anderson, C. A. Voigt, A. P. Arkin, *Mol. Syst. Biol.* **3**, 133 (2007).
5. G. Seelig, D. Soloveichik, D. Y. Zhang, E. Winfree, *Science* **314**, 1585 (2006).
6. Y. Benenson, B. Gil, U. Ben-Dor, R. Adar, E. Shapiro, *Nature* **429**, 423 (2004).
7. R. M. Dirks, N. A. Pierce, *Proc. Natl. Acad. Sci. U.S.A.* **101**, 15275 (2004).
8. M. N. Stojanovic, D. Stefanovic, *Nat. Biotechnol.* **21**, 1069 (2003).
9. R. Penchovsky, R. R. Breaker, *Nat. Biotechnol.* **23**, 1424 (2005).
10. R. R. Breaker, *Curr. Opin. Biotechnol.* **13**, 31 (2002).
11. M. P. Robertson, A. D. Ellington, *Nat. Biotechnol.* **17**, 62 (1999).
12. F. J. Isaacs, D. J. Dwyer, J. J. Collins, *Nat. Biotechnol.* **24**, 545 (2006).
13. B. Suess, J. E. Weigand, *RNA Biol.* **5**, 24 (2008).
14. K. Rinaudo *et al.*, *Nat. Biotechnol.* **25**, 795 (2007).
15. B. D. Brown *et al.*, *Nat. Biotechnol.* **25**, 1457 (2007).
16. M. Parisien, F. Major, *Nature* **452**, 51 (2008).
17. D. H. Mathews, D. H. Turner, *Curr. Opin. Struct. Biol.* **16**, 270 (2006).
18. M. N. Win, C. D. Smolke, *Proc. Natl. Acad. Sci. U.S.A.* **104**, 14283 (2007).
19. T. Hermann, D. J. Patel, *Science* **287**, 820 (2000).
20. A. Khvorova, A. Lescoute, E. Westhof, S. D. Jayasena, *Nat. Struct. Biol.* **10**, 708 (2003).
21. Materials and methods are available as supporting material on *Science* Online.
22. M. Mandal *et al.*, *Science* **306**, 275 (2004).
23. N. Sudarsan *et al.*, *Science* **314**, 300 (2006).
24. R. Welz, R. R. Breaker, *RNA* **13**, 573 (2007).
25. M. T. Woodside *et al.*, *Proc. Natl. Acad. Sci. U.S.A.* **103**, 6190 (2006).
26. D. L. Nelson, M. M. Cox, in *Lehninger Principles of Biochemistry* (Freeman, New York, ed. 4, 2005), pp. 167–174.

27. We thank Y. Chen, J. Liang, and D. Endy for critical reading of the manuscript and A. Babiskin for pRzS. This work was supported by the Center for Biological Circuit Design at the California Institute of Technology, the Arnold and Mabel Beckman Foundation, and the NIH. The authors declare competing financial interests in the form of a pending patent application.

Supporting Online Material

www.sciencemag.org/cgi/content/full/322/5900/456/DC1
Materials and Methods
SOM Text S1 to S6
Figs. S1 to S17
Tables S1 and S2
References

12 May 2008; accepted 12 August 2008
10.1126/science.1160311

Innate Immunity in *Caenorhabditis elegans* Is Regulated by Neurons Expressing NPR-1/GPCR

Katie L. Styer,[1] Varsha Singh,[1] Evan Macosko,[2] Sarah E. Steele,[1] Cornelia I. Bargmann,[2] Alejandro Aballay[1]*

A large body of evidence indicates that metazoan innate immunity is regulated by the nervous system, but the mechanisms involved in the process and the biological importance of such control remain unclear. We show that a neural circuit involving *npr-1*, which encodes a G protein–coupled receptor (GPCR) related to mammalian neuropeptide Y receptors, functions to suppress innate immune responses. The immune inhibitory function requires a guanosine 3′,5′-monophosphate–gated ion channel encoded by *tax-2* and *tax-4* as well as the soluble guanylate cyclase GCY-35. Furthermore, we show that *npr-1*– and *gcy-35*–expressing sensory neurons actively suppress immune responses of nonneuronal tissues. A full-genome microarray analysis on animals with altered neural function due to mutation in *npr-1* shows an enrichment in genes that are markers of innate immune responses, including those regulated by a conserved PMK-1/p38 mitogen-activated protein kinase signaling pathway. These results present evidence that neurons directly control innate immunity in *C. elegans*, suggesting that GPCRs may participate in neural circuits that receive inputs from either pathogens or infected sites and integrate them to coordinate appropriate immune responses.

Innate immune defense comprises a variety of mechanisms used by metazoans to prevent microbial infections. Activation of the innate immune system upon pathogen recognition results in a rapid and definitive microbicidal response to invading microorganisms that is fine-tuned to prevent deleterious deficiencies or excesses in the response. The nervous system, which can respond in milliseconds to many types of nonspecific environmental stimuli, has several characteristics that make it an ideal partner with the innate immune system to regulate nonspecific host defenses (*1*–*3*). However, even though a large body of evidence indicates that metazoan innate immunity is under the control of the nervous system, the mechanisms involved in the process and the biological importance of such control remain unclear. To provide insights into the neural mechanisms that regulate innate immunity, we have taken advantage of the simple and well-studied nervous and innate immune systems of *Caenorhabditis elegans*.

The powerful genetic approaches available to *C. elegans* research have been used to address central questions concerning the functions of the nervous system (*4*). With its 302 neurons and 56 glial cells, which represent 37% of all somatic cells in a hermaphrodite, the nervous system is perhaps the most complex organ of *C. elegans*. Ablation of different neurons has demonstrated that sensory neurons regulate a variety of physiological processes, including dauer formation and adult life span (*5*–*8*). In addition, *C. elegans* neurons are known to express numerous secreted peptides of the transforming growth factor–β (TGF-β) family, the insulin family, and neuropeptide families (*6*, *9*–*13*). This myriad of secreted factors has the potential to act at a distance to modulate various physiological processes by regulating the function of neuronal and nonneuronal cells throughout the animal.

Like other free-living nematodes, *C. elegans* lives in soil environments where it is in contact with soilborne microbes, including human microbial pathogens; it has evolved physiological mechanisms to respond to different pathogens by activating the expression of innate immune response genes that are conserved across metazoans (*14*–*19*). *C. elegans* also has behavioral responses to pathogenic bacteria such as *Bacillus thuringiensis* (*20*, *21*), *Microbacterium nematophilum* (*22*), *Photorhabdus luminescens* (*23*), *Pseudomonas aeruginosa* (*24*–*26*), and *Serratia marcescens* (*24*, *27*, *28*). Animals infected with these pathogens avoid lawns of the pathogen, or migrate away from pathogen odors. It is currently unknown how the nematode can sense pathogenic bacteria, although mutants in sensory-transduction molecules such as the Gi-like protein ODR-3 and the G protein–coupled receptor kinase GRK-2 are incapable of *S. marcescens* lawn avoidance (*28*). These results suggest that G protein–coupled receptors (GPCRs) may participate in neural circuits that receive inputs from either pathogens or infected sites and integrate them to coordinate appropriate defense responses.

To study the role of GPCRs in the regulation of innate immune response, we first determined the susceptibility of 40 *C. elegans* strains carrying mutations in GPCRs to the human opportunistic pathogen *P. aeruginosa* strain PA14, a clinical isolate capable of rapidly killing *C. elegans* at 25°C

[1]Department of Molecular Genetics and Microbiology, Duke University Medical Center, Durham, NC 27710, USA. [2]Howard Hughes Medical Institute and Laboratory of Neural Circuits and Behavior, Rockefeller University, New York, NY 10021, USA.

*To whom correspondence should be addressed. E-mail: a.aballay@duke.edu

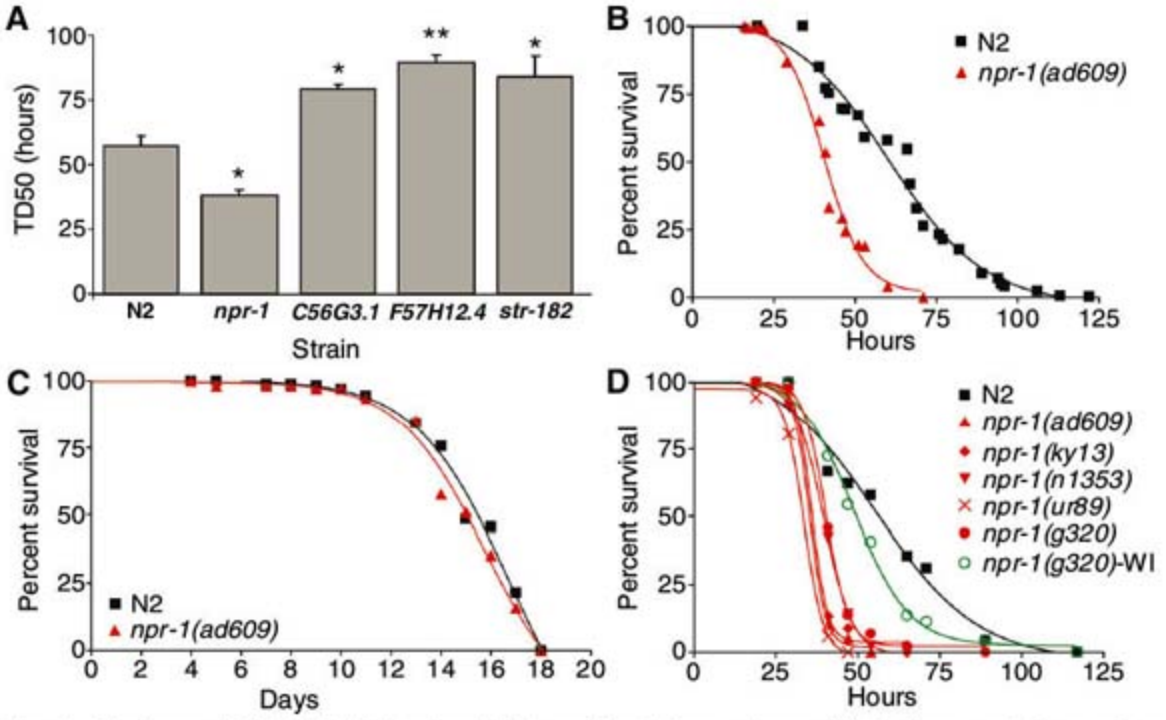

Fig. 1. *C. elegans* GPCR NPR-1 is involved in immunity to *P. aeruginosa*. (**A**) *C. elegans* strains carrying mutations in GPCRs were screened for altered survival on *P. aeruginosa*. *C56G3.1(ok1439)* (P = 0.0347), *F57H12.4(ok1504)* (P = 0.0071), and *str-182(ok1419)* (P = 0.0342) had enhanced resistance to *P. aeruginosa*, and *npr-1(ad609)* (P = 0.0246) had enhanced susceptibility to *P. aeruginosa*, relative to the wild type (N2). Shown is the time required for 50% of the nematodes to die (TD_{50}) as mean ± SEM corresponding to at least three independent experiments, each of which used at least 40 adult nematodes per strain. (**B**) Wild-type N2 and *npr-1(ad609)* (P = 0.0001) nematodes were exposed to *P. aeruginosa* and scored for survival over time. The graph represents combined results of four independent experiments ($n \geq 40$ adult nematodes per strain). (**C**) Wild-type N2 and *npr-1(ad609)* (P = 0.1411) nematodes were exposed to heat-killed *P. aeruginosa* and scored for survival over time. The graph represents the combined results of two independent experiments (n = 100 adult nematodes per strain). (**D**) Wild-type N2, *npr-1(ad609)* (P = 0.0001), *npr-1(ky13)* (P = 0.0001), *npr-1(n1353)* (P = 0.0001), *npr-1(ur89)* (P = 0.0001), *npr-1(g320)* (P = 0.0001), and the wild isolate *npr-1(g320)*-WI (P = 0.0922) were exposed to *P. aeruginosa* and scored for survival over time. Shown is a representative assay of at least three independent experiments (n = 48 adult nematodes per strain).

(*29*, *30*) (table S1). Of the 40 mutants studied, three mutants exhibited an enhanced resistance to *P. aeruginosa* and only one mutant exhibited an enhanced susceptibility to *P. aeruginosa* (Fig. 1, A and B). The strain exhibiting an enhanced susceptibility to *P. aeruginosa*–mediated killing carries a loss-of-function mutation in *npr-1*, which encodes a GPCR related to mammalian neuropeptide Y receptors (*31*).

To determine whether the enhanced susceptibility to *P. aeruginosa* exhibited by *npr-1(ad609)* animals (Fig. 1A) was due to a reduction in life span or a deficient response to potentially pathogenic bacteria, we fed *npr-1(ad609)* nematodes with heat-killed *P. aeruginosa* on plates supplemented with ampicillin. No difference in survival was seen between *npr-1(ad609)* and wild-type nematodes under these conditions, which suggests that the *npr-1* mutation affects the immune response to living pathogenic bacteria without altering the basic life span of the animals (Fig. 1C and fig. S1).

We confirmed that NPR-1 is required for *C. elegans* defense against *P. aeruginosa* by exposing five additional *npr-1* mutants to the pathogen and comparing their survival with that of wild-type animals (Fig. 1D). Strains carrying loss-of-function alleles *npr-1(ky13)*, *npr-1(n1353)*, or *npr-1(ur89)* or the reduced-function allele *npr-1(g320)* were more susceptible to *P. aeruginosa* than were the wild type, confirming that NPR-1 is required for the defense response to this pathogen. Although the German wild isolate RC301, which contains the *npr-1(g320)* allele (*31*), is not particularly susceptible to *P. aeruginosa* as compared with the

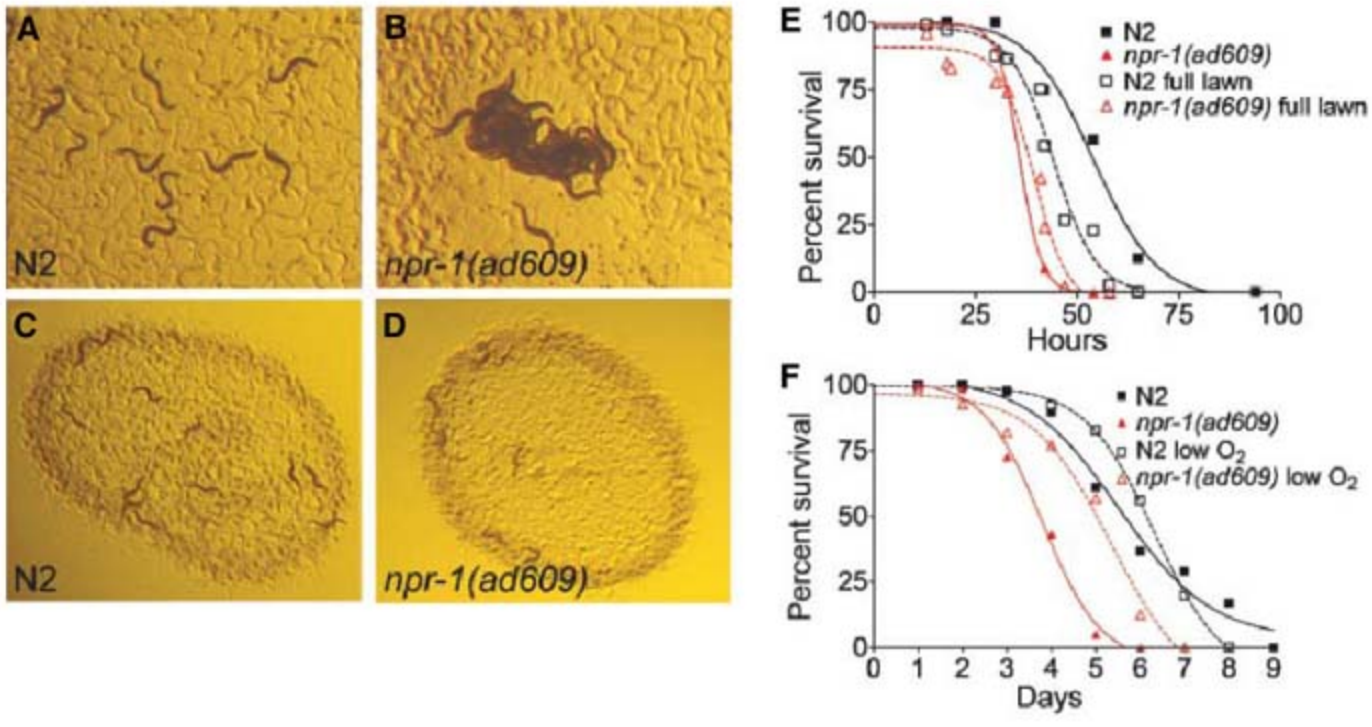

Fig. 2. Hyperoxia avoidance of NPR-1–deficient animals increases susceptibility to *P. aeruginosa*. (**A**) *C. elegans* wild-type N2 animals and (**B**) *npr-1(ad609)* mutants were propagated at 20°C as hermaphrodites on modified nematode growth agar plates seeded with *E. coli* strain OP50 and then visualized using a MZ FLIII stereomicroscope (Leica, Bannockburn, Illinois). The characteristic aggregate of *npr-1(ad609)* nematodes shown here is at the edge of the bacterial lawn. (**C**) Wild-type N2 and (**D**) *npr- 1(ad609)* nematodes (n = 12 each) were exposed to *P. aeruginosa* for 24 hours under standard killing assay conditions and visualized using a MZ FLIII stereomicroscope. Under these conditions, *npr-1(ad609)* nematodes do not form characteristic aggregates of the strain. (**E**) Wild-type N2 and *npr-1(ad609)* nematodes were exposed to either a full lawn or a center lawn of *P. aeruginosa* on a 3.5-cm-diameter plate and scored for survival over time. Under both conditions, *npr-1(ad609)* animals were more susceptible to *P. aeruginosa*–mediated killing (P = 0.0001). Wild-type animals on full lawns were more susceptible to *P. aeruginosa*–mediated killing than animals on center lawns (P = 0.0001); *npr-1(ad609)* animals were equally susceptible (P = 0.07). The graph represents combined results of three independent experiments ($n \geq 40$ adult nematodes per strain). (**F**) Wild-type N2 and *npr-1(ad609)* nematodes exposed to *P. aeruginosa* in either 21% or 8% oxygen at room temperature (~20° to 23°C) and scored for survival over time. Under both conditions, *npr-1(ad609)* animals were more susceptible to *P. aeruginosa*–mediated killing (P = 0.0001). *npr-1(ad609)* animals in 21% oxygen were more susceptible to *P. aeruginosa*–mediated killing than were animals in 8% oxygen (P = 0.0001); wild-type animals were equally susceptible (P = 0.95). The graph represents combined results of two independent experiments (n = 40 adult nematodes per strain).

wild type, the *npr-1(g320)* allele confers susceptibility to *P. aeruginosa* in an N2 background (Fig. 1D). These results suggest that the German isolate may have evolved a mechanism to compensate for the increased susceptibility to pathogens because of its reduced NPR-1 activity.

To determine whether the immune deficiency due to mutation in the *npr-1* gene is specific for *P. aeruginosa* infection, we exposed *npr-1(ad609)* nematodes to *Salmonella enterica* and *Enterococcus faecalis*, two human pathogens known to kill *C. elegans* (*32*–*34*). As shown in fig. S3, A and B, *npr-1(ad609)* nematodes exhibited an enhanced susceptibility to these pathogens, suggesting that NPR-1 is required for immune responses to pathogens in general.

NPR-1 is involved in a neural circuit that integrates behavioral responses to environmental oxygen, food, and other animals. In nature, NPR-1 is found in two allelic forms that differ in a single amino acid at position 215, NPR-1(215V) and NPR-1(215F) (*31*). The NPR1(215V) allele, which is found in the standard laboratory strain, has high activity, whereas the NPR-1(215F) allele has low activity (*35*, *36*). Wild-type *npr-1(215V)* animals avoid oxygen levels above 10% when food is absent, but fail to avoid high oxygen in the presence of *Escherichia coli* bacteria, the food provided to *C. elegans* in the laboratory. In contrast, *npr-1(215F)* and *npr-1* animals carrying loss-of-function (*lf*) alleles have strong hyperoxia avoidance in the absence or presence of *E. coli* (*37*). As a result, *npr-1(215F)* and *npr-1(lf)* show a preference for the thickest part of a bacterial lawn, the region in which oxygen levels are the lowest (*35*). In addition, because nematode aggregation into feeding groups decreases local oxygen concentrations, *npr-1(215F)* and *npr-1(lf)* form aggregates of nematodes when the animals are grown at densities high enough to allow this behavioral response (*37*).

One potential explanation for the reduced life span of *npr-1(lf)* mutants grown on bacterial pathogens is that aggregation increases nematode susceptibility to pathogen infection. However, the animal density in the assays where the susceptibility to pathogens is tested was not sufficient to elicit aggregation, making this possibility unlikely (Fig. 2D). Even though *npr-1(ad609)* animals did not aggregate, they still exhibited a preference for the thickest part of the lawn, where oxygen concentrations are lower (Fig. 2, C and D). In addition, long-term exposure to *P. aeruginosa* caused wild-type animals to leave the bacterial lawn, a potentially protective behavioral response, but leaving was not observed in *npr-1(ad609)* animals. Thus, we examined whether the behavior of *npr-1(ad609)* animals could affect susceptibility to pathogens. The number of bacterial cells in *npr-1(ad609)* animals was not found to be greater than that in wild-type animals (fig. S2) at early stages of the infection, suggesting that the increased susceptibility to pathogens of *npr-1(ad609)* animals is not caused by a higher dose of bacteria. In addition, we grew animals on agar plates that were completely covered in *P. aeruginosa*, a condition that eliminates both the lawn border (favored by *npr-1* animals) and the ability to leave the lawn (favored by wild-type animals). As shown in Fig. 2E, wild-type animals grown on plates completely covered by *P. aeruginosa* died at a higher rate than did animals grown on plates containing a small lawn of *P. aeruginosa* in the center of the plate. *npr-1(ad609)* animals were equally susceptible to *P. aeruginosa* when grown on full or center lawns. Together, these results indicate that the lawn-leaving behavior of wild-type animals contributes to their increased survival. However, *npr-1(ad609)* animals still exhibited enhanced susceptibility to *P. aeruginosa* relative to the wild type when the infections were performed in plates containing full lawns (Fig. 2E). These results indicate that lawn avoidance is part of the *C. elegans* defense response to *P. aeruginosa* but cannot account for all of the differences between wild-type and *npr-1(ad609)* animals.

To determine whether other elements of the oxygen response contribute to the enhanced susceptibility of *npr-1(ad609)* nematodes, we compared animals grown in 21% oxygen with those grown in 8% oxygen, a favorable oxygen environment that suppresses most behavioral phenotypes of *npr-1* mutants. Under 8% oxygen, *npr-1(ad609)* animals do not exhibit a preference for the bacterial border and are capable of leaving the *P. aeruginosa* lawn. As shown in Fig. 2F, *npr-1(ad609)* animals were more resistant to

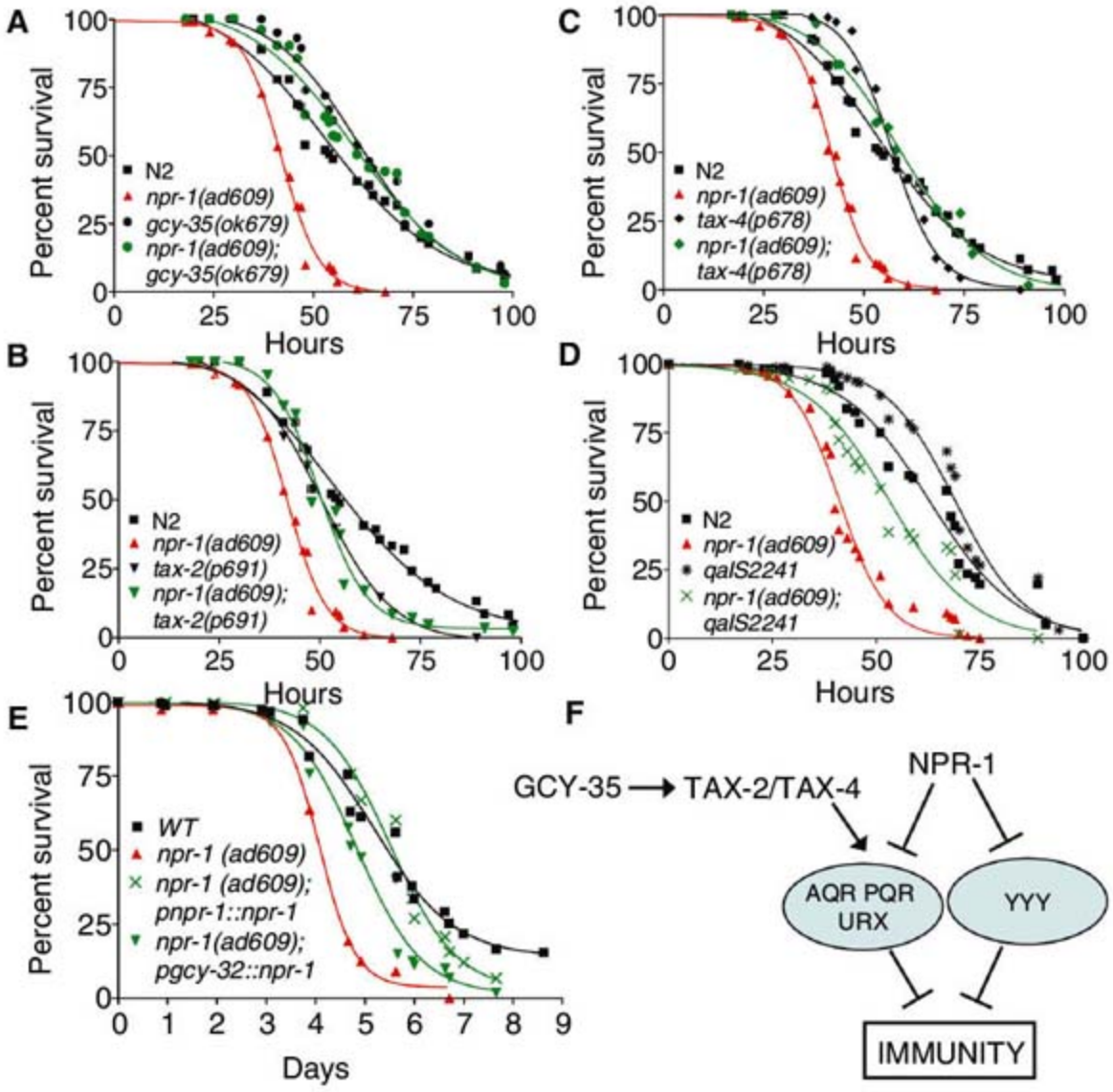

Fig. 3. The NPR-1 neural circuit regulates innate immunity. (**A**) Wild-type N2, *npr-1(ad609)* ($P = 0.0001$), *gcy-35(ok769)* ($P = 0.0125$), and *npr-1(ad609);gcy-35(ok769)* ($P = 0.0639$) were exposed to *P. aeruginosa*. (**B**) Wild-type N2, *npr-1(ad609)* ($P = 0.0001$), *tax-2(p691)* ($P = 0.0930$), and *npr-1(ad609);tax-2(p691)* ($P = 0.0031$) were exposed to *P. aeruginosa*. (**C**) Wild-type N2, *npr-1(ad609)* ($P = 0.0001$), *tax-4(p678)* ($P = 0.1673$), and *npr-1(ad609);tax-4(p678)* ($P = 0.3611$) were exposed to *P. aeruginosa*. (**D**) Wild-type N2, *npr-1(ad609)* ($P = 0.0001$), *qaIS2241* ($P = 0.0042$), a strain that lacks AQR, PQR, and URX neurons, and *npr-1(ad609);qaIs2241* ($P = 0.0001$) were exposed to *P. aeruginosa*. The graphs represent combined results of at least three independent experiments ($n \geq 40$ adult nematodes per strain). (**E**) Wild-type N2, *npr-1(ad609)* ($P = 0.0001$), *npr-1(ad609);pgcy-32::npr-1* ($P = 0.0001$), and *npr-1(ad609);pnpr-1::npr-1* ($P = 0.1939$) were exposed to *P. aeruginosa*. The graphs represent combined results of at least two independent experiments ($n \geq 100$ adult nematodes per strain). Killing assays were performed at 17°C, because low temperatures are known to increase the resolution of killing assays involving *P. aeruginosa*. (**F**) Model of the neural control of innate immunity in *C. elegans*. NPR-1 inhibits the activity of AQR, PQR, URX, and additional neuron(s) designated YYY that suppress innate immunity, whereas GCY-35, TAX-2, and TAX-4 are required for the activation of AQR, PQR, and URX neurons.

P. aeruginosa–mediated killing in 8% oxygen than 21% oxygen, but were still more susceptible than were wild-type animals in 8% oxygen. These results indicate that animals deficient in NPR-1 activity are more susceptible to *P. aeruginosa* because of two factors: decreased pathogen avoidance and decreased innate immune responses.

The increased susceptibility of *npr-1(ad609)* to *S. enterica* (fig. S3A), a pathogen that does not elicit an avoidance behavior (*38*), is consistent with a role of NPR-1 in the regulation of immune responses that are independent of pathogen avoidance. Because a small amount of *S. enterica* that passes through the pharyngeal grinder proliferates and colonizes the intestine in a process that is independent of the dose (*32*), and the pumping rates of *npr-1(ad609)* animals are comparable with those of the wild type (fig. S4), the results further support the function of NPR-1 in the regulation of immune responses.

Genetic studies have identified a chemosensory circuit that coordinates oxygen preference and aggregation in *npr-1* mutants (*35*, *37*, *39*–*42*). Aggregation and bordering of *npr-1(ad609)* nematodes depend on functional *gcy-35*, *tax-2*, or *tax-4* genes (*31*, *40*, *43*). GCY-35 is a soluble guanylyl cyclase (sGC) that binds directly to molecular oxygen, and TAX-2 and TAX-4 are two subunits of a guanosine 3′,5′-monophosphate–gated ion channel (*31*, *40*, *43*). Through the activity of GCY-35 and other guanylate cyclases and the subsequent activation of TAX-2/TAX-4, the AQR, PQR, and URX sensory neurons drive avoidance of high oxygen; these neurons are thought to be hyperactive in *npr-1* mutants (*40*). To determine whether this part of the NPR-1 neural circuit regulates innate immune response, we studied the pathogen susceptibility of *npr-1(ad609)* animals carrying loss-of-function mutations in *gcy-35*,

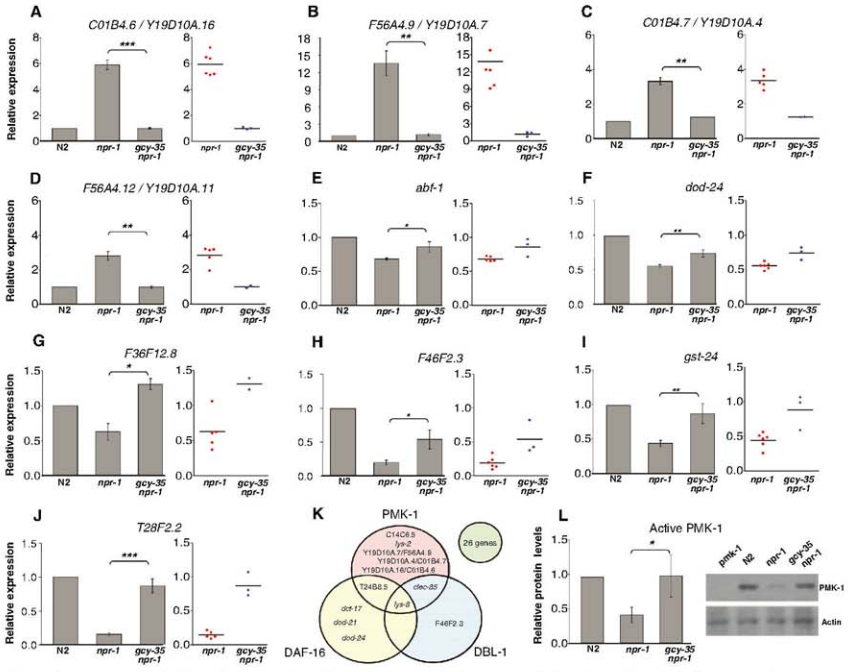

Fig. 4. The NPR-1 neural circuit regulates expression of innate immune genes. (**A** to **J**) QPCR analysis of *C01B4.6/Y19D10A.16*, *F56A4.9/Y19D10A.7*, *C01B4.7/Y19D10A.4*, *F56A4.12/Y19D10A.11*, *abf-1*, *dod-24*, *F36F12.8*, *F46F2.3*, *gst-24*, and *T28F2.2* expression in *npr-1(ad609)* and *npr-1(ad609);gcy-35(ok769)* nematodes relative to wild-type nematodes exposed to *P. aeruginosa*. Data were analyzed by normalization to pan-actin (*act-1,-3,-4*) and relative quantification using the comparative-cycle threshold method. Student's exact *t* test indicates that differences among the groups are significantly different; bar graphs correspond to mean ± SEM. Point graphs correspond to gene quantification in independent isolations of *npr-1(ad609)* ($n = 6$ independent experiments) and *npr-1(ad609);gcy-35(ok769)* ($n = 3$ independent experiments). (**K**) The Venn diagram lists the genes identified by microarray analysis to be regulated by both NPR-1 and one or more known innate immune pathways in *C. elegans*. Genes that lie within two or three circles are regulated by multiple innate immune pathways in addition to NPR-1. Twenty-six genes have not been previously connected to any of the innate immune pathways and are depicted in the solitary circle. (**L**) Immunological detection of active PMK-1. Active PMK-1 was detected in wild-type N2, *npr-1(ad609)*, and *npr-1(ad609);gcy-35(ok769)*. Animals were grown at 20°C until 1-day-old adult and whole-worm lysates were used to detect active PMK-1 with Western blotting using an antibody to human p38 (Promega). Actin was detected using a polyclonal antibody (Sigma). Quantity One analysis software (BioRad) was used to scan and analyze the Western blot.

tax-2, or *tax-4*. As shown in Fig. 3, the enhanced susceptibility to *P. aeruginosa* of *npr-1(ad609)* animals was rescued by mutations in *gcy-35*, *tax-2*, or *tax-4*. Similar results were obtained when the infections were performed in plates containing full lawns of *P. aeruginosa* (fig. S5).

NPR-1 is expressed in at least 20 different neurons, including the *gcy-35*–expressing sensory neurons AQR, PQR, and URX (*35*). To confirm that at least AQR, PQR, and URX neurons are part of a neural network that inhibits innate immunity, we studied the susceptibility to *P. aeruginosa* of a strain in which these neurons were genetically ablated by expressing the cell-death activator gene *egl-1* under the control of the *gcy-36* promoter (*42*). The strain lacking AQR, PQR, and URX neurons exhibited a significantly increased survival on *P. aeruginosa* (Fig. 3D), indicating that AQR, PQR, and URX neurons suppress innate immunity. In addition, lack of AQR, PQR, and URX neurons partially rescued the enhanced susceptibility to *P. aeruginosa* of *npr-1(ad609)* animals (Fig. 3D). Expression of *npr-1* under the control of the *gcy-32* promoter, which drives the expression of *npr-1* to the AQR, PQR, and URX neurons, also rescued the enhanced susceptibility to *P. aeruginosa* of *npr-1(ad609)* animals (Fig. 3E), providing additional evidence of the role of these neurons in the regulation of innate immunity. Consistent with the idea that additional NPR-1–expressing neurons regulate innate immunity (Fig. 3F), *npr-1* expression under the regulation of its own promoter fully rescued the enhanced susceptibility to *P. aeruginosa* phenotype of *npr-1(ad609)* animals (Fig. 3E). Taken together, these results indicate that genes and cells involved in the NPR-1 neural circuit modulate innate immune responses.

As in mammals, peristalsis, low pH, and antimicrobial substances prevent microbial colonization of the *C. elegans* intestine. In addition, accumulating evidence indicates that different genetic pathways regulate the expression of *C. elegans* genes that are markers of immune response (*14*–*19*). To provide insight into the immune function of the NPR-1 neural circuit, we used gene expression microarrays to find clusters of genes up-regulated or down-regulated in *npr-1(ad609)* mutants relative to wild-type animals grown on live *P. aeruginosa* (tables S2 and S3). There is a substantial enrichment in NPR-1–regulated genes that have at least one of three features: they are up-regulated by *P. aeruginosa* infection in wild-type animals, expressed in the intestine, and/or have already been linked to the *C. elegans* p38 mitogen-activated protein kinase PMK-1, which plays a crucial role in innate immunity (*17*, *44*–*47*) (table S4). Further analysis revealed that five of the genes most highly down-regulated by NPR-1 are found in a cluster on chromosome V that appears to have been duplicated further downstream on that chromosome (table S3). Of these five genes, three are also known to be down-regulated by the *C. elegans* PMK-1/p38 pathway. Overall, most of the genes regulated by pathways linked to innate immunity correspond to PMK-1–regulated genes (Fig. 4K). In addition, these genes are similarly misregulated in animals deficient in NPR-1 or PMK-1 function (tables S2 and S3). Because *pmk-1* is not transcriptionally regulated by NPR-1 (tables S2 and S3), we studied whether NPR-1 regulates PMK-1 at the post-transcriptional level. As shown in Fig. 4L, *npr-1 (ad609)* nematodes exhibited lower levels of active PMK-1 than did wild-type nematodes, suggesting that the NPR-1 neural circuit modulates the activation of PMK-1. Inhibition of *pmk-1* gene expression by RNA interference in *npr-1(ad609)* nematodes resulted in increased susceptibility (fig. S6), indicating that although the NPR-1–mediated immune pathway has overlapping targets with the PMK-1–mediated immune pathway, NPR-1 regulates both PMK-1–dependent and PMK-1–independent immune responses.

To obtain insight into the mechanism by which *gcy-35* mutation rescues the enhanced susceptibility to *P. aeruginosa* of *npr-1(ad609)* animals (Fig. 3A), we used quantitative real-time polymerase chain reaction (QPCR) to compare the expression levels of selected genes of *npr-1(ad609)* with that of *npr-1(ad609);gcy-35(ok769)* animals. As shown in Fig. 4, a *gcy-35* mutation in *npr-1(ad609)* animals rescues the altered expression of 10 out of 19 genes tested that are markers of the *C. elegans* immune response. These results indicate that the NPR-1 neural circuit modulates the expression of immune-related genes, many of which are known to be expressed in tissues that are in direct contact with pathogens during infection.

Our results provide evidence that specific genes and neurons in the nervous system are responsible for effective innate immune responses that are independent of behavioral phenotypes and may take place in tissues that are in direct contact with pathogens. It has recently been postulated that cell-nonautonomous signals from different neurons may act on nonneural tissues to regulate processes such as fat storage (*48*) and longevity (*8*). *C. elegans* neurons can regulate physiological processes through conserved neuroendocrine signals, including insulin-related peptides, TGF-β peptides, and neuropeptides. The URX, AQR, and PQR neurons that are part of the NPR-1 neural circuit that regulates innate immunity are exposed to the pseudocoelomic body fluid, which could communicate neuroendocrine signals to nonneural tissues involved in defense responses. The identification and characterization of the specific neuroendocrine signals that regulate innate immune responses in *C. elegans* should yield several insights into the mechanisms used by the nervous system to regulate similar processes across metazoans.

References and Notes

1. E. M. Sternberg, *Nat. Rev. Immunol.* **6**, 318 (2006).
2. J. Andersson, *J. Intern. Med.* **257**, 122 (2005).
3. K. J. Tracey, *Nature* **420**, 853 (2002).
4. D. B. Sattelle, S. D. Buckingham, *Invert. Neurosci.* **6**, 1 (2006).
5. C. I. Bargmann, H. R. Horvitz, *Science* **251**, 1243 (1991).
6. W. S. Schackwitz, T. Inoue, J. H. Thomas, *Neuron* **17**, 719 (1996).
7. J. Alcedo, C. Kenyon, *Neuron* **41**, 45 (2004).
8. N. A. Bishop, L. Guarente, *Nature* **447**, 545 (2007).
9. C. Li, L. S. Nelson, K. Kim, A. Nathoo, A. C. Hart, *Ann. N.Y. Acad. Sci.* **897**, 239 (1999).
10. W. Li, S. G. Kennedy, G. Ruvkun, *Genes Dev.* **17**, 844 (2003).
11. A. N. Nathoo, R. A. Moeller, B. A. Westlund, A. C. Hart, *Proc. Natl. Acad. Sci. U.S.A.* **98**, 14000 (2001).
12. S. B. Pierce *et al.*, *Genes Dev.* **15**, 672 (2001).
13. P. Ren *et al.*, *Science* **274**, 1389 (1996).
14. G. V. Mallo *et al.*, *Curr. Biol.* **12**, 1209 (2002).
15. S. Kerry, M. Tekippe, N. C. Gaddis, A. Aballay, *PLoS One* **1**, e77 (2006).
16. M. Shapira *et al.*, *Proc. Natl. Acad. Sci. U.S.A.* **103**, 14086 (2006).
17. E. R. Troemel *et al.*, *PLoS Genet.* **2**, e183 (2006).
18. D. Wong, D. Bazopoulou, N. Pujol, N. Tavernarakis, J. J. Ewbank, *Genome Biol.* **8**, R194 (2007).
19. D. O'Rourke, D. Baban, M. Demidova, R. Mott, J. Hodgkin, *Genome Res.* **16**, 1005 (2006).
20. H. Schulenburg, S. Muller, *Parasitology* **128**, 433 (2004).
21. M. Hasshoff, C. Bohnisch, D. Tonn, B. Hasert, H. Schulenburg, *FASEB J.* **21**, 1801 (2007).
22. K. Yook, J. Hodgkin, *Genetics* **175**, 681 (2007).
23. M. Sicard, S. Hering, R. Schulte, S. Gaudriault, H. Schulenburg, *Environ. Microbiol.* **9**, 12 (2007).
24. Y. Zhang, H. Lu, C. I. Bargmann, *Nature* **438**, 179 (2005).
25. E. Beale, G. Li, M. W. Tan, K. P. Rumbaugh, *Appl. Environ. Microbiol.* **72**, 5135 (2006).
26. T. R. Laws, H. S. Atkins, T. P. Atkins, R. W. Titball, *Microb. Pathog.* **40**, 293 (2006).
27. N. Pujol *et al.*, *Curr. Biol.* **11**, 809 (2001).
28. E. Pradel *et al.*, *Proc. Natl. Acad. Sci. U.S.A.* **104**, 2295 (2007).
29. M. W. Tan, S. Mahajan-Miklos, F. M. Ausubel, *Proc. Natl. Acad. Sci. U.S.A.* **96**, 715 (1999).
30. S. Mahajan-Miklos, M. W. Tan, L. G. Rahme, F. M. Ausubel, *Cell* **96**, 47 (1999).
31. M. de Bono, C. I. Bargmann, *Cell* **94**, 679 (1998).
32. A. Aballay, P. Yorgey, F. M. Ausubel, *Curr. Biol.* **10**, 1539 (2000).
33. A. Labrousse, S. Chauvet, C. Couillault, C. L. Kurz, J. J. Ewbank, *Curr. Biol.* **10**, 1543 (2000).
34. D. A. Garsin *et al.*, *Proc. Natl. Acad. Sci. U.S.A.* **98**, 10892 (2001).
35. J. C. Coates, M. de Bono, *Nature* **419**, 925 (2002).
36. C. Rogers *et al.*, *Nat. Neurosci.* **6**, 1178 (2003).
37. J. M. Gray *et al.*, *Nature* **430**, 317 (2004).
38. J. L. Tenor, A. Aballay, *EMBO Rep.* **9**, 103 (2008).
39. M. de Bono, D. M. Tobin, M. W. Davis, L. Avery, C. I. Bargmann, *Nature* **419**, 899 (2002).
40. B. H. Cheung, M. Cohen, C. Rogers, O. Albayram, M. de Bono, *Curr. Biol.* **15**, 905 (2005).
41. C. Rogers, A. Persson, B. Cheung, M. de Bono, *Curr. Biol.* **16**, 649 (2006).
42. A. J. Chang, N. Chronis, D. S. Karow, M. A. Marletta, C. I. Bargmann, *PLoS Biol.* **4**, e274 (2006).
43. B. H. Cheung, F. Arellano-Carbajal, I. Rybicki, M. de Bono, *Curr. Biol.* **14**, 1105 (2004).
44. D. H. Kim *et al.*, *Science* **297**, 623 (2002).
45. A. Aballay, E. Drenkard, L. R. Hilbun, F. M. Ausubel, *Curr. Biol.* **13**, 47 (2003).
46. D. H. Kim *et al.*, *Proc. Natl. Acad. Sci. U.S.A.* **101**, 10990 (2004).
47. D. L. Huffman *et al.*, *Proc. Natl. Acad. Sci. U.S.A.* **101**, 10995 (2004).
48. H. Y. Mak, L. S. Nelson, M. Basson, C. D. Johnson, G. Ruvkun, *Nat. Genet.* **38**, 363 (2006).

49. We thank the *Caenorhabditis* Genetics Center (University of Minnesota) for strains used in this study. A.A. is funded by the Whitehead Scholars Program, the NIH Southeast Regional Center of Excellence for Emerging Infections and Biodefense (grant U54 AI057157), and NIH grant GM070977. C.I.B. is an Investigator of the Howard Hughes Medical Institute.

Supporting Online Material

www.sciencemag.org/cgi/content/full/1163673/DC1
Materials and Methods
Figs. S1 to S6
Tables S1 to S4
References

24 April 2008; accepted 11 September 2008
Published online 18 September 2008;
10.1126/science.1163673
Include this information when citing this paper.

New Products Focus: Cell/Tissue Culture

Air Sterilization and Decontamination System

The Air Manager system is an air sterilization and decontamination system that destroys particulates, resulting in better air control and protection for sensitive laboratory applications. Rather than relying on filtering out airborne pathogens and particulates, the system destroys them through a patented sterilization technique based on close-coupled field technology (CCFT), in which an electrically generated plasma field sterilizes the passing atmosphere. Any particulates in the atmosphere, whether they are viable pathogens, pyrogenic material, chemical fumes, odors, viruses, or other offending materials, are "zapped" by the plasma field as a result of their own electrical charges. This "zapping" breaks down the chemical bonds of any materials and reduces the offending particulates, in most cases down to their elemental constituents. Heavier elemental constituents, which can be harmful, are generated by the breakdown of carbon dioxide in the atmosphere and are removed by the combination of the CCFT and the charged exhaust filter bed.

Scientific Laboratory Supplies
For information +44-(0)-1159-821-111
www.scientific-labs.com

Drug Interaction Study System

Cellport Technologies is a sophisticated assay system that provides the preclinical in vitro data on drug transporter–mediated drug-drug interactions needed when submitting a new drug application. The assay makes use of a series of novel cell lines in which transporter expression has been manipulated in the bidirectional assay format; the assay system clearly determines which efflux transporter(s) a test compound interacts with. The information can be used to determine whether or not a new drug is safe to use with other drugs. The system makes use of Caco-2, a human cell line that has been studied extensively. The cell lines were designed using RNA interference to knock down specific genes in a stable Caco-2 cell line, one at a time.

Absorption Systems
For information 610-280-7300
www.absorption.com

Cell Imaging System

Cellavista is an image-based system that can be used for rapid visualization of a broad range of cellular assays, while simultaneously performing image analysis. Combining brightfield and fluorescence optic capabilities, Cellavista enables users to acquire and analyze images for a wide array of cell-based assays, including single-cell cloning, cell confluence, suspension cell count, fluorescence-activated cell sorter seeding efficiency control, cell nuclei count and characterization, transfection efficiency, microplate quality control, viral plaque assays, fluorescent protein expression, and apoptosis assays. In as little as five minutes, Cellavista can scan a 96-well microplate with simultaneous image acquisition and analysis. It features specially designed optics combined with fast auto-focus. Assay-specific analysis algorithms have been developed to identify cell clusters or colonies and are applicable to stem cell research.

Innovatis
For information 800-286-1631
wwww.innovatis.com/cellavista

Human Epidermal Melanocytes

Primary Clonetics Adult Normal Human Epdidermal Melanocytes are highly characterized cells for use in diverse applications in dermal research, including malignant melanoma, dermal disorders, toxicology, pigmentation, and cosmetic studies. Clonetics Adult Melanocytes are available as cryopreserved amps, proliferating plates, or proliferating flasks. They are optimized for use with MGM-4 Melanocyte Growth Media BulletKit to deliver outstanding growth and survival in culture.

Lonza Group
For information 800-638-8174
www.lonza.com

Neural Stem Cell Lines

The MilliTrace primary rodent neural stem cell lines express green fluorescent protein (GFP) constitutively. GFP expression in these stem cells is the best way for researchers to monitor the behavior of specific populations of cells as they proliferate, migrate, and differentiate into various cell lineages, depending on the developmental context. The Millitrace cell lines are the first commercially available, GFP-expressing, karyotypically normal stem cell lines, and are supplied with optimized expansion medium. Validated for high levels of GFP expression, stem cell marker expression, and multipotency, MilliTrace GFP Reporter Neural Stem Cell Lines can improve reproducibility and data quality for a variety of applications.

Millipore
For information 800-548-7853
www.millipore.com

Stem Cell Workstation

The SCI-tive (stem cell investigations total in vitro environment) workstation is designed for both embryonic and adult stem cell isolation, optimization, differentiation, and incubation within a totally enclosed controlled culture environment. Working under controlled conditions is essential to ensure the cell differentiation process does not result in inappropriate cell types. Researchers can monitor the internal environment of the workstation and control temperature, humidity, and gas concentrations. The workstation features a small footprint, and reduces the need for other gas-controlled incubators and class 2 biological safety cabinets. All processes can be carried out within the workstation, with integrated microscopy and digital software making whole process monitoring, tracking, and calibration possible without disturbing the controlled atmosphere.

Ruskinn Technology
For information +44-(0)-1656-868540
www.ruskinn.com

Electronically submit your new product description or product literature information! Go to **www.sciencemag.org/products/newproducts.dtl** for more information.

Newly offered instrumentation, apparatus, and laboratory materials of interest to researchers in all disciplines in academic, industrial, and governmental organizations are featured in this space. Emphasis is given to purpose, chief characteristics, and availabilty of products and materials. Endorsement by *Science* or AAAS of any products or materials mentioned is not implied. Additional information may be obtained from the manufacturer or supplier.